Metal-Organic Frameworks for Chemical Reactions

From Organic Transformations to Energy Applications

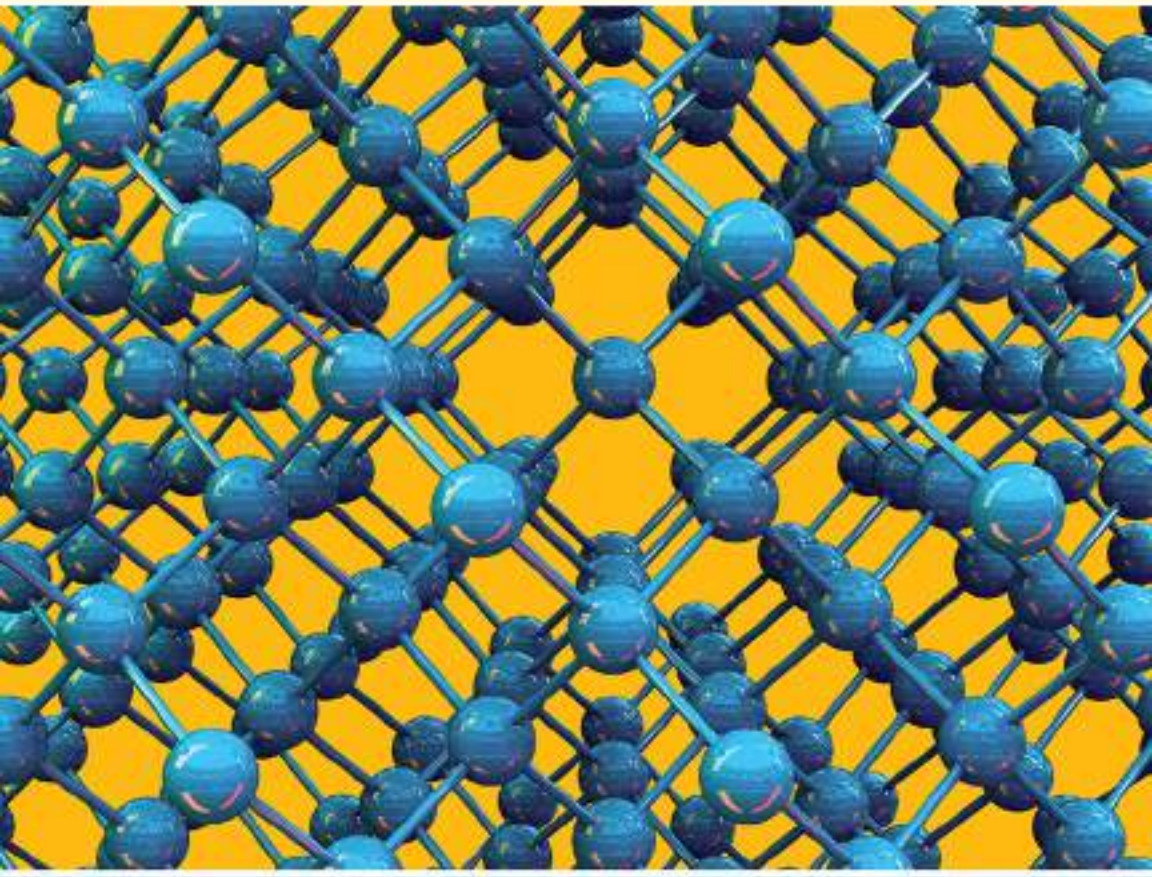

Edited by **Anish Khan, Francis Verpoort, Abdullah M. Asiri, Md Enamul Hoque, Anwar L. Bilgrami, Mohammad Azam, and K. Chandra Babu Naidu**

ELSEVIER

Metal-Organic Frameworks for Chemical Reactions

From Organic Transformations to Energy Applications

This page intentionally left blank

Metal-Organic Frameworks for Chemical Reactions

From Organic Transformations to Energy Applications

Edited by

Anish Khan
Center of Excellence for Advanced Materials Research, King Abdulaziz University, Jeddah, Saudi Arabia

Francis Verpoort
State Key Laboratory of Advanced Technology for Materials Synthesis and Processing, Wuhan University of Technology, Wuhan, China; Ghent University – Global Campus, Ywonsu-Gu, Incheon, Republic of Korea

Abdullah M. Asiri
Chemistry Department, Faculty of Science, King Abdulaziz University, Jeddah, Saudi Arabia; Center of Excellence for Advanced Materials Research, King Abdulaziz University, Jeddah, Saudi Arabia

Md Enamul Hoque
Department of Biomedical Engineering at the Military Institute of Science and Technology (MIST), Dhaka, Bangladesh

Anwar L. Bilgrami
Department of Entomology, Rutgers University, New Jersey, United States; Deanship of Scientific Research, King Abdulaziz University, Jeddah, Saudi Arabia

Mohammad Azam
Associate Professor of Chemistry, King Saud University, Riyadh, Saudi Arabia

K. Chandra Babu Naidu
GITAM School of Science (GSS), GITAM Deemed-to-Be University, Bangalore, India

ELSEVIER

Elsevier
Radarweg 29, PO Box 211, 1000 AE Amsterdam, Netherlands
The Boulevard, Langford Lane, Kidlington, Oxford OX5 1GB, United Kingdom
50 Hampshire Street, 5th Floor, Cambridge, MA 02139, United States

Notices
Knowledge and best practice in this field are constantly changing. As new research and experience broaden our understanding, changes in research methods, professional practices, or medical treatment may become necessary.

Practitioners and researchers must always rely on their own experience and knowledge in evaluating and using any information, methods, compounds, or experiments described herein. In using such information or methods they should be mindful of their own safety and the safety of others, including parties for whom they have a professional responsibility.

To the fullest extent of the law, neither the Publisher nor the authors, contributors, or editors, assume any liability for any injury and/or damage to persons or property as a matter of products liability, negligence or otherwise, or from any use or operation of any methods, products, instructions, or ideas contained in the material herein.

British Library Cataloguing-in-Publication Data
A catalogue record for this book is available from the British Library

Library of Congress Cataloging-in-Publication Data
A catalog record for this book is available from the Library of Congress

ISBN: 978-0-12-822099-3

Publisher: Susan Dennis
Acquisitions Editor: Emily M. McCloskey
Editorial Project Manager: Lena Sparks
Production Project Manager: Debasish Ghosh
Cover Designer: Victoria Pearson

Typeset by MPS Limited, Chennai, India

Contents

List of contributors

Ramon A. Alvarez-Puebla Department of Physical and Inorganic Chemistry and EMaS, Universitat Rovira I Virgili, Tarragona, Spain; ICREA, Barcelona, Spain

Rakesh Kumar Ameta School of Chemical Sciences, Central University of Gujarat, Gandhinagar, India; Department of Chemistry, Sri M M Patel Institute of Sciences and Research, Kadi Sarva Vishwavidhyalaya, Gandhinagar, Gujarat, India

Sambandam Anandan Department of Chemistry, National Institute of Technology, Trichy, India

Shahid Pervez Ansari Department of Applied Chemistry, Zakir Husain College of Engineering and Technology, Aligarh Muslim University, Aligarh, India

Abdullah M. Asiri Chemistry Department, Faculty of Science, King Abdulaziz University, Jeddah, Saudi Arabia; Center of Excellence for Advanced Materials Research, King Abdulaziz University, Jeddah, Saudi Arabia

D. Prakash Babu School of Applied Sciences, REVA University, Bangalore, India

Prasun Banerjee Department of Physics, GITAM (Deemed to be University), Bangalore, India; Instituto de Fisica, Universidade Federal de Goias, Goiania, Brazil

K. Chandra Babu Naidu Department of Physics, GITAM (Deemed to be University), Bangalore, India

C. Deepa Department of Computer Science and Engineering, KIT-Kalaignarkarunanidhi Institute of Technology, Coimbatore, India

Rajasekaran Elakkiya Materials Electrochemistry Laboratory, Department of Chemistry, SRM Institute of Science and Technology, Kattankulathur, Chennai, India

P C.V.V. Eswara Rao Department of Chemistry, GITAM School of Science, GITAM (Deemed to be University), Bangalore, India

Adolfo Franco, Jr Instituto de Fisica, Universidade Federal de Goias, Goiania, Brazil

Luca Guerrini Department of Physical and Inorganic Chemistry and EMaS, Universitat Rovira I Virgili, Tarragona, Spain

Rachna Gupta School of Chemical Sciences, Central University of Gujarat, Gandhinagar, India; Department of Biotechnology, Visva-Bharati, Santiniketan, Bolpur, India

Lakshmanan Gurusamy Department of Environmental Engineering and Science, Feng Chia University, Taichung, Taiwan

Antonio V. Herrera-Herrera Instituto Universitario de Bio-Orgánica Antonio González, Universidad de La Laguna (ULL), San Cristóbal de La Laguna, España

Ahmad Husain Department of Applied Chemistry, Zakir Husain College of Engineering and Technology, Aligarh Muslim University, Aligarh, India

S. Janardan Department of Chemistry, GITAM School of Science, GITAM (Deemed to be University), Bangalore, India

Anish Khan Chemistry Department, Faculty of Science, King Abdulaziz University, Jeddah, Saudi Arabia; Center of Excellence for Advanced Materials Research, King Abdulaziz University, Jeddah, Saudi Arabia

G. Ranjith Kumar School of Applied Sciences, REVA University, Bangalore, India

N. Suresh Kumar Department of Physics, JNTUA, Anantapuramu, India

N. Kuppuswamy Department of Aeronautical Engineering, KIT-Kalaignarkarunanidhi Institute of Technology, Coimbatore, India

Govindhan Maduraiveeran Materials Electrochemistry Laboratory, Department of Chemistry, SRM Institute of Science and Technology, Kattankulathur, Chennai, India

Parth Malik School of Chemical Sciences, Central University of Gujarat, Gandhinagar, India

H. Manjunatha Department of Chemistry, GITAM School of Science, GITAM (Deemed to be University), Bangalore, India

M. Muthukrishnan Department of Mechanical Engineering, KIT-Kalaignarkarunanidhi Institute of Technology, Coimbatore, India

Srinivasan Natarajan Solid State and Structural Chemistry Unit, Indian Institute of Science, Bangalore, India

Wei Ni Vanadium and Titanium Resource Comprehensive Utilization Key Laboratory of Sichuan Province, Panzhihua University, Panzhihua, P.R. China; Institute for Advanced Study, Chengdu University, Chengdu, P.R. China; Material Corrosion and Protection Key Laboratory of Sichuan Province, Sichuan University of Science and Engineering, Zigong, P.R. China

M. Noorjahaan Department of Chemistry, Palamuru University, Mahbubnagar, India

S. Praveen Department of Mechanical Engineering, KIT-Kalaignarkarunanidhi Institute of Technology, Coimbatore, India

M. Ramesh Department of Mechanical Engineering, KIT-Kalaignarkarunanidhi Institute of Technology, Coimbatore, India

S. Ramesh Department of Physics, GITAM (Deemed to be University), Bangalore, India

Bahram Ramezanzadeh Department of Surface Coatings and Corrosion, Institute for Color Science and Technology, Tehran, Iran

Mohammad Ramezanzadeh Department of Surface Coatings and Corrosion, Institute for Color Science and Technology, Tehran, Iran

L. Vaikunta Rao Department of Chemistry, GITAM School of Science, GITAM (Deemed to be University), Visakhapatnam, India

K. Venkata Ratnam Department of Chemistry, GITAM School of Science, GITAM (Deemed to be University), Bangalore, India

A. Ratnamala Department of Chemistry, GITAM School of Science, GITAM (Deemed to be University), Bangalore, India

G. Deepthi Reddy Department of Chemistry, Palamuru University, Mahbubnagar, India

K. Rama Krishna Reddy School of Applied Sciences, REVA University, Bangalore, India

Miguel Ángel Rodríguez Delgado Departamento de Química, Unidad Departamental de Química Analítica, Facultad de Ciencias, Universidad de La Laguna (ULL), San Cristóbal de La Laguna, España

Ruth Rodríguez-Ramos Departamento de Química, Unidad Departamental de Química Analítica, Facultad de Ciencias, Universidad de La Laguna (ULL), San Cristóbal de La Laguna, España

Álvaro Santana-Mayor Departamento de Química, Unidad Departamental de Química Analítica, Facultad de Ciencias, Universidad de La Laguna (ULL), San Cristóbal de La Laguna, España

Mohd Urooj Shariq Department of Chemistry, Aligarh Muslim University, Aligarh, India

A. Sivarmakrishna Department of Chemistry, School of Advanced Sciences, VIT University, Vellore, India

Bárbara Socas Rodríguez Department of Chemistry, Centre for Analysis and Synthesis, Lund University, Lund, Sweden

K. Srinivas Department of Physics, GITAM (Deemed to be University), Bangalore, India

N. Suresh Kumar Department of Physics, JNTUA, Anantapuramu, India

B. Venkata Shiva Reddy Department of Physics, GITAM (Deemed to be University), Bangalore, India

Jerry J. Wu Department of Environmental Engineering and Science, Feng Chia University, Taichung, Taiwan

Tolga Zorlu Department of Physical and Inorganic Chemistry and EMaS, Universitat Rovira I Virgili, Tarragona, Spain

This page intentionally left blank

Chapter 1

Metal-organic frameworks and their composites

M. Ramesh[1] and C. Deepa[2]
[1]Department of Mechanical Engineering, KIT-Kalaignarkarunanidhi Institute of Technology, Coimbatore, India, [2]Department of Computer Science and Engineering, KIT-Kalaignarkarunanidhi Institute of Technology, Coimbatore, India

1.1 Introduction

Metal-organic frameworks (MOFs), also called as porous polymers, created from inorganic ions with organic connectors, have emerged as a promising class of materials with many peculiar properties, such as high porosity, diverse composition, versatile pore structure, and flexible functionality [1−3]. Such are evolving adsorbent materials composed of metal ions or clusters of metal ions bound by organic linkers [4]. The MOFs attract a lot of interest because of their high crystallinity, porosity, and modularity [5]. The benefits of structural tuning and other physical or chemical properties, obtained by astute selection and variation in the shape of linkers, their scale and arrangement, and pre- and post-synthetic modification, have driven ever-expanding research into the use of MOFs in various fields and applications [6]. Through the advent of metal nanoparticles, metal oxides, graphene, carbon nanotubes (CNTs), quantum dots (QDs), biomolecules, polymers, polyoxometalates, organic chemicals, proteins, silica and polymers, etc., a variety of MOF composites have now been successfully synthesized [7−9]. The MOF composites are constructed of one or more MOF materials shown in Fig. 1.1 [1]. An analysis of Tang and Tanase's synthetic approaches [10] is for the production of MOFs and their composites. They observed that when compared to the performance of pure polymer membranes, MOFs embedded in polymer matrices increased mixture efficiency and permeability.

1.2 Metal-organic framework composites

MOFs themselves are part of the major composite material class. MOF composites are comparatively recent materials, used in diverse applications. It is,

Metal-Organic Frameworks for Chemical Reactions. DOI: https://doi.org/10.1016/B978-0-12-822099-3.00001-0

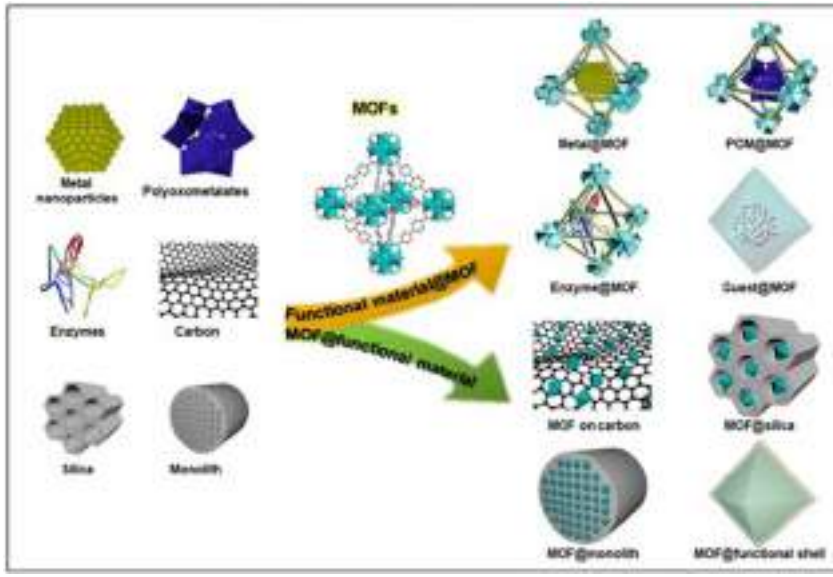

FIGURE 1.1 MOFs and other functional materials incorporated at MOF composites [1]. *MOFs*, Metal-organic frameworks.

however, necessary to find suitable complementary materials and adaptive pathways to form composites based on MOF. Its flexible crystalline architectures and compact units of metal ions and organic ligands are ideal for the further development of composites [11,12]. The composite architecture of MOF materials within the special porous structure offers the great practical ability to construct composite materials based on MOF [13–16]. Over the last decade, MOFs formed through the self-assembly phase of metal cations or metal clusters and smooth organic ligands received significant attention [17,18]. MOF-based composites are provided with high strength and good catalytic activity by integrating the functionalized nanoparticles into MOF structures that process the advantages over single-component MOFs [19].

1.2.1 Processing of metal-organic framework composites

For the preparation of MOF composites, three excellently developed techniques exist, such as ship-in-bottle, bottle-around-ship, and one-pot synthesis [1]. The ship-in-bottle method entails applying metal precursors to an MOF using various methods such as chemical vapor deposition, solvent impregnation, firm grinding, and microwave irradiation, followed by a reduction in metal precursors to form nanoparticles of metal. The bottle-around-ship methodology refers to the assembly around the metal of nanoparticles from MOFs. The trick to acquiring the core–shell structure is to prevent

aggregating metal nanoparticles and self-nucleating MOF shells. Due to reduced production costs, shorter processing times, and easy scaling, the one-pot method, through the direct mixing of the metal precursors and MOF precursors into one pot, has recently attracted much interest. Activated carbon @MIL-101(Cr) nanocomposite was prepared by MIL-101(Cr) in situ synthesis at a conversion rate of about 96%. The precursor MOF was treated with 25 mg activated carbon and autoclaved for 12 hours at 473K. The resulting stock was centrifuged and soaked at 353K for 60 minutes, to eliminate impurities. The powder, obtained through centrifugation, was dissolved in ethanol and heated at 353K for 12 hours. Finally, the synthesized green powder was centrifuged and dried at 373K in a vacuum oven for 12 hours. A schematic representation of the synthesis is shown in Fig. 1.2 [19].

1.2.2 Types of metal-organic framework composites

1.2.2.1 Metal-organic framework–polymer composites

Polymers are exceptional in their range of properties that include thermal, chemical, and softness stability. A synthesis of MOFs and polymers will generate innovative and versatile materials that show joint properties for frame stability and action enhancement [21]. Rowe et al. [22] prepared the gadolinium (Gd) MOF composites based on multi-functional polymer. Poly (*N*-isopropylacrylamide)-*co*-poly(*N*-acryloxysuccinimide)-*co*-poly(fluorescein *O*-methacrylate) copolymers were constructed through reversible additional fragmentation chain transfer (RAFT) polymerization. To bind a therapeutic agent such as methotrexate and a targeting ligand such as *H*-glycine-arginine-glycine-aspartate-serine-NH(2) peptide, succinimide's functionality was used as a scaffold. The use of a trithiocarbonate RAFT agent allowed the reduction of polymer end groups to thiolates and provided a means of copolymer attachment on the surface of Gd MOF particles through vacant orbitals on the Gd (3 +) ions. These versatile, nanoscale scaffolds have been demonstrated to be biocompatible and are capable of killing cancer cells, biomedical imaging, and treating diseases. This revolutionary approach offered a simple but versatile path for the production of polymer nanoparticles the agnostic materials with an unparalleled degree of flexibility in design, theoretically enabling customizable loading capacities and spatial loading of targeting or treatment agents, thereby combining bimodal imaging capabilities via both magnetic resonance and fluorescence microscopy.

1.2.2.2 Metal-organic framework–quantum dot composites

The combination of high surface area, microporosity, and flexible MOF compositions with QDs enables the preparation of composite materials with improved properties for many applications such as photocatalysis, energy storage, and gas storage and sensing [23]. Despite their unusual electronic

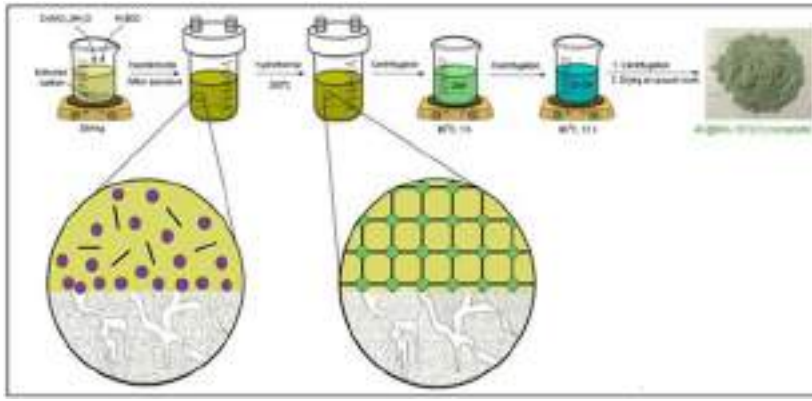

FIGURE 1.2 Synthesis procedure of activated carbon–based MOF composites [20]. *MOF*, Metal-organic framework.

and optical properties depending on dimension, QDs with a size range of 2–10 nm have received considerable attention. The encapsulation of QDs within MOFs will improve their stability and modulate rates of electron–hole part recombination. Different forms of QDs such as nitride-, oxide-, carbon-, and chalcogenide-based compounds have been integrated into MOFs, and the resultant composite materials have enhanced their properties and applications [7].

1.2.2.3 Metal-organic framework–metal nanoparticle composites

Metal nanoparticles have acquired a lot of interest because of their high chemical processes and specificities. Nevertheless, these particles have a high surface-to-volume ratio and high surface energy, and hence tend to collect and ignite. For example, arranging nanoparticles of metal into porous materials such as metal oxides, zeolites, mesoporous silicates, and carbon will effectively limit the accumulation of metal nanoparticles in restricted cavities. As a new class of porous materials [1,24–26], MOFs with large surfaces and porosity are suitable as supports for metal nanoparticles. MIL-100 (Fe) MOF composites and magnetic nanoparticles have also been shown to be quickly and easily absorbent for extracting acid dyes [27,28]. Shustova et al. [29] observed fluorescence in an otherwise nonemissive zinc-MOF sample. These researchers incorporated tetraphenylethylene cores into the MOF, and the resulting structure was observed to obtain fluorescence because of the matrix coordination's induced emission effect.

The semiconducting behavior of strontium MOF (Sr-MOF) has been demonstrated experimentally and by theoretical calculations [30]. Temperature-dependent current–voltage tests found the MOF had an

electrical conductivity value on the order on 106 S cm^{-1}. A change in the temperature at the annealing caused the MOF to exponentially increase its conductivity. Instead of the thermally mediated carriers and variable hopping, the Arrhenius conductivity plot showed Sr-MOF's semiconducting transport actions. For the development of a direct white light-emitting diode for solid-state lighting, an Sr-MOF composite formed with a semiconductive organic ligand (1,4,5,8-naphthalenetetracarboxylic acid hydrate) was documented [31]. The photoluminescence spectra of the above electroluminescent Sr-MOF confirmed the existence of unique emission peaks leading to intermetallic electronic transitions in strontium, transitions between metallic energy states, and metal-to-ligand conversion of charges.

1.2.2.4 Metal-organic framework–graphene oxide composites

The products better suited for MOF composite synthesis are graphene oxide (GO). Owing to its superior properties such as wide surface area, mechanical stability, robust electrical, and optical properties, GO, a functional oxygen-containing graphene with chemical groups, recently attracted resurgent interests [32]. The flexible, freestanding, and three-dimensional cobalt-based MOFs/reduced GO (CoMOF/rGO) composite was prepared with a simple electrochemical deposition of CoMOF on the surface of the rGO electrode [33]. Musyoka et al. [34] prepared a composite using in situ approach using zirconium-based MOF and rGO. This composite was used in storage applications and showed greater hydrogen storage efficiency compared with ZrMOF. Zhang et al. [35] synthesized GO nano-sheets with two-step co-based MOF using an in situ growth and calcination process. This material was used as a medium for electromagnetic absorption and demonstrated electromagnetic dissipation at high efficiency. Fang et al. [36] prepared and constructed uniform, high performance, and flexible nanofiltration membrane MOF composites based on Zr. Two phases were used to build the substratum: (1) doping GO sheets into a polyacrylonitrile (PAN) membrane casting solution and forming 2D–3D binding pores by phase immersion process and (2) immersing of the GO@PAN substratum into a dopamine solution for self-polymerization into macromolecular chains obtaining a highly stable and flexible substratum. Lin et al. [37] showed that the inclusion of rGO on Zr-based MOF increases both adsorptive and photocatalytic efficiency by eliminating acid colors.

1.2.2.5 Metal-organic framework–polyoxometalate composites

Polyoxometalates are a class of anionic metal–oxygen clusters with a wide range of additives, flexible shapes and proportions, solubility, redox potential, and high acidity. Such properties provide great opportunities in a variety of catalytic transformations, particularly in acid and oxidation reactions. However, their implementation is constrained by its low specific area and

low stability. The immobilization of polyoxometalates into MOFs is a promising approach for the stabilization and refining of polyoxometalates to boost their catalytic properties. Because of their compositional stability and structural strength, polyoxometalates can be used as versatile building blocks (nodes or bases, or prototypes inside the cages) for the construction of polyoxometalate-based MOF. In addition, polyoxometalates can be encapsulated in MOF pores by host−guest interactions to form MOF polyoxometalate composites [38,39].

1.2.2.6 Metal-organic framework−enzyme composites

Enzymes are a class of extremely efficient biocatalysts with high activity and mild chemo-, enantio-, and area selectivity, which are very effective in catalyzing various reactions. However, their extensive catalytic uses are greatly hindered by the delicate existence of enzymes, such as poor thermal stability, limited optimum pH ranges, and low resistance to organic solvents and denaturants. In addition, lengthy purification and isolation steps are required to contaminate the enzymes in the target products. MOFs have proved to be effective enzyme immobilization mechanisms to shield them from deactivating reaction conditions, improving their recyclability, and reducing product degradation. Precise regulation of pore depth, form, and composition of MOFs enables enzyme confinement with matched thickness, thereby reducing self-aggregation and enzyme leaching. In addition, MOF's inorganic nodes and functional linkers will create those enzyme interactions by coordination, covalent bonding, hydrogen bonding, and van der Waals to stabilize leaching enzymes [40−44]. The encapsulation of rhodamine was obtained in a bio-MOF based on adenine [45]. The resulting composite provided high quantum efficiency in color tuning to show the possible applicability of light-emitting devices and visible light communication. Several scholars have studied the different MOF composites with differing rhodamine ratios relative to specifications such as color tenability, emission efficiencies, and lifetime of emissions.

1.2.2.7 Metal-organic framework−cellulose composites

Cellulose has great potential as substrates because of its high strength, lightweight, low cost, water resilience, flexibility, nontoxicity, and excellent processability [46−49]. MOF dispersion on the cellulose surfaces is being successfully prepared to produce composite MOF−cellulose fabrics with new practical efficiency [50]. The MOF and cellulose aerogel composite materials were processed using the in situ growth technique at room temperature. Such materials have been described by a study of scanning electron microscopy (SEM), X-ray diffraction analysis (XRD), atomic absorption spectrometer, and thermogravimetry. The amount of adsorbed metal ions is equivalent to the number of MOFs and cellulose aerogels, indicating that the

MOFs are not blocked and therefore adsorbent after the development of cellulose aerogels. Composite plastic MOF−cellulose aerogels have been shown to be recyclable in water to adsorb Pb^{2+} and Cu^{2+} after quick washing. This result shows that these composite materials could adsorb heavy metal ions in water by preventing secondary contamination and demonstrate great potential in water treatment [51]. The composite MOF−cellulose aerogels were prepared at room temperature by simple in situ production. In the metal ion precursor, the pre-synthetic aerogel of cellulose is soaked, and then the organic ligand is added to allow the MOFs to build on the cellulose aerogel. The effectiveness of adsorbing heavy metal ions in water by cellulose aerogel has been investigated. The MOFs were still working, and the channels were not obstructed by comparing the adsorption equilibrium of heavy metal ions with cellulose aerogel, MOFs, and composite MOF−cellulose aerogel.

1.2.2.8 Metal-organic framework−silica composites

Silica particles and nanostructures have efficient mechanisms that have drawn significant interest in catalytic applications for performing various nanoscale functions such as porosity, stabilization, and hydrophilicity. The synthesis of silica with MOFs incorporates the essential properties of all materials and contributes to innovative applications. There are actually two main types of MOF−silica composites: SiO_2@MOFs and MOFs@SiO_2. The former includes the injection of dispersed silica particles into MOF pores/channels or the growth of an MOF shell into a preformed silica sphere, while the latter uses silica as a coating layer produced on the MOF surface or as an aid to the growth of MOF particles [52−54].

1.2.2.9 Metal-organic framework−activated carbon composites

MOF fibers, were synthesized for methane recovery and carbon dioxide capture by Kayal et al. [55]. Nevertheless, the effectiveness of MOF−activated carbon composites in aqueous conditions was not investigated for the removal of chemical species. These composites were synthesized by a simple hydrothermal cycle and used as the adsorbent organic dye. Through testing the adsorption kinetics under various conditions, such as adsorbent thickness, contact time, and dye concentration, the adsorption potential of the composite particles is shown to be superior to both activated carbon and MOF. The surface reaction technique depending on the core composite concept was used to determine the most effective conditions for the rapid and productive removal of dye. A potential organic dye structure and adsorption mechanism is given on carbon nanocomposite enabled with MIL-101(Cr). Mahmoodi et al. [56] synthesized the green MOF nanocomposite with 2, 5, and 10 wt.% activated carbon ratios based on cucumber peel activated carbon− and chromium-based MOF [MIL-101(Cr)]. Characterization of compounds was performed using TGA, Brunauer−Emmet−Teller (BET), XRD, SEM, and

Fourier-transform infrared spectroscopy (FTIR). The findings revealed octahedral crystal form, and composite materials exhibited the same morphology as MIL-101(Cr) crystals on an activated carbon surface. The findings revealed that the methods of the surface reaction model estimated the real data with high precision.

Hasanzadeh et al. [20] prepared the composites of the activated carbon−/chromium-based MOF [MIL-101(Cr)] with highly soluble adsorbents. The polymer has a high surface area and a gross volume of around 1.3 $cm^3\ g^{-1}$ in pore. To illustrate the efficacy of the composite as an adsorbent, the removal kinetics of anionic dyes from aqueous solutions are exhibited based on the volume of composite, adsorption time, dye concentration, and pH. MIL-101(Cr)-activated carbon composite kinetics was shown to be quicker than MIL-101(Cr) under near-neutral pH conditions. Half the processing time is roughly 3 minutes, and after 5 minutes 85% of the color is lost.

1.2.2.10 Metal-organic framework−aluminum composites

Aluminum tris(8-hydroxyquinoline) (Alq_3) was widely used as a solvent in metal chelates. Alq_3 thin films as electroluminescent materials have been reported to demonstrate high effectiveness and stability. Their use in commercial light-emitting systems has also drawn interest in thin film features. MOFs have been proposed as a host matrix for modulating the luminescence properties of Alq_3 molecules. The incorporation of Alq_3 molecules into MOF pores or nanochannels is very effective in avoiding their aggregation, which in turn helps to effectively increase the life span and the yield of the chromophore. For the MOF−Alq_3 composite, there was an increase in the lifetime of excited state emissions of as much as 65% relative to Alq_3 alone. In addition to this, a constant blue emission shift could be achieved by increasing the Alq_3 load in the composite. This activity was explained because of molecular interactions with the MOF in Alq_3. As such, the latter study can be considered one of the most important studies for understanding the tuning of emission properties of chromophores following their encapsulation in MOFs [57−59].

1.2.2.11 Metal-organic framework−molecular species composites

As tools for studying and imitating the functionalities of biological structures, homogeneous molecular species such as dye molecules, saline complexes, porphyrins, and metalloporphyrins were extensively researched. However, the lifetime of these molecules is shortened due to interactions between the active sites and oxidative self-degradation due to self-aggregation. The immobilization of molecular species in MOFs, where the active sites can be separated and protected, is a viable alternative to the heterogenization of homogeneous molecular catalysts, combining the benefits of

all catalyst groups and reducing the drawbacks. Molecular species can be incorporated in an MOF backbone via covalent bonding or encapsulated via noncovalent interaction within MOF pores. Direct encapsulation does not disturb the sphere of interaction between molecular species and thus retains the stability and properties of the molecular species. Furthermore, direct encapsulation can maintain the mobility of molecular molecules to some degree, enabling them to cooperate with the MOF backbone. Three-dimensional MOFs with wide cavities interconnected by small windows are especially ideal for stabilizing molecular species, given that the wide cavities can handle molecular species, and the small porous windows avoid leaching and aggregation of molecular species [60–64].

1.2.2.12 Metal-organic framework–hybrid composites

Monama et al. [65] produced a novel hybrid composite depending on 4-tetranitro copper(II)phthalocyanin (TNCuPc) produced from MOF as a noble, hydrogen-free catalyst. The composition, surface area, and morphology of the composite bare MOF, TNCuPc, and TNCuPc/MOF are characterized by XRD, FTIR spectroscopy, ultraviolet–visible spectroscopy, BET, SEM, transmission electron microscopy (TEM), and simultaneous thermal analysis. The composite developed exhibited high behavior against hydrogen reaction evolution, strong thermal stability, and excellent resistance. Thus the nonnoble electro-catalyst TNCuPc/MOF may be a promising electrochemical catalyst for the production of electrochemical hydrogen to replace platinum-based catalysts. The spectroscopic study indicated a strong composite synthesis of TNCuPc. The morphological findings showed that rod-like TNCuPc structures were being formed on the MOF sheet. The green solvothermal process for the preparation of the composite MOF (Cu-BTC) and MOF/graphene hybrid is to be used as an efficient adsorbent of the product fuels. The formulated adsorbents are distinguished by the application of various analytical techniques such as XRD, FTIR, BET, and TEM. Laboratory adsorption results revealed that, under optimal experimental conditions, the MOF/Gr composite content exhibits exceptionally strong adsorption of dibenzothiophene at an adsorption rate of 46.2 mgS g^{-1} [66].

1.3 Characterization of metal-organic framework composites

To advance the characterization of MOF particles for real-world applications, the wide range of materials such as activated carbons, rGO/GO, multiwalled CNTs, biomaterials, and nano-fibrous membranes have been regarded as support beds for stabilizing and creating better and better MOF nanocrystals. To date, MOF composites have been synthesized as thin films using a seeding and growth process or layer-by-layer growth of MOFs on different substrates, including porous oxide supports, graphite, CNT, and activated carbon

[67–72]. This chapter addressed the most important characterization techniques used by these MOF composites, such as XRD, X-ray photoelectron spectroscopy (XPS), FTIR, and SEM analytics.

1.3.1 X-ray diffraction analysis

Using the XRD process, the rGO, CoMOF/rGO composites, and CoMOF powder crystal structures were determined (Fig. 1.3). In the rGO paper, XRD spectrum the peak at 25.4 degrees was observed, referring to the typical crystal diffraction of the graphene structure (0 0 2). In CoMOF, XRD results from the peaks at roughly 35.4, 42.5, 61.7, and 73.4 degrees correspond to the (1 1 1), (2 2 0), (4 0 0), and (5 1 1), respectively, Co form. The XRD pattern of the CoMOF/rGO paper shows diffraction peaks of both rGO and CoMOF composition, suggesting the good preparation of the CoMOF/rGO composites [33].

1.3.2 X-ray photoelectron spectroscopy

The XPS experiments were conducted on a standard source spectrometer with Al X-ray. The CoMOF/rGO chemical composite electrode structure was calculated using XPS technique, as shown in Fig. 1.4. CoMOF/rGO's composite electrode consists of 46.432% C, 46.445% O, 4.721% Co, and 2.402% I. The CoMOF/rGO composite spectrum of C 1s (Fig. 1.4B) can be deconverted to three major peaks of 283.7, 285.5, and 287.6 eV binding energies, respectively. In Fig. 1.4C, O 1s range can be grouped into three peaks, respectively, at 530.4, 531.4, and 532.2 eV. The peaks correspond to various oxidation structures of Co, as shown in Fig. 1.4D, are Co^{2+} 2p 3/2 (780 eV), Co^{2+} 2p 1/2 (784 eV), and Co^{3+} 2p 3/2 satellite (796 eV). The high for I is due to HI used during the chemical reduction process when preparing the rGO film electrode. Since the CoMOF is formed on the surface of the rGO electrode using the electrochemical oxidation cycle, the rGO XPS spectrum showed relatively greater oxygen content. In evaluating these results, it was established that the CoMOF/rGO composite electrode was successfully prepared [33].

1.3.3 Fourier-transform infrared spectroscopy

FTIR spectrum of activated carbon strengthened MOF composites is seen in Fig. 1.5 [19]. The broadband around 3430 cm^{-1} is related to the O–H stretching vibration from water adsorbed by the air. The band appeared at 1400 cm^{-1} is due to the O–C–O symmetric vibration of the carboxylic acid group that indicates the presence of 1,4-benzene dicarboxylic acid (H_2BDC) ligand within the material structure. The low point at 1506 cm^{-1} is due to C = C of the benzene chain. The other motions at 1108, 1017, 888, and

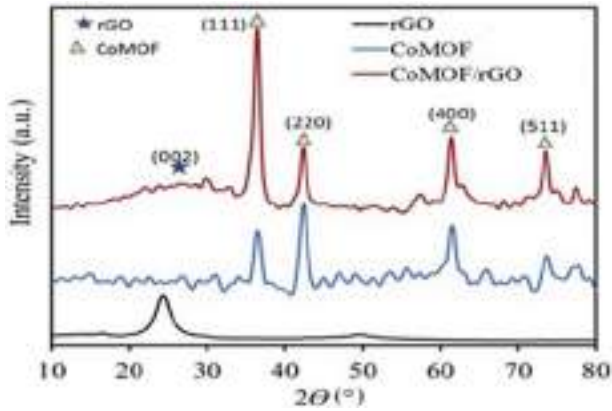

FIGURE 1.3 XRD patterns of rGO, CoMOF/rGO, and CoMOF composites [33]. *XRD*, X-ray diffraction analysis.

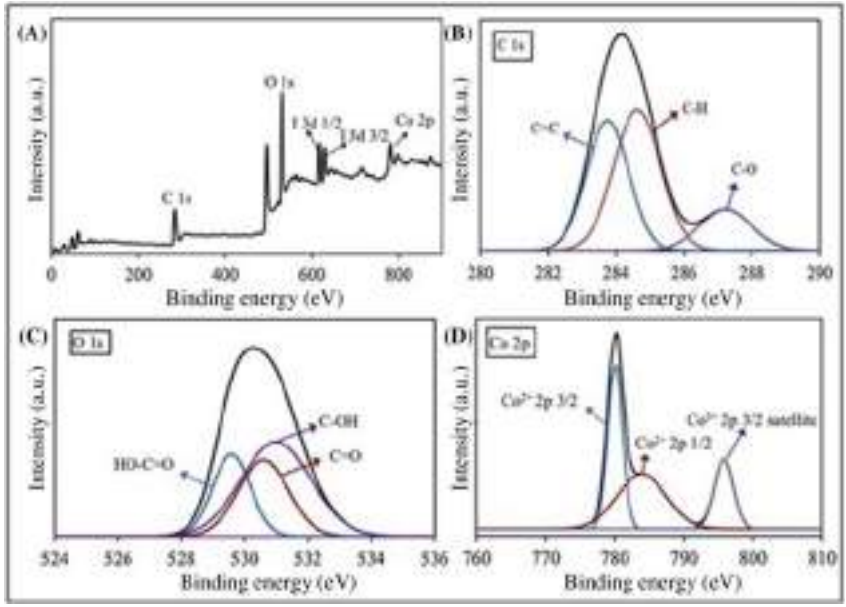

FIGURE 1.4 XPS spectra of CoMOF/rGO composite: (A) survey, (B) C 1s, (C) O 1s, and (D) Co 2p [33]. *XPS*, X-ray photoelectron spectroscopy.

749 cm^{-1} are due to C−H deformation of the benzene ring [55]. Reduction of the band strength at 1610 cm^{-1} (carboxylic acid C−O group) in combination with the formation of a new 1716 cm^{-1} absorption band (ester carbonyl group) for activated carbon−MOF composite enables the potential reaction of H_2BDC ligand to activated carbon. To map potential reactions between

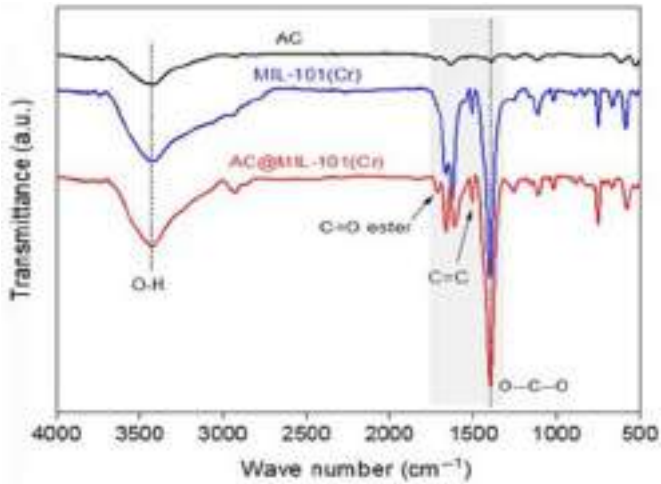

FIGURE 1.5 FTIR spectrum of activated carbon−reinforced MOF composites [20]. *FTIR*, Fourier-transform infrared spectroscopy, *MOF*, metal-organic framework.

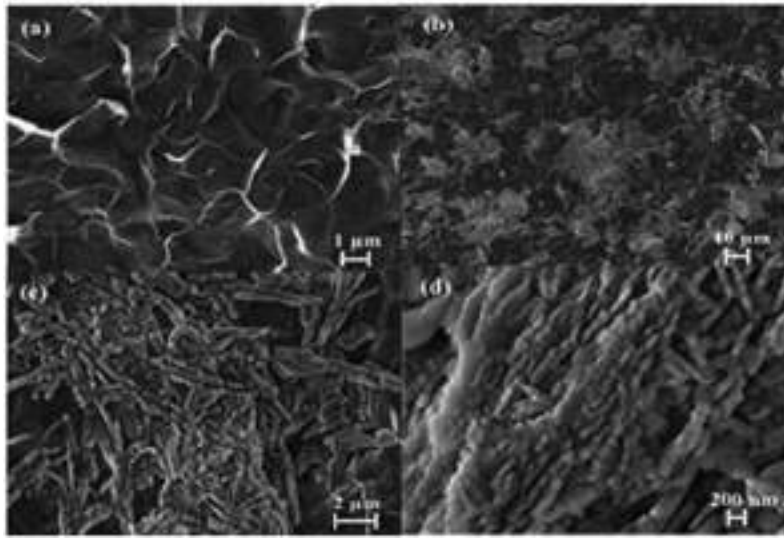

FIGURE 1.6 SEM images of (A) rGO, (B) CoMOF/rGO composite, and (C and D) low and high magnifications of CoMOF nanorods [33]. *SEM*, Scanning electron microscopy.

the activated carbon and H_2BDC ligand, the FTIR spectrum of activated carbon functionalized with H_2BDC molecules was measured. The peaks around 3430 and 1685 cm^{-1} correspond to the activated carbon stretching hydroxyl

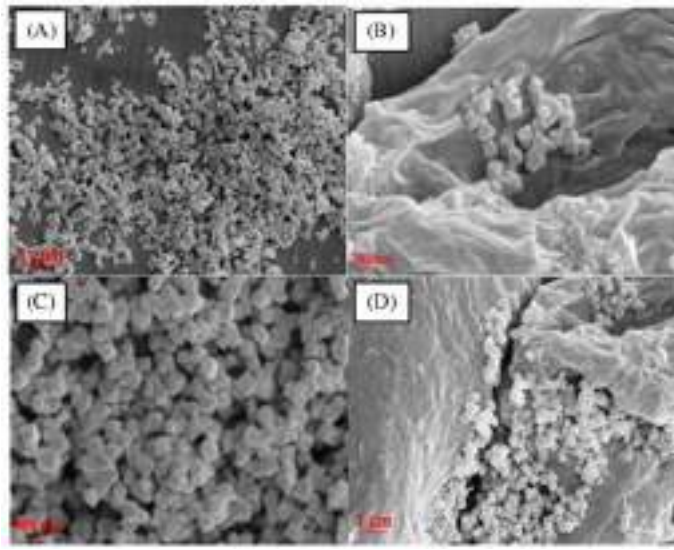

FIGURE 1.7 SEM images of the MOF composites (A and B) MIL-101(Cr) and (C and D) activated carbon/MIL-101(Cr) [56]. *MOF*, Metal-organic framework; *SEM*, scanning electron microscopy.

vibration, respectively, and the H_2BDC carbonyl group. According to the reaction between the activated carbon and H_2BDC, it was expected that an ester carbonyl group will form around 1716 cm^{-1}. FTIR spectroscopy has not shown such a peak that may be attributed to the high H_2BDC carbonyl group peak present in this level.

1.3.4 Scanning electron microscopy analysis

SEM photographs were gathered to analyze the morphology of the materials. The morphology of CoMOF/rGO composites was studied by SEM. Fig. 1.6 displays the SEM images of freestanding and robust composites rGO and CoMOF/rGO for morphological characterization. The characteristic wrinkled appearance of the graphene system's metallic gray surface was observed on the SEM picture of the rGO (Fig. 1.6A). Fig. 1.6B reveals that finger-like CoMOF nanorods shaped on the rGO surface and that these finger-like CoMOF structures coated the electrode surface homogeneously (Fig. 1.6C and D). A 3D surface was formed, as well as the surface's active surface area is increased by synthesized finger-like CoMOF structures on the rGO. Such 3D CoMOF structures are predicted to exhibit high efficiency on the rGO surface in electro-catalytic studies [33].

Fig. 1.7 revealed the SEM images of AC/MIL-101(Cr) 2% and AC/MIL-101(Cr) 10%. As for Fig. 1.7A and B, MIL-101(Cr) SEM photos revealed a

simple octahedral crystal form, and the composite materials displayed the same morphology as MIL-101(Cr) crystals on an activated carbon bed in Fig. 1.7C and D. As the difference between the pure MIL-101(Cr) SEM images and the composite form [AC/MIL-101(Cr) 5%] can be easily interpreted, the particle size of MOF nanocrystals has been limited, but MIL's octahedral faces seemed sharper and smoother. This phenomenon may be explained by the high ability of activated carbon negative surface to support metal cations and hence high nucleation velocity and stability of MOF crystals on the activated carbon surface [56].

1.4 Conclusion

The key purpose of this chapter is a study of the MOFs and their composites. MOF's approaches to developing and synthesizing and their composites, as well as their effects, have been studied. MOFs and a number of functional materials, such as metal nanoparticles, QDs, molecular species, enzymes, silica, and polymers, were incorporated into various well-developed MOF composite preparation techniques. From the literature, it is found that the MOF composites can be developed by adding functional nanomaterials to the MOF structure to significantly enhance the properties. MOF composites show synergistic effects between components, exhibiting outstanding features to significantly expand applications with high performance, selectivity, and flexibility for a wide variety of reactions. These MOF composites can, as has been found in many studies, improve the sensing properties to detect a wide variety of species, including heavy metal ions, anions, aromatic hydrocarbons, toxic phenolic compounds, and temperature. While there are still many hurdles, this modern form of functional material has been predicted well for the promising future by the rapid production of MOF composites in recent years. Sustained research activities should be expected to allow their realistic applications in this exciting area.

References

[1] Chen L, Xu Q. Metal-organic framework composites for catalysis. Matter 2019;1:57–89.

[2] Furukawa H, Cordova KE, O'Keeffe M, Yaghi OM. The chemistry and applications of metal–organic frameworks. Science 2013;341:974–86.

[3] Kitagawa S, Kitaura R, Noro S-I. Functional porous coordination polymers. Angew Chem Int Ed 2004;43:2334–75.

[4] Zhou H-C, Kitagawa S. Metal–organic frameworks (MOFs). Chem Soc Rev 2014;43:5415–18.

[5] Mahmoodi NM, Oveisi M, Panahdar A, Hayati B, Nasiri K. Synthesis of porous metal-organic framework composite adsorbents and pollutant removal from multicomponent systems. Mat Chem Phy 2020;243. Available from: https://doi.org/10.1016/j.matchemphys.2019.122572.

[6] Kaur H, Sundriyal S, Pachauri V, Ingebrandt S, Kim K-H, Sharma AL, et al. Luminescent metal-organic frameworks and their composites: potential future materials for organic light emitting displays. Coord Chem Rev 2019;401:213077.
[7] Aguilera-Sigalat J, Bradshaw D. Synthesis and applications of metal−organic framework−quantum dot (QD@MOF) composites. Coord Chem Rev 2016;307:267−91.
[8] Jin S, Son HJ, Farha OK, Wiederrecht GP, Hupp JT. Energy transfer from quantum dots to metal-organic frameworks for enhanced light harvesting. J Am Chem Soc 2013;135:955−8.
[9] Buso D, Jasieniak J, Lay MD, Schiavuta P, Scopece P, Laird J, et al. Highly luminescent metal-organic frameworks through quantum dot doping. Small 2012;8:80−8.
[10] Tang Y, Tanase S. Water-alcohol adsorptive separations using metal-organic frameworks and their composites as adsorbents. Micropor Mesopor Mater 2020;295. Available from: https://doi.org/10.1016/j.micromeso.2019.109946.
[11] Zhou Y, Yan B, Lei F. Postsynthetic lanthanides functionalization of nanosized metal-organic frameworks for highly sensitive ratiometric luminescent nanothermometers. Chem Commun 2014;50:15235−8.
[12] Pan M, Zhu YX, Wu K, Chen L, Hou YJ, Yin SY, et al. Epitaxial growth of hetero-Ln-MOF hierarchical single crystals for domain- and orientation controlled multicolor luminescence 3D coding capability. Angew Chem Int Ed 2017;56:14582−6.
[13] de Melo EF, Santana NC, Alves KG, de Sa GF, de Melo CP, Rodrigues MO, et al. LnMOF@PVA nanofiber: energy transfer and multicolor light-emitting devices. J Mater Chem C 2013;1:7574−81.
[14] Lian X, Yan B. Diagnosis of penicillin allergy: a MOFs-based composite hydrogel fordetecting β-lactamase in serum. Chem Commun 2019;55:241−4.
[15] Sava Gallis DF, Rohwer LES, Rodriguez MA, Nenoff TM. Efficient photoluminescence via metal-ligand alteration in a new MOFs family. Chem Mater 2014;29:2943−51.
[16] Lu Y, Yan B. Lanthanide organic-inorganic composite based on functionalized metal-organic frameworks (MOFs) for near-UV white LED. Chem Commun 2014;50:15443−6.
[17] Wu LL, Wang Z, Zhao SN, Meng X, Song XZ, Feng J, et al. A metal−organic framework/DNA hybrid system as a novel fluorescent biosensor for mercury (II) ion detection. Chemistry 2016;22:477−80.
[18] Peng Z, Jiang Z, Huang X, Li Y. A novel electrochemical sensor of tryptophan based on silver nanoparticles/metal−organic framework composite modified glassy carbon electrode. RSC Adv 2016;6:13742−8.
[19] Liao X, Fu H, Yan T, Lei J. Electroactive metal−organic framework composites: design and biosensing application. Biosens Bioelectron 2019;146:111743.
[20] Hasanzadeh M, Simchi A, Shahriyari Far H. Nanoporous composites of activated carbon-metal organic frameworks for organic dye adsorption: synthesis, adsorption mechanism and kinetics studies. J Indus Eng Chem 2019;81. Available from: https://doi.org/10.1016/j.jiec.2019.09.031.
[21] Kitao T, Zhang Y, Kitagawa S, Wang B, Uemura T. Hybridization of MOFs and polymers. Chem Soc Rev 2017;46:3108−33.
[22] Rowe MD, Thamm DH, Kraft SL, Boyes SG. Polymer-modifed gadoliniummetal-organic framework nanoparticles used as multifunctional nanomedicines for the targeted imaging and treatment of cancer. Biomacromolecules 2009;10:983−93.
[23] Ramesh M, Muthukrishnan M, Khan A, et al. Metal-organic-framework-quantum dots (QD@MOF) composites. In: Metal-organic framework composites II. 2019. Materials Research Forum LLC, p. 49−84.

[24] Li G, Zhao S, Zhang Y, Tang Z. Metal−organic frameworks encapsulating active nanoparticles as emerging composites for catalysis: recent progress and perspectives. Adv Mater 2018;30:1800702.
[25] Yang Q, Xu Q, Jiang H-L. Metal−organic frameworks meet metal nanoparticles: synergistic effect for enhanced catalysis. Chem Soc Rev 2017;46:4774−808.
[26] Chen L, Luque R, Li Y. Encapsulation of metal nanostructures into metal−organic frameworks. Dalton Trans 2018;47:3663−8.
[27] Fan J, Chen D, Li N, Xu Q, Li H, He J, et al. Adsorption and biodegradation of dye in wastewater with Fe_3O_4@MIL-100 (Fe) core−shell bio-nanocomposites. Chemosphere 2018;191:315−23.
[28] Wang T, Zhao P, Lu N, Chen H, Zhang C, Hou X. Facile fabrication of Fe_3O_4/MIL-101 (Cr) for effective removal of acid red 1 and orange G from aqueous solution. Chem Eng J 2016;295:403−13.
[29] Shustova NB, McCarthy BD, Dinca M. Turn-on fluorescence in tetraphenylethylene-based metal−organic frameworks: an alternative to aggregation-induced emission. J Am Chem Soc 2011;133:20126−9.
[30] Usman M, Mendiratta S, Batjargal S, Haider G, Hayashi M, RaoGade N, et al. Semiconductor behavior of a three-dimensional strontium-based metal−organic framework. ACS Appl Mater Interf 2015;7:22767−74.
[31] Haider G, Usman M, Chen T-P, Perumal P, Lu K-L, Chen Y-F. Electrically driven white light emission from intrinsic metal−organic framework. ACS Nano 2016;10:8366−75.
[32] Li F, Jiang X, Zhao J, Zhang S. Graphene oxide: a promising nanomaterial for energy and environmental applications. Nano Energy 2015;16:488−515.
[33] Ezgi T. Three-dimensional, free-standing, and flexible cobalt-based metal-organic frameworks/graphene composite paper: a novel electrochemical sensor for determination of resorcinol. Mate Rese Bull 2020;121:110629.
[34] Langmi HW, North BC, Musyoka NM, Mathe M, Bessarabov D, Ren J. Synthesis of rGO/Zr-MOF composite for hydrogen storage application. J Alloy Comp 2017;724:450−5.
[35] Jiang W, Sun M, Wu F, Dong W, Xie A, Zhang K. Electromagnetic dissipation onthe surface of metal organic framework (MOF)/reduced graphene oxide (rGO) hybrids. Mater Chem Phys 2017;199:340−7.
[36] Fang SU, Zhang P, Gong JL, Tang L, Zeng GM, Song B, et al. Construction of highly water-stable metal-organic framework UiO-66 thin film composite membrane for dyes and antibiotics separation. Chem Eng J 2019;385. Available from: https://doi.org/10.1016/j.cej.2019.123400.
[37] Lin KA, Yang H, Hsu F. Zr-Metal organic framework and derivatives for adsorptive and photocatalytic removal of acid dyes. Water Env Res 2018;90:144−54.
[38] Ye J-J, Wu C-D. Immobilization of polyoxometalates in crystalline solids for highly efficient heterogeneous catalysis. Dalton Trans 2016;45:10101−12.
[39] Du D-Y, Qin J-S, Li S-L, Su Z-M, Lan Y-Q. Recent advances in porous polyoxometalate-based metal−organic framework materials. Chem Soc Rev 2014;43:4615−32.
[40] Drout RJ, Robison L, Farha OK. Catalytic applications of enzymes encapsulated in metal−organic frameworks. Coord Chem Rev 2019;381:151−60.
[41] Lian X, Fang Y, Joseph E, Wang Q, Li J, Banerjee S, et al. Enzyme-MOF (metal−organic framework) composites. Chem Soc Rev 2017;46:3386−401.
[42] Doonan C, Ricco R, Liang K, Bradshaw D, Falcaro P. Metal−organic frameworks at the biointerface: synthetic strategies and applications. Acc Chem Res 2017;50:1423−32.

[43] Deng H, Grunder S, Cordova KE, Valente C, Furukawa H, Hmadeh M, et al. Large-pore apertures in a series of metal–organic frameworks. Science 2012;336:1018–23.
[44] Feng D, Liu T-F, Su J, Bosch M, Wei Z, Wan W, et al. Stable metal–organic frameworks containing single-molecule traps for enzyme encapsulation. Nat Commun 2015;6:5979.
[45] Chen W, Zhuang Y, Wang L, Lv Y, Liu J, Zhou T-L, et al. Color-tunable and high-efficiency dye-encapsulated metal–organic framework composites used for smart white-light-emitting diodes. ACS Appl Mater Interf 2018;10(22):18910–17.
[46] Arnaud D, Christian B, Claudia H, Arnaud R, Tatiana B. Cellulose–silica aerogels. Carbohyd Polym 2015;122:293–300.
[47] Liao Q, Su X, Zhu W, Hua W, Qian Z, Liu L, et al. Flexible and durable cellulose aerogels for highly effective oil/water separation. RSC Adv 2016;6:63773–81.
[48] Litschauer M, Neouze M-A, Haimer E, Henniges U, Potthast A, Rosenau T, et al. Silica modified cellulosic aerogels. Cellulose 2010;18(1):143–9.
[49] Cai J, Liu S, Feng J, Kimura S, Wada M, Kuga S, et al. Cellulose-silica nanocomposite aerogels by in situ formation of silica in cellulosegel. Angew Chem 2012;51(9):2076–9.
[50] Ren W, Gao J, Lei C. Recyclable metal-organic framework/cellulose aerogels for activating peroxymonosulfate to degrade organic pollutants. Chem Eng J 2018;349:766–74.
[51] Lei C, Gao J, Ren W, Xie Y, Abdalkarim SYH, Wang S, et al. Fabrication of metal-organic frameworks@cellulose aerogels composite materials for removal of heavy metal ions in water. Carbohyd Polym 2018;205. Available from: https://doi.org/10.1016/j.carbpol.2018.10.029.
[52] Uemura T, Hiramatsu D, Yoshida K, Isoda S, Kitagawa S. Sol–gel synthesis of low-dimensional silica within coordination nanochannels. J Am Chem Soc 2008;130:9216–17.
[53] Jo C, Lee HJ, Oh M. One-pot synthesis of silica@coordination polymercore–shell microspheres with controlled shell thickness. Adv Mater 2011;23:1716–19.
[54] Kou J, Sun L-B. Fabrication of metal–organic frameworks inside silica nanopores with significantly enhanced hydrostability and catalytic activity. ACS Appl Mater Interf 2018;10:12051–9.
[55] Kayal S, Chakraborty A. Activated carbon (type Maxsorb-III) and MIL-101(Cr) metal organic framework based composite adsorbent for higher CH_4 storage and CO_2 capture. Chem Eng J 2018;334:780–8.
[56] Mahmoodi NM, Taghizadeh M, Taghizadeh A. Activated carbon/metal-organic framework composite as a bio-based novel green adsorbent: preparation and mathematical pollutant removal modeling. J Mol Liq 2019;277:310–22.
[57] Desai P, Shakya P, Kreouzis T, Gillin W, Morley N, Gibbs M. Magnetoresistance and efficiency measurements of Alq_3-based OLEDs. Phys Rev B 2007;75:094423.
[58] Garbuzov D, Bulovic V, Burrows P, Forrest S. Photoluminescence efficiency and absorption of aluminum-tris-quinolate (Alq_3) thin films. Chem Phys Lett 1996;249:433–7.
[59] Yang G-S, Li M-N, Li S-L, Lan Y-Q, He W-W, Wang X-L, et al. Controllable synthesis of microporous, nanotubular and mesocage-like metal–organic frameworks by adjusting the reactant ratio and modulated luminescence properties of Alq_3@MOF composites. J Mater Chem 2012;22:17947–53.
[60] Wu C-D, Zhao M. Incorporation of molecular catalysts in metal–organicframeworks for highly efficient heterogeneous catalysis. Adv Mater 2017;29:1605446.
[61] Wang C, Liu D, Lin W. Metal–organic frameworks as a tunable platform for designing functional molecular materials. J Am Chem Soc 2013;135:13222–34.

[62] Kajiwara T, Fujii M, Tsujimoto M, Kobayashi K, Higuchi M, Tanaka K, et al. Photochemical reduction of low concentrations of CO_2 in a porous coordination polymer with a ruthenium(II)−CO complex. Angew Chem Int Ed 2016;55:2697−700.

[63] Niu Z, Bhagya Gunatilleke WDC, Sun Q, Lan PC, Perman J, Ma J-G, et al. Metal−organic framework anchored with a Lewis pair as a new paradigm for catalysis. Chem 2018;4:2587−99.

[64] Bogaerts T, Van Yperen-De Deyne A, Liu Y-Y, Lynen F, Van Speybroeck V, Van Der Voort P. Mnsalen@MIL101(al): a heterogeneous, enantioselective catalyst synthesized using a 'bottle around the ship' approach. Chem Commun 2013;49:8021−3.

[65] Monama GR, Hato MJ, Ramohlola KE, Maponya TC, Mdluli SB, Molapo KM, et al. Hierarchiral 4-tetranitro copper(II)phthalocyanine based metal organic framework hybrid composite with improved electrocatalytic efficiency towards hydrogen evolution reaction. Results Phys 2019;15:102564.

[66] Radwan DR, Matloob A, Mikhail S, Saad L, Guirguis D. Metal organic framework-graphene nano-composites for high adsorption removal of DBT as hazard material in liquid fuel. J Hazard Mat 2019;373:447−58.

[67] Sarker M, Song JY, Jhung SH. Adsorptive removal of anti-inflammatory drugs from water using graphene oxide/metal-organic framework composites. Chem Eng J 2018;335:74−81.

[68] Ramachandran R, Xuan W, Zhao C, Leng X, Sun D, Luo D, et al. Enhanced electrochemical properties of cerium metal−organic framework based composite electrodes for high-performance supercapacitor application. RSC Adv 2018;8:3462−9.

[69] Sohrabi S, Dehghanpour S, Ghalkhani M. A cobalt porphyrin-based metal organic framework/multi-walled carbon nanotube composite electrocatalyst for oxygen reduction and evolution reactions. J Mater Sci 2018;53:3624−39.

[70] Hadi M, Bayat M, Mostaanzadeh H, Ehsani A, Yeganeh-Faal A. Sensitive electrochemical detection of picloram utilising a multi-walled carbon nanotube/Cr-based metal-organic framework composite-modified glassy carbon electrode. Int J Environ Anal Chem 2018;98:197−214.

[71] Wu F, Zhao S, Chen L, Lu Y, Su Y, Jia Y, et al. Metalorganic frameworks composites threaded on the CNT knitted separator for suppressing the shuttle effect of lithium sulfur batteries. Energy Storage Mater 2018;14:383−91.

[72] Tanhaei M, Mahjoub AR, Safarifard V. Sonochemical synthesis of amide functionalized metal-organic framework/graphene oxide nanocomposite for the adsorption of methylene blue from aqueous solution. Ultrason Sonochem 2018;41:189−95.

Chapter 2

Metal-organic framework for batteries and supercapacitors

M. Ramesh[1], N. Kuppuswamy[2] and S. Praveen[1]
[1]*Department of Mechanical Engineering, KIT-Kalaignarkarunanidhi Institute of Technology, Coimbatore, India,* [2]*Department of Aeronautical Engineering, KIT-Kalaignarkarunanidhi Institute of Technology, Coimbatore, India*

2.1 Introduction

The demand for energy in modern society is growing, and issues are becoming increasingly serious about depleting and the resulting pollution caused by fossil fuels burnt [1]. Thus designing the technologies for the storage and conversion of abundant, secure, clean, and sustainable energy has become a hot topic of research [2]. This has attracted significant attractions in the scientific community in the design and development of sustainable, efficient, safe, and viable energy storage devices such as batteries, capacitors, and fuel cells. The most crucial electrochemical energy storage devices are rechargeable batteries and high-performance supercapacitors [3]. Lithium-ion batteries (LIBs) are primarily used for laptops, mobile phones, and compact and environment-friendly electric/hybrid electric vehicles and have considerable low weight and high energy capacity [4].

Similarly, supercapacitors, having long cycle life, competitive price, and substantial-high power density, are significantly popular and widely used in aerospace and electric vehicles [5]. The transport industry is growing demand for electric energy storage systems (EESs) with energy and power capacity. Hybrid cars, plug-in hybrid vehicles, and full electric vehicles were built in this case. Batteries and supercapacitors are two key technologies that emerge as the EES's leading component. All of them may not, however, fulfill all of the demands. Batteries have capacity to store higher densities of energy than supercapacitors, but consume less power. However, the highest energy available in batteries or supercapacitors, even if fully developed, is still inadequate to achieve such applications; levels of efficiency, life cycles, and battery protection are still need to be improved. Exploring new high-performance materials is a major challenge; and extensive research is being

Metal-Organic Frameworks for Chemical Reactions. DOI: https://doi.org/10.1016/B978-0-12-822099-3.00002-2

conducted in developing batteries and supercapacitors for the next decade [6]. Metal-organic frameworks (MOFs) are the subject of research because of the controllable and fascinating morphology, high-level structure, copious pores, and multifunctional characteristics [7].

2.2 Metal-organic frameworks

MOFs are also known as coordinating polymers that have had a strong and deep interest in the material and chemical community over the last decades [8]. MOFs provide a number of advantages over typical porous materials: for example, the most desirable crystal structures can be built rationally and crystal engineering. MOFs are typically made from metal sites and several organic mains [9]. The dense and large surface areas are tempted to be a good example of the promising electrode materials and high-performance energy storage systems of supercapacitors [10]. Furthermore, the batteries provide an excellent density of energy but low power. Conversely, supercapacitors are solid but have a low density of energy. MOF can, therefore, be customized for their ultimate applications, for instance, choosing certain metal sites to match power and energy densities and changing their pores. The single mechanism between unusual morphology, functional connections, different surfaces, and metal sites in MOFs and their subsequent electrochemical output is therefore significantly elucidated. In recent years, MOFs are being applied in electrochemical systems [11]. The application of MOFs in electrical energy storage is presented in Fig. 2.1, which is reproduced from [1].

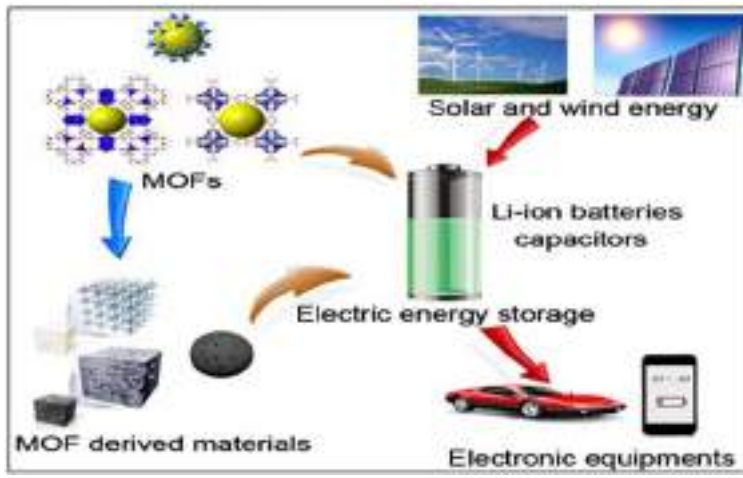

FIGURE 2.1 Applications of MOFs in electrical energy storage [1]. *MOF*, Metal-organic framework.

2.3 Metal-organic frameworks for batteries

2.3.1 Lithium-ion batteries

LIBs have an anode and electrode, as well as an electrolyte in three main components. When LIBs is charged, lithium ions are removed from the cathode electrode. The decomposition of lithium ions then travels through the electrolyte and transfers into the anode electrode, and the energy is stored in LIBs during this cycle. When the LIBs stop storing, the lithium ions move back to the cathode electrode; and the stored energy has been released. The selection of cathode and anode materials is very important, and this is the main focus of various researchers [12,13]. The conventional electrode material is subject to complicated synthesis, low energy/power density, and limited life cycle. MOFs are promising electro-materials for LIBs due to their unique character, nonspecific surfaces, well-developed porosity, and high storage ability. Metal captions serve as the active redox MOF site and enable efficient and reversible ion insert/extraction in open crystal frameworks [14]. Combarieu et al. [15] have been identified as a cathode material Li^+ to reversibly insert $Fe^{III}(OH)_{0.8}F_{0.2}[O_2C{-}C_6H_4{-}CO_2]$ [MIL-53(Fe)]. Experimental findings showed that MOFs are excellent cathode materials for LIBs, with no structural modification, up to 0.6 Li^+ per Fe^{3+} that could be split into MIL-53(Fe) at C/40. Except for cathode materials, MOFs may be used as anode materials for LIBs. Maiti et al. [16] synthesized a single solvothermal strategy for Mn-1,3,5-benzenetricarboxylate MOF. COO groups play a significant role in the insertion/extraction of Li^+ in Mn-BTC MOFs.

Lin et al. [17], with hydrophobic and polar-functionalized MOFs (bimetallic metal organic frameworks (BMOFs)), showed excellent thermal and chemical stability. They have demonstrated that lithium ions are deposited primarily by pores in BMOF. It also contributed to the highly required capacities of nitrogen atoms in BMOF amine groups. The maximum ability of the BMOF could be further increased by the maximum surface area, the pore volume, and the current nitrogen-rich functionality content. The prevailing concentrations were the small particle size and the rapid movement of lithium-ion through extensive open skeleton passages. Most of the MOFs in air and moisture are unstable [18]. In the complicated electrical climate of LIBs, chemical stability in MOFs is suffering from tougher challenges. Thus MOFs are in high demand for thermal, chemical, and structural stability that is critical in practical applications for LIBs cycling performance. Besides, for practical capabilities and rate efficiency, the electrical conductivity of MOFs is critical. For LIBs, MOFs are thus desirable electrode materials with high electrical conductivity and stability.

2.3.2 Sodium-ion batteries

The MOFs of sodium-ion batteries (SIBs) are required and as competitive as the LIBs potential alternatives; these are regarded as one of the ulterior and most promising batteries for advanced energy storage systems thanks to their widespread and low-cost sodium resources [19]. SIBs have a similar part and operating concept to LIBs. Various materials with proper storage of lithium are explored through correspondence with LIBs for efficient sodium storage applications. Nevertheless, due to the kinetics of the sodium-ion input week and the extraction caused by the greater radius size and the considerably heavier sodium atomic mass compared to lithium-ion injection, discovery of new sodium-ion input materials is limited [20]. Sodium ions require a larger tunnel size to disperse. However, the organic compound relative to inorganic compounds has both a structural variety and versatility.

Organic compounds are therefore known as fashionable and desirable materials for SIBs. MOFs are possible SIB electrode materials because they are connected to the metal ions and organic ligands. Wessells et al. [21] have described the bulk PBA nanoparticles for insertion/extraction of sodium and potassium ions into secure and cost-efficient aqueous electrolytes. The open-frame electrode materials are found to offer outstanding costs, extended cycle life, and excellent energy efficiency during the journey. The $Na_xCoFe(CN)_6$ (NaCoHCF) vacant-free nanocrystals by controlling the crystallization techniques and demonstrating a watery electrolyte's sodium-ion storage mechanism are recently prepared. In designing and building Prussian blue analog nanoparticles, $FeFe(CN)_6 \cdot xH_2O$ for flexible carbon fiber paper, Nie et al. [22] have reported substantial progress as a nonbonding cathode material for both organic and aqueous electrolytes. The construction of the electrodes is built with a sound conduction system to succeed in charging the active ingredients, effectively preventing the loss of current weight, making this material possible for the use of SIBs. As proof, the hybrid offers a specific capacity of 82 mA h g^{-1} to a current rate of 0.2 C, excellent cycling efficiency, and rate stability with a retention capacity of about 81.2% after 1000 cycles of charging−discharge. In addition, they reported excellent performance of the $FeFe(CN)_6$/carbon composite, benefiting from its unique architectures of electrode materials. The NaCoHCF nanocrystals displayed an increased specific ability of 130 mA h g^{-1}, consistent with the invertible insertion reaction of 1.7 sodium ions per cluster, using the incredible crystal structure and lattice integrity of the materials obtained.

In addition, NaCoHCF has shown excellent capacity retention over 800 cycles that indicate a reasonable way to improve the cyclability and storage of sodium ions in PBA. The PBA is encouraged by its excellent performance, versatile synthesis, and economical aqueous electrolytes as promising candidates for large-scale energy storage devices. The stable battery voltage cap to only 1.5 V is, however, hindered mainly due to electrochemically

stable water window activity in aqueous electrolytes. Besides, because of its great outlook for productive applications to SIBs, production of new ion intercalations is extremely attractive.

2.3.3 Li−O_2 batteries

The combination of O_2 and lithium-metallic anode is called Li−O_2 batteries. The anode in metal lithium releases lithium ions, and these ions are transmitted through the electrolyte to a cathode that reacts by oxidation (cathode) and then converts it to Li_2O and Li_2O_2 in cathode [23]. Li−O_2 batteries are very appealing, being able to store significant gravimetric energy with a capacity of 11,140 W h kg^{-1}, potentially stimulating the needs of potential applications of next-generation electric cars [24]. Nevertheless, in practical applications, Li−O_2 batteries continue to face numerous difficulties and issues, for example, the excessively lethargic kinetics of the main oxygen reduction and oxygen evolution (ORR and OER) reactions, which not only improve the overall battery efficiency but also increase overall performance and operation.

Besides, Li_2O_2 insoluble discharge product and the future generation of Li_2CO_3 side products are deposited on the cathode of oxygen, which gradually blocks catalytic sites along with electrolyte and oxygen distribution channels and inevitably leads to a considerable overall potential [25]. Thus the specific capacity of the practical Li−O_2 batteries, efficient rates, and high cyclic stability are yet limiting. As a result, the ideal catalog of catalytic materials, including porous structure, high activity and stability, is extremely important to reduce the sluggish kinetics of ORR and OER by channeling cathodes blocking and eventually improving the electrochemical performance of next-generation Li−O_2 batteries [26]. Because of their flexible structure, accessible metal sites, and high porous nature, the MOFs are good catalytic material for improving the cycling efficiency and the rate of Li−O_2 batteries cycles [27]. Wu et al. [28] reported that microspores at 273K under ambient pressure, which were 18 times higher than those pure oxygen concentrations, could increase the efficacy of O_2 in micropores. In comparison to the MOF−Super P cathode and the discharge profile of the Mn-MOF-74/Super P cathode atom, the performance exceeded four times that of 9420 mA h g^{-1} at 25°C under one O_2 atom.

Due to the more accessible metal sites and the excellent porosity of Mn-MOF-74, MOFs based on Li−O_2 material have an excellent electrochemical ability, which significantly increased the concentration of O_2 molecules in the micropores. More interestingly, heterometallic and hollow MOFs have received considerable attention recently, in particular, for the use of gases by catalytic reactions [29]. The hierarchical nanosheet Zn/Ni-MOF-2 is assembled by a scalable and straightforward operation, without any surfactant with hollow nanocubes. The hollow MOFs are fitted with a high specific area,

improved gas absorption/stockage characteristics, professional catalytic-active sites, and, above all, massive vacuum space for handling releases.

It can be used as a highly skilled electrical catalyst for superior Li−O_2 batteries by taking advantage of certain excellent inherent properties of the hollow MOFs. In particular, these hollow MOFs have an abundance of catalytic-active sites that enhance the overall electrical efficiency of Li−O_2 batteries when the active metal nanoparticles/nanocubes are inserted into the micropores. Substantial effects on catalytic properties were demonstrated by structural defects in MOF [30]. This approach, therefore, also provides groundbreaking opportunities to improve the catalytic efficiency of MOFs in Li−O_2 batteries. In short, MOFs materials not only serve as highly efficient nonprecious metallic catalysts in high-performance Li−O_2 batteries but also act as oxygen-reducing membranes when successfully applying Li−O_2 batteries in atmospheric conditions. MOFs with optimized morphology and structures should be used to provide efficiently distributed active catalytic sites, a high surface area, and excellent ionic and electronic conductivity. The combination of these extraordinary properties helps boost electrocatalytic operation of the Li−O_2 battery. In addition, bimetallic MOFs exhibit a distinctive structure and enhanced catalytic performance, which are also possible catalysts for high-performance Li−O_2 batteries.

2.3.4 Li−S batteries

Li−S batteries are currently considered to be one of the best batteries for energy storage because the sulfur cathode has a substantially increased capacity of 1675 mA h g^{-1} compared to conventional cathode materials in piratic LIBs [31]. Sulfur is also small in cost and is accessible naturally and environment-friendly. With metallic Li, Li−S batteries are mounted as an anode and cathode with sulfur. The porous MOFs are highly suitable for sulfur hosts as high specific surface and as large pores [32]. Cakan et al. [33] proposed for the first time in 2011 to use MOF materials in rechargeable Li−S batteries as desirable sulfur-host materials. A substantial improvement in performance retention was observable for Li−S batteries with a MIL-100 (Cr) with a large high specific surface area of 1485 m^2 g^{-1}.

Zhou et al. [34] researched sulfur-based composites with different MOFs for their electrochemical working. They have shown that small-sized MOF hosts are conducive to increased sulfur use. The small apertures with different functions show major affinity in polysulfide anions to the Lewis acid−base interactions that enable long stable cycling. They also found that an improved specific capacity ($>$950 mA h g^{-1}) was achieved when the particle size from ZIF-8 to $<$0.50 C was decreased by 20 nm, while the improved cycling efficiency could be achieved when the particle size of MOF was approximately 200 nm, approximately 75% after 250 cycles at the current density of 0.5 C. Besides, several groups benefit from the rich micropores and mesoporous that

exist in MOFs and better electronic conduction of carbon-based materials in order for potential sulfur hosts to generate hybrid nanocomposites to improve electrochemical efficiency and stable battery cycling. Zhao et al. [35] claimed that MIL-101(Cr) is an ideal host for sweat impregnation with ample microporous spaces and a mesoporous cage. The authors investigated the enhanced conduction network with an excellent physical container in which the graphene nanosheets (GNS) are enfolded on the MIL-101(Cr). The cycle stability and rate efficiency of the GNS-MIL-101(Cr)/S cathode substance were significantly increased thereby.

Selenium (Se), due to the similar chemical properties of sulfide, is currently considered one of the most promising electrode products. Sulfur also resembles lithiation and delithiation chemistry. Se also has a strong 678 mA h g^{-1} gravimetric potential and an outstanding volumetric capacity for general purposes (3253 mA h cm^{-3}) [36]. However, the cathodes of Se have also demonstrated the significant challenges associated with the dissolution of polyselenides, including the low Coulombic efficiency and low cycle performances [37]. The polycarbon−Se composites of porous materials can increase electronic conductivity and prevent Li polyselenides dissolution. For the synthesis of porous carbon materials, MOFs were considered to be a promising precursor. A mesoporous carbon material (Meso-C) has been developed by Lai et al. [38], and synthesized Meso-C displayed good power conductivity, large pores, and excellent specific surface areas.

2.4 Metal-organic frameworks for supercapacitors

Two different families will divide supercapacitors. One is double-layer electrochemical condensers. The second one is a fake condenser. The reaction of redox primarily occurs on the surface of the electrodes [39]. Supercapacitors are equipped with MOFs that are high in surface and tailored to the size of pores. Finally, in Co-based molecules in aqueous electrolytes, Han et al. [11] also found ethical conduct of pseudo-capacitors and retention of loads. The possibility for use in supercapacitor energy storage applications was investigated and developed into a range of different MOF nanocrystals, with various organic functionality, metal ions, and several structure types. The variations in the electrochemical properties of these nanocrystals were evident [40]. Sadly, since MOFs are often electrically isolated, the conductivity issue impedes practical application, resulting in a reduced efficiency rate and a degradation of capability over cycles.

In order to achieve this, the custom design [41] and the implementation of additives have been accomplished for MOFs with a unique structure [42]. A strategy for solving the isolation problem of MOFs by weaving flexibility ZIF-67 crystals/carbon cloth with conductive polyaniline will serve as bridge for the transport of electrons between the external circuit and the internal MOF surface. Wang et al. [43] developed an effective electrochemical

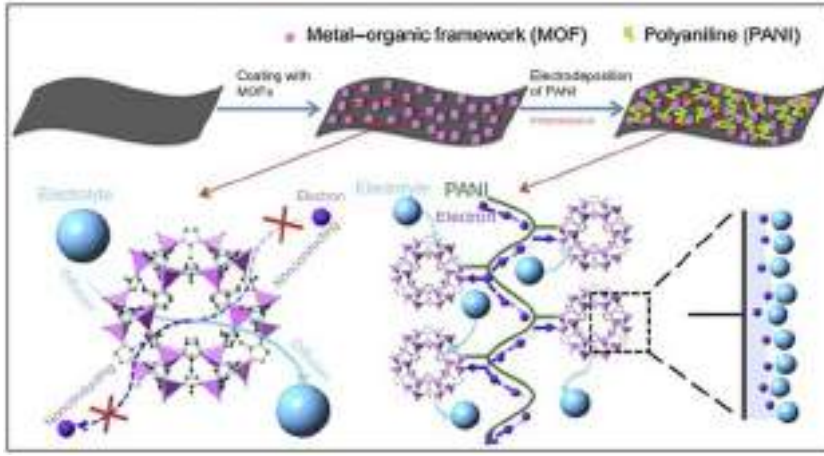

FIGURE 2.2 Synthesis route for polyaniline-ZIF-67-carbon cloth [43].

deposition strategy (Fig. 2.2). Results showed an exceptional capacity of 2146 mF cm^{-2} with a capacity of 10 mV s^{-1}. In addition, the installed flexible symmetric solid-state supercapacitor, the highest reported value of all MOF-based supercapacitors, achieved an excellent capacity of 35 mF cm^{-2} and a power density of 0.833 W cm^{-3} at 0.05 mA cm^{-2}.

As an electrodouble-layer supercapacitor material, reduced graphene oxide (rGO), has received a great deal of attention due to its high electrical conductivity, surface area, and outstanding electrochemical stability. Nevertheless, it has not been examined how MOFs/rGO composites are used in supercapacitors. MOF-5 nondoped with rGO was synthesized with gram size. The addition of a conductive reduces the resistance to charge transfer considerably, resulting in three times the potential as opposed to the algebraic sum of the two-component contributions [44]. Nickel was found to be engaged in an alkaline electrolyte with two-electron, reversible redox shuttles between Ni and Ni $(OH)_2$. A solvothermal method for asymmetric supercapacitor systems showing a high energy density of 36.6 W h kg^{-1} and an excellent cycle life, with just 5% loss of initial ability after 5000 deep cycles, was used for direct growth of Ni-MOFs on the carbon nanotube surface [45].

Due to their simple synthesis, ample octahedral space, and open ionic diffusion channels, it allows for quick and highly reversible intercalation of the alcalino ion, both in aqueous and organically formed electrolytes for storage applications. PBAs were first considered as possible electrode materials for supercapacitors in early 2008 [46]. The $Ni_3(Fe(CN)_6)2H_2O$ nanoscales, prepared in three different electrolytes such as 1 M KNO_3, 1 M $LiNO_3$, and 1 M -$1O_3$, were investigated using a coprecipitation cycle. At 0.2 A g^{-1} in 1 M KNO_3 solution a maximum capacitance of 574.7 F g^{-1}, with excellent capacitance retention following 1000 cycles, was achieved.

As an electrode material for high power condensers, Zhao et al. [47] reported the simple preparation of cobalt hexacyanoferrate (CoHCFe). With a high-speed capability of $>250\ F\ g^{-1}$, a steady rate, and ultrahigh cycling stability, CoHCFe had high capacity retention of 93.5% after 5000 cycles in neutral 0.5 M Na_2SO_4. The impressive work voltage of about 2.4 V, the high energy density of 34.4 W h kg^{-1}, and power capacity of up to 25 kW kg^{-1} could be supplied in combination with a carbon black−modified graphene negative electric to create an asymmetric supercapacitor. The pseudocapacitive behavior of several mesoporous metal hexacyanoferrates, M = Ni^{II}, Co^{II}, and Cu^{II}, was subsequently reported by Yue et al. [48]. Such efficiencies of capacitive materials were close to that of traditional nanostructured textiles hybrid graphene/MnO_2.

In addition, aqueous electrolyte was recorded in phenylboronic acids (PBAs), which showed decent specific capacity and cycling stability. The $Al_{0.2}$CuFe-PBA as a cathode was designed for a high-powered aluminum-ion asymmetric condenser and the anode for carbon activation. The discharge capacity remained above 65% at 1°C when the current density had been set at 100°C (34 mA cm^{-2}). After 1000 cycles at 5°C, the unit still retained about 90% of its original capacity, showing great promising results for future applications in energy storage. Recently, composites consisting of inorganic pseudo-capacity materials and MOFs have been investigated as potentials for electrode supercapacitors [49]. Because of its special ion transport nature, the separator membrane can be used for another important application [50].

2.4.1 Metallic oxides/sulfides for supercapacitors

The use of nanoporous NiO in supercapacitors has been demonstrated [51]. Thermal decomposition of two-dimensional metal−cyanide hybrid coordination polymers synthesized the nanoporous NiO, which was tunable porosity with crystallinity. Salunkhe et al. [52] recorded a two-to-one principle of supercapacitor design with a single precursor imidazole zeolite frame (ZIF-67), where nanoporous carbon and cobalt oxide (Co_3O_4) materials have begun to be selectively prepared by optimizing the conditions of clothing (Fig. 2.3). The produced asymmetric supercapacitors (Co_3O_4/carbon) can be operated with the optimum mass charge at a strong 0.0−1.6 V range, giving a high defined 36 W h kg^{-1} high speed and 8000 W kg^{-1} stated power at 2 A g^{-1}. Simple thermal decomposition of MOFs at a suitable temperature is widely used for the preparation of other metal oxides or carbon-based composites for supercapacitors such as CeO_2 [53], nitrogen-doped carbon/Mn_3O_4 composites [54], hollow Co_3O_4 [55], $ZnCo_2O_4$ nanoparticles [56], $Ni_xCo_3{-}_xO_4$ nanoparticles [57], Fe_3O_4/carbon composite [58], and Cu−Cu_2O−CuO/C composites [59].

A new structure-induced method for the exchange of Ni−Co PBA nanocubes into clearly defined cubic NiS nanoframes [60]. The NiS nanoframe showed enhanced electrochemical properties for condensers and hydrogen

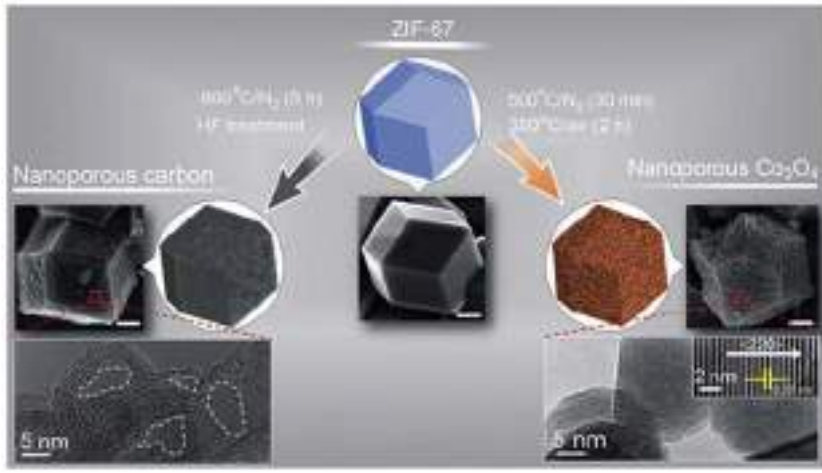

FIGURE 2.3 Preparation process of nanoporous carbon and nanoporous Co_3O_4 from a ZIF-67 polyhedron as the single precursor by optimized thermal treatment [52].

production in an alkaline electrolyte using their structural benefits, including three-dimensional (3D) hollow, porous structures, small nanoparticles size, and good structural resilience. Similarly, the ZIF-67 nanocrystal and 2-methyl imidazole amorphous cobalt sulfide nanocages from environmental conditions were obtained [61], the HKUST-1 porous $Cu_{1.96}S/C$ polyhedra, and sulfur powders and nanoribbons/carbon composites from Cr_2O_3 [62,63].

In addition, nanocytes from ZIF-67 have been synthesized, plus MOFs intend to synthesize binary oxides and composites and templates based on graphene. Using the $Co_3[Co(CN)_6]_2 \cdot nH_2O$ and the Fe(III) replaced MOF-5 (FeIII−MOF-5) as precursors and self-sacrificing templates, the stylish form porous $Co_3O_4/ZnFe_2O_4$ hollow nanocomposites can be prepared by a stepwise process [64]. The synergistic effect between Co_3O_4 and $ZnFe_2O_4$ enables nanocomposites to provide up to 326.7 F g^{-1}, a particular capacity, and 82.5 W h kg^{-1} high power density, at 675 W kg^{-1} strength. The first recording of rGO-wrapped MoO_3 compounds was the easy mixing of graphene oxide MOFs and a different atmosphere with a molybdenum-based process [65].

The resulting rGO/MoO_3 composite has shown excellent electrochemical properties, particularly in all-solid-state flexible supercapacitor systems, for high-performance supercapacitor applications. A high energy density and excellent retention rate of approximately revealed the flexible supercapacitor. For practical use in lightweight storage systems, the probability of a composite is 80% over 5000 cycles with 2 A g^{-1}. Recently produced was the direct carbonization of the MOFs for high-performance supercapacitor applications as another class of promising electrode materials, metal nanoparticles embedded in porous carbon [66].

2.4.2 Carbon for supercapacitors

MOF-derived carbon materials have a high specific pore volume surface [67], ensuring quick ion diffusion and improving the relationship between the electrolytes and the electrodes. These porous carbon materials also make suitable electrode materials promising for supercapacitors. Porous carbon materials produced through the direct carbonization method of MOFs (ZIF-8) [68] demonstrate superior electrochemical efficiency and excellent cycling stability. These synthesized carbon materials are also allowed by the treatment of potassium hydroxide in order to further enhance the exceptionally porous and excellent porous structure of carbon-related MOFs by direct carbonization [69]. The prepared porous carbon materials showed a higher average capacitance of 168 F g^{-1} at a fast scanning rate of 5 mV s^{-1}.

Furthermore, MOFs can also be synthesized explicitly by the nitrogen-doped porous carbon fiber. A highly specific capacitance channeling through a pseudocapacitive effect can significantly enhance the electrical conductivity and wettability of porous carbon materials [70]. A single hierarchical porous nitrogen-doped carbon (HNPC) was developed [71], using an isoretic MOF (IRMOF-3) nitron-containing precursor. The temperature of carbonization can regulate the primary surface area and amount of nitrogen. The resulting HNPC received a superior capacitance of 239 F g^{-1} due to the increased specific surface region, a wide pore volume, and a pseudocapacitance effect thanks to nitrogen doping when IRMOF-3 was measured at 950°C. Salunkhe et al. [72] have recently developed a two-for-one method to propose a supercapacitor, an asymmetric one, where the nanoporous of cobalt oxide (Co_3O_4) and carbon is selectively created by controlling the annealing conditions from a single zeolite imidazolate frame (ZIF-67). Such a nanoporous 3D form offers a highly open surface area for improved electrochemical applications. With increased available energy of about 36 W h kg^{-1} and good specific strength, around 8000 W kg^{-1} at 2 A g^{-1} can be accomplished in a broad range of potential windows (0.0−1.6 V) using synthetic asymmetrical supercapacitors (Co_3O_4/carbon) with optimized mass processing.

The technique to plan incorporation of nitrogen-doped carbon morphology has also recently been identified by Tang et al. [73] as the heart of the shells and as a very graphic carbon extracted from the thermal processing of MOFs, as shown in Fig. 2.4. With a wide surface area, this new carbon composite promises a high nitrogen content and robust graphics construction with the high current density of 2 A g^{-1} disclosing an immense maximum capability of 270 F g^{-1}. The unprecedented durability and excellent electrochemical efficiency have verified the potential benefits of the carbon composite for energy storage technology. The commercially available electrochemical double-layer condensers can be used to increase their specific energy capacity by about 6−7 W h kg^{-1} [74]. For a different type of electronic gadgets and in public transportation systems, electrochemical double-layer condensers can be used.

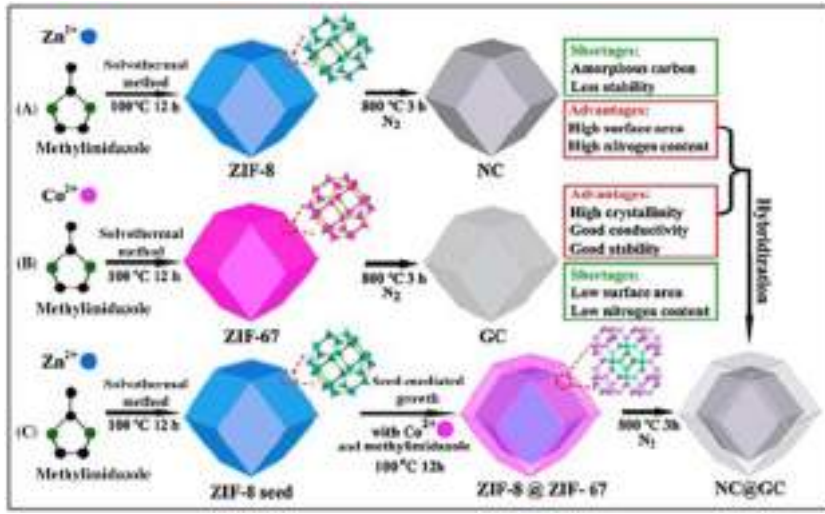

FIGURE 2.4 Preparation of (A) ZIF-8 crystals and NC, (B) ZIF-67 crystals and GC, and (C) core−shell ZIF-8@ZIF-67 crystals and NC@GC [73].

2.5 Conclusion

This chapter analyzes and examines the recent production of LIBs, SIBs, Li−O_2 and Li−S batteries, and supercapacitors based on scientific knowledge and experience that MOFs and their related materials are sufficient electrodes for these energy storages due to their controllable morphology. This chapter also explores the recent development of the MOFs and MOF-related materials. Nevertheless, the practical application of MOFs and MOF-related materials extracted from content remains challenging for further enhance the stability in moisture air that would make it possible to apply MOFs in any setting. MOFs can be processed conveniently and thoroughly in soil. At present, it is to explain the interaction between MOF and polysulfide/polyselenides that is essential for the Li−S and Li−Se batteries ultralong cycling performance.

To the practical application a thorough understanding of the processes used in energy storage by MOFs and their related materials is essential. Thus the demand for fast electric vehicle development, uncrewed aircraft, and portable electronic appliances can be fulfilled by MOFs and their materials. The incorporation of carbon products with the MOFs and their related materials is an excellent strategy to improve their composite electrodes electrical conductivity. While the several forms and morphologies of carbon materials extracted from MOFs display outstanding electrochemical properties, the volumes of their products are not sufficiently large. Its processing methods, excellent design, composition, and reaction chemical should, therefore, be

investigated to achieve highly desired energy storage solutions using inexpensive, efficient manufacturing, and high-performance electrode materials. MOFs and their composites are eventually leading to the production of high-performance batteries and supercapacitors. Improved technological efficiency will also be obtained through the addition of metals, metal oxides, and heteroatoms doping. While there are still many obstacles to be met, work into the rapid development of porous carbon-derived MOFs has opened the path for this new range of energy storage materials to a successful future.

References

[1] Wang L, Han Y, Feng X, Zhou J, Qi P, Wang B. Metal–organic frameworks for energy storage: batteries and supercapacitors. Coord Chem Rev 2016;307:361–81.

[2] Mehtab T, Yasin G, Arif M, Shakeel M, Korai RM, Nadeem M, et al. Metal-organic frameworks for energy storage devices: batteries and supercapacitors. J Energy Storage 2019;21:632–46.

[3] Miller EE, Hua Y, Tezel FH. Materials for energy storage: review of electrode materials and methods of increasing capacitance for supercapacitors. J Energy Storage 2018;20:30–40.

[4] Yu X, Manthiram A. Electrode-electrolyte interfaces in lithium-based batteries. Energy Env Sci 2018;11:527–43.

[5] Jun Y, Qian W, Tong W, Zhuangjun F. Recent advances in design and fabrication of electrochemical supercapacitors with high energy densities. Adv Energy Mater 2014;4:1300816.

[6] Bruce PG, Freunberger SA, Hardwick LJ, Tarascon JM. Li-O_2 and Li-S batteries with high energy storage. Nat Mater 2011;11:19–29.

[7] Nadeem M, Yasin G, Bhatti MH, Mehmood M, Arif M, Dai L. Pt-M bimetallic nanoparticles (M = Ni, Cu, Er) supported on metal organic framework-derived N-doped nanostructured carbon for hydrogen evolution and oxygen evolution reaction. J Power Sources 2018;402:34–42.

[8] Ramesh M, Muthukrishnan M, Khan A, Azam M. Metal-organic-framework-quantum dots (QD@MOF) composites. In: Metal-organic framework composites II. Materials Research Foundations; 2019;49–84.

[9] Janiak C, Vieth JK. MOFs, MILs and more: concepts, properties and applications for porous coordination networks (PCNs). N J Chem 2010;34:2366–88.

[10] Tong M, Liu S, Zhang X, Wu T, Zhang H, Wang G, et al. Two-dimensional CoNi nanoparticles@S,N-doped carbon composites derived from S,N-containing Co/Ni MOFs for high performance supercapacitors. J Mater Chem A 2017;5:9873–81.

[11] Han Y, Qi P, Li S, Feng X, Zhou J, Li H, et al. A novel anode material derived from organic-coated ZIF-8 nanocomposites with high performance in lithium ion batteries. Chem Commun 2014;50:8057–60.

[12] Xia W, Mahmood A, Zou R, Xu Q. Metal–organic frameworks and their derived nanostructures for electrochemical energy storage and conversion. Energy Env Sci 2015;8:1837–66.

[13] Eddaoudi M, Kim J, Rosi N, Vodak D, Wachter J, O'Keeffe M, et al. Systematic design of pore size and functionality in isoreticular MOFs and their application in methane storage. Science 2002;295:469–72.

[14] Wiers BM, Foo ML, Balsara NP, Long JR. A solid lithium electrolyte via addition of lithium isopropoxide to a metal–organic framework with open metal sites. J Am Chem Soc 2011;133:14522–5.

[15] Combarieu GD, Morcrette M, Millange F, Guillou N, Cabana J, Grey CP, et al. Influence of the benzoquinone sorption on the structure and electrochemical performance of the MIL-53 (Fe) hybrid porous material in a lithium-ion battery. Chem Mater 2009;21:1602–11.
[16] Maiti S, Pramanik A, Manju U, Mahanty S. Reversible lithium storage in manganese 1,3,5-benzenetricarboxylate metal–organic framework with high capacity and rate performance. ACS Appl Mater Interfaces 2015;7:16357–63.
[17] Lin Y, Zhang Q, Zhao C, Li H, Kong C, Shen C, et al. An exceptionally stable functionalized metal–organic framework for lithium storage. Chem Commun 2015;51:697–699.
[18] Zhang W, Hu Y, Ge J, Jiang HL, Yu SH. A facile and general coating approach to moisture/water-resistant metal–organic frameworks with intact porosity. J Am Chem Soc 2014;136:16978–81.
[19] Wook KS, Hwa SD, Xiaohua M, Gerbrand C, Kisuk K. Electrode materials for rechargeable sodium-ion batteries: potential alternatives to current lithium-ion batteries. Laser Phys Rev 2012;2:710–21.
[20] Song MK, Park S, Alamgir FM, Cho J, Liu M. Nanostructured electrodes for lithium-ion and lithium-air batteries: the latest developments, challenges, and perspectives. Mater Sci Eng R Rep 2011;72:203–52.
[21] Wessells CD, Peddada SV, Huggins RA, Cui Y. Nickel hexacyanoferrate nanoparticle electrodes for aqueous sodium and potassium ion batteries. Nano Lett 2011;11:5421–5.
[22] Nie P, Shen L, Pang G, Zhu Y, Xu G, Qing Y, et al. Flexible metal–organic frameworks as superior cathodes for rechargeable sodium-ion batteries. J Mater Chem A 2015;3:16590–7.
[23] Imanishi N, Yamamoto O. Rechargeable lithium–air batteries: characteristics and prospects. Mater Today 2014;17:24–30.
[24] Zhang P, Zhao Y, Zhang X. Functional and stability orientation synthesis of materials and structures in aprotic Li-O_2 batteries. Chem Soc Rev 2018;47:2921–3004.
[25] Xue H, Mu X, Tang J, Fan X, Gong H, Wang T, et al. A nickel cobaltite nanoparticle-decorated hierarchical porous N-doped carbon nanofiber film as a binder-free self-supported cathode for nonaqueous Li-O_2 batteries. J Mater Chem A 2016;4:9106–12.
[26] Kwak WJ, Lau KC, Shin CD, Amine K, Curtiss LA, Sun YK. A Mo_2C/carbon nanotube composite cathode for lithium–oxygen batteries with high energy efficiency and long cycle life. ACS Nano 2015;9:4129–37.
[27] Morozan A, Jaouen F. Metal organic frameworks for electrochemical applications. Energy Env Sci 2012;5:9269–90.
[28] Wu D, Guo Z, Yin X, Pang Q, Tu B, Zhang L, et al. Metal–organic frameworks as cathode materials for Li–O_2 batteries. Adv Mater 2014;26:3258–62.
[29] Atsushi N, Xiong C, Xiao F, Xuesong D, Zhaoqi G, Donglin J. A squaraine-linked mesoporous covalent organic framework. Angew Chem Int Ed 2013;52:3770–4.
[30] Olesia K, Ignacio L, Li X, Heshmat N, Max K, Bauke AH, et al. Multifunctional, defect-engineered metal–organic frameworks with ruthenium centers: sorption and catalytic properties. Angew Chem Int Ed 2014;53:7058–62.
[31] Ariel R, Elena M, Gregory S, Doron A, Arnd G, Francois CF. Review on Li-sulfur battery systems: an integral perspective. Adv Energy Mater 2015;5:1500212.
[32] Xu G, Ding B, Pan J, Nie P, Shen L, Zhang X. High performance lithium-sulfur batteries: advances and challenges. J Mater Chem A 2014;2:12662–76.
[33] Cakan RD, Morcrette M, Nouar F, Davoisne C, Devic T, Gonbeau D, et al. Cathode composites for Li–S batteries via the use of oxygenated porous architectures. J Am Chem Soc 2011;133:16154–60.

[34] Zhou J, Li R, Fan X, Chen Y, Han R, Li W, et al. Rational design of a metalorganic framework host for sulfur storage in fast, long-cycle Li-S batteries. Energy Env Sci 2014;7:2715–24.

[35] Zhao Z, Wang S, Liang R, Li Z, Shi Z, Chen G. Graphene-wrapped chromium MOF (MIL-101)/sulfur composite for performance improvement of high-rate rechargeable Li-S batteries. J Mater Chem A 2014;2:13509–12.

[36] Cui Y, Abouimrane A, Lu J, Bolin T, Ren Y, Weng W, et al. (De)lithiation mechanism of Li/SeSx (x = 0–7) batteries determined by in situ synchrotron X-ray diffraction and X-ray absorption spectroscopy. J Am Chem Soc 2013;135:8047–56.

[37] Chao L, Yujie Z, Yang W, Jingjing W, Chunsheng W. Carbonized polyacrylonitrile-stabilized SeSx cathodes for long cycle life and high power density lithium ion batteries. Adv Funct Mater 2014;24:4082–9.

[38] Lai Y, Gan Y, Zhang Z, Chen W, Li J. Metal-organic frameworks-derived mesoporous carbon for high performance lithium–selenium battery. Electrochim Acta 2014; 146:134–41.

[39] Salanne M, Rotenberg B, Naoi K, Kaneko K, Taberna PL, Grey CP, et al. Efficient storage mechanisms for building better supercapacitors. Nat Energy 2016;1:16070.

[40] Choi KM, Jeong HM, Park JH, Zhang YB, Kang JK, Yaghi OM. Supercapacitors of nanocrystalline metal-organic frameworks. ACS Nano 2014;8:7451–7.

[41] Tan Y, Zhang W, Gao Y, Wu J, Tang B. Facile synthesis and supercapacitive properties of Zr-metal organic frameworks (UiO-66). RSC Adv 2015;5:17601–5.

[42] Yang J, Xiong P, Zheng C, Qiu H, Wei M. Metal–organic frameworks: a new promising class of materials for a high performance supercapacitor electrode. J Mater Chem A 2014;2:16640–4.

[43] Wang L, Feng X, Ren L, Piao Q, Zhong J, Wang Y, et al. Flexible solid-state supercapacitor based on a metal–organic framework interwoven by electrochemically-deposited PANI. J Am Chem Soc 2015;137:4920–3.

[44] Banerjee PC, Lobo DE, Middag R, Ng WK, Shaibani ME, Majumder M. Electrochemical capacitance of Ni-doped metal organic framework and reduced graphene oxide composites: more than the sum of its parts. ACS Appl Mater Interfaces 2015;7:3655–64.

[45] Wen P, Gong P, Sun J, Wang J, Yanga S. Design and synthesis of Ni-MOF/CNT composites and rGO/carbon nitride composites for an asymmetric supercapacitor with high energy and power density. J Mater Chem A 2015;3:13874–83.

[46] Chen J, Huang K, Liu S, Hu X. Electrochemical supercapacitor behavior of Ni 3(Fe $(CN)_6)_2(H_2O)$ nanoparticles. J Power Sources 2009;186:565–9.

[47] Zhao F, Wang Y, Xu X, Liu Y, Song R, Lu G, et al. Cobalt hexacyanoferrate nanoparticles as a high-rate and ultra-stable supercapacitor electrode material. ACS Appl Mater Interfaces 2014;6:11007–12.

[48] Yue Y, Zhang Z, Binder AJ, Chen J, Jin X, Overbury SH, et al. Hierarchically super structured Prussian blue analogues: spontaneous assembly synthesis and applications as pseudocapacitive materials. ChemSusChem 2015;8:177–83.

[49] Gao Y, Zhang W, Tan Y, Gao J, Tang B, Zhao J. Synthesis of nickel carbonate hydroxide@zeolitic imidazolate framework-67 ($Ni_2CO_3(OH)_2$@ZIF-67) for pseudocapacitor applications. J Appl Electrochem 2015;45:541–7.

[50] Meng JP, Liu XL, Xu QJP. Crystal structure of diaquabis(3-(3,5-dibromophenyl)-5-(pyridin-2-yl)-1,2,4-triazol-4-ido-κ^2 N, N′) nickel(II) mono hydrate, $C_{26}H_{20}Br_4N_8NiO_3$. Dalton Trans 2015;44:5407–16.

[51] Zakaria MB, Hu M, Salunkhe RR, Pramanik M, Takai K, Malgras V, et al. Controlled synthesis of nanoporous nickel oxide with two-dimensional shapes through thermal decomposition of metal−cyanide hybrid coordination polymers. Chem Eur J 2015;21:3605−12.
[52] Salunkhe RR, Tang J, Kamachi Y, Nakato T, Kim JH, Yamauchi Y. Asymmetric supercapacitors using 3D nanoporous carbon and cobalt oxide electrodes synthesized from a single metal-organic framework. ACS Nano 2015;9:6288−96.
[53] Maiti S, Pramanik A, Mahanty S. Extraordinarily high pseudocapacitance of metal organic framework derived nanostructured cerium oxide. Chem Commun 2014;50:11717−20.
[54] Wang K, Shi X, Lu A, Ma X, Zhang Z, Lua Y, et al. High nitrogen-doped carbon/Mn_3O_4 hybrids synthesized from nitrogen-rich coordination polymer particles as supercapacitor electrodes. Dalton Trans 2015;44:151−7.
[55] Zhang YZ, Wang Y, Xie YL, Cheng T, Lai WY, Pang H, et al. Porous hollow Co_3O_4 with rhombic dodecahedral structures for high-performance supercapacitors. Nanoscale 2014;6:14354−9.
[56] Chen S, Xue M, Li Y, Pan Y, Zhu L, Zhang D, et al. Porous $ZnCo_2O_4$ nanoparticles derived from a new mixed-metal organic framework for supercapacitors. Inorg Chem Front 2015;2:177−83.
[57] Chen S, Xue M, Li Y, Pan Y, Zhu L, Qiu S. Rational design and synthesis of $Ni_xCo_{3-x}O_4$ nanoparticles derived from multivariate MOF-74 for supercapacitors. J Mater Chem A 2015;3:20145−52.
[58] Meng W, Chen W, Zhao L, Huang Y, Zhu M, Huang Y. Porous Fe_3O_4/carbon composite electrode material prepared from metal-organic framework template and effect of temperature on its capacitance. Nano Energy 2014;8:133−40.
[59] Khan IA, Badshah A, Nadeem MA, Haider N, Nadeem MA. A copper based metal-organic framework as single source for the synthesis of electrode materials for high-performance supercapacitors and glucose sensing applications. Int J Hydrogen Energy 2014;39:19609−20.
[60] Yu XY, Yu L, Wu HB, Wen X, Lou D. Formation of nickel sulfide nanoframes from metal−organic frameworks with enhanced pseudocapacitive and electrocatalytic properties. Angew Chem Int Ed 2015;127:5421−5.
[61] Jiang Z, Lu W, Li Z, Ho KH, Li X, Jiao X, et al. Synthesis of amorphous cobalt sulfide polyhedral nanocages for high performance supercapacitors. J Mater Chem A 2014;2:8603−6.
[62] Wu R, Wang DP, Kumar V, Zhou K, Law AWK, Lee PS. MOFs-derived copper sulfides embedded within porous carbon octahedra for electrochemical capacitor applications. Chem Commun 2015;51:3109−12.
[63] Ullah S, Khan IA, Choucair M, Badshah A, Khan I, Nadeem MA. A novel Cr_2O_3-carbon composite as a high performance pseudo-capacitor electrode material. Electrochim Acta 2015;171:142−9.
[64] Hu XW, Liu S, Qu BT, You XZ. Starfish-shaped Co_3O_4/$ZnFe_2O_4$ hollow nanocomposite: synthesis, supercapacity, and magnetic properties. ACS Appl Mater Interfaces 2015;7:9972−81.
[65] Cao X, Zheng B, Shi W, Yang J, Fan Z, Luo Z, et al. Reduced graphene oxide—wrapped MoO_3 composites prepared by using metal-organic frameworks as precursor for all-solid-state flexible supercapacitors. Adv Mater 2015;27:4695−701.
[66] Wu MS, Hsu WH. Nickel nanoparticles embedded in partially graphitic porous carbon fabricated by direct carbonization of nickel-organic framework for high-performance supercapacitors. J Power Sources 2015;274:1055−62.

[67] Zhang J, Wang Y, Xiao K, Cheng S, Zhang T, Qian G, et al. N-doped hierarchically porous carbon derived from heterogeneous core-shell ZIF-L(Zn)@ZIF-67 for supercapacitor application. N J Chem 2018;42:6719–26.

[68] Chaikittisilp W, Hu M, Wang H, Huang HS, Fujita T, Wu KCW, et al. Nanoporous carbons through direct carbonization of a zeolitic imidazolate framework for supercapacitor electrodes. Chem Commun 2012;48:7259–61.

[69] Qingfei W, Wei X, Wenhan G, Li A, Dingguo X, Ruqiang Z. Functional zeolitic-imidazolate-framework-templated porous carbon materials for CO_2 capture and enhanced capacitors. Chem Asian J 2013;8:1879–85.

[70] Xu G, Han J, Ding B, Nie P, Pan J, Dou H, et al. Biomass-derived porous carbon materials with sulfur and nitrogen dual-doping for energy storage. Green Chem 2015;17:1668–74.

[71] Jeon JW, Sharma R, Meduri P, Arey BW, Schaef HT, Lutkenhaus JL. In situ one-step synthesis of hierarchical nitrogen-doped porous carbon for high performance supercapacitors. ACS Appl Mater Interfaces 2014;6:7214–22.

[72] Salunkhe RR, Tang J, Kamachi Y, Nakato T, Kim JH, Yamauchi Y. Asymmetric supercapacitors using 3D nanoporous carbon and cobalt oxide electrodes synthesized from a single metal–organic framework. ACS Nano 2015;9:6288–96.

[73] Tang J, Salunkhe RR, Liu J, Torad NL, Imura M, Furukawa S, et al. Thermal conversion of core–shell metal–organic frameworks: a new method for selectively functionalized nanoporous hybrid carbon. J Am Chem Soc 2015;137:1572–80.

[74] Wang Y, Shi Z, Huang Y, Ma Y, Wang C, Chen M, et al. Supercapacitor devices based on graphene materials. J Phys Chem C 2009;113:13103–7.

This page intentionally left blank

Chapter 3

Titanium-based metal-organic frameworks for photocatalytic applications

A. Ratnamala[1], G. Deepthi Reddy[2], M. Noorjahaan[2], H. Manjunatha[1], S. Janardan[1], N. Suresh Kumar[3], K. Chandra Babu Naidu[4], Anish Khan[5,6] and Abdullah M. Asiri[5,6]

[1]Department of Chemistry, GITAM School of Science, GITAM (Deemed to be University), Bangalore, India, [2]Department of Chemistry, Palamuru University, Mahbubnagar, India, [3]Department of Physics, JNTUA, Anantapuramu, India, [4]Department of Physics, GITAM (Deemed to be University), Bangalore, India, [5]Chemistry Department, Faculty of Science, King Abdulaziz University, Jeddah, Saudi Arabia, [6]Center of Excellence for Advanced Materials Research, King Abdulaziz University, Jeddah, Saudi Arabia

3.1 Introduction

Since the first ever discovery of Ni-based complexes such as $Ni(CN)_2(NH)_3 \cdot C_6H_6$ done by Hofmann and Küspert in year 1897, an expedited advancement was seen in the utilization of metal-organic framework (MOF) for over about two centuries [1]. These frameworks are developed by connecting various metals with ligands, thus producing 1D, 2D, or 3D lattices and these are porous structures. One great advantage of these structures is that they could be tailored as per the need by choosing combinations of linker molecules and metal nodes. MOFs endorsed their third decade thorough studies in the beginning of 1990s [2–4]. In 20 years the class of MOF was developed unquestionably, captivating researchers across various fields along with nano-engineering [5–7], coordination chemistry [8–10], storage of gas and separation [11–16], optoelectronics and optics [17–21], catalysis [22–28], storage of energy and conversion [29–32], sensing [33–35], and biomedical science [36–39]. With respect to the chemical nature of the MOFs, the eventual purpose of the chemists is to develop MOFs through the different elements in a predesigned and well-controlled approach. Thousands of MOFs have been reported, which are constructed by using divalent or trivalent ions of third group *d*-block transition metals, third group *p*-block metals [40–44], and lanthanides [45,46]. However, the development of MOFs using

Metal-Organic Frameworks for Chemical Reactions. DOI: https://doi.org/10.1016/B978-0-12-822099-3.00003-4

high-valent metal ions remains as a challenge till now [47,48]. In view point of photocatalytic applications, the MOFs behave as light harvesting sites and, upon photoexcitation, trigger the metal clusters of MOFs and enhance the photocatalytic activity.

Metal cations such as Cu, Zn, Co, and Ni aid in the formation of numerous open frameworks with exceptional porosity but are not stable in the presence of water. The increase in the metal cation charge well balanced with its polarization power and charge over ionic radius are the effective strategies to intensify the bond strength of cation and ligand thus increasing the stability of coordination polymer. Although the trivalent cations such as Cr, Fe, and Al have succeeded in deriving water-stable porous MOFs, the tetravalent-derived MOFs are still found deficient and this is because of highly reactive nature of the cations causes precipitation of their oxides or leads to the formation of crystallized and amorphous polymers. However, one conspicuous exception is the Zr.

3.1.1 The Ti-chemistry

Creating inexhaustible, economical, and biological assets has become one of the real fundamental concerns so as to conquer the issue of the dubious conventional energy sources. Mirroring the characteristic photosynthesis is by all accounts an exceptionally better option. Ti dioxide, TiO_2, is viewed as one of the best photocatalysts (PCs) because of its effectiveness, chemical stability, high supply, and rather low harmfulness. In addition, MOFs, among different materials, have been demonstrated to be extremely encouraging sacrificial precursors holding properties such as very high surface area, excellent dispersion toward the active regions, and long-range ordering for heterogeneous catalysis, and can be synthesized along with diversified metal oxides adopting various thermal treatment strategies.

Ti is located simply above Zr in the chemical table. With a smaller range of Ti^{4+} high affinity toward oxygen in contrasting with Zr^{4+} makes it extremely stable. Such steadiness is acquired by titanium-based MOFs (Ti-MOFs) built from Ti-oxo-carboxylate secondary building units (SBUs) with solid Ti−O linkages. The most prominent characteristics of Ti are its multifunctionality, redox action, photochemical property, and bioaffinity [49]. The work in these lines has drawn attention mainly due to the sequential reasons such as plausibility to tune the gap between conduction band and valence band, variation, and alteration of ligands [50−53].

3.2 Preparation of titanium-based metal-organic frameworks and the selection of precursors

Manufacture of Ti-MOFs is the bottleneck point in MOFs' field. It has been reported that Ti-MOFs are found rarely when compared to other metals.

Such circumstance is presumably because of the uniqueness of Ti cations and relating Ti combinations, which are utilized as Ti source in MOFs' combination. Ti(IV) is found to be stable at room temperature, while Ti(III) upon exposure to air immediately oxidizes back to Ti(IV), though it is stable in reductive state. Because of the low electronegativity and solid polarizing capacity, Ti^{4+} is exceptionally reactive and hydrolyzes in humid conditions. This extraordinary reactivity during the MOFs' amalgamation causes quick and wild nucleation and erratic framework development, consequently leading to the development of amorphous polymers and clusters. Thus the reactivity of the Ti precursors is vital in Ti-MOFs amalgamation that concentrates more on the choice of solution blend, fixation, time and heat, and, if required, modulator addition and technological processes such as microwave, ultrasonication, along with the source of Ti have also been taken into consideration.

Ti precursors utilized in MOFs amalgamation include hydrous TiO_2, Ti-alkoxides, Ti-chlorides, Ti-oxo-groups, and Ti edifices. Hydrous form of TiO_2 was utilized earlier for the synthesis of few Ti natural phosphonates, such as MIL-25 [54] and MIL-22 [55]. Compounds like this, however, are made out of profoundly requested frameworks, are less organically derived, and do not have open porosity, taking after inorganic phosphates of Ti than the MOFs. Outstandingly, MIL-91 was produced with hydrous forms of TiO_2 and *N*,*N*′-piperazinebismethylenephosphonic acid in aqueous conditions [56]. This is the first Ti-MOF with tancoite architecture reported by Serre and coworkers and is proved as the promising candidates for CO_2 capture (Fig. 3.1) [56]. The constraint of hydrous form of TiO_2 along with high temperature of $>200^{\circ}C$, time (3−4 days), and response media of 40% hydrofluoric acidseriously blocked its use in MOFs' manufacturing.

Ti-chlorides are scarcely utilized in Ti-MOFs' amalgamation because of their hydrolysis discharging hydrochloride fumes in surrounding conditions [57]. One of the exemptions is $TiCl_3$, utilized in the synthesis of Ti(III)-Ti-MIL-101, where Ti(IV) species could not be used because of imbalanced charge, and ionic range. Due to its reductive nature, Ti^{3+} needs gentle activity during the preparation, and if exposed to air it would prompt failure of the synthesis [58]. Mason and his coworkers excelled in the synthesis of $Ti_3O(OEt)(bdc)_3(DMF)_2$ (Ti-MIL-101) using $TiCl_3$ and terepthalic acid in N_2 protection by a method of solvothermal technique the first MOF with Ti (III) centers [58].

Commonly used source of Ti in the making of MOFs are Ti-alkoxides and are preferred over $TiCl_4$ owing to the difficulties in handling/controlling $TiCl_4$. Presence of alkoxy bunches with steric obstructions halts the Ti^{4+} hydrolysis and the reactivity can be adjusted by altering the alkoxy chain. Apart from alkoxides, other bidentate ligands such as carboxylates, diketonates, catecholates, and phosphonates also show the stability in humid conditions (Fig. 3.2) [58].

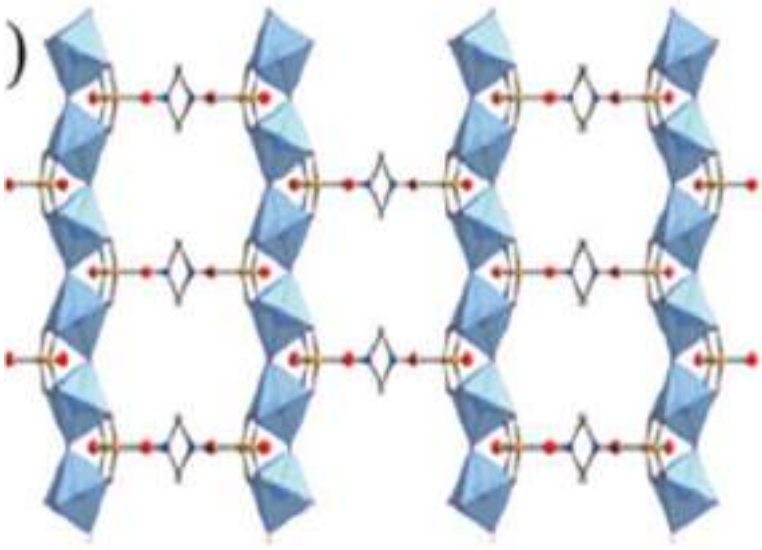

FIGURE 3.1 MIL-91 or $Ti^{IV}O(H_2\text{-}L)\text{-}nH_2O$ (n E 4.5) with $L = O_3P{-}CH_2{-}NC_4H_8N{-}CH_2{-}PO_3$ or *N,N′*-piperazinebismethylenephosphonate. *Copyright permission is taken from Serre C, Groves JA, Lightfoot P, Slawin AMZ, Wright PA, Stock N, et al., Synthesis, structure and properties of related microporous* N,N′*-piperazinebismethylenephosphonates of aluminum and titanium. Chem Mater 2016;18:1451−7.*

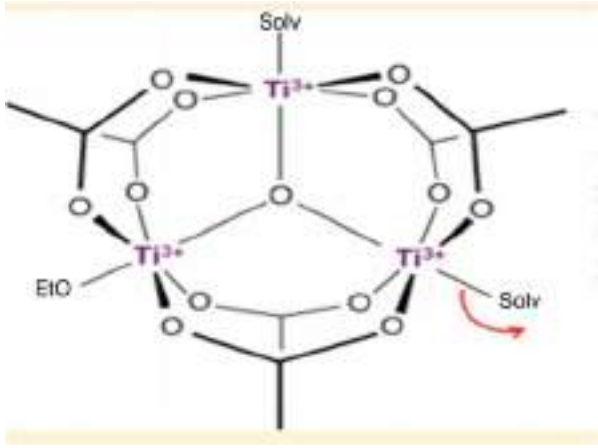

FIGURE 3.2 Presentation of proposed composition of the Ti_3O clusters after heating at 150°C vacuum. *Copyright permission is taken from Mason JA, Darago L.E, Lukens WW, Long JR. Synthesis and O2 reactivity of a titanium(III) metal-organic framework. Inorg Chem 2015;54:10096−104.*

Usage of six-faced Ti-clusters or $Ti_nO_m(OR/Cl) \times (L)y$ is a method to mediate the reaction rate during the MOFs' arrangement [59–61]. On account of the abilities of Ti, an assortment of Ti-groups with various size, coordination numbers and geometry could be chosen as building material of MOFs. For instance, in the amalgamation of PCN-22, $Ti_6O_6(iOPr)_6(abz)_6$ was utilized as source of Ti, however Ti_6-oxo group have been metamorphed into a different Ti_7O_6-oxo SBU units in the resultant 3D-MOFs [61]. Porous coordination network is abbreviated as PCN. It is prepared from titanium oxocluster and a linker molecule tetrakis (4-carboxyphenyl)-porphyrin by solvothermal method in the presence of benzoic acid. Similarly, a hexametric form of Ti-group was protected as SBU within the arrangement of MOF-901 and MOF-902 [62,63]. These are prepared by combining the approaches of MOFs and covalent organic frameworks (COFs) using imine condensation reactions (Fig. 3.3) [63].

3.2.1 Direct synthesis

Direct synthesis includes traditional hydro/solvothermal application, yet the most generally utilized strategy for Ti-MOFs synthesis. Organic ligands

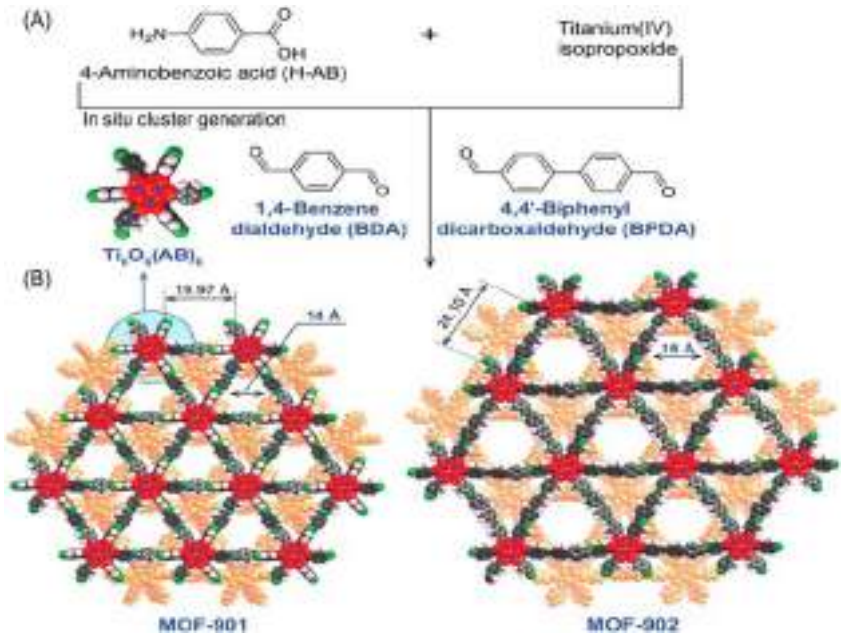

FIGURE 3.3 Structures of MOF-901 and MOF-902. *MOF*, Metal-organic frameworks. *Copyright permission is taken from Nguyen HL, Vu TT, Le D, Doan TLH, Nguyen VQ, Phan NTS. Titanium–organic framework: engineering of the band-gap energy for photocatalytic property enhancement. ACS Catal A 2017;7:338–42.*

along with precursors of Ti are mixed in appropriate solvents and stacked into a steel autoclave lined with Teflon or airtight Pyrex containers, and with internal pressure it was heated with a reaction period of few hours to days. In the crystallinity of end products, solvents have a significant influence, and frequently the best choice of solvents must be established through hit-and-trial method. The concentration of reactants is an additional aspect in determining the MOFs' morphology. In one case, general change in the starting solution concentration, microcrystals of amine-functionalized MIL-125 (NH_2-MIL-125) can be framed to octahedron from circular plate [64].

3.2.2 Solvothermal synthesis

Initially, hydrothermal reactions were utilized for the development of oxalatotitanates [65] and titanophosphates [54–56]. Serre et al., using solvothermal reactions, obtained Ti-MOF as well as MIL-125, the first porous and crystalline and carboxylate Ti-MOF [66]. Titanium isopropoxide on reaction with terephthalic acid, an organic ligand along with solvent mixtures [*N*,*N*-dimethyl formamide (DMF) and methanol] at 423K for 15 hours effectively yielded the MIL-125 as white powdered crystals. The amine-functionalized MIL-125 and likewise processed under solvothermal reaction with the replacement of terephthalic acid to 2-aminoterephthalic acid [67].

Various Ti-salicylate MOFs were reported by solvothermal techniques via $Ti(iOPr)_4$ and 2,5-dihydroxyterephthalic acid. Red and hexagonal crystals of Ti-MOF, NTU-9, have been orchestrated by Zhang and coworkers by means of solvothermal techniques of $Ti(iOPr)_4$ with H_4DOBDC in acid, which were actually stable in water, air, and basic, natural solvents (Fig. 3.4) [83]. While Devic and coworkers researched NTU-9 framework by altering the trial parameters, four Ti-MOFs such as NTU-9, MIL-168, MIL-169, and MIL-167 have been effectively developed via solvothermal responses in between precursors of Ti and the ligands of H_4DOBDC [60].

Yaghi and coworkers reported 3D broadened Ti-catecholate MOF effectively utilizing solvothermal techniques at about 180°C and 4 hours, by joining the Ti particle and catecholate linker, 2,3,6,7,9,11-hexahydroxytriphenylene [69]. Zhou et al. synthesized PCN-22 that is porphyrin based with a metal source of $Ti_6O_6(OiPr)_6(abz)_6$ and tetrakis(4-carboxyphenyl) porphyrin as a linker molecule in the presence of benzoic acid and *N*,*N*-DEF (diethylformamide) (Fig. 3.5) [61]. By utilizing a strong organometallic Ti precursor, dicyclopentadienyl Ti(IV) dichloride, De Vos et al. demonstrated Ti-MOF, COK-69, from solvothermal method of $[Cp_2Ti^{IV}Cl_2]$ using *trans*-1,4-cyclohexanedicarboxylic acid in solvent dimethyl formamide along with acetic acid at 110°C for about 2 days in an inert and oxidizing environment [70]. Long et al. developed Ti(III) form of MIL-101 by solvothermal method using theterephthalic acid and $TiCl_3$ at 120°C in solvents' anhydrous DMF and ethanol medium in N_2 atmosphere for about 18 hours [58].

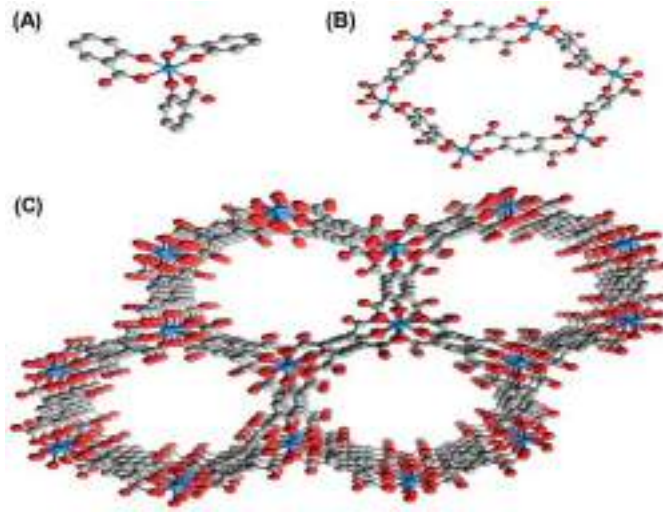

FIGURE 3.4 (A) The coordination mode of the Ti atom in NTU-9. (B) The coordination of the DOBDC ligand in NTU-9. (C) 1D channels of NTU-9 viewed along the *c*-axis. Color representation: red, O; gray, C; blue, Ti. H atoms are removed for clarity. *Copyright permission is taken from Gao J, Miao J, Li P-Z, Teng WY, Yang L, Zhao Y, et al. A p-type Ti(iv)-based metal–organic framework with visible-light photo-response, Chem Commun 2014;50:3786–8.*

Along with Ti-complexes as main inorganic parts in Ti-MOFs, few of the bimetallic Ti-MOFs were developed by means of solvothermal technique. Chun et al. reported orange precious stones of ZTOF-1 from Zn $(NO_3)_2 \cdot 6H_2O$, $Ti(OiPr)_4$ and 2-hydroxyterephthalic acid in solvent dimethyl formamide. When zinc nitrate and $Ti(iOPr)_4$ are brought together, an orange precious stones of zinc–Ti, ZTOF-2, were synthesized from with 3-hydroxy-2,7-naphthalenedicarboxylic acid and 1,4-diazabicyclo-[2.2.2]octane in solvent dimethyl formamide [71,72]. Therefore solvothermal techniques are mostly utilized for fabrication of Ti-MOFs.

3.2.3 Ultrasonic and microwave-assisted synthesis

Apart from solvothermal strategies, ultrasonic- [73] or microwave- [74,75] assisted techniques have been advantageously used to fabricate porous Ti-MOFs, which aid in crystallization at low temperature requiring a short span of time. In addition, Ti-MOFs developed by these methods possess a distinctive molecular sizes and shapes that influence their nature. Kim et al. reported the microwave-assisted synthesis of NH_2-MIL-125 and reduced the reaction time from 16 to 1 hour by solvothermal technique [74]. Through ultrasonication, the development and breakdown of air pockets developed within the solution led to high pressure and temperature therefore bring about very quick temperature changes, which aid in developing fine

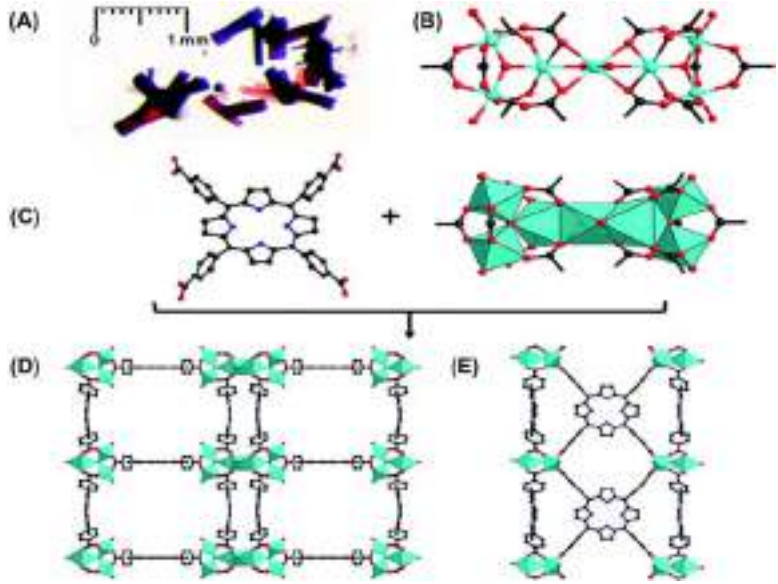

FIGURE 3.5 (A) Microscope image of PCN-22 crystals. (B) Structure of the Ti_7O_6 cluster. (C) Structures of tetratopic TCPP linker (left) and 12-connected Ti_7O_6 cluster (right). Structural views of PCN-22 along (D) *a* axis and (E) *b* axis. *PCN*, Porous coordination network, TCPP, tetrakis(4-carboxyphenyl)porphyrin. *Copyright permission is taken from Yuan S, Liu T-F, Feng D, Tian J, Wang K, et al. A single crystalline porphyrinic titanium metal−organic framework, Chem Sci 2015;6:3926−30.*

crystallite forms. The high shear rates can prompt the development of energized atoms, encouraging the disintegration of the initial components and the process of bond breakage. Han and coworkers have documented that NH_2-MIL-125 developed through ultrasonic solvothermal technique that showed uniform size dissemination of 300 nm [73]. Utilizing solvothermal/ultrasonic and microwave consolidated technique, a perfect Ti-MOF film on porous TiO_2 was effectively synthesized [76].

3.2.4 The method of coordination−covalent combination

In spite of the fact that the vast majority of the documented Ti-MOFs developed by direct synthesis, this methodology shows serious concerns with respect to the Ti-chemistry in controlling the final structure and unwanted products. In majority of the cases the significant results are observed in novel Ti-clusters. The control over the structure to some extent was achieved by usage of Ti-oxoclusters. Joining the MOFs and COFs is a best strategy to maintain the desired structure, which does not disturb the Ti−O bonding in the clusters [77,78]. Nguyen et al. displayed the first and foremost case of such a technique [62]. A Ti-cluster for which structure is already known

along with the amine carboxyl ligands, $Ti_6O_6(iOPr)_6(abz)_6$, was utilized as source of Ti. This involves in situ generation of an amine-functionalized titanium oxocluster that was linked with benzene-1,4-dialdehyde (BDA) using imine condensation reactions, a pattern in the COFs' development, they made an attempt to fabricate Ti-MOFs with already known structure and topology.

Constrained by the lower dissolvability of acquired cluster in a solvent assortment, only amorphous solids have been resulted in the entire process. The in situ blend along with BDA has led to Ti-MOF, MOF-901. In this way, while altering from benzene 1,4-dialdehyde to 4,4′-biphenyldicarboxaldehyde (BPDA), the MOF-902 was achieved by using the similar strategy [63] in a single reaction setup. Development of covalent and coordination bonds could continue at the same time without intruding on one another, permitting the in situ development of Ti-groups along with framework congregation. The different complexes of Ti-groups and extenders may show the advancements in Ti-MOFs' field, particularly by taking in the functionality and connectivity that can be joined over the extenders.

3.2.5 Method of postsynthetic cation exchange

In general, the conventional methods for MOF synthesis result in unpredicted structures. While the cation exchange method is a valuable technique for the arrangement of Ti-MOFs with desired pore and topography [79,80]. This method can also avoid highly reactive nature and Ti precursors with exceptional hydrolysis. The metal ion exchange was readily occurred in Zr-MOF, UiO-66, and was reported to be a better option for Ti-MOF, which is relatively difficult to prepare and reported as the main model for the post-Ti-transfer by Cohen [81]. After the cation exchange, it was checked that more than 90% of the MOFs' particles consist of Ti(IV), with around 38 wt.% Ti (IV) in the taken sample. They also observed that Cr(III) ion exchange was not seen in MIL(101) due to kinetic inertness of the chromium.

There are four components that impact this strategy's success: the first one being the cations in the MOFs that could not be reduced through Ti(III), the metal sites that are open should be within and this could aid in the speeding up of metathesis rate, the metal cations' coordination environment in the MOFs must be similar to Ti(III), and the ligand−metal bonds in the MOFs must be easy for metal ion exchange process. In all, the Ti ion exchange process gives a new approach to produce novel Ti-MOFs with already known structures.

3.2.6 Vapor-assisted crystallization method

Though Ti-MOFs have displayed greater potential as a form of heterogeneous catalysts, the main constraint is the surface area or intrinsic micropores

for the passage of large reactant molecules (>7 Å) However, developing mesopores in the structure of MOFs is one of the solutions. Hicks brought a method called chelating-free vapor-assisted crystallization method on microporous metal organic framework MIL-125. By this method the mesoporosity was generated by using cetyltrimethyl ammonium bromide (Fig. 3.6) [82], which acts as the capping agent and useful in the confinement of the precursors. In the prepared materials, two types of pores are resulted. The formation of micropores was due to the breakdown of the matrix in the solvent during the solvothermal activity; however, cetyl trimethyl ammonium bromide restrained the growth of particle and aided in the formation of mesopore between the nanoparticles (NPs) of MOFs. The resultant MOFs displayed oxidation of dibenzothiophene by using TBHP (tertbutylhydroperoxide) because of the existence of availability of active metal sites.

3.2.7 Synthesis of titanium-based metal-organic framework composites

Composite nanomaterials were prepared to increase the dispersion of metals such as Ag [83,84], gold [73], platinum [85], and palladium [86–88], and also other nonmetal NPs such as Ni [89] were effectively embedded into Ti-MOFs. For example, Pd NPs were anchored into NH_2-MIL-125 by means of

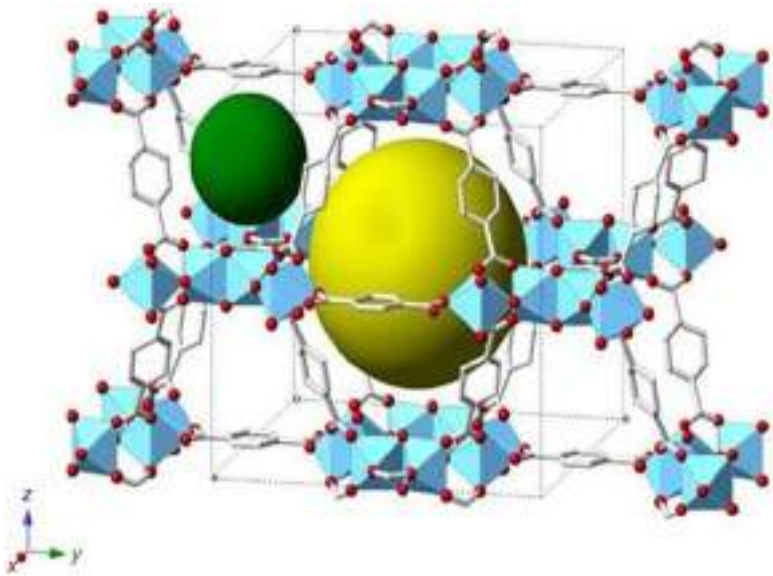

FIGURE 3.6 MIL-125 structure. *Copyright permission is taken from McNamara ND, Hicks JC. Chelating agent-free, vapor-assisted crystallization method to synthesize hierarchical microporous/mesoporous MIL-125 (Ti), ACS Appl Mater Inter 2015;7:5338–46.*

photodeposition strategy by Yamashita [87], which showed enhanced reactivity. Meantime, the MoS_2 sheets, CdS, Ag_2S, and CuS quantum dots are accumulated onto the MIL-125 and a set of Ti-MOF complexes were developed in UV light. These complexes have been used as PC for the reduction of Cr (VI) in visible light [90]. For instance, graphitic carbon nitride, reduced form of graphene, and TiO_2 was combined with NH_2-MIL-125 showed to enhance photoelectric, photocatalytic, optical, and electrochemical activities.

3.3 The structure of titanium-based metal-organic frameworks

Though the construction of Ti-MOFs was extensively studied, documentation on 3D frameworks with Ti-based structures and porosity are still limited. Based on the research reports, ligands possess greater directing effect toward the resultant Ti-oxo SBUs. Based on the type of ligand, it is classified as shown in Fig. 3.7. In Fig. 3.8 [72], the trigonal prism pinwheel network of ZTOF-2 is shown.

3.3.1 Photocatalytic application of titanium-based metal-organic frameworks

Ever since the discovery of photocatalytic activity of TiO_2 by Fujishima and Honda [91], TiO_2 is known to be the benchmark PC with TiO_2 because of low

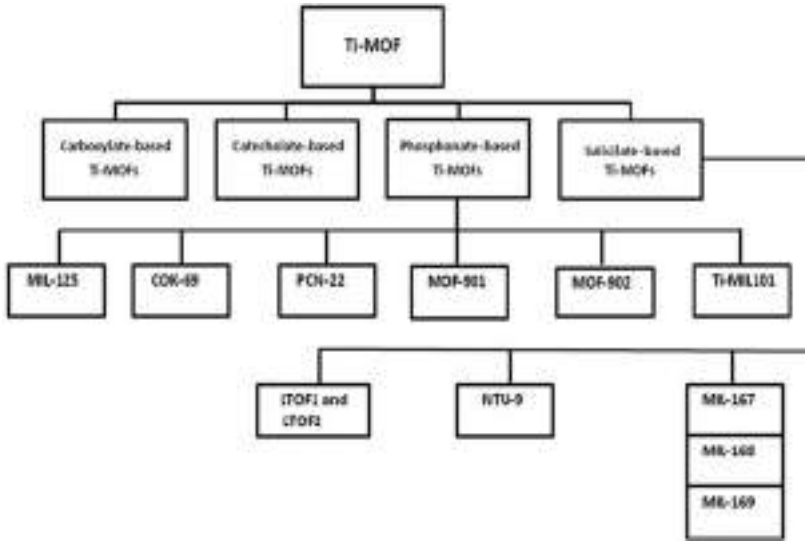

FIGURE 3.7 Classification of Ti-MOFs. *Ti-MOFs*, Titanium-based metal-organic frameworks.

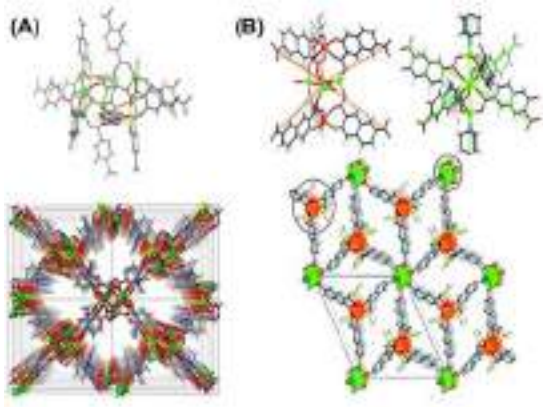

FIGURE 3.8 (A) Zn_6Ti_2 SBU (upper) and (B) 6-connecting trigonal prism and 8-connected pinwheel SBUs (upper) and overall network viewed along the *c*-axis (lower) for ZTOF-2. *Copyright permission is taken from Hong K, Chun H. Unprecedented and highly symmetric (6,8)-connected topology in a porous metal−organic framework through a Zn−Ti heterometallic approach. Chem Commun 2013;49:10953−55.*

cost, stability, and nontoxicity, but it is active only in UV light [49]. It is hard to gather the photons in visible light region with different issues of lower conversion rate of solar energy, simple agglomeration, and reduced recyclability constraining their wide applications as shown in Fig. 3.9 [92−94]. By introducing Ti particles into the MOFs, agglomeration could be minimized. Apart from different MOFs, Ti-MOFs possess photoactivity; greater porosity makes them profoundly encouraging materials in photocatalytic oxidation, H_2 production, CO_2 reduction, photocatalyst sensors, and degradation of pollutant molecules as shown in diagram next. The MIL-125 and NH_2-MIL-125, the main carboxylate Ti-MOFs, paved the way for making the new MOFs and photochemical reactions [66]. Spontaneous photochromic effect discovered over NH_2-MIL125 due to photoreduction of Ti^{4+} to Ti^{3+}.

Bandgap is a key feature of any PC, minimal energy required for an assimilated photon to develop e−h pair that could transfer to the active centers and promote redox reactions. MIL-125, with an optical bandgap of c.3.6 eV, was photoactive only in UV radiation [66,95]. This bandgap of 3.6 eV was brought down in MIL-125 with incorporation of mono-aminated and diaminated ligands with an exploratory bandgap of 1.3 eV (shifted to IR region) (Fig. 3.10) [63].

Hendon consolidated exploratory and computational techniques to study the impact of ligand functionalization on the bandgap [96]. Postalteration, the amino gathering of NH_2-MIL-125, is another way to fine-tune the bandgap. By utilizing methyl viologen as the acceptor for electron and *N*,*N*,*N*,*N*-tetramethyl-*p*-phenylene-diamine as the donor, the separation of charges was observed by García et al. in the case of NH_2-MIL-125 [97].

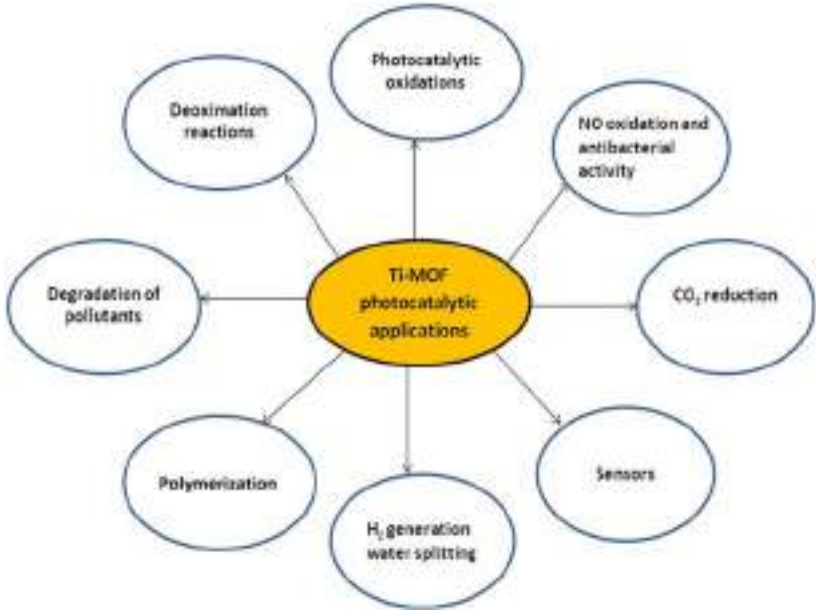

FIGURE 3.9 Photocatalytic applications of Ti-MOFs. *Ti-MOFs*, Titanium-based metal-organic frameworks.

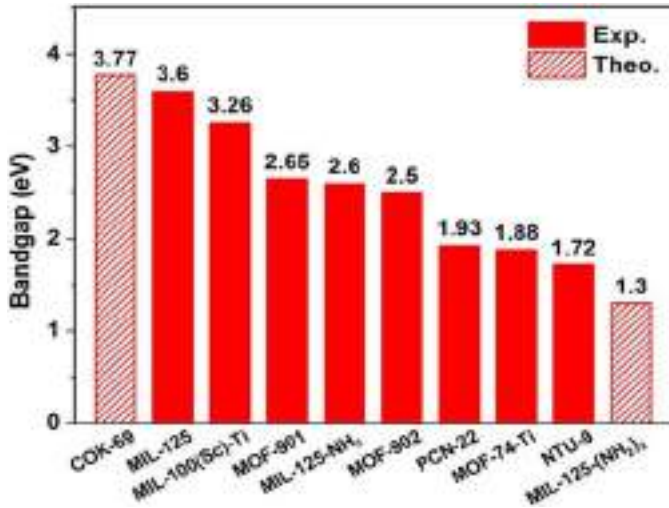

FIGURE 3.10 Bandgap of Ti-MOFs. *Ti-MOFs*, Titanium-based metal-organic frameworks.

MIL-125 analogs' functionalization has shown motivating outcomes, but capability of such methodology is constrained. In spite of that it is not likely simple to additionally bring down the bandgap to beneath 1.3 eV; hence, the development of novel structure and topologies is a significant way to engineer Ti-MOFs' bandgap, yet certainly a more complex one. These novel structures indicated captivating characteristic light retaining properties (Fig. 3.10) [63]. By incorporating aromatic ligands in MOFs, the bandgap can also be reduced as seen in the case of MOF-901 (2.65 eV) [62] and MOF-902 (2.50 eV) [63]. The bandgap was further reduced in PCN-22 up to 1.93 eV [61]. Increasing the catalytically active sites (by incorporating the noble metals such as Pt and Ru) is one of the well-adopted strategies to enhance the activity of PCs. Similarly metals such as Pt, Pd, and Au NPs are encapsulated within the porous frameworks and drastically increase the photocatalytic activity [98,99].

3.4 Photocatalytic oxidation reaction

The TiO_2 incorporated in Ti-MOFs and its composites have gained prominence in heterogeneous light-induced green organic transformations with reusability of catalyst systems and have been utilized for the process of photocatalytic oxidation aromatics, alcohol, alkylphenols, hydrazine, etc. Liu et al. reported the photocatalytic oxidation of amines to imines over UiO-66-NH_2 in the presence of air and anaerobic conditions with decent conversion and high selectivity. They confirmed holes and superoxide ions are responsible for oxidation in the presence of air. These holes also generate nitrogen-centered and carbon-centered radicals that are responsible for selectivity in anaerobic conditions [100]. The same reaction converting amines to imines was carried out using the catalyst NH_2-MIL-125 in oxygen atmosphere, but the difference is in visible range of the spectrum. The obtained selectivities are in the range of 75%−93% using different substituents. The catalyst systems studied were photoactive and reusable up to 3−4 runs without the collapse of the structure of MOFs.

3.4.1 Titanium-based metal-organic framework composites

The metal NPs such as Au, Pd, and Pt decorated on Ti-MOF show improved activity and selectivity as reported by Wu and his group. The M/MIL-125-NH_2 was prepared by postsynthetic method with a size range of 3−9 nm based on metals such as Au, Pd, or Pt. These systems improve selective photocatalytic oxidation activity due to minimizing the e−h recombination and also increasing the photoinduced electron transfer as detailed by Wu [85]. In photocatalytic oxidation taking benzyl alcohol as an example, the conversion is 36%, 32.7%, and 26.4% on the catalysts Au at MIL-125, Pd

over MIL-125, and Pt over MIL-125, respectively, for 4 hours at 298K, which is more than MIL-125 with 18.9% conversion.

Fu et al. reported the photocatalytic activity of Ni-NH_2-MIL-125 in the aromatic alcohol aerobic oxidation and converting them into aldehydes by utilizing O_2 as an oxidant [89]. The Ni metal decorated on NH_2-MIL-125 (Ni particles size 3 nm inside the pores) was found to be more photoactive NH_2-MIL-125, Ni-NH_2-MIL-125, in converting of *p*-methyl benzyl alcohol into its aldehyde from 25.8% to 43.2%. The Ni incorporated in NH_2-MIL-125 was found highly active due to light-induced charge transfer and stable even after the third cycle without any change in crystallinity and porosity as proven from the results of X-ray diffraction and N_2 adsorption and desorption studies.

Xu et al. reported a nano-layered hybrid of UiO-66-NH_2 and graphene prepared by in situ self-assembling and solvothermal method. They have fabricated these materials by sandwiching the graphene oxide with 2-aminoterephthalate acid anchored on pyrene [trimethyl-(2-oxo-2-pyreen-1-yl-ethyl)-ammonium bromide] by electrostatic interaction. The photocatalytic oxidations of 4-methylbenzyl alcohol, 4-nitrobenzyl alcohol, and 4-fluorobenzyl alcohol were taken as examples to investigate these photocatalytic systems in visible light range under milder conditions of temperature [101]. It was indicated that the inclusion of rGO enhanced photocatalytic execution of MOFs regardless of the phenyl ring groups. The enhanced activity is due to separation and transfer of photogenerated electrons and reduces O_2 to O_2^-. In this manner, under visible light the generated e^- rapidly moves on the surface of graphene layer, and O_2 assimilated is broken down to (O_2). Meantime, the aromatic alcohols get transformed through oxidation to carbonium particles by deprotonation.

3.4.2 Photocatalytic NO oxidation and antibacterial activity

Zhu et al. synthesized silver-doped NH_2-MOF(Ti) by microwave-assisted technique using 2-aminoterephthalic acid and tetra-*n*-butyl titanate and then assembling the silver NPs. These materials exhibited excelling activity against NO oxidation under visible light mainly due to the production of electron hole pairs along with the generation of OH and O_2^- active species. The photocatalytic systems were active for many cycles without significant change in morphology and physicochemical properties. These materials also show the antibacterial activity, but further studies on the exact reason for bactericidal action either due to Ag or MOF were not clear [102].

3.4.3 Photocatalytic CO_2 reduction

An alluring methodology for diminishing CO_2 present in air is to build a new material in visible light illumination. Ti-MOFs that are photoactive

become perfect contender for such use. The photocatalytic decrease of CO_2 to formate ion under triethanol amine in visible light on NH_2-MIL-125(Ti) was studied by Li [95]. The fabrication of the amino group was demonstrated vital for the photocatalytic reaction of NH_2-MIL-125 in visible light. The absorption band prompted by the amino clusters firmly took up visible light, producing charge separation. The Ti^{3+} locales function as active regions to diminish CO_2 while triethanolamine (TEOA) acts as both e^- donor and Lewis base, Li et al. examined the photocatalytic reduction of CO_2 is carried out in visible light in saturated CO_2 over Pt, Au/NH_2-MIL-125(Ti) [98]. For the first time it is reported the overflow of H_2 from Pt to the framework of NH_2-MIL-125(Ti) rather than Au/NH_2-MIL-125.

Postsynthetic exchange of Ti(IV) cation into Zr(IV)-based MOF is reported by Lee et al., as a powerful PC for conversion of CO_2 to HCOOH in visible light illumination with the help of 1-benzyl-1,4-dihydronicotinamide and TEOA [103]. When compared with UiO-66(Zr/Ti)-NH_2, 1(Zr/Ti) MOF produced greater number of the Ti site toward CO_2, demonstrating that a larger number of electrons were taken in by Ti than Zr to promote catalytic conversion of CO_2. Furthermore, the presence of $(NH_2)_2$-substituted ligands incredibly upgraded the photocatalytic capacity by producing additional levels of energy for light retention and transfer of charge. Zr/Ti-MOF shows high photocatalytic activity in visible irradiation and exhibits good stability and catalyst recyclability.

3.4.4 Photocatalytic H_2 generation from water splitting

The porosity and unique structure of MOFs makes them interesting candidates for solar light harvesting and photocatalytic water splitting [104]. Horiuchi et al. reported the photocatalytic water splitting activity under visible light over Ti-MOF-NH2, which was prepared by solvothermal synthesis method. Pt was photodeposited on to the Ti-MOF-NH2. Studies have shown that the Ti-MOF PCs can be utilized to advance photocatalytic H2 via splitting of water [104]. Matsuoka and coworkers studied production of H2 from a fluid medium over NH2-MIL-125, Pt/NH2-MIL-125, MIL-125, and Pt/MIL-125 in visible light at wavelengths of 500 nm, where Pt was stacked on to the MOF by the strategy of photodeposition [99]. NH2-MIL-125 displayed somewhat lower photocatalytic reaction, while Pt/MIL-125 demonstrated no activity under similar conditions. In this way, ANH2 clusters in natural ligands and Pt NPs as coimpetuses performed a fundamental job on advancing the photocatalytic hydrogen creation in visible light range. Wu and associates examined H2 production by means of water splitting method over M/MIL-125 complexes arranged from another Ti3+ strategy [85], and with Pt/MIL-125-PD arranged by photodeposition technique, Pt/MIL-125 (30.2) was 80% greater, demonstrating that the encapsulation strategy essentially affects the synergist properties of metal NPs/Ti-MOF complexes.

Other nonnoble metals combined Ti-MOF complexes were likewise used for photocatalytic water splitting and H2 production. Nasalevich revealed a productive and completely recyclable synergist framework, cobaloxime-determined Ti-MOF PC, for H2 advancement through water in within visible light range [105]. The presentation of chemically dynamic sites prompted a 20-overlay of H2 activity when compared to NH2-MIL-125. The occurrence of high-turn Co(II) species enhances the photocatalytic action of the entire framework. The Ni/NH2-MIL-125 composite containing an exceptionally dynamic proton-decreasing nickel(II) impetus [Ni(dmobpy)(2-mpy)2] was arranged and examined as H2 developing impetus from water split by Meyer [106]. It was demonstrated that, in 5 v/v% TEOA conditions, the measure of delivered hydrogen over Ni/NH2-MIL-125 composite was higher than that of NH2-MIL-125, Ni species. In 2 v/v% water and acetonitrile blend, the Ni/NH2-MIL-125 indicated 28 mol H2 g (Ni)1 h1 frequency with greater firmness photocatalytic reactivity.

As of late, researches likewise demonstrated that, utilizing MIL-167, H2 production was distinguished from the method of water splitting in UV illumination [60]. The purpose behind no reactant activity in visible light was not yet completely comprehended. More profound examinations are as yet required.

3.4.5 Photocatalytic degradation of organic pollutants

MOFs were considered as another class of PC in ecological fields like pollutant decontamination [107−110]. P-type semiconductor NTU-9 showed a bandgap of 1.72 eV, as contrasted the bandgap of TiO_2 (3.2 eV for anatase), the absorption of NTU-9 demonstrated clear shift. In visible light range ($\lambda > 420$ nm), NTU-9 showed exceptional activity and photostability in the degradation of rhodamine B and methylene blue solution and completed after 80 and 20 minutes, respectively [68].

A few strategies have been created to make novel PCs dependent on Ti-MOFs for pollutant disintegration, which consists of postmanufactured changes and metal NPs loading [83,84]. For example, Ag NP-MIL-125(Ti) microspheres (Ag/MIL-125) were produced [84], where the Ag NPs were scattered on the outside of MIL-125 with a uniform size of around 40 nm as shown in reference [84]. Modified Ag/MIL-125 displayed magnificent visible photocatalytic activity and by photogenerated radical scavengers $[O_2]^{\bullet-}$ and $^{\bullet}OH$ from encompassing O_2 and hydroxyl bunches serve as a fundamental reactive species in the photodisintegration of RhB. In visible light illumination, RhB was totally degraded in 40 minutes by 3 wt.% Ag NPs, and the photocatalytic activity of the composite was higher than P25. In addition, the PC can be reused at any rate multiple times without clear loss in photocatalytic activity.

Ag/rGO/MIL-125 ternary forms, showed efficient photocatalytic degradation of RhB under visible light illumination [111]. The photocatalytic action

of Ag/rGO/MIL-125 marginally diminished because of the loss of PC in reusing photocatalytic tests, demonstrating the strength of Ag/rGO/MIL-125 for the degradation of RhB. The Ag NPs act as efficient electron pool and rGO acts as electron transporter and gatherer, thus prompting effective charge separation. NH2-MIL-125(Ti) proposed by Abdelhameed et al. effectively improved the photocatalytic nature and steadiness by modified Cr(III) and Ag NPs into the perfect MOF, where the amino clusters were treated with acetylacetone [83]. In visible range, MB was totally degraded with Cr-MIL-125-AC and Ag-MIL-125-AC, where Cr(III) acts as hole acceptor and Ag NPs as the e acceptor, advancing the partition of hole–e pairs and expanding the recombination time. The modified Ag-MIL-125-AC was an efficient PC in degradation of methylene blue with a consistent rate of 0.10 min1 up to five cycles. NH2-MIL-125(Ti) proposed by Abdel Hameed et al. [116] effectively improved the photocatalytic nature and steadiness by modified Cr(III) and Ag NPs into the perfect MOF, where the amino clusters were treated with acetylacetone [107].

Not the same as metal-doped PCs, other heterostructure Ti-MOF complexes are detailed, for example, g-C_3N_4/MIL-125 [112], core shell In_2S_3/MIL-125 [113], and BiOBr/NH2-MIL-125 [114], and utilized as effective PCs for the photodisintegration of colors, pesticides and antitoxins in visible light. Critically, these 2D layers were found with photocatalysis in visible light. The improved photocatalytic execution in visible light could frequently be credited to the $Ti^{3+}-Ti^{4+}$ intervalence e transfer and synergistic impact, bringing about higher effectiveness of photogenerated e sets during the photocatalytic response. Besides, N-doped anatase/rutile-blended stage TiO_2 (A/R N-TiO_2) was effectively synthesized by means of the pyrolysis of MIL-125 and toughening at various temperature in ammonia environment [115,116]. The disintegration of RhB for A/R N-TiO2, acquired for next cycle of processing at 500°C, rises to 93% in 240 minutes, which is greater than TiO2 (32%) in visible light.

3.4.6 Photocatalytic polymerization

Nguyen et al. reported the visible light responsive MOF-901 and MOF-902 for polymerization reactions. Upon the incorporation of imine linking units MOF-902 was able to absorb light at red shift region and correspondingly there is lowering of the bandgap energy. The enhancement in the photocatalytic activity was studied by the polymerization of methyl methacrylate, benzyl methacrylate, and styrene in the presence of initiator α-bromophenyl acetate. The resultant polymers has high molecular weight of 31,465 g mol^{-1} and yield as high as 84% with uniform distribution (low polydispersity index of 1.11). Because of its high conjugated system of imine building units, MOF-902 stabilizes the free radicals and enhances the polymerization reaction than compared to MOF-901 and other commercial catalysts (P 25-TiO_2),

other MOFs of similar bandgap [62]. These PCs showed the reusability up to three cycles without significant loss of activity.

3.4.7 Photocatalytic deoximation reaction

Abedi and Morsali reported used Plueronic 123 as a structure directing agent for the synthesis of NH_2-MIL-125 and were named SMIL-NH_2 by adopting solvothermal technique [117]. These MOFs has very high surface area and photocatalytic property of SMIL-NH_2 was assessed for deoximation reactions. The catalytic activity of these systems is much higher than compared to other photoactive systems with 100% yields that were produced for the conversion of acetophenone oxime into corresponding ketone in 10 hours. The ring activating groups such as methyl and methoxy groups attached to benzene ring were found to be more active and reactions completed within 6 and 4.5 hours. These photocatalysts can be easily recyclable and reused without losing the photoactivity.

3.4.8 Photocatalytic sensors

Apart from the various photocatalytic applications, MOF-based sensors [118,119] have shown excellent potential for detecting a range of organic molecules and ions (as well as detecting radiation). Though many of the MOFs are reported as sensors, achieving the high selectivity of analyte and stability always remains a challenge. Pioneering work in this field was carried out by Li and coworkers and they prepared $[Zn_2(oba)_2(bpy)]$ dimethyl acetamide and used for the detection of nitro aromatic compounds. Coming to the Ti-MOFs, Hu et al. used NH_2-MIL-125(Ti) along with carbon paste electrodes for the detection of Mn^{2+} ions in tea samples. They have used cathodic stripping cyclic voltammetry method for photooxidation activity of Mn^{2+} at pH of 8.5 using buffer 0.04 M NH_3−NH_4Cl in visible light irradiation. The peak current are proportional to Mn^{2+} ion concentration with detection limit of 4.0×10^{-9} M and results are comparable with that of atomic adsorption spectroscopy method. The reusability of the sensors were also checked for 100 cycles showing the same peak heights and peak intensities and stable for long-term storage at room temperature for 30 days and retained 96.5% of its response [120]. The same group has detected clethodim herbicide in soil samples using the same MOFs but used the glassy carbon electrode. They quantified the herbicide concentration range from 0.2 to 25 $\mu mol\ L^{-1}$ and 10 $nmol\ L^{-1}$ detection limit. These photoelectrochemical sensors showed good repeatability, reproducibility, and good long-term stability for 7 days in humidity environment at 4°C retaining 94.1% original response [121].

3.5 Conclusion

Ti-MOFs are the most captivating yet testing points in MOF investigation, particularly their high chemical, thermal stability, and photocatalytic properties. Despite many years of endeavors bringing about the Ti-group coordination science, the path breaking advancement of Ti-MOF research has been recently developed with the disclosure of MIL-125 is a breakthrough in this arena. In this current chapter, various aspects of the chemistry of Ti-MOF such as structures and strategies, photocatalytic uses of Ti-MOFs and their complexes, along with oxidation, CO_2 decrease, hydrogen advancement, pollutant degradation, photocatalytic sensors, polymerization, and deoximation were detailed. Ti-MOFs have displayed diversity in their structures in different MOFs. They exhibit special topologies, amassed from remarkable SBUs, and different natural ligands such as salicylates, organodiphosphonates, catecholates, and carboxylates.

One major challenge is its synthesis in Ti-MOF research, because of the poly-condensation of Ti^{4+} that results in production of unwanted byproducts. Factors such as time, solvent composition, temperature, modulators, and surfactants also impact the porosity, structure, morphology, and crystallinity of resultant products. Solvothermal synthesis is the mostly used method for the synthesis of Ti-MOFs. Hence, we pen down three strategies for the development of novel Ti-MOFs: oxidation and high valence metathesis method [98,104]. Nonetheless, cation exchange could be known as the beneficial method to produce Ti-MOFs, where the majority of them could not be produced by solvothermal synthesis. The second is the process of isoreticular expansion and the next is the covalent−coordination combined strategy. By making use of these strategies along with other techniques, target-oriented synthesis Ti-MOFs is possible with chemical functionality and predesigned topology. Using different methods, it may be conceivable to accomplish union of Ti-MOFs with preplanned morphology and artificial usefulness, while an initial step should be Ti-MOF with three-dimensional interconnected instead of two-dimensional layered structures.

Ti-MOF complexes show incredible focal points in the applications of photocatalysis particularly in visible light. By and large, the nearness of metal NPs as cocatalysts, incorporated into Ti-MOFs, assumes a significant job in upgrading photocatalytic exercises. Linking with other materials with reasonable bandgap is achievable to bring down the gap and boost the photocatalytic movement. For example, semiconductors such as TiO_2, metal sulfides, and g-C_3N_4 as the support for Ti-MOFs offer a proficient electron hole separation, photon capture, and electron transport because of their synergistic impacts.

As far as photocatalytic uses of Ti-MOF are concerned, the one of a kind Ti^{4+}/Ti^{3+} reversible redox transformation upon visible light along with chemical or thermal dependability on fluid and natural frameworks make

Ti-MOFs incredible in a wider scope of photo-driven synergist redox responses. The Ti-MOF bandgap can be modified by functionalization of the ligands and advancements in the synthesis of novel structures. The synergist effect can be enhanced by coupling with exceptionally dynamic species such as NPs and graphene. Among the little available Ti-MOFs, MIL-125 and NH_2-MIL-125 have grabbed much attention because of their high stability and photocatalytic activity. Noteworthy, Ti-MOFs, photocatalytic applications ought to be additionally reached out to other Ti-MOFs. In the interim, novel Ti-MOFs and Ti-MOF-based complexes with very much characterized texture and low bandgap ought to be investigated [122,123].

References

[1] Hofmann KA, Küspert F. Verbindungen von Kohlenwasserstoffen mit Metallsalzen. Anorg Chem 1897;15:204.

[2] Yaghi OM, Li G, Li H. Selective binding and removal of guests in a microporous metal−organic framework. Nature 1995;378:703−6.

[3] Furukawa H, Cordova KE, O'Keeffe M, Yaghi OM. The chemistry and applications of metal-organic frameworks. Science 2013;341:1230444.

[4] Zhao Y. Emerging applications of metal−organic frameworks and covalent organic frameworks. Chem Mater 2016;28:8079−81.

[5] Morris RE, Brammer L. Coordination change, lability and hemilability in metal−organic frameworks. Chem Soc Rev 2017;46:5444−62.

[6] Furukawa S, Reboul J, Diring S, Sumida K, Kitagawa S. Structuring of metal−organic frameworks at the mesoscopic/macroscopic scale. Chem Soc Rev 2014;43:5700−34.

[7] Lu W, Wei Z, Gu ZY, Liu T-F, Park J, et al. Tuning the structure and function of metal−organic frameworks via linker design. Chem Soc Rev 2014;43:5561−93.

[8] Doherty CM, Buso D, Hill AJ, Furukawa S, Kitagawa S, Falcaro P. Using functional nano- and microparticles for the preparation of metal−organic framework composites with novel properties. Acc Chem Res 2014;47:396−405.

[9] Chen L, Luque R, Li Y. Controllable design of tunable nanostructures inside metal−organic frameworks. Chem Soc Rev 2017;46:4614−30.

[10] Carne A, Carbonell C, Imaz I, Maspoch D. Nanoscale metal−organic materials. Chem Soc Rev 2011;40:291−305.

[11] Adil K, Belmabkhout Y, Pillai RS, Cadiau A, Bhatt PM, Assen AH, et al. Gas/vapour separation using ultra-microporous metal−organic frameworks: insights into the structure/separation relationship. Chem Soc Rev 2017;46:3402−30.

[12] Ramsahye NA, Trens P, Shepherd C, Gonzalez P, Trung TK, Ragon F, et al. The effect of pore shape on hydrocarbon selectivity on UiO-66(Zr), HKUST-1 and MIL-125(Ti) metal organic frameworks: insights from molecular simulations and chromatography. Microporous Mesoporous Mater 2014;189:222−31.

[13] Liu J, Thallapally PK, McGrail BP, Brown DR, Liu J. Progress in adsorption-based CO_2 capture by metal−organic frameworks. Chem Soc Rev 2012;41:2308−22.

[14] Li P-Z, Wang X-J, Zhang K, Nalaparaju A, Zou R, Zou R, et al. "Click"-extended nitrogen-rich metal−organic frameworks and their high performance in CO_2-selective capture. Chem Commun 2014;50:4683−5.

[15] Li P-Z, Zhao Y. Nitrogen rich porous adsorbents for CO_2 capture and storage. Chem Asian J 2013;8:1680–91.
[16] Barea E, Montoro C, Navarro JAR. Toxic gas removal – metal–organic frameworks for the capture and degradation of toxic gases and vapours. Chem Soc Rev 2014;43:5419–30.
[17] Corma A, García H, Llabrés Xamena FX. Engineering metal organic frameworks for heterogeneous catalysis. Chem Rev 2010;110:4606–55.
[18] Liu J, Chen L, Cui H, Zhang J, Zhang L, Su C-Y. Applications of metal–organic frameworks in heterogeneous supramolecular catalysis. Chem Soc Rev 2014;43:6011–61.
[19] Sun L-B, Liu X-Q, Zhou H-C. Design and fabrication of mesoporous heterogeneous basic catalysts. Chem Soc Rev 2015;44:5092–147.
[20] Wang S, Wang X. Multifunctional metal–organic frameworks for photocatalysis. Small 2015;11:3097–112.
[21] Zhang T, Lin W. Metal–organic frameworks for artificial photosynthesis and photocatalysis. Chem Soc Rev 2014;43:5982–93.
[22] Rogge SMJ, Bavykina A, Hajek J, Garcia H, Olivos-Suarez AI, et al. Metal–organic and covalent organic frameworks as single-site catalysts. Chem Soc Rev 2017;46:3134–84.
[23] Liang J, Liang Z, Zou R, Zhao Y. Heterogeneous catalysis in zeolites, mesoporous silica, and metal–organic frameworks. Adv Mater 2017;29:1701139.
[24] Medishetty R, Zareba JK, Mayer D, Samoc M, Fischer RA. Fabrication of zinc-dicarboxylate- and zinc-pyrazolate-carboxylate-framework thin films through vapour–solid deposition. Chem Soc Rev 2017;46:4976–5004.
[25] Hu Z, Deibert BJ, Li J. Luminescent metal–organic frameworks for chemical sensing and explosive detection. Chem Soc Rev 2014;43:5815–40.
[26] Stavila V, Talin AA, Allendorf MD. MOF-based electronic and opto-electronic devices. Chem Soc Rev 2014;43:5994–6010.
[27] Sheberla D, Sun L, Blood-Forsythe M, Er S, Wade CR, Brozek CK, et al. High electrical conductivity in Ni_3(2,3,6,7,10,11-hexaiminotriphenylene)2, a semiconducting metal–organic graphene analogue. J Am Chem Soc 2014;136:8859–62.
[28] Kim WY, Kim KS. Tuning molecular orbitals in molecular electronics and spintronics. Acc Chem Res 2010;43:111–20.
[29] Campbell MG, Liu SF, Swager TM, Dinca M. Chemiresistive sensor arrays from conductive 2D metal–organic frameworks. J Am Chem Soc 2015;137:13780–3.
[30] Stassen I, Burtch N, Talin A, Falcaro P, Allendorf M, Ameloot R. An updated roadmap for the integration of metal–organic frameworks with electronic devices and chemical sensors. Chem Soc Rev 2017;46:3185–241.
[31] Chen B, Xiang S, Qian G. Metal–organic frameworks with functional pores for recognition of small molecules. Acc Chem Res 2010;43:1115–24.
[32] Chen X, Li C, Gratzel M, Kostecki R, Mao SS. Nanomaterials for renewable energy production and storage. Chem Soc Rev 2012;41:7909–37.
[33] Mahmood A, Guo W, Tabassum H, Zou R. Metal-organic framework-based nanomaterials for electrocatalysis. Adv Energy Mater 2016;6:1600423.
[34] Wang H, Zhu Q-L, Zou R, Xu Q. Metal-organic frameworks for energy applications. Chem 2017;2:52–80.
[35] Xia W, Mahmood A, Zou R, Xu Q. Metal–organic frameworks and their derived nanostructures for electrochemical energy storage and conversion. Energy Environ Sci 2015;8:1837–66.

[36] Horcajada P, Gref R, Baati T, Allan PK, Maurin G, Couvreur P, et al. Metal–organic frameworks in biomedicine. Chem Rev 2012;112:1232–68.
[37] Lian X, Fang Y, Joseph E, Wang Q, Li J, et al. Enzyme–MOF (metal–organic framework) composites. Chem Soc Rev 2017;46:3386–401.
[38] Horcajada P, Chalati T, Serre C, Gillet B, Sebrie C, et al. Porous metal–organic-framework nanoscale carriers as a potential platform for drug delivery and imaging. Nat Mater 2010;9:172–8.
[39] McKinlay AC, Morris RE, Horcajada P, Férey G, Gref R, et al. BioMOFs: metal–organic frameworks for biological and medical applications. Angew Chem Int Ed 2010;49:6260–6.
[40] Devic T, Serre C. High valence 3p and transition metal based MOFs. Chem Soc Rev 2014;43:6097–115.
[41] Nasalevich MA, Hendon CH, Santaclara JG, Svane K, van der Linden B, et al. Electronic origins of photocatalytic activity in d0 metal organic frameworks. Sci Rep 2016;6:23676.
[42] Erxleben A. Structures and properties of Zn(II) coordination polymers. Coord Chem Rev 2003;246:203–28.
[43] Yan Y, Yang S, Blake AJ, Schröder M. Studies on metal–organic frameworks of Cu(II) with isophthalate linkers for hydrogen storage. Acc Chem Res 2014;47:296–307.
[44] Crystal engineering of Cu-containing metal–organic coordination polymers under hydrothermal conditions. In: Lu JY, editor. Coord Chem Rev, 246. 2003. p. 327–47.
[45] Cui Y, Chen B, Qian G. Lanthanide metal-organic frameworks for luminescent sensing and light-emitting applications. Coord Chem Rev 2014;273–274:76–86.
[46] Pagis C, Ferbinteanu M, Rothenberg G, Tanase S. Lanthanide-based metal organic frameworks: synthetic strategies and catalytic applications. ACS Catal 2016;6:6063–72.
[47] Bon V, Senkovskyy V, Senkovska I, Kaskel S. Zr(IV) and Hf(IV) based metal–organic frameworks with reo-topology. Chem Commun 2012;48:8407–9.
[48] Schaate A, Roy P, Godt A, Lippke J, Waltz F, Wiebcke M, et al. Modulated synthesis of Zr-based metal–organic frameworks: from nano to single crystals. Chem Eur J 2011;17:6643–51.
[49] Schneider J, Matsuoka M, Takeuchi M, Zhang J, Horiuchi Y, Anpo M, et al. Understanding TiO_2 photocatalysis: mechanisms and materials. Chem Rev 2014;114:9919–86.
[50] Fang W-H, Wang J-F, Zhang L, Zhang J. Titanium–oxo cluster based precise assembly for multidimensional materials. Chem Mater 2017;29:2681–4.
[51] Fang W-H, Zhang L, Zhang J. A 3.6 nm Ti_{52}–oxo nanocluster with precise atomic structure. J Am Chem Soc 2016;138:7480–3.
[52] Liu J-X, Gao M-Y, Fang W-H, Zhang L, Zhang J. Bandgap engineering of titanium–oxo clusters: labile surface sites used for ligand substitution and metal incorporation. Angew Chem Int Ed 2016;55:5160–5.
[53] Santiago Portillo A, Baldoví HG, García Fernandez MT, Navalón S, Atienzar P, et al. LiC Ti as mediator in the photoinduced electron transfer of mixed-metal NH_2–UiO-66(Zr/Ti): transient absorption spectroscopy study and application in photovoltaic cell. J Phys Chem 2017;121:7015–24.
[54] Serre C, Férey G. Hybrid open frameworks. 8. Hydrothermal synthesis, crystal structure, and thermal behavior of the first three-dimensional titanium(IV) diphosphonate with an open structure: $Ti_3O_2(H_2O)_2(O_3P–(CH_2)–PO_3)_2 \cdot (H_2O)_2$, or MIL-22. Inorg Chem 1999;38:5370–3.

[55] Serre C, Férey G. Hydrothermal synthesis and structure determination from powder data of new three-dimensional titanium(IV) diphosphonates $Ti(O_3P{-}(CH_2)_n{-}PO_3)$ or MIL-25*n* ($n = 2, 3$). Inorg Chem 2001;40:5350–3.

[56] Serre C, Groves JA, Lightfoot P, Slawin AMZ, Wright PA, Stock N, et al. Synthesis, structure and properties of related microporous *N*,*N*′-piperazinebismethylenephosphonates of aluminum and titanium. Chem Mater 2016;18:1451–7.

[57] Cassaignon S, Koelsch M, Jolivet J-P. Selective synthesis of brookite, anatase and rutile nanoparticles: thermolysis of $TiCl_4$ in aqueous nitric acid. J Mater Sci 2007;42:6689–95.

[58] Mason JA, Darago LE, Lukens WW, Long JR. Synthesis and O_2 reactivity of a titanium (III) metal–organic framework. Inorg Chem 2015;54:10096–104.

[59] Rozes L, Sanchez C. Titanium oxo-clusters: precursors for a Lego-like construction of nanostructured hybrid materials. Chem Soc Rev 2011;40:1006–30.

[60] Assi H, Pardo Pérez LC, Mouchaham G, Ragon F, Nasalevich M, et al. Investigating the case of titanium(IV) carboxyphenolate photoactive coordination polymers. Inorg Chem 2016;55:7192–9.

[61] Yuan S, Liu T-F, Feng D, Tian J, Wang K, et al. A single crystalline porphyrinic titanium metal–organic framework. Chem Sci 2015;6:3926–30.

[62] Nguyen HL, Gándara F, Furukawa H, Doan TLH, Cordova KE, Yaghi OM, et al. Framework as an exemplar of combining the chemistry of metal– and covalent–organic frameworks. J Am Chem Soc 2016;138:4330–3.

[63] Nguyen HL, Vu TT, Le D, Doan TLH, Nguyen VQ, Phan NTS. Titanium–organic framework: engineering of the band-gap energy for photocatalytic property enhancement. ACS Catal A 2017;7:338–42.

[64] Hu S, Liu M, Li K, Zuo Y, Zhang A, et al. Solvothermal synthesis of NH_2-MIL-125(Ti) from circular plate to octahedron. CrystEngComm 2014;16:9645–50.

[65] Fu Y, Liu Y, Shi Z, Li B, Pang W. Hydrothermal synthesis and characterization of four oxalatotitanates with $Ti_4O_4(C_2O_4)_8$ tetramers as basic building blocks. J Solid State Chem 2002;163:427–35.

[66] Dan-Hardi M, Serre C, Frot T, Rozes L, Maurin G, Sanchez C, et al. A new photoactive crystalline highly porous titanium(IV) dicarboxylate. J Am Chem Soc 2009;131:10857–9.

[67] Zlotea C, Phanon D, Mazaj M, Heurtaux D, Guillerm V, et al. Effect of NH_2 and CF_3 functionalization on the hydrogen sorption properties of MOFs. Dalton Trans 2011;40:4879–81.

[68] Gao J, Miao J, Li P-Z, Teng WY, Yang L, Zhao Y, et al. A p-type Ti(IV)-based metal–organic framework with visible-light photo-response. Chem Commun 2014;50:3786–8.

[69] Nguyen NTT, Furukawa H, Gándara F, Trickett CA, Jeong HM, et al. Three-dimensional metal-catecholate frameworks and their ultrahigh proton conductivity. J Am Chem Soc 2015;137:15394–7.

[70] Bueken B, Vermoortele F, Vanpoucke DEP, Reinsch H, Tsou C-C, et al. A flexible photoactive titanium metal–organic framework based on a $[Ti^{IV}_3(\mu_3O)(O)_2(COO)_6]$ cluster. Angew Chem 2015;127:14118–23.

[71] Hong K, Bak W, Chun H. Unique coordination-based heterometallic approach for the stoichiometric inclusion of high-valent metal ions in a porous metal–organic framework. Inorg Chem 2013;52:5645–7.

[72] Hong K, Chun H. Unprecedented and highly symmetric (6,8)-connected topology in a porous metal–organic framework through a Zn–Ti heterometallic approach. Chem Commun 2013;49:10953–5.

[73] Han Y, Han L, Zhang L, Dong SA. Ultrasonic synthesis of highly dispersed Au nanoparticles supported on Ti-based metal−organic frameworks for electrocatalytic oxidation of hydrazine. J Mater Chem 2015;3:14669−74.
[74] Kim S-N, Kim J, Kim H-Y, Cho H-Y, Ahn W-S. Adsorption/catalytic properties of MIL-125 and NH_2-MIL-125. Catal Today 2013;204:85−93.
[75] George P, Dhabarde NR, Chowdhury P. Rapid synthesis of titanium based metal organic framework (MIL-125) via microwave route and its performance evaluation in photocatalysis. Mater Lett 2017;186:151−4.
[76] Lee Y-R, Cho S-M, Baeck S-H, Ahn W-S, Cho W-S. Ti-MIL-125-NH_2 membrane grown on a TiO_2 disc by combined microwave/ultrasonic heating: facile synthesis for catalytic application. RSC Adv 2016;6:63286−90.
[77] Ding S-Y, Wang W. Covalent organic frameworks (COFs): from design to applications. Chem Soc Rev 2013;42:548−68.
[78] Feng X, Ding X, Jiang D. Covalent organic frameworks. Chem Soc Rev 2012;41:6010−22.
[79] Evans JD, Sumby CJ, Doonan CJ. Post-synthetic metalation of metal−organic frameworks. Chem Soc Rev 2014;43:5933−51.
[80] Brozek CK, Dincă M. Cation exchange at the secondary building units of metal−organic frameworks. Chem Soc Rev 2014;43:5456−67.
[81] Kim M, Cahill JF, Fei H, Prather KA, Cohen SM. Postsynthetic ligand and cation exchange in robust metal−organic frameworks. J Am Chem Soc 2013;134:18082−8.
[82] McNamara ND, Hicks JC. Chelating agent-free, vapor-assisted crystallization method to synthesize hierarchical microporous/mesoporous MIL-125 (Ti). ACS Appl Mater Inter 2015;7:5338−46.
[83] Abdelhameed RM, Simões MMQ, Silva AMS, Rocha J. Enhanced photocatalytic activity of MIL125 by post synthetic modification with CrIII and Ag nanoparticles. Chem Eur J 2015;21:11072−81.
[84] Guo H, Guo D, Zheng Z, Weng W, Chen J. Visible light photocatalytic activity of Ag@MIL125(Ti) microspheres. Appl Organomet Chem 2015;29:618−23.
[85] Shen L, Luo M, Huang L, Feng P, Wu L. A clean and general strategy to decorate a titanium metal−organic framework with noble-metal nanoparticles for versatile photocatalytic applications. Inorg Chem 2015;54:1191−3.
[86] Martis M, Meicheng W, Mori K, Yamashita H. Fabrication of metal nanoparticles in metal organic framework NH_2-MIL-125 by UV photo-assisted methods for optimized catalytic properties. Catal Today 2014;235:98−102.
[87] Martis M, Mori K, Fujiwara K, Ahn W-S, Yamashita H. Amine-functionalized MIL-125 with imbedded palladium nanoparticles as an efficient catalyst for dehydrogenation of formic acid at ambient temperature. J Phys Chem C 2013;117:22805−10.
[88] Puthiaraj P, Ahn W-S. Highly active palladium nanoparticles immobilized on NH_2-MIL-125 as efficient and recyclable catalysts for Suzuki−Miyaura cross coupling reaction. Catal Commun 2015;65:91−5.
[89] Fu Y, Sun L, Yang H, Xu L, Zhang F, Zhu W. Visible-light-induced aerobic photocatalytic oxidation of aromatic alcohols to aldehydes over Ni-doped NH_2-MIL-125(Ti). Appl Catal B Environ 2016;187:212−17.
[90] Wang H, Yuan X, Wu Y, Chen X, Leng L, Zeng G. Photodeposition of metal sulfides on titanium metal−organic frameworks for excellent visible-light-driven photocatalytic Cr (VI) reduction. RSC Adv 2015;5:32531−5.

[91] Fujishima A, Honda K. Electrochemical photolysis of water at a semiconductor electrode. Nature 1972;238:37–8.
[92] Liu W, Cai J, Ding Z, Li Z. TiO_2/RGO composite aerogels with controllable and continuously tunable surface wettability for varied aqueous photocatalysis. Appl Catal B Environ 2015;174–175:421–6.
[93] Hou H, Shang M, Gao F, Wang L, Liu Q, Zheng J, et al. Highly efficient photocatalytic hydrogen evolution in ternary hybrid TiO_2/CuO/Cu thoroughly mesoporous nanofibers. ACS Appl Mater Inter 2016;8:20128–37.
[94] Qin N, Liu Y, Wu W, Shen L, Chen X, Li Z, et al. One-dimensional CdS/TiO_2 nanofiber composites as efficient visible-light-driven photocatalysts for selective organic transformation: synthesis, characterization, and performance. Langmuir 2015;31:1203–9.
[95] Fu Y, Sun D, Chen Y, Huang R, Ding Z, Fu X, et al. An amine functionalized titanium metal–organic framework photocatalyst with visible light induced activity for CO_2 reduction. Angew Chem 2012;124:3420–3.
[96] Hendon CH, Tiana D, Fontecave M, Sanchez C, D'arras L, Sassoye C, et al. Engineering the optical response of the titanium-MIL-125 metal–organic framework through ligand functionalization. J Am Chem Soc 2013;135:10942–5.
[97] de Miguel M, Ragon F, Devic T, Serre C, Horcajada P, García H. Evidence of photoinduced charge separation in the metal–organic framework MIL125(Ti)NH_2. Chem Phys Chem 2012;13:3651–4.
[98] Sun D, Liu W, Fu Y, Fang Z, Sun F, Fu X, et al. Noble metals can have different effects on photocatalysis over metal–organic frameworks (MOFs): a case study on M/NH_2MIL125(Ti) (M = Pt and Au). Chem Eur J 2014;20:4780–8.
[99] Horiuchi Y, Toyao T, Saito M, Mochizuki K, Iwata M, Higashimura H, et al. Visible-light-promoted photocatalytic hydrogen production by using an amino-functionalized Ti (IV) metal–organic framework. J Phys Chem C 2012;116:20848–53.
[100] Sun D, Ye L, Li Z. Visible-light-assisted aerobic photocatalytic oxidation of amines to imines over NH_2-MIL-125(Ti). Appl Catal B Environ 2015;164:428–32.
[101] Xu J, He S, Zhang H, Huang J, Lin H, Wang X, et al. Layered metal–organic framework/graphene nanoarchitectures for organic photosynthesis under visible light. J Mater Chem A 2015;3:24261–71.
[102] Zhu W, Liu P, Xiao S, Wang W, Zhang D, Li H. Microwave-assisted synthesis of Ag-doped MOFs-like organotitanium polymer with high activity in visible-light driven photocatalytic NO oxidization. Appl Catal B Environ 2015;172–173:46–51.
[103] Lee Y, Kim S, Kang JK, Cohen SM. Photocatalytic CO_2 reduction by a mixed metal (Zr/Ti), mixed ligand metal–organic framework under visible light irradiation. Chem Commun 2015;51:5735–8.
[104] Meyer K, Ranocchiari M, van Bokhoven JA. Metal organic frameworks for photocatalytic water splitting. Energy Environ Sci 2015;8:1923–37.
[105] Nasalevich MA, Becker R, Ramos-Fernandez EV, Castellanos S, Veber SL, et al. Co@NH_2-MIL-125(Ti): cobaloxime-derived metal–organic framework-based composite for light-driven H_2 production. Energy Environ Sci 2015;8:364–75.
[106] Meyer K, Bashir S, Llorca J, Idriss H, Ranocchiari M, van Bokhoven JA. Photocatalyzed hydrogen evolution from water by a composite catalyst of NH_2MIL125(Ti) and surface nickel(II) species. Chem Eur J 2016;22:13894–9.
[107] Wu Z, Yuan X, Zhang J, Wang H, Jiang L, Zeng G. Photocatalytic decontamination of wastewater containing organic dyes by metal–organic frameworks and their derivatives. ChemCatChem 2017;9:41–64.

[108] Wang C-C, Li J-R, Lv X-L, Zhang Y-Q, Guo G. Photocatalytic organic pollutants degradation in metal−organic frameworks. Energy Environ Sci 2014;7:2831−67.
[109] Kozlova EA, Panchenko VN, Hasan Z, Khan NA, Timofeeva MN, Jhung SH. Photoreactivity of metal-organic frameworks in the decolorization of methylene blue in aqueous solution. Catal Today 2016;266:136−43.
[110] Dhakshinamoorthy A, Asiri AM, García H. Metal−organic framework (MOF) compounds: photocatalysts for redox reactions and solar fuel production. Angew Chem Int Ed 2016;55:5414−45.
[111] Yuan X, Wang H, Wu Y, Zeng G, Chen X, Leng L, et al. One pot self-assembly and photoreduction synthesis of silver nanoparticles decorated reduced graphene oxide/MIL125(Ti) photocatalyst with improved visible light photocatalytic activity. Appl Organomet Chem 2016;30:289−96.
[112] Li J, Xu X, Liu X, Qin W, Wang M, Pan L. Metal-organic frameworks derived cake-like anatase/rutile mixed phase TiO_2 for highly efficient photocatalysis. J Alloys Compd 2017;690:640−6.
[113] Wang H, Yuan X, Wu Y, Zeng G, Chen X, Leng L, et al. Synthesis and applications of novel graphitic carbon nitride/metal-organic frameworks mesoporous photocatalyst for dyes removal. Appl Catal B Environ 2015;174−175:445−54.
[114] Zhu S-R, Liu P-F, Wu M-K, Zhao W-N, Li G-C, Tao K, et al. Enhanced photocatalytic performance of BiOBr/NH_2-MIL-125(Ti) composite for dye degradation under visible light. Dalton Trans 2016;45:17521−9.
[115] Li J, Xu X, Liu X, Qin W, Wang M, Pan L. Metal-organic frameworks highly efficient visible light photocatalysis. J Alloys Compd 2017;690:640−6.
[116] Li J, Xu X, Liu X, Qin W, Pan L. Metal-organic frameworks derived cake-like anatase/rutile mixed phase TiO_2 for highly efficient photocatalysis. Ceram Int 2017;43:835−40.
[117] Jin D, Xu Q, Yu L, Hu X. Photoelectrochemical detection of the herbicide clethodim by using the modified metal-organic framework amino-MIL-125(Ti)/TiO_2. Microchim Acta 2015;182:1885−92.
[118] Abedi S, Morsali A. Improved photocatalytic activity in a surfactant-assisted synthesized Ti-containing MOF photocatalyst under blue LED irradiation. New J Chem 2015;39:931−7.
[119] Kreno LE, Leong K, Farha OK, Allendorf M, Van Duyne RP, Hupp JT. Metal−organic framework materials as chemical sensors. Chem Rev 2012;112:1105−25.
[120] Zhang Y, Fu B, Liu K, Zhang Y, Li X, Wen S, et al. Humidity sensing properties of $FeCl_3$-NH_2-MIL-125(Ti) composites. Sens Actuators B Chem 2014;201:281−5.
[121] Xu Q, Wang Y, Jin G, Jin D, Li K, Mao A, et al. Photooxidation assisted sensitive detection of trace Mn^{2+} in tea by NH_2-MIL-125 (Ti) modified carbon paste electrode. Sens Actuators B Chem. 2014;201:274−80.
[122] Abdelhameed RM, Simões MMQ, Silva AMS, Rocha J. Enhanced photocatalytic activity of MIL-125 by post-synthetic modification with Cr^{III} and Ag nanoparticles. Chemistry - A European Journal 2014;21(31).
[123] Sedigheh Abediand, Ali Morsali. Improved photocatalytic activity in a surfactant-assisted synthesized Ti-containing MOF photocatalyst under blue LED irradiation. New J. Chem. 2015;39:931−7. Available from: https://doi.org/10.1039/C4NJ01536C.

This page intentionally left blank

Chapter 4

Electrochemical aspects of metal-organic frameworks

H. Manjunatha[1], S. Janardan[1], A. Ratnamala[1], K. Venkata Ratnam[1], L. Vaikunta Rao[2], S. Ramesh[3], K. Chandra Babu Naidu[3], N. Suresh Kumar[4], Anish Khan[5,6] and Abdullah M. Asiri[5,6]

[1]Department of Chemistry, GITAM School of Science, GITAM (Deemed to be University), Bangalore, India, [2]Department of Chemistry, GITAM School of Science, GITAM (Deemed to be University), Visakhapatnam, India, [3]Department of Physics, GITAM (Deemed to be University), Bangalore, India, [4]Department of Physics, JNTUA, Anantapuramu, India, [5]Chemistry Department, Faculty of Science, King Abdulaziz University, Jeddah, Saudi Arabia, [6]Center of Excellence for Advanced Materials Research, King Abdulaziz University, Jeddah, Saudi Arabia

4.1 Introduction

Metal-organic frameworks (MOFs), broadly known as coordination polymers are a new class of porous, crystalline solid materials formed by coordinate bond linkages between electron-donating organic bridging ligands and inorganic metals ions in three-dimensional spaces [1,2]. More precisely, MOFs are inorganic−organic hybrid materials with metal ions or metal clusters, forming the inorganic moieties (such as Fe^{2+}, Co^{2+}, Ni^{2+}, Cu^{2+}, Zn^{2+}, Mg^{2+}, Mn^{2+}, Al^{3+}, and Fe^{3+}) and usually mono-, di-, tri-, or tetravalent ligands containing oxygen or nitrogen forming the organic linkers as shown in Fig. 4.1. MOFs have gained more significance and attention due to their unique features such as tunable pore sizes, controllable structures and a large specific surface area. Though the MOFs are known since the early 1960s [4,5], they drew greater attention and significance only from the end of the last century. The research and development of MOFs was restarted by the works of Robson et al. [6] Kitagawa et al. [7] Yaghi and Li [8], Lee and Moore [9], and Riou and Ferey [10] among others. The pore sizes of the microporous characters of MOFs can be fine-tuned from several angstroms to several nanometers by length control of the rigid organic linkers or ligands.

The wide choice of choosing from variety of metal ions or clusters, organic linkers, and structural moieties provide an essentially infinite number of possible combinations [3,11]. Thus the structures of MOFs can be

Metal-Organic Frameworks for Chemical Reactions. DOI: https://doi.org/10.1016/B978-0-12-822099-3.00004-6

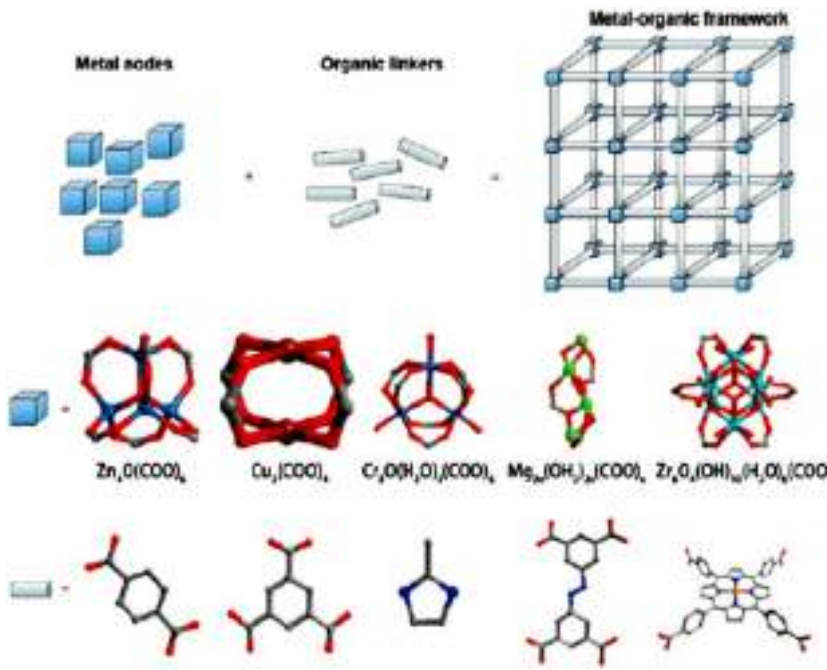

FIGURE 4.1 Schematic illustration of the composition of MOFs. *MOFs*, Metal-organic frameworks. *Reproduced from Howarth AJ, Liu Y, Li P, Li Z, Wang TC, Hupp JT, et al. Chemical, thermal and mechanical stabilities of metal–organic frameworks. Nat Rev Mater 2016;1:15018 [3] with permission of the Nature Publishing Group.*

designed for different target molecules. Importantly, versatile framework functionalities beyond the accessible porosity could be produced from the metal centers (e.g., electricity, catalysis, and magnetism), organic ligands (e.g., luminescence, fluorescence, and chirality), or a combination of both [12–15]. Till date, approximately 20,000 MOFs with variety of composition, structure, and morphologies have been reported [16,17]. MOFs have the large internal pore volumes (up to 90% free volume) with well-defined pore sizes and highest specific surface areas (Starting from 1000 $m^2 g^{-1}$ going beyond a Langmuir surface area of 10,000 $m^2 g^{-1}$) among the reported porous materials. MOFs offer unrivalled degree of tunability for variety of applications such as gas storage [18], separation [19], catalysts [20], sensors [21], and biomedicine [22].

The electrochemical applications of MOFs are driven by their high specific surface area which is greater than 10,000 $m^2 g^{-1}$. The pore size of MOFs can be adjusted to a maximum value of 9.8 nm or to a size according to the desired application by altering the organic linkers. The electrochemical aspects of MOFs such as electrochemical synthesis and their applications in the areas of batteries, supercapacitors, electrocatalysis, electrochemical sensors, electrochromism, etc.,

have been reported by many research groups. All the above applications depend on the two driving forces, that is, high specific surface area and tunable pore size. For example, few reports have summarized different approaches for synthesizing MOF-based on electrochemical principles and have used MOFs as precursors for the synthesis of nanoparticles, nanosheets, nanorods, nanospheres, etc. [23,24]. Similarly, other researchers have given a brief summary of recent applications of nanostructured MOFs and their derivatives in the field of batteries and super capacitors [2,25–29].

Recently the potential of MOFs as electrocatalysts has attracted the interest of many researchers particularly in the field of energy conversion reactions such as oxygen reduction reaction (ORR), oxygen evolution reaction (OER), and hydrogen evolution reaction (HER) in addition to Li–air batteries and CO_2 reduction reactions [30–32]. Electrochemical sensing is another potential, promising application of MOFs and there are some reports summarizing the applications of MOFs and their composites in sensors [22,33]. This chapter gives brief information of about electrochemical aspects of MOFs and their composites starting from their electrochemical methods of synthesis to their various electrochemical applications.

4.2 Electrochemical synthesis of metal-organic frameworks

Most of the present applications of MOFs in crystal engineering, catalysis, biomedicine, fuel cell, battery, etc., depend on the use materials (MOFs) synthesized by conventional approaches such as sonochemical, hydrothermal, microwave-assisted, mechanochemical, solvothermal, and liquid phase epitaxy methods. In order to expand the use of MOFs in advanced research areas such as sensors, membranes, and/or integrated electronic devices, the preparation of MOF in the form of thin films on a substrate is essential. To achieve the goal, electrochemical synthesis methods are the most suitable methods. These methods have several advantages and considered having a niche over all other conventional methods mentioned previously for the synthesis of MOFs. The shorter synthesis time, milder synthesis conditions, and real-time monitoring of the synthesis process there by enabling us to influence the reaction directly to get the desired properties in the synthesized material make the electrochemical synthesis methods very attractive [34]. Electrochemical methods offer both control and the ability to synthesis the MOFs continuously. The localized synthesis of electrochemical methods permits the formation of directed thin films without the requirement of pretreatment of surfaces unlike other conventional methods. Electrochemical methods use mild temperature conditions for the synthesis of MOFs thin films to overcome the disadvantage of hydrothermal method (most commonly used method for synthesizing MOFs), that is, the use of high temperature, which generally lead to film cracking. The following section will discuss

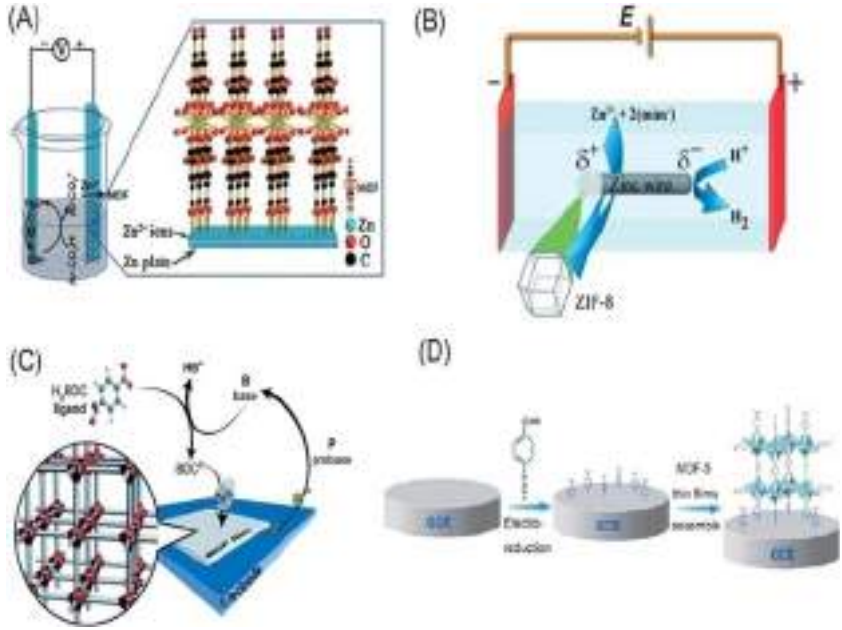

FIGURE 4.2 Selected methods for electrosynthesis of MOFs: (A) Anodic dissolution, (B) indirect bipolar electrodeposition, (C) probase electro reduction, and (D) anchoring a linker. *MOFs*, Metal-organic frameworks. *Reproduced from Kutubi HA, Gascon J, Sudhölter EJR, Rassaei L. Electrosynthesis of metal-organic frameworks: challenges and opportunities. ChemElectroChem 2015;2:462–74 with permission from Wiley-VCH Verlag.*

briefly various electrochemical methods used for the synthesis of MOFs. An overview of the various electrosynthesis methods of MOFs is shown next and also in Fig. 4.2.

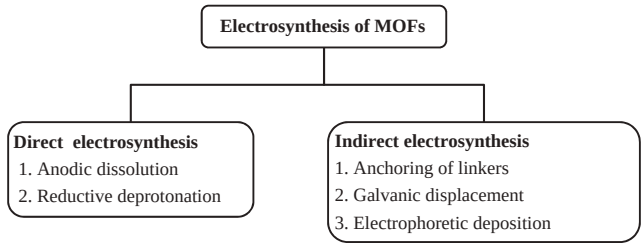

4.2.1 Direct electrosynthesis of metal-organic frameworks

Direct electrosynthesis allows control of entire synthesis process of MOFs by electrochemical means. There are two types of direct electrosynthesis process, namely, anodic dissolution and reductive deprotonation.

4.2.1.1 Anodic dissolution

Developed for the first time and patented by BASF in 2005, this is the most popular electrosynthesis method [35]. Here, a metal electrode acting as a source of metal ions is placed in a solution of an organic linker containing an electrolyte. When suitable voltage or current is applied to the electrode, the metal dissolves and the metal ions are released into the electrical double layer close to the electrode surface. The metal ions thus formed react with the organic linkers in the solution to form MOFs in the immediate vicinity of the electrode surface. Unlike the other synthetic methods where the metal ions are supplied by a salt precursor in the solution, in electrosynthesis approach, the metal ions are supplied by the dissolution of the electrode avoiding any disturbances arising from the source of metal precursor on the kinetics of MOF formation. Another advantage of this method is that the oxidation state of the metal ion can be controlled by applying suitable voltage (amperometry technique) or current (potentiometry technique) to the electrode. Since the process is performed in a two electrode cell with no reference electrode, the cell geometry and a constant distance between the electrodes is very important to order to get uniform distribution of throughout the electrosynthesis process. On the other hand, metal ions reduction instead of oxidation at the electrode cannot be ruled out. This can be prevented by any one of the following methods: (1) The use of protic solvents (acidic) that ensure the evolution of hydrogen instead of reduction of metal ions, (2) use of an auxiliary electrode with a suitable over potential for H_2 evolution, and/or (3) by adding of a compound which sacrificially undergoes reduction in place of metal ion into the electrolyte solution.

Anodic dissolution method is more often used for the synthesis of MOFs, $Cu_3(BTC)_2$ also known as HKUST-1 and its synthesis was first reported in 1999. The MOFs is made up of copper nodes bonded to trimesic acid (H_3BTC/BTC) linkers [36]. In electrosynthesis method the parameters such as applied voltage, current density, distance between the electrodes, synthesis time, types of solvent, linker, and concentration of electrolyte affect the properties of the MOFs synthesized. Muller et al. [37] studied the properties of HKUST-1 synthesized by the method and found that the electrosynthesized MOFs have larger specific surface area of 1820 $m^2\ g^{-1}$ compared 917 $m^2\ g^{-1}$ for the samples synthesized by other methods. The lower surface area observed in samples synthesized by solvothermal method are due to the blocking of pores by nitrate moieties of the precursor.

Hartman et al. [38] studied the effect of solvent and synthesis conditions on the separation properties of HKUST-1 for isobutane and isobutene in mixture of BTC and methyltributylammonium methylsulfate (MTBS). The electrolyte was prepared using pure ethanol or ethanol/water (50:50 v/v) mixture. They found that the HKUST-1 synthesized using pure ethanol was having more surface area compared to that synthesized from a mixture of

ethanol/water solvents. Later, effect of supporting electrolyte concentration and current density on particle size of HKUST-1 was studied by Kulandainathan et al. [39] for using it as electrocatalyst for the reduction of *p*-nitrophenol by $NaBH_4$. The yield of the MOFs increased with increase in current density and the concentration of supporting electrolyte.

De Vos et al. [34] found that by varying the synthesis conditions during the formation of HKUST-1 dense films, the crystal size can be adjusted between 2 and 50 μm. Raising the applied potential from 2.5 to 25 V led to the formation of smaller particles according to the nucleation theory. Larger applied potential makes the electrode dissolve more and raises the number of metal ions close to the electrode surface which lead to smaller particles. Higher amounts of water and synthesis time results in longer crystals, high density, and intergrown films. Thus ideal conditions for the formation of more dense and integrated MOFs are shorter synthesis time and mild conditions. Later, Denayer et al. [40] upon depositing HKST-1 thin films on copper mesh found that higher solution conductivity makes the electrode dissolve more and damages the mesh structure with poor crystal adhesion. Also, more control over the synthesis can be achieved when the solution has no conducting salt in it. They also found that the ethanol/water ratio also has a greater impact on the crystal morphology. When the water content was between 10% and 35%, the average crystal size increased from 2 to 11 nm in 30 min allowing fine tuning of the crystals. However, when it was 50%, it resulted in detachment of crystals and at more than 50% water content led to the formation of nonporous structure.

Gascon et al. [41] electrosynthesized MOFs, HKUST-1, MIL-53(Al), NH_2-MIL-53, MIL-100(Al), and ZIF-8 with an emphasis on the effect of temperature, type of solvent, and voltage−current density on the synthesis process. HKUST-1 shows a small variation in the surface area with increase in temperature during its electrosynthesis. Their investigations led to the conclusion that addition of a salt resulted in higher conductivity of electrolyte with lowered ohmic drop and higher yield in the production of MOFs. On the other hand, the ZIF-8 thin films require a template layer for initiating the deposition on the electrode. This is attributed to the fact that they are formed in the solution and not on the electrode surface, which demands equilibrium time period (incubation) before the nucleation to occur and metal ions move away from the electrode. Surprisingly, when the temperature is varied, ZIF-8 crystals were formed at very low temperature as low as 0°C with higher rate of formation. MIL materials are named after *Material Institute Lavoisier* and are made up of carboxylate linkers and aluminum as metal ions. The low cost of aluminum make the MOFs cost-effective and interesting for industrial applications. However, the low electrical conductivity of aluminum when oxidized makes the synthesis of the MOFs very difficult. Among the three MIL materials studied, MIL-100(Al) also known as "giant-pore MOFs" made up of mesocages (25−29 Å) connected through pores (5−9 Å) with BTC as linker. The pH of the electrochemical cell increases due to HERs complicating

the electrosynthesis of MIL-100 which should be carried out at low pH. Other two MOFs, MIL-53(Al) and NH_2-MIL-53, are synthesized under diverse conditions.

Ionic liquids (ILs) can also be employed for the electrosynthesis of MOFs as solvents. They have several advantages compared to conventional solutions based on water, methanol, ethanol, and DMF. ILs are made up of organic anions and cations. Organic anions act as linkers and cations act as structure directing agents. Also ILs represent a class of solvents with unique properties such as nonflammability, low vapor pressure, high thermal stability, and most important for electrosynthesis point of view the wide electrochemical stability window. Such properties of solvents render their design easy for various applications [42]. The use of ionic liquids enhanced the electrical conductivity and due to strong interactions between the ionic liquids and organic linkers, the MOF-5 acquired attractive flower-like or rod-like crystal morphology [43,44]. Table 4.1 summarizes the anodic dissolution conditions for electrosynthesis of different MOFs.

4.2.1.2 Reductive deprotonation

The principle behind this new method for electrosynthesis of MOFs is to use electrochemical methods to raise the pH of solution, which subsequently led to the deprotonation of the linker. This causes the nucleation of MOFs crystals and a thin film is formed near the electrode. Dinca and Li [48] first introduced and patented this method for the synthesis MOF-5 on a fluorine-doped tin oxide (FTO) electrode. They used $Zn(NO_3)_2$ as the source of the metal, tetrabutylammonium hexafluorophosphate $[(NBu_4)PF_6]$ as electrolyte, FTO as working electrode, DMF/water mixture as electrolyte and Ag/Ag $(cryptand)^+$ as a reference electrode. The reaction raises the pH of the solution upon electro-reduction of oxoanions such as NO_3^-. The linker 1,4-benzenedicarboxylic acid (H_2BDC) then undergoes deprotonation in the alkaline conditions to react with metal precursor in accordance with the following equations:

$$NO_3^- + H_2O + 2e^- \rightarrow NO_2^- + 2OH^- \tag{4.1}$$

$$H_2BDC + OH^- \rightarrow HDBC^+ + H_2O \tag{4.2}$$

One of the drawback of this method is that the potential required for the electroreduction of NO_3^- [− 1.75 V vs Ag/Ag$(cryptand)^+$] was greater than that of the Zn [− 1.00 V vs Ag/Ag$(cryptand)^+$]. This results in codeposition of Zn along with MOF, and the problem was later addressed with the use of a probase, trimethylammonium(Et_3NH^+) which undergoes reduction at low negative potential [− 0.5 V vs Ag/Ag$(cryptand)^+$] on Pt electrode. Reduction of the probase led to the formation of trimethylamine(Et_3N) and

TABLE 4.1 Anodic dissolution electrosynthesis conditions for different metal-organic frameworks (MOFs).

MOF	Applied potential (V)	Applied current (mA)	Solvent	Electrolyte	References
HKUST-1	12–19	1300	Methanol		[37]
HKUST-1	15	0.05	Water/ethanol 50:50 (v/v)	MTBS	[38]
HKUST-1	10–20	–	Methanol	TBATFB	[39]
HKUST-1	2–25	–	Water/ethanol 50:50 (v/v)	MTBS	[34]
HKUST-1	0–5	–	Water/ethanol 50:50 (v/v)	None	[40]
HKUST-1	–	10	–	MTBS	[41]
MIL-100 (Fe)	–	2–20	–	–	[45]
Li-doped MIL-100 (Fe)		38	Methanol	MTBS	[33]
ZIF-8	–	10	Water, methanol, water/methanol, water/acetonitrile, DMF	MTBS, KCl	[41]
ZIF-8	5–7	–	Water	Na_2SO_4	[46]
MIL-100 (Al)	–	10	Water/ethanol 25:75(v/v)	None	[41]
MIL-53 (Al)	–	2–20	Water/DMF 90:10 (v/v)	MTBS, KCl	[41]
NH_2-MIL-53 (Al)	–	2–20	Water/DMF 90:10 (v/v)	KCl	[41]
MOF-5	–	2.5	DMF	BMIN bromine	[43]

(*Continued*)

TABLE 4.1 (Continued)

MOF	Applied potential (V)	Applied current (mA)	Solvent	Electrolyte	References
MOF-5	0.5–2	–	Water	NH_4F	[44]
Gd-BTC	–	1	Water/ ethanol 50:50 (v/v)	MTBS	[47]

Source: Reproduced with permission from Kutubi HA, Gascon J, Sudhölter EJR, Rassaei L. Electrosynthesis of metal-organic frameworks: challenges and opportunities. ChemElectroChem 2015;2:462–74.

H_2, which does not interfere with the formation of the MOF as shown in the equations below.

$$2R_3NH^+ + 2e^- \rightarrow 2R_3N + H_2 \tag{4.3}$$

$$2H_2BDC + 2e^- \rightarrow H_2 + 2\,HBDS^- \tag{4.4}$$

Later, Yang et al. [49] synthesized Europium-based MOF making use of benzophenone-3,3′,4,4′-tetracarboxylic dianhydride (BTDA) and $Eu(NO_3)_3 \cdot 6H_2O$ in DMF based on the same principle discussed earlier. Reduction deprotonation has advantages as well as disadvantages. It has the advantage of allowing the formation of MOF on variety of conducting substrates, provided the probase is carefully selected to avoid any undesired by products and eliminates the need for extreme voltages for electrosynthesis of MOFs. The disadvantages of the method stem from the need for extremely negative potential even with the use of trimethylamine, making the methods not suitable in presence of readily reduced metals such as copper.

4.2.2 Indirect electrosynthesis of metal-organic frameworks

Electrochemical methods can also become one among several steps involved in the synthesis of MOFs and such methods are termed indirect electrosynthesis methods. There different types of indirect electrosynthesis of MOFs.

4.2.2.1 Anchoring of a linker

This method is used to synthesis thin films of MOF and involves anchoring a linker to the substrate surface by chemical or electrochemical methods. The adsorbed linker on the substrate acts as a nucleation site for the

formation of MOFs. Telfer et al. [50] synthesized HKUST-1 MOF on a glassy carbon electrode (GCE, a substrate electrode) by two approaches. First approach involves grafting 4-carboxyphenyl radicals to the surface of the GCE by the reduction of 4-carboxybenzenediazonium cations. The GCE was then placed in a mixture of $Cu(NO_3)_2$ and BTC dissolved in ethanol at higher temperature. Second approach involves creating a rough surface on glassy carbon electrode using abrasive SiC paper, which introduces functional groups containing oxygen such as COO^-. These functional groups themselves behave as anchored groups of the first method. Repeated cycling with cyclic voltammetry in $Cu(NO_3)_2$ and BTC solution then induces the growth of HKUST-1. The first approach yields relatively discontinuous and open network of HKUST-1 crystals, whereas second approach forms dense, intergrown, and continuous film. Later, Hu et al. [51] electrosynthesized MOF-5 on a GCE using the first approach.

4.2.2.2 Galvanic displacement

This method works on the principle where a more noble metal is displaced by a less noble metal when they come in contact with each other. It is well known from the electrochemical series that, whenever, two metals with different reduction potentials (E^0) are in contact with each other, the of less noble metal (substrate electrode in electrosynthesis) displaces the more noble metal (in the solution) and makes the substrate undergo oxidation. This process releases metal ions to the solution and MOF is formed. This method does not require external current for the formation of metal ions. Galvanostatic displacement method was developed by De Vos et al. [52] for the formation of HKUST-1 on glass substrate. They used metallic copper decorated on the glass substrate and a mixture of $AgNO_3$ and BTC in DMF as electrolyte. $AgNO_3$ was then spin-coated on the top of copper-decorated glass substrate, and the sample was heated to 80°C. As a result, the silver ions get reduced and Cu^{2+} ions released into the solution form HKUST-1.

4.2.2.3 Electrophoretic deposition

Electrophoretic deposition works on electrophoresis, a phenomenon in which the charged particles are separated by the application of electric field between two electrodes placed to a colloidal solution or charged biofluids placed. This idea was first used by Hupp et al. [53] for depositing MOFs and they proved the versatility of this method for synthesizing not only the well-known HKUST-1 but also Al- and Zr-based MIL-53(Al), UiO-66, and NU-1000 thin films. The negative charge of the solution placed between two FTO plates comes from the intrinsic defects present in the structure of MOFs, and thin films are formed on the electrode upon applying a potential of 90 V for 3 hours. The strength of this technique is that two different

MOFs can be deposited on the same electrode surface. The investigations on the reversible electrochromism of NU-1000 found that the MOFs particles that are not in contact with the FTO electrode also participated in the electrochemical reaction indicating the existence of particle−particle redox communication. One of the important requirements for this technique is that the MOF particle must be able to give a stable colloidal suspension, and use of organic solvents is a must in order to avoid any side reactions.

4.2.2.4 Self-templated synthesis from metal oxide/hydroxide nanostructures

In this method the metal oxides/hydroxides are first prepared by an electrochemical method, and once they are formed, they themselves act as a source of metal and nucleation sites for the formation of MOFs. For example, ZIF-8 was grown on ZnO nanorods by electrodeposition [54]. First, ZnO nanorods acting as both template as well as source of Zn were electrodeposited for 50 minutes on an FTO electrode by galvanostatic method from a mixture of aqueous $Zn(NO_3)_2 \cdot 6H_2O$ and hexamethylenetetramine (HMTA, as an electrolyte additive). The ZnO nanorod arrays modified−FTO electrode is then placed in an autoclave containing 2-methylimidazole, H_2O/DMF solvent mixture, and heated to 70°C for 24 hours to yield ZnO−ZIF-8 nanorod arrays. Similarly, Yang et al. [55] electrodeposited $Eu(OH)_2$ on to an electrode surface and subsequently a thin MOF film was formed by a solvothermal step.

4.3 Electrochemical applications of metal-organic frameworks

The electrochemical applications of MOFs are mainly due to their specific surface area generally varying from 1000 to 10,000 $m^2\,g^{-1}$ which is very large compared to all the other known porous materials. Fig. 4.3 shows various electrochemical applications of MOFs.

4.3.1 Battery applications of various metal-organic frameworks

MOFs and their derivatives represent two classes of functional materials for energy storage and conversion due to their high porosity, diverse structures, and controllable chemical compositions. These offer immense possibilities in the search for suitable electrode materials for rechargeable batteries. Despite these advantageous features, MOFs and their derivatives face several challenges as electrode materials that impede their practical applications. In this context, we present both the opportunities and challenge that MOFs and their composites materials offer for rechargeable batteries including lithium-ion batteries, lithium-sulfur batteries, sodium-ion batteries, and other battery systems. Among all the abovementioned

FIGURE 4.3 The schematic diagram of MOFs and MOF composites for electrochemical application. *MOFs*, Metal-organic frameworks. *Reproduced from Xu Y, Li Q, Xue H, Pang H. Metal-organic frameworks for direct electrochemical applications. Coord Chem Rev 2018;376:292–318 with permission from Elsevier.*

battery systems, lithium-based batteries are widely accepted and appreciated for use in variety of portable electronic devices due to their high energy density.

4.3.1.1 Metal-organic frameworks for Li-ion batteries

Owing to their high surface area, porosity, diverse structures, tunable redox properties, and low cost, MOFs have become a new class of porous crystalline electrode materials for lithium-ion batteries (LIBs) [56,57]. High surface area and porosity favor interfacial charge transport during lithium insertion/extraction in LIBs. MOFs have been used as positive electrode, negative electrode and electrolytes for LIBs. Many metal-based MOFs such as Fe-MOF [58–60], Co-MOFs [61–68], Cu-MOFs [69–72], Mn-MOFs [73–76], Ni-MOFs [77,78], Cd-MOFs [79], and Zn-MOFs [80] have been reported as electrode materials for LIBs.

Among the three Fe-based MOFs reported such as MIL-53(Fe) [58], MIL-101(Fe) [59], and Fe-MIL-88B [60], Fe-MIL-88B exhibited a superior electrochemical performance by delivering high specific capacity of 744.4 mAh g^{-1} over 400 cycles in a half battery and maintains a capacity of

86.8 mAh g^{-1} over 100 cycles in a full-battery. The morphological structure of Fe-MIL-88B is as shown in Fig. 4.4A and B. The nanostructured polyhedral nanorods of the synthesized material is found to play a crucial role by holding the metal organic skeleton together throughout the battery operation signifying the use of nanostructured MOFs for stable Li^+ interaction/deintercalation processes compared to their bulk counterparts. MIL-53(Fe), though first used in battery applications since 2007, suffers from low capacity (75 mAh g^{-1}) and cycle stability [56]. The redox reaction (Fe^{2+}/Fe^{3+}) was not 100% reversible and a more functionalized form, that is, MIL-101(Fe) SBU shows some improvement in the reversibility of the redox reaction. Co-based MOFs are also used as electrodes for LIBs [61−64,67,68]. Among Co-BDC MOF [62] and S-Co-MOF [63], Co-BDC MOF delivered a high capacity of 1090 mAh g^{-1} at 200 mA g^{-1}, whereas the later suffered from

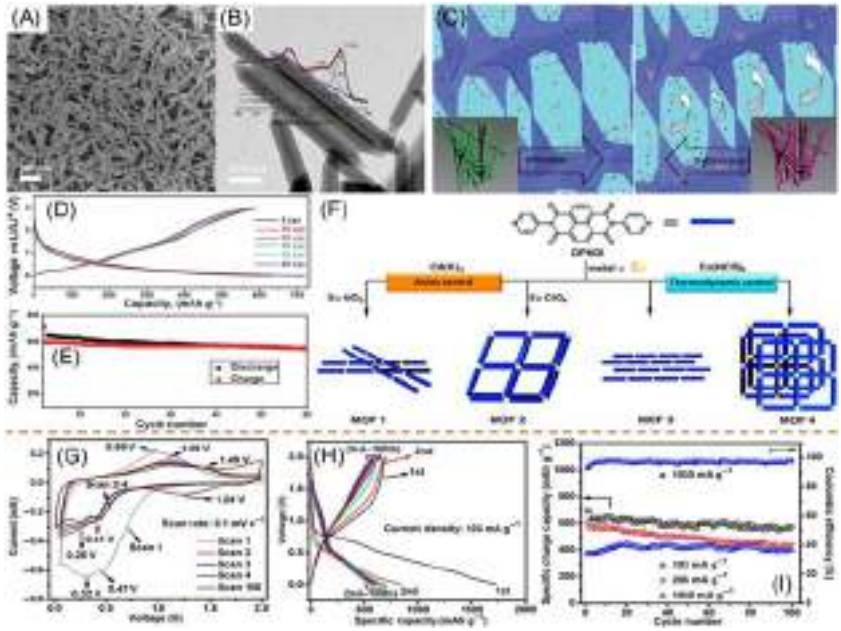

FIGURE 4.4 (A and B) SEM and TEM images of the Fe-MIL-88B, (C) schematic diagram of CoCOP nanowires with the robust framework structure and abundant interpenetrating tunnels for Li-ion transport in lithiation−delithiation processes, (D) selected cycles, (E) capacity versus cycle number plot of $Zn_3(HCOO)_6$ [current density of 60 mA g^{-1} (0.11 C, 1 C = 520 mA g^{-1})] was used within 0.005−3 V, (F) conceptual schematic presentation of crystal engineering of naphthalenediimide-based MOFs 1−4, (G) cyclic voltammograms of Mn-BTC MOF at 0.1 mV s^{-1}, (H) galvanostatic discharge−charge curves of Mn-BTC MOF, and (I) cycle stability of Mn-BTC MOF. *MOFs*, Metal-organic frameworks. *Reproduced from Xu Y, Li Q, Xue H, Pang H. Metal-organic frameworks for direct electrochemical applications. Coord Chem Rev 2018;376:292−318 with permission from Elsevier.*

low lithium-ion storage capacity. In another work a one-dimensional cobalt coordination polymer (CoCOP) nanowires [64] (Fig. 4.4F) synthesized by hydrothermal method delivered a capacity of 1090 mAh g^{-1} at 20 mA g^{-1}. Later, Li et al. [66] prepared Co-BTC coordination polymers (Co-BTC CPs) using the same hydrothermal method with three different solvents to get CPs with different morphologies. Almost same cycling stabilities were obtained for all the three CoBTC CPs at 100 mA g^{-1} and the current density increased up to 2 A g^{-1}.

The first Cu-based MOFs, microporous Cu(2,7-AQDC) (AQDC = anthraquinone dicarboxylate) was reported in 2014 [69]. When tested as cathode material for LIBs, it exhibited a very good reproducibility indicating that the frame is strong and vigorous. Later, another copper-based MOF, Cu-TCA (H_3TCA = tricarboxytriphenyl amine) with the electrochemically active metal coexisting with the organic linker was reported as cathode for LIBs [70]. The material achieved long cycle stability and good rate capability. A new 2D Mn-based MOF, [Mn-(tfbdc) (4,40-bpy)$(H_2O)_2$] (Mn-LCP) was reported by Liu et al. [74]. However, it had low lithium storage capacity. The capacity of Mn-based MOF was improved later by Maiti et al. [73] who designed and synthesized an Mn-1,3,5-benzenetricarboxylate MOF (Mn-BTC MOF) and when used as anode, it exhibited good electrochemical performance in LIBs as shown in Fig. 4.4G–I. Cd-based MOFs are particularly attractive for LIBs due to their ability to reversibly accommodate Li^+ ion. Tian et al. [79] synthesized two Cd-MOFs with same structures using naphthalenediimide having different porosities. The metal node and porosity significantly affected the electrochemical performance of these MOFs. There are several Zn-based MOFs such as $Zn_3(HCOO)_6$, $Co_3(HCOO)_6$, and $Zn_{1.5}Co_{1.5}(HCOO)_6$. $Zn_3(HCOO)_6$ have been successfully applied for Li-storage, and the studies revealed that $Zn_3(HCOO)_6$ shows the best electrochemical performance of around 600 mA g^{-1} over 60 cycles as shown in Fig. 4.4D and E [80]. In another work, nanosized UiO-66 [81] showed little change in volume during Li^+ insertion when used as electrode for LIBs.

MOFs have also been explored as electrolyte materials for all solid state Li^+-ion batteries. Mg-based MOF (Mg-BTC-MOFs) [82] and Ti-based MOFs [NH_2-MIL-125(Ti) [83] and intercalated MOF(iMOF, 2,6-Naph $(COOLi)_2$] [84] have been investigated as electrolytes. NH_2-MIL-125(Ti)-coated battery separators provided long life service for Li|Cu and Li|Li batteries which are free from dendrites during Li deposition. This study showed that MOFs can be used for protecting Li anode. Lithiated MOFs [iMOFs, 2,6-Naph $(COOLi)_2$] were proposed as electrode material for high-voltage bipolar batteries. The iMOF-based electrode materials are found to undergo very small volumetric change (0.33%) during Li^+ insertion and help to design batteries with high energy density and with good safety. Some bimetallic MOFs have also been reported for Li-ion storage such as

Fe/Co-BTC nanotubes [85] and MnCo-BTC MOFs [86]. Since Mn-BTC MOFs have poor cyclability, doping them with cobalt improved battery performance with a high capacity of 901 mAh g^{-1} at 100 mA g^{-1} even after 150 cycles.

All the above MOFs discussed for LIBs are pure MOFs and their conductivity is poor. In order to enhance their electrical conductivity and alter the electrochemical performance, MOF composites were explored by many researchers by combining them with conductive materials such as metal oxides [87,88], carbon materials [89–92], conducting polymers [93], and single metals [94,95]. Among various approaches to modify the electrochemical performance of MOFs, the novel MOF sandwich coating (MOF-SC) method using single metal (Si) as conductive additives for preparing mixed electrodes for LIBs was promising. The micro Si-MOF electrode, C/Si/ZIF-8 [94] when used as anodes for LIBs exhibited areal capacity of 1.7 mAh cm^{-2} at 265 Ah cm^{-2} and maintained a capacity of 0.850 mAh cm^{-2} over 50 cycles. The higher pore volume ratio of MOF layer along with high surface area accommodates more electrolytes and facilitates faster Li^+-ion diffusion, increasing the reproducibility of the electrode material. Carbon-based conducting materials also play a crucial role in improving the electrochemical performance of certain MOFs. MOF/reduced grapheme oxide composites of Co- and Cd-based MOFs showed better performance compared their pristine ones. Co(L)MOF/rGO-delivered a discharge capacity of 639 mAh g^{-1} and retained 500 mAh g^{-1} of discharge capacity even after 120 cycles. MOF composites are also used as electrolytes for LIBs. For example, Al-BTC MOF with poly(ethylene oxide) conducting polymer nanocomposite (NCPE) exhibited good stability for lithium metal storage for longer time [94]. Another ionic liquid impregnated MOF nanocrystals (Li-IL@MOF) when used as solid electrolyte exhibited a good ionic conductivity [96].

4.3.1.2 Metal-organic frameworks for Li–S batteries and other batteries

Li–S batteries are gaining significance as next generation rechargeable batteries due to their high theoretical capacity (1675 mAh g^{-1}) and natural abundance of sulfur. The applications of MOFs for Li–S batteries are still in the early stage of development and the factor hindering their applications is the "shuttle problem" of polysulfides [97]. Shuttle problem in Li–S batteries refers to a phenomenon where fast capacity fading of the battery occurs due to shuttling of soluble polysulfides between electrodes. MIL-100(Cr) [98], S-ZIF-8 [97,99,100], sulfur containing noncarbonized (S-MOF) [101], zirconium-metal porphyrin framework (MOF-525(Cu) [102], and sulfur containing S@MOF-525 (Cu) [102] have been investigated as electrode materials for Li–S batteries. It is found that MIL-100(Cr) significantly

enhanced the capacity retention of Li−S batteries due to its unique topography, balanced polarity, and high chemical stability. On the other hand, ZIF-8/S MOF showed best electrochemical performance with significantly improved sulfur storage and long-term cycle performance when the particle size was around 200 nm. The noncarbonized MOF(S-MOF) delivered an initial discharge capacity of 1476 mAh g^{-1} and retained a capacity of 609 mAh g^{-1} after 200 cycles with nearly no fading. However, the best performance was noticed for S@MOF-525 (Cu) as cathode which exhibited a discharge capacity of 700 mAh g^{-1} at 0.5C over 200 cycles.

MOF composites were also reported to improve the properties of pure MOF as electrode materials for Li−S batteries [103−106]. MOF/graphene composites found to have higher electrical conductivity than the pristine MOF [MIL-101(Cr)]. They also found to address one of the main hindrances in the performance of Li−S, that is, "shuttle problem." For example, $Cu_3(BTC)_2$@GO was proposed [104] as battery separator for Li−S batteries which showed less capacity fading of 0.02% for each cycle for 1500 cycle owing to the combined effect of the MOF particles with GO sheets. Similarly a Zn-based Zn(II)-MOF@Go separator was also proposed; however, its electrochemical stability is less than the $Cu_3(BTC)_2$@GO [105]. In another attempt, MOF/CNTs composites have also been having porous morphology for flexible and foldable Li−S batteries [106]. The resulting Li−S batteries are able to maintain good electrical contact withstanding large volume expansion during lithium insertion/extraction reaction and impart great deal of flexibility and integrity through CNT networks penetrating the MOF. Once the problems of insulating property, shuttling problem, and volume change of sulfur electrodes are resolved, Li−S batteries become attractive owing to their high energy density.

MOFs have also been used widely in other battery systems apart from LIBs. Important to mention are Li−O_2 batteries [107,108], sodium-ion batteries (SIBs) [89], and potassium-ion batteries (PIBs) [109]. The theoretical specific energy of Li−O_2 batteries is about 5200 Wh kg^{-1} which is higher than Li−S batteries. Among various MOFs researched as electrode materials for Li−O_2 batteries, Mn-MOF-74 reported by Wu et al. [108] is found to deliver highest specific capacity of 9420 mAh g^{-1} at 50 mA g^{-1} in O_2 environment. This best performance of the MOF is assigned to the accessible metal sites in the uniform channel that enable easy intake of more O_2 molecules by the pores increasing the efficiency of the reaction. Dong et al. [89] prepared Co(L) MOF and Cd(L) MOF by solvothermal methods and Co(L) MOF/rGO composite when used as anode in SIBs delivered excellent discharge capacity of 206 mAh g^{-1} 15,500 mA g^{-1} over 330 cycles. Recently, L-$Co_2(OH)_2$ BDC has been reported as anode material for potassium-ion batteries, and it showed excellent potassium ion storage capability [109]. The battery performance of various MOF and MOF composites have been summarized in Table 4.2.

TABLE 4.2 Battery performance of various metal-organic frameworks (MOFs) and MOF composites.

Samples	Discharge capacity ($mAh\ g^{-1}$)	Capacity retention(%) /cycle number	Coulombic efficiency (%)	Electrode	References
Fe-MIL-88 B	1507.4	93/400	100	Anode	[60]
$Co_2(OH)_2BDC$	1385	–/100	72.8	Anode	[61]
Co-BDC	1963.6	70.7/100	99.46	Anode	[62]
S–Co-MOF	1946	–/200	80.4	Anode	[63]
CoCOP	1620	100/1000	100	Anode	[64]
Co-BTC MOF	1739	–/200	79	Anode	[65]
CoBTC–EtOH	1790.3	97.4/100	100	Anode	[66]
Co-MOF	600	84.2/150	99.8	Anode	[67]
Co_2(DOBDC) MOF	1409	–/200	99	Anode	[68]
Cu(2,7-AQDC)	–	–/50	–	Cathode	[69]
$[Cu_3(BTC)_2]$ MOF	1497	100/50	98	Anode	[70]
Cu-TCA	102.2	22/200	96.5	Cathode	[71]
Mn-LCP	1807	–/50	–	Anode	[74]
Mn-BTC MOF	1717	100%/100	97	Anode	[73]
Ni–Me_4bpz	320	–/100	>98	Anode	[77]
Ni-MOF	1984	–/100	100	Anode	[78]
Cd(II) MOFs	45	>70/50	–	Cathode	[79]

(*Continued*)

TABLE 4.2 (Continued)

Samples	Discharge capacity ($mAh\ g^{-1}$)	Capacity retention(%) /cycle number	Coulombic efficiency (%)	Electrode	References
$Zn_3(HCOO)_6$	1344	–/60	–	Anode	[80]
Fe/Co-BTC	859.1	–/50	95	Anode	[85]
Fe_3O_4@MOF	1266.2	–/100	–	Anode	[87]
ZIF8-10	1125.7	–/20	–	Anode	[88]
Co(L) MOF/rGO	951.8	–/330	98	Anode	[89]
CoCGr-5	2566	–/400	>99	Anode	[110]
$Ni_3(HCOO)_6$/CNT-50	–	–/400	58	–	[90]
Fe-MOF/rGO	2055.9	–/200	43.3	Anode	[91]
Mn-MOF/rGO_{10}	1677.5	98/100	100	Anode	[92]
S/ZIF-8	1055	75/300	–	Cathode	[99]
S–Zn-MOF	1476	41.3/200	–	Cathode	[101]
S@MOF-525(Cu)	–	–/200	100	Cathode	[102]
MIL-101(Cr)/S	715	95/134	96.6	Cathode	[103]
MOF@GO	1126	71/1500	100	Cathode	[104]
Zn-based MOF@GO	1118	–/1000	98.8	–	[105]
L–$Co_2(OH)_2$BDC	742	–/600	100	Anode	[109]

Source: Reproduced with permission from Xu Y, Li Q, Xue H, Pang H. Metal-organic frameworks for direct electrochemical applications. Coord Chem Rev 2018;376:292–318.

4.3.2 Supercapacitors applications of various metal-organic frameworks

Supercapacitors (SCs) differ from traditional rechargeable batteries in terms of fast discharge rates, high power density, and longer cycle life. MOFs have attracted the interest of many researchers as potential electrode materials for SC due to their high surface area and easily tunable pore size. However, their application directly as electrode is hampered by their chemical instability and poor electrical and mechanical properties. For application in super capacitors, organic linkers are made to react with metal salts of transition elements such as Co, Ni, Mn, Cu, and Zn to form MOFs. Commonly used organic linkers are as shown in Fig. 4.5. Many pure MOFs such as Ni-based MOFs [111–115], Co-based MOFs [116–121], a series of different nanocrystals of MOF (nMOF) [122], MOF nanowire assay (MOF NWSs) [123], Zr-based MOF [124–126], and bimetallic MOF [127,128] have been reported and studied as electrode materials for SCs.

Among various Ni-based MOFs, hierarchical 2D structured Ni-MOFs [111,129] shows good electrochemical performance with a high energy density of 55.8 Wh kg^{-1} and power density of 7000 W kg^{-1}. In another work an accordion such as Ni-MOF, $[Ni(OH)_2(C_8H_4O_4)_2(H_2O)_4] \cdot 2H_2O$//activated carbon displayed good capacitance and cycling stability with the retention of 98.8% of capacitance after 5000 cycles. This excellent performance was attributed to the special structure of synthesized Ni-MOFs with layered micro plates, which means thousands of nanochannels to enhance the diffusion of

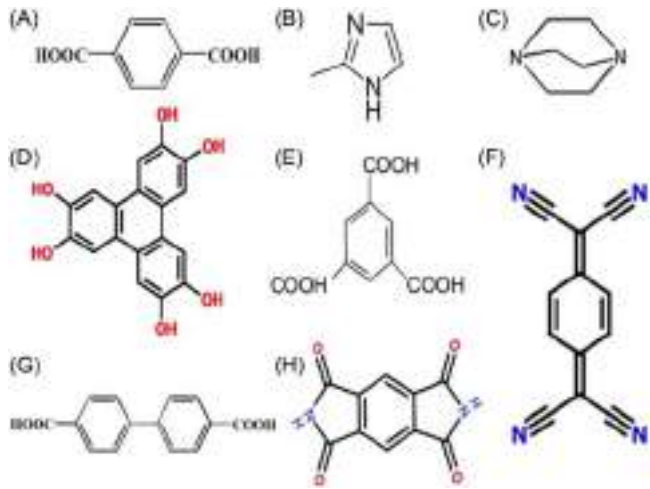

FIGURE 4.5 Schematic representation of 1,4-H_2bdc (A), $C_4H_6N_2$ (B), $C_6H_{12}N_2$ (C), $C_{18}H_{12}O_6$ (D), H_3BTC (E), $C_{12}H_4N_4$ (F), 4,40-H_2bpc (G), and $C_{10}H_4O_4N_2$ (H). *Reproduced from Xu Y, Li Q, Xue H, Pang H. Metal-organic frameworks for direct electrochemical applications. Coord Chem Rev 2018;376:292–318 with permission from Elsevier.*

ions and electrolytes. Apart from hierarchical Ni-based MOFs, other nano materials have also been reported [112,114,115] and used as electrodes for SCs. Among them, Ni-DMC-ADC exhibits highest stability of more than 98% after 16,000 cycles at 10 A g^{-1}. Co-based MOF, Co_8-MOF-5 was reported by Diaz et al. [116] as electrode material for SCs and its electrochemical performance was found to be restricted by spatial MOF and electrolyte. The best performance among Co-based MOFs was observed for Co-MOF nanosheets [118] which when tested as electrode delivered a high capacitance of 2564 F g^{-1} at 1 A g^{-1} and an excellent cyclability of 98% over 3000 cycles. To understand the high capacitance and longer cycle behavior, a family of nanocrystal MOFs (nMOFs) with varying organic linkers and metal nodes having different pore size, shapes, and structures were also reported [130]. Here, pure MOFs were doped with graphene to solve the problem of low conductivity. Out of these nMOFs, Zirconium-based MOF showed the stack and an aerial capacitance of 0.64 and 5.09 mF cm^{-2} which was found to be six times greater than the commercially available carbon material−based SCs. Such findings become the key in the development of a high capacitance SCs. On the other hand, bimetallic MOFs which are made up of two different metal nodes included into the same structure offer additional degree of structural stability [127,128]. Pure MOFs lack capacitance due to their poor conductivity and replacing part of Ni^{2+} by Co^{2+} or Zn^{2+} significantly enhanced the capacitance of mixed MOFs (M-MOFs), and the enhanced performance is assigned to improved electrical conductivity, high surface area, increased pore size, increased contact between the electrode and electrolyte, and shortened diffusion path.

Another way to overcome these intrinsic drawbacks of poor conductivity and chemical stability of pure MOFs is to combine them with conductive additives such as carbon materials [131−134], conducting polymers [135−142], and so on [143] to form MOF composites [130,134,141,142,144−147]. Among carbon-based MOFs composites, Ni-doped MOF-5 and rGO composite delivered a power density of 37.8 Wh kg^{-1} at 227 W kg^{-1} [136] with increased charge storage capacity as shown in Fig. 4.6D−G. In another work, rGO-HKUST-1 composite was synthesized by ultrasonic mixing method. The surface morphologies are as shown in Fig. 4.6A and B. Addition of rGO to HKUST-1 results in the formation of 8.2 nm pore size with mesoporous structure, high specific surface area, and specific capacitance compared to that of the pure HKUST-1. Graphene and CNTs are also found to have a profound effect on the performance of Ni-MOFs [133,134,148,149] (Fig. 4.6C−E). The insulating properties of MOFs can also be solved by combining them with appropriate conducting polymers to realize high-performance SCs.

Among the reported conducting polymers [135−139], PANI-electrodeposited ZIF-67 on a carbon cloth reported by Wang et al. [135] exhibited the best electrochemical performance. ZIF-67 was synthesized on a carbon cloth (cc)

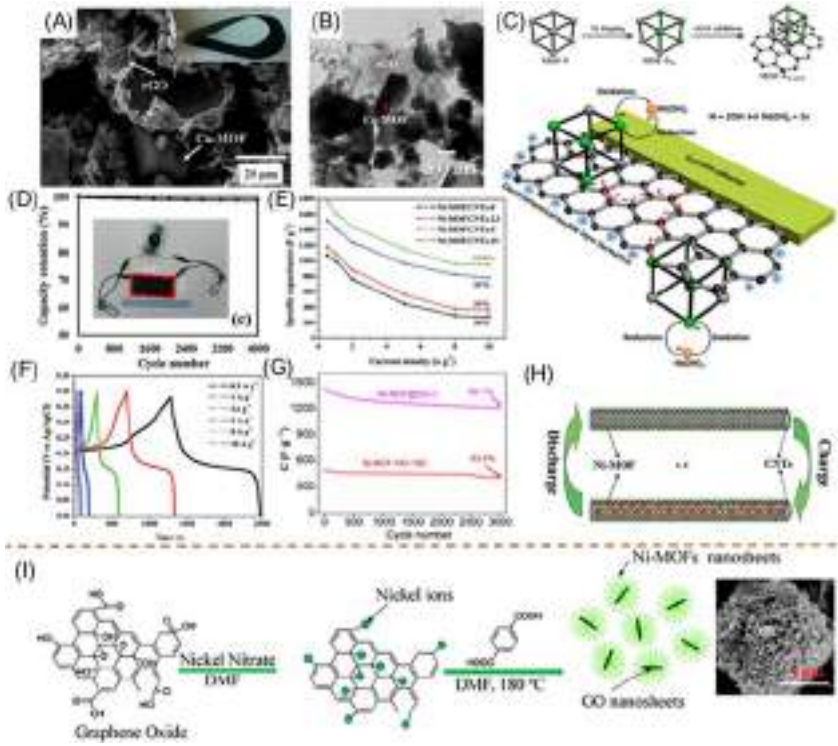

FIGURE 4.6 (A and B) SEM and TEM images of rGO-HKUST-1 composite. (C) Scheme showing the formation of a composite of rGO and Ni-doped MOF-5. (D) Capacity versus cycle no. of a single cell supercapacitor. (E) Specific capacitance of different Ni-MOF/CNTs. (F) Charge−discharge curves of Ni-MOF/CNT-5 at 0.5−10 A g^{-1}. (G) Capacitance cycling performance of Ni-MOF-HCl-180 and Ni-MOFs@GO-3 at 10 A g^{-1}. (H) The storage and release of electrons in the Ni-MOF/CNT composite. (I) Illustration of in situ compound of Ni-MOFs with GO nanosheets. *MOFs*, Metal-organic frameworks. *Reproduced from Xu Y, Li Q, Xue H, Pang H. Metal-organic frameworks for direct electrochemical applications. Coord Chem Rev 2018;376:292−318 with permission from Elsevier.*

and on top of that PANI was electrodeposited to get a flexible electrode (PANI-ZIF-67-CC). This modification decreased the total resistance of the MOF with no structural change. It exhibited superior areal capacitance of 2146 mF cm^{-2} in 3 M KCl solution, and this value reported was found to be greater than most of the SCs studied in the literature. In addition to carbon and polymer conducting materials, some researchers have also used nickel hydroxyl compounds, Zn-doped MOFs, and MnO_x-activated carbon materials to enhance the conductivity of MOFs [130,144−147], and among them, the MnO_x-MHCF nanocube electrode exhibited a good specific capacitance of 1200 F g^{-1} at 10 A g^{-1} [147]. The SC performance of various MOFs has been summarized in Table 4.3.

4.3.3 Electrocatalysis applications of various metal-organic frameworks

Nowadays, the need for clean and safe energy technologies is growing and electrochemical energy conversion and storage making use of fuels such as methanol, ethanol, CO_2, H_2O_2, H_2, and glucose are a gaining lot of significance. As alternative energy sources, they can replace traditional fossil fuels which are not environmentally friendly. In this connection, MOFs form a new class of electrocatalysts for electrochemical energy conversion reactions such as OERs, ORRs, and HERs and have attracted the interest of many researchers. Many MOFs have been studied for their electrocatalytic properties such as Cu-based MOFs [156–158], Fe-, Co-, Ni-based MOFs [30,159–168], bimetallic MOFs [169–171], inkjet-printed MOFs [172,173], and other MOFs [174,175]. Cu-based MOFs include Cu-bipy-BTC MOF [156,157] and $[Cu(adp)(BIB)(H_2O)]_n$ (BIB = 1,4-bisimidazolebenzene; H_2adp = adipic acid) [158]. Among them, Cu-bipy-BTC MOF shows good ORR electrocatalytic activity in phosphate buffer (pH = 6) [156]. In addition, Cu-based MOF modified electrodes also has good catalytic activity toward the oxidation of H_2O_2 and glucose.

Among iron-, cobalt-, and nickel-based MOFs, Fe-MOF-525 [176] was found to be good as catalyst for CO_2 reduction reaction. High porosity and excellent chemical and structural stabilities make the MOF-525 a good electrocatalyst. Later, porphyrinic PCN-223-Fe frameworks [166] were found to have good catalytic activity and selectivity for H_2O/H_2O_2. These finding pave the way for improving MOF-based ORR catalysts by choosing H^+ sources best adjusted to the internal pore environment. Co-based, cobalt-citrate MOFs (UTSA-16) showed very good electrocatalytic OER activity in alkaline medium [159]. An over potential 408 mV at 10 mA cm^{-2} was reported for UTSA-16 which was superior among all the MOF-based electrocatalysts and the standard Co_3O_4 counterparts. This superior electrocatalytic activity of UTSA-16 was attributed its favorable structure, uniform distribution of electroactive metal center (cobalt) in the framework, large accessible surface, and electronic motion. Among bimetallic MOFs as electrocatalysts [20,169,171], the NiFe-MOF [163] electrode had excellent OER and HER properties (240 mV at 10 mA cm^{-2}, a small Tafel plots of 34 mV dec^{-1}) and good stability of 12,000 seconds which was superior compared to its bulk NiFe-MOF and Ni-MOF.

Functionalized MOFs are found to be effective on the OER reaction thermodynamics and to understand it, Musho et al. [173] designed UiO-66(Zr) MOFs. Later, polyoxometalate-based MOFs (POMOFs) were studied as promising electrocatalysts for HER [167,177]. Among the two POMOFs, NENU-500 and NENU-501 that are synthesized [178], NENU-500 exhibited an initial over potential of 180 mV, and in acidic conditions, it shows an over potential of 237 mV at 10 mA cm^{-2} which were far higher than that reported for similar materials. Coordination of unsaturated metal sites (CUMSs) as the catalytic centers for OER reactions is another popular field of research. However, controlling the CUMSs in MOFs is a challenging task [174,175].

TABLE 4.3 Performance of various metal-organic frameworks (MOFs) and MOF composites in SCs.

MOFs as electrodes	Electrolyte	Current density	Specific capacitance	Capacity retention (%)/cycle number	References
Ni-MOF-24	6 M KOH	0.5	1127	>90/3000	[111]
$Ni_3(HITP)_2$	1 M $TEABF_4$/CAN	0.1	117	90/10,000	[112]
$([Ni_3(OH)_2(C_8H_4O_4)_2(H_2O)_4] \cdot 2H_2O$	3 M KOH	1.4	988	96.5/5000	[113]
Ni-DMOF-ADC013	2 M KOH	50	395	>98/16,000	[114]
$Ni(HOC_6H_4COO)_{1.48}(OH)_{0.52} \cdot 1.1H_2O$	6 M KOH	1	1698	94.8/1000	[115]
Co_8-MOF-5	0.1 M $TBAPF_6$ in C_2H_3N	0.01	0.3	92/1000	[116]
Co-LMOF	1 M KOH	1	2474	94.3/2000	[117]
Co-MOF	5 M KOH	1	2564	95.8/3000	[118]
Co-MOF	1 M LiOH	0.6	206.76	98.5/1000	[119]
Co-BPDC	0.5 M LiOH	–	179.2	94.3/1000	[120]
Cu-CAT NWAs	3 M KCl	0.5	120	80/5000	[123]
$\{[Cu_2Cl(OH)(L)_2](CH_3OH)_4\}_n$	6 M KOH	0.5	1148	90/2000	[150]
CIRMOF-3-950	1 M H_2SO_4	–	239	–/10,000	[151]
UiO-66	6 M KOH	–	920	–/5000	[124]

(*Continued*)

TABLE 4.3 (Continued)

MOFs as electrodes	Electrolyte	Current density	Specific capacitance	Capacity retention (%)/cycle number	References
Zr-MOF	6 M KOH	–	1144	–/2000	[125]
HP-UiO-66	6 M KOH	0.2	849	68.8/2000	[126]
Ni/Co-MOF	3 M KOH	1	1049	97.4/5000	[152]
Ni/Co-MOF	1 M LiOH	1	530.4	99.75/2000	[127]
Co/Ni-MOF	3 M KOH	–	–	–/5000	[128]
Zn/Ni-MOF	3 M KOH	–	–	–/5000	[128]
NiCo-NFA	–	1	129.8	94.1/5000	[153]
$^{MOF\text{-}5}$Ni50% rGO50%	1 M KOH	–	758	–/500	[131]
10 wt.% rGO/HKUST-1	0.5 M Na_2SO_4	1	385	–/4000	[132]
ZIF-8/GO	6 M KOH	–	400	–/1500	[133]
ZIF-67/GO	6 M KOH	–	252	76/1500	[133]
Ni-MOFs@GO-3	2 M KOH	1	2192.4	85.1/3000	[148]
Ni-MOF/CNT-5	6 M KOH	0.5	1765	95/5000	[149]
CNTs@Mn-MOF	1 M Na_2SO_4	1	203.1	88/3000	[154]
MOF-5/AC-C nsp 850	6 M KOH	1.5	300	91.5/3000	[155]
PANI-ZIF-67-CC	3 M KCl	–	371	>80/2000	[135]
PEDOT/H-15G-CNTF	3 M KCl	–	–	89.8/2000	[136]

MOF/PANI	1 M H_2SO_4	1	477	>90/100	[137]
POAP/ZIF-67	0.1 M $HClO_4$	–	724	–/–	[138]
POAP/$Cu(btec)_{0.5}$DMF	0.1 M $HClO_4$	–	241	91/1000	[139]
POAP/Cu-bipy-BTC	0.1 M $HClO_4$	–	422	–/1000	[140]
ZIF-PPy-2	1 M Na_2SO_4	0.5	554.4	90.7/10,000	[141]
Zn/Ni-MOF@PPy	3 M KOH	1	160.1	91.8/3000	[142]
$Ni_2CO_3(OH)_2$/ZIF-8	6 M KOH	–	851	–/5000	[130]
$Ni_3(NO_3)_2(OH)_4$@Zr-MOF	6 M KOH	–	992	–/3000	[144]
NiC_2O_4/ZIF-67	6 M KOH	–	1019.7	73/2000	[145]
MOF-2	6 M KOH	0.25	1620	>91/3000	[146]
MnO_x–MHCF	1.0 M Na_2SO_4	10	1200	>94.7/10,000	[147]

Source: Reproduced with permission from Xu Y, Li Q, Xue H, Pang H. Metal-organic frameworks for direct electrochemical applications. Coord Chem Rev 2018;376:292–318.

Apart from the above discussed pure MOFs for electrocatalysis, MOF composites have also been proposed to overcome the inherent poor conductivity of pure MOFs [179,180]. GO-incorporated Cu-MOF composites [181], CNTs incorporated Co-MOF [179,182], CuS-doped nano-CuS@Cu-BTC [183], ε-MnO_2/MOF(Fe) composite [184], and (CoBDC)-$Ti_3C_2T_x$ nanosheet hybrid have been proposed and studied to improve the electrocatalytic performance of the respective MOFs as catalysts for HER, OER, and/or ORR. Among the various GO incorporated MOFs, the (GO 8 wt.%)@Cu-MOF exhibited the best HER performance [181]. The CNTs are also good at improving electron transport in CNTs@Co-MOF [179] and when the weight ratio of CNTs was 5%, the catalytic activity of the MOF nanocomposites were almost comparable with that of RuO_2 and 20 wt.% Pt/C catalysts. The excellent catalytic activity was assigned to the unique three-dimensional layered structure and the combined effect of redox active Co(II), organic linker, and CNTs. Though efforts have been made to improve the electrocatalytic performance of MOFs using GO and CNTs [182], their performances were not satisfactory.

CuS pore inclusion into Cu-BTC to get nano-CuS(x wt.%)@Cu-BTC is found to have greater impact on the ORR catalytic activity of the MOF than the single pure component. The amount of CuS incorporated into the Cu-BTC MOF found to affect the porosity and conductivity the MOF. The nano-CuS(x wt.%)@Cu-BTC had increased current density compared to that of pure Cu-BTC and/or nano-CuS(99 wt.%). Later, Zhao et al. [185] reported a two-dimensional cobalt 1,4-benzenedicarboxylic acid (CoBDC)-$Ti_3C_2T_x$ lamellar nano-hybrid material synthesized by interdiffusion reaction for OER applications. The hybrid composite material developed an excellent double-layer capacitance and a Tafel slope of 48.2 mV dec^{-1} in 0.1 M KOH electrolyte. This value was significantly higher than that of the standard IrO_2-based catalysts. The electrocatalytic performance of various MOFs and MOF composites are summarized in Table 4.4.

4.3.4 Electrochemical sensing applications of various metal-organic frameworks

MOFs have been used rarely in the past for electrochemical sensing due to their insulating properties or poor conductivity. However, introduction of redox and catalytically active sites through metal nodes and ligands into the MOFs have achieved some progress in the electrochemical determination of H_2O_2, glucose, heavy metals, and so on (Table 4.5). The pure MOFs reported for electrochemical sensing include ZIF-67 crystallites [189] and Co-MOFs [190] for H_2O_2 sensing, Cu-based MOFs for glucose sensing [158,191], porphyrin MOFs for nitrite sensing [192], DNA functionalized ion-porphyrinic MOF for Pb^{2+} sensing [193], TMU-16-NH_2 MOF for Cd^{2+} sensing [194], synthetic MOFs as electrochemical chiral sensors and bifunctional luminescent sensors [206,207] and Cd-, Ni-based MOFs for nitrobenzene and glucose sensing [208]. In addition to these

MOFs, other MOFs have been applied for successful detection of analytes as shown in Table 4.5. Among all these various MOFs, Cu-based MOFs are found to be having lowest detection limit of 0.1 μM for the detection of catechol and hydroquinone [177] making them the best electrochemical sensors. They are also found to be good in electrochemical detection of glucose and H_2O_2.

Due to the inherent insulating properties of pure MOFs, MOFs composites with improved electrical conductivity and electrochemical sensitivity to H_2O_2 and glucose have also been studied by many researchers. Nanocomposites are particularly attractive for electrochemical sensing application owing to their high electrical conductivity. Nanocomposites of Cu-based MOFs and carbon materials particularly graphene and its derivatives have always been the focus of many researchers [177,195−197]. A nonenzymatic sensor, GO(SGO)@HKUST-1 designed by Wang et al. [198] by solvothermal reduction (SGO) has a higher effective surface area due to its flower-like structure as shown in Fig. 4.7 and has high selectivity and sensitivity to H_2O_2 detection. Ninety-seven percent of its initial current response was retained after storing the electrode for 15 days.

In another work, nanosized electrochemically reduced graphene oxide (nERGO) modified Cu-MOF, Cu-TDPAT-nERGO exhibited excellent electrocatalytic activity toward the detection of H_2O_2, highlighting the importance of nERGO. Gold nanoparticles (Au NPs) and silver (Ag NPs) have also been combined with MOFs to obtain Au-MOF-5(Zn) and Ag@MOF-5 (Zn) [200,209]. These MOF nanocomposites were applied for the determination of nitrite and nitrobenzene which are considered harmful pollutants. Many other MOF composites such as Cu_xONPs@ZIF-8 polyhedra with core−shell heterostructures (Fig. 4.7) and others have also been reported apart from the above-discussed important MOF composites for electrochemical sensing [202−205,210−212]. Due to the advances in nanoscience and technology, MOF-based sensors are gaining more significance in clinical, environmental, and industrial applications. Compared to pure MOF which suffer from low sensitivity, narrow linear range and poor stability, MOF composites particularly when combined with graphene, CNTs, and metal NPs offer better electrochemical sensing and overcome the drawbacks of pure MOFs.

4.3.5 Other electrochemical applications of metal-organic frameworks

MOFs have found applications in other electrochemical fields apart from batteries, supercapacitors, electrocatalysis, and electrochemical sensing [213,214]. The MOF, NU-901 film grown on a glass substrate was found to exhibit reversible and fast electrochromism (reversible color change due to the stabilization of radical cation of pyrene linker by the rigid MOF) [213]. In another work, Zn_4O(1,4-benzenedicarboxylate)$_3$ (MOF-5) [214] was electrodeposited from $Zn_4O(O_2C-)_6$, and the findings proved that

TABLE 4.4 Electrocatalytic performance of various metal-organic frameworks (MOFs) and MOF composites for oxygen evolution reaction (OER) and oxygen reduction reaction (ORR).

Material	Testing condition	E_{onset}/V[a] (V vs RHE)	$E_{j=10}$ V[b] (V vs RHE)	Tafel slope (mV dec^{-1})	References
OER					
UTSA-16	1.0 M KOH	1.6	1.638	77	[159]
Co-MOF/NF	1.0 M KOH	1.61	1.541	77	[160]
NiPc-MOF	1.0 M KOH	1.48	1.58	74	[161]
NiCo-UMOFNs	1.0 M KOH	1.42	1.48	42	[186]
NiFe-MOF	0.1 M KOH	–	1.47	34	[20]
MOF(Fe_1−Co_3)$_{550}$N	0.1 M KOH	–	1.62	72.9	[187]
Fe/$Ni_{2.4}$/$Co_{0.4}$-MIL-53	1.0 M KOH	–	1.449	52.2	[170]
ZIF-67	0.5 M KBi	1.58	1.78	74.9	[174]
CUMSs-ZIF-67	0.5 M KBi	1.50	1.64	53.7	[174]
CoCd-BNN	0.1 M KOH	–	1.583/1 mA cm^{-2}	110	[175]
(GO 8 wt.%) Cu-MOF	0.5 M H_2SO_4	1.19	1.34/2 mA cm^{-2}	65	[181]
Co-MOF@CNTs (5 wt.%)	1.0 M KOH	1.51	1.57	69	[179]
$Ti_3C_2T_x$-CoBDC	0.1 M KOH	1.51	1.64	48.2	[185]
ORR			Half-wave potential ($E_{1/2}$)		

Ni/Co-MOF	0.1 M KOH	0.76	0.82	–	[71]
Fe-MOF@CNTs-G	0.1 M $HClO_4$	0.839	0.715	121.7	[182]
ε-MnO_2/MOF(Fe)	0.1 M KOH	0.84	0.64	117	[184]
HER					
(GO 8 wt.%) Cu-MOF	0.5 M H_2SO_4	0.087	–	84	[188]
NENU-500	0.5 M H_2SO_4	1.41	–	96	[178]

HER, Hydrogen evolution reaction.
[a]E_{onset} *for onset potential.*
[b]E_j *= 10 for overpotential required for the current density of 10 mA* cm^{-2}.
Source: Reproduced with permission from Xu Y, Li Q, Xue H, Pang H. Metal-organic frameworks for direct electrochemical applications. Coord Chem Rev 2018;376:292–318.

TABLE 4.5 Electrochemical performance of various metal-organic framework (MOF) and MOF composites in sensors.

MOFs	Modified electrode	Detection limit (mM)	Linear range (μM)	Test sample	References
ZIF-67	ZIF-67	–	0.125–400	Glutathione	[189]
Co-MOF	$Co(pbda)(4,4\text{-bpy})\ 2H_2O]_n$	3.76	5–9000	H_2O_2	[190]
Cu-MOF	$Cu(adp)(BIB)(H_2O)]_n$	0.068	0.1–2.75	H_2O_2	[158]
Cu-MOF	MOF-14	1	1–900	H_2O_2	[176]
Cu-MOF	$[Cu_3(btc)_2]$	–	0.125–2250	Glucose	[191]
Zr-MOF	MOF-525	2.1	20–800	nitrite	[192]
$(Fe\text{-}P)_n$-MOF	$(Fe\text{-}P)_n$-MOF-Au	0.02×10^{-3}	0.03×10^{-3}–1	Pb^{2+}	[193]
TMU-16-NH_2	TMU-16-NH_2	0.2 mg L^{-1}	0.7–120 mg L^{-1}	Cd^{2+}	[194]
Cu-MOF	Cu-MOF–GN-3/GCE	2	10–11,180	H_2O_2	[195]
Cu-MOF	Cu-MOF–GN-3/GCE	0.02	0.5–6965.5	Ascorbic acid	[195]
Cu-MOF	Cu-hemin MOFs/CS-rGO	0.019	0.065–410	H_2O_2	[196]
Cu-based MOF-199	MOF-ERGO-5/GCE	0.1	0.1–566	Catechol	[177]
Cu-based MOF-199	MOF-ERGO-5/GCE	0.1	0.1–476	Hydroquinone	[177]
$\{[Cu_2(bep)(ada)_2]H_2O\}_n$	Cu-MOF/AB-2%/GCE	0.014	0.05–3	H_2O_2	[197]
HKUST-1	SGO@HKUST-1	0.49	1.0–5600	H_2O_2	[198]
Cu-TDPAT	Cu-TDPAT-nERGO	0.17	4–12,000	H_2O_2	[199]
MOF-5	GC/Au-MOF-5	1	–	Nitrite	[200]

MOF-5	GC/Au-MOF-5	15.3	–	Nitrobenzene	[200]
Zn-TSA	IL/Mb/Ag@Zn-TSA-CPE	0.15	0.3–20,000	H_2O_2	[201]
Zn-TSA	IL/Mb/Ag@Zn-TSA-CPE	0.5	1.3–133,000	NO_2	[201]
Zn-TSA	IL/GO_x/Ag@Zn-TSA-CPE	0.8	2.0–1022	Glucose	[201]
ZIF-8	Cu_xO NPs@ZIF-8	0.15	1.5–21,442	H_2O_2	[202]
UiO-66-NH_2	UiO-66-NH_2@PANI/GCE	0.3 mg L^{-1}	0.5–600 mg L^{-1}	Cd^{2+}	[203]
Ni-MOF	Ni-MOF/MWCNTs	3	10–1120	Urea	[204]
PCN-333 (Al)	3D-KSC/PCN-333 (Al)@MP-11	0.127	0.387–1725	H_2O_2	[205]

Reproduced with permission from Xu Y, Li Q, Xue H, Pang H. Metal-organic frameworks for direct electrochemical applications. Coord Chem Rev 2018;376:292–318.

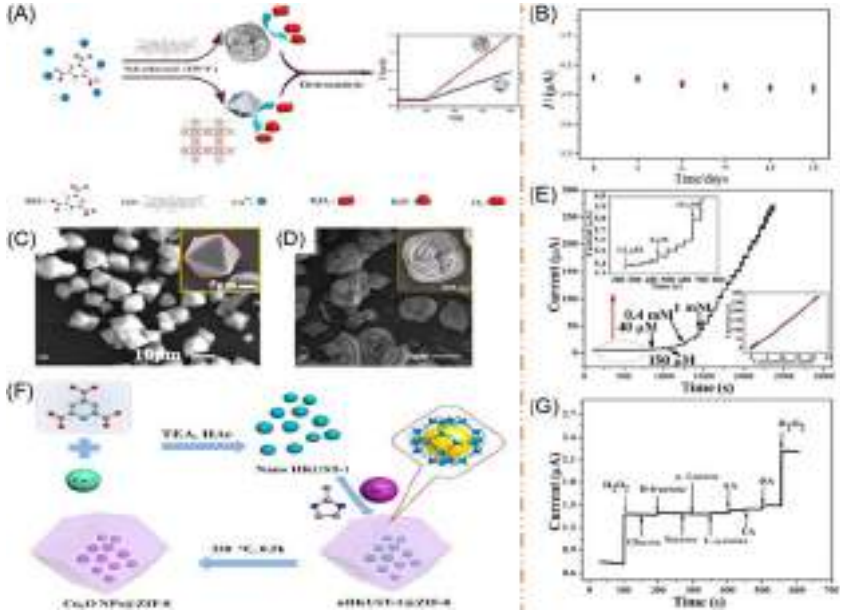

FIGURE 4.7 (A) Scheme showing the synthesis of SGO@HKUST-1 and its sensor application, (B) reproducibility study of CS-SGO@HKUST-1/GCE in the presence of 0.2 mM H_2O_2 in PBS at pH 7.0 tested every 3 days over 15 days, (C) SEM images ofSGO@HKUST-1, (D) addition of GO during synthesis was 0.13 mg mL^{-1}, (E) amperometric response curves of Cu_xONPs@ZIF-8/GCE upon successively adding H_2O_2 at 0.7 V. Left inset: amperometric response of H_2O_2 at lower concentration and right inset: the relationship between current signal and H_2O_2 concentration, (F) illustration of the synthesis of Cu_xO NPs@ZIF-8, and (G) current response of Cu_xO NPs@ZIF-8/GCE to 50 μM H_2O_2 and other biomolecules. *Reproduced from Xu Y, Li Q, Xue H, Pang H. Metal-organic frameworks for direct electrochemical applications. Coord Chem Rev 2018;376:292−318 with permission from Elsevier.*

electrochemical processes responsible for crystallization of MOF-5 is relatively complex in nature.

4.4 Conclusion

An insight into the electrochemical aspects of MOFs and their composites has been presented from their synthesis to applications. Electrochemical synthesis methods have been used so far mostly to synthesis MOFs sensing applications. Electrochemical synthesis methods are particular useful for the formation of MOF thin films. However, more research is required to investigate the effects of various synthesis parameters such as solvent properties, conductivity, applied current and voltage, synthesis time better understanding of the effect of side reactions in the electro formation of MOFs for other electrochemical applications such as batteries and supercapacitors. Poor

electrical conductivity hampers the direct applications of MOFs, and MOF composites formed by the combination of MOF with conductive additives such as graphene, CNTs, and conducting polymers appears to overcome the problem. Mesoporous MOFs and MOF composites with high surface area can increase the diffusion kinetics by shortening the path length for electron and ion transport in batteries. Compared to transition metal oxides, the capacitance of MOFs is low due to their poor conductivity, and their conductivity can be enhanced by doping with other conducting materials. MOFs and their composites hold potential application in the electrochemical fields due to their unique properties. However, finding a method for large-scale production of MOF and MOF composites is the key for rapid growth and development of this interesting field of science.

Acknowledgment

This work has been supported by the Science and Engineering Research Board (SERB), DST, Govt. of India (project no. ECR/2016/00046).

References

[1] Jian-Ke S, Qiang X. Functional materials derived from open framework templates/precursors: synthesis and applications. Energy Environ Sci 2014;7:2071–100.

[2] Xu G, Nie P, Dou H, Ding B, Li L, Zhang X. Exploring metal organic frameworks for energy storage in batteries and supercapacitors. Mater Today 2017;20:191–209.

[3] Howarth AJ, Liu Y, Li P, Li Z, Wang TC, Hupp JT, et al. Chemical, thermal and mechanical stabilities of metal–organic frameworks. Nat Rev Mater 2016;1:15018.

[4] Kinoshita Y, Matsubara I, Higuchi T, Saito Y. The crystal structure of bis(adiponitrilo) copper (l) nitrate. Bull Chem Soc Jpn 1959;32:1221–6.

[5] Aleksandra AB, Matveeva NG. Polymeric chelate compounds. Russ Chem Rev 1960;29:119–28.

[6] Hoskins BF, Robson R. Design and construction of a new class of scaffolding-like materials comprising infinite polymeric frameworks of 3D-linked molecular rods. A reappraisal of the zinc cyanide and cadmium cyanide structures and the synthesis and structure of the diamond-related frameworks $[N(CH_3)_4][Cu^{I}Zn^{II}(CN)_4]$ and Cu^{I}[4,4′,4″,4‴-tetracyanotetraphenylmethane] $BF_{4.x}C_6H_5NO_2$. J Am Chem Soc 1990;112:1546–54.

[7] Kitagawa S, Matsuyama S, Munakata M, Tsunehiko E. Synthesis and crystal structures of novel one-dimensional polymers, $[\{M(bpen)X\}_\infty]$[$M = Cu^{I}$, $X = PF_6^-$; $M = Ag^{I}$, $X = ClO_4^-$; bpen = *trans*-1,2-bis(2-pyridyl)ethylene] and $[\{Cu(bpen)(CO)(CH_3CN)(PF_6)\}_\infty]$. J Chem Soc Dalton Trans 1991;2869–74.

[8] Yaghi OM, Hailian L. Hydrothermal synthesis of a metal-organic framework containing large rectangular channels. J Am Chem Soc 1995;117:10401–2.

[9] Gardner GB, Venkataramani D, Moore JS, Lee S. Spontaneous assembly of a hinged coordination network. Nature 1994;374(7):92–795.

[10] Riou D, Ferey G. Hybrid open frameworks (MIL-*n*). Part 3 Crystal structures of the HT and LT forms of MIL-7: a new vanadium propylenediphosphonate with an

open-framework. Influence of the synthesis temperature on the oxidation state of vanadium within the same structural type. J Mater Chem 1998;8:2733–5.
[11] Stuart LJ. Metal-organic frameworks. Chem Soc Rev 2003;32:276–88.
[12] Omar KF, Joseph TH. Rational design, synthesis, purification and activation of metal–organic framework materials. Acc Chem Res 2010;43:1166–75.
[13] Chenghong W, Xinlei L, Nilay KD, Chen JP, Li K. Applications of water stable metal–organic frameworks. Chem Soc Rev 2016;45:5107–34.
[14] Carne A, Carbonell C, Imaz I, Maspoch D. Nanoscale metal–organic materials. Chem Soc Rev 2011;40:291–305.
[15] Tard AB, Fischer RA. Metal–organic framework thin films: from fundamentals to applications. Chem Rev 2012;112:1055–83.
[16] Xiehong C, Chaoliang T, Melinda S, Zhang H. Hybrid micro-/nano-structures derived from metal–organic frameworks: preparation and applications in energy storage and conversion. Chem Soc Rev 2017;46:2660–77.
[17] Jyotsana M, Neha B, Sanjeev KB, Kim KH, Akash D. Recent advances in enzyme immobilization techniques: metal-organic frameworks as novel substrates. Coord Chem Rev 2016;322:30–40.
[18] Chao-Ying G, Hong-Rui T, Jing A, Lei-Jiao L, Dang S, Ya-Qian L, et al. A microporous Cu-MOF with optimized open metal sites and pore spaces for high gas storage and active chemical fixation of CO_2. Chem Commun 2016;52:11147–50.
[19] Anindita C, Syamantak R, Muthusamy E, Maji TK. Flexible MOF–aminoclay nanocomposites showing tunable stepwise/gated sorption for C_2H_2, CO_2 and separation for CO_2/N_2 and CO_2/CH_4. J Mater Chem 2017;A5:8423–30.
[20] Duan J, Chen S, Zhao C. Ultrathin metal-organic framework array for efficient electrocatalytic water splitting. Nat Commun 2017;8:15341.
[21] Zhichao H, Benjamin JD, Jing L. Luminescent metal–organic frameworks for chemical sensing and explosive detection. Chem Soc Rev 2014;43:5815–40.
[22] Fei-Yan Y, Dongxiao C, Meng-Ke W, Han L, Jiang H. Chemical sensors based on metal–organic frameworks. ChemPlusChem 2016;81:675–90.
[23] Norbert S, Shyam B. Synthesis of metal-organic frameworks (MOFs): routes to various MOF topologies, morphologies, and composites. Chem Rev 2012;112:933–69.
[24] Liyu C, Rafael L, Yingwei L. Controllable design of tunable nanostructures inside metal–organic frameworks. Chem Soc Rev 2017;46:4614–30.
[25] Hao BW, Xiong W(D)L. Metal-organic frameworks and their derived materials for electrochemical energy storage and conversion: promises and challenges. Sci Adv 2017;3:9252.
[26] Wang L, Han Y, Feng X, Zhou J, Qi P, Wang B. Metal–organic frameworks for energy storage: batteries and supercapacitors. Coord Chem Rev 2016;307:361–81.
[27] Yang Z, Zhongxin S, Li X, Sun Q, Cheng N, Lawes S, et al. Metal organic frameworks for energy storage and conversion. Energy Storage Mater 2016;2:35–62.
[28] Xu Y, Li Q, Xue H, Pang H. Metal-organic frameworks for direct electrochemical applications. Coord Chem Rev 2018;376:292–318.
[29] Shasha Z, Xinran L, Bingyi Y, Qin H, Yuxia X, Xiao X, et al. Transition-metal (Fe, Co, Ni) based metal-organic frameworks for electrochemical energy storage. Adv Energy Mater 2017;7:1602733.
[30] Mahmood A, Guo W, Tabassum H, Zou R. Metal-organic framework-based nanomaterials for electrocatalysis. Adv Energy Mater 2016;6:1600423.

[31] Kutubi HA, Gascon J, Sudhölter EJR, Rassaei L. Electrosynthesis of metal-organic frameworks: challenges and opportunities. ChemElectroChem 2015;2:462–74.
[32] Qihao Y, Qiang X, Hai-Long J. Metal–organic frameworks meets metal nanoparticles: synergistic effect for enhanced catalysis. Chem Soc Rev 2017;46:4774–808.
[33] Jianping L, Ruocan Q, Pinghual L, Lin C, Huangxian J. Design and sensing applications of metal–organic framework composites. TrAC Trends Anal Chem 2014;58:71–8.
[34] Rob A, Linda S, Jan F, Luc A, Bert FS, De Vos DE. Patterned growth of metal-organic framework coatings by electrochemical synthesis. Chem Mater 2009;21:2580–2.
[35] Mueller U, Puetter H, Hesse M, Wessel H. WO2005049892 – Method for electrochemical production of a crystalline porous metal organic skeleton material. Patent scope. 2005.
[36] Stephen S-YC, Samuel M-FL, Jonathan PHC, Orpen AG, Williams ID. A chemically functionalizable nanoporous material $[Cu_3(TMA)_2(H_2O)_3]_n$. Science 1999;283:1148–50.
[37] Mueller U, Schubert M, Teich F, Puetter H, Schierle-Arndt K, Pastre J. Metal–organic frameworks—prospective industrial applications. J Mater Chem 2006;16:626–36.
[38] Hartmann M, Sebastian K, Dieter H, Oliver T, Stefan E, Alex W. Adsorptive separation of isobutene and isobutane on $Cu_3(BTC)_2$. Langmuir 2008;24:8634–42.
[39] Senthil KR, Senthil Kumar S, Anbu Kulandainathan M. Efficient electrosynthesis of highly active $Cu_3(BTC)_2$-MOF and its catalytic application to chemical reduction. Microporous Mesoporous Mater 2013;168:57–64.
[40] Tom RCVA, Gert D, Rob A, Dirk EDV, Herman T, Denayer JFM. Electrochemical synthesis of thin HKUST-1 layers on copper mesh. Microporous Mesoporous Mater 2012;158:209–13.
[41] Alberto MJ, Jana J-A, Pablo S-C, Freek K, Gascon J. Electrochemical synthesis of some archetypical Zn^{2+}, Cu^{2+}, and Al^{3+} metal organic frameworks. Cryst Growth Des 2012;12:3489–98.
[42] Russell EM. Ionothermal synthesis—ionic liquids as functional solvents in the preparation of crystalline materials. Chem Commun 2009;2990–8.
[43] Yang HM, Song XL, Yang TL, Liang ZH, Fan CM, Hao XG. Electrochemical synthesis of flower shaped morphology MOFs in an ionic liquid system and their electrocatalytic application to the hydrogen evolution reaction. RSC Adv 2014;4:15720–6.
[44] Wei JL, Jian L, Shui-Ying G, Qiao-Hong L, Rong C. Electrochemical preparation of metal–organic framework films for fast detection of nitro explosives. J Mater Chem A 2014;2:19473–8.
[45] Nicolo C, Tom VA, Tom B, Joeri D, Koen B, Dirk EDV, et al. High pressure, high temperature electrochemical synthesis of metal–organic frameworks: films of MIL-100 (Fe) and HKUST-1 in different morphologies. J Mater Chem A 2013;1:5827–30.
[46] Yadnum S, Roche J, Lebraud E, Negrier P, Garrigue P, Bradshaw D, et al. Inside back cover: site-selective synthesis of Janus-type metal-organic framework composites. Angew Chem 2014;126:4082–6.
[47] Nicolo C, Ernesto RS, Dirk EDV, Koen B, Jan F. Luminescent terbium-containing metal–organic framework films: new approaches for the electrochemical synthesis and application as detectors for explosives. Chem Commun 2014;50:12545–7.
[48] Dinca M, Li M. Methods for electrochemically induced cathodic deposition of crystalline metal-organic frameworks. US patent. 2012.
[49] Huiping L, Hongming W, Tianshu C, Minghao Y, Yang Y. An electrodeposited lanthanide MOF thin film as a luminescent sensor for carbonate detection in aqueous solution. J Mater Chem C 2014;2:8683–90.
[50] Sivakumar B, Alison JD, Tefler SG. HKUST-1 growth on glassy carbon. J Mater Chem 2011;21:19207–9.

[51] Chuantao H, Jinyun P, Qin X, Zhengping J, Hu X. Elaborate fabrication of MOF-5 thin films on a glassy carbon electrode (GCE) for photoelectrochemical sensors. RSC Adv 2012;2:12696–8.

[52] Ameloot R, Pandey L, Mark VA, Luc A, Bert FS, De Vos ED. Patterned film growth of metal–organic frameworks based on galvanic displacement. Chem Commun 2010;46:3735–7.

[53] Idan H, Wojciech B, David MK, Pravas D, Chung-Wei K, Michael JK, et al. Directed growth of electroactive metal-organic framework thin films using electrophoretic deposition. Adv Mater 2014;26:6295–300.

[54] Wen-wen Z, Qin K, Jian-zhang Z, Xiang-jian K, Zhao-xiong X, Lan-sun Z. Semiconductor@metal–organic framework core–shell heterostructures: a case of ZnO@ZIF-8 nanorods with selective photoelectrochemical response. J Am Chem Soc 2013;135:1926–33.

[55] Yi-Min Z, Cheng-Hui Z, Tian-Shu C, Hong-Ming W, Yang YY, Ye-Xiang T, et al. A novel highly luminescent LnMOF film: a convenient sensor for Hg^{2+} detecting. J Mater Chem A 2013;1:11312–19.

[56] Gerard F, Franck M, Mathieu M, Christian S, Marie-Liesse D, Jean-Marc G, et al. Mixed-valence Li/Fe-based metal–organic frameworks with both reversible redox and sorption properties. Angew Chem Int Ed 2007;46:3259–63.

[57] Zhang L, Zheng S, Wang L, Tang H, Xue H, Wang G, et al. Fabrication of metal molybdate micro/nanomaterials for electrochemical energy storage. Small 2017;13:1700917.

[58] Combarieu GD, Morcrette M, Millange F, Guillou N, Cabana J, Grey CP, et al. Influence of the benzoquinone sorption on the structure and electrochemical performance of the MIL-53 (Fe) hybrid porous material in a lithium-ion battery. Chem Mater 2009;21:1602–11.

[59] Jae Wook S, Min K, Jordi C, Shawn C, Gregory JH, Thomas AY, et al. MIL-101(Fe) as a lithium-ion battery electrode material: a relaxation and intercalation mechanism during lithium insertion. J Mater Chem A 2015;3:4738–44.

[60] Shen L, Song H, Wang C. Metal-organic frameworks triggered high-efficiency Li storage in Fe-based polyhedral nanorods for lithium-ion batteries. Electrochim Acta 2017;235:595–603.

[61] Lei G, Li-Min H, Yong-Xin S, Shou-Long M, Xiao-Yong F, Lei X, et al. One-pot synthesis of a metal–organic framework as an anode for Li-ion batteries with improved capacity and cycling stability. J Solid State Chem 2014;210:121–4.

[62] Xiaoshi H, Huiping H, Chao L, Tian L, Xiaobing L, Qun C, et al. Cobalt-based metal organic framework with superior lithium anodic performance. J Solid State Chem 2016;242:71–6.

[63] Li C, Hu X, Lou X, Zhang L, Wang Y, Amoureux JP, et al. The organic-moiety-dominated Li^+ intercalation/deintercalation mechanism of a cobalt-based metal–organic framework. J Mater Chem A 2016;4:16245–51.

[64] Song H, Shen L, Wang J, Wang C. Reversible lithiation–delithiation chemistry in cobalt based metal organic framework nanowire electrode engineering for advanced lithium-ion batteries. J Mater Chem 2016;A4:15411–19.

[65] Danhua G, Jie P, Genlong Q, Geng H, Deng Y, Wu J, et al. Nanostructured Co(II)-based MOFs as promising anodes for advanced lithium storage. New J Chem 2016;40:9238–44.

[66] Li C, Xiaobing L, Ming S, Xiaoshi H, Zhi G, Yong W, et al. High anodic performance of Co 1,3,5-benzenetricarboxylate coordination polymers for Li-ion battery. ACS Appl Mater Interfaces 2016;8:15352–60.

[67] Sengodu P, Bongu C, Perumal M, Paramasivam M. Easy synthesis of microporous/mesoporous cobalt organic framework as binder less lithium-ion battery electrode. J Alloy Compd 2017;714:603–9.
[68] Liao Y, Li C, Lou X, Wang P, Yang Q, Shen M, et al. Highly reversible lithium storage in cobalt 2,5-dioxido-1,4-benzenedicarboxylate metal-organic frameworks boosted by pseudocapacitance. J Colloid Interface Sci 2017;506:365–72.
[69] Zhang Z, Yoshikawa H, Awaga K. Monitoring the solid-state electrochemistry of Cu(2,7-AQDC) (AQDC = anthraquinone dicarboxylate) in a lithium battery: coexistence of metal and ligand redox activities in a metal–organic framework. J Am Chem Soc 2014;136:16112–15.
[70] Maiti S, Pramanik A, Manju U, Mahanty S. Cu3(1,3,5-benzenetricarboxylate)$_2$ metal-organic framework: a promising anode material for lithium-ion battery. Microporous Mesoporous Mater 2016;226:353–9.
[71] Zhe P, Xiaohui Y, Zixuan L, Shang J, Wang D. Triphenylamine-based metal–organic frameworks as cathode materials in lithium-ion batteries with coexistence of redox active sites, high working voltage, and high rate stability. ACS Appl Mater Interfaces 2016;8:14578–85.
[72] Kaveevivitchai W, Allan JJ. Exploration of vanadium benzenedicarboxylate as a cathode for rechargeable lithium batteries. J Power Sources 2015;278:265–73.
[73] Maiti S, Pramanik A, Manju U, Mahanty U. Reversible lithium storage in manganese 1,3,5-benzenetricarboxylate metal–organic framework with high capacity and rate performance. ACS Appl Mater Interfaces 2015;7:16357–63.
[74] Liu Q, Lili Y, Ying W, Yunzhou J, Horvat J, Cheng M, et al. Manganese-based layered coordination polymer: synthesis, structural characterization, magnetic property and electrochemical performance in lithium-ion batteries. Inorg Chem 2013;52:2817–22.
[75] Zhang Z, Yoshikawa H, Awaga K. Discovery of a "bipolar charging" mechanism in the solid-state electrochemical process of a flexible metal–organic framework. Chem Mater 2016;28:1298–303.
[76] Zhang L, Cheng F, Shi W, Chen J, Cheng P. Transition-metal-triggered high-efficiency lithium ion storage via coordination interactions with redox-active croconate in one-dimensional metal–organic anode materials. ACS Appl Mater Interfaces 2018;10:6398–406.
[77] An T, Wang Y, Tang J, Wang Y, Zhang L, Zheng G. A flexible ligand-based wavy layered metal–organic framework for lithium-ion storage. J Colloid Interface Sci 2015;445:320–5.
[78] Zhang Y, Niu Y, Liu T, Li Y, Wang M, Hou J, et al. A nickel-based metal-organic framework: a novel optimized anode material for Li-ion batteries. Mater Lett 2015;161:712–15.
[79] Tian B, Ning G, Gao Q, Tan L, Tang W, Chen Z, et al. Metal-organic frameworks for direct electrochemical applications. ACS Appl Mater Interfaces 2016;8:31067–73.
[80] Saravanan K, Nagarathinam M, Balaya P, Vittal JJ. Lithium storage in a metal organic framework with diamondoid topology – a case study on metal formats. J Mater Chem 2010;20:8329–35.
[81] Tang B, Huang S, Fang Y, Hu J, Malonzo C, Truhlar DG, et al. Mechanism of electrochemical lithiation of a metal-organic framework without redox-active nodes. J Chem Phys 2016;144:194702.
[82] Angulakshmi N, Kumar RS, Kulandainathan MA, Stephan AM. Composite polymer electrolytes encompassing metal organic frame works: a new strategy for all-solid-state lithium batteries. J Phys Chem C 2014;118:24240–7.

[83] Liu W, Mi Y, Weng Z, Zhong Y, Wu Z, Wang H. Functional metal−organic framework boosting lithium metal anode performance *via* chemical interactions. Chem Sci 2017;8:4285−91.

[84] Ogihara N, Yasuda T, Kishida Y, Ohsuna T, Miyamoto K, Ohba N. Organic dicarboxylate negative electrode materials with remarkably small strain for high-voltage bipolar batteries. Angew Chem 2014;126:11651−6.

[85] Xu X, Chen S, Chen Y, Sun H, Song L, He W, et al. Polyoxometalate cluster-incorporated metal-organic framework hierarchical nanotubes. Small 2016;12:2982−90.

[86] Li T, Li C, Hu X, Lou X, Hu H, Pan L, et al. Reversible lithium storage in manganese and cobalt 1,2,4,5-benzenetetracarboxylate metal−organic framework with high capacity. RSC Adv 2016;6:61319−24.

[87] Sun X, Gao G, Yan D, Feng C. Synthesis and electrochemical properties of Fe_3O_4@MOF core-shell microspheres as an anode for lithium ion battery application. Appl Surf Sci 2017;405:52−9.

[88] Zheng X, Li Y, Xu Y, Hong Z, Wei M. Metal−organic frameworks: promising materials for enhancing electrochemical properties of nanostructured Zn_2SnO_4 anode in Li-ion batteries. CrystEngComm 2012;14:2112−16.

[89] Dong C, Xu L. Cobalt- and cadmium-based metal−organic frameworks as high-performance anodes for sodium ion batteries and lithium ion batteries. ACS Appl Mater Interfaces 2017;9:7160−8.

[90] Gou L, Liu PG, Liu D, Wang C, Lei H, Li ZY, et al. Rational synthesis of $Ni_3(HCOO)_6$/CNT ellipsoids with enhanced lithium storage performance: inspired by the time evolution of the growth process of a nickel formate framework. Dalton Trans 2017;46:6473−82.

[91] Jin Y, Zhao C, Sun Z, Lin Y, Chen L, Wang D, et al. Facile synthesis of Fe-MOF/RGO and its application as a high performance anode in lithium-ion batteries. RSC Adv 2016;6:30763−8.

[92] He S, Li Z, Ma L, Wang J, Yang S. Graphene oxide-templated growth of MOFs with enhanced lithium-storage properties. New J Chem 2017;41:14209−16.

[93] Gerbaldi C, Nair JR, Kulandainathan MA, Kumar RS, Ferrara C, Mustarelli P, et al. Innovative high performing metal organic framework (MOF)-laden nanocomposite polymer electrolytes for all-solid-state lithium batteries. J Mater Chem A 2014;2:9948−54.

[94] Han Y, Qi P, Zhou J, Feng X, Li S, Fu X, et al. Metal−organic frameworks (MOFs) as sandwich coating cushion for silicon anode in lithium ion batteries. ACS Appl Mater Interfaces 2015;7:26608−13.

[95] Han Y, Qi P, Feng X, Li S, Fu X, Li H, et al. In situ growth of MOFs on the surface of Si nanoparticles for highly efficient lithium storage: Si@MOF nanocomposites as anode materials for lithium-ion batteries. ACS Appl Mater Interfaces 2015;7:2178−82.

[96] Wang Z, Tan R, Wang H, Yang L, Hu J, Chen H, et al. A metal−organic-framework-based electrolyte with nanowetted interfaces for high-energy-density solid-state lithium battery. Adv Mater 2018;30:1704436.

[97] Meng-Ting L, Yu S, Kai-Sen Z, Zhao W, Xin-Long W, Zhong-Min S, et al. Metal−organic framework with aromatic rings tentacles: high sulfur storage in Li−S batteries and efficient benzene homologues distinction. ACS Appl Mater Interfaces 2016;8:33183−8.

[98] Demir-Cakan R, Morcrette M, Nouar F, Davoisne C, Devic T, Gonbeau D, et al. Cathode composites for Li−S batteries via the use of oxygenated porous architectures. J Am Chem Soc 2011;133:16154−60.

[99] Zhou J, Li R, Fan X, Chen Y, Han R, Li W, et al. Rational design of a metal−organic framework host for sulfur storage in fast, long-cycle Li−S batteries. Energy Environ Sci 2014;7:2715−24.
[100] Junwen Z, Yu X, Fan X, Wang X, Li H, Zhang Y, et al. The impact of the particle size of a metal−organic framework for sulfur storage in Li−S batteries. J Mater Chem A 2015;3:8272−5.
[101] Shanthi PM, Hanumantha PJ, Gattu B, Sweeney M, Datta MK, Kumta PN. Understanding the origin of irreversible capacity loss in non-carbonized carbonate − based metal organic framework (MOF) sulfur hosts for lithium − sulfur battery. Electrochim Acta 2017;229:208−18.
[102] Wang Z, Wang B, Yang Y, Cui Y, Wang Z, Chen B, et al. Metal-organic frameworks for direct electrochemical applications. ACS Appl Mater Interfaces 2015;7:20999−1002.
[103] Zhao Z, Wang S, Liang R, Li Z, Shi Z, Chen G. Graphene-wrapped chromium-MOF (MIL-101)/sulfur composite for performance improvement of high-rate rechargeable Li−S batteries. J Mater Chem A 2014;2:13509−12.
[104] Bai S, Liu X, Zhu K, Wu S, Zhou H. Metal−organic framework-based separator for lithium−sulfur batteries. Nat Energy 2016;1:16094.
[105] Bai S, Zhu K, Wu S, Wang Y, Yi J, Ishida M, et al. A long-life lithium−sulphur battery by integrating zinc−organic framework based separator. J Mater Chem 2016;A4:16812−17.
[106] Mao Y, Li G, Guo Y, Li Z, Liang C, Peng X, et al. Foldable interpenetrated metal-organic frameworks/carbon nanotubes thin film for lithium−sulfur batteries. Nat Commun 2017;8:1−8.
[107] Li Q, Xu P, Gao W, Ma S, Zhang G, Cao R, et al. Graphene/graphene-tube nanocomposites templated from cage-containing metal-organic frameworks for oxygen reduction in Li−O_2 batteries. Adv Mater 2014;26:1378−86.
[108] Wu D, Guo Z, Yin X, Pang Q, Tu B, Zhang L, et al. Metal−organic frameworks as cathode materials for Li−O_2 batteries. Adv Mater 2014;26:3258−62.
[109] Li C, Hu X, Hu B. Cobalt(II) dicarboxylate-based metal-organic framework for long-cycling and high-rate potassium-ion battery anode. Electrochim Acta 2017;253:439−44.
[110] Li C, Lou X, Yang Q, Zou Y, Hu B. Remarkable improvement in the lithium storage property of $Co_2(OH)_2$BDC MOF by covalent stitching to graphene and the redox chemistry boosted by delocalized electron spins. Chem Eng J 2017;326:1000−8.
[111] Yang J, Xiong P, Zheng C, Qiu H, Wei M. Metal−organic frameworks: a new promising class of materials for a high performance supercapacitor electrode. J Mater Chem 2014; A2:16640−4.
[112] Sheberla D, Bachman JC, Elias JS, Sun C, Shao-Horn Y, Dinca M. Conductive MOF electrodes for stable supercapacitors with high areal capacitance. Nat Mater 2017;16:220−4.
[113] Yan Y, Gu P, Zheng S, Zheng M, Pang H, Xue H. Facile synthesis of an accordion-like Ni-MOF superstructure for high-performance flexible supercapacitors. J Mater Chem 2016;A4:19078−85.
[114] Qu C, Jiao Y, Zhao B, Chen D, Zou R, Walton KS, et al. Nickel-based pillared MOFs for high-performance supercapacitors: design, synthesis and stability study. Nano Energy 2016;26:66−73.
[115] Xu J, Yang C, Xue Y, Wang C, Cao J, Chen Z. Facile synthesis of novel metal-organic nickel hydroxide nanorods for high performance supercapacitor. Electrochim Acta 2016;211:595−602.

[116] Díaz R, Orcajo MG, Botas JA, Calleja G, Palma J. Co_8-MOF-5 as electrode for supercapacitors. Mater Lett 2012;68:126–8.
[117] Liu X, Shi C, Zhai C, Cheng M, Liu Q, Wang G. Cobalt-based layered metal–organic framework as an ultrahigh capacity supercapacitor electrode material. ACS Appl Mater Interfaces 2016;8:4585–91.
[118] Yang J, Ma Z, Gao W, Wei M. Layered structural Co-based MOF with conductive network frames as a new supercapacitor electrode. Chemistry 2017;23:631–6.
[119] Lee DY, Yoon SJ, Shrestha NK, Lee S, Ahn H, Han S. Unusual energy storage and charge retention in Co-based metal–organic-frameworks. Microporous Mesoporous Mater 2012;153:163–5.
[120] Lee DY, Shinde DV, Kim E, Lee W, Oh I, Shrestha NK, et al. Supercapacitive property of metal–organic-frameworks with different pore dimensions and morphology. Microporous Mesoporous Mater 2013;171:53–7.
[121] Meng J, Gong Y, Lin Q, Zhang MM, Zhang P, Shi H, et al. Metal–organic frameworks based on rigid ligands as separator membranes in supercapacitor. Dalton Trans 2015;44:5407–16.
[122] Choi KM, Jeong HM, Park JH, Zhang Y, Kang JK, Yaghi OM. Supercapacitors of nanocrystalline metal–organic frameworks. ACS Nano 2014;8:7451–7.
[123] Li W, Ding K, Tian H, Yao M, Nath B, Deng W, et al. Conductive metal–organic framework nanowire array electrodes for high-performance solid-state supercapacitors. Adv Funct Mater 2017;27:1702067.
[124] Yang F, Li W, Tang B. Facile synthesis of amorphous UiO-66 (Zr-MOF) for supercapacitor application. J Alloy Compd 2018;733:8–14.
[125] Tan Y, Zhang W, Gao Y, Wu J, Tang B. Facile synthesis and supercapacitive properties of Zr-metal organic frameworks (UiO-66). RSC Adv 2015;5:17601–5.
[126] Gao W, Chen D, Quan H, Zou R, Wang W, Luo X, et al. Fabrication of hierarchical porous metal–organic framework electrode for aqueous asymmetric supercapacitor. ACS Sustain Chem Eng 2017;5:4144–53.
[127] Xia H, Zhang J, Yang Z, Guo S, Guo S, Xu Q. 2D MOF nanoflake-assembled spherical microstructures for enhanced supercapacitor and electrocatalysis performances. Nano-Micro Lett 2017;9:43.
[128] Jiao Y, Pei J, Chen D, Yan C, Hu Y, Zhang Q, et al. Mixed-metallic MOF based electrode materials for high performance hybrid supercapacitors. J Mater Chem 2017;A5:1094–102.
[129] Jiao Y, Pei J, Yan C, Chen D, Hu Y, Chen G. Layered nickel metal–organic framework for high performance alkaline battery-supercapacitor hybrid devices. J Mater Chem 2016;A4:13344–51.
[130] Gao Y, Wu J, Zhang W, Tan Y, Gao J, Tang B, et al. Synthesis of nickel carbonate hydroxide/zeolitic imidazolate framework-8 as a supercapacitors electrode. RSC Adv 2014;4:36366–71.
[131] Banerjee PC, Lobo DE, Middag R, Ng WK, Shaibani ME, Majumder M. Electrochemical capacitance of Ni-doped metal organic framework and reduced graphene oxide composites: more than the sum of its parts. ACS Appl Mater Interfaces 2015;7:3655–64.
[132] Srimuk P, Luanwuthi S, Krittayavathananon A, Sawangphruk M. Solid-type supercapacitor of reduced graphene oxide-metal organic framework composite coated on carbon fiber paper. Electrochim Acta 2015;157:69–77.
[133] Zhang W, Tan Y, Gao Y, Wu J, Hu J, Stein A, et al. Nanocomposites of zeolitic imidazolate frameworks on graphene oxide for pseudocapacitor applications. J Appl Electrochem 2016;46:441–50.

[134] Worrall SD, Mann H, Rogers A, Bissett MA, Attfield MP, Dryfe RAW. Electrochemical deposition of zeolitic imidazolate framework electrode coatings for supercapacitor electrodes. Electrochim Acta 2016;197:228–40.
[135] Wang L, Feng X, Ren L, Piao Q, Zhong J, Wang Y, et al. Flexible solid-state supercapacitor based on a metal–organic framework interwoven by electrochemically-deposited PANI. J Am Chem Soc 2015;137:4920–3.
[136] Fu D, Li H, Zhang X, Han G, Zhou H, Chang Y. Flexible solid-state supercapacitor fabricated by metal-organic framework/graphene oxide hybrid interconnected with PEDOT. Mater Chem Phys 2016;179:166–73.
[137] Guo S, Zhu Y, Yan Y, Min Y, Fan J, Xu Q, et al. (Metal-organic framework)-polyaniline sandwich structure composites as novel hybrid electrode materials for high-performance supercapacitor. J Power Sources 2016;316:176–82.
[138] Boorboor AF, Kowsari E, Ehsani A. P-type conductive polymer/zeolitic imidazolate framework-67 (ZIF-67) nanocomposite film: synthesis, characterization, and electrochemical performance as efficient electrode materials in pseudocapacitors. J Colloid Interface Sci 2018;509:189–94.
[139] Naseri M, Fotouhi L, Ehsani A, Dehghanpour S. Facile electrosynthesis of nano flower like metal-organic framework and its nanocomposite with conjugated polymer as a novel and hybrid electrode material for highly capacitive pseudocapacitors. J Colloid Interface Sci 2016;484:314–19.
[140] Qi K, Hou R, Zaman S, Qiu Y, Xia BY, Duan H. Construction of metal–organic framework/conductive polymer hybrid for all-solid-state fabric supercapacitor. ACS Appl Mater Interfaces 2018;10:18021–8.
[141] Xu X, Tang J, Qian H, Hou S, Bando Y, Hossain MSA, et al. Three-dimensional networked metal–organic frameworks with conductive polypyrrole tubes for flexible supercapacitors. ACS Appl Mater Interfaces 2017;9:38737–44.
[142] Jiao Y, Chen G, Chen D, Pei J, Hu Y. Bimetal–organic framework assisted polymerization of pyrrole involving air oxidant to prepare composite electrodes for portable energy storage. J Mater Chem A 2017;5:23744–52.
[143] Gao Y, Wu J, Zhang W, Tan Y, Zhao J, Tang B. The electrochemical performance of SnO_2 quantum dots@zeolitic imidazolate frameworks-8 (ZIF-8) composite material for supercapacitors. Mater Lett 2014;128:208–11.
[144] Li Z, Tan Y, Zhang W, Tang B. Flower-like $Ni_3(NO_3)_2(OH)_4$@Zr-metal organic framework (UiO-66) composites as electrode materials for high performance pseudocapacitors. Ionics 2016;22:2545–51.
[145] Gao Y, Wu J, Zhang W, Tan Y, Gao J, Zhao J, et al. Synthesis of nickel oxalate/zeolitic imidazolate framework-67 (NiC_2O_4/ZIF-67) as a supercapacitor electrode. New J Chem 2015;39:94–7.
[146] Yang J, Zheng C, Xiong P, Li Y, Wei M. Zn-doped Ni-MOF material with a high supercapacitive performance. J Mater Chem 2014;A2:19005–10.
[147] Zhang YZ, Cheng T, Wang Y, Lai W, Pang H, Huang W. A simple approach to boost capacitance: flexible supercapacitors based on manganese oxides@MOFs via chemically induced in situ self-transformation. Adv Mater 2016;28:5242–8.
[148] Zhou Y, Mao Z, Wang W, Yang Z, Liu X. In-situ fabrication of graphene oxide hybrid Ni-based metal–organic framework (Ni–MOFs@GO) with ultrahigh capacitance as electrochemical pseudocapacitor materials. ACS Appl Mater Interfaces 2016;8:28904–16.

[149] Wen P, Gong P, Sun J, Wang J, Yang S. Design and synthesis of Ni-MOF/CNT composites and rGO/carbon nitride composites for an asymmetric supercapacitor with high energy and power density. J Mater Chem 2015;A3:13874–83.

[150] Xiong X, Zhou L, Cao W, Liang J, Wang Y, Hu S, et al. Metal–organic frameworks based on halogen-bridged dinuclear-Cu-nodes as promising materials for high performance supercapacitor electrodes. CrystEngComm 2017;19:7177–84.

[151] Jeon J, Sharma R, Meduri P, Arey BW, Schaef, Lutkenhaus JL, et al. In situ one-step synthesis of hierarchical nitrogen-doped porous carbon for high-performance supercapacitors. ACS Appl Mater Interfaces 2014;6:7214–22.

[152] Gholipour-Ranjbar H, Soleimani M, Naderi HR. Application of Ni/Co-based metal–organic frameworks (MOFs) as an advanced electrode material for supercapacitors. New J Chem 2016;40:9187–93.

[153] Yu D, Wu B, Ran J, Ge L, Wu L, Wang H, et al. An ordered ZIF-8-derived layered double hydroxide hollow nanoparticles-nanoflake array for high efficiency energy storage. J Mater Chem 2016;A4:16953–60.

[154] Zhang Y, Lin B, Sun Y, Zhang X, Yang H, Wang J. Carbon nanotubes@metal–organic frameworks as Mn-based symmetrical supercapacitor electrodes for enhanced charge storage. RSC Adv 2015;5:58100–6.

[155] Khan IA, Badshah A, Khan I, Zhao D, Nadeem MA. Soft-template carbonization approach of MOF-5 to mesoporous carbon nanospheres as excellent electrode materials for supercapacitor. Microporous Mesoporous Mater 2017;253:169–76.

[156] Mao J, Yang L, Yu P, Wei X, Mao L. Electrocatalytic four-electron reduction of oxygen with copper (II)-based metal-organic frameworks. Electrochem Commun 2012;19:29–31.

[157] Jia G, Gao Y, Zhang W, Wang H, Cao Z, Li C, et al. Metal-organic frameworks as heterogeneous catalysts for electrocatalytic oxidative carbonylation of methanol to dimethyl carbonate. Electrochem Commun 2013;34:211–14.

[158] Zhang C, Wang M, Liu L, Yang X, Xu X. Electrochemical investigation of a new Cu-MOF and its electrocatalytic activity towards H_2O_2 oxidation in alkaline solution. Electrochem Commun 2013;33:131–4.

[159] Jiang J, Huang L, Liu X, Ai L. Bioinspired cobalt–citrate metal–organic framework as an efficient electrocatalyst for water oxidation. ACS Appl Mater Interfaces 2017;9:7193–201.

[160] Zhang X, Sun W, Du H, Kong RM, Qu F. A Co-MOF nanosheet array as a high-performance electrocatalyst for the oxygen evolution reaction in alkaline electrolytes. Inorg Chem Front 2018;5:344–7.

[161] Jia H, Yao Y, Zhao J, Gao Y, Luo Z, Du P. A novel two-dimensional nickel phthalocyanine-based metal–organic framework for highly efficient water oxidation catalysis. J Mater Chem 2018;A6:1188–95.

[162] Song G, Wang Z, Wang L, Li G, Huang M, Yin F. Preparation of MOF (Fe) and its catalytic activity for oxygen reduction reaction in an alkaline electrolyte. Chin J Catal 2014;35:185–95.

[163] Lions M, Tommasino JB, Chattot R, Abeykoon B, Guillou N, Devic T, et al. Insights into the mechanism of electrocatalysis of the oxygen reduction reaction by a porphyrinic metal organic framework. Chem Commun 2017;53:6496–9.

[164] Xu YX, Li B, Zheng SS, Wu P, Zhan JY, Xue HG, et al. Ultrathin two-dimensional cobalt–organic framework nanosheets for high-performance electrocatalytic oxygen evolution. J Mater Chem A 2018. Available from: https://doi.org/10.1039/C8TA03128B.

[165] Hod I, Sampson MD, Deria P, Kubiak CP, Farha OK, Hupp JT. Fe-porphyrin-based metal−organic framework films as high-surface concentration, heterogeneous catalysts for electrochemical reduction of CO_2. ACS Catal 2015;5:6302−9.

[166] Usov PM, Huffman B, Epley CC, Kessinger MC, Zhu J, Maza WA, et al. Study of electrocatalytic properties of metal−organic framework PCN-223 for the oxygen reduction reaction. ACS Appl Mater Interfaces 2017;9:33539−43.

[167] Miner EM, Gul S, Ricke ND, Pastor E, Yano J, Yachandra VK, et al. Mechanistic evidence for ligand-centered electrocatalytic oxygen reduction with the conductive MOF Ni_3 (hexaiminotriphenylene)$_2$. ACS Catal 2017;7:7726−31.

[168] Rui K, Zhao G, Chen Y, Lin Y, Zhou Q, Chen J, et al. Hybrid 2D dual-metal−organic frameworks for enhanced water oxidation catalysis. Adv Funct Mater 2018;28:1801554.

[169] Chen YZ, Wang C, Wu ZY, Xiong Y, Xu Q, Yu SH, et al. From bimetallic metal-organic framework to porous carbon: high surface area and multicomponent active dopants for excellent electrocatalysis. Adv Mater 2015;27:5010−16.

[170] Li FL, Shao Q, Huang X, Lang JP. Nanoscale trimetallic metal−organic frameworks enable efficient oxygen evolution electrocatalysis. Angew Chem Int Ed 2017;28. Available from: https://doi.org/10.1002/anie.201711376.

[171] Wang H, Yin F, Li G, Chen B, Wang Z. Preparation, characterization and bifunctional catalytic properties of MOF (Fe/Co) catalyst for oxygen reduction/evolution reactions in alkaline electrolyte. Int J Hydrog Energy 2014;39:16179−86.

[172] Su C, Kung C, Chang T, Lu H, Ho K, Liao YC. Inkjet-printed porphyrinic metal−organic framework thin films for electrocatalysis. J Mater Chem 2016;A4:11094−102.

[173] Musho T, Li J, Wu N. Thermodynamics of the oxygen evolution electrocatalysis in a functionalized UiO-66 metal-organic frameworks. Int J Quantum Chem 2016;116:1153−9.

[174] Tao L, Lin CY, Dou S, Feng S, Chen D, Liu D, et al. Creating coordinatively unsaturated metal sites in metal-organic-frameworks as efficient electrocatalysts for the oxygen evolution reaction: insights into the active centers. Nano Energy 2017;41:417−25.

[175] Maity K, Bhunia K, Pradhan D, Biradha K. Co(II)-doped Cd-MOF as an efficient water oxidation catalyst: doubly interpenetrated boron nitride network with the encapsulation of free ligand containing pyridine moieties. ACS Appl Mater Interfaces 2017;93:7548−37553.

[176] Zhang D, Zhang J, Zhang R, Shi H, Guo Y, Guo X, et al. 3D porous metal-organic framework as an efficient electrocatalyst for nonenzymatic sensing application. Talanta 2015;144:1176−81.

[177] Chen Q, Li X, Min X, Cheng D, Zhou J, Li Y, et al. Determination of catechol and hydroquinone with high sensitivity using MOF-graphene composites modified electrode. J Electroanal Chem 2017;789:114−22.

[178] Qin JS, Du DY, Guan W, Bo XJ, Li YF, Guo LP, et al. Ultrastable polymolybdate-based metal−organic frameworks as highly active electrocatalysts for hydrogen generation from water. J Am Chem Soc 2015;137:7169−77.

[179] Fang Y, Li X, Li F, Lin X, Tian M, Long X, et al. Self-assembly of cobalt-centered metal organic framework and multiwalled carbon nanotubes hybrids as a highly active and corrosion-resistant bifunctional oxygen catalyst. J Power Sources 2016;326:50−9.

[180] Nohra B, El Moll H, Rodriguez Albelo LM, Mialane P, Marrot J, Mellot-Draznieks C, et al. Polyoxometalate-based metal organic frameworks (POMOFs): structural trends, energetics, and high electrocatalytic efficiency for hydrogen evolution reaction. J Am Chem Soc 2011;133:13363−74.

[181] Li JS, Li SL, Tang YJ, Li K, Zhou L, Kong N, et al. Heteroatoms ternary-doped porous carbons derived from MOFs as metal-free electrocatalysts for oxygen reduction reaction. Sci Rep 2014;4:5130.

[182] Yang W, Zhang Y, Liu X, Chen L, Jia J. In situ formed Fe−N doped metal organic framework@carbon nanotubes/graphene hybrids for a rechargeable Zn−air battery. Chem Commun 2017;53:12934−7.

[183] Cho K, Han S, Suh MP. Copper−organic framework fabricated with CuS nanoparticles: synthesis, electrical conductivity, and electrocatalytic activities for oxygen reduction reaction. Angew Chem Int Ed 2016;55:15301−5.

[184] Wang H, Yin F, Chen B, Li G. Synthesis of an ε-MnO_2/metal−organic-framework composite and its electrocatalysis towards oxygen reduction reaction in an alkaline electrolyte. J Mater Chem 2015;A3:16168−76.

[185] Zhao L, Dong B, Li S, Zhou L, Lai L, Wang Z, et al. Inter diffusion reaction-assisted hybridization of two-dimensional metal−organic frameworks and $Ti_3C_2T_x$ nanosheets for electrocatalytic oxygen evolution. ACS Nano 2017;11:5800−7.

[186] Zhao S, Wang Y, Dong J, He C, Yin P, An H, et al. Ultrathin metal−organic framework nanosheets for electrocatalytic oxygen evolution. Nat Energy 2016;1:16184.

[187] Han Y, Zhai J, Zhang L, Dong S. Direct carbonization of cobalt-doped NH_2-MIL-53 (Fe) for electrocatalysis of oxygen evolution reaction. Nanoscale 2016;8:1033−9.

[188] Jahan M, Liu Z, Loh KP. A Graphene oxide and copper-centered metal organic framework composite as a tri-functional catalyst for HER, OER, and ORR. Adv Funct Mater 2013;23:5363−72.

[189] Zhao J, Wei C, Pang H. Zeolitic imidazolate framework-67 rhombic dodecahedral microcrystals with porous {110} facets as a new electrocatalyst for sensing glutathione. Part Part Syst Charact 2015;32:429−33.

[190] Yang L, Xu C, Ye W, Liu W. An electrochemical sensor for H_2O_2 based on a new Co-metal-organic framework modified electrode. Sens Actuators, B: Chem 2015;215:489−96.

[191] Liu Y, Zhang Y, Chen J, Pang H. Copper metal−organic framework nanocrystal for plane effect nonenzymatic electro-catalytic activity of glucose. Nanoscale 2014;6:10989−94.

[192] Kung C, Chang T, Chou L, Hupp JT, Farha OK, et al. Porphyrin-based metal−organic framework thin films for electrochemical nitrite detection. Electrochem Commun 2015;58:51−6.

[193] Wang X, Yang C, Zhu S, Yan M, Ge S, Yu J. 3D origami electrochemical device for sensitive Pb^{2+} testing based on DNA functionalized iron-porphyrinic metal-organic framework. Biosens Bioelectron 2017;87:108−15.

[194] Roushani M, Valipour A, Saedi Z. Electroanalytical sensing of Cd^{2+} based on metal−organic framework modified carbon paste electrode. Sens Actuators, B: Chem 2016;233:419−25.

[195] Yang J, Zhao F, Zeng B. One-step synthesis of a copper-based metal−organic framework−graphene nanocomposite with enhanced electrocatalytic activity. RSC Adv 2015;5:22060−5.

[196] Wang L, Yang H, He J, Zhang Y, Yu J, Song Y. Cu-hemin metal-organic-frameworks/chitosan-reduced graphene oxide nanocomposites with peroxidase-like bioactivity for electrochemical sensing. Electrochim Acta 2016;213:691−7.

[197] Meng W, Xu S, Dai L, Li Y, Zhu J, Wang L. An enhanced sensitivity towards H_2O_2 reduction based on a novel Cu metal−organic framework and acetylene black modified electrode. Electrochim Acta 2017;230:324−32.

[198] Wang Q, Yang Y, Gao F, Ni J, Zhang Y, Lin Z. Graphene oxide directed one-step synthesis of flowerlike graphene@HKUST-1 for enzyme-free detection of hydrogen peroxide in biological samples. ACS Appl Mater Interfaces 2016;8:32477–87.
[199] Li C, Zhang T, Zhao J, Liu H, Zheng B, Gu Y, et al. Boosted sensor performance by surface modification of bifunctional rht-type metal–organic framework with nanosized electrochemically reduced graphene oxide. ACS Appl Mater Interfaces 2017;9:2984–94.
[200] Yadav DK, Ganesan V, Sonkar PK, Gupta R, Rastogi PK. Electrochemical investigation of gold nanoparticles incorporated zinc based metal-organic framework for selective recognition of nitrite and nitrobenzene. Electrochim Acta 2016;200:276–82.
[201] Dong S, Zhang D, Suo G, Wei W, Huang T. Exploiting multi-function metal-organic framework nanocomposite Ag@Zn-TSA as highly efficient immobilization matrixes for sensitive electrochemical biosensing. Anal Chim Acta 2016;934:203–11.
[202] Yang J, Ye H, Zhao F, Zeng B. A novel Cu_xO nanoparticles@ZIF-8 composite derived from core–shell metal–organic frameworks for highly selective electrochemical sensing of hydrogen peroxide. ACS Appl Mater Interfaces 2016;8:20407–14.
[203] Wang Y, Wang L, Huang W, Zhang T, Hu X, Perman JA, et al. A metal–organic framework and conducting polymer based electrochemical sensor for high performance cadmium ion detection. J Mater Chem 2017;A5:8385–93.
[204] Tran TQN, Das G, Yoon HH. Nickel-metal organic framework/MWCNT composite electrode for non-enzymatic urea detection. Sens Actuators B: Chem 2017;243:78–83.
[205] Gong C, Shen Y, Chen J, Song Y, Chen S, Song Y, et al. Microperoxidase-11@ PCN-333 (Al)/three-dimensional macroporous carbon electrode for sensing hydrogen peroxide. Sens Actuators B: Chem 2017;239:890–7.
[206] Yang L, Lian C, Li X, Han Y, Yang L, Cai T, et al. Highly selective bifunctional luminescent sensor toward nitrobenzene and Cu^{2+} ion based on microporous metal–organic frameworks: synthesis, structures, and properties. ACS Appl Mater Interfaces 2017;9:17208–17.
[207] Deng CH, Li T, Chen JH, Ma J, Cheng P. The electrochemical discrimination of pinene enantiomers by a cyclodextrin metal–organic framework. Dalton Trans 2017;46:6830–4.
[208] Xiao X, Zheng S, Li X, Zhang G, Guo X, Xue H, et al. Facile synthesis of ultrathin Ni-MOF nanobelts for high-efficiency determination of glucose in human serum. J Mater Chem B 2017;5:5234–9.
[209] Yadav DK, Ganesan V, Marken F, Gupta R, Sonkar PK. Metal@ MOF materials in electroanalysis: silver-enhanced oxidation reactivity towards nitrophenols adsorbed into a zinc metal organic framework—Ag@ MOF-5 (Zn). Electrochim Acta 2016;219:482–91.
[210] Kung C, Li Y, Lee M, Wang S, Chiang WH, Ho KC. In situ growth of porphyrinic metal–organic framework nanocrystals on graphene nanoribbons for the electrocatalytic oxidation of nitrite. J Mater Chem 2016;A4:10673–82.
[211] Ling P, Lei J, Ju H. Porphyrinic metal-organic framework as electrochemical probe for DNA sensing via triple-helix molecular switch. BiosensBioelectron 2015;71:373–9.
[212] Shu Y, Yan Y, Chen J, Xu Q, Pang H, Hu X. Ni and NiO nanoparticles decorated metal–organic framework nanosheets: facile synthesis and high-performance nonenzymatic glucose detection in human serum. ACS Appl Mater Interfaces 2017;9:22342–9.
[213] Kung W, Wang TC, Mondloch JE, Fairen-Jimenez D, Gardner DM, Bury W, et al. Metal–organic framework thin films composed of free-standing acicular nanorods exhibiting reversible electrochromism. Chem Mater 2013;25:5012–17.
[214] Li MM, Dinca M. Pt electrodes enable the formation of μ_4-O centers in MOF-5 from multiple oxygen sources. ACS Appl Mater Interfaces 2017;93:3528–33532.

This page intentionally left blank

Chapter 5

Permeable metal-organic frameworks for fuel (gas) storage applications

S. Janardan[1], P C.V.V. Eswara Rao[1], H. Manjunatha[1], K. Venkata Ratnam[1], A. Ratnamala[1], K. Chandra Babu Naidu[2], A. Sivarmakrishna[3], Anish Khan[4,5] and Abdullah M. Asiri[4,5]

[1]*Department of Chemistry, GITAM School of Science, GITAM (Deemed to be University), Bangalore, India,* [2]*Department of Physics, GITAM (Deemed to be University), Bangalore, India,* [3]*Department of Chemistry, School of Advanced Sciences, VIT University, Vellore, India,* [4]*Chemistry Department, Faculty of Science, King Abdulaziz University, Jeddah, Saudi Arabia,* [5]*Center of Excellence for Advanced Materials Research, King Abdulaziz University, Jeddah, Saudi Arabia*

5.1 Introduction

There is a constant demand for the production and storage of alternative fuels to overcome the problems associated with the fossil fuels [1]. Among the strategies reported, metal-organic frameworks (MOFs) are promising alternatives. They are crystalline materials that consist of organic linkers, metal clusters, or metal ions [2–4]. In recent years, these novel crystalline classes of porous materials have gathered a significant attention due to their permanent porosity and huge surface area. These molecules are synthesized by linking inorganic and organic moieties through a strong chemical bond, and the organic units are divalent or polyvalent and forming three-dimensional (3D) structure with a specific distribution of pore sizes as showed in Fig. 5.1 [5] when it links with metal units such as Ni^{+2}, Cu^{+2}, Co^{2+}, and Zn^{+2}. The pore size and the surface area of the MOFs range up to 9.8 nm and 1000–10,000 $m^2\ g^{-1}$, respectively, depending upon both the organic and inorganic units present in the MOFs [6–9]. According to the literature reported, for the past few decades, so many MOFs (more than 20,000) have been synthesized by varying the size, functionality, and constituents and represented the crystal structure [2]. The development in the field of MOFs is an important area of research to assess the property

Metal-Organic Frameworks for Chemical Reactions. DOI: https://doi.org/10.1016/B978-0-12-822099-3.00005-8

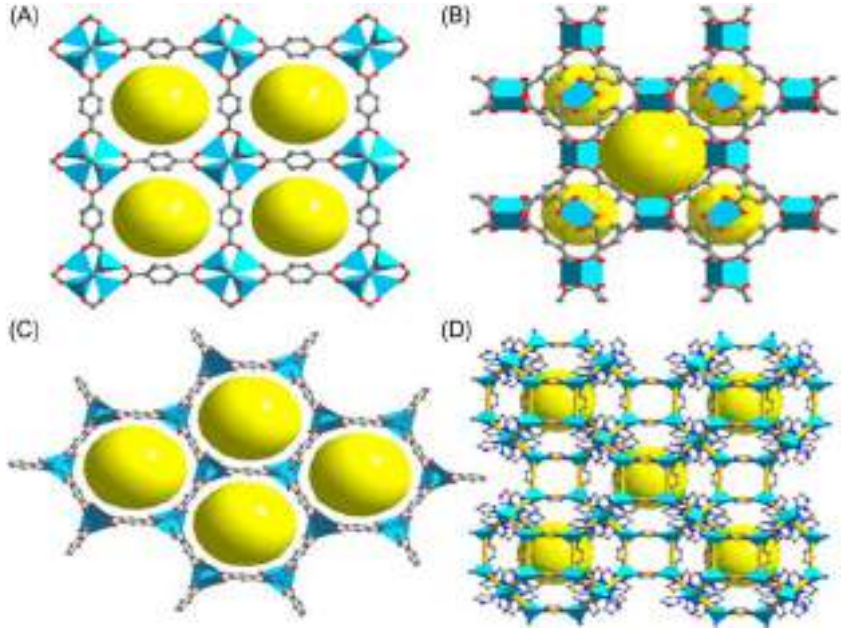

FIGURE 5.1 Representative crystal structures of four MOFs: (A) MOF-5, (B) HKUST-1, (C) Mg-MOF-74, and (D) ZIF-8 [5]. *MOF*, Metal-organic framework.

investigations such as conductivity, nonlinear optics, chirality, magnetism, catalysis, luminescence, spin transition (spin crossover), and porosity or zeolitic behavior for the storage of small molecules for energy applications.

5.2 Concept of porosity in fuel storage

Porous MOFs have been synthesized mainly by assembling the metal-incorporated clusters referred to as secondary building units with polydentate ligands such as sulfonates, tetrazoles, or carboxylates through coordination bonds to form 3D networks [10]. The pore size of the MOFs can be easily modified by using reticular synthesis from several angstroms to nanometers with the help of organic ligand chain length [11–13]. The most interesting factor for porosity is the surface area where MOF-177 shows high surface area 5640 $m^2 g^{-1}$ and followed by MOF-177 exhibits 5900 $m^2 g^{-1}$. In addition to this, the highest surface area recorded is 6000 $m^2 g^{-1}$ [14,15]. Since this high surface area enhances the nanopore space in the MOFs, this property triggers to store various gases, and some of the breakthroughs of the MOFs over time line are represented in Table 5.1.

TABLE 5.1 Important achievements in the field of metal-organic frameworks (MOFs) for gas storage applications in time line.

S. no	Year	Important breakthrough in MOFs in gas storage	Refs.
1	1997	$[Co_2(bpy)_3(NO_3)_4]$: CH_4 storage	[16]
2	2002	IRMOF-6: high CH_4 storage	[13]
3	2003	MOF-5: H_2 storage	[17]
4	2005	$[Cu_2(pzdc)_2(pyz)]$: C_2H_2 storage	[18]
5	2009	Open metal sites for high C_2H_2	[19]
6	2010	MOF-210: 17.6% of total gravimetric uptake of H_2 at 77K and 80 bar	[7]
7	2013	HKUST-1: 267 $cm^3\ cm^{-3}$ high total volumetric capacity of CH_4 at 298K and 65 bar	[20]
8	2014	UTSA-76: 197 $cm^3\ cm^{-3}$ high total volumetric working capacity of CH_4 5 and 65 bar	[21]
9	2015	Al-soc-MOF-1: record high total gravimetric CH_4 uptake of 579 $cm^3\ g^{-1}$ at 298K and 65 bar	[22]
10	2017	MFM-188 reported high gravimetric C_2H_2 uptake of 232 $cm^3\ g^{-1}$ at 295K and 1 bar. $[Cd_3(vtz)_6]$: record high volumetric C_2H_2 working capacity of 45 $cm^3\ cm^{-3}$ at 298K, 1.5/1.0 bar	[23,24]
11	2018	HKUST-1 with the highest BET surface area 1615 $m^2\ g^{-1}$ with high yield 84.1% with CO_2 uptake capacity of 4.2 mmol g^{-1}	[25]
12	2019	MonoUiO-66_D showed extremely high CH_4 gas uptake of 211 and 296 cm^3 (STP) cm^{-3} at 65 and 100 bar and CO_2 284 cm^3 (STP) cm^{-3} at 40 bar	[26]
13	2020	$Cu_{0.5}(tztp) \cdot 0.5DMA$ with both hydrophobic and hydrophilic ends with N-functionality with high CO_2 adsorption	[27]

5.3 Permeable metal-organic frameworks for H_2 storage application

The growth of population, the rapid industrialization, and transport developmental activities toward enhancement of the economy have been consuming huge amounts of fuels and intern, the situation overexploits the present fossil fuels as well as creating more damage to the environment. This further requires a significant attention to reduce the carbon gas emissions. Recently, a lot of attention has been centered on alternative energy fuels; among them

the H_2 gas occupies a prominent place with zero carbon gas emissions. However, the major problem with H_2 fuel is the low energy density at ambient conditions with less volume, and this drives the researchers to focus on the construction of highly efficient H_2 storage materials. The efficient materials for H_2 storage applications are required to show the following volumetric and gravimetric capacities, and it will be 30 g L^{-1}, 4.5 wt.% and operating temperature will be at −40°C to 60°C with a pressure of maximum 100 bar that reduces the cost of compression and storage vessel in order to facilitate proper storage capacities. Due to the week van der Waals interactions between the MOFs and H_2 gas, it is always difficult to store H_2 gas and use for applications at ambient temperature.

Yaghi et al. [11] reported the first MOFs for H_2 storage that is MOF-5 in 2003, and this facilitated the investigation of hundreds of MOFs and their H_2 uptake capacities as given in Table 5.2 [28−33]. It is clear from the investigations that the enhancement of pore size and surface area will enrich the H_2 storage capacity at 77 kat high pressure includes NOTT-122, NU-100/PCN-610, NU-111 total H_2 gravimetric uptake of 10.0, 16.4, and 13.6 wt.% at 80 bar and 77K with the BET surface areas as 3800, 6143, and 4930 m^2 g^{-1}, respectively [8,34−36]. Furukawa reported that MOF-210 MOF can take the highest H_2 (17.6 wt.%) at 80 bar and 77K [7]. However, some metals incorporated in MOFs can enhance the isosteric H_2 heat of adsorption for about 12 kJ mol^{-1}, which is deviated from the theoretical H_2 heat of adsorption 15 kJ mol^{-1} for high H_2 storage capacities at optimum temperatures [37]. Several theoretical simulation studies revealed that the H_2 storage density is increased with the high gravimetric capacity with moderate volumetric capacities for their enhancement in their pore size, and weak MOFs and H_2 interactions that promote the scientists to synthesize several remarkable MOFs possessing high H_2 gravimetric capacities include IRMOF-20 with following gravimetric and volumetric capacities 9.1 wt.% and 51.0 g L^{-1}, respectively, at a pressure and temperature of 5 bar and 160K [38]. Kapelewski et al. reported a high performed physisorptive MOFs based on Ni_2(*m*-dobdc) with high H_2 uptake capacities of 11−23.0 g L^{-1} with the enhancement of the temperature from −75°C to 25°C at 100 and 5 bar pressure, due to the interaction of unsaturated metal sites with H_2 [39]. The selected H_2 gas storage MOFs with their crystal structures, their BET surface areas, and uptake capacities at various parameters were listed in Table 5.2 [40].

5.4 Permeable metal-organic frameworks for CH_4 storage applications

Various types of MOFs such as Ni MOF-74, NU-125, HKUST-1, UTSA-20, PCN-14, and NU-111 were examined for methane gas uptake capacities with the help of an efficient protocol by Peng et al. in 2013, which clearly depend

TABLE 5.2 Important metal-organic frameworks (MOFs) examples for H_2 storage.

MOFs	Surface area ($m^2\ g^{-1}$)	Total gravimetric capacity (wt.%)	Pressure (bar)	Total volumetric capacity ($g\ L^{-1}$)	Temperature (K)	Ref.
NU-111	5930	13.6	70	–	77	[8]
NU-100/PCN-610	6143	16.4	70	–	77	[34]
MOF-210	6240	17.6	80	44	77	[7]
MOF-5	3800	10	100	66	77	[70]
NOTT-122	3800	10	77	50.3	77	[35]
IRMOF-20	4073	9.1	–	51.0	–	[38]
MOF-205	4460	12.0	80	46	77	[7]
Mg-MOF-74	1510	4.9	100	49	77	[71]
MOF-200	4530	16.3	80	36	77	[7]
NOTT-115[a]	3394	7.5	60	49.3	78	[72]
Mn-BTT	2100	6.9	90	60	77	[73]
Ni_2(*m*-dobdc)[b]	1321	–	–	11.0	298	[39]
SNU-16	2590	10.0	70	–	77	[74]
PCN-46	2500	6.88	97	45.7	77	[75]

[a]Usable capacities are measured with temperature and pressure ranging 77K and 100 bar to 160K and 5 bar.
[b]Volumetric capacities measured between 5 and 100 bar.

upon the factors such as pore volume, inverse density of MOFs with the BET surface area. Among the group of molecules, NU-111 with the highest BET surface ($4930\ m^2\ g^{-1}$) showed higher gravimetric uptake of CH_4 ($0.37\ g\ g^{-1}$) [20]. Li et al. developed an empirical formula for calculating the gravimetric CH_4 uptake and examined the effect of temperature on CH_4 gravimetric uptake, and it showed with reduction in the temperature, there is gradual enhancement in the gravimetric CH_4 uptake by using the following formula:

$$C_{\text{total}} = -70.463 \times {V_p}^2 + 460.543 \times V_p - 2.709$$

where C_{total} is the total gravimetric CH_4 uptake at 270K and 65 bar, and V_p is the pore volume ($cm^3\ g^{-1}$) [41]. From the abovementioned observation, it is clearly revealed that the uptake capacity of methane gas is increased with an increase in the porosity and Brunauer-Emmett-Teller (BET) surface area. Later on, many MOFs were synthesized having high porosity volume and high surface area, for example, aluminum-based MOF (Al-soc-MOF-1) was reported by Alezi et al. in 2015 which displays significant porosity ($2.3\ cm^3\ g^{-1}$) and high surface area ($5585\ m^2\ g^{-1}$) with the highest methane gas uptake $580\ cm^3$ (STP) g^{-1}, $0.42\ g\ g^{-1}$ at 65 bar and 298K reported so far [22].

Moreover, creating a favorable pore size is one of the necessity criteria, which is influenced by the nature of organic linker framework with shrinkages to accommodate CH_4 molecules. Various kinds of MOFs (MOF-905-Me_2, MOF-905, MOF-905-Naph, and MOF-905-NO_2) were synthesized by changing the peripheral phenylene ring of BTB linker and acrylate links in MOF-205 with double-bond spacer by Jiang et al. in 2016 [42].

In addition, Wen et al. introduced extended linker systems with nitrogen functional sites in MOFs, significantly known as UTSA-76 (surface area: $2820\ m^2\ g^{-1}$ and nitrogen content: $2.64\ mmol\ cm^{-3}$) in 2013 [43], which inspired the synthesis of analogous MOF such as UTSA-110a ($3241\ m^2\ g^{-1}$ and $3.94\ mmol\ cm^{-3}$) with higher BET surface area and large nitrogen functional sites showing greater volumetric [$241\ cm^3$ (STP) cm^{-3}] and gravimetric [$402\ cm^3$ (STP) g^{-1}] uptake of methane gas. Further, the theoretical calculations also suggested that enhanced porosity and nitrogen functionalities increase the gravimetric uptake due to enhancement in the interaction between CH_4 and MOF.

By introducing the functionalized linker backbones in MOFs, Yan et al. reported a new class of MOFs with significant molecular dynamics with the 3-, 24-connected MOFs such as MFM-112a, MFM-112a, MFM-115a, and MFM-132a with different functionalized backbone linkers in 2017 [44]. Lin et al. reported an MOF in 2016 without any open metal sites, which is quite suitable with the shape and size of CH_4 molecule. However, MAF-38 in

2016 has two kinds of nanocages with a diameter of 8.6 and ~6.2, with greater total volumetric methane uptake of 263 cm^3 (STP) cm^{-3} as well as with 187 cm^3 (STP) cm^{-3} working capacity made the MOFs to bound strongly with CH_4 molecules [45,46]. The selected CH_4 gas storage of MOFs, their BET surface areas, and uptake capacities at various parameters were listed in Table 5.3 [40].

TABLE 5.3 Significant examples of metal-organic frameworks (MOFs) for CH_4 storage.

MOFs	BET surface area	Total uptake[a] (cm^3 g^{-1})		Working capacity		Refs.
Co(bdp)	2911	–	203 (161)	–	197 (155)	[47]
Al-soc-MOF-1	5585	579 (362)	197 (123)	518 (306)	176 (104)	[22]
HKUST-1	1850	302 (257)	267 (227)	215 (170)	190 (150)	[20]
UTSA-76	2820	363 (302)	257 (211)	282 (216)	197 (151)	[21]
UTSA-110	3241	402 (312)	241 (187)	317 (227)	190 (136)	[43]
MOF-905	3490	377 (264)	207 (145)	331 (219)	182 (120)	[42]
NJU-Bai 43	3090	396 (315)	254 (202)	308 (228)	182 (110)	[48]
MOF-177	4500	475 (307)	203 (131)	426 (258)	182 (110)	[41]
MAF-38	2022	346 (297)	263 (226)	246 (197)	187 (150)	[45,46]
MFM-115[a]	3394	389 (204)	238 (186)	312 (226)	191 (138)	[44]
LIFM-82	1624	267 (214)	245 (196)	209 (156)	192 (143)	[49]
NU-125	3286	395 (315)	232 (182)	312 (226)	183 (133)	[20]
NU-111	4930	503 (337)	206 (138)	437 (271)	179 (111)	[20]

[a]65 (35) bar pressure at room temperature.

5.5 Permeable metal-organic frameworks for C_2H_2 storage applications

C_2H_2 molecule is abundantly used in the industrial sector in order to synthesize value-added products for the modern world, but because of its violent reactions on storing over 0.2 MPa under compressed pressure made, the storage of acetylene gas itself is a challenging task to researchers. Also, the current storage methodology in porous materials with the usage of acetone is not a cost-effective and eco-friendly method, because acetone is a toxic component toward the nature concern, which triggers the researchers to focus on synthesizing a new class of materials with high porosity, more safety, and eco-friendly materials where MOFs gather attention. Matsuda et al. in 2005 reported the $[Cu_2(pzdc)_2(pyz)]$ as the first MOFs for storing C_2H_2 gas. Optimization of the pore size and impregnating the open metal sites are two major features of an efficient MOFs for storing C_2H_2 molecule, which has implemented first by Xiang et al. in 2009 by introducing open metal sites in the MOFs for enhancing the uptake capacity of the respective gas molecule [19]. In addition, several MOFs (MOF-505, MIL-53, ZIF-8, HKUST-1, MOF-508, and MOF-5) were tested for their C_2H_2 uptake capacities and it was identified that the HKUST-1 was the best MOF among all of them possessing 201 $cm^3\ g^{-1}$ C_2H_2 uptake capacity at 1 atm and 295K, which was mainly due to the strong interactions of the C_2H_2 molecules with the Cu(II) open metal sites present in the MOFs. Moreover, the same phenomenon was implemented with other groups of molecules with various metal frameworks, including M-MOF-74 [M = Mn(II), Zn(II), Mg(II), Co(II)], where the Co-based MOF has showed greater C_2H_2 uptake capacities (197 $cm^3\ g^{-1}$ at 1 bar at 298K) over other metal frameworks [50]. Incorporating amide- and pyridyl-based organic linkers also enhances the C_2H_2 uptake capacities [23,51]. MOFs such as ZJU-5 showed greater uptake (193 $cm^3\ g^{-1}$ at 298K and 1 atm) than its reticular analog NOTT-101 (184 $cm^3\ g^{-1}$ at 298K and 1 atm) due to the replacement of the more efficient pyridine ring with N-functionality with less efficient benzene spacer that was reported by Rao et al. in 2013 [51]. Further modification of the same benzene spacer with pyrazine ring has been increased the acetylene uptake capacity (216 $cm^3\ g^{-1}$ at 298K and 1 bar) due to its greater affinity with C_2H_2 molecule with more Lewis basic nitrogen sites in isoreticular MOF such as ZJUT-40. Cu(II)-based MOF (MFM-188) showed significantly high uptake capacity (232 $cm^3\ g^{-1}$ at 295K, and 1 bar) even with moderate porosity, and it was evidenced by neutron diffraction and inelastic neutron scattering with amide-C_2D_2 bond interactions. Zhang et al. in 2017 examined NJU-Bai-17 with the highest uptake capacity material of 222.4 $cm^3\ g^{-1}$ at 296K and 1 bar [52]. Similarly, FJI-H8 MOF showed the extremely highest volumetric capacity [196 cm^3 (STP) cm^{-3}] and the highest gravimetric C_2H_2 uptake capacity [224 cm^3 (STP) g^{-1} at 298K and 1 atm] [53]. Moreover, the theoretical

calculations also state that more than 60% of the uptake capability mainly depends upon the porosity of the materials. Furthermore, the working capacity of C_2H_2 was limited because one cannot operate the respective MOFs at high pressure due to explosive nature of C_2H_2, so always one can deliver the fuel at an optimum pressure conditions ranging from 1.0 to 1.5 atm. MAF-2-type MOFs showed a moderate uptake capacity [70 cm^3 (STP) g^{-1} of C_2H_2] with significant 40-fold enhancement in the working capacity and energy deliverable amount within the range of 1.0−1.5 atm [54]. Cd metal−based MOF, $[Cd_3(Vtz)_6]$, showed the highest working capacity (1.99 mmol cm^{-3}) with 98 times greater than gas cylinder [24]. The selected C_2H_2 gas storage MOFs, their BET surface areas, and uptake capacities at various parameters were listed in Table 5.4 [40].

TABLE 5.4 Important examples of metal-organic frameworks (MOFs) for C_2H_2 gas storage.

MOFs	BET surface area (m^2 g^{-1})	Total gravimetric capacity (wt.%)	Temperature (K)	Total volumetric capacity (g L^{-1})	Ref.
ZJU-5	2823	193	298	–	[51]
ZJU-8	2501	195	298	134	[55]
Co-MOF-74	1056	197	295	230	[50]
Mn-MOF-74	1102	168	295	182	[50]
MAF-2	–	70	298	82	[54]
$[Cd_3(vtz)_6]$	–	50	298	77	[24]
Mg-MOF-74	1332	184	295	–	[56]
SIFSIX-1-Cu	1178	190	298	164	[46]
HKUST-1	1780	201	295	177	[19]
MOF-505	1694	148	295	137	[19]
FJI-H8	2025	224	295	196	[53]
MFM-188	2568	232	298	–	[23]
ZJU-40	2858	216	298	–	[57]
NJU-Bai 17	2423	222.4	296	176	[52]

5.6 Permeable metal-organic frameworks for CO_2 storage applications

CO_2 capturing technologies are gradually increased throughout the world and gather the attention of scientific researchers. There are several materials, especially solid adsorbents such as activated carbons, zeolites, polymer materials, and MOFs are used. Among these molecules, MOFs occupied a significant position due to their selective pore size and flexible tuning properties, and the easily modifiable interacting sites made these molecules prominent to capture and store them. Various MOFs were examined for their significant CO_2 adsorbents [58–63].

Pan et al. in 2003 reported a complex $[Er_2(pda)_3]$ that can selectively absorb CO_2 molecule through the 3D frameworks with 1D channels that were supported by unsaturated Eu^{III} sites. These MOFs specifically absorb CO_2 over other gases due to the suitable pore size with 3.4 Å with the molecule diameter 3.3 Å and the unsaturated metal sites that were involved in the coordination of CO_2 molecule. In addition to this, the quadruple moment also helps the CO_2 molecule to interact with the electrical field and enhances the absorption energy [64]. Similarly, Wang et al. in 2008 examined that the MOFs (ZIF-95 and ZIF-100) selectively absorb the CO_2 molecule with the suitable cavities (3.65 Å) and pore that were straitened (3.35 Å) [65]. Xiang et al. in 2012 reported the UTSA-16 with excellent absorption capacity [160 cm^3 cm^{-3}/(volumetric)] and best selectivity against CH_4 and N_2 gas due to the suitable pore size and the efficient binding sites [66]. Dybtsev et al. reported the selective absorption of CO_2 molecule completely that depends upon the compatible pore size with its kinetic diameter of the molecule [67]. Further, the porosity one can be enhanced to store the CO_2 gas capacity by using open metal sites within the metal framework by Dietzel et al. [68]. Some of the important CO_2 storage MOFs were listed in Table 5.5 [69].

5.7 Conclusion

As stated in the above information, MOFs are significant materials in the storage of gases such as hydrogen, acetylene, methane, and carbon dioxide due to their suitable pore size, open metal sites, and excellent surface area in various industrial, domestic, and academic sectors from the last two decades, but still many challenges are associated with commercialization and stability of the compounds. Moreover, it is always necessary to construct MOFs with high volumetric and gravimetric fuel storage capacities with high energy deliverable amounts requires a prominent attention.

Due to the week van der Waals interactions of H_2 molecules with MOFs, one cannot store at the highest working temperatures because uptake capacity gradually decreases with the rise in the temperature, which can be

TABLE 5.5 Important examples of metal-organic frameworks (MOFs) for CO_2 gas storage [69].

MOF	Reason for selectivity	Pore size (Å)	Absorption (selective)	CO_2 uptake	T (K)	P	Ref.
MIL-96	Size/shape exclusion	2.5–3.5	CO_2 than CH_4	~3.7 mmol g^{-1}	303	3.5 bar	[58]
$Zn_2(cnc)_2(dpt)$	Both	~3.7	CO_2 than CH_4	~150 mL g^{-1}	195	$1P/P_1$	[59]
$Zn_2(ndc)_2(dpni)$	Adsorbate–adsorbent	4–5	CO_2 than CH_4	4.3 mmol g^{-1}	296	1750 kPa	[60]
$Er_2(pda)_3$	Both	~3.4	CO_2 than N_2 and Ar	~24 mg g^{-1}	273	760 Torr	[64]
ZIF-100	Both	3.35	CO_2 than CH_4, N_2 and CO	~0.95 mmol g^{-1}	298	850 Torr	[65]
MIL-102	Adsorbate–adsorbent	~4.4	CO_2 than CH_4 and N_2	~3.4 mmol g^{-1}	304	3 MPa	[61]
CUK-1	Adsorbate–adsorbent	11.1	CO_2 than CH_4	~88 mL g^{-1}	298	760 Torr bar	[62]
Zn(OH)(p-cdc)$_{2.5}$	Adsorbate–adsorbent	3×5	CO_2 than CH_4	~0.586 mmol g^{-1}	298	0.5 bar	[63]

overcome with increasing the surface area at low temperatures (77K) by introducing various functionalities such as metal sites, organic ligands. In addition to this, it is necessary to produce MOFs with large densities of H_2 molecule at room temperature with efficient adsorption sites that shall be the major task for the future researchers and can be achieved by exchanging the organic linkers, cations with other dopants (metals). However, even though the uptake capacities are good enough in the case of C_2H_2 and CH_4 gases, but the problems such as kinetics of storage capacities and the binding efficiency of the molecules with the MOFs are yet to be solved. The emerging potential of tuning the robust structure and porosity triggers the scientific community to focus on the synthesis of MOFs with extremely greater affinity, storage, and working capacities with reusable and cost-effective manner.

Acknowledgment

Dr. Sannapaneni Janardan is highly grateful to Management of GITAM (Deemed to be University), Bengaluru Campus for the constant support and encouragement.

References

[1] Thangaraja J, Sivaramakrishna A, Desikan R. Bio fuels from renewable biomass resources: an overview of technologies for production, environmental and economic impacts. In: Akhilendra PS, Yogesh CY, Nirendra NM, Avinash KA, editors. Alternative fuels and their utilization strategies in internal combustion engines. Singapore: Springer; 2020. p. 25–47.

[2] (a) Furukawa H, Cordova KE, Okeffe M, Om Y. The chemistry and applications of metal-organic frameworks. Science 2013;34:1230444.
(b) Das MC, Xiang S, Zang Z, Chen B. Functional mixed metal-organic frameworks with metallo-ligands. Angew Chem Int Ed 2011;50:10510–20.

[3] Lu W, Wei Z, Gu ZY, Liu TF, Park J, Tian J, et al. Tuning the structure and function of metal-organic frameworks via linker design. Chem Soc Rev 2014;43:5561–93.

[4] Stock N, Biswas S. Synthesis of metal organic frameworks (MOFs): routes to various MOF topologies, morphologies, and composites. Chem Rev 2012;112:933–69.

[5] Wang H, Zhu Q, Zou R, Xu Q. Metal-organic frameworks for energy applications. Chemistry 2017;2:52–80.

[6] Furukawa H, Yaghi OM. Storage of hydrogen, methane, and carbon dioxide in highly porous covalent organic frameworks for clean energy applications. J Am Chem Soc 2009;31:8875–83.

[7] Furukawa H, Ko N, Go YB, Aratani N, Choi SB, Choi E, et al. Ultra high porosity in metal-organic frame works. Science 2010;329:424–8.

[8] Farha OK, Wilmer CE, Eryazici I, Hauser BG, Parilla PA, Sarjeant AA, et al. Designing higher surface area metal-organic frameworks: are triple bonds better than phenyls. J Am Chem Soc 2012;134:9860–3.

[9] Deng H, Grunder S, Cordova KE, Valente C, Furukawa H, Hmadeh M, et al. Large-pore apertures in a series of metal-organic frame works. Science 2012;336:1018–23.

[10] Tranchemontagne DJ, Mendoza-Cortes JL, O'Keeffe M, Yaghi OM. Chem Soc Rev 2009;38:1257–83.
[11] Yaghi OM, O'Keeffe MN, Ockwig W, Chae HK, Eddaoudi M, Kim J. Nature 2003;423:705–14.
[12] O'Keeffe M. Design of MOFs and intellectual content in reticular chemistry: a personal view. Chem Soc Rev 2009;38:1215–17.
[13] Eddaoudi M, Kim J, Rosi N, Vodak D, Wachter J, O'Keeffe M, et al. Systematic design of pore size and functionality in isoreticular MOFs and their application in methane storage. Science 2002;295:469–72.
[14] Ferey G. Hybrid porous solids: past, present, future. Chem Soc Rev 2008;37:191–214.
[15] Suh MP, Cheon YE, Lee EY. Syntheses and functions of porous metallosupramolecular networks. Coord Chem Rev 2008;252:1007–26.
[16] Kondo M, Yoshitomi T, Matsuzaka H, Kitagawa S, Seki K. Three-dimensional framework with channelling cavities for small molecules: $\{[M_2(4,4\text{-bpy})_3(NO_3)_4]\ xH_2O\}_n$ (M = Co, Ni, Zn). Angew Chem Int Ed 1997;36:1725–7.
[17] Rosi NL, Eckert J, Eddaoudi M, Vodak DT, Kim J, O'Keeffe M, et al. Hydrogen storage in microporous metal-organic frameworks. Science 2003;300:1127–9.
[18] Matsuda R, Kitaura R, Kitagawa S, Kubota Y, Belosludov RV, Kobayashi TC, et al. Highly controlled acetylene accommodation in a metal-organic microporous material. Nature 2005;436:238–41.
[19] Xiang S, Zhou W, Gallegos JM, Liu Y, Chen B. Exceptionally high acetylene uptake in a microporous metal-organic framework with open metal sites. J Am Chem Soc 2009;131:12415–19.
[20] Peng Y, Krungleviciute V, Eryazici I, Hupp JT, Farha OK, Yildirim T. Methane storage in metal-organic frameworks: current records, surprise findings, and challenges. J Am Chem Soc 2013;135:11887–94.
[21] Li B, Wen HM, Wang H, Wu H, Tyagi M, Yildirim T, et al. A porous metal-organic framework with dynamic pyrimidine groups exhibiting record high methane storage working capacity. J Am Chem Soc 2014;136:6207–10.
[22] Alezi D, Belmabkhout Y, Suyetin M, Bhatt PM, Weselinski ŁJ, Solovyeva V, et al. MOF crystal chemistry paving the way to gas storage needs: aluminum-based soc-MOF for CH_4, O_2, and CO_2 storage. J Am Chem Soc 2015;137:13308–18.
[23] Moreau F, Da Silva I, Al Smail NH, Easun TL, Savage M, Godfrey HGW, et al. Unravelling exceptional acetylene and carbon dioxide adsorption within a tetra-amide functionalized metal-organic framework. Nat Commun 2017;8:14085.
[24] He CT, Ye ZM, Xu YT, Zhou DD, Zhou HL, Chen D, et al. Hyperfine adjustment of flexible pore-surface pockets enables smart recognition of gas size and quadrupole moment. Chem Sci 2017;8:7560–5.
[25] Yipei C, Mu X, Edward L, Tao W. High efficiency synthesis of HKUST-1 under mild conditions with high BET surface area and CO_2 uptake capacity. Prog Nat Sci: Mater Int 2018;28:584–9.
[26] Connolly BM, Aragones-Anglada M, Gandara-Loe J, Danaf NA, Lamb DC, Mehta JP, et al. Tuning porosity in macroscopic monolithic metal-organic frameworks for exceptional natural gas storage. Nat Commun 2019;10:2345.
[27] Li XY, Li Y, Ma LN, Hou L, He CZ, Wang Y, et al. Efficient gas and alcohols uptake and separation driven by two types of channels in a porous MOF: experimental and theoretical investigation. J Mater Chem A 2020. Available from: https://doi.org/10.1039/x0xx00000x.

[28] Allendorf MD, Hulvey Z, Gennett T, Ahmed A, Autrey T, Camp J, et al. An assessment of strategies for the development of solid-state adsorbents for vehicular hydrogen storage. Energ Environ Sci 2018;11:2784–812.
[29] Gomez-Gualdron DA, Colon YJ, Zhang X, Wang TC, Chen YS, Hupp JT, et al. Evaluating topologically diverse metal–organic frameworks for cryo-adsorbed hydrogen storage. Energ Environ Sci 2016;9:3279–89.
[30] Yan Y, Yang S, Blake AJ, Schroder M. Studies on metal-organic frameworks of Cu(II) with isophthalate linkers for hydrogen storage. Acc Chem Res 2014;47:296–307.
[31] Dinc M, Long JR. Hydrogen storage in microporous metal-organic frameworks with exposed metal sites. Angew Chem Int Ed 2008;47:6766–79.
[32] Xiao B, Wheatley PS, Zhao XB, Fletcher AJ, Fox S, Rossi AG, et al. High-capacity hydrogen and nitric oxide adsorption and storage in a metal-organic framework. J Am Chem Soc 2007;129:1203–9.
[33] Murray LJ, Dinca M, Long JR. Hydrogen storage in metal-organic frameworks. Chem Soc Rev 2009;38:1294–314.
[34] Farha OK, Ozgur Yazaydın A, Eryazici I, Malliakas CD, Hauser BG, Kanatzidis MG, et al. De novo synthesis of a metal-organic framework material featuring ultrahigh surface area and gas storage capacities. Nat Chem 2010;2:944.
[35] Yan Y, Lin X, Yang S, Blake AJ, Dailly A, Champness NR, et al. Exceptionally high H_2 storage by a metal-organic polyhedral framework. Chem Commun 2009;9:1025–7.
[36] Yuan D, Zhao D, Sun D, Zhou HC. An isoreticular series of metal-organic frameworks with dendritic hexacarboxylate ligands and exceptionally high gas-uptake capacity. Angew Chem Int Ed 2010;49:5357–61.
[37] Bhatia SK, Myers AL. Optimum conditions for adsorptive storage. Langmuir 2006;22:1688–700.
[38] Ahmed A, Liu Y, Purewal J, Tran LD, Wong Foy AG, Veenstra M, et al. Balancing gravimetric and volumetric hydrogen density in MOFs. Energ Environ Sci 2017;10:2459–71.
[39] Kapelewski MT, Runcevski T, Tarver JD, Jiang HZH, Hurst KE, Parilla PA, et al. Record high hydrogen storage capacity in the metal-organic framework Ni_2(m-dobdc) at near-ambient temperatures. Chem Mater 2018;30:8179–89.
[40] Li H, Li L, Lin RB, Zhou W, Zhang Z, Xiang S, et al. Porous metal-organic frameworks for gas storage and separation: status and challenges. Energy Chem 2019;1:100006.
[41] Li B, Wen HM, Zhou W, Xu Jeff Q, Chen B. Porous metal-organic frameworks: promising materials for methane storage. Chemistry 2016;1:557–80.
[42] Jiang J, Furukawa H, Zhang YB, Yaghi OM. High methane storage working capacity in metal-organic frameworks with acrylate links. J Am Chem Soc 2016;138:10244–51.
[43] Wen HM, Li B, Li L, Lin RB, Zhou W, Qian G, et al. A metal-organic framework with optimized porosity and functional sites for high gravimetric and volumetric methane storage working capacities. Adv Mater 2018;30:1704792.
[44] Yan Y, Kolokolov DI, Da Silva I, Stepanov AG, Blake AJ, Dailly A, et al. Porous metal-organic polyhedral frameworks with optimal molecular dynamics and pore geometry for methane storage. J Am Chem Soc 2017;139:13349–60.
[45] Lin JM, He CT, Liu Y, Liao PQ, Zhou DD, Zhang JP, et al. A metal-organic framework with a pore size/shape suitable for strong binding and close packing of methane. Angew Chem Int Ed 2016;55:4674–8.
[46] Cui X, Chen K, Xing H, Yang Q, Krishna R, Bao Z, et al. Pore chemistry and size control in hybrid porous materials for acetylene capture from ethylene. Science 2016;353:141–4.

[47] Mason JA, Oktawiec J, Taylor MK, Hudson MR, Rodriguez J, Bachman JE, et al. Methane storage in flexible metal-organic frameworks with intrinsic thermal management. Nature 2015;527:357–61.

[48] Zhang M, Zhou W, Pham T, Forrest KA, Liu W, He Y, et al. Fine tuning of MOF-505 analogues to reduce low-pressure methane uptake and enhance methane working capacity. Angew Chem Int Ed 2017;56:11426–30.

[49] Chen CX, Wei ZW, Jiang JJ, Zheng SP, Wang HP, Qiu QF, et al. Dynamic spacer installation for multirole metal-organic frameworks: a new direction toward multifunctional MOFs achieving ultrahigh methane storage working capacity. J Am Chem Soc 2017;139:6034–7.

[50] Xiang S, Zhou W, Zhang Z, Green MA, Liu Y, Chen B. Open metal sites within isostructural metal-organic frameworks for differential recognition of acetylene and extraordinarily high acetylene storage capacity at room temperature. Angew Chem Int Ed 2010;49:4615–18.

[51] Rao X, Cai J, Yu J, He Y, Wu C, Zhou W, et al. A microporous metal-organic framework with both open metal and Lewis basic pyridyl sites for high C_2H_2 and CH_4 storage at room temperature. Chem Commun 2013;49:6719–21.

[52] Zhang M, Li B, Li Y, Wang Q, Zhang W, Chen B, et al. Finely tuning MOFs towards high performance in C_2H_2 storage: synthesis and properties of a new MOF-505 analogue with an inserted amide functional group. Chem Commun 2016;52:7241–4.

[53] Pang J, Jiang F, Wu M, Liu C, Su K, Lu W, et al. A porous metal-organic framework with ultrahigh acetylene uptake capacity under ambient conditions. Nat Commun 2015;6:7575.

[54] Zhang JP, Chen XM. Optimized acetylene/carbon dioxide sorption in a dynamic porous crystal. J Am Chem Soc 2009;131:5516–21.

[55] Cai J, Wang H, Wang H, Duan X, Wang Z, Cui Y, et al. An amino-decorated NbO-type metal-organic framework for high C_2H_2 storage and selective CO_2 capture. RSC Adv 2015;5:77417–22.

[56] Cui Y, Yue Y, Qian G, Chen B. Luminescent functional metal-organic frameworks. Chem Rev 2012;112:1126–62.

[57] Wen HM, Wang H, Li B, Cui Y, Wang H, Qian G, et al. A microporous metal-organic framework with Lewis basic nitrogen sites for high C_2H_2 storage and significantly enhanced C_2H_2/CO_2 separation at ambient conditions. Inorg Chem 2016;55:7214–18.

[58] Loiseau T, Lecroq L, Volkringer C, Marrot J, Ferey G, Haouas M, et al. MIL-96, a porous aluminum trimesate 3D structure constructed from a hexagonal network of 18-membered rings and μ3-oxo-centered trinuclear units. J Am Chem Soc 2006;128:10223–30.

[59] Xue M, Ma S, Jin Z, Schaffino RM, Zhu GS, Lobkovsky EB, et al. Robust metal-organic framework enforced by triple-framework interpenetration exhibiting high H_2 storage density. Inorg Chem 2008;47:6825–8.

[60] Bae YS, Mulfort KL, Frost H, Ryan P, Punnathanam S, Broadbelt LJ, et al. Separation of CO_2 from CH_4 using mixed-ligand metal-organic frameworks. Langmuir 2008;24:8592–8.

[61] Surble S, Millange F, Serre C, Duren T, Latroche M, Bourrelly S, et al. Synthesis of MIL-102, a chromium carboxylate metal-organic framework, with gas sorption analysis. J Am Chem Soc 2006;128:14889–96.

[62] Yoon JW, Jhung SH, Hwang YK, Humphrey SM, Wood PT, Chang JS. Gas-sorption selectivity of CUK-1: a porous coordination solid made of cobalt(II) and pyridine-2,4-dicarboxylic acid. Adv Mater 2007;19:1830–4.

[63] Bae YS, Farha OK, Spokoyny AM, Mirkin CA, Hupp JT, Snurr RQ. Carborane-based metal-organic frameworks as highly selective sorbents for CO_2 over methane. Chem Commun 2008;35:4135–7.

[64] Pan L, Adams KM, Hernandez HE, Wang X, Zheng C, Hattori Y, et al. Porous lanthanide-organic frameworks: synthesis, characterization, and unprecedented gas adsorption properties. J Am Chem Soc 2003;125:3062–7.

[65] Wang B, Cote AP, Furukawa H, Okeeffe M, Yaghi OM. Colossal cages in zeolitic imidazolate frameworks as selective carbon dioxide reservoirs. Nature 2008;453:207.

[66] Xiang S, He Y, Zhang Z, Wu H, Zhou W, Krishna R, et al. Microporous metal-organic framework with potential for carbon dioxide capture at ambient conditions. Nat Commun 2012;3:954.

[67] Dybtsev DN, Chun H, Yoon SH, Kim D, Kim K. Microporous manganese formate: a simple metal-organic porous material with high framework stability and highly selective gas sorption properties. J Am Chem Soc 2004;126:32–3.

[68] Dietzel PD, Besikiotis V, Blom R. Application of metal-organic frameworks with coordinatively unsaturated metal sites in storage and separation of methane and carbon dioxide. J Mater Chem 2009;19:7362–70.

[69] Ghanbari T, Abnisa F, Ashri Wan Daud WM. A review on production of metal organic frameworks (MOF) for CO_2 adsorption. Sci Total Environ 2020;707:135090.

[70] Kaye SS, Dailly A, Yaghi OM, Long JR. Impact of preparation and handling on the hydrogen storage properties of Zn_4O-(1,4-benzenedicarboxylate)$_3$ (MOF-5). J Am Chem Soc 2007;129:14176–7.

[71] Sumida K, Brown CM, Herm ZR, Chavan S, Bordiga S, Long JR. Hydrogen storage properties and neutron scattering studies of Mg_2(dobdc) a metal-organic framework with open Mg^{2+} adsorption sites. Chem Commun 2011;47:1157–9.

[72] Yan Y, Blake AJ, Lewis W, Barnett SA, Dailly A, Champness NR. Modifying cage structures in metal-organic polyhedral frameworks for H_2 storage. Chem Eur J 2011;17:11162–70.

[73] Dinca M, Dailly A, Liu Y, Brown CM, Neumann DA, Long JR. Hydrogen storage in a microporous metal-organic framework with exposed Mn^{2+} coordination sites. J Am Chem Soc 2006;128:16876–83.

[74] Park HJ, Suh MP. Mixed-ligand metal-organic frameworks with large pores: gas sorption properties and single crystal to single crystal transformation on guest exchange. Chem Eur J 2008;14:8812–21.

[75] Zhao D, Yuan D, Yakovenko A, Zhou HCA. NbO-type metal-organic framework derived from a polyyne coupled di isophthalate linker formed in situ. Chem Commun 2010;46:4196–8.

Chapter 6

Excessively paramagnetic metal organic framework nanocomposites

B. Venkata Shiva Reddy[1], N. Suresh Kumar[2], K. Chandra Babu Naidu[1], K. Srinivas[1], H. Manjunatha[3], A. Ratnamala[3], Anish Khan[4,5] and Abdullah M. Asiri[4,5]

[1]Department of Physics, GITAM (Deemed to be University), Bangalore, India, [2]Department of Physics, JNTUA, Anantapuramu, India, [3]Department of Chemistry, GITAM School of Science, GITAM (Deemed to be University), Bangalore, India, [4]Chemistry Department, Faculty of Science, King Abdulaziz University, Jeddah, Saudi Arabia, [5]Center of Excellence for Advanced Materials Research, King Abdulaziz University, Jeddah, Saudi Arabia

6.1 Introduction

The invention of atomic force microscopy and surface electron microscopy along with development of cluster science made a revolution in nanotechnology and nanoscience. Nanomaterials are different from the bulk materials in electrical properties, magnetic properties, dielectric properties, chemical properties, strength of the materials, etc. For example, gold shines at bulk form, but when it is in nanoscale loses its shining and also becomes red in color and acts as semiconductor. The silicon at nanoscale is an insulator. The properties of nanoscale mentioned previously are due to increase of surface-to-volume ratio and quantum effects. As a result of extensive and intensive research in nanotechnology or nanoscience have been developed nanocomposites with many applications to develop science and technology. Nanocomposites are present hybrid science composed of multiphase solid material and one of the phases has one, two, or three dimensions less than 100 nm. The composition may be only metals, insulators, or both. We can take metals and organic composition for better applications, for example, titanium carbide (Ti_3C_2) exhibits highly antibacterial property. Stable reduced silver, titanium carbide, and cuprous oxide ($AgTiC_2Cu_2O$) shows very good antibacterial properties and efficient photocatalytic bactericides for antifouling. Marine biofouling is a major environmental challenge as it damages economy and health every year.

Metal-Organic Frameworks for Chemical Reactions. DOI: https://doi.org/10.1016/B978-0-12-822099-3.00006-X

So, preventing and treating marine biofouling are major and popular research in present days.

The two-dimensional (2D) materials coupled with nanocomposites exhibit unique characteristics to eradicate some medical and environmental problems such as bacterial infections, savage water purification, and bactericides for antifuming. In 2D materials MXenes are used for effective work and the general formula is $M_{n+1}X_nT_X$ where M is early transition metal, X is carbon or nitrogen, and T is surface termination group like $-OH$, $-F$ and $=O$. Titanium-based substances are promising materials in various fields, such material is Ti_2C_3 used in energy storage, catalysis, and photochemical therapy due to hydrophilic functional group, strong redox reactivity, and more efficient electron transfer ability. Even though MXenes discharge their good duties but little bit shortcomings are there in charge recombination. Hence to improve this shortcoming heterojunctions are to be formed, such as TiO_2 and g-C_3N_4 [1]. Organic chitosan (CS) (nontoxic) is coated with copper oxide (CuO) nanocomposite for enhanced industrial dye removal from aqueous solutions and antibacterial properties to maintain eco-biocompatibility in environment. The biogenic synthesis of chitosan-coated copper oxide (CS−CuO) nanocomposites is prepared by using *Psidium guajava* aqueous leaf extract. However, chemically synthesized metal oxide nanoparticles will affect environment due to their toxic solvent contents and hazardous chemical usage as a reducing agent, such reducing agents such as hydrazinium hydroxide sodium hypophosphite and sodium borohydride. These chemicals are very adverse in nature, which can damage on atmosphere and ecosystem. The green synthesis of CuONPs has drawn very good attention due to their significant applications in physicochemical and biological applications in gas sensors, dye sensitize solar cells, lithium ion batteries, ink jet printers, and in optics. In addition to this application, CuONPs exhibit as an antioxidant, anticancer activities and use in textiles and pesticide industry. The biodegradable biopolymer of chitosan has all kinds of biological properties. This chitosan is a natural polysaccharide composed of β-(1→4)-2-amino-2-deoxy-D-glucopyranose and it is deacetylated in the form of chitin. Chitosan is extracted from crab shells, lobsters, crawfish, bacteria, and fungi and also from various biological systems [2].

Since prehistoric and ancient times of Egyptian and Babylonian, composite materials were used in their daily life for their specific purpose, for example, animal hair and straw were used in order to strengthen the baked clay and masonry mortars. Hence, addition or reinforcement of other elements into single component system gives more applications. Silica aerogels are prepared by sol−gel chemistry and possess very good nano-porosity with a wide range of physical properties. This aerogel can be used in various fields such as aerospace technology, insulation of sound and heat, catalyst carrier for chemical reaction, storage of energy, biomedical science, and automotive sector. However, the major concern is its brittleness on collapse and sudden

swift thing in applications. Hence, in order to compensate its shortcomings, we can add or reinforce carbon nanotubes (CNTs) and graphene. These reinforcement materials have very good mechanical properties; however, these composites possess high mechanical strength and toughness. Therefore these materials could facilitate widespread use in space technology and the automotive industry [3]. The gamma radiation incidence or treatment on the metal organic nanocomposites gives good physical strength due to the formation of carbon-rich clusters and declaim of amorphous nature and intermolecular cross-linking [4].

The use of nondegradable things such as plastic is the most environmental contamination issue in this world, due to human's reckless activities. In order to overcome or mitigate this hazardous threat, research is going on and some solutions have been found. Biodegradable materials are such things that are used in food pockets instead of petroleum-based polymers that are dangerous to health. These biodegradable materials are generally made up of starch, cellulose, and chitosan and few multipurpose polymers such as polylactic acid, polyglycolic acid, polybutylene succinate, and polyhydroxybutyrate. These compounds are ecofriendly, biodegradable, and nontoxic with highly crystalline in nature. But these polymers or biodegradable materials have its own shortcomings in some aspects such as strength or mechanical properties and thermal properties. In order to overcome these shortcomings, we add silver nanoparticles and some clay particles [5]. The plant extract−based synthesis is most biocompatibility to alleviate the global environmental issues and problems. The plant extracts are more economical than other extracts and give good results when added into nano-paramagnetic materials to form magnetic−organic nanocomposites. These plant extracts generally contain proteins, sugars, terpenoids, polyphenols, alkaloids, and phenolic acids. These bioactive materials involve in the reduction metal ions into its nanostructure [6].

The silver nanoparticles in the literature have got supreme place as an antimicrobial agent when it is combined with plant extracts. The number of silver particles in nanocomposites determines its antimicrobial activity due to increase of surface area or surface-to-volume ratio or density. Silver is the highest form of antimicrobial element than any other element in the periodic table, because it is most toxic to the pathogenic microorganism, very low toxic to the animal cell, and to be preferred against antibiotic-resistant bacteria [7]. The silver nanoparticles (Ag) are also most important material in the preparation of epoxy nanosheets from epoxy resin and 4,4′-diamino-diphenylmethane [8]. In the preparation of nanotubes, injection of tangled silver gives rise to advanced properties in the polythiophene-functionalized multiwalled carbon nanotube, such as low cost, efficiency, high electrical conductivity, and thermal properties [9].

The gold is important and excellent material in the preparation of nanocomposites. The sunlight is coupled with nanocomposites to remove toxic

elements in the savage water and decomposition of toxic organic substances. Au@CNT@TiO_2 nanocomposite acts as a very good catalyst in the degradation of toxic organic dyes, reduction of *p*-nitrophenol into *p*-aminophenol and coumarin molecule to 7-hydroxycoumarin. The hexavalent chromium is extremely water-soluble and also dangerous to human carcinogen when it enters the human body and thus damages the cell structure. If the hexavalent chromium is entered through cell membrane develop unstable toxic intermediates and poisonous reactive oxygen [10].

6.2 Discussion and applications

Paramagnetic substances are weekly magnetized substances when placed in the direction of magnetic field. Organic substances are carbon containing chain linked with hydrogen, oxygen, or nitrogen through covalent bond. Paramagnetic and organic substances or combination of both in the nanoscale dimensions gives rise to more advantages. In the savage water management and antibacterial treatment, we can employ paramagnetic−organic nanocomposites. Contamination of water is major challenge than any other environmental issues and harmful to the living organisms. The contamination of water is caused due to the carcinogenic pollutants, nondegradable color dyes, discharged by the leather, paper, and textile industries. In addition, another group of compounds is being treated as chemical contaminants of emerging concern. At present, all over the world research groups are focusing to degrade the dyes by different strategies. Among them most effective method is advanced oxidation process. In this process the nanocomposite is used to remove contaminants, among them C_3N_4−TiO_2 is most effective nanocomposite. This nanocomposite works without any external reagents and works based on the sunlight incidence. TiO_2 is photocatalytic in nature and generates reactive oxygen. TiO_2 possess high electron/hole recombination pairs and its bandgap is 3.2 eV but this will not help in photocatalytic activity under visible light; hence, it fails in practical applications. So, in order to modify TiO_2 bandgap and to work under visible light incidence, the methods employed are (1) doping impurities that may be metal or nonmetal (2) dye sensitization, (3) surface modification by controlling morphology, (4) constructing heterojunction, and (5) semiconductor coupling. Among the abovementioned strategies, making the nanocomposites will be an impactful method to enhance the photocatalytic activity with improved optical and electronic properties. Here carbon nitride (g-C_3N_4) is the best material for making nanocomposite with TiO_2; in this case heterojunction is formed between these two substances. In these nano-compositions interfacial connection is formed and retards the electron transfer rate. In addition to g-C_3N_4 is photocatalyst of metal free with a bandgap of 2.7−2.8 eV that possesses high thermal and chemical stability. This heterojunction is used as a photocatalyst in the removal of NO, H_2 production, hydrocarbon oxidation, etc. the

optical and synergic electron transfer behavior of g-C_3N_4 will enhance the optoelectronic behavior of the TiO_2 materials. And, thus, light absorption in the visible range is possible in heterojunction nanocomposites [11].

In semiconductor advanced hybrid oxidation process, there is a complete removal of organic, inorganic, and microbial pollutants under ambient reactions. Semiconductors containing photocatalysts are efficient in nature without posttreatment sludge formation and secondary pollutants. These photocatalysts can be recycled due to their inertness in aqueous solution and chemical stability. Fig. 6.1 illustrates the degradation of organic pollutants present in water. When photocatalyst is exposed to sunlight of photon of equal or greater than bandgap energy, then electrons jump from valance band to conduction band. The holes in valance band and electrons in conduction band form the electron−hole pair. These electron−hole pairs move to the surface of the photocatalyst and thus involve in photodegradation reaction [12].

The energy crisis is major problem across the world, because we are using nonrenewable or traditional resources to build the economy of a country and to reach public needs. But the major drawbacks of using traditional (or conventional or nonrenewable) are unlimited in nature. Hydrogen is used as good source of energy; hence, it is produced by the water gas method or electrolytic route in industry but it is less effective. Hence, in contrast to this method, photocatalytic decomposition of water by semiconductor is simple, economical, and greenway to produce hydrogen energy to meet the demands. In this process solar energy is utilized, hence, no pollution. The heterostructure nanocomposites used in this process are TiO_2 and g-C_3N_4, which is good combination to get the hydrogen from the water and to convert the CO_2 or reduction of CO_2. But in order to enhance the photocatalytic activity,

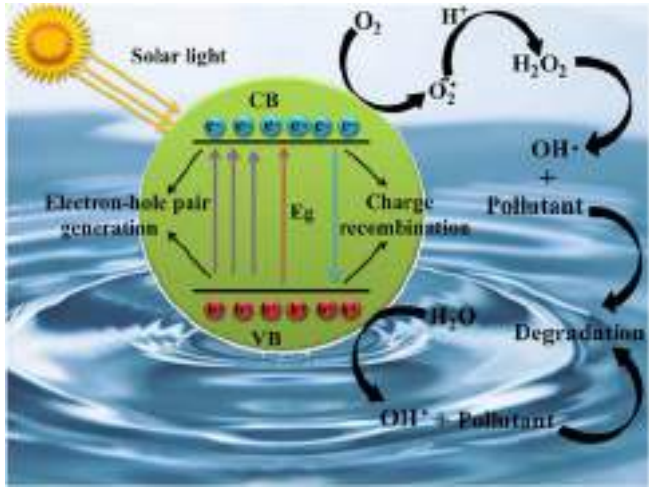

FIGURE 6.1 Degradation of organic pollutants present in water [12].

CN is doped with TiO_2 so that to form CN@TiO_2 becomes hexagonal double-shell tubular heterostructure due to C_3N_4 precursor. Thus this nanocomposite reaches a good catalytic activity and performance is 10.10 mmol h^{-1} g^{-1} [13]. In this composition g-C_3N_4 possess heptazine ring structure and high condensation degree, which accounts for physiochemical stability and good electronic structure [14].

In the heterojunction nanocomposite structures, the light harvesting in photocatalytic reaction depends on the materials used. The g-C_3N_4 is not costly, has great stability, and is easily available, but its efficiency of working depends on metal in which heterojunction is formed. In order to increase its efficiency, gold nanoroads are used. This gold combination with graphene containing urea is used in which the hydrogen evolution rate is four times greater than Pt combination with g-C_3N_4. In the Pt combination with g-C_3N_4 the hydrogen evolution rate is 68.9 μmol g^{-1} h^{-1} under visible light, but gold rods in combination with g-C_3N_4 give hydrogen evolution rate that is 350.6 μmol g^{-1} h^{-1} under visible and near-infrared light. Hence, gold nanorods carry great importance in the light harvesting in both visible and near-infrared range and good hope in future to solve the energy crisis by evolving more amount of hydrogen that is used as substitution to petroleum products. Noble metals in the nano-form possess special nature that is surface plasmon resonance (SPR) effect. SPR can produce hot electrons that improve visible and near-infrared range of light absorption in the gold nanorods [15]. The schematic representation of synthetic root of g-C_3N_4 nanosheets and schematic illustration of synthetic root of Au-g-C_3N_4 are shown in Figs. 6.2 and 6.3, respectively.

Gold and graphene oxide nanoparticles combined with poly vinyl alcohol (PVA) form cross-linked composite films that are biodegradable in nature. This biodegradable film is used in the food packaging to protect the shelf-life of food. It not only helps in protecting the shelf-life of food but also enhances the safety so that health risks of consumers can reduce. PVA is water-soluble and nontoxic biosynthetic biocompatible polymer. PVA possess excellent hydrophobic and film-forming capacity in nature so it can be used as synthetic and natural polymer blends. In the backbone of this PVA

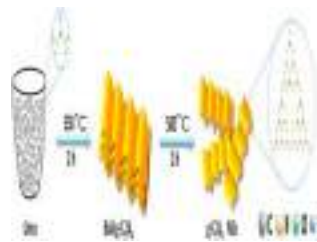

FIGURE 6.2 Preparation root of g-C_3N_4 nanosheets [15].

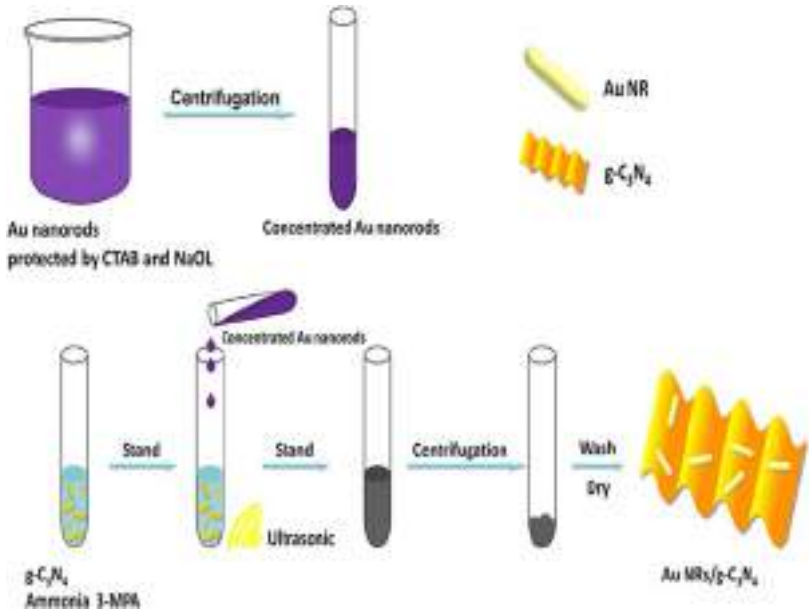

FIGURE 6.3 Preparation root of Au-g-C_3N_4 nanocomposite [15].

has hydroxyl group (−OH) where other many potential chemical compounds can interact to toiler the required shape of packaging film. In this case cross-linking agents are added, which act as antimicrobial agents such as smallest dialdehyde, glyoxal and glutaraldehyde with antiseptic properties. The mechanical strength of the PVA can be improved by fillers such as gold and graphene oxide nanoparticles and also silver can be added via electrospun technique [16].

In the water treatment nickel oxide nanoparticles (NOP) are also being used as a photocatalyst as they possess bandgap varying from 3.6 to 4.0 eV. Hence, NOP plays an important role in the environmental issues as it finds huge applications in the degradation process of hazardous dyes, inorganic pollutants, and biological aspects. Some specific studies have been done on nanocomposites such as antimicrobial potentiality and degradation of organic substance with the visible sunlight irradiation. Anyway, the single nickel NOP has its own shortcomings; hence, it can be clubbed with reduced graphene oxide (RGO) to make good application. The RGO can be prepared by the phytoextract as a reductant for the synthesis of RGO and the nanoclusters, which has been extracted from the *P. guajava* (guava) leaf. This leaf contains leucocyanidin flavonoids and exhibits hydroxyl group (−OH), which can reduce graphene oxide by tautomeric conversion of flavonoids to keto from enol form [17]. Fig. 6.4 shows the schematic representation of chemical reduction of graphene oxide with aqueous phytoextract.

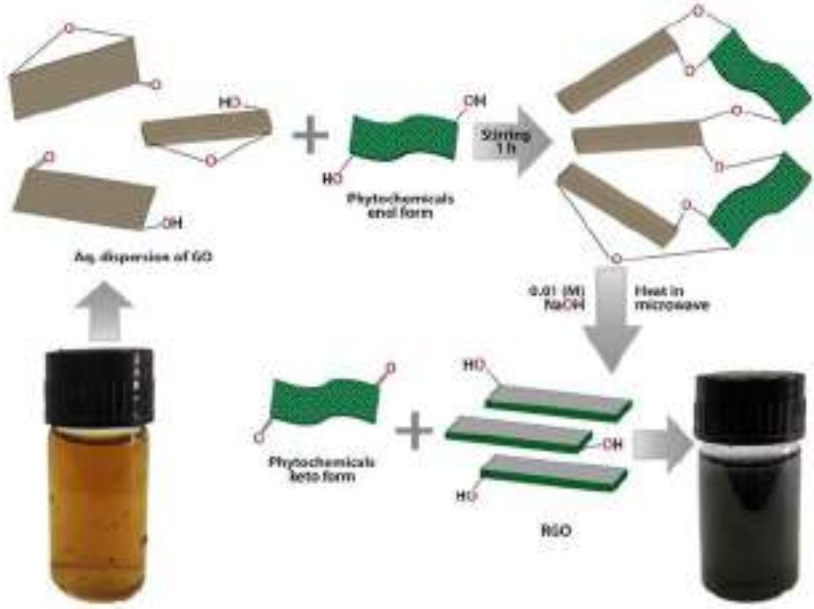

FIGURE 6.4 Scheme of reaction showing the chemical reduction of graphene oxide with aqueous phytoextract [17].

If we go through literature the silver (Ag) nanoparticles are prominently found that as an excellent antimicrobial agent, because of its nanosize in which the surface-to-volume ratio is maximum. The silver is preferred as an antimicrobial agent because of its high toxic nature to the pathogens and low toxic nature to the animal cell and also viable alternative against antibiotic-resistant bacteria. Silver nanoparticles possess many applications such as in water purification, food packing, cosmetics, nanoelectronics, biomedicine, biosensors, and bone prostheses and nano-plasmonics. In pharmacological applications, they are used as antiplasmodial, anticancer, antiinflammatory, and antifungal agents. The synthesis of Ag nanoparticles can be done by various methods among which we can select green methods as it is an eco-friendly nature and will utilize natural reducing agent. Preparation of Ag nanoparticles by green synthesis is shown in Fig. 6.5. This method includes the use of microorganisms, enzymes, plant extracts, and plant exudates as possible ecologically correct alternatives to conventional methods. The cashew gum is excellent exudates extracted from the *Anacardium occidentale* L. tree. The clay [Palygorskite (Pal), $Si_8Mg_5O_{20}(OH)_2(OH_2)_4 \cdot 4H_2O$] is also added as a supportive matrix into the nanostructure for immobilization of nanoparticles [18].

The organic−inorganic (paramagnetic only) nanocomposites can exhibit a wide range of novel advantages. In this nanocomposition, organic materials

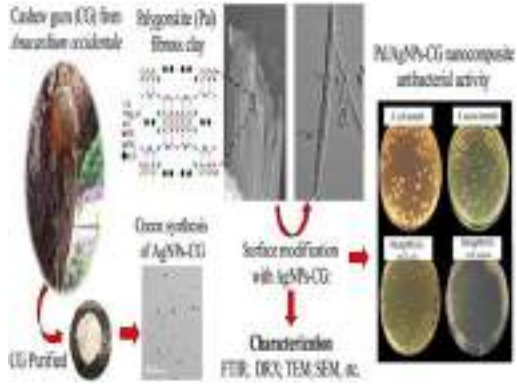

FIGURE 6.5 Schematic representation of green synthesis [18].

separate the inorganic materials with enhancing catalytic, magnetic, and electronic properties. Organic materials are easy to mold and have good permeability and biocompatibility. Inorganic materials possess good catalytic, electronic, magnetic, and redox reaction properties but will not possess good biocompatibility and prone to agglomerate with each other. Hence, binding or organic materials on inorganic materials enhances the biocompatibility. Such inorganic materials are Au, Ag, Co, Ni, Ru, Pt, and Pd and their metal oxides that can be incorporated into organic structures include CNT, graphene, and various polymers. Example of addition of TiO_2 into graphene (TiO_2−graphene) shows enhanced photocatalytic reaction in NO_x reaction than mere TiO_2 due to electron−hole pairs effectively separated. The organic and inorganic composites can be susceptible to external stimulus such as chemical, light, heat, electric field, magnetic field, and mechanical force by modifying internal structure and composition. For the stimulus, nanocomposites show distinguishable states (ON and OFF), which can be applied to switch system. In the composites nanomaterials are important which gives different properties on different compositions and nanomaterials are classified into (1) zero-dimensional (quantum dots), (2) one−dimensional, (3) 2D, and (4) three-dimensional. The schematic representation of nano materials has shown in Fig. 6.6 [19].

A novel electrochemiluminescence biosensor can be constructed from the organic−inorganic nanocomposition. The nanocomposite $ZnCO_2O_4$ is used as an efficient emitter and accelerator in the detection of specific sequence in DNA. The sequence identification in the DNA helps to diagnose and prevent the diseases. From these nanocomposites we can develop enzyme-free electrochemiluminescence biosensor [20]. The natural enzymes involve in catabolic and anabolic reactions of animal body. The bioassays are developed relayed on unique activity of enzymes toward specific substrates. However, they deactivate when they open to extreme environmental factors such as temperature,

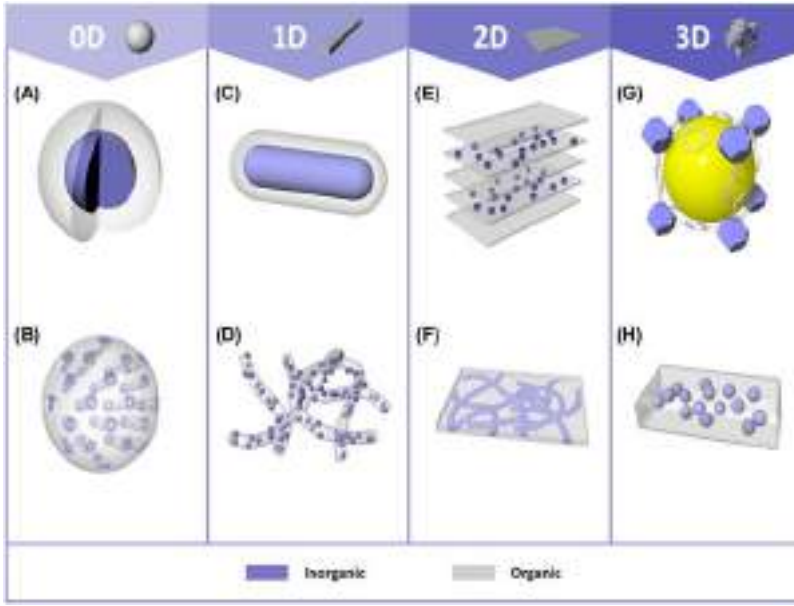

FIGURE 6.6 Various structures of nanocomposites [19]: (A) core−shell nanoparticle, (B) porous support-functional group, (C) core−shell nanorod, (D) nanofiber, (E) multilayer, (F) nanofiber-embedded nanocomposite, (G) crystal, (H) inorganic plum−organic pudding.

pH, ionic strength, and organic solvents. To overcome the abovementioned shortcomings, we developed artificial enzymes or enzyme- like nanocomposites, which are called nanozymes. These nanozymes are stable alternative to the natural enzymes is bimetallic in nature such as Ag/Pt nanoclusters, Pd@Au nanorods, Pt−Se nanostructure, CeO_2/NiO nanocomposites, $CuWO_4$ nanoparticles, and porous $NiCO_2O_4$ nanoparticles [21]. The bioactive inorganic and organic nanocomposites can be used to heal the wound and regeneration of skin tissue [22].

6.3 Conclusion

Industrial revolution and globalization of the world are two historical situations in the world, which leads to advantages and disadvantages as well. Advantages are employment opportunities for unemployed youth and economic growth and development of a country. No doubt that international peace and cooperation is developed between the many countries from the previous two historical situations, but the adverse effects on the environment is indelible. Due to industrial revolution and globalization, the atmosphere has been polluted like anything across the globe. The major pollutions in the atmosphere are water pollution and air pollution, which damages the flora and fauna structures. The water from the outlets of industry contains many

poisonous elements that can damage the aquatic life and smoke from the industry and automobiles releases carbon dioxide and carbon monoxide, which can cause increase of the Earth's temperature. Present international problem is global warming that can raise the temperature of the Earth and leads to the melting of ice in the mountains. The melted ice can reach to the sea or ocean causing rise of water level, leading to the land encroachment by sea or ocean.

The one more major issue across the world is health issue that is a major challenge to the WHO and modern government as well to fight against the new diseases. We have been seen the bacterial infections (foe bacteria) and skin disease that can cause irritation to the living organisms and threat too. These bacterial infections are also due to effluents from industry and irresponsible governments. So, in order to mitigate environmental pollution and health issues like bacterial infections, the exclusively paramagnetic nanocomposites are being fabricated according to the need. These nanocomposites can filter the effluents and convert them into useful energy and biodegradation by the catalytic activity. This biodegradation and energy storage by nanocomposites leads to the ecofriendly environment, which keeps clean and green around us and reduces some health problems such as breathing and skin allergy issues. Hence, across the world laboratories, these advanced nanocomposites and technologies are to be developed in order to mitigate the environmental and health issues.

References

[1] Feng H, Wang W, Zhang M, Zhu S, Wang Q, Liu J, et al. 2D titanium carbide-based nanocomposites for photocatalytic bacteriostaticapplications. Appl Catal B Environ 2020;266:118609.

[2] Sathiyavimal S, Vasantharaj S, Kaliannan T, Pugazhendhi A. Eco-biocompatibility of chitosan coated biosynthesized copper oxide nanocomposite for enhanced industrial (Azo) dye removal from aqueous solution and antibacterial properties. Carbohydr Polym 2020;241:116243. Available from: https://doi.org/10.1016/j.carbpol.2020.116243.

[3] Patila Sandeep P, Shendyea Parag, Markerta Bernd. Molecular dynamics simulations of silica aerogel nanocomposites reinforced by glass fibers, graphene sheets and carbon nanotubes: a comparison study on mechanical properties. Composites B Eng 2020;190:107884.

[4] Nouh SA, Benthami K, Samy RM, El-Hagg AA. Effect of gamma radiation on the structure and optical properties of polycarbonate−polybutylene terephthalate/silver nanocomposite films. Chem Phys Lett 2020;741:137123.

[5] Manikandan NA, Pakshirajan K, Pugazhenthi G. Preparation and characterization of environmentally safe and highly biodegradable microbial polyhydroxybutyrate (PHB) based graphene nanocomposites for potential food packaging applications. Int J Biol Macromol 2020;154:866−77.

[6] Ansari Z, Singh P, Sen K. Facile synthesis of polyphenol mediated metal nanocomposites for selective sensing of methylmercury. J Environ Chem Eng 2020;8(4):103838.

[7] Araújo CM, das Virgens Santana M, do Nascimento Cavalcante A, Nunes LCC, Bertolino LC, de Sousa Brito CAR, et al. Cashew-gum-based silver nanoparticles and palygorskite as green nanocomposites for antibacterial applications. Mater Sci Eng C 2020;115:110927. Available from: https://doi.org/10.1016/j.msec.2020.110927.

[8] Bogdanova L, Lesnichaya V, Spirin M, Shershnev V, Irzhak V, Kydralieva K, et al. Mechanical properties of polycondensate epoxy nanocomposites filled with Ag nanoparticles synthesized in situ. Mater Today Proc 2020. Available from: https://doi.org/10.1016/j.matpr.2020.02.138.

[9] Swathy TS, Jinish Antony M. Tangled silver nanoparticles embedded polythiophene-functionalized multiwalled carbon nanotube nanocomposites with remarkable electrical and thermal properties. Polymer 2020;189:122171.

[10] Misra M, Chowdhury SR, Lee TIL. Sunlight driven decomposition of toxic organic compound, coumarin, *p*-nitrophenol, and photo reduction of Cr(VI) ions, using a bridge structure of Au@CNT@TiO_2 nanocomposite. Appl Catal B Environ 2020;272:118991.

[11] Sutar RS, Barkul RP, Delekar SD, Patil MK. Sunlight assisted photocatalytic degradation of organic pollutants using g-C_3N_4−TiO_2 nanocomposites. Arab J Chem 2020;13(4):4966−77.

[12] Sudhaik A, Raizada P, Shandilya P, Jeong D-Y, Lim J-H, Singh P. Review on fabrication of graphitic carbon nitride based efficient nanocomposites for photodegradation of aqueous phase organic pollutants. J Ind Eng Chem 2018;67:28−51.

[13] Li F, Xiao X, Zhao C, Liu J, Li Q, Guo C, et al. TiO_2-on-C_3N_4 double-shell microtubes: in-situ fabricated heterostructures toward enhanced photocatalytic hydrogen evolution. J Colloid Interface Sci 2020;572:22−30.

[14] Sim LC, Koh KS, Leong KH, Chin YH, Aziz AA, Saravanan P. In situ growth of g-C_3N_4 on TiO_2 nanotube arrays: construction of heterostructures for improved photocatalysis properties. J Environ Chem Eng 2020;8(1):103611.

[15] Tian H, Liu X, Liang Z, Qiu P, Qian X, Cui H, et al. Gold nanorods/g-C_3N_4 heterostructures for plasmon-enhanced photocatalytic H_2 evolution in visible and near-infrared light. J Colloid Interface Sci 2020;557:700−8.

[16] Chowdhury S, Teoh YL, Ong KM, Rafflisman Zaidi NS, Mah S-K. Poly(vinyl) alcohol crosslinked composite packaging film containing gold nanoparticles on shelf life extension of banana. Food Packag Shelf Life 2020;24:100463.

[17] Sadhukhan S, Bhattacharyya A, Rana D, Ghosh TK, Orasugh JT, Khatua S, et al. Synthesis of RGO/NiO nanocomposites adopting a green approach and its photocatalytic and antibacterial properties. Mater Chem Phys 2020;247:122906.

[18] Araújo CM, das Virgens Santana M, do Nascimento Cavalcante A, Nunes LCC, Bertolino LC, de Sousa Brito CAR, et al. Cashew-gum-based silver nanoparticles and palygorskite as green nanocomposites for antibacterial applications. Mater Sci Eng C 2020;115:110927. Available from: https://doi.org/10.1016/j.msec.2020.110927.

[19] Lee W, Kim D, Lee S, Park J, Oh S, Kim G, et al. Stimuli-responsive switchable organic-inorganic nanocomposite materials. Nano Today 2018;23:97−123.

[20] Li Y, Chu Y, Li Y, Ma C, Li L. A novel electrochemiluminescence biosensor: inorganic-organic nanocomposite and $ZnCo_2O_4$ as the efficient emitter and accelerator. Sens Actuators B Chem 2019;303:127222.

[21] Lien C-W, Yu P-H, Chang H-T, Hsu P-H, Wu T, Lin Y-W, et al. DNA engineered copper oxide-based nanocomposites with multiple enzyme-like activities for specific detection of mercury species in environmental and biological samples. Anal Chim Acta 2019;1084:106−15.

[22] Wang X, Chang J, Wu C. Bioactive inorganic/organic nanocomposites for wound healing. Appl Mater Today 2018;11:308−19.

Chapter 7

Expanding energy prospects of metal-organic frameworks

K. Rama Krishna Reddy[1], D. Prakash Babu[1], N. Suresh Kumar[2], G. Ranjith Kumar[1], K. Chandra Babu Naidu[3] and Anish Khan[4,5]

[1]School of Applied Sciences, REVA University, Bangalore, India, [2]Department of Physics, JNTUA, Anantapuramu, India, [3]Department of Physics, GITAM (Deemed to be University), Bangalore, India, [4]Chemistry Department, Faculty of Science, King Abdulaziz University, Jeddah, Saudi Arabia, [5]Center of Excellence for Advanced Materials Research, King Abdulaziz University, Jeddah, Saudi Arabia

7.1 Introduction

Nowadays, metal-organic frameworks (MOFs) are receiving much attention as an interesting class of highly ordered crystalline and porous materials possessing extensively huge porosity, morphology, and framework tunability [1−6]. The various combinations via the coordinate bonding among the organic linkers and metal clusters result in more advantages for altering their properties in different approaches [7−11]. MOFs are identified efficient materials to detect the structure of molecule with gas separation and storage, secondary battery electrode materials, catalysis, control of medicine releasing, etc. [7,12].

MOFs consisting of extensive specific surface area that employs them to adsorb impurities that are unfavorable for lithium-ion batteries in the process of cycling and can also develop steric effects and some have inherent Lewis acidic or empty coordination sites on their surface [13,14]. These various properties exist due to the dissipation and transport of Li^+ ions from the associated lithium salt, [15,16] because the MOFs perform selective for potential fillers of PEO-based solid electrolyte (SE) to increase the prospects of lithium-ion batteries. While comparing with nanomaterials such as carbon, zeolite, and silica, MOFs consist of huge advantages such as size tunable porosity, structural diversity, and increased surface area.

In general, MOFs consisting of metal ions and organic linkers are a new class of high surface materials. The organic units are divalent or polyvalent organic carboxylates, which when linking to metal-containing units (e.g., Zn^{2+}, Co^{2+}, Cu^{2+}, Mg^{2+}, Ni^{2+}, and Al^{3+}) can result in three-dimensional network having

Metal-Organic Frameworks for Chemical Reactions. DOI: https://doi.org/10.1016/B978-0-12-822099-3.00007-1

proper pore size distributions. The surface area of MOFs typically ranges from 1000 to 10,000 $m^2 g^{-1}$, and pore size is possible to change as large as 9.8 nm obtained by altering the organic and metal-containing units. Within the past few decades, more than 20,000 different MOFs with different geometry, size, and functionality are reported and studied [17,18]. Transition metals (e.g., Zn, Co, Cu, Fe, and Ni); alkaline earth elements (e.g., Sr and Ba); *p*-block elements (e.g., In and Ga); actinides (e.g., U and Th); and mixed metals have been utilized for the synthesis of MOFs. These are produced from supramolecular assembly of inorganic components possessing materials that can provide different structures and morphologies. As the formation of porous structures using MOFs as precursors/templates may generates extensive functional nanomaterials.

7.2 Metal-organic frameworks in Li-ion batteries

Nowadays, lithium-ion batteries play a vital role in the field of automobile industry because of high selectivity, high package of storage capacity of grid energy, and viable energy storage. The materialistic lithium-ion batteries comprise both electrodes, such as the cathode and anode. Cathodes are generally designed by Li transition metal oxide (e.g., $LiCoO_2$, $LiMn_2O_4$, and $LiFePO_4$), but anodes are designed by the carbonaceous materials (e.g., activated carbon) [19–22]. The abovementioned compounds are usually laminated structure, so that the lithium ions can easily transfer into the compound. Generally, lithium-ion batteries are fabricated with discharged compounds segregated by a non-aqueous electrolyte, since lithium possesses high reactivity in the presence of aqueous medium. Nevertheless those materials generally possess very poor conductivity, so that it leads to small separation occurring between the electrodes. In the course of first charging of the battery, nearly 5%–20% lithium is absorbed in the production of an SE interface (SEI) at the surface of anodic metal [23]. But, in the former succession, a small amount of lithium is absorbed for SEI. This SEI layer consists of highly dense inorganic compounds (Li_2O, Li_2CO_3, and LiF) near the anodic surface and mixture of the inorganic and organic composites ($ROCO_2Li$ and Li_2CO_3) present at the electrolyte material. The existence of SEI in lithium-ion batteries is unfavorable due to its unconfined extension. However, the dazzling phase of the SEI surface produced is shielded batteries in the process of overpotential and limits the dissolution of the material [24,25]. In Fig. 7.1 the Li-ion battery schematic representation is shown [24].

In the beginning, lithium batteries were introduced by Whittingham in 1970 with titanium(IV) sulfide and lithium metal as cathode and anode, respectively [26]. In 1973 Adam Heller introduced the lithium thionyl chloride battery, designed by metallic lithium as an anode and liquid thionyl chloride ($SoCl_2$) as a cathode; it has long life, high energy density, and good operating temperature of 55°C [27]. But, the electrochemistry of these batteries was not reversible, and the electrolyte utilized was highly hazardous with a high tendency to react with water [28]. Moreover, high cost and safety concerns restrict their experimental

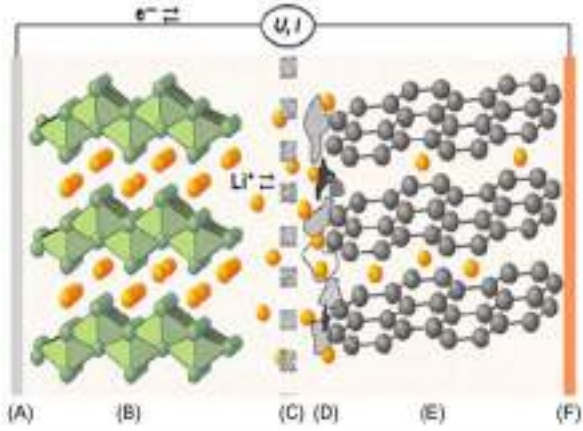

FIGURE 7.1 Schematic illustration of a typical Li-ion battery: (A) aluminum current collector; (B) oxide active material; (C) porous separator soaked with liquid electrolyte; (D) inhomogeneous SEI layer; (E) graphite active material; and (F) copper current collector. *SEI*, Solid electrolyte interface.

advantages. In 1981 two scientists Goodenough and Mizushima suggested a rechargeable cell with a voltage in 3.2 V range using lithium cobalt oxide ($LiCoO_2$) as a cathode and lithium metal as an anode material [29]. Nevertheless, the utilization of a lithium metal anode was restricted because of the issue of lithium dendrite formation on the anode surface while charging process. These dendrites are the causes of the growth of needle-like metal particles on the anode surface. This process helps in producing graphite as an interesting anode material for lithium-ion batteries that can alter the lithium metal. In 1983 Basu suggested an effective lithium-embedded graphite electrode at Bell Labs, which is effective replacement to the anode materials generally in lithium-ion batteries [30]. In 1983 Thackeray et al. also indicated manganese spinel as an alternate positive material to replace $LiCoO_2$ [31]. In 1989 Manthiram and Goodenough introduced the cathode material containing polyanions, these can be utilized to evolve higher voltages than oxides due to the induction effect of the polyanions [32]. Finally, in 1990, Sony Corporation synthesized the first commercial lithium-ion battery in which lithium cobalt oxide and graphite were utilized as cathode and anode materials, respectively [33]. Moreover, very less cyclability and high cost of $LiCoO_2$ propelled the need for better alternatives. In 1996 Padhi et al. introduced lithium iron phosphate ($LiFePO_4$) and other phosphoolivine materials as a cathode for lithium-ion batteries [20]. But, very less conductivity of oxide was a limitation, which leads to the loss of Coulombic efficiency of the battery. In 2002 Chiang and his group studied the n-type conductivity of the synthesized materials via supervalent cation doping (Mg^{2+}, Al^{3+}, Ti^{4+}, Zr^{4+}, Nb^{5+}, or W^{6+}), and results increase the overall performance very extensively [34].

Battery efficiency also depends on the material morphology and particle size. In 2004 Chiang suggested that iron phosphate having a particle size of $<$100 nm can effectively increase the efficiency of batteries [35]. The reason for the increased efficiency of lithium-ion batteries was attributed to the reduced particle density and increased specific surface area. In 2007 Chan et al. introduced silicon nanowire-based anodes for lithium-ion batteries [36]. This silicon nanowire can produce effective strain without pulverization on volume changes (400%) during charging or discharging. Moreover, in 2012, these nanowires were added with impurities to enhance their electrochemistry and to increase the efficiency [37]. Yet, necessary requirements for upgrading the lithium-ion batteries of general consequences are volume changes and the deterioration of original electrode surface during lithiation or delithiation. More volume expansion provided in the process of lithiation or delithiation, which can alter the morphology of the active material. Because of these limitations, results decrease in the capacity of the battery. Till today, various metal oxides and carbon-based materials have been utilized as anode materials for lithium-ion batteries for instance, nitrogen-doped or graphitic carbon [38]; metal oxides (NiO [39], MoO_3 [40], Fe_2O_3 [41], VS_2 [42], Co_3O_4 [43], SnO_2 [44,45], and TiO_2 [46]); SnS_2 [47]; MnO_2 [48]; Co_9S_8 [49]; metal sulfides (MoS_2 [50]); and lithium alloys (Sn, Si, and Sb)/multinary alloys [51−53]. Nevertheless, almost all compounds lead to very less electrical conductivity, poor structural stability, and high electrode pulverization since large volume expansion or contraction of the materials in the process of charging or discharging cycles.

7.3 Applications of metal-organic frameworks as electrode material for lithium-ion batteries

Li et al., in 2006 [54], introduced extensive applications of MOFs as efficient electrode material for the lithium-ion batteries. They have synthesized a compound that is polycrystalline MOF-177 [Zn_4O (1,3,5-benzene tribenzoate)$_2$] in various architectures and introduced its suitable application in the devices of lithium storage. The authors found to explore shape-controlled design by changing reaction pathways such as variation of temperature, time, reactant concentration, and molar ratio of Zn^{2+} to H_3BTB. Yet, the experimental evidences show the very least working of MOF-177 for the usage of reversible lithium storage devices. The capacitance of MOF-177 in the next discharge process was only 105 mAh g^{-1}, down from 400 mAh g^{-1} noted in the first cycle [54]. From a morphological point of view, microcubes produced very high rate of charge/discharge capacities as compared to microcuboids. Since the synthesized MOF-177 microcubes are strewing in nature, the microcuboids are accumulated one on another. The disseminated structure allows the connection among the active material and electrolyte, the usage of productive microcubes is greater than that of microcuboids [54].

Though the MOF-177 is not efficient, the rate of storage competence of such high porous MOFs was expected because of the more reaction sites and architectural uses. In 2009 Combarieu et al. reported the first ever proof of reversible lithium storage using MOFs [MIL-53(Fe)] [55]. This Fe-MOF exhibited high electrochemical capability since the lithium ion (Li^+) was embedded into the lattice of Fe-MOF due to the oxidation of Fe^{2+} to Fe^{3+}. Nevertheless, very few lithium ions are embedded (0.6 Li^+ per Fe^{3+}) and very poor conductivity of MIL-53(Fe) reduces the capacity to 68 mAh g^{-1}. To avoid the abovementioned constraint, a redox arbitrator (1,4-benzoquinone) was accumulated in the MIL-53 (Fe) lattice, and it increases the electron transfer ($2e^-$ per molecule). In the process of discharge the quinone molecules were reduced to quinolate species, these are in-soluble in electrolyte, to retain the crystal structure. Nevertheless, the quinone molecules are more liable to dissipate with the loss of quinine molecules in view of charging process, the results of which decrease the capacity over five cycles from 95 to 68 mAh g^{-1}. Majority of MOFs are not stable under moist conditions because of loss of framework structure. But the harsh conditions of electrochemical environments demand extremely stable MOFs. Lin et al. changed the structure of MOFs by the addition of hydrophobic functionalities through postsynthetic modifications. Moreover the inner pores of the MOFs were functionalized via the chemical grafting of polar groups, these can able to connect through guest molecules. The final architecture was considered as bifunctionalized MOF possessing both hydrophobic and polar groups. The synthesized bifactionalized MOF employed the capacity of 190 mAh g^{-1} per 100 charging/discharging cycles. A Coulombic efficiency of near 100% was reached by possessing huge current density of 400 mAh g^{-1} per 200 cycles. Generally, in the processes of lithiation or delithiation processes, the transition metal involves in the altering mechanism, this results in the deterioration of the MOF. Moreover, the active material also experiences the deterioration or destruction when it intercalates into the structure. To overcome these drawbacks, the utilization of organic linkers with the rigid inorganic cluster can be devised to produce redox active properties possessing a high degree of flexibility.

7.4 Applications of high conductive metal-organic frameworks

The metallic compounds with the insertion of conductive MOFs found to have huge current densities and very good working performance. For instance, consider cobalt-based MOF has been indicated as very good electrode component for sodium ion batteries [56]. The two-dimensional MOF is consisting of hexa amino benzene (HAB) attached by Co(II) centers. Possessing the high degree of delocalization in this graphene-like network, Co-HAB has been produced conductivity of 1.57 S cm^{-1}. Furthermore, the transition capacity of the cobalt

centers and the aromatic compound is capable of standard capacities of 200 mAh g^{-1} per100 cycles at high rate of 4 A g^{-1}. The cobalt-HAB also indicated worthy of attention showing at high rates (up to 12 A g^{-1}) and the capacity to regain attention while it back to the high-moderate cycling rates. The productive high charge/discharge rates were also indicated by one more active MOF (Cu-CuPc, having conductivity 1.6×10^{-6} S cm^{-1}) possessing extensive capability to reach ~150 mAh g^{-1} at a rate of 5.2 A g^{-1} for lithium-ion batteries [57]. The abovementioned examples exhibit the efficient suitable synthesis approaches, MOF have the capability to bear astonishing cycling conditions.

7.5 Utilization of metal-organic frameworks as electric double-layer capacitors (supercapacitors)

The electric double-layer capacitors or supercapacitors performed at applied potential produce the ions at the interface of electrolyte and electrode. The capacitance of ELDCS produces the current in the form of static charges on the surface of electrode, unlike the conversion of chemical energy into electricity in the galvanic cells. Since, there are no issues from the kinetics of redox reactions, electric double-layer capacitors produced high energy efficiency, long life, huge power density, and quick charging and discharging. Usually the extensive capacitance produced on the surfaces of the high porous anode and cathode materials.

7.5.1 Applications of optimizing the surface area

The internal structure and extensive porosity of MOFs make these consummate for the developing charge storage capacity in small package. The substantial production control over MOF lattice form, morphology, size of the particle, and surface composition furnish distinctive methods for resisting pore limitations and developing connection with the active mass. A relative study of 23 nano-size lattice MOFs (nMOFs) provides the usage of MOF graphene electrodes for the double-layer capacitors [58]. The decreased particle sizes of nMOFs are consummate for designing the huge surface area of electrodes with momentary dissemination tracks. A device using nMOF-867 was given next to produce a specific capacitance of 726 F g^{-1}. The MOF was suggested to increase charge storage capacity by affording the active groups in the bipyridine linker to join with the separated ions. Likewise, supercapacitors that possess smaller UiO-66 (Universitetet i Oslo) particles produced higher charge storage capacity than those having largest particle size. For instance, the size of the particles range ~100 nm in diameter obtained capacitance of 1144 F g^{-1} at a scan rate of 5 mV s^{-1}, whereas the largest size of the particle 400 nm was a mere 207 F g^{-1}. The storage capabilities will improve dramatically by the favored crystalline facets particularly in MOFs having the pseudo-behavior. A laminated Ni-benzene dicarboxylate MOF with advantageous bare of (1 0 0)

facets were produced as a double-layer capacitor electrode [59]. The appliances checked were exhibited specific capacitance of 1127 F g^{-1} at a charge rate of 0.5 A g^{-1}, and over 90% of which were holding on to 3000 cycles. The huge concentration of vulnerable Ni atoms on the (1 0 0) facet was suggested to increase the action by incorporating the additional redox sites and also ionic conductivity. Likewise, this regularizes the structure of nickel MOF nanosize sheets with a controlled growth upon a surface of carbon produces a specific capacitance of 1962 F g^{-1} at a current density of 1 A g^{-1} [60]. Over 1200 cycles and 97% of the specific capacitance were retained. Moreover, driving the current to 32 A g^{-1} provides the 996 F g^{-1} of specific capacitance. The huge pore accessibility will be attained by the very controlled morphology of the electrode, which will increase the device performance. The combined examples of MOFs having the accurate crystallographic regulate the application of storage capacity of the MOFs.

7.6 Utilization of lithium−oxygen as separators

The advantages of the MOFs are separators to permit the usage of organic redox arbitrators. Redox arbitrators allow greater efficient oxygen reduction reaction (ORR) inside the cathode structure and reduce the passivation of the $Li-O_2$ electrode. But, those compounds react with the lithium anode and decline the resultant capacity and cyclicability. Due to this problem, a film of HKUST-1(Hong Kong University of Science and Technology) was grown on a Celgard separator to avoid the arbitrator from insertion to the Li anode, permitting the battery to maintain cell functioning for over 100 cycles [61].

7.7 Utilization of solid-state electrolytes

Generally, the cell consists of the electrolytes of flammable organic solvents, which are highly explosive in nature. To overcome the threat by replacing with solid-state electrolytes is of great interest. These materials should possess the great conductivity ($>10^{-4}$ S cm^{-1} at 25°C) and consummate Li^+ transport number. Moreover, these electrolytes should behave as insulator to avoid the shortening of the battery and should be strong enough mechanically and chemically with the accomplishing temperature and electrochemical property. Solid-state inorganic materials are very interesting materials, since they possess huge ionic mobilities ($\sim 10^{-2}$ S cm^{-1} at RT) and which can function under the conditions of thermal and electrochemical window. Nevertheless, they are more brittle and chemically unstable within the conditions that restrict the usage. Moreover, due to the dearth of constitutional and atomistical control from top-down synthesis, avoid the sensible compounds produced. MOFs also can extensively allow ion conductivity from soft chemical interactions, solvent insertion, and open channels. Furthermore, these are more accessible with carbon-based electrodes than solid inorganic materials.

MOFs have been proposed for SEs formerly but have been rarely utilized in full device testing. Even the gel active masses are also favorable components possessing high ionic mobility and quite ease of synthesis. Nevertheless, they are very poor and chemically inert under the high potential; hence, advanced storage devices are currently required. Gel polymers normally possess ether, amine, and ionic groups that make possible in solvating ions for charge conduction. Those functional groups have already been inserted into MOFs intrinsically or via postsynthetic modifications.

7.8 Applications of electrode–electrolyte alliances

Usually the MOFs are also employed to steady the SE alliance. Generally, the native SEI is produced upon the plane of the electrode by the plating of the diffusion of electrolyte material in a battery. The SEI usually possesses the passivation and avoids the humiliation; however, it will damage periodically the SEI. An introduction of MOFs of SEI serves the purpose of those problems by avoiding the decaying of electrolyte, encouraging ion transference, and obliging volumetric changes. For instance, there are various scientific results of usage of MOF coatings on silicon anodes in lithium-ion batteries. The MOF coating enhances the periodicity by the contribution a safeguarding cushion for the volume variation as well as by lowering the cell resistances and improves ion conduction in the electrolyte-filled MOFs. MOF separators on top of the Li metals have also been indicated to encourage even Li deposition to avoid dendrite formation. Furthermore, the usage of MOFs as protective layers should possess ionic conductivity, strength and compatibility to synthesis, and deposition process on the surface of electrode. The multifaceted property of MOFs permits researchers to follow variable approaches, in situ and ex situ characterization techniques to study electrolyte and SEIs.

7.9 Fuel cell applications

A typical fuel cell is a class of electrochemical cell that converts chemical energy of a fuel into electricity, by the pursuing supply of fuel, such as hydrogen, natural gas, or methanol, and oxidant such as oxygen, air, or hydrogen peroxide. Every fuel cell contains an anode, a cathode, and conductive electrolyte, which permit ions to move back and forth in the fuel cell, which accompany the basic functional exercise inside the membrane of the polymeric fuel cell (PEMFC). Generally, hydrogen gas (H_2) as a fuel is provided at anodic compartment where the oxidation occurs and generates protons and electrons. The protons move through the electrolyte and enter the cathodic compartment. During this process of movement of electrons through the circuit produces the electricity that can be utilized for the external purpose. Near the cathode, by the assistance of catalyst, oxygen (O_2)

combines with protons and electrons producing water and releasing some thermal energy. MOFs, as described earlier, are customized to have a high surface area and porosity. With the adjustment of its structure through best handpicked metallic clusters and multifunctional groups, the desired product of MOFs could be outlined with precious metals (e.g., Co, Fe, and Cu), nitrogen, and carbon sites, which would be beneficial for producing excellent electrochemical catalysts. In the discipline of fuel cells, MOFs procured nanosize materials working as high-performance electrochemical catalyst have been extensively reported.

7.10 Electrocatalytic applications

MOFs consisting of metal clusters can be constituted of electrochemically active metals. By the logical designing of the composition of frameworks and considering the advantages of the natural properties of MOFs, it is very easy to synthesize the chemically active functional frameworks containing the catalytic properties. For instance, the usage of MOFs as an electrocatalysts for ORR was introduced by Lanqun Mao's group. They have synthesized different Cu-based MOFs. [Cu(II) benzene-1,3,5-tricarboxylate] and [Cu(II)-2,2′-bipyridinebenzene-1,3,5-tricarboxylate]. The second compound of [Copper(II)-2,2′-bipyridinebenzene-1,3,5-tricarboxylate] MOF was introduced to possess a very good and steady electrocatalytic activity toward four-electron reduction of oxygen. Due to the outstanding catalytic property of Cu-MOFs, graphene and Cu-MOF composites were reported to overcome the least conducting behavior of copper-MOFs and later it enhances the incitation property and stability. In 2013 Maryam Jahan and coworkers introduced a graphene oxide (GO)-incorporated Cu-MOF composite (GO−Cu-MOFs), which have been possessing good incitation property for ORR, oxygen evolution reaction, and hydrogen evolution reaction with the extensive three functional catalytic incitation properties; graphene oxide copper MOF composites possess lower overpotentials and higher currents for all three electrocatalytic reactions and showed good stability in acid media. Generally, a significant enhancement of cathodic peak at 0.29 V (vs reversible hydrogen electrode) in O_2-saturated H_2SO_4 for (GO 8 wt.%)-copper MOFs, which is higher than pure Cu-MOFs at 0.16 V (vs reversible hydrogen electrode), it is recommended that the inclusion of graphene oxide into the MOFs develops the electrocatalytic property. The power density of frameworks 110.5 mW cm^{-2} was achieved for (GO 8 wt.%)-copper MOFs, which is 76% that of Pt/C. As the excellent electrocatalytic behavior along with more economic and simplistic synthesis makes GO−Cu-MOFs hybrids, if it is considered a trust worthy substitute to platinum catalysts in fuel cell applications. Excluding the Cu-based MOFs, graphene−Fe-MOFs were produced and considered as ORR catalyst by KPL (Kian Ping Loh) group in 2012. The reduced graphenes that are serviceable upon double sides of the surface with pyridine ligands, these functional reduced graphene as swagger to link metalloporphyrin (FeP) junction to form

the reduced graphene MOF hybrids. It was suggested that the weight percentage of serviceable reduced graphene add-on to the framework plays a very important role in the structure and electrochemical property of the (r-GO−FeP) MOFs, since the functionalized r-GO can affect the crystallization process of MOFs. If certain amount of 50 wt.% r-GO is added, (r-GO-50 wt.%-FeP) nMOFs show the good oxygen reduced reaction performance with the onset potential of −0.23 V (vs Ag/AgCl). Since reduced graphene oxide behaves collaborated with FeP catalysts to provide simplistic four-electron oxygen reduced reaction pathway and this kind of MOFs composite also contained the reduced methanol crossover effects relative to platinum catalyst.

7.11 Conclusion

MOFs have potential applications in different areas such as energy conversion devices, high surface electrode materials, supercapacitors, conducting separators, electrodes, and electrolytes of batteries. In this chapter, we have discussed the high surface area of the MOFs used to design and synthesis of nanostructured mesoporous metal oxides, composite materials for the applications in supercapacitors, batteries, and fuel cells. The internal structure of the MOFs and porosity provides the extensive capability to store the charges in capacitors. Also, we have highlighted the future prospects and trends for the different applications of MOFs.

References

[1] Rowsell JLC, Yaghi OM. Metal−organic frameworks: a new class of porous materials. Microporous Mesoporous Mater 2004;73:3−14.
[2] Zhou HC, Long JR, Yaghi OM. Introduction to metal-organic frameworks. Chem Rev 2012;112(2):673−4.
[3] O'Keeffe M, Yaghi OM. Deconstructing the crystal structures of metal−organic frameworks and related materials into their underlying nets. Chem Rev 2012;112:675−702.
[4] Lu W, Wei Z, Gu ZY, Liu TF, Park J, Park J, et al. Tuning the structure and function of metal-organic frameworks via linker design. Chem Soc Rev 2014;43(16):5561−93.
[5] Maurin G, Serre C, Cooper A, Ferey G. The new age of MOFs and of their porous-related solids. Chem Soc Rev 2017;46:3104−7.
[6] Ferey G. Hybrid porous solids: past, present, future. Chem Soc Rev 2008;37:191−214.
[7] Furukawa H, Cordova KE, O'Keeffe M, Yaghi OM. The chemistry and applications of metal-organic frameworks. Science 2013;341(6149):1230444.
[8] Tranche Montagne DJ, Mendoza-Cortes JL, O'Keeffe M, Yaghi OM. Secondary building units, nets and bonding in the chemistry of metal-organic frameworks. Chem Soc Rev 2009;38:1257−83.
[9] Chen L, Luque R, Li Y. Controllable design of tunable nanostructures inside metal−organic frameworks. Chem Soc Rev 2017;46:4614−30.
[10] Stock N, Biswas S. Synthesis of metal-organic frameworks (MOFs): routes to various MOF topologies, morphologies, and composites. Chem Rev 2012;112(2):933−69.

[11] Almeida Paz FA, Klinowski J, Vilela SMF, Tome JPC, Cavaleiro JAS, Rocha J. Ligand design for functional metal–organic frame works. Chem Soc Rev 2012;41:1088–110.
[12] Liang W, D'Alessandro DM. Microwave-assisted solvothermal synthesis of zirconium oxide-based metal-organic frameworks. Chem Commun 2013;49(35):3706–8.
[13] Zhang Z, Zhao Y, Gong Q, Li Z, Li J. MOFs for CO_2 capture and separation from flue gas mixtures: the effect of multifunctional sites on their adsorption capacity and selectivity. Chem Commun 2013;49(7):653–61.
[14] Paszkowicz W. Genetic algorithms, a nature-inspired tool: a survey of applications in materials science and related fields: part II. Mater Manuf Process 2013;28(7):708–25.
[15] Horike S, Kamitsubo Y, Inukai M, Fukushima T, Umeyama D, Itakura T, et al. Post synthesis modification of a porous coordination polymer by LiCl to enhance H^+ transport. J Am Chem Soc 2013;135(12):4612–15.
[16] Gao X, Dong Y, Li S, Zhou J, Wang L, Wang B. MOFs and COFs for batteries and supercapacitors. Electrochem Energy Rev 2020;3:81–126.
[17] Park SS, Tulchinsky Y, Dincă M. Single-ion Li^+, Na^+, and Mg^{2+} solid electrolytes supported by a mesoporous anionic cu-azolate metal-organic framework. J Am Chem Soc 2017;139:13260–3.
[18] Gerbaldi C, Nair JR, Kulandainathan MA, Kumar RS, Ferrara C, Mustarelli P, et al. Innovative high performing metal organic framework (MOF)-laden nanocomposite polymer electrolytes for all-solid-state lithium batteries. J Mater Chem A 2014;2:9948–54.
[19] Goodenough JB, Park KS. The Li-ion rechargeable battery: a perspective. J Am Chem Soc 2013;135:1167–76.
[20] Padhi A, Nanjundaswamy K, Goodenough JB. $LiFePO_4$: a novel cathode material for rechargeable batteries. Electrochem Soc Meet Abstr 1996;1:73.
[21] Armand M, Grugeon S, Vezin H, Laruelle S, Ribière P, Poizot P, et al. Conjugated dicarboxylate anodes for Li-ion batteries. Nat Mater 2009;8(2):120–5.
[22] Tarascon JM, Armand M. Issues and challenges facing rechargeable lithium batteries. Mater Sustain Energy 2010;171–9.
[23] An SJ, Li J, Daniel C, Mohanty D, Nagpure S, Wood III DL. The state of understanding of the lithium-ion battery graphite solid electrolyte interphase (SEI) and its relationship to formation cycling. Carbon 2016;105:52–76.
[24] Verma P, Maire P, Novák P. A review of the features and analyses of the solid electrolyte interphase in Li-ion batteries. Electrochim Acta 2010;22(55):6332–41.
[25] Wang A, Kadam S, Li H, Shi S, Qi Y. Review on modelling of the anode solid electrolyte interphase (SEI) for lithium-ion batteries. npj Comput Mater 2018;4:15.
[26] Whittingham MS. Lithium batteries and cathode materials. Chem Rev 2004;104:4271–302.
[27] Levy SC, Bro P. Lithium/thionyl chloride batteries. In: Battery hazards and accident prevention. New York: Plenum Press; 1994.
[28] Mallela VS, Ilankumaran V, Rao NS. Trends in cardiac pacemaker batteries. Indian Pacing Electrophysiol J 2004;4(4):201–12.
[29] Goodenough JB, Mizuchima K. Electrochemical cell with new fast ion conductors. Google patents. 1981.
[30] Basu S. Ambient temperature rechargeable battery. Google patents. 1983.
[31] Thackeray M, David W, Bruce P, Goodenough J. Lithium insertion into manganese spinels. Mater Res Bull 1983;18:461–72.
[32] Manthiram A, Goodenough J. Lithium insertion into $Fe_2(SO_4)_3$ frameworks. J Power Sources 1989;26:403–8.
[33] Crabtree G, Kocs E, Trahey L. The energy-storage frontier: lithium-ion batteries and beyond. MRS Bull 2015;40(12):1067–78.

[34] Chung SY, Bloking JT, Chiang YM. Electronically conductive phospho-olivines as lithium storage electrodes. Mater Sustain Energy 2010;205–10.
[35] In the search of perfect battery. <https://www.economist.com/technology-quarterly/2008/03/08/in-search-of-the-perfect-battery>, 2008.
[36] Chan CK, Peng H, Liu G, McIlwrath K, Zhang XF, Huggins RA, et al. High- performance lithium battery anodes using silicon nanowires. Mater Sustain Energy 2011;187–91.
[37] Chakrapani V, Rusli F, Filler MA, Kohl PA. Silicon nanowire anode: improved battery life with capacity-limited cycling. J Power Sources 2012;205:433–8.
[38] Xie Z, He Z, Feng X, Xu W, Cui XJ, Zhang C, et al. Hierarchical sandwich-like structure of ultrafine N-rich porous carbon nanospheres grown on graphene sheets as superior lithium-ion battery anodes. ACS Appl Mater Interfaces 2016;8:10324–33.
[39] Ju Z, Guo C, Qian Y, Tang B, Xiong S. Direct large-scale synthesis of 3D hierarchical mesoporous NiO microspheres as high-performance anode materials for lithium ion batteries. Nanoscale 2014;6:3268–73.
[40] Meduri P, Clark E, Kim JH, Dayalan E, Sumanasekera GU, Sunkara MK. MoO_{3-x} nanowire arrays as stable and high-capacity anodes for lithium ion batteries. Nano Lett 2012;12:1784–8.
[41] Su Q, Xie D, Zhang J, Du G, Xu B. In situ transmission electron microscopy observation of the conversion mechanism of Fe_2O_3/graphene anode during lithiation-de-lithiation processes. ACS Nano 2013;7(10):9115–21.
[42] Fang W, Zhao H, Xie Y, Fang J, Xu J, Chen Z. Facile hydrothermal synthesis of VS_2/graphene nanocomposites with superior high-rate capability as lithium-ion battery cathodes. ACS Appl Mater Interfaces 2015;7:13044–52.
[43] Sennu P, Kim HS, An JY, Aravindan V, Lee VS. Synthesis of 2D/2D structured mesoporous Co_3O_4 nanosheet/N-doped reduced graphene oxide composites as a highly stable negative electrode for lithium. Chem—Asian J 2015;10:1776–83.
[44] Xu W, Zhao K, Niu C, Zhang L, Cai Z, Han C, et al. Heterogeneous branched core–shell SnO_2–PANI nanorod arrays with mechanical integrity and three dimensional electron transport for lithium batteries. Nano Energy 2014;8:196–204.
[45] Zhang L, Zhao K, Xu W, Dong Y, Xia R, Liu F, et al. Integrated SnO_2 nanorod array with poly pyrrole coverage for high-rate and long-life lithium batteries. PCCP 2015;7:7619–23.
[46] Liu J, Zhang Q, Yang J, Ma H, Tade MO, Wang S, et al. Facile synthesis of carbon-doped mesoporous anatase TiO_2 for the enhanced visible-light driven photocatalysis. Chem Commun 2014;50:13971–4.
[47] Luo B, Fang Y, Wang B, Zhou J, Song H, Zhi L. Two-dimensional graphene SnS_2 hybrids with superior rate capability for lithium ion storage. Energy Environ Sci 2012;5:5226–30.
[48] Zheng X, Song X, Wang X, Zhang Z, Sun Z, Guo Y. Nickel–copper bimetal organic framework nanosheets as a highly efficient catalyst for oxygen evolution reaction in alkaline media. New J Chem 2018;42:8346–50.
[49] Ding Y, Bai W, Sun J, Wu Y, Memon MA, Wang C, et al. Cellulose tailored anatase TiO_2 nano spindles in three-dimensional graphene composites for high-performance supercapacitors. ACS Appl Mater Interfaces 2016;8:12165–75.
[50] Cao X, Shi Y, Shi W, Rui X, Yan Q, Kong J, et al. Preparation of MoS_2-coated three-dimensional graphene networks for high-performance anode material in lithium-ion batteries. Small 2013;9:3433–8.
[51] Zhu Y, Han X, Xu Y, Liu Y, Zheng S, Xu K, et al. Electrospun Sb/C fibers for a stable and fast sodium-ion battery anode. ACS Nano 2013;7:6378–86.

[52] Xu Y, Liu Q, Zhu Y, Liu Y, Langrock A, Zachariah AR, et al. Uniform nano-Sn/C composite anodes for lithium ion batteries. Nano Lett 2013;13:470–4.
[53] Hong YJ, Son MY, Kang YC. One-pot facile synthesis of double-shelled SnO_2 yolk-shell-structured powders by continuous process as anode materials for Li-ion batteries. Adv Mater 2013;25:2279–83.
[54] Li X, Cheng F, Zhang S, Chen J. Metal organic frameworks composites for lithium battery applications. Power J Sources 2006;160:542–7.
[55] de Combarieu G, Morcrette G, Millange F, Guillou N, Cabana J, et al. Enhanced electrochemical performance of Li–Co-BTC ternary metal–organic frameworks as cathode materials for lithium-ion batteries. Chem Mater 2009;21:1602–11.
[56] Park J, et al. Stabilization of hexaaminobenzene in a 2D conductive metal- organic framework for high power sodium storage. J Am Chem Soc 2018;140:10315–23.
[57] Nagatomi H, Yanai N, Yamada T, Shiraishi K, Kimizuka N. Synthesis and electric properties of a two-dimensional metal-organic framework based on phthalocyanine. Chem A Eur J 2018;24:1806–10.
[58] Choi KM, et al. Supercapacitors of nanocrystalline metal-organic frameworks. ACS Nano 2014;08:7451–7.
[59] Yang J, Xiong P, Zheng C, Qiu H, Wei M. Metal-organic frameworks: a new promising class of materials for a high-performance supercapacitor electrode. J Mater Chem A 2014;2:16640–4.
[60] Deng T, et al. Vertically co-oriented two-dimensional metal-organic frameworks for packaging enhanced supercapacitive performance. Commun Chem 2018;1:6.
[61] Qiao Y, et al. MOF-based separator in an Li-O_2 battery: an effective strategy to restrain the shuttling of dual redox mediators. ACS Energy Lett 2018;3:463–8.

This page intentionally left blank

Chapter 8

Metal-organic framework–based materials and renewable energy

Prasun Banerjee[1,2], Adolfo Franco, Jr[2], K. Chandra Babu Naidu[1], Anish Khan[4,5], Abdullah M. Asiri[4,5] and Srinivasan Natarajan[3]

[1]Department of Physics, GITAM (Deemed to be University), Bangalore, India, [2]Instituto de Fisica, Universidade Federal de Goias, Goiania, Brazil, [3]Solid State and Structural Chemistry Unit, Indian Institute of Science, Bangalore, India, [4]Chemistry Department, Faculty of Science, King Abdulaziz University, Jeddah, Saudi Arabia, [5]Center of Excellence for Advanced Materials Research, King Abdulaziz University, Jeddah, Saudi Arabia

8.1 Introduction

The overall reserve of the fossil fuel is depleting very quickly and also causing extensive damage to our environment due to its extensive use [1,2]. Hence, renewable technologies that use a clean, green, and sustainable source of energy are undoubtedly the only alternative to these problems [3–6]. Hence, processes such as electrocatalysis and photocatalysis, which can convert the energy from the renewable sources, are high in demand [7–11]. But there exist a lot of scopes to improve the present-day photocatalytic and electrocatalytic technologies. For example, the poor stability and low porosity in generally developed in photocatalytic materials because of the use of the complex synthesis techniques [12]. These directly influence the light absorption power of the photocatalysis material, which results in very poor efficiency of the energy conversion power [13,14]. On the other hand, the high cost, short lifetime, and slow kinetics make the electrocatalyst material less popular for the extensive applications [15]. In addition, if we look at the battery technologies, we can observe that reduced stability of the cycling, low capability rate, and small energy density is a big challenge because of the poor hydrogen evaluation reaction (HER), oxygen reduction reaction (ORR), and oxygen evolution reaction (OER) [16–24]. Hence, to solve these issues advanced materials are highly desirable at this stage. Multifunctional properties along with a high surface area with porous structure materials are highly required to overcome these problems. All these

Metal-Organic Frameworks for Chemical Reactions. DOI: https://doi.org/10.1016/B978-0-12-822099-3.00008-3

properties along with adjustable node of metal and linkers with organic nature with ordered structure can be found into metal-organic framework–based materials (MOFMs) [25–28]. Advanced nanoparticles (NPs) of MOFMs can substantially offer new metal nodes and their superior designs with new chemical and physical properties can obliterate all issues of the energy conversions using renewable sources [29,30]. Not only that the NPs–MOFMs can further be mixed with molecules and graphene to generate composite MOFMs [31]. Hence, broadly we can classify the MOFMs into 0D, 1D, 2D, and 3D classes according to their nanoarchitectures along with composite MOFMs.

Hence, in this book chapter we tried to focus on the new and advanced 0D-NPs-MOFMs, 1D-NPs-MOFMs, 2D-NPs-MOFMs, 3D-NPs-MOFMs, and composite MOFMs available for energy conversions using renewable sources.

8.2 0D-metal-organic framework–based materials-nanoparticles

Downsizing the particle sizes of MOFMs to nano-range using a top-down approach is the first alternative to create 0D nanoarchitecture. Broadly we can classify it into two types: multishell 0D-MOFMs-NPs and hollow 0D-MOFMs-NPs.

8.2.1 Multishell 0D-metal-organic framework–based materials-nanoparticles

Multishell MOFMs of Sb_2S_3 shown in Fig. 8.1 are the examples of such a nanoarchitecture that can be obtained from zeolitic imidazolate framework-8 (ZIF-8) [32]. In this case the energy density and the stability can be

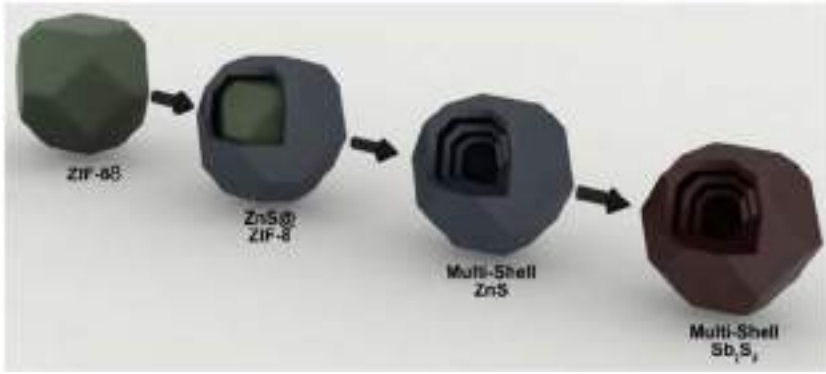

FIGURE 8.1 Schematic illustration route of synthesis to obtain multishell Sb_2S_3 from ZIF-8. *Reprint with the permission from Xie F, Zhang L, Gu Q, Chao D, Jaroniec M, Qiao SZ. Multishell hollow structured Sb_2S_3 for sodium-ion batteries with enhanced energy density. Nano Energy 2019;60:591–9. ©2019, Elsevier.*

enhanced in many folds with respect to the single-wall structure of the Sb_2S_3 networks. It is believed that the hollow structure of the 0D nanoarchitecture is responsible for the enhancement of the electrochemical properties with high reversible capacity. Such a system is indeed a good replacement as an anode material for the energy conversion system from renewable sources of energy.

8.2.2 Hollow 0D-metal-organic framework–based materials-nanoparticles

Hollow mesoporous nanospheres of Co_9S_8 shown in Fig. 8.2 are the examples of another 0D nanoarchitecture with MOFMs-NPs [33]. This hollow structure when sintered at 650°C temperature exhibits performance of 1122 mAh g^{-1} even after 100 cycles at 200 mA g^{-1}. Even a further coating of C can further enhance the performance rate with a recovery of the capacity after cycling. This feature undoubtedly makes cobalt sulfide nanospheres of MOFMs-NPs as another suitable choice as anode material for the energy conversion system with using renewable source of energy.

8.3 1D-metal-organic framework–based materials-nanoparticles

Alternatively, nanoarchitecture with the use of 1D structure such as nanorods, nanotubes, and nanowire MOFMs-NPs can be an effective way to enhance energy conversion capability. The added advantages of the 1D structures such as short-distance diffusion of ions, fast transport of electrons along the axis of the 1D structures, easy relaxation strain capabilities, and excellent diffusion between the porous structure and high surface area make it a good choice in addition to the 0D-MOFMs-NPs. Not only that the 1D structures are the building blocks for the design of the 3D-MOFMs-NPs.

8.3.1 Nanotube 1D-metal-organic framework–based materials-nanoparticles

Single crystal long nanotube of 1D-MOFMs-NPs shown in Fig. 8.3 can show a better ORR activity. These 1D structures are beneficial to convert it to 3D structures with nanotubes as a branch, nanofiber as trunks with immobilized Co ions in the system. The observed power density can move up to 220 mW cm^{-2} although the time of use is of 133 hours with 400 cycles with a constant potential of 1.46 V. This makes it a superior candidate for wide range of electrocatalyst applications for the conversion of energy from a renewable source of energies.

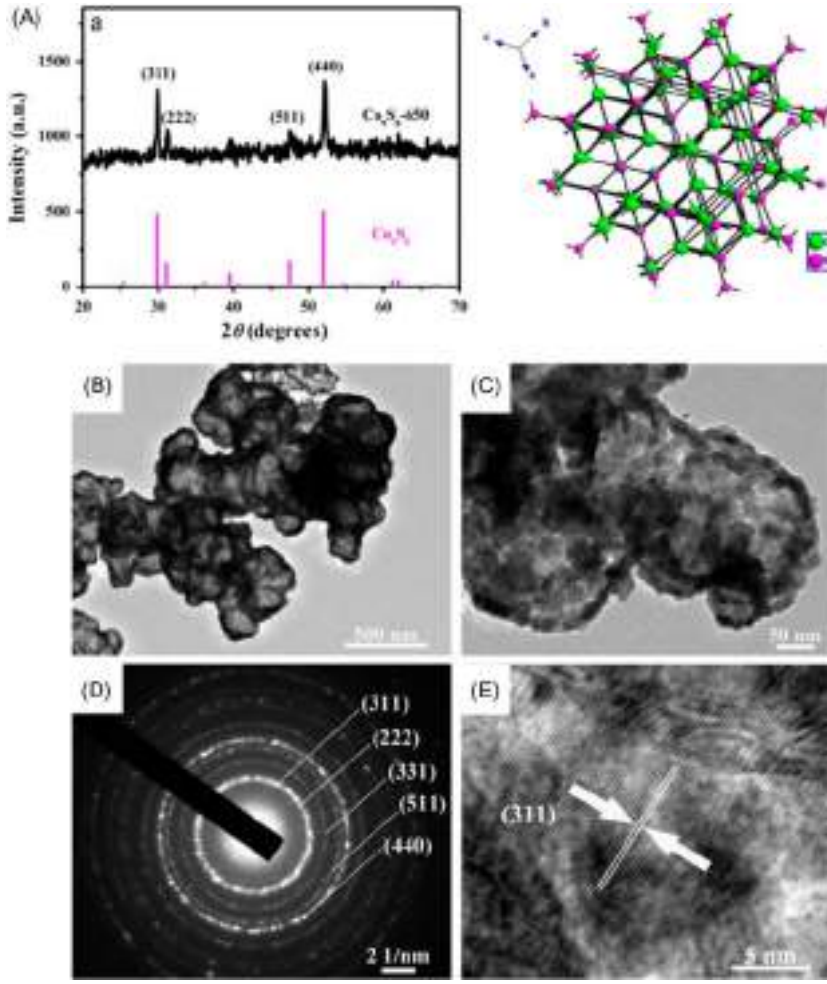

FIGURE 8.2 (A) XRD and crystal structure, (B–C) TEM, (D) SAED, and (E) HRTEM images of the Co_9S_8 mesoporous nanospheres of 0D-MOFMs-NPs. *MOFMs*, Metal-organic framework–based materials; *NPs*, nanoparticles. XRD, X-Ray Diffraction, TEM, transmission electron microscopy, SAED, selected area electron diffraction, HRTEM, high-resolution transmission electron microscopy. *Reprint with the permission from Zhou Y, Yan D, Xu H, Feng J, Jiang X, Yue J, et al. Hollow nanospheres of mesoporous Co_9S_8 as a high-capacity and long-life anode for advanced lithium ion batteries. Nano Energy 2015;12:528–37. ©2015, Elsevier.*

8.3.2 Nanorod 1D-metal-organic framework–based materials-nanoparticles

The MOFMs can further be embedded with semiconductor structures for the application of the sensor applications. The 1D nanorod MOFMs with the combination of the ZnO semiconductor, ZIF-8 MOFMs are shown in Fig. 8.4 [35].

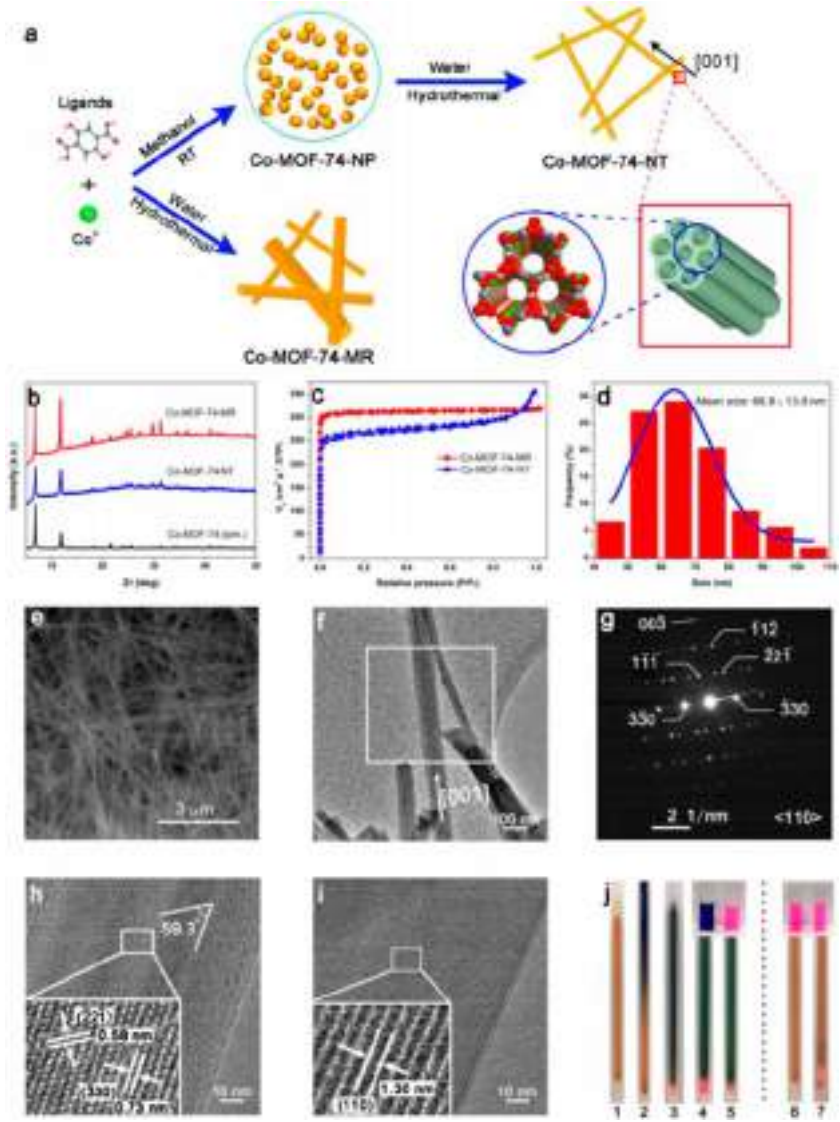

FIGURE 8.3 (A) Synthesis, (B) XRD, (C) N_2 absorption isotherms, (D) histogram of distribution of the diameter (E) SEM, (F) TEM, (G) SAED, (H–I) HRTEM, and (J) photograph images of the Co-MOFMs-NT. *MOFMs*, Metal-organic framework–based materials. XRD, X-ray diffraction, SEM, scanning electron microscope, TEM, transmission electron microscopy, SAED, selected area electron diffraction, HRTEM, high-resolution transmission electron microscopy, CO, cobalt, NT, nano tubes. *Reprint with the permission from Zou L, Hou CC, Liu Z, Pang H, Xu Q. Superlong single-crystal metal–organic framework nanotubes. J Am Chem Soc. 2018;140 (45):15393–401 [34]. ©2018, ACS.*

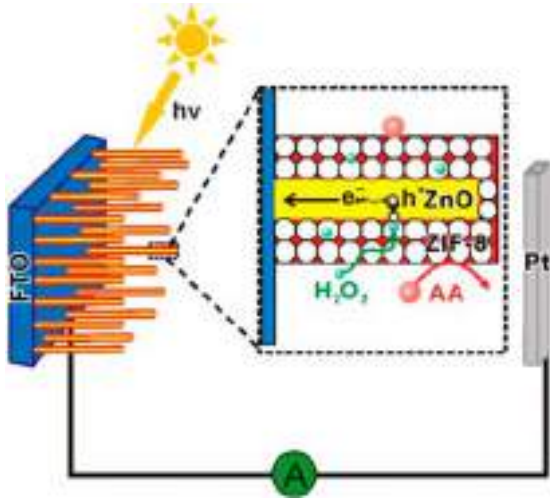

FIGURE 8.4 Schematic illustration of nanorod 1D-MOFMs-NPs for sensor applications. *MOFMs*, Metal-organic framework–based materials; *NPs*, nanoparticles. *Reprint with the permission from Zhan WW, Kuang Q, Zhou JZ, Kong XJ, Xie ZX, Zheng LS. Semiconductor@metal–organic framework core–shell heterostructures: a case of ZnO@ZIF-8 nanorods with selective photoelectrochemical response. J Am Chem Soc. 2013;135(5):1926–33. ©2013, ACS.*

The combination of ZnO with ZIF-8 enhances the photocurrent in many folds. In these cases the porous structure of ZIF-8 acts as a catalyst to disintegrate the hydrogen peroxide into hydrogen and oxygen by the acceptance of the holes by the zinc oxide semiconductor. In the process the electrons generated to get an axial direction due to the nanorod architecture enhancing the photocurrent.

8.3.3 Nanowire 1D-metal-organic framework–based materials-nanoparticles

Carbonization of the MOFMs in copper foil can create a nanowire 1D-MOFMs-NPs with Co_3O_4C. Fig. 8.5 shows that the OER activity in this 1D-MOFMs-NPs with nanowire activity is far superior to any known electrocatalyst with cobalt as the material [36]. The large surface area, porous structure, the stability of the structure, and high transport of charges may be responsible for the observable effect of the nanowire 1D-MOFMs-NPs on its OER activity.

8.4 2D-metal-organic framework–based materials-nanoparticles

The other way to improve the charge transport by using 2D structure as it is having an excessively low thickness. For example, cobalt dithiolene known to

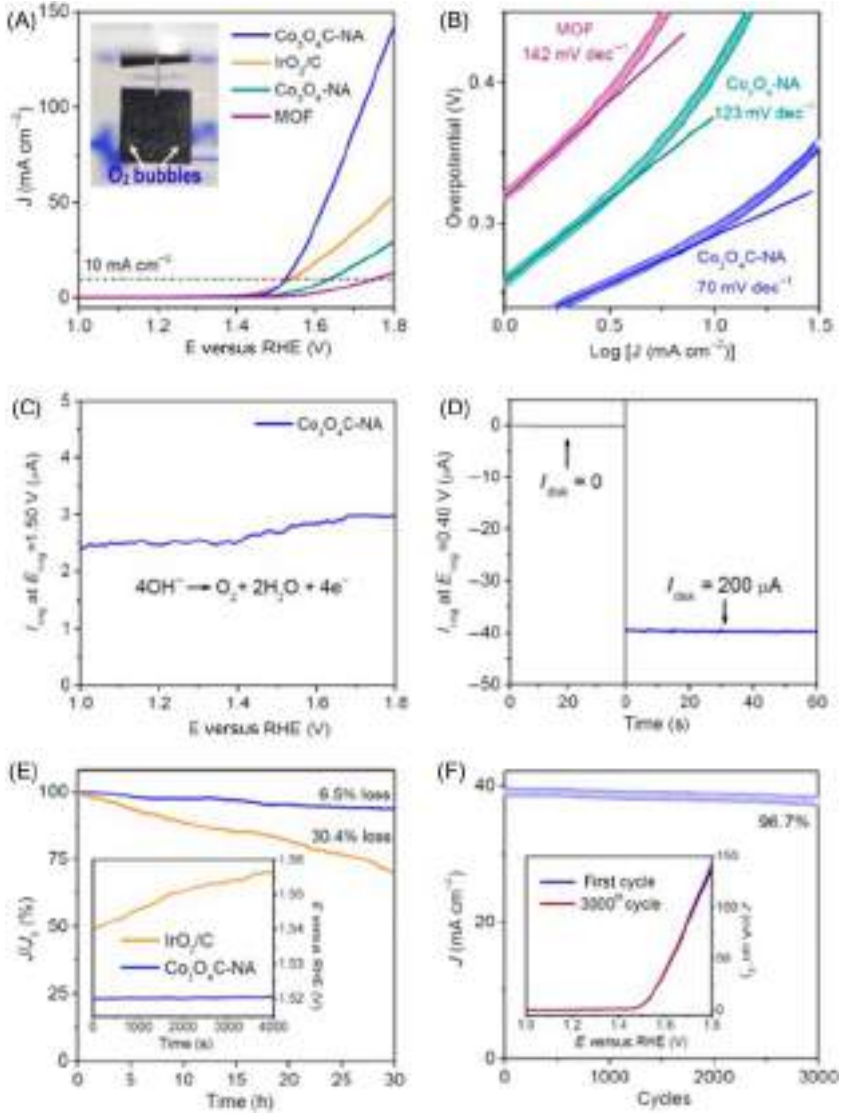

FIGURE 8.5 (A) Polarization, (B) Tafel, (C) ring current in oxygen, (D) ring current in nitrogen, (E) chronoamperometric and (F) current density of the Co-MOFMs-NPs. MOFMs, Metal-organic framework–based materials. *CO*, Cobalt, *NPs*, nanoparticles, *HRTEM*, high-resolution transmission electron microscopy, *SAED*, Selected area electron diffraction. *Reprint with the permission from Ma TY, Dai S, Jaroniec M, Qiao SZ. Metal–organic framework derived hybrid Co3O4-carbon porous nanowire arrays as reversible oxygen evolution electrodes. J Am Chem Soc. 2014;136(39):13925–31. ©2014, ACS.*

be a cathode material for the generation of H_2 from H_2O can be integrated with MOFMs to enhance its performances as reported [37]. In general, we can classify it into two types: nanosheet 2D-MOFMs-NPs and holey 2D-MOFMs-NPs.

8.4.1 Nanosheet 2D-metal-organic framework–based materials-nanoparticles

2D-MOFMs-NPs with nanosheet architecture can be synthesized from ZIF-67 into Co_3O_4 thin sheets shown in Fig. 8.6 [38]. Here also it can be observed that the OER activity enhances due to the presence of active cobalt ions, porous nanosheet structure with large surface area, and presence of oxygen defects. Hence, it presents a better electrochemical application of such nanosheet 2D-MOFMs-NPs.

8.4.2 Holey 2D-metal-organic framework–based materials-nanoparticles

2D-MOFMs-NPs with holey architecture can be derived from cobalt-based MOFMs into h-Co_4S_3 [39]. It can outperform any other cobalt sulfides in terms of the high capacity, retention, and stability of the cycles due to the presence of large no. of holes in it. These properties made these holey 2D-MOFMs-NPs for the direct application in the energy conversion devices ranging from batteries to the supercapacitors.

8.5 3D-metal-organic framework–based materials-nanoparticles

Stacking issues as well as the aggregation in 0D-MOFMs-NPs, 1D-MOFMs-NPs, and 2D-MOFMs-NPs can result in accessibility as well as permeability issue along with the electrolyte. Hence, a 3D-MOFMs-NPs structure is more promising for energy conservation from renewable sources. This skeleton of 3D structure can easily be built from the 0D-MOFMs-NPs, 1D-MOFMs-NPs, and 2D-MOFMs-NPs as building blocks. It always enhances the durability, stability, efficiency, and kinematics in this kind of application. We can broadly classify it into three types: array 3D-MOFMs-NPs, hierarchical 3D-MOFMs-NPs, and superstructure 3D-MOFMs-NPs.

8.5.1 Array 3D-metal-organic framework–based materials-nanoparticles

The array nanoarchitecture can be synthesized into 3D-MOFMs-NPs. Initially, in an aqueous solution, the substrate and the metal salts need to mix homogeneously. Thereafter, an organic ligand needs to place into the structure. Finally, with the use of crystallization dissolution techniques 3D

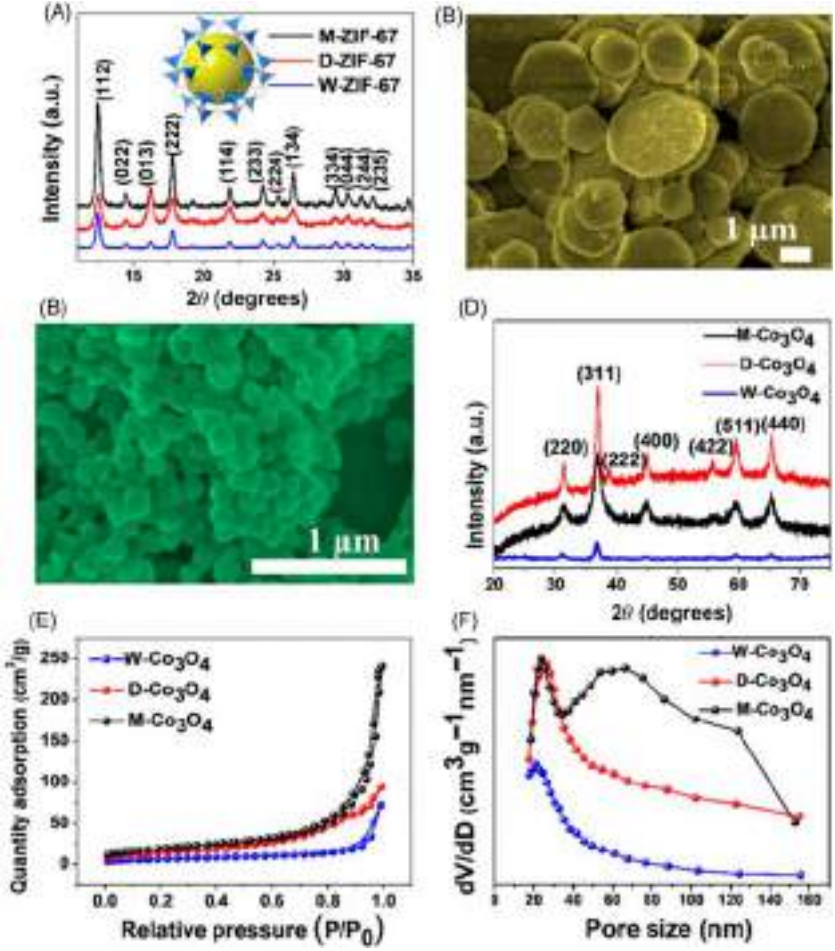

FIGURE 8.6 (A) XRD for ZIF-67, (B and C) SEM, (D) XRD for Co_3O_4, (E) absorption isotherm, and (F) pore size distribution for Co_3O_4 nosheets MOFMs-NPs. *MOFMs*, Metal-organic framework–based materials; *NPs*, nanoparticles; *SEM*, scanning electron microscope; *XRD*, x-ray diffraction. . *Reprint with the permission from Wei G, Zhou Z, Zhao X, Zhang W, An C. Ultrathin metal–organic framework nanosheet-derived ultrathin Co_3O_4 nanomeshes with robust oxygen-evolving performance and asymmetric supercapacitors. ACS Appl Mater Interfaces. 2018;10(28):23721–30. ©2018, ACS.*

array structure of MOFMs-NPs grows on the surface of the substrate [40]. This way the synthesis of an array Ni–Fe 3D-MOFMs-NPs can present a better performance of OER activity with a long duration of operation as an electrocatalyst up to 333 minutes. The 3D array structure of MOFMs-NPs can further be extended to HER activity for the splitting of H_2 from renewable sources of energy like H_2O.

8.5.2 Hierarchical 3D-metal-organic framework–based materials-nanoparticles

Bimetallic 3D-MOFMs-NPs synthesized with a hierarchical approach with porous structure have been shown in Fig. 8.7 [41]. This composite hierarchical 3D-MOFMs-NPs structure presents better performance as an anode material for the energy conversion systems with capacity 2.061 Ah g^{-1} even after the use of 300 cycles due to the composite nature of the two metallic ions. The excellent cycle process in this structure is also linked to the porous structure with stable hierarchical networks, which creates a pseudo-nature to its capacitance.

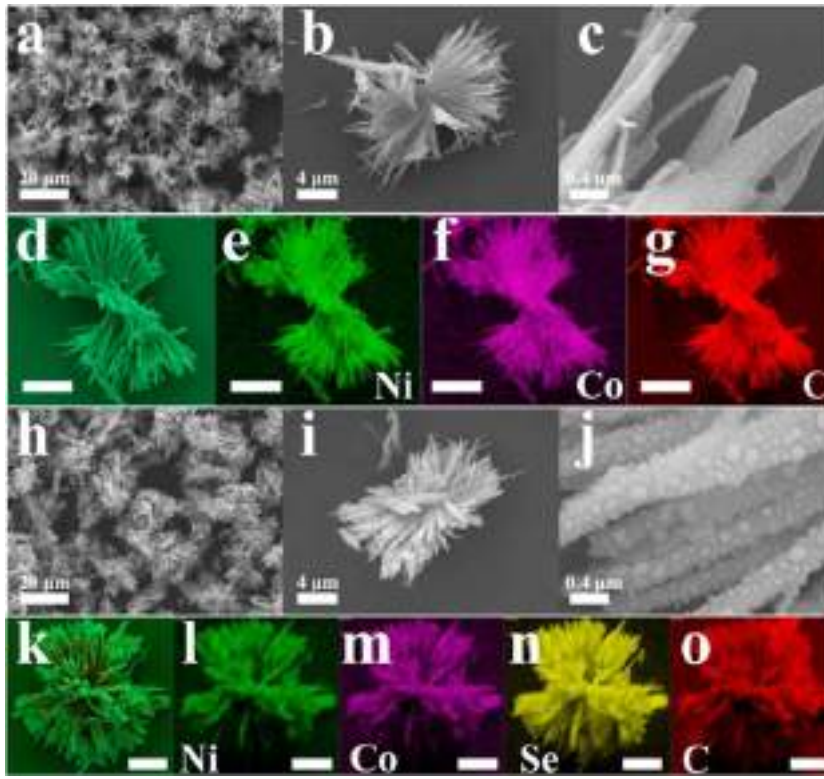

FIGURE 8.7 (A–D) SEM, (E) EDS, (F) Co mapping, (G) C mapping, (H–K) SEM for composites, (L) Ni mapping, (M) Co mapping, (N) Se mapping, and (O) C mapping; *EDS*, Energy dispersive x-ray spectroscopy; *SEM,* scanning electron microscope. *Reprint with the permission from Yang T, Liu Y, Yang D, Deng B, Huang Z, Ling CD, et al. Bimetallic metal-organic frameworks derived Ni-Co-Se@C hierarchical bundle-like nanostructures with high-rate pseudocapacitive lithium ion storage. Energy Storage Mater 2019;17:374–84.*

8.5.3 Superstructured 3D-metal-organic framework–based materials-nanoparticles

The superstructure can enhance the connectivity between the walls while retaining to the porosity of the 3D network. Hence, a cage-like core–shell structure with zinc and cobalt on a MOFMs derived from ZIF, ZIF-8, and ZIF-67 can lead to a superstructured 3D-MOFMs-NPs [42]. The OER and ORR activities can be enhanced using these superstructured 3D-MOFMs-NPs due to the presence of the C cages and metallic ions. The use of superstructured 3D-MOFMs-NPs as an electrode in the energy conversion device can show the excellent capacity of 0.789 Ah g^{-1} with power density 0.1903 W cm^{-2}, whereas the energy density can reach up to the value of the 1012 Wh kg^{-1}. The catalytic activity of the two metal ions along with the fast effective mass as well as the electron transport is responsible for these enhanced performances. On the other hand, the porous structure and superstructured architecture are also associated with the better performances of the material. Hence, this type of the superstructured 3D-MOFMs-NPs opens a new avenue for the application as energy conversion of the renewable sources of the energy.

8.6 Conclusion

In summary, a new design of materials is required for energy conversion from the renewable source of energy. Especially nanoarchitecture of such kind of materials is very popular for their superior behavior. The OER, ORR, and HER activities can be enhanced many folds with the use of the NPs. The inorganic–organic platform of the MOFMs provides an excellent platform with a porous nature. Modeling the MOFMs with NPs can provide excellent design credibility into the energy conversion techniques. Hence, engineering MOFMs-NPs into 0D, 1D, 2D, and 3D architecture can provide excellent stability, durability, and accessibility with fast pathways of transfer of charges. So the malleability of the MOFMs in the energy conversion applications greatly depends on the nanoarchitecture. Especially the 3D skeleton of such MOFMs-NPs provides excellent more active sites, better loading of the masses, and high charge transport properties for the future application of such material for the energy conversion from the renewable source of energy. Although there is further scope to address the challenge of the complex synthesis process of such MOFMs-NPs, which always leads to structural errors or damages very far from the targeted one, it can be believed that in-depth study of such MOFMs-NPs can improve the understanding of the nanoarchitecture of such materials for the better application in the energy conversion from the renewable source of energy.

Acknowledgments

The authors would like to thank UGC, New Delhi for start-up grant with no. F.30−457/2018 (BSR). We also acknowledge the support provided to A. Franco Jr. by CNPq, Brazil with grant No. 307557/2015-4.

References

[1] Hoel M, Kverndokk S. Depletion of fossil fuels and the impacts of global warming. Resour Energy Econ 1996;18(2):115−38.
[2] Höök M, Tang X. Depletion of fossil fuels and anthropogenic climate change—a review. Energy Policy 2013;52:797−809.
[3] Hosseini SE, Wahid MA. Hydrogen production from renewable and sustainable energy resources: promising green energy carrier for clean development. Renew Sustain Energy Rev 2016;57:850−68.
[4] Saravanan KK, Stalin DN, Jayasuthahar ST. Review of renewable energy resources in clean green environment. Int J Emerg Trends Electr Electron 2013;1(1):54−8.
[5] Elliott D. Renewable energy and sustainable futures. Futures 2000;32(3−4):261−74.
[6] Omer AM. Green energies and the environment. Renew Sustain Energy Rev 2008;12(7):1789−821.
[7] Jiao Y, Zheng Y, Jaroniec M, Qiao SZ. Design of electrocatalysts for oxygen-and hydrogen-involving energy conversion reactions. Chem Soc Rev 2015;44(8):2060−88.
[8] Faber MS, Jin S. Earth-abundant inorganic electrocatalysts and their nanostructures for energy conversion applications. Energy Environ Sci 2014;7(11):3519−42.
[9] Zhu YP, Guo C, Zheng Y, Qiao SZ. Surface and interface engineering of noble-metal-free electrocatalysts for efficient energy conversion processes. Acc Chem Res 2017;50(4):915−23.
[10] Wang C, Astruc D. Nanogold plasmonic photocatalysis for organic synthesis and clean energy conversion. Chem Soc Rev 2014;43(20):7188−218.
[11] Wang W, Tadé MO, Shao Z. Research progress of perovskite materials in photocatalysis-and photovoltaics-related energy conversion and environmental treatment. Chem Soc Rev 2015;44(15):5371−408.
[12] Kanhere P, Chen Z. A review on visible light active perovskite-based photocatalysts. Molecules 2014;19(12):19995−20022.
[13] Zhang G, Liu G, Wang L, Irvine JT. Inorganic perovskite photocatalysts for solar energy utilization. Chem Soc Rev 2016;45(21):5951−84.
[14] Grabowska E. Selected perovskite oxides: characterization, preparation and photocatalytic properties—a review. Appl Catal B: Environ 2016;186:97−128.
[15] Li D, Xu HQ, Jiao L, Jiang HL. Metal-organic frameworks for catalysis: state-of-the-art, challenges, opportunities. EnergyChem 2019;1:100005.
[16] Yan W, Guo Z, Xu H, Lou Y, Chen J, Li Q. Downsizing metal−organic frameworks with distinct morphologies as cathode materials for high-capacity Li−O_2 batteries. Mater Chem Front 2017;1(7):1324−30.
[17] Bai S, Sun Y, Yi J, He Y, Qiao Y, Zhou H. High-power Li-metal anode enabled by metal-organic framework modified electrolyte. Joule 2018;2(10):2117−32.
[18] Kim SH, Lee YJ, Kim DH, Lee YJ. Bimetallic metal−organic frameworks as efficient cathode catalysts for Li−O_2 batteries. ACS Appl Mater Interfaces 2018;10(1):660−7.

[19] Baumann AE, Aversa GE, Roy A, Falk ML, Bedford NM, Thoi VS. Promoting sulfur adsorption using surface Cu sites in metal–organic frameworks for lithium sulfur batteries. J Mater Chem A 2018;6(11):4811–21.

[20] Naresh U, Kumar RJ, Ramesh S, Naidu KC, Basha DB, Banerjee P, et al. 3: Conducting polymer-derived materials for batteries. In: Conducting polymers based energy storage materials, vol. 10; 2019. **CRC Press**, p. 65–78

[21] Banerjee P, Junior AF, Basha DB, Naidu KC, Ramesh S. Zinc-based materials for supercapacitors. Inorganic nanomaterials for supercapacitor design. CRC Press; 2019. p. 17–31.

[22] Banerjee P, Junior AF, Basha DB, Naidu KC, Srinivas K. Niobium based materials for supercapacitors. Inorganic nanomaterials for supercapacitor design. CRC Press; 2019. p. 1–15.

[23] Srinivas K, Naidu KC, Balakrishna G, Reddy BV, Kumar NS, Ramesh S., et al. Magnetic nanomaterials for supercapacitors. In: Magnetochemistry – materials and applications, vol. 66; 2020. **Materials Research Forum LLC**, p. 259.

[24] Banerjee P, Junior AF, Basha DB, Naidu KC. Magnetic nanomaterials for spintronics. In: Magnetochemistry – Materials and Applications, vol. 66; 2020. Materials Research Forum LLC, p. 323.

[25] Wang L, Han Y, Feng X, Zhou J, Qi P, Wang B. Metal–organic frameworks for energy storage: batteries and supercapacitors. Coord Chem Rev 2016;307:361–81.

[26] Chen YZ, Wang C, Wu ZY, Xiong Y, Xu Q, Yu SH, et al. From bimetallic metal-organic framework to porous carbon: high surface area and multicomponent active dopants for excellent electrocatalysis. Adv Mater 2015;27(34):5010–18.

[27] Liu B, Shioyama H, Akita T, Xu Q. Metal-organic framework as a template for porous carbon synthesis. J Am Chem Soc 2008;130(16):5390–1.

[28] Mahmood A, Guo W, Tabassum H, Zou R. Metal-organic framework-based nanomaterials for electrocatalysis. Adv Energy Mater 2016;6(17):1600423.

[29] Shen K, Chen X, Chen J, Li Y. Development of MOF-derived carbon-based nanomaterials for efficient catalysis. ACS Catal 2016;6(9):5887–903.

[30] Wang H, Zhu QL, Zou R, Xu Q. Metal-organic frameworks for energy applications. Chem 2017;2(1):52–80.

[31] Zhang W, Wu ZY, Jiang HL, Yu SH. Nanowire-directed templating synthesis of metal–organic framework nanofibers and their derived porous doped carbon nanofibers for enhanced electrocatalysis. J Am Chem Soc 2014;136(41):14385–8.

[32] Xie F, Zhang L, Gu Q, Chao D, Jaroniec M, Qiao SZ. Multi-shell hollow structured Sb_2S_3 for sodium-ion batteries with enhanced energy density. Nano Energy 2019;60:591–9.

[33] Zhou Y, Yan D, Xu H, Feng J, Jiang X, Yue J, et al. Hollow nanospheres of mesoporous Co_9S_8 as a high-capacity and long-life anode for advanced lithium ion batteries. Nano Energy 2015;12:528–37.

[34] Zou L, Hou CC, Liu Z, Pang H, Xu Q. Superlong single-crystal metal–organic framework nanotubes. J Am Chem Soc 2018;140(45):15393–401.

[35] Zhan WW, Kuang Q, Zhou JZ, Kong XJ, Xie ZX, Zheng LS. Semiconductor@metal–organic framework core–shell heterostructures: a case of ZnO@ZIF-8 nanorods with selective photoelectrochemical response. J Am Chem Soc 2013;135(5):1926–33.

[36] Ma TY, Dai S, Jaroniec M, Qiao SZ. Metal–organic framework derived hybrid Co_3O_4-carbon porous nanowire arrays as reversible oxygen evolution electrodes. J Am Chem Soc 2014;136(39):13925–31.

[37] Clough AJ, Yoo JW, Mecklenburg MH, Marinescu SC. Two-dimensional metal−organic surfaces for efficient hydrogen evolution from water. J Am Chem Soc 2015;137(1):118−21.

[38] Wei G, Zhou Z, Zhao X, Zhang W, An C. Ultrathin metal−organic framework nanosheet-derived ultrathin Co_3O_4 nanomeshes with robust oxygen-evolving performance and asymmetric supercapacitors. ACS Appl Mater Interfaces 2018;10(28):23721−30.

[39] Dong Y, Shi W, Lu P, Qin J, Zheng S, Zhang B, et al. 2D holey cobalt sulfide nanosheets derived from metal−organic frameworks for high-rate sodium ion batteries with superior cyclability. J Mater Chem A 2018;6(29):14324−9.

[40] Duan J, Chen S, Zhao C. Ultrathin metal-organic framework array for efficient electrocatalytic water splitting. Nat Commun 2017;8(1):1−7.

[41] Yang T, Liu Y, Yang D, Deng B, Huang Z, Ling CD, et al. Bimetallic metal-organic frameworks derived Ni-Co-Se@C hierarchical bundle-like nanostructures with high-rate pseudocapacitive lithium ion storage. Energy Storage Mater 2019;17:374−84.

[42] Hou CC, Zou L, Xu Q. A hydrangea-like superstructure of open carbon cages with hierarchical porosity and highly active metal sites. Adv Mater 2019;31(46):1904689.

Chapter 9

Applications of metal-organic frameworks in analytical chemistry

Ruth Rodríguez-Ramos[1], Álvaro Santana-Mayor[1], Bárbara Socas Rodríguez[2], Antonio V. Herrera-Herrera[3] and Miguel Ángel Rodríguez Delgado[1]

[1]Departamento de Química, Unidad Departamental de Química Analítica, Facultad de Ciencias, Universidad de La Laguna (ULL), San Cristóbal de La Laguna, España, [2]Department of Chemistry, Centre for Analysis and Synthesis, Lund University, Lund, Sweden, [3]Instituto Universitario de Bio-Orgánica Antonio González, Universidad de La Laguna (ULL), San Cristóbal de La Laguna, España

9.1 Introduction

Metal-organic frameworks (MOFs), a particular class of coordination polymers, have attracted attention in different areas of science. In fact, a quick search, using metal-organic framework or MOFs on typical scientific databases, provides 35,456 or 25,959 results in Scopus; 61,882 or 21,658 in Web of Science; and 2,560,000 or 102,000 results in Google Scholar (early March 2020). The inherent tunability of MOFs makes them ideal for numerous applications in diverse fields such as gas absorption and/or separation [1,2], biomedical applications (including drug delivery [3,4], enzyme stabilization or mimic [5,6] and photodynamic therapy [7,8]), photovoltaic applications [9], energy storage [10], catalysis [11], sensor technology [12], and magnetic applications [13]. Although the term "coordination polymer" appeared in 1960, it was not until 1995 when Yaggi et al. [14] invented the term "MOF" promoting a significant evolution in this field [15].

Despite the important amount of small-molecule crystal structures classified as MOFs (in fact, more than 75,600 MOFs arrangements have been described so far [16]), there is not a unified criteria to define what an MOF is. Frequently, this definition depends on the projected research. In this regard, the Division of Inorganic Chemistry at the International Union of Pure and Applied Chemistry (IUPAC) developed the project entitled

Metal-Organic Frameworks for Chemical Reactions. DOI: https://doi.org/10.1016/B978-0-12-822099-3.00009-5

"Coordination polymers and metal-organic frameworks: terminology and nomenclature guidelines" [17]. One of the first reports from this project concluded that, despite the prolific research using coordination polymers and MOFs in inorganic chemistry and crystal engineering, there was no consensus about a unique definition [18]. IUPAC considered that the term "coordination polymer" could be suitable from a strict nomenclature point of view. However, this label could only include straight-chain polymers (1D) and not 2D or 3D compounds. Another term frequently used is "hybrid inorganic–organic materials." However, it is considered inadequate because it refers, in a very general way, to the composition of the material. For these reasons and keeping in mind that MOF is a widely employed name, as well as that the IUPAC's recommendation would not eliminate the use of such name, a definition was still needed. As a result, the "Terminology of metal-organic frameworks and coordination polymers (IUPAC Recommendations 2013)" was published [19]. It defines an MOF as "a coordination network with organic ligands containing potential voids" [19]. Such definition includes noncrystalline MOFs since different factors (temperature, pressure, etc.) influence the systems structure, modifying the porosity and the potential occupation of voids. Coordination networks, for their part, are defined in the same document [19] as "a coordination compound extending, through repeating coordination entities, in 1 dimension, but with cross-links between two or more individual chains, loops or spiro-links, or a coordination compound extending through repeating coordination entities in 2 or 3 dimensions" [19].

MOFs are extended coordination entities composed of clusters or nodes of metal ions connected by organic linker ions or molecules (usually called bridging ligands). Due to the high number of possible metal ions, organic ligands, structural arrangements, and plausible postsynthetic modifications, the number of potentially obtainable MOFs is practically infinite. Almost all cations up to tetravalent atoms could be nuclear atoms in MOFs, whereas inorganic coordination networks are limited to Al, Si, and chalcogens [20]. Some particular coordinating functional groups, such as carboxylates, amines, nitriles, phosphates, and sulfonates, are frequently part of the ligand compound. Fig. 9.1 illustrates some examples of typical inorganic subunits, organic linkers, and functional groups of MOFs. As can be expected, the physicochemical properties of MOFs depend on the metal components, the organic linkers, and the solvent used for their synthesis [21]. A great number of available experimental structures [16], together with the computational modeling, have allowed the predesign of MOFs with specific properties for specific applications [22,23].

Similarly to definition, nomenclature of MOFs is quite heterogeneous. Some researchers prefer to use a descriptive name with the sequential number of synthesis (i.e., MOF-*n*). Frequently, they are named to highlight the institution or university of discovery by using an acronym made with the name of that place [e.g., Materials of Institute Lavoisier (MIL-*n*), Hong Kong

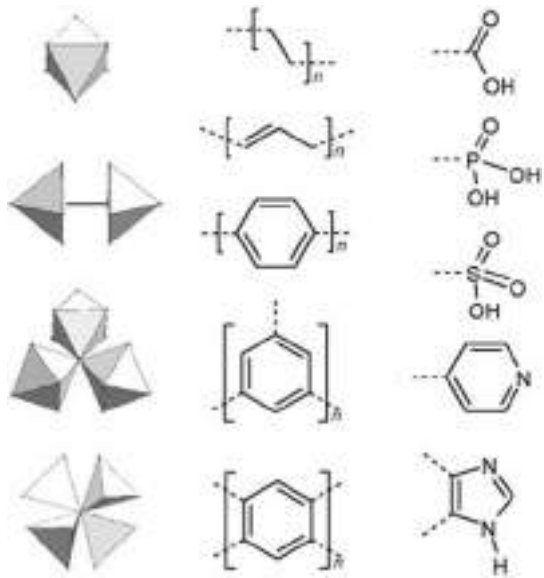

FIGURE 9.1 Typical inorganic subunits, organic linkers, and complex functions encountered in MOFs. *MOFs*, Metal-organic frameworks. *Reprinted from Devic T, Serre C. Porous metal organic frameworks: from synthesis to applications. In: Valtchev V, Mintova S, Tsapatsis M, editors. Ordered porous solids. Elsevier; 2009. p. 77–99 with permission from Elsevier. [24]*

University of Science and Technology (HKUST-*n*), Universitetet i Oslo (UiO-*n*), Saint Andrews MOF (STAM-*n*), and University of Michigan Crystalline Material (UMCM-*n*)]. Other authors use an abbreviation describing the material [e.g., zeolitic imidazolate Framework (ZIF-*n*, porous interpenetrated Zr-organic frameworks (PIZOF-*n*), porous coordination network (PCN-*n*), rare-earth polymeric framework (RPF-*n*), and metal peptide framework (MPF-*n*)]. Finally, some investigators use the formula unit (if it is not too complicated) to facilitate that other scientists can easily understand which is the compound of interest.

Apart from the conventional MOFs (e.g., ZIF, HKUST-1, MIL, and UiO series), there are others with high interest for their use in analytical chemistry: covalent organic frameworks (COFs), homochiral MOFs, magnetic MOFs (MMOFs), and MOF-derived nanoporous carbons. COFs are a particular type with organic building units entirely composed of light elements (B, C, N, O, and Si) linked by strong covalent bonds [25] and produced by a reticular synthesis. COFs are mainly classified into three different groups: the boronate ester-linked, the hydrazone- and imine-linked, and the cyano-contained covalent triazine-based [26]. The use of the homochiral MOFs, with defined pore structures capable of differentiating between enantiomers, in chiral separations, heterogeneous asymmetric catalysis, and nonlinear

optical materials, has increased the interest of the scientific community for these materials [27]. Such class of compounds is produced from stereochemically pure chiral ligands, from achiral metal and ligands in the presence of a chiral reagent that forces the MOF to form a specific chiral network, or even using achiral ligands and metals without chiral auxiliary reagent by spontaneous resolution during crystal growth [28]. The predisposition of metal ions/clusters to adopt particular geometries and the features of chiral ligands (bond angles, length, etc.) has a great influence on the final framework structure. MMOFs, for their part, combine some properties of magnetic particles with those of MOFs. In this case the porous MOFs are combined with magnetic nanoparticles (m-NPs) through chemical or physical methods [29]. Thus materials with superparamagnetism, large surface areas, quick adsorption/desorption cycle, and high recycling rates are obtained. It should be mentioned that magnetism is one of the many characteristics of MOFs that can be obtained by using magnetic moment carriers (paramagnetic metals or open-shell organic ligands) [13]. Based on that, in this text, the term "MMOFs" involves the inclusion of "extra" magnetic particles to the MOFs. Another interesting type of these materials is the MOF-derived nanoporous carbons [30]. Due to their particular properties, MOFs seem to be ideal templates to synthesize porous carbon materials for several applications. Those substances are obtained by direct carbonization or by a combination of carbonization and polymerization after the impregnation of MOF precursor with furfuryl alcohol [30].

The obtaining of MOFs by a simple combination of metal ions and linkers is a matter of coincidence since ions produce little directionality and, consequently, more than one possible structure is obtained [20]. The synthesis of such materials, in both aqueous and nonaqueous media, has been carried out through different procedures [15]. Such processes comprise the following steps: nucleation, oligomerization, particle aggregation, growth, and cooling [29]. One-step methodologies, in which the metal ions and organic linkers are mixed in a suitable solvent to produce the frameworks by self-assembly, are very frequent. Initially, crystallization procedures were used. This term includes two different methods: slow evaporation at room temperature and diffusion of solutions of metal salts through mixtures of organic linkers and weak bases (deprotonate organic ligands and, at the same time, prevent competitive coordination of unreacted ions and linkers) [29]. However, the low yields obtained and the long times employed favored the development of alternative approaches [15]. Solvothermal protocols, in which metal salts and organic ligands are electrically heated at high temperatures, are the most commonly employed methods. Since no complicated apparatus are required and good crystal growth is obtained, this technique is used by different companies for the commercialization of MOFs [15]. The mechanochemical solid-state or liquid-assisted grinding was also utilized. The application of microwave-assisted techniques allows a reduction of the

synthetic time, a uniform and rapid heating, and the obtaining of nanosized polymers [15]. Sonochemical-assisted syntheses are promising owing to a rapid growth and fast crystallization and precipitation (due to the extremely high local temperatures and pressures). Nevertheless, such methods are not universally applicable [29]. On the contrary, electrochemical synthesis by the anodic dissolution of metals in the mixtures of ligands and electrolytes requires short reaction times and mild conditions [15]. Other alternative methods such as chemical vapor deposition, decomposition of precursors, or templated production have also been employed [15]. Apart from the components, the conditions applied during the synthetic protocol (e.g., stoichiometry, temperature, time, solvent type and proportion, the addition of modifiers and their nature, pH, size of the reactor, ionic strength, and nature of counterions [29]), strongly influence the properties and structure of the obtained MOF, so that small variations provide a dramatic alteration of the characteristics.

Thanks to their unique properties, MOFs have been employed in many analytical applications, including sample preparation [29,31], sensors [12], chromatographic and electrophoretic separations [31], and matrix-assisted laser desorption ionization (MALDI) analyses [21]. Regarding MALDI applications, MOFs seem to be promising materials to overcome the traditional problems of this technique when small molecules are analyzed [32]. Typical matrix materials usually present inadequate signal-to-noise ratio and poor reproducibility for small compounds. However, MOFs have proven to be more efficient because of their high surface area, efficient photon absorption, and stable structure [32]. Because of the large number of published MOF applications, this chapter is centered only on recent uses in sample preparation, separation techniques, and sensors. The main objective is to provide an overview of the most relevant employments, as well as the main trends and evolution of these materials.

9.2 Desirable characteristics of MOFs for analytical chemistry applications

Apart from their large specific surface area, other important features of MOFs such as the large pore aperture (from micropores to mesopores), the low density, the charge-transfer ability between metal and ligand, the thermal stability, the conducting effects, and the pH-sensitive stability play an important role for their use in analytical science [30]. Moreover, ideally, MOFs used in analytical chemistry applications should allow an easy adaptation to microanalytical techniques, provide suitable interactions with target analytes, allow the development of quick methodologies, have a reduced cost, be in line with green analytical chemistry (GAC) principles, and offer an appropriate performance. Furthermore, considering the GAC principles, the ideal MOFs would be those that can be infinitely reused [33]. Frequently,

particular applications are hindered by the analytical requirements or process characteristics. For instance, water-unstable MOFs could not be used for direct extraction of compounds from aqueous matrices or thermally labile MOFs cannot be used in combination with high temperatures. As an example, Gu et al. [34] found that MOF-5 offered good performance for formaldehyde extraction and preconcentration on air samples with relative humidity less than 45%; however, the extraction efficiency decreased remarkably with a further increase of moisture, limiting the application.

Although milli-to-micrometer-sized MOFs are frequently used, they sometimes produce inhomogeneous solutions in aqueous media and, thus, their use in many analytical applications is restricted [35]. This fact is particularly important from a GAC perspective, which considers water the ideal solvent [33]. The tunability of MOFs allows accurate control of the size to obtain nanosized MOFs successfully applicable to analytical science due to an effective dispersion in water [21]. The stability in water can be explained by the Hard Acid Soft Base Theory. In this regard, stronger bonds are formed when hard acids react with hard bases [small, weakly polarizable and with high charge states, e.g., Fe(III), Zr(IV), Hf(IV), and carboxylate] and soft acids interact with soft bases [e.g., Ag (I) and thiol] [21]. In addition to the selection of metals and ligands interacting through strong bonds, the stability of MOFs in water solutions has been improved via introduction of hydrophobic groups in the network, fabrication of core−shell structures, and linkers' functionalization [36].

The sorption qualities of MOFs depend on multiple characteristics (apart from the specific surface area and pore size) such as their morphologies, their capability to participate in hydrogen bonds, hydrophobic effects, $\pi-\pi$ interactions, surface charge and polarity, and wettability. As for any other sorbents, MOFs should be able to retain and release analytes in different media (being stable in such solvents). The existence of an unsaturated metal site improves the sorption capability of MOF by direct interaction of the metal with target molecules. These unsaturated nuclei are produced by the existence of unstable ligands that are released as a consequence of heating or drying without changing the framework [29]. Hydrophobic interactions between linkers in the framework and target analytes contribute to the extraction of suitable compounds, and the presence of delocalized electrons in some molecules allows the establishment of $\pi-\pi$ interactions and complexation between aromatic rings of target molecules and linkers and/or Lewis acid sites of MOFs [36]. Generally speaking, presence of large cavities is better for the incorporation of target analytes. However, the cavities must not be too large to avoid the structure collapse. The structural stability of specific MOFs can be inadequate for certain applications [29] and only a strict control of synthetic conditions can overcome this problem. The selection of the components (and their ratios) used for the synthesis is

fundamental to regulate not only the pore size and the porous structure but also the stability of the material.

Fortunately, MOFs can be precisely designed to increase the recognition of target compounds [22,23]. Thus MOFs have been used as sorbents for sample preparation and extraction of either organic or metal compounds from a wide range of matrices, including environmental, biological, or food samples. The flexible synthetic design of MOFs makes possible modifications on their nature without changing their topology (the so-called isoreticular principle). In this way, MOFs can be conceived to trap from small discrete compounds to macromolecules. The additional possible postsynthetic modification of MOFs through functional groups into the framework increases the sorption possibilities over other porous materials [20].

Frequently, MOFs are compared with zeolites due to their analogous use and their similar characteristics [12,21]: large surface areas ($1000-10{,}400\ m^2\ g^{-1}$) [37], extensive tunable porosity, and high degree of crystallinity (although, as it was previously mentioned, crystallinity is not a necessary condition to define MOFs). However, their use in industrial applications is limited for some of them due to the fact that their thermal and chemical stability could be inadequate (−Si−O and Al−O in zeolites are much more strong bonds than coordination links) [15].

MOFs must have an appropriate permeability and high mechanical, thermal, and electrical stability to be used as chromatographic/electrophoretic stationary phases [31]. Their porosity favors their use as stationary phases since high flow rates can be applied and low back pressures are produced. However, the irregularity and the broad size distribution of particles are the main challenges for the use of MOFs in chromatographic separations [20]. Moreover, large amounts of MOFs are needed to fill packed columns and, thus, the cost is relatively superior to other classical or novel materials. The combination with other materials to produce hybrid MOFs improves their properties, including the advantages of the combined material and excluding some disadvantages of MOFs [20].

Some important characteristics of MOFs have favored their application in sensors. In this regard, their semiconductor-like properties and optical features, their selectivity and reusability, as well as their electric behavior make this material a good alternative to other classical substances used in this field. The effective employment of MOFs in chemical sensors depends on the sensitivity, response time, regeneration, selectivity, and stability [12]. Sensitivity is highly related to the dynamic of analyte transport in the sensor (low transference provides long response times not distinguishable from baseline drift) and to the strength of binding [stronger binding provides lower limits of detection (LODs)]. The response and reusability are governed by the thermodynamic and sorption kinetic [12]. Usually, sorbates are physically sorbed and thus the application of vacuum and/or temperatures should be enough to reactivate the sensors. The velocity of this step is determined by

the particle size and/or film thickness and the rate of analyte diffusion within the pores (slower diffusion is expected when solvent molecules are within MOFs pores). Selectivity depends on the pore size, metal and linker shapes and sizes, directional orientation of ligand functional groups, framework catenation, and chemical interactions of analytes with the MOF internal surface [12]. MOFs have a tendency to adsorb a high amount of water and thus such possible interference should be considered when MOFs-based sensors are designed [12].

9.3 Recent applications

9.3.1 Recent applications in sample preparation

As indicated previously, the extraordinary properties that MOFs offer, such as large surface area, high porosity, and their structured cavities, have boosted their use in the area of sample preparation as can be seen in Tables 9.1–9.5 in which some recent applications of these sorbents in food, environmental, and biological analysis have been compiled.

9.3.1.1 Solid-phase extraction

Solid-phase extraction (SPE) is a sorption method based on the transfer of the compounds contained in a liquid sample, in some cases gas samples or supercritical fluids, to a solid sorbent. During the initial development and application of this technique in the area of analytical chemistry, conventional sorbents such as octyl- (C_8) or octadecylsilane (C_{18}) and hydrophilic–lipophilic balance copolymer, among others, have been applied. However, the necessity of more selective systems, with better adsorption efficiency and easier synthesis procedures, as well as lower cost, has led to the development and utilization of new materials. Among them, MOFs have attracted special interest, not only due to their unique characteristics but also due to the possibility of modification or functionalization. In this sense, MOFs have been applied in SPE, principally, for the extraction of organic species from environmental [38,41,42], biological [38], or food [39,40] samples (see Table 9.1), but the evaluation of inorganic species has also been reported [36].

Among the different types of MOFs that have been applied as SPE sorbents, MIL-101 or MIL-101-based composites have been the most used in a wide group of samples, including environmental, food, and biological samples, among others, even if other MOFs such as UiO-66, MOF-5, or ZIF-8 have also been widely applied [31,36,43]. MIL-101 is a chromium-based MOF that exhibits high surface area, large pore size and windows, great stability, and active metal sites. In addition, the existence of different functional groups allows it to establish $\pi-\pi$ and hydrophobic interactions, and hydrogen bonds with target analytes, which make it an excellent SPE sorbent [43].

TABLE 9.1 Recent applications of metal-organic frameworks (MOFs) as solid-phase extraction (SPE) sorbents in sample preparation.

Analytes	Matrix	MOF	Determination technique	Recovery (%)	LOD	Comments	Reference
Nitrazepam and oxazepam	Wastewater, plasma, and urine (750 μL)	PAN/MIL-53 NFs (5 mg)	HPLC–DAD	92–100	1.5–2.5 μg L^{-1}	– A PT–SPE method was developed – Plasma samples were pretreated with HCl and TFA for protein precipitation while urine and water samples were only centrifuged and filtered, respectively – Real samples of wastewater, plasma, and urine were analyzed	[38]
Six SAs	Milk (3 g), pork meat (6 g), and lake water (2 mL)	MIL-68-NH_2@COF (8 mg)	HPLC-VWD	69–104	1–10 μg L^{-1}	– A PT–SPE method was developed – Milk samples were pretreated with $HClO_4$ to eliminate proteins while pork samples were initially submitted to an US-SLE using ACN – The sorbent could be reused after 100 adsorption/desorption cycles	[39]
	Vegetables (5 g)		HPLC-FD	84–111	0.01–0.02 μg L^{-1}		[40]

(*Continued*)

TABLE 9.1 (Continued)

Analytes	Matrix	MOF	Determination technique	Recovery (%)	LOD	Comments	Reference
Four		UiO-66@PAN NFs (5 mg)				– A PT–SPE method was developed – A previous extraction with MeOH was carried out – The sorbent could be reused for 10 adsorption/desorption cycles – The method was applied to the analysis of real watermelon and mung bean sprouts samples	
Eight PAHs	Environmental water (10 mL)	MIL-101 (2 mg)	GC–(Q)-MS	84–105	0.20–1.9 ng L^{-1}	– An in-syringe SPE method was developed – The sorbent could remain stable for at least 7 days on the device	[41]

						– Real tap and river water samples were analyzed	
Four SAs	Environmental water (60 mL)	MIL-101 (40 mg)	UHPLC–(QqQ)–MS/MS	84–107	0.03–0.08 μg L^{-1}	– A μ-SPE procedure was carried out – MIL-101 and MIL-100 were investigated as SPE sorbents – A computational study by molecular docking technique was carried out to recognize the interactions between SAs and MIL-101	[42]

μ-SPE, micro-solid-phase extraction; *ACN*, acetonitrile; *COF*, covalent organic framework; *DAD*, diode array detector; *FD*, fluorescence detector; *GC*, gas chromatography; *HPLC*, high-performance liquid chromatography; *LOD*, limit of detection; *MeOH*, methanol; *MIL*, Materials of Institute Lavoisier; *MS*, mass spectrometry; *MS/MS*, tandem mass spectrometry; *NF*, nanofiber; *$-NH_2$*, amino-functionalized; *PAH*, polycyclic aromatic hydrocarbon; *PAN*, polyacrylonitrile; *PT*, pipette tip; *Q*, single quadrupole; *QqQ*, triple quadrupole; *SA*, sulfonamide; *SLE*, solid–liquid extraction; *TFA*, trifluoroacetic acid; *UHPLC*, ultrahigh-performance liquid chromatography; *UiO*, Universitetet i Oslo; *US*, ultrasound; *VWD*, variable wavelength detector.

TABLE 9.2 Recent applications of metal-organic frameworks (MOFs) as dispersive solid-phase extraction (dSPE) sorbents in sample preparation.

Analytes	Matrix	MOF	Determination technique	Recovery (%)	LOD	Comments	Reference
Seven PGRs	Fruit and vegetables (5 g)	Fe_3O_4@COF (TpDA) (15 mg)	HPLC–DAD	83–105	4.68–7.51 μg L^{-1}	– An m-μ-dSPE method was developed – Samples were initially submitted to an US–SLE using methanol – Real samples of cucumber, tomato, apple, and orange were analyzed	[45]
Methamphetamine	Urine (5 mL)	ZIF-8-COOH (40 mg)	HPLC-UV	100	10 μg L^{-1}	– A μ-dSPE method was developed – ZIF-8 and carboxylated@ZIF-8 adsorbents were compared – The sorbent could be reused up to eight times without showing any loss in extraction capacity	[46]

Cu(II)	Vegetable (1 g) and water (200 mL)	ligand@MIL-101 (30 mg)	FAAS	92–98	0.47 μg L^{-1}	– A μ-dSPE method was developed – Vegetables were initially ground and pretreated before μ-dSPE – An interference study using other cations was carried out – The sorbent could be reused up to five times without showing any significative loss in extraction capacity – Real samples of sea and drinking water, potato, and mushroom were analyzed	[47]
5 SAs	Meat (2 g)	Fe_3O_4@JUC-48 (25 mg)	HPLC–DAD	76–103	1.73–5.23 μg kg^{-1}	– An m-μ-dSPE method was developed – Samples were initially submitted to an US-SLE using ACN	[48]

(*Continued*)

TABLE 9.2 (Continued)

Analytes	Matrix	MOF	Determination technique	Recovery (%)	LOD	Comments	Reference
						– The sorbent could be reused up to 7 times without showing any significative loss in extraction capacity – Real samples of chicken, pork, and shrimp were analyzed	
6 PAHs	Air and water (20 mL)	Fe_3O_4@pDA/ZIF-7 (18 mg)	GC-(QqQ)-MS	82–99	0.71–5.79 ng L^{-1}	– An m-μ-dSPE method was developed – The sorbent could be reused up to 10 times without showing any significative loss in extraction capacity – Real samples of rainwater and $PM_{2.5}$ were analyzed	[49]

μ-dSPE, micro-dispersive solid-phase extraction; *ACN*, acetonitrile; *COF*, covalent organic framework; *−COOH*, carboxylate-functionalized; *DA*, 2,6-diaminoanthraquinone; *DAD*, diode array detector; *FAAS*, flame atomic absorption spectrometry; *GC*, gas chromatography; *HPLC*, high-performance liquid chromatography; *JUC*, Jilin University China; *LOD*, limit of detection; *m-μ-dSPE*, magnetic-micro-dispersive solid-phase extraction; *MIL*, Materials of Institute Lavoisier; *MS/MS*, tandem mass spectrometry; *MS*, mass spectrometry; *PAH*, polycyclic aromatic hydrocarbon; *pDA*, polydopamine; *PGR*, plant growth regulator; $PM_{2.5}$, particulate matter (diameter of 2.5 μm or less); *QqQ*, triple quadrupole; *SA*, sulfonamide; *SLE*, solid–liquid extraction; *Tp*, 1,3,5-triformylphloroglucinol; *US*, ultrasound; *UV*, ultraviolet; *ZIF*, zeolitic imidazolate framework.

TABLE 9.3 Recent applications of metal-organic frameworks (MOFs) as solid-phase microextraction (SPME) sorbents in sample preparation.

Analytes	Matrix	MOF	Determination technique	Recovery (%)	LOD	Comments	Reference
5 PBDEs	Milk (10 mL)	UiO-66-OH (–)	GC–(QqQ)–MS/MS	75–118	0.15–0.35 ng L^{-1}	– A DI–SPME method was developed – The SPME procedure was optimized using an experimental design – The method was applied to the analysis of real milk samples	[53]
4 NSAIDs	Biological fluids and tablet formulation (5 mL)	Fe_3O_4/$Cu_3(BTC)_2$ (–)	HPLC–UV	94–102	0.03–0.05 μg L^{-1}	– A DI–SPME method was developed – Capillary glass tubes were used as substrates to prepare SPME fiber – Synthesized SPME fiber could be reused for 110 times – The SPME procedure was partially optimized using an experimental design – The method was applied to the analysis of real biological samples (human urine, serum, and plasma) and tablet formulation samples	[54]

(*Continued*)

TABLE 9.3 (Continued)

Analytes	Matrix	MOF	Determination technique	Recovery (%)	LOD	Comments	Reference
16 PAHs and 11 NPAHs	Environmental waters (15 mL)	ZIF-8 (–)	GC–(Q)-MS	66–105	0.3–27 ng L^{-1}	– ZIF-8 was synthesized by solvothermal, stirring, and ball- milling methods – A DI–SPME method was developed – The HS–SPME mode was also investigated – A comparison between hydrothermal ZIF-8 and commercial and etched stainless fibers was carried out – The method was applied to the analysis of real environmental water samples (tap water, surface water, and wastewater)	[55]
7 CPs	Honey (4.2 g) and canned-yellow-peach (5.0 g)	TpBD COF (–)	GC–(Q)-MS	70–113	0.3–1.8 μg kg^{-1}	– An HS–SPME method was developed – A derivatization step was carried out – Synthesized SPME fiber could be reused for 150 times – The method was applied to the analysis of real honey and canned-yellow-peach samples	[56]

5 Triazole fungicides	Fruits and vegetables (1.0 g)	MOF-5/GO (–)	GC-μ-ECD	86–106	0.05–1.6 μg kg^{-1}	– A DI–SPME method was developed – The extraction capabilities of GO, MOF-5, and MOF-5/GO were compared – A comparison between $Zn_4O(BDC)_3$/GO and commercial fibers was carried out – Synthesized SPME fiber could be reused for 120 times – The method was applied to the analysis of fruit and vegetable samples (grape, apple, cucumber, celery cabbage, pear, cabbage, and tomato)	[57]

μ-ECD, micro-electron capture detector; *BD*, benzidine; *BDC*, 1,4-benzenedicarboxylate; *BTC*, 1,3,5-benzenetricarboxylate; *COF*, covalent organic framework; *CP*, chlorophenol; *DI*, direct immersion; *GC*, gas chromatography; *GO*, graphene oxide; *HPLC*, high-performance liquid chromatography; *HS*, headspace; *LOD*, limit of detection; *MS*, mass spectrometry; *MS/MS*, tandem mass spectrometry; *NPAH*, nitro polycyclic aromatic hydrocarbon; *NSAID*, nonsteroidal antiinflammatory drug; *–OH*, hydroxyl-functionalized; *PAH*, polycyclic aromatic hydrocarbon; *PBDE*, polybrominated diphenyl ether; *Q*, single quadrupole; *QqQ*, triple quadrupole; *Tp*, 1,3,5-triformylphloroglucinol; *UiO*, Universitetet i Oslo; *UV*, ultraviolet; *ZIF*, zeolitic imidazolate framework.

TABLE 9.4 Recent applications of metal-organic frameworks (MOFs) as matrix solid-phase dispersion (MSPD) sorbents in sample preparation.

Analytes	Matrix	MOF	Determination technique	Recovery (%)	LOD	Comments	Reference
3 Pyrethroids	Wheat (0.24 g)	Fe-based MOF–MIP (0.36 g)	GC–(QqQ)–MS/MS	96–109	1.8–2.8 μg kg^{-1}	– Cyhalothrin was used as template molecule and APTES and TEOS as functional monomers and cross-linking agents – Binding experiments for MOF–MIP and MOF–NIP were carried out – The method was applied to the analysis of real wheat samples	[60]
15 PAEs	Agricultural soil and sand (1.0 g)	Fe-BTC (30 mg)	UHPLC–(QqQ)–MS/MS	70–120	0.14–2.7 μg kg^{-1} dw[a])	– GO and MWCNTs were also investigated as dispersion sorbents – The MSPD procedure was partially optimized using an experimental design	[61]

						– The method was applied to the analysis of real agricultural soil and sand samples	
3 TCs	Milk powder (0.18 g)	Al-based MOF–MIP (0.27 g)	UHPLC–(QqQ)–MS/MS	85–94	0.217–0.318 μg kg^{-1}	– TC was used as template molecule and APBA as a functional monomer and a cross-linking agent – Binding experiments for MOF–MIP and MOF–NIP were carried out – The method was applied to the analysis of real milk samples	[62]
8 Pesticides	Peppers (500 mg)	$[(La_{0.9}Sm_{0.1})_2(DPA)_3(H_2O)_3]_\infty$ (350 mg)	GC-(Q)-MS	48–135	16–67 μg kg^{-1}	– Na_2SO_4 (1.0 g) and silica (500 mg) were used as dehydrating and cleanup agents, respectively – The MSPD procedure was optimized using an experimental design	[63]

(*Continued*)

TABLE 9.4 (Continued)

Analytes	Matrix	MOF	Determination technique	Recovery (%)	LOD	Comments	Reference
						– The method was applied to the analysis of real pepper samples	
7 Pesticides	Coconut palm stem (0.25 g)	$[Zn(BDC)_{0.9}(NH_2\text{-}BDC)_{0.1}(H_2O)_2]_n$ (1.0 g)	HPLC–DAD	64–76	10–50 μg kg^{-1}	– $[Zn(BDC)(H_2O)_2]_n$, $[Zn(BDC)_{0.99}(NH_2\text{-}BDC)_{0.01}(H_2O)_2]_n$, and $[Zn(BDC)_{0.95}(NH_2\text{-}BDC)_{0.05}(H_2O)_2]_n$ were also tested as dispersion sorbents in the MSPD process – A comparison between $[Zn(BDC)_{0.9}(NH_2\text{-}BDC)_{0.1}(H_2O)_2]_n$ and two different commercial sorbents (e.g., Al_2O_3 and C_{18}) was carried out	[64]

APBA, 3-aminophenylboronic acid; *APTES*, 3-aminopropyltriethoxysilane; *BDC*, 1,4-benzenedicarboxylate; *BTC*, 1,3,5-benzenetricarboxylate; *C_{18}*, octadecylsilane; *DAD*, diode array detector; *DPA*, dipicolinic acid; *dw*, dry weight; *GC*, gas chromatography; *GO*, graphene oxide; *HPLC*, high-performance liquid chromatography; *LOD*, limit of detection; *MIP*, molecularly imprinted polymer; *MS*, mass spectrometry; *MS/MS*, tandem mass spectrometry; *MWCNT*, multiwalled carbon nanotube; *NIP*, nonimprinted polymer; *PAE*, phthalic acid ester; *Q*, single quadrupole; *QqQ*, triple quadrupole; *TC*, tetracycline; *TEOS*, tetraethoxysilane; *UHPLC*, ultrahigh-performance liquid chromatography.
[a]*Limit of quantification.*

TABLE 9.5 Recent applications of metal-organic frameworks (MOFs) as stir bar sorptive extraction (SBSE) sorbents in sample preparation.

Analytes	Matrix	MOF	Determination technique	Recovery (%)	LOD	Comments	Reference
5 PAEs	Solid and liquid children's food (50 mL)	ZIF-8@GO HF (5 mg)	GC-(Q)-MS	72–100	0.15–0.60 μg L^{-1} 0.75–2.20 μg kg^{-1}	– Jam samples were diluted up to 60 mL with double distilled water and submitted to the SBSE procedure – A comparison of HF, ZIF-8 HF, GO HF, and ZIF-8@GO HF stir bars was carried out – Synthesized stir bar could be reused for 120 times – CiCi beverage, pear juice, and jam real samples were analyzed	[66]
Benzylpenicillin	Human blood plasma (–), urine (–), and milk (1 mL)	Zn–Al–LDH@ZIF-8 (–)	HPLC–UV	95–110	0.05 μg L^{-1}	– Urine and plasma samples were pretreated with trichloroacetic	[67]

(*Continued*)

TABLE 9.5 (Continued)

Analytes	Matrix	MOF	Determination technique	Recovery (%)	LOD	Comments	Reference
						and perchloric acids to precipitate proteins. The supernatant was submitted to the extraction procedure – Milk samples were pretreated with ACN and TFA to eliminate proteins and fats. The supernatant was diluted to 10 mL with water – Multivariate optimization strategy was carried out by Plackett–Burman design and Box–Behnken model assisted by response surface methodology	

						– Anodized Al/Zn–Al–LDH/ZIF-8, anodized Al/Zn–Al–LDH, anodized Al, and bare Al stir bars were compared – Real samples of milk were analyzed	
5 NSAIDs	Environmental water (10 mL)	MIL-101@PVA/PEG (–)	HPLC–(QqQ)–MS	77–102	0.011–0.035 μg L^{-1}	– MIL-101@PVA/PEG cryogel was used as an SBSE sorbent – MIL-101@PVA/PEG and MIL-101@PVA were compared as extraction sorbents – 60 mg mL^{-1} of MIL-101 was selected as optimal amount of sorbent – Real samples of lake water, pharmaceutical wastewater, and feedwater were analyzed	[68]

(*Continued*)

TABLE 9.5 (Continued)

Analytes	Matrix	MOF	Determination technique	Recovery (%)	LOD	Comments	Reference
5 Phytohormones	Fruit (1 g)	ZIF-8@poly-(MMA-EGDMA) (–)	HPLC–UV	83–111	0.11–0.51 $\mu g\ L^{-1}$	– Samples were pretreated with 4 mL of MeOH/water mixture. The supernatant was concentrated, diluted up to 30 mL with water, and submitted to the SBSE procedure – Commercial PEG coating and the synthesized stir bars were compared – Synthesized stir bar could be reused, at least, for 40 times – Real samples of apple and pear were analyzed	[69]
2 PCBs	Fish (20 g)	Apt-MOF-5 (–)	GC–(Q)-MS	89–97	0.15–0.22 $ng\ kg^{-1}$	– Samples were grinded, freeze-dried, and extracted twice	[70]

						with 50 mL of *n*-hexane. The extract was filtered, dried, and dispersed in PBS buffer for the SBSE procedure – Apt-MOF-5 selectivity was evaluated adding other PCBs, chlorobenzene and parathion-methyl – Apt-MOF-5 fiber and Apt fiber were compared – Commercial PA, PDMS, PDMS/DVB, and Apt-MOF-5 SBSE fibers were compared were also compared – Real samples of fish were analyzed	

ACN, acetonitrile; *Apt*, aptamer; *DVB*, divinylbenzene; *EGDMA*, ethylene glycol dimethacrylate; *GC*, gas chromatography; *GO*, graphene oxide; *HF*, hollow fiber; *HPLC*, high-performance liquid chromatography; *LDH*, layered double hydroxide; *LOD*, limit of detection; *MeOH*, methanol; *MIL*, Materials of Institute Lavoisier; *MMA*, methyl methacrylate; *MS*, mass spectrometry; *NSAID*, nonsteroidal antiinflammatory drug; *PA*, polyacrylate; *PAE*, phthalic acid ester; *PBS*, phosphate-buffered solution; *PCB*, polychlorinated biphenyl; *PDMS*, polydimethylsiloxane; *PEG*, polyethylene glycol; *PVA*, polyvinyl alcohol; *Q*, single quadrupole; *QqQ*, triple quadrupole; *TFA*, trifluoroacetic acid; *UV*, ultraviolet; *ZIF*, zeolitic imidazolate framework.

As an example of the different approaches in which MOFs have been applied as SPE sorbents, Dai et al. [42] prepared a Cr-based MOF, MIL-101, for the micro-SPE (μ-SPE) of four sulfonamides (SAs) from environmental water samples prior their separation and determination by ultrahigh-performance liquid chromatography (UHPLC)−tandem mass spectrometry (MS/MS). In order to establish the adequate extraction conditions, different parameters, such as SPE sorbent, load flow rate, pH and volume of sample, as well as type and volume of elution solvent, were evaluated. Under optimized conditions, 60 mL of water sample at pH 4 was passed through the previously conditioned cartridge at a flow rate of 2 mL min^{-1}. The cartridge, packed with a suspension of 40 mg of MIL-101 in methanol (MeOH), was conditioned with 5 mL of MeOH and 5 mL of water. After sample loading, the cartridge was washed with water and dried using vacuum. The target analytes were eluted with 4 mL of MeOH at a flow rate of 0.3 mL min^{-1}, the eluate filtered through 0.22 μm membrane filter and dried under nitrogen steam. The extract was redissolved with mobile phase and injected into the UHPLC−MS/MS system. Recovery values of 84%−107% and LODs between 0.03 and 0.08 μg L^{-1} were obtained. In addition, the authors carried out a computational study in order to estimate the binding mode between MOFs and SAs and showed that it is generated from coordination bonds between the open sites in MOFs and SA groups of the compounds of interest, intramolecular hydrogen bonds between carboxyl groups and amino groups in MOFs and SAs, respectively, and π−π and hydrophobic interactions between phenyl rings of MOFs and SAs.

Another example is the work carried out by Amini et al. [38], who synthesized nanofibers (NFs) of polyacrylonitrile (PAN) and MIL-53 type MOF by electrospinning method and used it as sorbent for pipette tip (PT)-SPE to determine two benzodiazepines, nitrazepam and oxazepam, in wastewater and biological samples, including plasma and urine, using a high-performance liquid chromatography (HPLC)−diode array detector (DAD) system. Under the optimum conditions, recovery values and LODs were obtained in the ranges 92%−100% and 1.5−2.5 μg L^{-1}, respectively. The synthesized composite allowed the extraction of drugs using a low volume of sample (750 μL) and amount of sorbent (5 mg). In addition, the nanosize and porous structure of that MOF, and the existence of different functional groups, allow its application for the evaluation of other pollutants [i.e., pesticides, polycyclic aromatic hydrocarbons (PAHs), dopamine, and ions] through hydrophobic, hydrogen bonds, and π−π interactions. Despite these advantages, the application of the sorbent is limited for the analysis of lower sample volumes and the PT-SPE system may be clogged when biological samples are analyzed.

Despite the many advantages that the use of MOFs provides in SPE performance, in recent years the application of such nanomaterials in this approach has decrease in respect to those that imply greater operational

simplicity or speed, such as dispersive SPE (dSPE), magnetic-SPE (m-SPE), and solid-phase microextraction (SPME). As an example, the application of MOFs in SPE for the extraction of organic compounds from environmental samples represents 9% of the total applications, versus of 32% of m-SPE and SPME [44].

9.3.1.2 Dispersive solid-phase extraction

The diverse drawbacks that conventional SPE approach presents, such as high back pressure, cartridge clogging, or time consumption, can be solved by dSPE. This procedure follows the same principles than classic SPE, but its dispersion mode not only improves the extraction efficiency, but also avoids critical stages and the strict control of such parameters that SPE requires. In addition, dSPE approach allows the use of small amounts of sorbents in the order of milligrams or micrograms giving rise to the so-called micro-dSPE (μ-dSPE). In this respect and supported by the great advance of nanoscience in recent decades, different sorbents have been used for this purpose. Among them, MOFs are not an exception thanks to their inherent properties. Therefore, they have been applied in all types of matrices for the determination of both organic [45,46,48,49] and inorganic species [47] (see Table 9.2). As an example, Taghvimi et al. [46] developed a method for the analysis of methamphetamine in urine. With this purpose, the authors used 40 mg of carboxylated@ZIF-8 sorbent in a μ-dSPE combined with HPLC−ultraviolet (UV) determination obtaining a recovery of 100% and an LOD of 10 $\mu g\ L^{-1}$. These results and the selectivity, velocity, and cost that the developed method showed make it suitable for clinical and forensic laboratory analysis.

Another significant improvement of conventional SPE is the inclusion of m-NPs giving rise to the m-dSPE. This modality adds to the abovementioned advantages of the dSPE, the easy separation of the sorbent through the application of an external magnetic field. In this regard, Li et al. [45] combined the benefits of COFs with m-NPs. The sorbent was applied for the extraction of seven plant growth regulators (PGRs) from fruits and vegetables, including cucumber, tomato, apple, and orange, prior to their separation and determination by HPLC−DAD. For the magnetic-μ-dSPE (m-μ-dSPE) procedure, 15 mg of Fe_3O_4@COF, using 1,3,5-triformylphloroglucinol (Tp) and 2,6-diaminoanthraquinone (DA) as building blocks, was dispersed in 10 mL of sample solution containing the PGRs. After the extraction, assisted by vortex, the sorbent was collected by an external magnet and the compounds desorbed with 1 mL of acetonitrile (ACN) 0.1% formic acid (v/v) for subsequent chromatographic analysis. Recovery values between 83% and 105% and LODs of 4.68−7.51 $\mu g\ L^{-1}$ were obtained.

In the field of environmental analysis, Zhang et al. [49] developed an interesting application of an MMOF for the m-μ-dSPE of six PAHs from

environmental water. An ultrasound-assisted-m-μ-dSPE procedure was performed using 20 mL of sample and 18 mg of Fe_3O_4@polydopamine (pDA)/ZIF-7 sorbent. The nanocomposite was easily formed in situ by mixing 3 mg of Fe_3O_4@pDA dispersed into the sample solution with 15 mg of ZIF-7, using pDA as the covalent linker. The solution was sonicated for 1 min, the sorbent was then isolated using an external magnet, and the analytes were reextracted with 200 μL of ethyl acetate (EtOAc). The extract was collected and injected into a gas chromatography (GC)−mass spectrometry (MS) system. The procedure was also applied for the evaluation of air samples. With this purpose, airborne particulate matter with a diameter of 2.5 μm or less ($PM_{2.5}$) was collected over 24 hours onto a quartz-fiber filter since these particles usually act as carriers of PAHs in the environment. The filter was cut into small pieces, extracted with 10 mL of acetone, and evaporated to dryness under vacuum. The extract was redissolved in 500 μL of MeOH and 50 μL was diluted with 20 mL of water and submitted to the m-μ-dSPE previously described. The developed method afforded recovery values between 82% and 99% and LODs of 0.71−5.79 ng L^{-1}.

9.3.1.3 Solid-phase microextraction

SPME constitutes one of the most widely used sample preparation techniques due to its inherent advantages such as robustness, simplicity, reusability, and reduction of extraction time and solvent consumption [50]. This approach is based on the sorption of the target analytes onto the sorbent-coated fiber [36]. In this respect, SPME can be applied in two modes, direct immersion (DI)−SPME and headspace (HS)−SPME, and both have been tested using different coating materials, including commercial materials such as polydimethylsiloxane (PDMS), polyacrylate (PA), and PAN, or even new materials such as nanoparticles (NPs), carbon-based materials, and MOFs [36,51]. This last group of materials has been applied in a great number of SPME applications due to their large surface areas and stable and homogeneous porosities, as well as their good thermal stabilities and low amounts required to achieve high extraction efficiencies for both polar and nonpolar compounds, good reproducibility, high sensitivity, and acceptable reusability [36,52] (see Table 9.3).

As an example, Kong et al. [55] evaluated the performance of ZIF-8 fibers synthesized by three different methods, including solvothermal, stirring, and ball-milling methods, as coating materials for the SPME of 16 PAHs [i.e., naphthalene (Nap), acenaphthene (Ace), acenaphthylene (Acy), fluorene (Flu), phenanthrene (Phe), anthracene (Ant), fluoranthene (Fla), pyrene (Pyr), benzo[a]anthracene (BaA), chrysene (Chr), benzo[b]fluoranthene (BbF), benzo[k]fluoranthene (BkF), benzo[a]pyrene (BaP), dibenzo[a,h]anthracene (DahA), benzo[g,h,i]perylene (Bghip), and indeno[1,2,3-c,d]pyrene (IcdP)] and 11 nitro PAHs [i.e., 2-nitronaphthalene (2-nNap), 2-nitrobiphenyl

(2-NB), 5-nitroacenaphthene (5-nAce), 2-nitrofluorene (2-nFlu), 9-nitroanthracene (9-nAnt), 9-nitrophenanthrene (9-nPhe), 1-nitropyrene (1-nPyr), 2-nitrofluoranthene (2-nFla), 3-nitrofluoranthene (3-nFla), 2,7-dinitrofluorene (2,7-nFlu), and 6-nitrochrysene (6-nChr)] in environmental waters (i.e., tap water, surface water, and wastewater), followed by GC-single quadrupole (Q)-MS analysis. Authors investigated the performance of the materials obtained from the different synthetic procedures in both DI and HS modes. As can be seen in Fig. 9.2, the studies demonstrated that the ZIF-8 solvothermal MOF gave rise to the best extraction capacity for most of the target compounds using DI−SPME, especially for compounds with high rings. In addition, the authors proposed a possible extraction mechanism of the ZIF-8 fiber based on the high hydrophobicity of the studied analytes, which resulted to be an advantage for their transfer from the aqueous phase to the fibers, as well as on their smaller molecular lengths and volume than the pore size of the prepared material, which allowed their penetration into the ZIF-8 channel. Moreover, hydrophobic, electrostatic, and hydrogen-bonding interactions as well as π−π stacking interactions between aromatic rings of target compounds and ZIF-8 were also considered. Finally, under the optimized conditions, the analytical method was validated obtaining recovery values and limits of quantification (LOQs) in the ranges 66%−105% and 0.3−27 ng L^{-1}, respectively, and applied to the analysis of real water samples, including tap water, surface water, and wastewater.

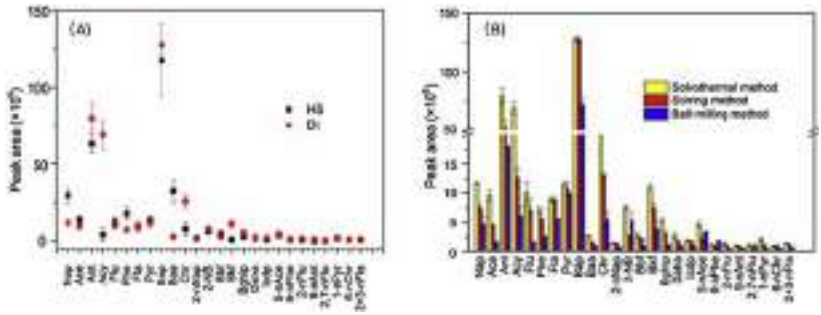

FIGURE 9.2 Graphical representation of the extraction capacity 16 PAHs and 11 NPAHs at 2 μg L^{-1} by (A) different modes of SPME and (B) different synthetic procedures. (DI mode: pH value: 6.0, without salt addition, extraction time: 45 min, extraction temperature: 35°C, desorption temperature: 260°C, and desorption time: 5 min; HS mode: pH value: 6.0, without salt addition, extraction time: 45 min, extraction temperature: 85°C, desorption temperature: 260°C, and desorption time: 5 min). DI, Direct immersion; *NPAHs*, nitro polycyclic aromatic hydrocarbons; *PAH*, polycyclic aromatic hydrocarbons; *SPME*, solid-phase microextraction. *Reprinted from Kong J, Zhu F, Huang W, He H, Hu J, Sun C, et al. Sol−gel based metal-organic framework zeolite imidazolate framework-8 fibers for solid-phase microextraction of nitro polycyclic aromatic hydrocarbons and polycyclic aromatic hydrocarbons in water samples. J Chromatogr A 2019;1603:92−101 [55] with permission from Elsevier.*

As previously indicated, the structure of MOFs can be easily modified by modification of their structure or through their combination with other materials in order to improve their chemical stability and promote their application in the field of sample preparation [50]. In this respect, one of the most relevant modifications of MOFs is their combination with m-NPs, since MMOFs integrate both characteristics of MOFs and m-NPs [29,58]. As an example, Mirzajani et al. [54] developed capillary glass tubes coated with a nanocomposite material based on Fe_3O_4 m-NPs and Cu_3[1,3,5-benzenetricarboxylate (BTC)]$_2$ MOF for the DI−SPME of four nonsteroidal antiinflammatory drugs (NSAIDs) in biological fluids and tablet formulation samples, followed by their determination by HPLC−UV. The authors investigated the lifetime of the SPME fiber coating material through different experiments, finding that the nanocomposite could be used up to 100−110 runs without reducing its extraction efficiency. Besides, the study also showed the high chemical stability of the material in acidic, alkaline, and organic solvent environments. The SPME procedure was optimized using a step-by-step strategy for desorption conditions (i.e., type, volume, and pH of desorption solvent and desorption time) and a Box−Behnken design for adsorption conditions (i.e., pH of sample solution, extraction time, salt concentration, and stirring rate) in order to establish the experimental conditions that gave rise to the maximum extraction efficiency. The best results for the adsorption step were as follows: pH sample solution of 3.5, extraction time of 35 min, NaCl 0% (w/v), and stirring rate 600 r.p.m., while for the desorption step the highest recovery values were achieved using 300 μL of ACN/water (6/4, v/v) at pH 8. Finally, the methodology was validated in human plasma, serum, urine, and tablet samples, obtaining recovery values and LOQs in the ranges 94%−102% and 0.12−0.18 μg L^{-1}, respectively.

As can be noticed in the examples described previously, as well as from those showed in Table 9.3, the application of SPME using MOFs as coating materials has attracted attention in the field of sample preparation for the analysis of, mainly, organic compounds in different areas, including food [53,56,57], environmental [55], and biological samples [54], since it provides high extraction efficiency and good selectivity, as well as low LODs for target analytes [36].

9.3.1.4 Matrix solid-phase dispersion

Matrix solid-phase dispersion (MSPD) was introduced to avoid problems related to solid and semisolid samples processing. It usually involves the use of inert solid materials, as, for example, sand and diatomaceous earth, which ensure the complete disruption of the matrix [59]. However, other conventional SPE sorbents, such as alumina, silica, Florisil, C_8, or C_{18}, have also been applied to improve the selectivity of the procedure, as well as to simultaneously perform the extraction and the cleanup steps [59]. In recent years,

new sorbent materials, such as MOFs, have been used in MSPD applications for the analysis, mainly, of organic compounds in food [60,62–64] and environmental samples [61] (See Table 9.4).

As an example, Santos-Barreto et al. [63] synthesized and characterized an MOF based on lanthanum ions and dipicolinic acid (DPA) linkers and employed it as dispersion sorbent in the MSPD procedure for the extraction of seven pesticides, including atrazine, bifenthrin, bromuconazole, clofentezine, fenbuconazole, flumetralin, procymidone, and pirimicarb, from fresh peppers, followed by GC–MS analysis. The authors used a factorial experimental design for the optimization of the MSPD extraction procedure parameters, which included the type and volume of elution solvent, matrix mass, matrix:sorbent ratio, and the type of sorbent for cleanup. The best results obtained for the fixed mass of 350 mg of $[(La_{0.9}Sm_{0.1})_2(DPA)_3(H_2O)_3]_\infty$ were 500 mg of the matrix, elution with 10 mL dichloromethane (DCM), and silica for cleanup. The analytical methodology was validated obtaining recovery values in the range 48%–135%, which were similar to those previously reported in the literature for the same group of compounds and matrix using commercial materials in the extraction procedures, and LOQs between 50 and 200 $\mu g\ kg^{-1}$. Finally, the MSPD–GC–MS method was applied to the analysis of six samples. Results showed that pesticides concentrations were below the LOQ even though the samples were produced using conventional agriculture techniques.

Similarly, Liang et al. [60] proposed a method for the analysis of three pyrethroid pesticides in wheat by an MSPD extraction based on the use of an Fe-based MOF molecularly imprinted polymer (MIP) as dispersion sorbent followed by GC–MS/MS analysis. Isothermal, kinetics, thermodynamics, and selective binding experiments were carried out in order to demonstrate that the introduction of the MIP in the dispersion sorbent structure gave rise to higher extraction efficiency, decreased adsorption time, and involved lower organic solvent consumption compared to the use of Fe-based MOF-nonimprinted polymer. The MSPD procedure was optimized following a step-by-step strategy in which the sample pH, dispersant/sample ratio, dispersion time, washing solvent, and elution solvent were the parameters investigated. Under the optimized conditions, 0.24 g of wheat samples and 0.36 g of MOFs–MIPs were blended for 10 minutes and transferred to a 5-mL syringe, to which 2.0 mL of the washing solvent (ACN/water, 2/8, v/v) was added to remove the impurities, and then 3.0 mL of the eluent (acetic acid (HOAc)/ACN, 5/95, v/v) was added to carry out the elution of the target analytes. The eluent was dried using nitrogen and reconstituted with *n*-hexane prior to GC–MS/MS analysis. Finally, the method was validated obtaining recovery values and LODs in the ranges 96%–109% and 1.8–2.8 $\mu g\ kg^{-1}$, respectively, and applied to the analysis of six wheat samples.

9.3.1.5 Stir bar sorptive extraction

One of the most commonly applied sorbent-based extraction techniques is the stir bar sorptive extraction (SBSE) procedure. This technique is generally performed by the use of a stir bar in contact with the sample for the extraction of compounds in liquid or gas phase. The sample is stirred and then, the analytes adsorbed on the stir bar coating are desorbed by thermal desorption (TD) or liquid desorption. This second approach is most largely applied in recent publications, due to the development of new nanomaterial-based coating that have low temperature resistance required in TD mode [65]. As can be seen in Table 9.5 in which some examples of the most recent publications are compiled, MOFs have been employed as sorbents in SBSE procedures for the analysis of food [66,67,69,70], biological [67], and environmental [68] samples, and, mainly, for the extraction of organic compounds. One of the limitations of SBSE is its use for the extraction of polar and thermolabile compounds. Nevertheless, the development of different coatings has allowed the expansion of the technique to a wide range of compounds with different properties [51,71]. In this regard, MOFs can be modified with different ligands that improve their selectivity and applicability, which added to their large surface area and porosity, and make them appropriate for SBSE applications [69].

An example that shows the potential of these materials for SBSE is the work carried out by Lin et al. [70] who prepared a novel sorbent based on aptamer (Apt)-functionalized MOF-5 for the extraction of two polychlorinated biphenyls (PCBs), 2,3′,5,5′-tetrachlorobiphenyl (PCB72) and 2′,3′,4′,5,5′-pentachlorobiphenyl (PCB106) from fish samples, prior to GC−MS analysis. The Apt (simple chain of nucleic acids) was 5′-CAC TCG GAC CCC ATT CTC CTT CCA TCC CTC ATC CGT CCAC-3′. The Apt-functionalized stir bar coating overcomes time consumption and complex preparation of MOFs' synthesis and functionalization by the use of electrodeposition technique on a stainless-steel wire. In this case, the cation, poly-(diallyldimethylammonium chloride), was modified on MOF to attract the negative charge of the Apt. The optimized SBSE procedure consisted of the application of the coated stir bar into the sample solution and incubated for 1 hour at room temperature. The fiber was rinsed twice with phosphate-buffered solution (PBS) to remove undesirable species. To desorb the analytes the stir bar was put into 5 mL of methylene chloride-pH 3/glycine-HCl buffer (1/10, v/v) and stirred at 500 r.p.m. The combination of both solvents allowed the extraction of PCBs, changing the structure of the Apt. The final extract was dried under nitrogen gas, redissolved in 20 μL of *n*-hexane, and injected into the GC−MS system for the determination of PCBs. The method provided recovery values and LODs of 89%−97% and 0.15−0.22 ng kg^{-1}, respectively. In addition, the selectivity of the synthesized SBSE coating was evaluated with the addition of other PCBs, as well as chlorobenzene and

parathion-methyl as possible interference compounds. The results showed that the recovery values of the PCBs determined in this work were higher than those of the other compounds, less than 15% for the other PCBs and 1% for chlorobenzene and parathion-methyl. The extraction capacity of the Apt-MOF coating was also tested by comparing the material with Apt fiber without MOF, showing that the presence of MOF could increase the adsorption capacity and ability due to its higher surface area, as it is shown in Fig. 9.3. Moreover, Apt-MOF fiber was compared with commercial SBSE fibers, including PA, PDMS, PDMS/divinylbenzene (DVB) fibers, and indicated that the synthesized fiber not only has better enrichment factors than commercial fibers on complex samples but also has a better cleanup performance resulting in less chromatographic interferences.

Other modification of MOFs was proposed by Khoobi et al. [67], who prepared a nanoporous Zn−Al-layered double hydroxide (LDH)@ZIF-8 composite by in situ growth of ZIF-8 on the surface of the LDH. The nanocomposite was applied in SBSE for the extraction of benzylpenicillin (penicillin G) from human blood plasma, urine and milk prior to determination by HPLC−UV. Recovery values in the range 95%−110% and an LOD of 0.05 $\mu g\ L^{-1}$ were obtained. In order to study the different variables that can affect the extraction procedure, a Placket−Bumman design was carried out

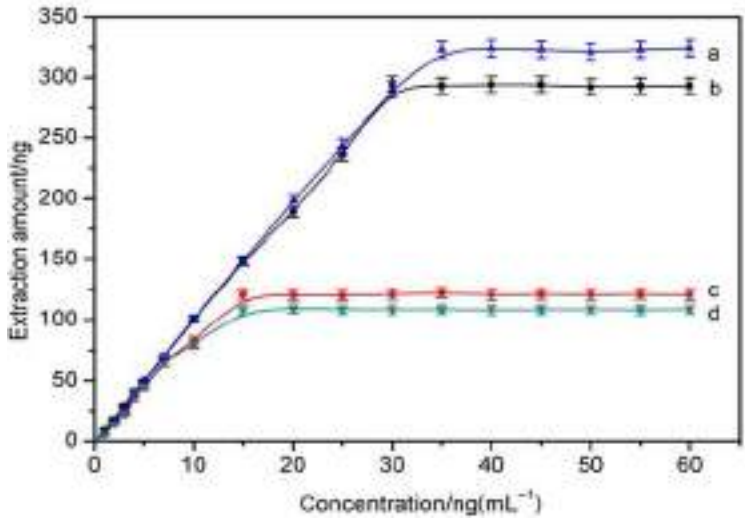

FIGURE 9.3 Extraction capacity of Apt-MOF (a for PCB106, b for PCB72) and Apt (without MOF, c for PCB106, d for PCB72). *MOFs*, Metal-organic frameworks. *Redrawn from Lin S, Gan N, Zhang J, Qiao L, Chen Y, Cao Y. Aptamer-functionalized stir bar sorptive extraction coupled with gas chromatography−mass spectrometry for selective enrichment and determination of polychlorinated biphenyls in fish samples. Talanta 2016;149:266−74 with permission from Elsevier.*

to identify critical independent variables, and then a Box–Behnken model assisted by response surface methodology was used for optimizing the significant factors. In addition, the extraction efficiency of modified and bare stirs bars was evaluated by comparing anodized Al/Zn–Al–LDH/ZIF-8, anodized Al/Zn–Al–LDH, anodized Al, and bare Al stir bars. The results demonstrated that the first one showed the best extraction efficiency due to the capacity of the coating to establish hydrogen bonds, electrostatic and hydrophobic interactions, and π–π-stacking, and also by the pore size and large surface area of the nanomaterial.

9.3.2 Recent applications in chromatography

Although the application of MOFs in chromatography and electrophoretic separations, as stationary or pseudo-stationary phases, is reduced compared with their use as sorbents in sample preparation procedures, some works in which MOFs are employed with this aim can be found in the literature, as shown in Table 9.6. Apart from their general properties in terms of surface area, efficiency, selectivity, or stability, the interest of the application of these kinds of materials in this area is especially related to their high and versatile porosity, their easy functionalization, or the ease to link them to other surfaces, as well as the possibility to synthesize chiral center MOFs to performance chiral separations [82].

9.3.2.1 Gas chromatography

Among the different nanomaterials used to date as stationary phases for GC separations, MOFs have been the most widely used [31]. The main reasons are the high thermal stability and stable framework, as well as their large surface area and nano- to micro-sized porosity [31,83]. Likewise, the synthesis of chiral MOFs has allowed the performance of chiral separations enabling the separations of enantiomers, which is a very important aspect in the field of pharmacology [31]. As an example, Yang et al. [74] synthesized a porous chiral MOF consisted of clusters of Cd and L-(−)-thiazolidine-4-carboxylic acid (LTP), $[Cd(LTP)2]_n$ and incorporated it into a permethylated β-cyclodextrin (β-CD) column to performance a GC separation of 14 chiral compounds, including (±)-limonene, (±)-dihydrocarvyl acetate, (±)-citronellal, (±)-rose oxide, (±)-1-phenylethylamine, (±)-1-cyclohexylamine, (±)-1-phenylethanol, (±)-menthol, (±)-2-hexanol, (±)-2-amino-1-butanol, (±)-2-methyl-1-butanol, (±)-2-phenyl-1-propanol, DL-alanine, and DL-arginine. To demonstrate the capacity of the prepared column, its performance was compared with a chiral $[Cd(LTP)_2]_n$ column, and a permethylated β-CD- and NaCl-based columns. Whereas the column that only contained the chiral MOF only separated three isomers, and the one containing NaCl could only separate six enantiomers, the stationary phase synthesized in this

TABLE 9.6 Recent applications of metal-organic frameworks (MOFs) as stationary and pseudo-stationary phases in chromatography and electrophoretic separations.

Analytes	Matrix	Nanomaterial	Phase characteristics	Mobile phase (flow rate)	Determination technique	LOD	Comments	Reference
Gas chromatography								
H_2 and D_2	He-H_2-D_2 mixture	CPL-1@γ-Al_2O_3 and $MnCl_2$@CPL-1@γ- Al_2O_3	Stainless steel column (1.0 m × 2.0 mm i.d.)	–	GC–TCD	–	– GDX-102 commercial column was used as reference column for H_2/D_2 separation – He was used as carrier gas – The separation was performed under liquid nitrogen temperature	[72]
Heptane and octane isomers, *cis*/*trans*-dichloropropene, *cis*/*trans*-naphthane, substituted Nap and benzene isomers	Commercial reagents of analytical grade	Graphene@ZIF-8	Capillary (10 m × 0.25 mm i.d.)	–	GC–FID	-	– N_2 was used as carrier gas – Graphene@ZIF-8, neat graphene, neat ZIF-8, and HP-5MS capillary columns were compared – Minor isomer impurities in commercial reagent samples of analytical grade were determined to test the feasibility of the column	[73]
14 Chiral compounds	-	$[Cd(LTP)_2]_n$ and permethylated β-CD	Capillary (20 m × 0.25 mm i.d.)	-	GC–FID	–	– Chiral $[Cd(LTP)_2]$, and permethylated β-cyclodextrin and sodium chloride capillary columns were also tested	[74]

(*Continued*)

TABLE 9.6 (Continued)

Analytes	Matrix	Nanomaterial	Phase characteristics	Mobile phase (flow rate)	Determination technique	LOD	Comments	Reference
Liquid chromatography								
Xylene isomers and ethylbenzene	-	1. Salen-based COF 2. Metallosalen-based COF	SiO_2 column (250 mm × 2.1 mm i.d., particle size 0.3 and 5 μm for COFs and SiO_2, respectively)	Hexane/DCM (95/5, v/v) (i) (0.5 mL min^{-1}) (ii) (0.25 mL min^{-1})	HPLC–UV	–	– Zn(salen)- and Zn (metallosalen)-based COFs were also tested	[75]
PAHs, phenols, anilines, NSAIDs, and benzothiophenes	–	Poly-(TpPa-1-MA-*co*-EDMA)	Stainless-steel monolithic column (50 mm × 4.6 mm i.d.)	ACN/H_2O (1 mL min^{-1})	HPLC–UV	–	– C_{18} silica gel was used as reference packed column – Poly-(St-*co*-DVB) and poly-(MMA-*co*-EDMA) monolithic columns were also prepared and compared – Different mobile phase compositions were used	[76]
(±)-Methyl phenyl sulfoxide	–	[Zn_2(BDC)(L-lactic acid)(DMF)](DMF)	Poly-(4-VP-*co*-EDMA) capillary monolithic column (30 cm × 100 μm i.d.)	Hexane/IPA (97/3, v/v) (1 μL min^{-1})	Nano-LC–UV	–	– Poly-(4-VP-*co*-EDMA) and the chiral-MOF-based monolithic columns were compared	[77]
Electrophoretic separations								
6 Cationic and 4 neutral analytes	Urine	ZIF-8	OT-fused silica capillary (30 cm × 75 μm i.d.)	–	CEC–DAD	0.26–0.52 mg L^{-1}	– Separation was performed using 15% (v/v) MeOH in 20 nM NaOAc/HOAc buffer solution – Recovery values in the range 92%–109% were achieved	[78]

3 Cephalosporin antibiotics	Lake water	APTES@[Cu(L-(−)-malic acid)(bpy)] · H_2O	OT-capillary (21 cm × 75 μm i.d.)	–	CEC–DAD	0.1 mg L^{-1}	– Separation was performed using 10% (v/v) ACN in 40 nM NaOAc/HOAc buffer solution and 7.5 nM SDS – Results were compared with those from common capillary column – Recovery values in the range 88%–106% were achieved	[79]
Acidic, neutral, and alkaline compounds	–	MOF-180	OT-capillary (25 cm × 50 μm i.d.)	–	CEC–DAD	-	– Separation was performed using 10% (v/v) MeOH in 10 nM Na_2HPO_4 – MOF-180 and MOF-199 capillary columns were compared	[80]
Acidic, neutral, and alkaline substituted benzenes	–	MOF-5	Carboxyl-terminated OT-capillary (22.5 cm × 50 μm i.d.)	–	CEC–DAD	-	– APTES and glutaraldehyde were used as covalent linkers – Separation was performed using 10 nM Na_2HPO_4	[81]

ACN, acetonitrile; *APTES*, 3-aminopropyltriethoxysilane; *BDC*, 1,4-benzenedicarboxylate; *bpy*, 4,4′-bipyridyl; *CEC*, capillary electrochromatography; *COF*, covalent organic framework; *CPL-1*, {[Cu^2(pyrazine-2,3-dicarboxylate)2(pyrazine)] · $2H_2O$}$_n$; *DAD*, diode array detector; *DCM*, dichloromethane; *DMF*, dimethylformamide; *DVB*, divinylbenzene; *EDMA*, ethylene dimethacrylate; *FID*, flame ionization detector; *GC*, gas chromatography; *HOAc*, acetic acid; *HPLC*, high-performance liquid chromatography; *IPA*, isopropanol; *LC*, liquid chromatography; *LOD*, limit of detection; *LTP*, L-(−)-thiazolidine-4-carboxylic acid; *MA*, methacrylate; *MeOH*, methanol; *MMA*, methyl methacrylate; *NaOAc*, sodium acetate; *Nap*, naphthalene; *NSAID*, nonsteroidal antiinflammatory drug; *OT*, open tubular; *PA-1*, 1,4-phenylenediamine; *PAH*, polycyclic aromatic hydrocarbon; *salen*, *N*,*N*′-bis(salicylidene) ethylenediamine; *SDS*, sodium dodecyl sulfate; *St*, styrene; *TCD*, thermal conductivity detector; *Tp*, 1,3,5-triformylphloroglucinol; *UV*, ultraviolet; *VP*, 4-vinylpyridine; *ZIF*, zeolitic imidazolate framework; *β-CD*, β-cyclodextrin.

work perfectly separated all 14 chiral compounds. This improvement is related to the inherent characteristics of the MOF employed (helical channels and 3D-supramolecular reticular structure) combined with β-CD, which result in a superior chiral microenvironment between the chiral channel framework and the conformational forms of the racemates.

The combination of nanomaterials has also opened a new window in the field of chromatographic separations, taking advantage of the properties of each component to form an improved material. In this sense, Yang et al. [73] developed a stationary phase composed by graphene@ZIF-8 composite for capillary GC−flame ionization detector separation of branched alkane isomers (including heptane isomers such as 2,2,3-trimethylbutane, 2,3-dimethylpentane and heptane, and octane isomers such as 2,2,4-trimethylpentane, 2,2-dimethylhexane, 3-methylheptane and octane) and geometric *cis*/*trans*-isomers, including 1,3-dichloropropene and naphthene, and aromatic positional isomers of substituted Nap (1-Nap and 2-Nap; 1,2-, 1,3-, 2,3-, and 2,6-dimethyl-Nap; and 1- and 2-naphthol) and substituted benzene (tert-, iso-, and *n*-butylbenzene; *m*-, *p*- and *o*-iso-propyltoluene; iso- and *n*-propylbenzene; 1,3,5-, 1,2,4-, and 1,2,3-trichlorobenzene; *o*-, *m*-, and *p*-nitrotoluene; and 2,3-, 2,4-, 2,6-, 3,4-, and 3,5-dimethylphenol). Compared with graphene or ZIF-8 capillary columns in the separation of iso-propyltoluene and nitrotoluene isomer mixtures, graphene@ZIF-8 column provided better separation due to its increased surface area enhancing its interaction with the compounds, as can be seen in Fig. 9.4. In addition, the separation performance of the graphene@ZIF-8 column was compared with the widely used commercial HP-5MS capillary column for the separation of a complex mixture of 18 analytes, including iso-butylbenzene, *m*-dichlorobenzene, bromoheptane, *m*-bromotoluene, *n*-undecane, methyl octanoate, 1,6-dichlorohexane, ethyl benzoate, 1,2,4-trichlorobenzene, 1,2,3-trichloro-benzene, *n*-tridecane, 1-decanol, *n*-tetradecane, 1-undecanol, methyl dodecanoate, acenaphthylene, diethyl phthalate, and fluorine. The results showed that whereas the synthesized column separated well almost all analytes with resolution values higher than 1.21, with the HP−5MS column, four pairs of analytes were overlapped. To evaluate the feasibility of the column to carry out the separation of the analytes in real samples, commercial reagents of analytical grade were analyzed for the determination of minor isomer impurities, such as of tert- and iso-butylbenzene, *o*- and *m*-nitrotoluene, 1,2,4-trichlorobenzene, *cis*/*trans*-naphthane, and 1,2,4-trimethylbenzene. Results showed good agreement with its labeled purity and indicated the viability of the developed method for the determination of isomers impurities in real samples.

9.3.2.2 Liquid chromatography

As in GC, the use of MOFs as stationary phases in liquid chromatography (LC) has allowed the separation of positional isomers and chiral compounds

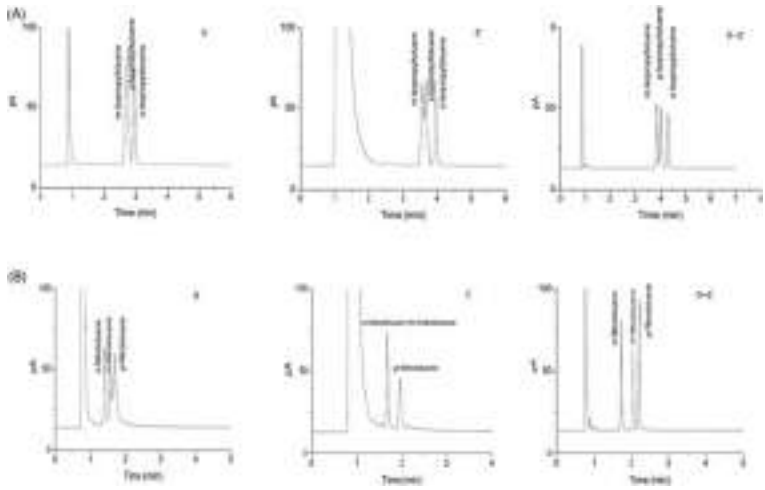

FIGURE 9.4 Comparison of graphene@ZIF-8 (G−Z) capillary column, with the neat graphene (G) and ZIF-8 (Z) columns on their separation performance for isomer mixtures of (A) isopropyltoluenes at 50°C and (B) nitrotoluenes at 100°C. *Reprinted from Yang X, Li C, Qi M, Qu L. Graphene-ZIF8 composite material as stationary phase for high-resolution gas chromatographic separations of aliphatic and aromatic isomers. J Chromatogr A 2016;1460:173−80 with permission from Elsevier.*

that cannot be achieved with conventional phases such as C_8 or C_{18} [31]. Huang et al. [75] leveraged the unique properties of COFs, in terms of solvent stability and surface area, to prepare 3D microporous *N*,*N*′-bis(salicylidene)ethylenediamine (salen)- and Zn(salen)-based COFs through Schiff-base condensation of ethanediamine with tetrahedral tetra(salicylaldehyde)-silane or -methane derivatives with or without Zn ions, for the HPLC separation of xylene isomers and ethylbenzene. The synthesized COFs presented great porosity (seven-fold interpenetrated diamonded open framework with about 7.8 Å wide tubular channels), high thermal stability, and chemical resistance. The two columns were able to baseline separate xylene isomers and ethylbenzene with good efficiency, repeatability, and provided high resolution and selectivity. In addition, when these columns were compared with Zn-based columns, the latter did not provide a good resolution. The incorporation of Zn ions improves the intermolecular interactions between C_8 aromatic compounds and Zn(salen)-COFs, which probably causes very similar adsorptions of the isomers.

MOFs-based monoliths have been widely explored as stationary phase materials for HPLC applications through the combination of MOFs characteristics, such as pore size and volume, high surface area, tunability, or controllable shape, with the permeability of organic monoliths [84]. As an example, Wang et al. [77] developed a monolithic [Zn_2(1,4-benzenedicarboxylate (BDC)) (L-lactic acid) dimethylformamide (DMF)] for the

enantioseparation of (±)-methyl phenyl sulfoxide by nano-LC−UV. The chiral MOF was prepared using zinc nitrate, 1,4-benzenedicarboxylic acid, and L-lactic acid, and it was incorporated into a poly(4-vinylpyridine (VP)-*co*-ethylene dimethacrylate (EDMA)). The prepared column combined the selectivity of the chiral MOF with the properties of the monolith, achieving baseline separations of the enantiomers, whereas using the parent monolith phase, the separation was not observed.

In the same way, Liu et al. [76] reported the preparation of methacrylate (MA)-bonded COF monolithic columns [poly-(Tp-1,4-phenylenediamine (Pa-1)-MA-*co*-EDMA)] for the HPLC separation of small molecules such as PAHs, phenols, anilines, NSAIDs, and benzothiophenes. With this strategy the authors managed to avoid the general problems that limit the application of COFs synthesized by traditional methods as HPLC stationary phases, such as irregular shape, broad size distribution, or submicrometer size [26]. The prepared column exhibited high efficiency and good resolution due to the interactions between TpPa-1 COF and the small molecules.

9.3.2.3 *Electrophoretic separations*

In the case of electrophoresis or capillary electrophoresis, the use of MOFs in these techniques has come up with a clear improvement of efficiency, selectivity, and rapidity of the separations. Among the different approaches in which MOFs have been employed as stationary or pseudo-stationary phases for electrophoretic separations, including electrokinetic chromatography, the most recent applications of MOFs in this field have been mainly in capillary electrochromatography (CEC). CEC combines the characteristics of HPLC and capillary electrophoresis obtaining high selectivity and efficiency in the separation [85]. As shown in Table 9.6, open tubular (OT)−CEC is the most common mode applied for CEC performance. This technique exhibits low back pressure and easy coating modification, which favor the selectivity of separation [81]. However, OT capillaries usually present a relative low column capacity and phase ratio because of the small surface area of the coatings [80]. In this context, the inclusion of MOFs, as porous material with high surface area, allows overcoming such limitations [80].

In this regard, Pan et al. [78] developed a one-dimensional CEC−DAD using a synthesized ZIF-8-coated OT-capillary column for the simultaneous separation and detection of six cationic monoamine neurotransmitters and analogs, and four neutral flavonoids compounds in urine, in a single run. The results obtained demonstrated the capacity of the material and the good sensitivity of the developed method with LODs in the order of few mg L^{-1}. The main advantage of the methodology is the analysis of different species by CEC without the use of a switching buffer solution, thanks to the interactions established between cationic functional groups and the imidazolium group in

ZIF-8 MOF, as well as the hydrophobic interaction between the neutral compounds and the microporous coating material.

Another work that should be highlighted in this area is the one carried out by Wang et al. [79] who performed a 3-aminopropyltriethoxysilane (APTES)-functionalized [Cu(L-(−)-malic acid)(4,4′-bipyridyl (bpy))] · H_2O MOF for the determination of three different cephalosporin formulations, such as ceftiofur, cefixime, and cefapirin, in Kunming Lake water (Beijing) by CEC with DAD. The developed method was compared with capillary zone electrophoresis, micellar electrokinetic chromatography, and UHPLC methods, obtaining lower LODs for the group of cephalosporins studied, and recovery values in the range 88%−106%. In addition, the MOF-coated column showed good separation, stability, and reproducibility. The synthesized MOF, using the L-(−)-malic acid ligand, provided more reactions sites for cephalosporins due to the chiral structure of this compound.

An interesting and thorough study of the performance of MOF-based separation was developed by Tang et al. [80]. In this case, authors carried out an in situ preparation of MOF-180 on the inner wall of an OT-capillary column for CEC−DAD. The MOF-180 exhibited exceptional porosity, specific recognition of tested compounds, and size selectivity when it was compared with MOF-199-modified capillary column. As can be seen in Fig. 9.5, for MOF-199, toluene and Nap peaks are overlapped, whereas MOF-180 allowed the complete separation of toluene, Nap, and 4-methylbiphenyl. To elucidate this fact a thorough study was carried out based on the size of analytes and pores of both MOFs, as well as the hydrophobic interactions between the compounds and the stationary phase. The study revealed that in MOF-199, toluene and Nap can freely pass through the channels but their slight different hydrophobicity as well as the weaker hydrophobic interactions with the stationary phase than the one shown by MOF-180 brings about the coelution of the two compounds. The larger pore size and the presence of a large number of specific sites, such as ethyne groups and benzene rings, made that MOF-180 has stronger hydrophobic interactions. On the contrary, despite that the higher size of 4-methylbiphenyl should lead to be the first to elute, the strong π−π interaction shown makes that 4-methylbiphenyl eluted as the last one. The developed Zn-based MOF stationary phase demonstrated good separation for acidic (phthalic acid, aspirin, and benzoic acid), basic (β-phenylethylamine, *N*,*N*-dimethylaniline, aniline), and neutral compounds (three peptides, including Gly−L-Phe, L-Phe−Gly−Gly, and L-Phe−Gly) showing a clear improvement of the separation performance respect to the application of bare OT-column. The reproducibility of the column as well as the CEC method performance was evaluated for mixtures of alkylbenzenes (methylbenzene, ethylbenzene, and *n*-propylbenzene) and chlorobenzenes (chlorobenzene, odichlorobenzene, and 1,2,4-trichlorobenzene), obtaining good repeatability, reproducibility, and stability in terms of relative standard

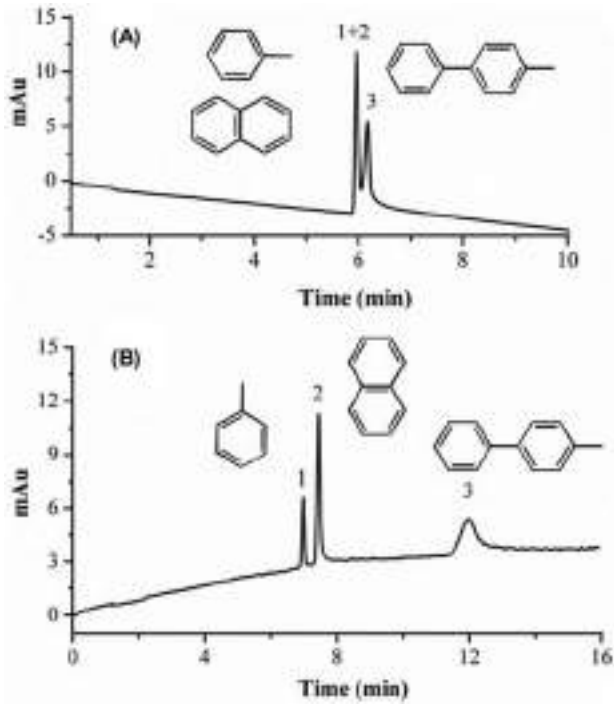

FIGURE 9.5 Comparison of the separation performance between (A) MOF-199- and (B) MOF-180-modified capillary column. Peak identification: (1) toluene, (2) Nap, and (3) 4-methylbiphenyl. Mobile phase: 10 mM PBS (pH 7) with 40% (v/v) MeOH. Injection: 10 mbar × 5 s. Voltage: 15 Kv. UV detection at 214 nm. Temperature: 25°C. Capillary column: 25/33.5 cm (effective length/total length) × 50 μm i.d. *Reprinted from Tang P, Bao T, Chen Z. Novel Zn-based MOFs stationary phase with large pores for capillary electrochromatography. Electrophoresis 2016;37:2181–9 with permission from Wiley.*

deviations (RSDs) of retention time, peak area, and width, as well as run-to-run, day-to-day, and column-to-column RSDs.

9.3.3 Recent applications in sensor development

The tunable MOFs' structures and their intrinsic properties make these nanomaterials excellent candidates for sensing applications [86]. Depending on their metallic center and the organic ligands, in terms of type and number, their chemical, physical, and even biological properties can change [87]. Based on the fact that any change of MOFs properties can produce a signal modification in the sensor response, they have been applied in electrochemical and luminescent sensors, including fluorescent and colorimetric sensors [86,88,89]. Herein, recent applications of MOFs for sensing are listed in Table 9.7.

TABLE 9.7 Recent applications of metal-organic frameworks (MOFs) in detection systems.

Analytes	Matrix	Nanomaterial	Determination technique	Recovery (%)	LOD	Comments	Reference
Electrochemical methods							
Cd(II), Pb(II) and Cu(II)	Tap water (–)	rGO/Fc-UiO-66-NH_2 (10.5 μg)	DPASV	91–105	0.6–8.5 nM	– One mg of rGO and 20 mg of Fc-UiO-66-NH_2 were dispersed in 20 mL of ultrapure water. 10 μL was used for preparation of modified electrodes – GCE, SCE, and platinum electrode, were used as working, reference, and counter electrodes, respectively – A selectivity study was carried out using Zn(II), Al(III), Ca(II), Ni(II), Mn (VII), Zr(IV), Na(I), and K(I), as interfering metal ions	[90]

(*Continued*)

TABLE 9.7 (Continued)

Analytes	Matrix	Nanomaterial	Determination technique	Recovery (%)	LOD	Comments	Reference
						– The method was applied to the analysis of real tap water samples	
XA, HXA, BPA and *p*-CP	Plasma and urine (200 μL), shopping receipt (1 g) and wastewater (5 mL)	Cu-BTC@graphene NSs (10 μg)	DPV	–	1.1–7.3 μg L^{-1}	– GCE, SCE, and platinum electrode were used as working, reference, and counter electrodes, respectively – A selectivity study was carried out using glucose, dopamine, ascorbic acid, uric acid, or L-cysteine as XA and HXA interferences, Cd(II), Pb(II), hydroquinone, catechol, *p*-nitrophenol, and phenol as BPA and *p*-CP interferences – For real sample analysis, plasma and urine samples were high-speed centrifuged, and	[91]

						200 μL of plasma or urine supernatants were added to 5 mL of PBS; for shopping receipt 1 g of receipt sample was pretreated with 20 mL of MeOH, and 200 μL of extract added to 5 mL of PBS; 5 mL of wastewater was mixed with 5 mL of PBS – XA and HXA were measured in biological samples, BPA in receipt and *p*-CP in wastewater, and the results were compared with those obtained by HPLC	
Nitrofurazone	Pork liver, crayfish (2.5 g), milk (100 μL), and honey (1 g)	Hollow MIL-101 (20 μg)	DPV	91–107	10 nM	– GCE, SCE, and platinum wire were used as working, reference, and counter electrodes, respectively	[92]

(*Continued*)

TABLE 9.7 (Continued)

Analytes	Matrix	Nanomaterial	Determination technique	Recovery (%)	LOD	Comments	Reference
						– Pork liver or crayfish were pretreated with 10 mL of ACN/water (8/2, v/v). The final extract was redissolved with 1 mL ACN/water (2/80, v/v). Honey samples were dissolved into 10 mL of hot water before measurements. 100 μL sample solution was added into 5 mL of acetate buffer solution – A selectivity study was carried out using Sn(II), Mg(II), Mn(II), Sr(II), Co(II), Ca(II), Cr(III), Zn(II), Pb(II), Ni (II), Al(III), glycine, aspartic acid, urea, ascorbic acid, and glucose, as interfering species	

						– Electrochemical and HPLC–FD real samples results were compared	
Chlorpyrifos	Cucumber, capsicum, and brinjal (10 g)	AChE@ZIF-8 (–)	DPV	94–99	6 ng L^{-1}	– An electrochemical micro analytical device was developed and integrated into a portable potentiostat for CV and DPV measurements – Samples were crushed and centrifuged in PBS. The supernatant was employed for DPV measurements – A selectivity study was carried out using cartap hydrochloride as interference compound	[93]
Vomitoxin and salbutamol	Wine (5 μL) and pork (5 g)	Ab@516-MOFs (10 μg)	EIS	98–102	0.4–0.7 ng L^{-1}	– $Anti_{vomitoxin}$ and $Anti_{salbutamol}$ were employed as antibodies – Gold electrode, Ag/AgCl electrode, and	[94]

(*Continued*)

TABLE 9.7 (Continued)

Analytes	Matrix	Nanomaterial	Determination technique	Recovery (%)	LOD	Comments	Reference
						platinum slide were employed as working, reference, and counter electrodes, respectively – A selectivity study for vomitoxin was carried out using oxytetracycline, doxycycline, kanamycin, ofloxacin, and streptomycin, as interfering agents – A selectivity study of salbutamol was carried out using solutions of salbutamol with or other environmentally relevant constituents – Ab@515-MOF and Ab@516-MOF were compared	

						– Chopped pork samples were pretreated with EtOAc and K_2CO_3, the supernatant was dried and redissolved in MeOH and reconstituted in PBS. 5 μL of the supernatants were used – Rice samples and pork samples were used for recovery study of vomitoxin and salbutamol, respectively	
Electroluminescent/optical methods							
Cl_2, HClO, and ClO^-	Environmental water (5 mL)	Hf-UiO-66-$(NH_2)_2$ (5 mg)	FD	93–112	0.02 μM	– A selectivity study was carried out in the presence of different cationic and anionic possible interferers – The probe could be reused for five cycles	[95]

(*Continued*)

TABLE 9.7 (Continued)

Analytes	Matrix	Nanomaterial	Determination technique	Recovery (%)	LOD	Comments	Reference
						– The stability of the materials was tested in different solvents and pH media – Hf-based MOF portable paper strips were also developed for the on-site sensing of chlorine – The method was applied to the analysis of environmental water samples (tap water and swimming pool water)	
TBHQ	Edible oil (1 mL)	[Sm (DCPP) $(H_2O)_4]_n \cdot 2nH_2O$ (2 mg)	FD	101–103	5.6 μg L^{-1}	– Two grams of oil samples was pretreated with ethanol for the extraction of TBHQ – A selectivity study was carried out in the presence of different cationic possible interferers	[96]

						– The method was applied to the analysis of a soybean oil sample	
Human prolactin	Serum (10 mL)	$_n$[Pr(AIP)(Phen)$Cl_2(DMF)_2(H_2O)_2$] (10 mL)	FD	100–102	0.251 μg L^{-1}	– A selectivity study was carried out in the presence of different hormones and drugs as possible interferers – The method was applied to the analysis of females and males blood real samples	[97]
NMF	Human urine (3 mL)	Eu@MOF-1 (3 mg)	FD	–	0.36 μM	– Water and pH stability of the Eu(III)@MOF-1 were evaluated at different conditions – A selectivity study was carried out in the presence of different urine chemicals – The Eu-based MOF probe could be reused for seven cycles	[98]

(*Continued*)

TABLE 9.7 (Continued)

Analytes	Matrix	Nanomaterial	Determination technique	Recovery (%)	LOD	Comments	Reference
						– The optical sensor was tested in a real human urine sample	
DBP	Beverages and environmental water (–)	Cu-based MOF@Ab_2 (0.5 mg)	UV/Vis	88–103	1.0 μg L^{-1}	– The developed colorimetric immunosensor-based procedure was compared with ELISA – The method was applied to the analysis of liqueur, milk, red wine, and pure and pond water real samples	[99]

Ab, antibody; *Ab_2*, second antibody; *AChE*, acetylcholinesterase enzyme; *ACN*, acetonitrile; *AIP*, 5-aminoisophthalic acid; *BPA*, bisphenol A; *BTC*, 1,3,5-benzenetricarboxylate; *CV*, cyclic voltammetry; *DBP*, dibutyl phthalate; *DCPP*, 3-(2,4-dicarboxylate phenyl)-2-pyridinecarboxylate; *DMF*, dimethylformamide; *DPASV*, differential pulse anodic stripping voltammetry; *DPV*, differential pulse voltammetry; *EIS*, electrochemical impedance spectroscopy; *ELISA*, enzyme-linked immunosorbent assay; *EtOAc*, ethyl acetate; *Fc*, ferrocenecarboxylic acid; *FD*, fluorescence detector; *GCE*, glassy carbon electrode; *HPLC*, high-performance liquid chromatography; *HXA*, hypoxanthine; *LOD*, limit of detection; *MeOH*, methanol; *MIL*, Materials of Institute Lavoisier; *$-NH_2$*, amino-functionalized; *NMF*, *N*-methylformamide; *NS*, nanosheet; *PBS*, phosphate-buffered solution; *p-CP*, *p*-chlorophenol; *Phen*, 1,2-phenylenediamine; *rGO*, reduced graphene oxide; *SCE*, saturated calomel electrode; *TBHQ*, tertiary butylhydroquinone; *UiO*, Universitetet i Oslo; *UV/vis*, ultraviolet/visible; *XA*, xanthine; *ZIF*, zeolitic imidazolate framework.

9.3.3.1 Electrochemical sensors

Electrochemical sensors are based on electrical signal changes produced as a result of chemical reactions between the target compounds and the recognition elements of an electrode surface [100]. In the last years the application of MOFs in electrochemical devices has been scarce because of their insulating or poorly conductive properties. However, with the advance of nanoscience and nanotechnology, different approaches have been carried out to overcome this problem, including structural modifications or (bio)composites fabrication by linking precious metal NPs polymers, biopolymers and biomolecules, or carbon-based materials with MOFs [86,101,102], which can give rise with the synergistic effect of the properties of both materials [103]. The superior electrochemical or electrocatalytic properties of MOFs-based materials can be due to their large surface area and high porosity, which could also provide high selectivity and sensitivity for electrochemical applications [103,104].

In this regard, Liu et al. [94] developed two immunosensors made of aluminum-based MOFs and 4,4′,4″-nitrilotribenzoate (NTB) as linker, for the detection of two antigens, vomitoxin and salbutamol, in wine and pork samples by electrochemical impedance spectroscopy (EIS), reporting LODs of 0.7 and 0.4 ng L^{-1}, and recovery values in the ranges 98%−100% in wine samples, and 100%−102% in pork samples, for vomitoxin and salbutamol, respectively. For electrochemical measurements, a three-electrode system was employed, consisting of a modified gold electrode, an Ag/AgCl electrode (saturated in KCl), and a platinum slide, as working, reference, and counter electrodes, respectively. EIS curves were obtained in 0.5 mM $[Fe(CN)_6]^{3-/4-}$ solution containing 0.1 M KCl. To fabricate the immunosensors, 10 μL of a solution containing MOFs at a concentration of 1 mg mL^{-1} was dropped into clean gold electrodes. After drying the modified electrodes were incubated with solutions of $Anti_{vomitoxin}$ and $Anti_{salbutamol}$ antibodies (Abs), and subsequently rinsed with PBS, and dried for further measurements. In order to compare the biosensing performance of both immunosensors, cyclic voltammetry and EIS measurements of 515- and 516-based MOF immunosensors were carried out. The results suggested that even though 516-MOF was better in terms of water stability, both electrodes exhibited excellent recognition toward the target antigens. In addition, to investigate the selectivity of the immunosensors, two different studies, using interfering compounds or ions, for vomitoxin and salbutamol were tested, through the measurement of the charge-transfer resistance responses of each antigen, given by the charge-transfer kinetics of the $[Fe(CN)_6]^{3-/4-}$ redox system. As a result, the same response was obtained with the individual solution of the target analytes and the solutions containing the interferences, even at a concentration 100-fold or 1000-fold higher for vomitoxin and salbutamol, respectively. These results not only reveal the high sensitivity that the use of

MOFs as biosensing materials provide, but also the great selectivity for these compounds in the presence of other contaminants or environmentally relevant compounds.

Most applications of MOFs in electrochemical systems involve a three-electrode system consisting of a modified working electrode (gold [94] or glassy carbon electrode [90–92]), a reference electrode (saturated calomel electrode (SCE) [90–92] or Ag/AgCl [94]), and an auxiliary platinum electrode [90–92,94]). As an example of this setup, a voltammetric sensor based on hollow MIL-101 was developed by Gan et al. [92] for the detection of nitrofurazone in complex matrices, including pork liver, crayfish, milk, and honey, obtaining a high sensitivity (LOD of 10 nM) and selectivity. In addition, Li et al. [91] developed a sensitive electrochemical device consisted of Cu-BTC MOF in situ integrated on graphene nanosheets (NSs), which exhibited the properties of both materials, but prevented the aggregation of MOF thanks to the graphene NSs. The sensor was applied for the detection of biomolecules such as xanthine (XA) and hypoxanthine (HXA) in plasma and urine, bisphenol A (BPA) in shopping receipt, and *p*-chlorophenol (*p*-CP) in wastewater, and the results compared with those obtained by HPLC were in good concordance, indicating the high suitability of the method, with LODs of 1.1–7.3 $\mu g\ L^{-1}$. Another example is the work carried out by Wang et al. [90] who constructed a ratiometric sensing platform consisted of a composite of ferrocenecarboxylic acid (Fc)-functionalized MOF, NH_2-UiO-66, and thermally reduced graphene oxide (rGO) for the detection of multiple heavy metals, including Cd(II), Pb(II), and Cu(II) in tap water. The use of MOF with porous structure and large surface area allowed the adsorption and preconcentration of the ions while Fc and rGO improved the conductivity and electrochemical properties of the material, respectively. Fc was also used as internal reference for ratiometric detection. This method provided low LODs of 8.5, 0.6, and 0.8 nM for Cd(II), Pb(II), and Cu(II), respectively, and selectivity against the presence of other mono-, di-, or polyvalent metal ions.

In another way, Nagabooshanam et al. [93] harnessed the inhibition mechanism of the acetylcholinesterase enzyme (AChE) by organophosphate pesticides (OPPs) to develop an electrochemical microanalytical device consisted of ZIF-8 deposited on a gold microelectrode, and immobilized AChE, for the detection of the OPP chlorpyrifos in vegetables, including cucumber, capsicum, and brinjal. The fabricated biosensor exhibited an LOD of 6 $ng\ L^{-1}$ and recovery values of 94%–99%. As shown in Fig. 9.6, the bioconjugated MOF was grafted on a gold microelectrode on an all-in-one microfluidic platform, the analysis consisting on the measurement of the signal decrease as a result of the block of active sites of AChE by chlorpyrifos that inhibit the interaction of the substrate acetylthiocholine (ATCh) with AChE, and thus, the regulation of ATCh levels in the body. Furthermore, the device demonstrated a good selectivity when the sensor was exposed to other pesticide, as the thiocarbamate cartap, which not contains a phosphate group,

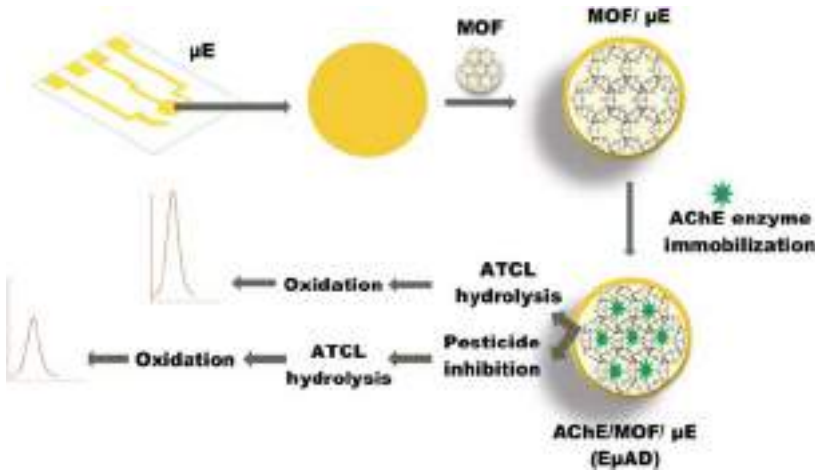

FIGURE 9.6 Scheme of the stepwise electrode fabrication for the detection of chlorpyrifos. The system includes the gold microelectrode with the all-in-one microfluidic platform and electrochemical analyzer for the detection of electroactive species. *Reprinted from Nagabooshanam S, Roy S, Mathur A, Mukherjee I, Krishnamurthy S, Bharadwaj LM. Electrochemical micro analytical device interfaced with portable potentiostat for rapid detection of chlorpyrifos using acetylcholinesterase conjugated metal organic framework using Internet of things. Sci Rep 2019;9:19862 with permission from Nature Research.*

suggesting that the system had a selective nature for phosphate-containing compounds. In addition, the biosensor demonstrated a good stability with a stable signal up to 20 days. For real samples analysis the electrochemical microdevice was integrated in a portable potentiostat, allowing the real-time analysis for the detection of chlorpyrifos that compared with conventional electrochemical workstations provided comparable or even better signals at several concentrations. In addition to these advantages, it should be noted the low response time (50 seconds, including the incubation time of 20 seconds) and the low volume of sample required (2 μL). The authors also highlighted that given the few scientific skills that the use of this device requires, it makes it viable to be used by farmers and others who do not have technical knowledge, to carry out on-site analyses.

9.3.4 Electroluminescent/optical sensors

Electroluminescent/optical sensors rely on luminescence processes that occur when excited electrons return to the ground state via photon emission [88]. In this context, luminescent MOFs are one of the most widely investigated types of MOFs as optical sensors to date. They have several advantages such as high sensitivity and selectivity, fast response, reusability, and simplicity since they can be used directly as powder without processing steps, among

others [12,82,105]. In fact, luminescent MOF sensors make possible the qualitative and quantitative analysis of different target compounds by quenching or enhancing the luminescent process, and even by the movement of the emission wavelength, during host−guest interactions [88]. As can be seen in Table 9.7, MOFs have been used as sensing elements for detection of inorganic species [95] and organic compounds [96−99] in food [96,99], environmental [95], and biological samples [97,98].

As an example, Sheta et al. [97] developed a method based on praseodymium-MOF-NFs optical sensor for the determination of human prolactin in serum samples. The authors characterized the synthesized material using different spectroscopic tools, which served to deduce the formula of the Pr-MOF-NFs was *n*[Pr(5-aminoisophthalic acid (AIP))(1,2-phenylenediamine (Phen))$Cl_2(DMF)_2(H_2O)_2$]. The photoluminescence study suggested that the fluorescent behavior of Pr-MOF-NFs was due to the π-molecular orbital transitions that occurred within aromatic rings of the carboxylate and diamine ligands. In this sense, when prolactin entered the Pr-MOF-NFs structure, the amine groups acted as Lewis basic sites binding prolactin molecules by their lone electron pair. Moreover, the aromatic chromophore groups could also be attached to the active site of prolactin. Both interactions resulted in an enhancement of the luminescence, which was useful for the detection of the biological target at clinically relevant concentrations, even in the presence of different interfering hormones and drugs. Finally, the method showed a low LOD of 0.251 $\mu g\, L^{-1}$ and recovery values ranging between 100% and 102%, indicating its successful performance for prolactin quantification in human serum without sample preparation and pretreatment steps.

Similarly, Liu et al. [96] presented a "turn off−on" samarium-based MOF fluorescence sensor for the detection of tertiary butylhydroquinone (TBHQ) in edible oil. As it is shown in Fig. 9.7, the "turn off−on" process consisted of completely quenching the orange-red luminescence exhibited by

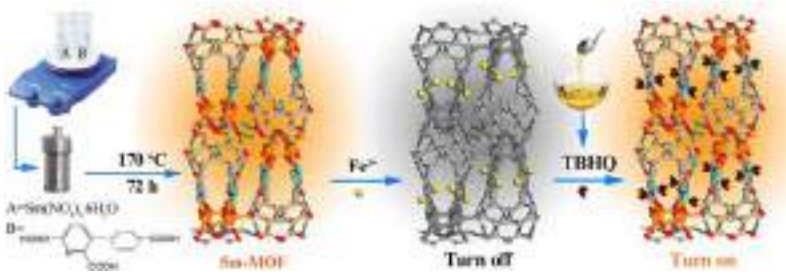

FIGURE 9.7 The detection mechanism of the "turn off−on" sensor for TBHQ. *Reprinted from Liu X, Zhang X, Li R, Du L, Feng X, Ding Y. A highly sensitive and selective "turn off-on" fluorescent sensor based on Sm-MOF for the detection of tertiary butylhydroquinone. Dye Pigment 2020;178:108347 with permission from Elsevier.*

the Sm-MOF in the presence of Fe (III) ions, by forming Sm-MOF@Fe(III) complex (turn off), and then it was recovered in the presence of TBHQ due to the competitive formation of TBHQ@Fe(III) and release of Sm-MOF (turn on). The selectivity of the sensor was evaluated for both responses of fluorescence quenching and recovery processes by adding different possible interfering substances. In this respect, the authors found out that other mono-, di-, and trivalent metal ions could not influence the "turn off" process of Sm-MOF as much as Fe(III) ions, due to its small ion radius and high charge density. In the case of "turn on" process, mono- and divalent metal ions, anions, and even other antioxidants showed a little or noninfluence on the fluorescence recovery, suggesting a high selectivity of the quenched Sm-MOF@Fe(III) system for TBHQ detection. Under the optimum Fe(III) concentration level, the method showed a low LOD of 5.6 $\mu g\, L^{-1}$ and recovery values ranging between 101% and 103%, which make the sensor reliable and effective for the proposed goal.

9.4 Conclusion and future remarks

In the middle of nanoscience effervescence, MOFs have appeared as a very interesting group of nanomaterials, which present particular characteristics that make them excellent candidates for a wide range of applications and fields as demonstrates the impressive number of publications related to this issue in the last years. Apart from the common features shared by most of nanomaterials such as high surface area, easy functionalization, and unique thermal and electrical properties, MOFs also present a great ease to be tuned. In fact, taking into account the huge number of metal ions and linkers that can be used in their synthesis, the possibilities of obtaining different MOFs is infinite.

This versatility has led to the application of MOFs in diverse areas, and chemistry has not been an exception. In this context, such materials have allowed improving the efficiency of many procedures carried out in different areas of this discipline. Particularly, in analytical chemistry, their use as sorbents has been the most common application. Diverse types of MOFs, both commercially available or laboratory prepared, have been used, especially to perform extraction or cleanup procedures in sample preparation.

Although to a lesser extent, they have also been used in other approaches within this area. Indeed, MOFs constitute one of most widely applied nanomaterials for the preparation of stationary phases in separation analytical techniques, including the different modalities of GC and LC, as well as electrophoretic separations with good results. However, still there are certain limitations in the performance of these applications that should be overcome, which describes a large area of study.

Apart from that, the sharp development of the very sensitive detection technique based on the preparation of sensors or microscale devices has

found a good ally in MOFs since the abovementioned characteristics make these nanomaterials as excellent substrates for the preparation of this kind of setup. Moreover, their combination with other nanomaterials has also resulted to be a feasible strategic to synergistically enhance the advantages provided by their properties.

All in all, so far, MOFs have shown a great performance of diverse applications in analytical chemistry and the development of customized synthetic procedures has further favor their use in the area. In addition, the good results obtained in the latest reported publications shown that still there exists a wide range of applications toward this issue that seem to the promising and need to be studied.

Acknowledgement

This work has been supported by the Spanish Ministry of Economy, Industry and Competitiveness (project AGL2017-89257-P).

References

[1] Flaig RW, Popp TMO, Fracaroli AM, Kapustin EA, Kalmutzki MJ, Altamimi RM, et al. The chemistry of CO_2 capture in an amine-functionalized metal-organic framework under dry and humid conditions. J Am Chem Soc 2017;139:12125−8.

[2] Sutrisna PD, Hou J, Zulkifli MY, Li H, Zhang Y, Liang W, et al. Surface functionalized UiO-66/Pebax-based ultrathin composite hollow fiber gas separation membranes. J Mater Chem A 2018;6:918−31.

[3] Teplensky MH, Fantham M, Li P, Wang TC, Mehta JP, Young LJ, et al. Temperature treatment of highly porous zirconium-containing metal−organic frameworks extends drug delivery release. J Am Chem Soc 2017;139:7522−32.

[4] Wu M-X, Yang Y-W. Metal−organic framework (MOF)-based drug/cargo delivery and cancer therapy. Adv Mater 2017;29:1606134.

[5] Lian X, Fang Y, Joseph E, Wang Q, Li J, Banerjee S, et al. Enzyme−MOF (metal−organic framework) composites. Chem Soc Rev 2017;46:3386−401.

[6] Nath I, Chakraborty J, Verpoort F. Metal organic frameworks mimicking natural enzymes: a structural and functional analogy. Chem Soc Rev 2016;45:4127−70.

[7] Ma Y, Li X, Li A, Yang P, Zhang C, Tang B, et al. Nanoparticle photosensitizer for effective photodynamic therapy against cancer with controllable singlet-oxygen release. Angew Chem Int Ed 2017;56:13752−6.

[8] Zhang Y, Wang F, Liu C, Wang Z, Kang L, Huang Y, et al. Nanozyme decorated metal−organic frameworks for enhanced photodynamic therapy. ACS Nano 2018;12:651−61.

[9] Stavila V, Talin AA, Allendorf MD. MOF-based electronic and opto-electronic devices. Chem Soc Rev 2014;43:5994−6010.

[10] Hong X-J, Tan T-X, Guo Y-K, Tang X-Y, Wang J-Y, Qin W, et al. Confinement of polysulfides within bi-functional metal−organic frameworks for high performance lithium−sulfur batteries. Nanoscale 2018;10:2774−80.

[11] Nandi S, Collins S, Chakraborty D, Banerjee D, Thallapally PK, Woo TK, et al. Ultralow parasitic energy for postcombustion CO_2 capture realized in a nickel isonicotinate metal−organic framework with excellent moisture stability. J Am Chem Soc 2017;139:1734−7.
[12] Kreno LE, Leong K, Farha OK, Allendorf M, Van Duyne RP, Hupp JT. Metal-organic framework materials as chemical sensors. Chem Rev 2012;112:1105−25.
[13] Kurmoo M. Magnetic metal−organic frameworks. Chem Soc Rev 2009;38:1353−79.
[14] Yaghi OM, Li H. Hydrothermal synthesis of a metal-organic framework containing large rectangular channels. J Am Chem Soc 1995;117:10401−3.
[15] Pettinari C, Marchetti F, Mosca N, Tosi G, Drozdov A. Application of metal−organic frameworks. Polym Int 2017;66:731−44.
[16] Cambridge Crystallographic Data Centre (CCDC). <http://www.ccdc.cam.ac.uk/> [accessed 10.02.20].
[17] Coordination polymers and metal organic frameworks: terminology and nomenclature guidelines. <http://www.iupac.org/web/ins/2009-012-2-200> [accessed 02.03.20].
[18] Batten SR, Champness NR, Chen XM, Garcia-Martinez J, Kitagawa S, Öhrström L, et al. Coordination polymers, metal−organic frameworks and the need for terminology guidelines. CrystEngComm 2012;14:3001−4.
[19] Batten SR, Champness NR, Chen XM, Garcia-Martinez J, Kitagawa S, Öhrström L, et al. Terminology of metal−organic frameworks and coordination polymers (IUPAC Recommendations 2013). Pure Appl Chem 2013;85:1715−24.
[20] Yusuf K, Aqel A, ALOthman Z. Metal-organic frameworks in chromatography. J Chromatogr A 2014;1348:1−16.
[21] Xu M, Yang S-S, Gu Z-Y. Two-dimensional metal-organic framework nanosheets: a rapidly growing class of versatile nanomaterials for gas separation, MALDI-TOF matrix, and biomimetic applications. Chem Eur J 2018;24:15131−42.
[22] Farha OK, Yazaydin AO, Eryazici I, Malliakas CD, Hauser BG, Kanatzidis MG, et al. De novo synthesis of a metal−organic framework material featuring ultrahigh surface area and gas storage capacities. Nat Chem 2010;2:944−8.
[23] Ryan P, Farha OK, Broadbelt LJ, Snurr R. Computational screening of metal-organic frameworks for Xenon/Krypton separation. AIChE J 2011;57:1759−66.
[24] Devic T, Serre C. Porous metal organic frameworks: from synthesis to applications. In: Valtchev V, Mintova S, Tsapatsis M, editors. Ordered porous solids. Elsevier; 2009. p. 77−99.
[25] Diercks CS, Yaghi OM. The atom, the molecule, and the covalent organic framework. Science 2017;355:eaal1585.
[26] Qian H-L, Yang C-X, Wang W-L, Yang C, Yan X-P. Advances in covalent organic frameworks in separation science. J Chromatogr A 2018;1542:1−18.
[27] Xie S-M, Yuan L-M. Recent progress of chiral stationary phases for separation of enantiomers in gas chromatography. J Sep Sci 2017;40:124−37.
[28] Scriba GKE. Chiral recognition in separation science − an update. J Chromatogr A 2016;1467:56−78.
[29] Gao Y, Liu G, Gao M, Huang X, Xu D. Recent advances and applications of magnetic metal-organic frameworks in adsorption and enrichment removal of food and environmental pollutants. Crit Rev Anal Chem 2019.
[30] Manousi N, Zachariadis GA, Deliyanni EA, Samanidou VF. Applications of metal-organic frameworks in food sample preparation. Molecules 2018;23:2896.

[31] Wang X, Ye N. Recent advances in metal-organic frameworks and covalent organic frameworks for sample preparation and chromatographic analysis. Electrophoresis 2017;38:3059–78.
[32] Liu H-L, Chang Y-J, Fan T, Gu Z-Y. Two-dimensional metal–organic framework nanosheets as a matrix for laser desorption/ionization of small molecules and monitoring enzymatic reactions at high salt concentrations. Chem Commun 2016;52:12984–7.
[33] Armenta S, Esteve-Turrillas FA, Garrigues S, de la Guardia M. Green analytical chemistry: the role of green techniques. In: Ibañez E, Cifuentes A, editors. Comprehensive analytical chemistry. Green extraction techniques: principles, advances and applications. Elsevier; 2017. p. 1–25.
[34] Gu Z-Y, Wang G, Yan X-P. MOF-5 Metal–organic framework as sorbent for in-field sampling and preconcentration in combination with thermal desorption GC/MS for determination of atmospheric formaldehyde. Anal Chem 2010;82:1365–70.
[35] Gu Z-Y, Yang C-X, Chang N, Yan X-P. Metal–organic frameworks for analytical chemistry: from sample collection to chromatographic separation. Acc Chem Res 2012;45:734–45.
[36] Hashemi B, Zohrabi P, Raza N, Kim K-H. Metal-organic frameworks as advanced sorbents for the extraction and determination of pollutants from environmental, biological, and food media. TrAC—Trend Anal Chem 2017;97:65–82.
[37] Wen Y, Chen L, Li J, Liu D, Chen L. Recent advances in solid-phase sorbents for sample preparation prior to chromatographic analysis. TrAC—Trend Anal Chem 2014;59:26–41.
[38] Amini S, Ebrahimzadeh H, Seidi S, Jalilian N. Polyacrylonitrile/MIL-53(Fe) electrospun nanofiber for pipette-tip micro solid phase extraction of nitrazepam and oxazepam followed by HPLC analysis. Microchim Acta 2020;187:1–10.
[39] Chen Z, Yu C, Xi J, Tang S, Bao T, Zhang J. A hybrid material prepared by controlled growth of a covalent organic framework on amino-modified MIL-68 for pipette tip solid-phase extraction of sulfonamides prior to their determination by HPLC. Microchim Acta 2019;186:1–11.
[40] Yan Z, Wu M, Hu B, Yao M, Zhang L, Lu Q, et al. Electrospun UiO-66/polyacrylonitrile nanofibers as efficient sorbent for pipette tip solid phase extraction of phytohormones in vegetable samples. J Chromatogr A 2018;1542:19–27.
[41] Zhang X, Wang P, Han Q, Li H, Wang T, Ding M. Metal–organic framework based in-syringe solid-phase extraction for the on-site sampling of polycyclic aromatic hydrocarbons from environmental water samples. J Sep Sci 2018;41:1856–63.
[42] Dai X, Jia X, Zhao P, Wang T, Wang J, Huang P, et al. A combined experimental/computational study on metal-organic framework MIL-101(Cr) as a SPE sorbent for the determination of sulphonamides in environmental water samples coupling with UPLC-MS/MS. Talanta 2016;154:581–8.
[43] Wang P-L, Xie L-H, Joseph EA, Li J-R, Su X-O, Zhou H-C. Metal–organic frameworks for food safety. Chem Rev 2019;119:10638–90.
[44] Manousi N, Zachariadis GA, Deliyanni EA. On the use of metal-organic frameworks for the extraction of organic compounds from environmental samples. Env Sci Pollut Res 2020.
[45] Li N, Wu D, Li X, Zhou X, Fan G, Li G, et al. Effective enrichment and detection of plant growth regulators in fruits and vegetables using a novel magnetic covalent organic framework material as the adsorbents. Food Chem 2020;306:125455.

[46] Taghvimi A, Tabrizi AB, Dastmalchi S, Javadzadeh Y. Metal organic framework based carbon porous as an efficient dispersive solid phase extraction adsorbent for analysis of methamphetamine from urine matrix. J Chromatogr B 2019;1109:149–54.
[47] Nilash MM, Hashemzadeh A, Fakhari AR, Amini MM. Novel Schiff base-functionalized metal–organic framework nanoparticles for dispersive solid phase extraction of copper ions from vegetable and water samples. Anal Methods 2019;11:2683–91.
[48] Xia L, Liu L, Lv X, Qu F, Li G, You J. Towards the determination of sulfonamides in meat samples: a magnetic and mesoporous metal-organic framework as an efficient sorbent for magnetic solid phase extraction combined with high-performance liquid chromatography. J Chromatogr A 2017;1500:24–31.
[49] Zhang S, Yao W, Ying J, Zhao H. Polydopamine-reinforced magnetization of zeolitic imidazolate framework ZIF-7 for magnetic solid-phase extraction of polycyclic aromatic hydrocarbons from the air-water environment. J Chromatogr A 2016;1452:18–26.
[50] Rocío-Bautista P, Termopoli V. Metal–organic frameworks in solid-phase extraction procedures for environmental and food analyses. Chromatographia 2019;82:1191–205.
[51] Płotka-Wasylka P, Szczepańska N, de la Guardia M, Namieśnik J. Miniaturized solid-phase extraction techniques. TrAC—Trend Anal Chem 2015;73:19–38.
[52] Rocío-Bautista P, Pacheco-Fernández I, Pasán J, Pino V. Are metal-organic frameworks able to provide a new generation of solid-phase microextraction coatings?—a review. Anal Chim Acta 2016;939:26–41.
[53] Jiang H-L, Li N, Wang X, Wei X-Y, Zhao R-S, Lin J-M. A zirconium-based metal-organic framework material for solid-phase microextraction of trace polybrominated diphenyl ethers from milk. Food Chem 2020;317:126436.
[54] Mirzajani R, Kardani F, Ramezani Z. Preparation and characterization of magnetic metal–organic framework nanocomposite as solid-phase microextraction fibers coupled with high performance liquid chromatography for determination of non-steroidal anti-inflammatory drugs in biological fluids and tablet formulation samples. Microchem J 2019;144:270–84.
[55] Kong J, Zhu F, Huang W, He H, Hu J, Sun C, et al. Sol–gel based metal-organic framework zeolite imidazolate framework-8 fibers for solid-phase microextraction of nitro polycyclic aromatic hydrocarbons and polycyclic aromatic hydrocarbons in water samples. J Chromatogr A 2019;1603:92–101.
[56] Wu T, Zang X, Wang M, Chang Q, Wang C, Wu Q, et al. Covalent organic framework as fiber coating for solid-phase microextraction of chlorophenols followed by quantification with gas chromatography–mass spectrometry. J Agric Food Chem 2018;66:11158–65.
[57] Zhang S, Yang Q, Wang W, Wang C, Wang Z. Covalent bonding of metal–organic framework-5/graphene oxide hybrid composite to stainless steel fiber for solid-phase microextraction of triazole fungicides from fruit and vegetable samples. J Agric Food Chem 2016;64:2792–801.
[58] Soares-Maciel EV, de Toffoli AL, Lanças FM. Recent trends in sorption-based sample preparation and liquid chromatography techniques for food analysis. Electrophoresis 2018;39:1582–96.
[59] Capriotti AL, Cavaliere C, Foglia P, Samperi R, Stampachiacchiere S, Ventura S, et al. Recent advances and developments in matrix solid-phase dispersion. TrAC—Trend Anal Chem 2015;71:186–93.
[60] Liang T, Wang S, Chen L, Niu N. Metal organic framework-molecularly imprinted polymer as adsorbent in matrix solid phase dispersion for pyrethroids residue extraction from wheat. Food Anal Methods 2019;12:217–28.

[61] Rodríguez-Ramos R, Socas-Rodríguez B, Santana-Mayor Á, Rodríguez-Delgado MÁ. Nanomaterials as alternative dispersants for the multiresidue analysis of phthalates in soil samples using matrix solid phase dispersion prior to ultra-high performance liquid chromatography tandem mass spectrometry. Chemosphere 2019;236:124377.

[62] Wang S, Zhang J, Li C, Chen L. Analysis of tetracyclines from milk powder by molecularly imprinted solid-phase dispersion based on a metal−organic framework followed by ultra high performance liquid chromatography with tandem mass spectrometry. J Sep Sci 2018;41:2604−12.

[63] Santos-Barreto A, de Cassia da Silva Andrade P, Meira Farias J, Menezes Filho A, Fernandes de Sá G, Alves-Junior S. Characterization and application of a lanthanide-based metal−organic framework in the development and validation of a matrix solid-phase dispersion procedure for pesticide extraction on peppers (*Capsicum annuum* L.) with gas chromatography−mass spectrometry. J Sep Sci 2018;41:1593−9.

[64] de Jesus JR, Wanderley KA, Alves-Junior S, Navickiene S. Evaluation of a novel metal−organic framework as an adsorbent for the extraction of multiclass pesticides from coconut palm (*Cocos nucifera* L.): an analytical approach using matrix solid-phase dispersion and liquid chromatography. J Sep Sci 2017;40:3327−34.

[65] David F, Ochiai N, Sandra P. Two decades of stir bar sorptive extraction: a retrospective and future outlook. TrAC—Trend Anal Chem 2019;112:102−11.

[66] Shen C, Wu T, Zang X. Hollow fiber stir bar sorptive extraction combined with GC−MS for the determination of phthalate esters from children's food. Chromatographia 2019;82:683−93.

[67] Khoobi A, Salavati-Niasari M, Ghani M, Ghoreishi SM, Gholami A. Multivariate optimization methods for in-situ growth of LDH/ZIF-8 nanocrystals on anodized aluminium substrate as a nanosorbent for stir bar sorptive extraction in biological and food samples. Food Chem 2019;288:39−46.

[68] Wang Y, Jia M, Wu X, Wang T, Wang J, Hou X. PEG modified column MIL-101(Cr)/PVA cryogel as a sorbent in stir bar solid phase extraction for determination of non-steroidal anti-inflammatory drugs in water samples. Microchem J 2019;146:214−19.

[69] You L, He M, Chen B, Hu B. One-pot synthesis of zeolitic imidazolate framework-8/poly (methyl methacrylate-ethyleneglycol dimethacrylate) monolith coating for stir bar sorptive extraction of phytohormones from fruit samples followed by high performance liquid chromatography-ultraviolet detection. J Chromatogr A 2017;1524:57−65.

[70] Lin S, Gan N, Zhang J, Qiao L, Chen Y, Cao Y. Aptamer-functionalized stir bar sorptive extraction coupled with gas chromatography−mass spectrometry for selective enrichment and determination of polychlorinated biphenyls in fish samples. Talanta 2016;149:266−74.

[71] Carasek E, Morés L, Merib J. Basic principles, recent trends and future directions of microextraction techniques for the analysis of aqueous environmental samples. Trend Environ Anal Chem 2018;19:e00060.

[72] Yang S, Xie H, Zhu H, Zhang L, Zhou Y, Zhang H, et al. Highly effective hydrogen isotope separation by cryogenic gas chromatography in a new stationary phase material $MnCl_2$@CPL-1@g-Al_2O_3. Int J Hydrogen Energy 2018;43:7973−81.

[73] Yang X, Li C, Qi M, Qu L. Graphene-ZIF8 composite material as stationary phase for high-resolution gas chromatographic separations of aliphatic and aromatic isomers. J Chromatogr A 2016;1460:173−80.

[74] Yang J-r, Xie S-m, Zhang J-h, Chen L, Nong R-y, Yuan L-m. Metal−organic framework $[Cd(LTP)_2]_n$ for improved enantioseparations on a chiral cyclodextrin stationary phase in GC. J Chromatogr Sci 2016;54:1467−74.
[75] Huang J, Han X, Yang S, Cao Y, Yuan C, Liu Y, et al. Microporous 3D covalent organic frameworks for liquid chromatographic separation of xylene isomers and ethylbenzene. J Am Chem Soc 2019;141:8996−9003.
[76] Liu L-H, Yang C-X, Yan X-P. Methacrylate-bonded covalent-organic framework monolithic columns for high performance liquid chromatography. J Chromatogr A 2017;1479:137−44.
[77] Wang X, Lamprou A, Svec F, Bai Y, Liu H. Polymer-based monolithic column with incorporated chiral metal−organic framework for enantioseparation of methyl phenyl sulfoxide using nano-liquid chromatography. J Sep Sci 2016;39:4544−8.
[78] Pan C, Lv W, Wang G, Niu X, Guo H, Chen X. Simultaneous separation of neutral and cationic analytes by one dimensional open tubular capillary electrochromatography using zeolitic imidazolate framework-8 as stationary phase. J Chromatogr A 2017;1484:98−106.
[79] Wang X, An J, Li J, Ye N. A capillary coated with a metal-organic framework for the capillary electrochromatographic determination of cephalosporins. Microchim Acta 2017;184:1345−51.
[80] Tang P, Bao T, Chen Z. Novel Zn-based MOFs stationary phase with large pores for capillary electrochromatography. Electrophoresis 2016;37:2181−9.
[81] Bao T, Tang P, Mao Z, Chen Z. An immobilized carboxyl containing metal-organic framework-5 stationary phase for open-tubular capillary electrochromatography. Talanta 2016;154:360−6.
[82] Rocío-Bautista P, Taima-Mancera I, Pasan J, Pino V. Metal-organic frameworks in green analytical chemistry. Separations 2019;6:33.
[83] Yu Y, Ren Y, Shen W, Deng H, Gao Z. Applications of metal-organic frameworks as stationary phases in chromatography. TrAC—Trend Anal Chem 2013;50:33−41.
[84] Zajickova Z, Špánik I. Applications of monolithic columns in gas chromatography and supercritical fluid chromatography. J Sep Sci 2019;42:999−1011.
[85] Zhang J, Chen Z. Metal-organic frameworks as stationary phase for application in chromatographic separation. J Chromatogr A 2017;1530:1−18.
[86] Qiu Q, Chen H, Wang Y, Ying Y. Recent advances in the rational synthesis and sensing applications of metal-organic framework biocomposites. Coord Chem Rev 2019;387:60−78.
[87] Ji L, Jin Y, Wu K, Wan C, Yang N, Tang Y. Morphology-dependent electrochemical sensing performance of metal (Ni, Co, Zn)-organic frameworks. Anal Chim Acta 2018;1031:60−6.
[88] Fang X, Zong B, Mao S. Metal−organic framework-based sensors for environmental contaminant sensing. Nano-Micro Lett 2018;10:64.
[89] Kumar P, Deep A, Kim K-H. Metal organic frameworks for sensing applications. TrAC—Trend Anal Chem 2015;73:39−53.
[90] Wang X, Qi Y, Shen Y, Yuan Y, Zhang L, Zhang C, et al. A ratiometric electrochemical sensor for simultaneous detection of multiple heavy metal ions based on ferrocene-functionalized metal-organic framework. Sens Actuators, B: Chem 2020;310:127756.
[91] Li X, Li C, Wu C, Wu K. Strategy for highly sensitive electrochemical sensing: in situ coupling of a metal−organic framework with ball-mill-exfoliated graphene. Anal Chem 2019;91:6043−50.

[92] Gan T, Li J, Xu L, Yao Y, Liu Y. Construction of a voltammetric sensor based on MIL-101 hollow cages for electrocatalytic oxidation and sensitive determination of nitrofurazone. J Electroanal Chem 2019;848:113287.
[93] Nagabooshanam S, Roy S, Mathur A, Mukherjee I, Krishnamurthy S, Bharadwaj LM. Electrochemical micro analytical device interfaced with portable potentiostat for rapid detection of chlorpyrifos using acetylcholinesterase conjugated metal organic framework using internet of things. Sci Rep 2019;9:19862.
[94] Liu C-S, Sun C-X, Tian J-Y, Wang Z-W, Ji H-F, Song Y-P, et al. Highly stable aluminum-based metal-organic frameworks as biosensing platforms for assessment of food safety. Biosens Bioelectron 2017;91:804–10.
[95] Nandi S, Biswas S. A diamino functionalized metal-organic framework for fluorometric recognition of free chlorine in environmental water samples. Microporous Mesoporous Mater 2020;299:110116.
[96] Liu X, Zhang X, Li R, Du L, Feng X, Ding Y. A highly sensitive and selective "turn off-on" fluorescent sensor based on Sm-MOF for the detection of tertiary butylhydroquinone. Dye Pigment 2020;178:108347.
[97] Sheta SM, El-Sheikh SM, Abd-Elzaher MM. A novel optical approach for determination of prolactin based on Pr-MOF nanofibers. Anal Bioanal Chem 2019;411:1339–49.
[98] Sun N, Yan B. Fluorescence detection of urinary *N*-methylformamide for biomonitoring of human occupational exposure to *N*,*N*-dimethylformamide by Eu(III) functionalized MOFs. Sens Actuators, B: Chem 2018;261:153–60.
[99] Zhu N, Zou Y, Huang M, Dong S, Wu X, Liang G, et al. A sensitive, colorimetric immunosensor based on Cu-MOFs and HRP for detection of dibutyl phthalate in environmental and food samples. Talanta 2018;186:104–9.
[100] Zhang X, Li G, Wu D, Zhang B, Hu N, Wang H, et al. Recent advances in the construction of functionalized covalent organic frameworks and their applications to sensing. Biosens Bioelectron 2019;145:111699.
[101] Lei J, Qian R, Ling P, Cui L, Ju H. Design and sensing applications of metal–organic framework composites. TrAC—Trend Anal Chem 2014;58:71–8.
[102] Yin D, Liu J, Bo X, Li M, Guo L. Porphyrinic metal-organic framework/macroporous carbon composites for electrocatalytic applications. Electrochim Acta 2017;247:41–9.
[103] Liu L, Zhou Y, Liu S, Xu M. The applications of metal-organic frameworks in electrochemical sensors. ChemElectroChem 2018;5:6–19.
[104] Kempahanumakkagari S, Vellingiri K, Deep A, Kwon EE, Bolan N, Kim K-H. Metal–organic framework composites as electrocatalysts for electrochemical sensing applications. Coord Chem Rev 2018;357:105–29.
[105] Anik Ü, Timur S, Dursun Z. Metal organic frameworks in electrochemical and optical sensing platforms: a review. Microchim Acta 2019;186:196.

Chapter 10

Modified metal-organic frameworks as photocatalysts

Wei Ni[1,2,3] and Anish Khan[4]

[1]*Vanadium and Titanium Resource Comprehensive Utilization Key Laboratory of Sichuan Province, Panzhihua University, Panzhihua, P.R. China,* [2]*Institute for Advanced Study, Chengdu University, Chengdu, P.R. China,* [3]*Material Corrosion and Protection Key Laboratory of Sichuan Province, Sichuan University of Science and Engineering, Zigong, P.R. China,* [4]*Center of Excellence for Advanced Materials Research, King Abdulaziz University, Jeddah, Saudi Arabia*

10.1 Introduction

To address the intensively increasing concerns of global energy and environment, solar energy conversion and storage is very promising [1−3]. Photocatalysis, including water splitting, CO_2 reduction, and organic transformations, is playing a key role in solar energy conversion and environmental protection [4−10]. Compared to conventional inorganic semiconductor and homogeneous photocatalysts, metal-organic frameworks (MOFs) have recently attracted significant attention for photocatalysis, owing to their extraordinary structural variability and richness [namely, engineering synergies between the metal nodes, functional linkers, and incorporated substrates/nanoparticles (NPs) for multiple and selective heterogeneous interactions/activations in these well-defined and tailorable porous MOF-based nanocatalysts] for superior sunlight utilization, charge separation, and exposure of active sites as well as further understanding of the structure−activity relationship [3,8−13]. MOFs, combining the benefits of heterogeneous catalysis and homogeneous catalysis, provide a powerful and versatile platform for photocatalysis, which mainly involves three key processes, that is, light harvesting, electron−hole (e−h) separation, and surface redox reactions, as can be rationally improved [8,11,14−22].

Although, under appropriate light irradiation, the organic bridging ligands (or named linkers) of MOFs can function as antennas to harvest light and activate the metal nodes/clusters by means of a linker-to-cluster charge transition (LCCT) with a featured semiconductor-like behavior [10,23], pristine MOFs as photocatalysts (also nicknamed "opportunistic" photocatalysts [24]) are limited and hard to

Metal-Organic Frameworks for Chemical Reactions. DOI: https://doi.org/10.1016/B978-0-12-822099-3.00010-1

be readily tuned; also, most of them are only sensitive to ultraviolet (UV) light and the lifetimes of the excited states are usually too short to perform the photocatalytic activity, which restricts the practicability under solar illumination [18]. Thus the exploitation of new MOFs that response to visible light is highly desirable, and modifications to MOFs would be a sensible and effective choice.

Herein, we timely and systematically overview the very recent progress and achievements on the design, synthesis, and photocatalysis applications with emphasis on the promising hydrogen production and water splitting. Beginning with the introduction of characteristics of structural advantages of modified MOFs, structural engineering and hybridization strategies for high-efficiency photocatalysts are analyzed and discussed in detail. The roles of MOFs in the photocatalytic systems as photocatalysts, cocatalysts, and photocatalytic hosts are highlighted. This specific review will provide fundamental guidance to rational design of efficient MOF-based photocatalyst materials as well as perspectives of future research direction, critical challenges, and potential solutions. It is hoped that this recent progress on modified MOF-based photocatalysts will boost more research interests and inspirations for efficient photocatalytic energy conversion technology.

10.2 Structure, merits, and strategies

MOFs, also called porous coordination polymers, are a class of intriguing two-dimensional (2D) or three-dimensional porous crystalline materials formed via self-assembly of inorganic metal ions (or clusters) and organic ligands connected by coordination interactions [3,9,25–27]. MOFs have been playing a central role and recently been explored toward photocatalysis beyond traditional semiconductors owing to their unique and significant advantages in the following aspects: (1) high porosity allowing enhanced exposure/accessibility of active sites for photocatalysis and facile mass transport, (2) structural tunability (e.g., tunable catalytic metal active sites and functionalizable organic ligands) endowing extended light response, (3) eliminated structural defects (usually e−h recombination centers) of crystalline greatly suppressing charge recombination, (4) shortened migration paths for charge carriers prior to their reaction with substrates and the improved e−h separation created by the porous structure, and (5) enhanced spatial separation of e−h pairs by the flexibly positioned photosensitizer or the cocatalyst (on the framework or in the pore space of MOFs) [8,28]. Besides the classic LCCT mechanism for charge transport within the frameworks, some new theories such as charge transport pathway via node-to-node communication in both ground and excited states of MOFs are also emerging [29]. Moreover, the well-defined and tailorable MOF structures are beneficial for the further in-depth understanding of the structure−activity relationship of photocatalysis [8,30]. Owing to these merits, great efforts have been devoted to the development of MOF-based materials toward photocatalysis in recent years.

The different roles that MOFs have played in emerging heterogeneous photocatalysis may be classified to provide fundamental and important guidance for researchers to rationally design and study MOF-related photochemical systems in the future; according to their different functions in the photocatalytic systems, the MOFs may serve as photocatalysts (i.e., hard-core light-energy units that absorb light and produce photogenerated charge carriers for subsequent photoredox reactions), cocatalysts (i.e., active components that promote kinetic processes of charge separation and catalytic reactions along with dyes or semiconductors), and hosts (i.e., no/weak catalytic activity but may obtain enhanced performance after anchoring/encapsulating other functional moieties) [9].

To gain insight into the relationship between the photocatalytic performance and structural tailorability of MOFs and to further enhance their practical application in photocatalysis, different strategies have been developed, and a series of modified MOFs (e.g., via direct solvothermal synthesis [31], postsynthetic modification [3,32–35], and hybridization [36]) with tailored structures and enhanced photocatalysis [24,37] has been rationally fabricated to improve the light absorption, charge separation, and subsequent utilization [8], namely, to meet the high requirements on longer lifetime of excited states and enhanced spectral sensitivity for efficient photocatalysis [18]. Of course, some cases refer to the synergistic effects, for example, by integration of homogeneous molecular photosensitizer and cocatalyst [38], plasmonic effects and Schottky junctions [39], and plasmon and upconversion [40].

Specific methods have been developed to improve the light absorption (e.g., via furnishing functionalized conjugated/aromatic carboxylate ligands [31,35,41–45], porphyrin ligands [46–49], or integrated functional metal complexes) [50], charge separation (e.g., via noble-metal cocatalysts, nonprecious metal-based proton reduction catalysts [24,51], framework interpenetration [52], spatial charge separation [53–55], defect engineering [56,57], and introducing or substitution by new components [58]), and subsequent utilization (i.e., via promoted redox reaction) [8]. For example, the development of pristine MOFs as photocatalysts is mainly focused on the extension from UV light–driven ($E_g > 3.1$ eV, $\lambda < 400$ nm) to visible light–driven ($E_g < 3.1$ eV, $\lambda > 400$ nm) photocatalysis [18]; by further tuning the light absorption the light response may thus be extended to 600 nm and even high up to 800 nm (for porphyrin ligands), which effectively enhances the light absorption of these MOF-based photocatalysts from the UV ($\sim$5%) to visible ($\sim$42%–45%) and even the near-infrared (NIR) (>50% in the spectrum) region for improved solar energy utilization [8,40,59].

10.3 Metal-organic framework modification

The great structural versatility of MOFs allows the exchange of metal nodes, adaption of the nature of linkers, or encapsulation/hybridization of functional components for the required semiconductor properties [3,18,20,55,60,61], as

well as the promising applications in MOF-mediated solar-to-chemical energy conversion reactions, including photocatalytic water splitting, CO_2 reduction, organic transformation, and pollutant degradation [62,63].

10.3.1 Ligands and clusters

Ligand modification is an effective strategy to tune the optical response and has given great prospects for the application of these MOFs for visible light−driven photocatalysis, and the related modification methods may be classified into several categories, including ligand-exchange method [64], ligand functionalization/substitution [35,65−68], ligand defect engineering [69], and ligand decoration [70].

The ligand modification may directly change the bandgap and color of photocatalysts (via electronic localization of the conjugated motifs and valence band control), enhance the visible-light absorption and the photocurrent response or photocatalytic activity/stereoselectivity thereof [31,35,71−76]. For example, a specific proportional ligand of pristine MIL-125(Ti) can be replaced by methylthio- or aminoterephthalate with electron-donating substituents via solvent-assisted ligand-exchange method [23,64]; sulfur secondary building units, including methylthio ($-SCH_3$), are recently evidenced as a kind of more efficient functional group to achieve desirable photocatalysis [65,77]; and disubstituted linkers show larger shifts than the monosubstituted variants [75]. UiO-66-NH_2 red-shifted modifications can be further realized by using a diazo-coupling reaction (with naphthol and aniline) [78]. The introduction of photosensitizers such as porphyrins (a group of well-known redox-active photosensitizers) [49] can give rise to self-sensitized MOFs with enhanced visible-light absorption and remarkable long lifetime of triplet excited state [47,59,79]. Moreover, the photocatalytic properties of MOF defect structures mainly depend on the coordination of constituent nodes, and the nodes with the strongest local distortions affect the electronic structure most. Thus defects (e.g., missing linker) may provide an alternative pathway to tune photocatalytic properties beyond the linker modification and node metal substitution [56].

The formation of metal-coordinated MOF catalysts by incorporation of additional metal active sites (e.g., noble-metal Ru [80], noble metal−free Ni−Mo cluster [81], Ti(IV) coordination sites [82] via postsynthetic metal exchange, and grafting or doping [83−86]) can contribute to the preferable electronic structure and therefore enhance the photocatalytic activity, for example, for H_2 evolution, which are much higher than those of pure MOF and usually superior to those of metal nanoparticle (MNP)−loaded MOFs or monometallic photocatalysts.

10.3.2 Metals

To improve the e−h separation ability, cocatalysts such as MNPs are usually encapsulated into the coordination interspaces of MOFs (MNP@MOF)

[3,36,87], where a Schottky barrier could be formed at the interface and enhance the photogenerated electrons from the lowest unoccupied molecular orbital (LUMO) of MOFs to MNPs as well as the consequent photocatalytic performance [59]. And these MNPs can be divided into noble-metal NPs (e.g., Pt, Pd, and Au) [39,88–90] and noble metal–free NPs (e.g., Cu, Co, and Ni) [91].

10.3.3 Semiconductors

Controllable semiconductors with superior light absorption, charge separation/transfer, photocatalytic activity, and/or structural protection can be incorporated with MOFs for enhanced photocatalysis and/or stability [36,58,92]. And these semiconductive cocatalysts include TiO_2 (MIL-125-NH_2@TiO_2 core–shell particles [92,93], double-shell TiO_2@ZIF-8 hollow nanospheres [94]), Cu_2O-encapsulated NH_2-MIL-125(Ti) [95], dye molecule Eosin Y (EY)–sensitized ZIF-9/CuO [96], Bi_2WO_6/MIL-100(Fe) [97]; CdS (CdS/UiO-66 [92], CdS/MIL-101 [98], CdS-loaded 2D MOF [99]), 1T-MoS_2/MIL-125-NH_2 [100]; bimetal sulfides ($Cd_{0.2}Zn_{0.8}S$@UiO-66-NH_2 [101], $ZnIn_2S_4$@NH_2-MIL-125(Ti) [102], $CdLa_2S_4$/MIL-88A(Fe) [103], flower-like UiO-66/$CdIn_2S_4$ [104]); ternary MoS_2/UiO-66/CdS composites [105], UiO-66/CdS/RGO [106], g-C_3N_4@ZIF-67/NiS_x [107], MoS_2 nanosheets decorated with UiO-66-$(COOH)_2$/$ZnIn_2S_4$ [108], mesoporous NH_2-MIL-125(Ti)@$ZnIn_2S_4$/CdS [109], polyoxo-titanium cluster (PTC)/CdS/MIL-101 [110].

It is noteworthy that polymeric graphitic carbon nitride (g-C_3N_4) [111,112] or graphene [113] may also work as a kind of efficient flexible semiconductive cocatalyst due to their high chemical stability, visible-light absorption capacity, and low cost. The 2D structure allows them a versatile platform to create the intimately contacted interface and therefore enhanced photocatalysis; typical examples include UiO-66/g-C_3N_4 heterojunction [114], ZIF-8/g-C_3N_4 composite [115], nanocomposites of carbon nitride nanosheets/MIL-100(Fe) [116], and partially reduced graphene oxide/coordination polymer nanoplates [117].

10.3.4 Dyes

The use of photosensitizers (via dye sensitization), usually in combination with an inorganic semiconductor, is also an effective solution to extend the light absorption of normal MOFs from UV region into visible. Thus dye fixation on the MOF surface improves the electron transfer process via the enhanced visible-light absorption and excited electron transfer into the MOF semiconductor conduction band [3]. These dyes include *cone*-calixarene-based dye (Calix-3) [118], molecular Ru–photosensitizer [38,71,119–122], fluorescein [122], EY [96,123], Erythrosin B dye [124], and polyaniline (PANI) [125] etc.

10.3.5 Composites/hybrids

Multicomponent composites/hybrids are also emerging, such as GO-wrapped Pt@UiO-66-NH_2 [126], core−shell-structured upconversion nanoparticles (UCNPs)−Pt@MOF/Au composites [40], MOF/covalent organic framework (COF) hybrids [127,128], Pd-doped MOFs@COFs core−shell hybrid [129], MOF/metal-organic cage (MOC) [or photochemical molecular device (PMD)] hybrid [130], polyoxometalate (POM)@MOF [122], POM-Pt NPs@NH_2-MIL-53 [131], MXene/MOF hybrid [132,133], MIL-125(Ti)/few-layer black phosphorus composite [134], MOF−quantum dot composites [135,136], and single-site (or single-atom) MOF photocatalysts [137−140]. Among, incorporation of carbons with MOFs via surface modification or encapsulation is another key approach to enhance electron transfer and photocatalytic activity thereof. For example, graphene as a surface modifier or encapsulating carbon nanodots can stay in close contact with MOFs and result in superior electron transfer efficiency [141−143].

10.4 Applications

The applications of modified MOFs mainly focus on energy-related (e.g., hydrogen production and overall water splitting [30,58,111,144−147], CO_2 reduction, organic transformations, and nitrogen fixation) and environmental-related fields (e.g., water depollution and dyes degradation) [3,148,149].

10.4.1 Hydrogen production

Paralleling electrocatalysis, photocatalysis via MOF, is increasingly investigated for H_2 evolution from H_2O as well as H_2 release from hydrogen storage materials [3]. Photocatalytic hydrogen evolution reaction (HER) with relatively small activation energy (theoretically 1.23 eV, around 1000 nm light irradiation) is especially attractive [59]. MOF-based materials possess unique advantages to offer attractive functionalities in HER processes by lowing reaction potentials and speeding up reaction rates [30].

In MOFs the MOF linker can serve as a semiconductor that transfers the light-generated electron to the nearby metal node by ligand-to-metal charge transfer (similar to LCCT), and the reduced metal node can then transfer the electron to the surface of the transition-metal cocatalyst for proton reduction, where the cocatalyst, for example, MNPs (M = Pd, Pt), metal clusters, or metal complexes are usually essential to mediate the highly competitive annihilation/recombination reaction [3,83,150,151]. For example, Li et al. fabricated a hybrid of well-distributed Pt-NPs immobilized within confined coordination interspaces of self-sensitized porphyrin MOF for highly efficient photocatalytic HER via the synergistic effect [between Pd-porphyrin photosensitizers of long-lived phosphorescence and Pt-NP cocatalysts,

~3 nm width, confined within nanoscale coordination interspaces, 3.7 nm diameter, incorporating hydrophilic Hf(IV)-oxo clusters] (Fig. 10.1) [59]. The as-prepared Pt@Pd-PCN-222(Hf) [also denoted as Pt@Pd-PMOF-2(Hf)] displays superior photocatalytic activity under visible-light irradiation, that is, an unprecedented maximum H_2 production rate of 22,674 μmol g^{-1} h^{-1} with a turnover number of 4131 in 32 hours, and the highest turnover frequency (TOF) of 482.5 h^{-1}.

The ligand modification for enhanced visible-light absorption can improve the photocurrent density and photocatalytic H_2 evolution rate thereof beyond UV irradiation [43,47,74,152,153]. For example, a specific proportional ligand of pristine MOF [MIL-125(Ti)] can be replaced by methylthio- or aminoterephthalate via solvent-assisted ligand-exchange method [23,64]. The methylthio-functionalized MOF decorated with Pt cocatalyst demonstrates a high quantum yield (8.90%) and a high H_2 production rate of 3814 μmol g^{-1} h^{-1} at visible irradiation (420 nm) by using triethanolamine (TEOA) as sacrificial agent (Fig. 10.2) [64], which is higher than that of amino-functionalized Pt/MOF photocatalyst (Pt/MIL-125-NH_2) [23]. The thioether-functionalization of MOFs with greater visible-light response is worthy of further investigation for more efficient MOF-based photocatalysts [65]. Furthermore, simultaneously engineering both electronic states and nanostructures could be realized, for example, through design of low-dimensional novel MOFs [e.g., one-dimensional (1D) titanium phosphonate MOF] [154]. By homogeneously incorporation of organophosphonic linkers that can narrow the bandgap and shift the light absorption to visible portion of the spectrum, as well as the unique 1D nanowire topology that can enhance the photoinduced charge carrier transport/separation with increased exposure of photoactive sites, the highly stable 1D phosphonate-based MOF delivers a remarkably improved photocatalytic H_2 evolution activity under irradiation of either visible light or a full-spectrum light, compared to conventional MOFs or TiO_2 NPs [154], partly owing to the long-term photostability [155].

Defect engineering is a versatile method to modulate the band and electronic structures as well as the material performance thereof. For example, Jiang et al. investigated a tailored MOF with controlled ligand defects, namely, defective UiO-66-NH_2-X (X represents the molar equivalents of the modulator to the linker in synthesis). The structural defects show remarkable effect on the photocatalysis, namely, switching on the photocurrent and photocatalytic H_2 production, which implies that the creation of structural defects with optimized contents (Pt@UiO-66-NH_2-100) is vital to promoting the efficient separation of photogenerated e−h pairs and the highest photocatalytic activity thereof. In other words, moderate structural defects possess the fastest relaxation kinetics and highest charge separation efficiency, while excessive defects retard the relaxation and reduce the charge separation efficiency, that is, a volcano-type trend of photocatalytic activity with increased structural defects (Fig. 10.3) [69].

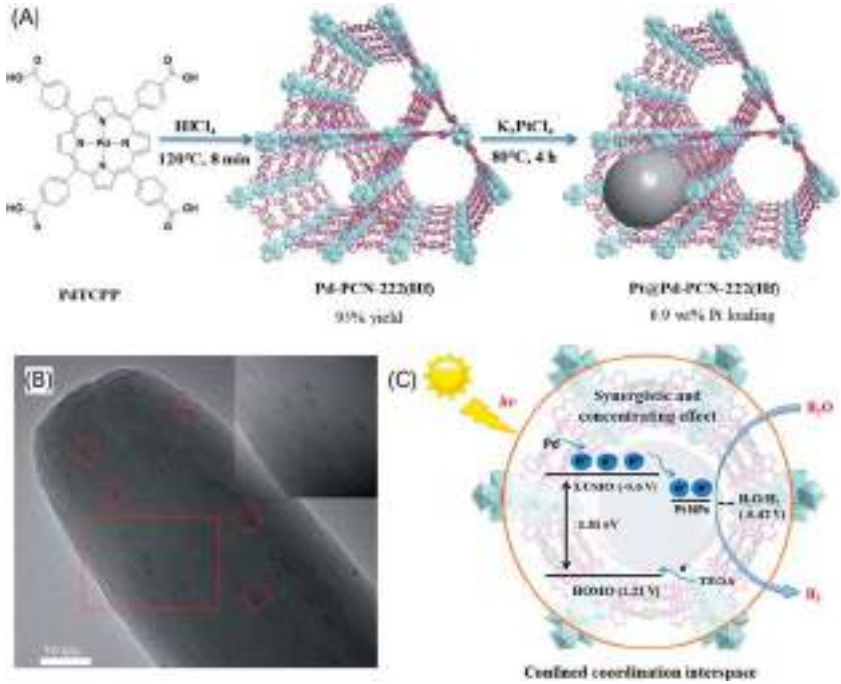

FIGURE 10.1 (A) The synthesis of well-distributed Pt-nanoparticles within confined coordination interspaces of self-sensitized porphyrin MOFs: Pd-PCN-222(Hf) and Pt@Pd-PCN-222(Hf). (B) TEM and high-magnification TEM (insert) images of Pt@Pd-PCN-222(Hf). (C) Schematic illustration of the structure and photocatalytic HER behavior of Pt@Pd-PCN-222(Hf). *HER*, hydrogen evolution reaction; *TEM*, transmission electron microscopy. *Reprinted from Li S, Mei HM, Yao SL, Chen ZY, Lu YL, Zhang L, et al. Well-distributed Pt-nanoparticles within confined coordination interspaces of self-sensitized porphyrin metal-organic frameworks: synergistic effect boosting highly efficient photocatalytic hydrogen evolution reaction. Chem Sci 2019;10 (45):10577–85. (Open Access under CC BY-NC 3.0).*

Single-atom catalysts (SACs, also named single-site catalysts), with isolated metal atoms anchored on supports and maximized utilization of metal atoms, are a novel and hot research frontier in catalysis [7,137,156–159]; and for integrating the strengths of both SACs and MOFs, single atoms immobilized on MOFs especially those with unique nanostructures have drawn significant attention in the application of catalysis but remain a great challenge [140,159]. To improve the dispersion and usage of noble-metal cocatalysts, which is beneficial to charge transfer in photocatalysis, Jiang et al., for the first time, designed a modified MOF with Pt atomically dispersed in a conventional MOF, that is, a kind of SAC named Al-TCPP-Pt [TCPP = 4,4′,4″,4‴-(porphyrin-5,10,15,20-tetrayl)tetrabenzoate or tetrakis(4-carboxyphenyl)porphyrin] via Pt(II) ions implanting into the center of porphyrin linkers of Al-TCPP followed by chemical reduction; thus, the

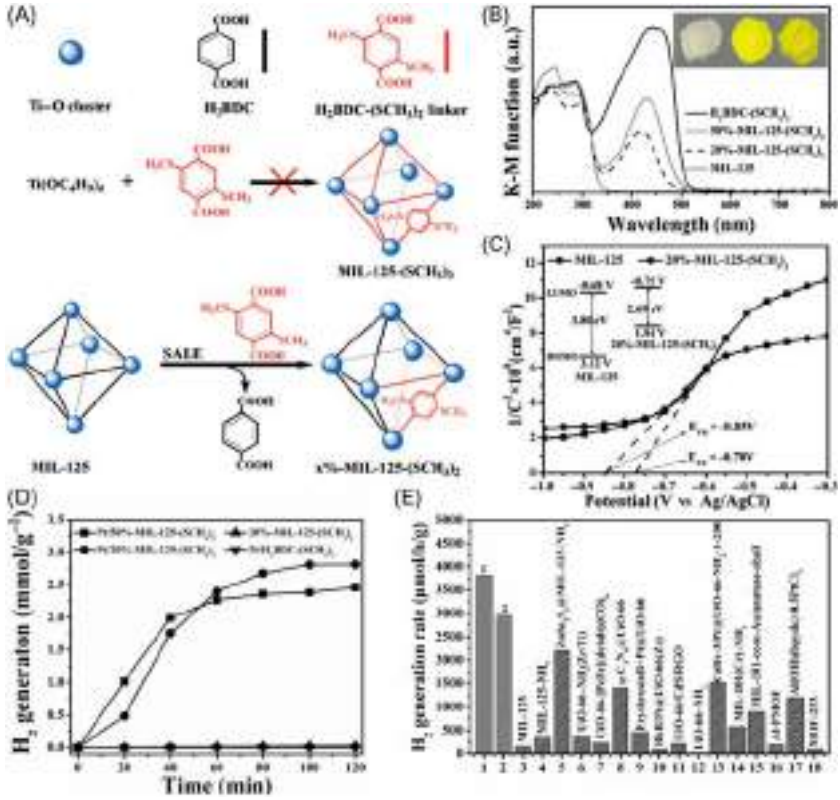

FIGURE 10.2 (A) Schematic diagram of the SALE process to obtain the methylthio-functionalized MOF photocatalyst *x*%-MIL-125-$(SCH_3)_2$ by using MIL-125 as the parent MOF and H_2BDC-$(SCH_3)_2$ as the exterior exchange linker. (B) UV/Vis spectra [inset: powder colors of MIL-125, 20%-MIL-125-$(SCH_3)_2$, and 50%-MIL-125-$(SCH_3)_2$]. (C) Mott−Schottky plots of MIL-125 and 20%-MIL-125-$(SCH_3)_2$ in 0.1 M Na_2SO_4 [inset shows the bandgaps of MIL-125 and 20%-MIL-125-$(SCH_3)_2$]. (D) Time course of photocatalytic H_2 production under 400−800 nm irradiation. (E) Activity of splitting water into H_2 under visible-light irradiation by using 20%-MIL-125-$(SCH_3)_2$ (1), 50%-MIL-125-$(SCH_3)_2$ (2), and those representative photocatalytic MOFs (3−18) (for details please refer to original content). *SALE*, solvent-assisted ligand exchange; *UV*, ultraviolet; *Vis*, visible. *Reprinted with permission from Han SY, Pan DL, Chen H, Bu XB, Gao YX, Gao H, et al. A methylthio-functionalized-MOF photocatalyst with high performance for visible-light-driven H_2 evolution. Angew Chem Int Ed 2018;57(31):9864−9. ©2018 Wiley-VCH Verlag GmbH & Co. KGaA, Weinheim.*

electrons can facilely transfer from the MOF (photosensitizer) to the Pt (acceptor) for H_2 production by water splitting under visible-light irradiation ($\lambda > 380$ nm) [138]. Due to the highly efficient electron transfer channels and the improved hydrogen binding energy, the single Pt atoms confined in the MOF exhibit a superb photocatalytic H_2 production activity (129 μmol g^{-1} h^{-1}), showing a TOF of 35 h^{-1}, ≈30 times that of Pt NPs

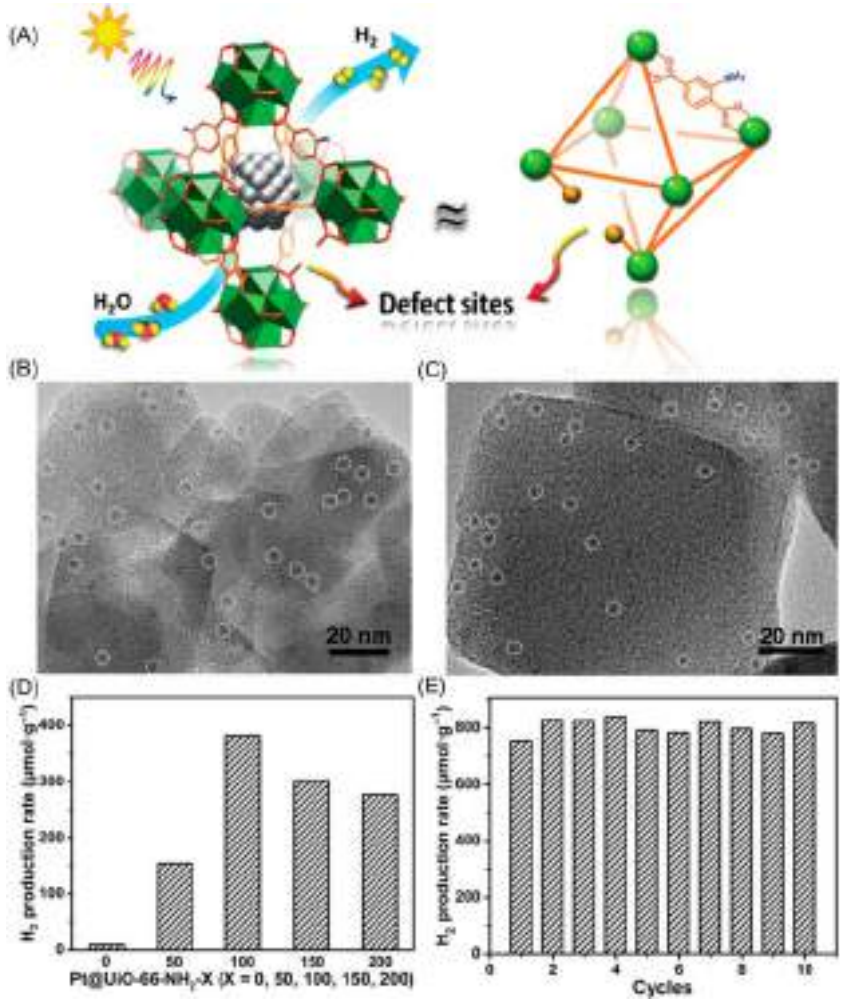

FIGURE 10.3 Switching on the photocatalysis of MOFs by engineering structural defects: (A) Schematic photocatalytic hydrogen production over Pt@UiO-66-NH_2-X with structural defects. (B and C) Typical TEM images of Pt@UiO-66-NH_2-0 and Pt@UiO-66-NH_2-100. (D) Photocatalytic H_2 performance from water splitting over varied catalysts in MeCN/TEOA/H_2O (10.8:1:0.2 v/v, 30 mL) under light irradiation, and (E) recycling performance of Pt@UiO-66-NH_2-100 (2 h cycle^{-1}). *Reprinted with permission from Ma X, Wang L, Zhang Q, Jiang HL. Switching on the photocatalysis of metal-organic frameworks by engineering structural defects. Angew Chem Int Ed 2019;58(35):12175–9. ©2019 Wiley-VCH Verlag GmbH & Co. KGaA, Weinheim.*

(~3 nm) stabilized by the same MOF and superior to all previously reported Pt-MOF composites on a per Pt-atom basis. Moreover, the photocatalytic H_2 production efficiency could be further enhanced by the incorporation of 2D

MOFs with much more accessible active sites and suppressed undesirable e−h recombination due to the minimized transport distance for photon-generated carriers from the interior to the surface [139]. Zuo et al. exploited an ultrathin MOF nanosheet with ultrahigh loading of single Pt atoms (12.0 wt.%) for efficient visible light−driven photocatalytic H_2 evolution via a surfactant-stabilized coordination strategy. The freestanding 2D SACs with an ultrathin thickness of 2.4 ± 0.9 nm exhibit a record-high photocatalytic H_2 evolution rate of 11,320 $\mu mol\ g^{-1}\ h^{-1}$ via water splitting under visible-light irradiation ($\lambda > 420$ nm) among those reported MOF-based photocatalysts (Fig. 10.4A−E). The interlinkage of Pt-TCPP by Cu^{2+} ions to form the MOF nanosheets (PtSA-MNSs), which is beneficial to the photon-generated electron transfer among the connected photosensitive porphyrin rings, contributes to the highly efficient photocatalysis. Such a synergistic action between Pt and Cu in the MOF nanosheets leads to a high H_2 generation rate. Also, these MOF-based 2D SACs nanosheets can be readily drop-casted onto solid substrates, forming thin films while retaining high photocatalytic activity, which is highly desirable for future practical solar H_2 production (Fig. 10.4F and G) [139]. Besides the 2D architectures, these SACs could also be manipulated into 1D morphology, for example, Wang et al. immobilized a series of noble-metal (Ir, Pt, Ru, Au, Pd) single atoms on zirconium−porphyrinic MOF hollow nanotubes (HNTM) structures by a facile solvothermal strategy, since the porphyrin units possess well-defined square-planar anchoring sites for these single atoms [140]. Due to the hollow structure and excellent photoelectrochemical performance, the HNTM-Ir/Pt bimetal SAC exhibits excellent catalytic activity in the visible-light photocatalytic H_2 evolution from water splitting, which is about 27 and 3.6 times higher than that of HNTM-Ir and HNTM-Pt, respectively, that is, the synergistic effect generated by porphyrin−Pt units (acting as catalyst) and porphyrin−Ir units (acting as photosensitizer) enhances the catalytic performance (Fig. 10.5) [140]. In addition, it should be noticed that these porphyrin-based MOF are usually hydrophobic, and organic solvents (e.g., acetonitrile) along with sacrificial reagents (e.g., TEOA, ascorbic acid) are unavoidably used; however, the 2D SACs with higher dispersibility can be directly utilized in water.

The incorporation of homogenous molecular catalyst (or organometallic complex) with favorable HER activity into MOFs (usually as photosensitizer and/or host matrix) can be utilized for enhanced photoinduced charge transfer and increased rate of photo-assisted transformation as well as enhanced stability of these molecular catalysts [24,53,160]. These diverse and typical molecular proton reduction catalysts/complexes include biomimetic diiron complexes (i.e., [FeFe]-hydrogenases) [24,161,162], cobaloximes [51,53,163,164], Pt complexes [50,70,165], and some other transition-metal Ni, Ru, Ir complexes [160] or transition-metal ions (Co^{2+}, Cu^{2+}, and Ni^{2+}) [86]. For example, PMD based on MOC with integrated light-harvesting and catalytic

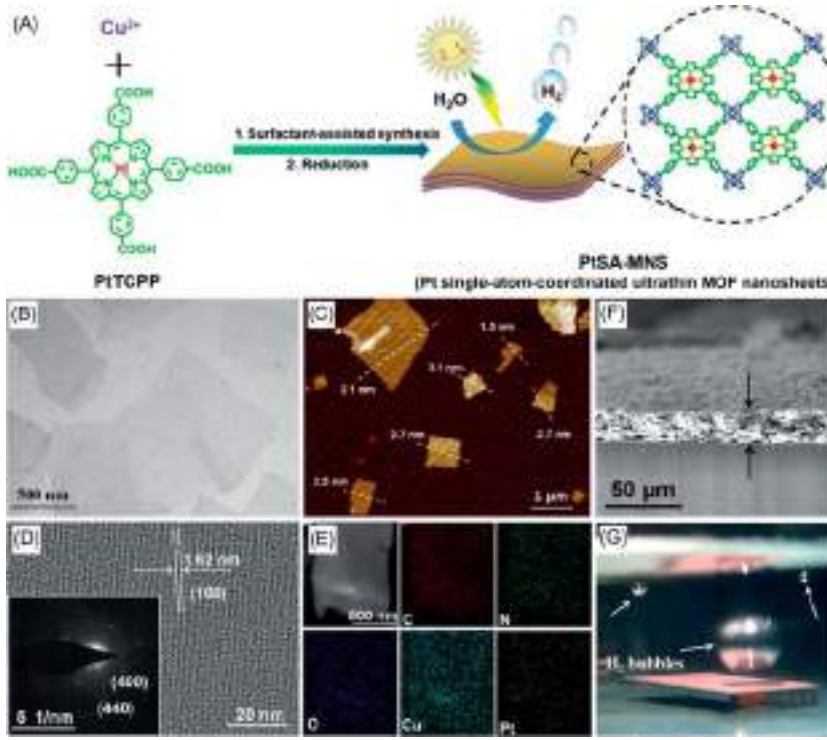

FIGURE 10.4 (A) Illustration of the synthetic route toward PtSA-MNSs through a surfactant-stabilized coordination strategy for efficient visible light−driven photocatalytic H_2 production. Morphological and structural characterizations of PtSA-MNSs: (B) TEM image, (C) AFM height profile, (D) HRTEM image (inset: SAED pattern), and (E) elemental mapping images. Photocatalytic activity characterizations: (F) sectional-view SEM image of the PtSA-MNS thin film prepared by drop-casting (inset: photograph of the thin film on glass), and (G) photograph of the film producing hydrogen gas. *PtSA-MNS*, Pt single atom−coordinated ultrathin MOF nanosheet. *AFM*, atomic force microscopy; *HRTEM*, high-resolution TEM; *TEM*, transmission electron microscopy; *SAED*, selected-area electron diffraction; *SEM*, scanning electron microscopy. *Reprinted with permission from Zuo Q, Liu TT, Chen CS, Ji Y, Gong XQ, Mai YY, et al. Ultrathin metal-organic framework nanosheets with ultrahigh loading of single Pt atoms for efficient visible-light-driven photocatalytic H_2 evolution. Angew Chem Int Ed 2019;58 (30):10198−203. ©2019 Wiley-VCH Verlag GmbH & Co. KGaA, Weinheim.*

centers is a high-efficiency molecular catalyst while often confronted with rapid deactivation because of photodegradation, detrimental aggregation, or inconvenient recovery; incorporation of these PMDs into MOFs will solve the problem. Luo et al. developed a method of heterogenization of the PMD via embedding an MOC, $[Pd_6(RuL_3)_8]^{28+}$ (MOC-16), into a ZIF-8-derived matrix, carbonate matrix of $Zn_x(MeIm)_x(CO_3)_x$ (CZIF), to promote proton and electron transfer. The hybridized MOC-16@CZIF inherits the highly efficient and directional electron transfer of MOC-16 and greatly increases

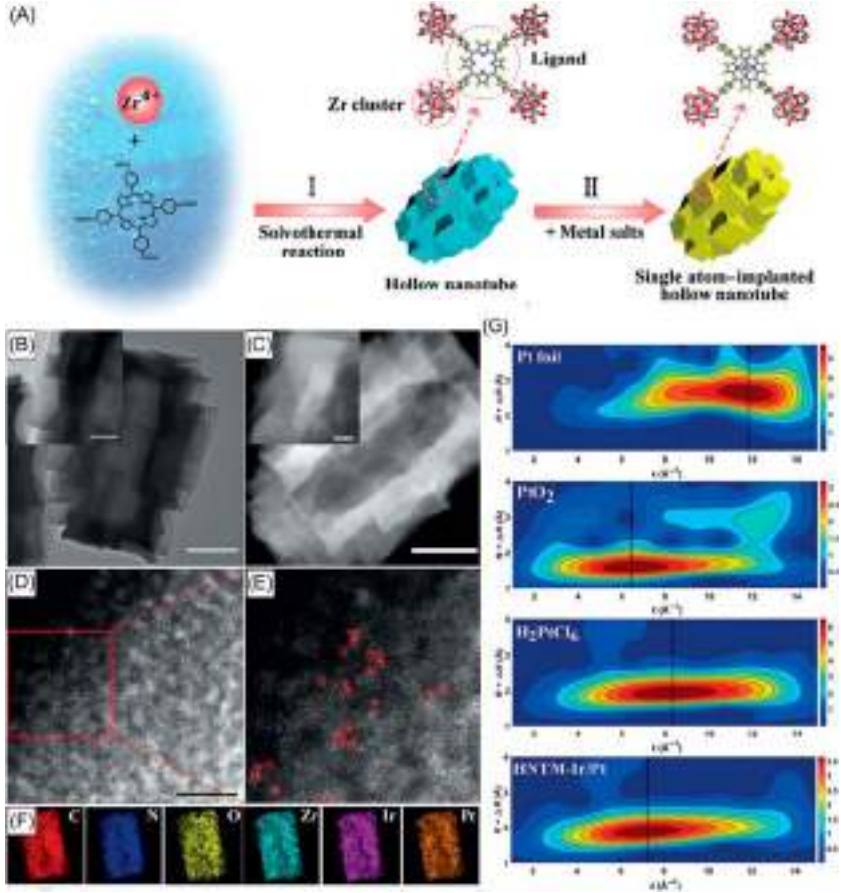

FIGURE 10.5 (A) Formation of the zirconium−porphyrin-based hollow nanotube MOF (HNTM) and the derived single atom-immobilized hollow nanotube MOF (HNTM-M). Characterization of HNTM-Ir/Pt: (B) TEM (scale = 100 nm; inset: high-magnification TEM image, scale = 50 nm); (C) HAADF-STEM (scale = 100 nm; inset: high-magnification STEM image, scale = 20 nm); (D) HAADF-STEM image (scale = 5 nm); (E) enlarged image (single Ir and Pt atoms are indicated by red circles); (F) EDX elemental mapping; (G) WT of Pt foil, PtO_2, H_2PtCl_6, and HNTM-Ir/Pt (Pt) samples. For WT contour plot of HNTM-Ir/Pt, it displays only one intensity maximum at 7.2 $Å^{-1}$ corresponding to Pt−N/Cl coordination (no intensity maximum of 11.8 $Å^{-1}$ associated with the Pt−Pt contribution for Pt foil), that is, the atomic dispersion of Pt atoms. *TEM*, transmission electron microscopy; *HAADF-STEM*, high-angle annular dark-field scanning transmission electron microscopy; *EDX*, energy-dispersive X-ray spectroscopy; *WT*, wavelet transform. *Reprinted with permission from He T, Chen S, Ni B, Gong Y, Wu Z, Song L, et al. Zirconium−porphyrin-based metal−organic framework hollow nanotubes for immobilization of noble-metal single atoms. Angew Chem Int Ed 2018;57(13):3493−8. ©2018 Wiley-VCH Verlag GmbH & Co. KGaA, Weinheim.*

the excited state electron lifetime as well as water wettability and proton delivery by the incorporation of CZIF matrix (note: the hydrophilic CO_3^{2-} in the CZIF matrix assists in proton delivery to proximal catalytic sits for efficient chemical reactions, while the hydrophobic ZIF-8 matrix does not work on H_2 evolution). Due to these synergistic effects, the heterogeneous MOC-16@CZIF exhibits a TOF of 0.43 s^{-1} ($\sim$1500 h^{-1}) in photocatalytic H_2 generation (based on Pd centers), increased by 50-fold over that of the homogeneous PMD (MOC-16). The heterogenization example sheds light on the design of multifunctional PMD@MOF hybrid to facilitate the molecular catalysts for practical photoconversion (Fig. 10.6) [130]. Another interesting case is that the metal location in metalloporphyrin matters, that is, the unusual OOP (out-of-plane) porphyrin-based MOF exhibits unexpectedly high photocatalytic H_2 production activity, far superior to the isostructural in-plane porphyrin-based MOF counterparts. The special phenomenon can be explained by the structure−property relationship, that is, the additional metal ions, for example In(III), locating above the porphyrin plane instead of fitting in a coplanar fashion into the cavity, form unusual OOP porphyrin that can readily detach from the porphyrin rings under light irradiation, inhibiting the e−h recombination and therefore greatly improving the e−h separation efficiency and photocatalytic performance [166].

The incorporation of inorganic materials (e.g., semiconductors) of narrow/reduced bandgaps with MOFs will not only enhance the visible-light absorption but also be beneficial to the improvement of charge separation dynamics [36,58,92]. Numerous related composites/hybrids have been recently reported, for example, CdS/MIL-101 [98], CdS-loaded 2D MOF [99], UiO-66/g-C_3N_4 [114], ZIF-8/g-C_3N_4 [115], g-C_3N_4/ultrathin bimetallic organic nanosheets (UMOFNs) (2D/2D, UMOFNs) [167], $Cd_{0.2}Zn_{0.8}S$@UiO-66-NH_2 [101], $ZnIn_2S_4$@NH_2-MIL-125(Ti) [102], $Zn_{0.8}Cd_{0.2}S$ NPs dispersed Co-based metal-organic layers [168], Cu_2O-encapsulated NH_2-MIL-125(Ti) [95], graphene well-wrapped UiO-66-NH_2 octahedrons [141], Ni-CPNS@CdS [Ni-CPNS: Ni(II) coordination polymer nanosheets] [169], p−n heterojunction of graphene/MOF [117], ternary ZnO/GO/Cu-MOF [170], MoS_2/UiO-66/CdS [105], UiO-66/CdS/RGO [106], g-C_3N_4@ZIF-67/NiS_x [107], and g-C_3N_4/MOF/MoS_2 [171]. Taking CdS as an example, in the CdS NP−decorated MOF composite systems (CdS/UiO-66), the effective electron transfer from excited CdS to UiO-66 significantly inhibits the recombination of photogenerated charge carriers, which ultimately boosts the photocatalytic activity for H_2 evolution. These insights into the enhanced charge separation dynamics (i.e., the generation of long-lifetime electrons) via synergistic effect unveiled by femtosecond transient absorption spectroscopy will afford the future fabrication of advanced composite/hybrid photocatalysts (Fig. 10.7) [92]. And by the adoption of 2D MOF with ultrathin thickness, highly exposed active sites and favorable band structure, the improved interactive nature (i.e., strong electronic coupling) between CdS

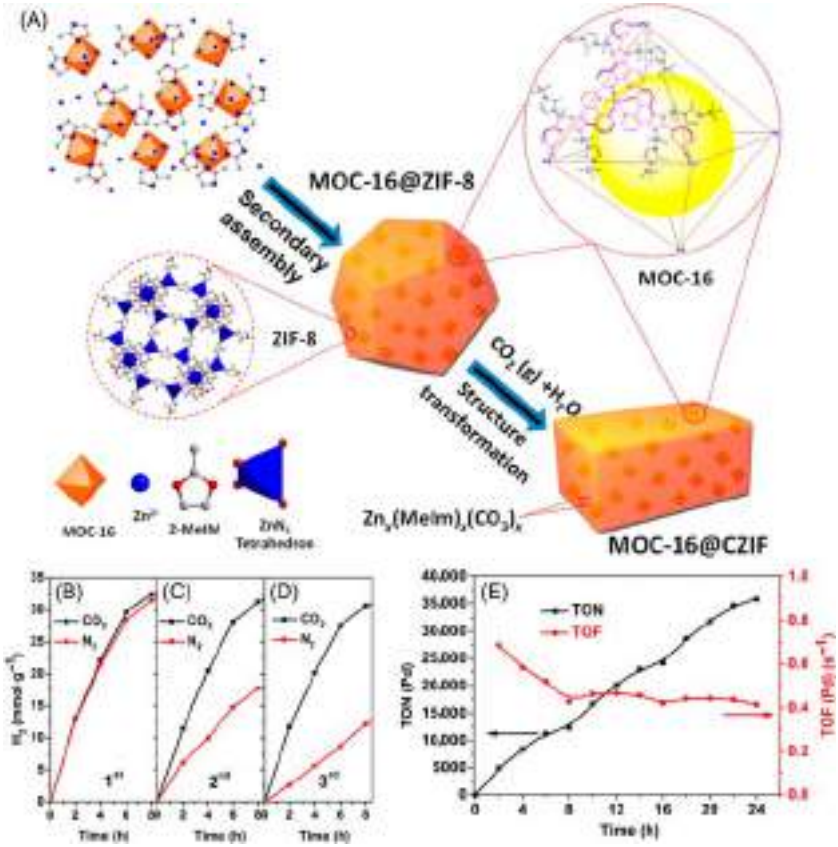

FIGURE 10.6 (A) Concept of heterogenization of photochemical molecular devices: schematic process to incorporate an MOC-16 into the ZIF-8 matrix, via coordination-assisted secondary assembly followed by transforming the ZIF-8 structure to the CZIF matrix in the presence of CO_2 and water, to promote proton and electron transfer. H_2 evolution curves with prolonged irradiation time for MOC-16@CZIF photocatalyst under N_2 and CO_2 atmospheres: (B) first cycle run, (C) second cycle run, (D) third cycle run, and (E) accumulated TONs and TOFs based on the Pd center in the catalyst durability test over 24 h under CO_2 atmosphere. TON = $n(H_2)/n$ (Pd), TOF = $d_{(TON)}/dt$. Visible light ($\lambda > 420$ nm) irradiation with 100 mW cm^{-2} intensity. *ZIF*, zeolitic imidazolate framework; *CZIF*, carbonated ZIF; *MOC*, metal-organic cage; *TOF*, turnover frequency; *TON*, turnover number. *Reprinted with permission from Luo YC, Chu KL, Shi JY, Wu DJ, Wang XD, Mayor M, et al. Heterogenization of photochemical molecular devices: embedding a metal–organic cage into a ZIF-8-derived matrix to promote proton and electron transfer. J Am Chem Soc 2019;141(33):13057–65.* ©*2019 American Chemical Society.*

and 2D MOF synergistically contributes to the significant photocatalytic performance (exhibiting a superior H_2 production activity of 45,201 μmol h^{-1} g^{-1}, exceeding that of Pt-loaded CdS by 185%) [99]. In addition, some polymeric semiconductor cocatalysts are also emerging and

showing promising application for modified MOF-based photocatalytic H_2 production [114,115]. Moreover, the incorporation of UV-harvesting semiconductor such as TiO_2 will also improve the charge separation and transfer although probably in a reverse way, that is, the photogenerated electron transfer from MOF to TiO_2, for example, double-shell TiO_2@ZIF-8 hollow nanospheres [94], NH_2-MIL-125(Ti)/TiO_2 nanorod heterojunction [172]. It is noteworthy that these TiO_2-based shells can also enhance the photochemical structural stability of the MOF matrices and the MOF-based composites thereof [93]. About the photocatalysis mechanisms [173], besides the common type-II, direct Z-scheme system with stronger redox ability and higher solar energy utilization efficiency has also been proposed (Fig. 10.8) [103,108,174,175].

POM clusters, including crystalline PTCs, with tunable energy band structures and facile incorporation into MOFs are a class of promising materials for photocatalytic application [110,176–178]. For example, Jiang et al.

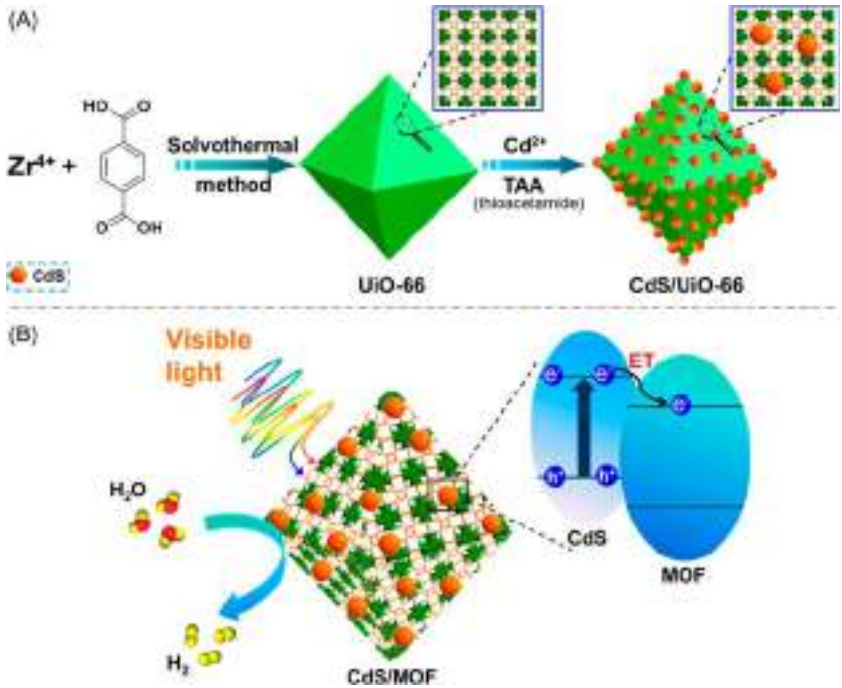

FIGURE 10.7 Schematic illustrations showing (A) synthetic process for CdS/UiO-66 composite and (B) charge separation dynamics (electron transfer dynamics from CdS to UiO-66) in the composite for enhanced photocatalytic activity of H_2 generation. *Reprinted with permission from Xu HQ, Yang S, Ma X, Huang J, Jiang H-L Unveiling charge-separation dynamics in CdS/metal–organic framework composites for enhanced photocatalysis. ACS Catal 2018;8 (12):11615–21. ©2018 American Chemical Society.*

developed a series of ternary PTC/CdS/MIL-101 materials with different organic ligands in PTCs via a stepwise solvothermal strategy (Fig. 10.9A) [110]. The bandgaps and absorption properties of these PTCs can be effectively modified by the organic ligands sensitization or changing the functional ligands, making it possible to tailor the photocatalytic activities of the obtained composites via structural chemistry methods (i.e., the increase of aromatic decorations in PTCs enhances the H_2 evolution activities of the ternary photocatalysts) (Fig. 10.9B and C). For the photocatalytic mechanism of the ternary catalyst, CdS produces photogenerated electrons under visible-light irradiation, PTCs promote the e−h separation/transfer, and the MOF provides massive catalytic sites for absorbing and splitting water molecules into hydrogen, that is, the synergistic effect of the three components gives rise to the highly efficient visible light−range photocatalytic H_2 production. The POM clusters may work as an effective molecular tool to tune the photocatalytic properties of MOF-based catalysts for promising application [110].

Some COFs with similar structural merits to MOFs but usually featured by their 2D layered structures, extended optical response, and beneficial charge carrier separation may also be integrated for better photocatalytic H_2 evolution [128]. Lan et al. developed a Schiff base−based COF (i.e., TpPa-1-COF), inspired by the physical appearance of the family (usually with *orange* to *dark red color*) and their large conjugation system for broader light harvesting (Fig. 10.10A−E) [128]. The optimized NH_2-UiO-66/TpPa-1-COF (4:6) demonstrates a maximum photocatalytic H_2 evolution rate of

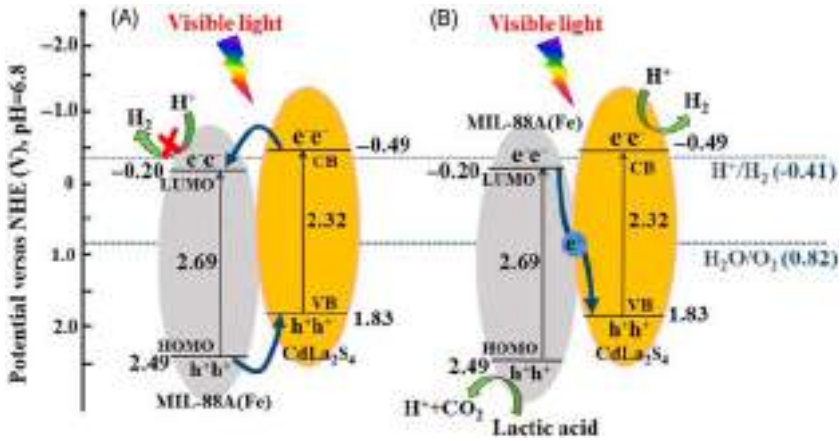

FIGURE 10.8 Possible electron transfer mechanism over a semiconductor/MOF composite, for example, $CdLa_2S_4$/MIL-88A(Fe): (A) type-II heterojunction and (B) direct Z-scheme. *Reprinted with permission from Chen Q, Li J, Cheng L, Liu H. Construction of $CdLa_2S_4$/MIL-88A(Fe) heterojunctions for enhanced photocatalytic H_2-evolution activity via a direct Z-scheme electron transfer. Chem Eng J 2020;379:122389. ©2019 Elsevier B.V.*

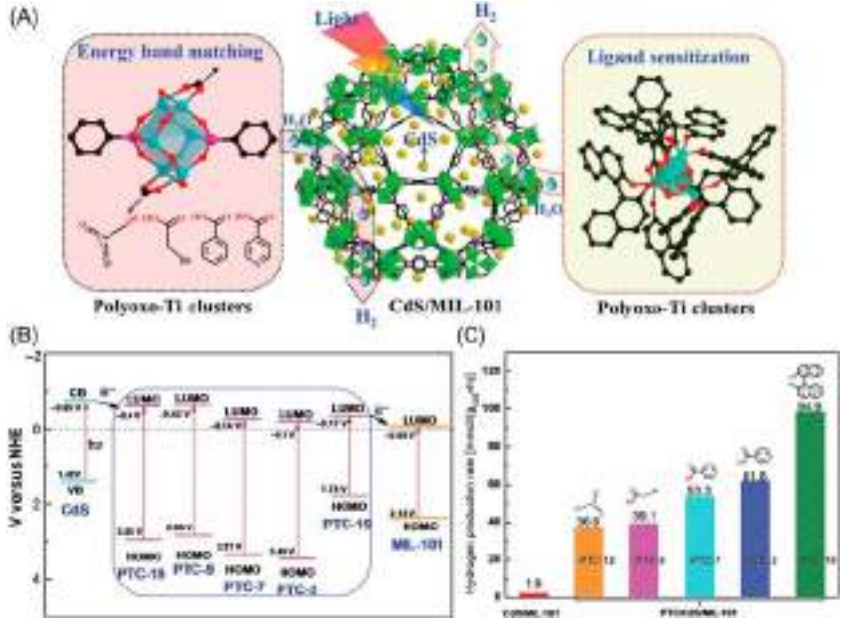

FIGURE 10.9 Assembling crystalline PTC and CdS nanoparticles to a porous matrix for efficient and tunable visible light−driven H_2 evolution activities: (A) strategy for constructing ternary PTC/CdS/MIL-101 photocatalysts; (B) the energy band position diagram of CdS, PTC, and MIL-101, demonstrating the proposed electron transfer process; and (C) H_2 production rates under visible-light (>420 nm) irradiation by different photocatalysts. *PTC*, polyoxo-titanium clusters. *Reprinted with permission from Jiang ZQ, Liu JX, Gao MY, Fan X, Zhang L, Zhang J. Assembling polyoxo-titanium clusters and CdS nanoparticles to a porous matrix for efficient and tunable H_2-evolution activities with visible light. Adv Mater 2017;29(5):1603369. ©2016 WILEY-VCH Verlag GmbH & Co. KGaA, Weinheim.*

23.4 mmol g^{-1} h^{-1} (with TOF of 402 h^{-1}), which is c. 20 times higher than that of the individual TpPa-1-COF and is one of the best performance photocatalysts for H_2 production among the state-of-the-art MOF- and COF-based photocatalysts (Fig. 10.10F and G). Further density functional theory (DFT) calculation reveals that the effective viable-light absorption of TpPa-1-COF, well-matching bandgaps between TpPa-1-COF and NH_2-UiO-66, and the efficient charge separation across the covalent heterojunction interface in the MOF/COF hybrid greatly contribute to the ultrahigh H_2 production rate of the hybrid materials [128]. The integration of MOFs and COFs provides a new insight into the design strategy and enriches the hybrid family [127,128].

Synergistic effects (or the integration of more than two effects) play an effective role for enhanced photocatalysis, for example, to offer a wide range of light absorption and rapid e−h separation/transfer that are desired for efficient photocatalysis [39]. More and more related cases are emerging, for

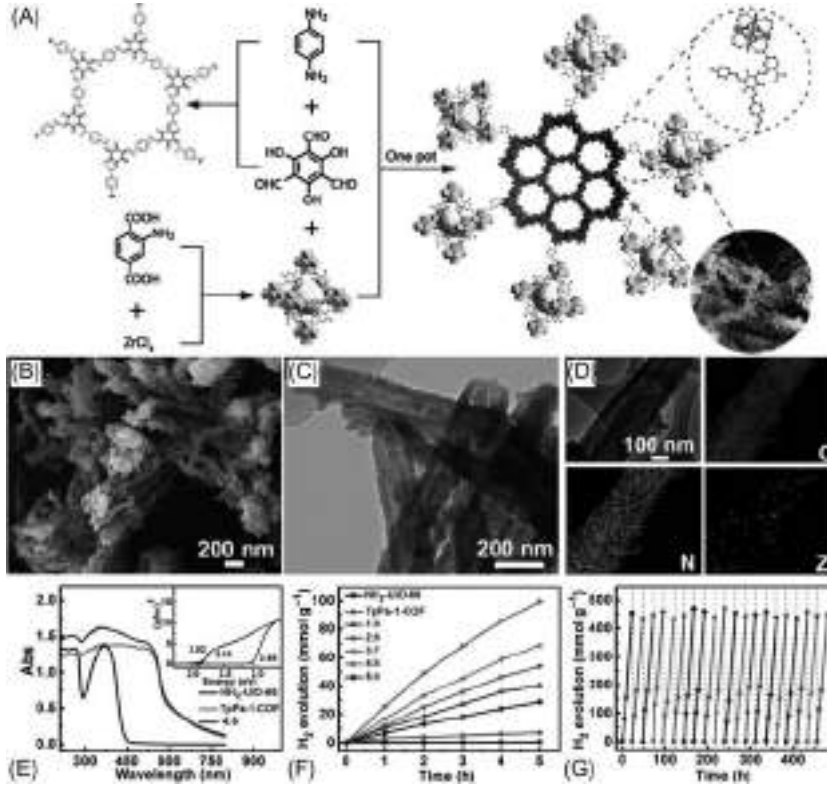

FIGURE 10.10 Rational design of MOF/COF hybrid materials for photocatalytic H_2 evolution: (A) schematic illustration of the synthesis of NH_2-UiO-66/TpPa-1-COF hybrid material; (B) SEM and (C) TEM images; (D) the corresponding elemental mappings of NH_2-UiO-66/TpPa-1-COF (4:6); (E) UV/Vis DRS and bandgap energies (inset); (F) the photocatalytic H_2 evolution activities; and (G) the photocatalytic stability of NH_2-UiO-66/TpPa-1-COF (4:6). *COF*, covalent organic framework; *DRS*, diffuse reflectance spectra; *UV*, ultraviolet; *Vis*, visible. *Reprinted with permission from Zhang FM, Sheng JL, Yang ZD, Sun XJ, Tang HL, Lu M, et al. Rational design of MOF/COF hybrid materials for photocatalytic H_2 evolution in the presence of sacrificial electron donors. Angew Chem Int Ed 2018;57(37):12106–10.* ©*2018 Wiley-VCH Verlag GmbH & Co. KGaA, Weinheim.*

example, Au@CdS/MIL-101 heterostructure [179], MIL-101 core–Au/anatase shell material [180], POM-Pt NPs@NH_2-MIL-53 [131], WP/UiO-66/CdS [181], sodium-doped C_3N_4/MOF heterojunction (Na_x-C_3N_4/Pt@UiO-66) [182], UiO-66–PANI–Co_3O_4 [125], carbon nanodots@NH_2–UiO-66/g-C_3N_4 [143], MXene Ti_3C_2/TiO_2/UiO-66-NH_2 hybrid [132], dye-sensitized composites/systems (Pt@UiO-66 [118,183], ZIF-9/CuO [96], UiO-66/WP [123], CoP/MIL-125-NH_2 [184], RGO/MOF/Co-Mo-S [185], NH_2-MIL-125 (Ti)/g-C_3N_4/NiPd [186], Pt-loaded UiO-66 [124], and MIL-101 loaded with Ni/NiO_x NPs [187], graphene well-wrapped UiO-66-NH_2 octahedrons [141],

Pt/NH_2-MIL-101 [188]), and hybrid Ru-M-UIO-67 with incorporated molecular Ru−photosensitizer and M-catalyst (M = Pt, Co) [38,119]. As a typical example, Jiang et al. designed a Pt@MOF/Au catalyst via the integration of plasmonic effects and Schottky junctions into MOF composites to steer charge flow for enhanced visible-light photocatalysis. In the Pt@MOF/Au composite, two types of metal−MOF interfaces with effective spatial separation of Pt and Au particles integrate the surface plasmon resonance [90] excitation of Au nanorods with a Schottky junction of Pt-MOF, which not only extends the light absorption of the pristine MOF from the UV to the visible region (via long-wavelength light−driven injection of plasmonic hot electrons into the LUMO of the MOF) but also steers the formation of charge flow and significantly accelerates charge transfer (via establishing the Schottky barrier as charge "pump"). As a result, the Pt@MOF/Au demonstrates a superior photocatalytic H_2 production rate in water splitting under visible-light irradiation, much higher than that of conventional Pt/MOF/Au, MOF/Au, and MOF/Pt with similar Pt/Au contents, highlighting the important synergistic role of each component and their location (e.g., Pt) in the catalyst (Fig. 10.11) [39]. Moreover, the incorporation of additional photosensitizer into MOFs, that is, dye sensitization, is another strategy for improved visible-light harvesting and enhanced hydrogen evolution efficiency thereof [118,183].

The exploitation of photocatalysts that harvest solar spectrum as broad as possible, for example, from UV to NIR region, remains a high priority but challenging target. Jiang et al. further rationally fabricated a specific photon upconversion−based MOF composite, that is, core−shell-structured UCNPs-Pt@MOF/Au, to achieve such broadband spectral response, in which the MOF is responsive to UV and a bit visible light, the plasmonic Au NPs accept visible light, and the UCNPs absorb NIR light to emit UV and visible light that are harvested by the MOF and Au once again (Fig. 10.12A−C). Moreover, the MOF not only facilitates the spatial separation of Au and Pt NPs on its surface but also provides necessary access from catalytic substrates to Pt active sites. As a result, the optimized composite exhibits excellent photocatalytic H_2 production activity ($280\ \mu mol\ g^{-1}\ h^{-1}$) under simulated solar light (consisting of UV, visible, and NIR irradiation). And the involved photocatalytic mechanisms under light irradiation falling in different wavelength ranges can be elucidated as follows, that is, the integration of plasmon and upconversion effects into MOF composites greatly extends light absorption, and Pt further boosts the charge separation, realizing the unique photocatalysis toward all three regions in full solar light (Fig. 10.12D) [40]. However, the wavelength-dependent photocatalytic H_2 production should be also noticed, that is, the NIR and visible irradiations contribute relatively less to the H_2 production than UV.

In addition, it should be noticed that some other chemicals (hydrogen carriers) can also be exploited for photocatalytic H_2 production via

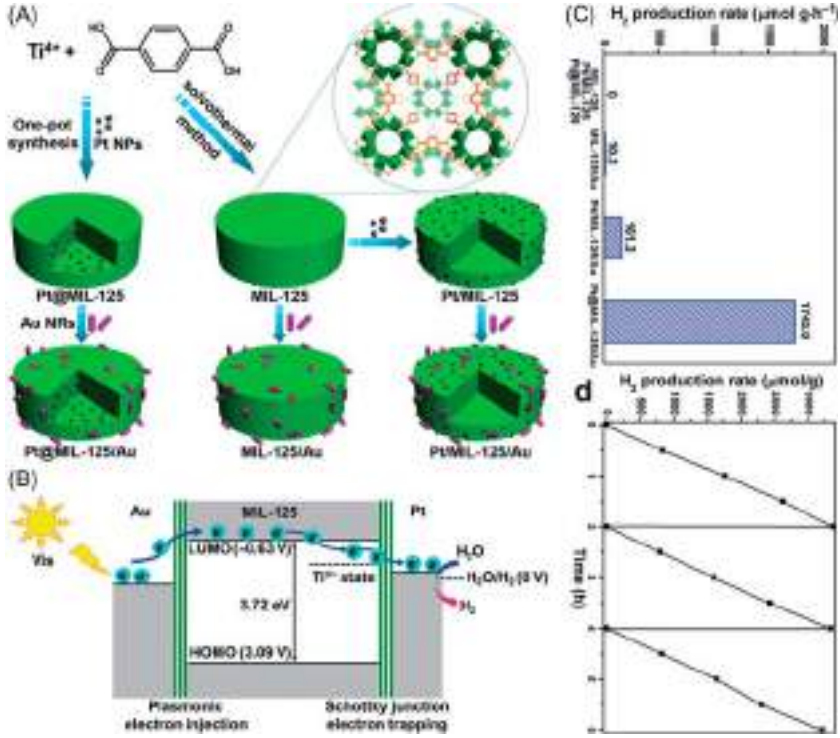

FIGURE 10.11 Integration of plasmonic effects and Schottky junctions into MOF composites to steer charge flow for enhanced visible-light photocatalysis: (A) schematic illustration for the synthesis of Pt@MIL-125/Au and the corresponding Pt/MIL-125/Au and MIL-125/Au analogues. (B) Schematic illustration showing the electron migration at the two metal−MOF interfaces based on the energy levels. (C) Photocatalytic H_2 production rates of different catalysts and (D) recycling performance of Pt@MIL-125/Au. The reaction with photocatalyst (5 mg) in MeCN/TEOA/H_2O (9:1:0.15 v/v, 20 mL) is irradiated by 380−800 nm light with a 300 W Xe lamp. *Reprinted with permission from Xiao JD, Han LL, Luo J, Yu SH, Jiang HL. Integration of plasmonic effects and Schottky junctions into metal-organic framework composites: steering charge flow for enhanced visible-light photocatalysis. Angew Chem Int Ed 2018;57(4):1103−7. Copyright 2018 Wiley-VCH Verlag GmbH & Co. KGaA, Weinheim.*

dehydrogenation, for example, hydrogen storage material ammonia borane (NH_3BH_3) [91,129,189] and formic acid (HCOOH) [190]; and these cases usually show enhanced catalytic activity of dehydrogenation under visible-light irradiation. And the performance of H_2 production is dependent on not only the photocatalysts, including the chemical components (e.g., mixed-node MOFs [120]) and structural design (e.g., mesoporous MOF [80], low-dimensional 1D or 2D MOFs [43,47,168]), but also many other parameters, including sacrificing electron donors [65,141], value-added oxidation half reaction [151], and solvents [120].

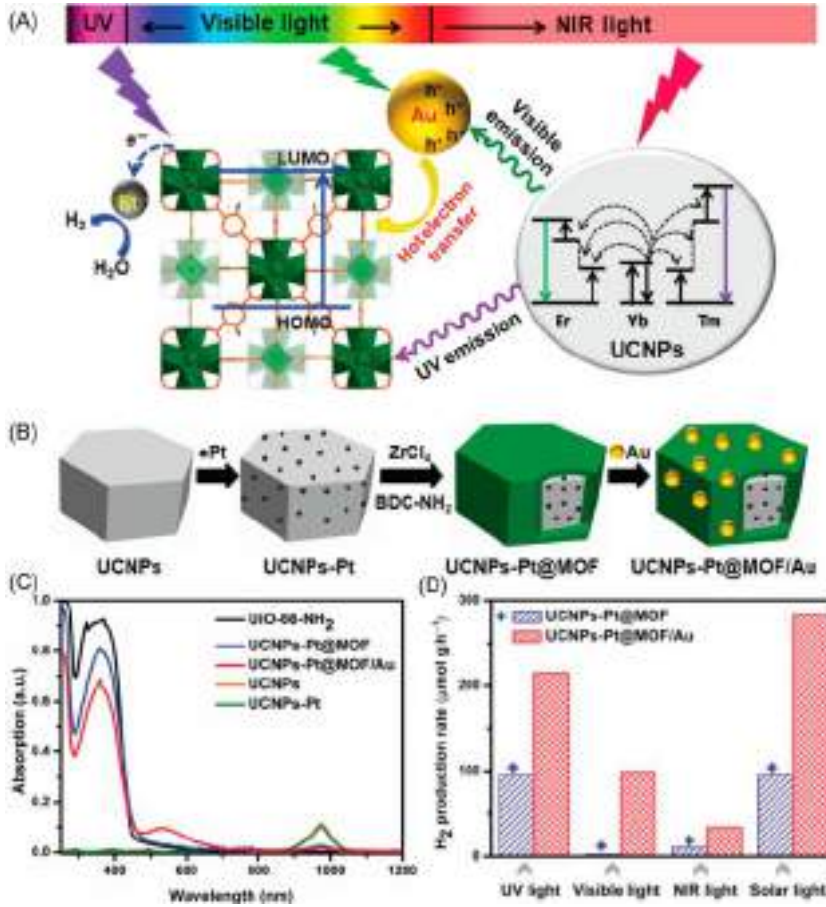

FIGURE 10.12 Plasmon and upconversion enhanced photocatalysis by from UV to NIR light-responsive MOF composites: (A) the light absorption of each component in the MOF composites and involved mechanism for photocatalytic hydrogen production. (B) Schematic illustration of synthetic process for the UCNPs-Pt@MOF/Au composites. (C) UV−vis−NIR absorption spectra. (D) Comparison of H_2 production rate of UCNPs-Pt@MOF and UCNPs-Pt@MOF/Au under UV (200−400 nm), visible (420−800 nm), NIR (980 nm), and simulated solar light irradiation. *NIR*, near-infrared; UCNP, upconversion nanoparticle; UV, ultraviolet; *Vis*, visible. *Reprinted with permission from Li DD, Yu SH, Jiang HL. From UV to near-infrared light-responsive metal-organic framework composites: plasmon and upconversion enhanced photocatalysis. Adv Mater 2018;30(27):1707377. ©2018 WILEY-VCH Verlag GmbH & Co. KGaA, Weinheim.*

10.4.2 Water splitting

The development of bifunctional MOFs with both water reduction and oxidation, especially under visible-light irradiation, is highly desirable for promising photocatalytic overall water splitting [54,122,191]. Xiao et al. synthesized a Cd-based MOF with π-conjugated layered framework

[Cd-TBAPy, H_4TBAPy = 1,3,6,8-tetrakis(*p*-benzoic acid)pyrene] and good visible-light absorption (bandgap of ~2.15 eV) [191]. The n-type Cd-MOF loaded with Pt or CoPi cocatalyst is active for water reduction/oxidation in the presence of hole/electron scavengers (Fig. 10.13). Especially, for the O_2 evolution, it exhibits a high rate of 81.7 μmol h^{-1} and optimized apparent quantum efficiency of 5.6% at 420 nm, much superior to previously reported MOF-based photocatalysts [e.g., MIL-101(Fe) [192], bismuth-based MOF [193]]. The CoPi and Pt can also be simultaneously deposited into MOFs, for example, MIL-125(Ti)-CoPi-Pt [54], from which stoichiometric H_2 and O_2 can be produced from pure water with no external bias voltage, not only showing decreased overpotential of H_2 and O_2 evolution but also improved photogenerated charge separation efficiency. More and more cocatalysts such as Pt, RuO_x, and CoO_x have shown positive influence on the photocatalytic activity of MOFs, including MIL-125(Ti)-NH_2 in the overall water splitting, and the presence of bimetallic Pt−RuO_x cocatalyst shows superior H_2 and O_2 production rate [194]. Although some noble metal−free photocatalysts such as POM@MOF (consisting of oxidative POM clusters and reductive MOF nodes) with high initial activity have been developed, their life span or stability should be further improved for the promising application of low-cost visible light−driven heterogeneous photosystems [122]. In addition, the electron-donating amine-substitution in MOFs, for example, NH_2-MIL-53(Fe), can decrease the gap energy and efficiently separate the

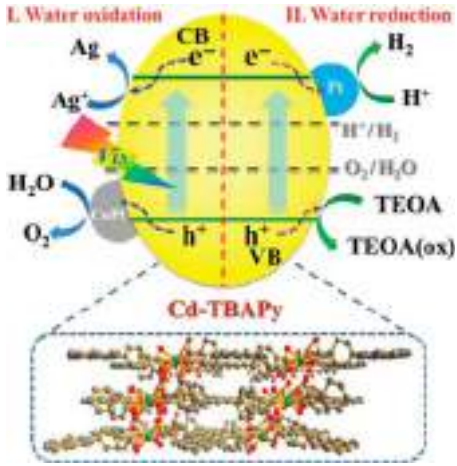

FIGURE 10.13 The proposed mechanism for visible light−driven photocatalytic H_2 and O_2 evolution over a cadmium-based MOF (Cd-TBAPy, loading of suitable cocatalysts such as Pt and CoPi). *Reprinted with permission from Xiao Y, Qi Y, Wang X, Wang X, Zhang F, Li C. Visible-light-responsive 2D cadmium−organic framework single crystals with dual functions of water reduction and oxidation. Adv Mater 2018;30(44):1803401. ©2018 WILEY-VCH Verlag GmbH & Co. KGaA, Weinheim.*

photoinduced e−h pairs that are beneficial for enhanced photocatalytic performance toward water oxidation [121], whereas adding electron-withdrawing groups by fluoro-substitution, for example, can prevent or slow the hydroxylation rate of the linkers (arising from the degradation of the linker through hydroxylation, that is, side reaction of the linkers with the created highly oxidizing/reactive intermediates such as hydroxyl radicals from monoelectronic oxidation of H_2O) via reducing the electron density of the benzene ring, thus stabilizing the organic linker and promoting the photocatalytic water oxidation reaction [68]. Further mechanism study reveals that the photogenerated holes and hydroxyl radicals are probably responsible for the photocatalytic water oxidation; however, the latter one may be a double-edged sword [68,121]. Further, in-depth mechanism investigation is needed.

Incorporation of compounds of transition-metal ions such as Ni^{2+} cations into the MOF pores through coordination to the amino groups can also form an efficient photocatalyst for overall water splitting. The Ni^{II} coordination to the Al-based MOF made from 2-aminoterephthalate sheds light on the design of MOF-based photocatalysts with assembled H_2 and O_2 evolution units in close proximity, where the transition-metal cation coordinated to the amino group acts as the H_2 evolution site and enhances the O_2 evolution at the benzene ring bearing the amino group [195].

In addition, some photocatalytic half reactions, including O_2 production (i.e., oxygen evolution reaction) arising from MOF-based hybrid photocatalysts are also investigated to further the development of overall water splitting via overcoming the bottleneck of water oxidation step (forming O−O bond) with higher energy barrier [196], for example, bismuth-based MOF (Bi-mna, mna = 2-mercaptonicotinic acid) [193], ultrasmall CoO_x@MIL-101 (Cr) [197], ZnO@M@ZIF-67 arrays (M = Au, Pt, and Ag) [198], MIL-100 (Fe)@$BiVO_4$ [196], Mo:$BiVO_4$−MIL-53(Fe) [199], mesoporous NH_2-MIL-125(Ti)@Bi_2MoO_6 core−shell heterojunction [200], and Fe_2O_3:Ti/NH_2-MIL-101(Fe) core−shell nanorod composite [72]. These MOFs usually not only enhance the visible-light absorption and interfacial e−h separation/transfer but also reduce the photocorrosion, thus improving the O_2 evolution rate [72,196,198]. And it can be expected that by regulating the morphology/structure with reduced thickness/size or with enhanced mesopores/defects, the electron transfer and mass transport will be facilitated and thus further boost the catalytic activity [200]. Moreover, the photoelectrochemical water splitting could also be a solution by the assistance of applied bias voltage [201].

10.4.3 Other applications

Due to the specific advantages of MOF-based photocatalysts with distinctive structure and superior properties, they can be applied to some other

promising fields that are now intensively studied, for example, CO_2 reduction, organosynthesis, and other environment-related fields.

The photocatalytic conversion of CO_2 into fuels or useful chemicals is another amazing solution to tackle the global warming and energy crisis [202−206]. As an emerging family of photocatalysts, MOF-based materials have the major advantages of light absorption, charge separation, and adsorption/activation (of a massive amount of CO_2 on the surface and in numerous internal pores) for enhanced photocatalysis [202]. Generally, constructing MOF−cocatalyst hybrid structures with desirable interfacial contact for enhanced electron transfer is believed to further improve CO_2 photoreduction. There are some recent reviews on the topic for reference [207−216].

Photocatalytic organosynthesis, or named organic transformation, has raised increasing interest for developing renewable energy or chemicals; MOF-based multifunctional photocatalytic materials with unique structural characteristics and properties promoted by photoactive inorganic nodes or organic ligands in MOFs have been playing a key role, and some references are listed for further information [208,217].

There are several main aspects to extend the MOF-based photocatalysts to environmental (remediation) applications [218−220], for example, organic pollutants degradation [221,222], toxic heavy metals removal [223,224], water depollution or wastewater decontamination [225−229], and air purification and disinfection [218].

10.5 Conclusion and outlook

Despite being in its infancy, the field of MOF-mediated photocatalysis has demonstrated promising applications. The improved photocatalytic performance of MOF-based materials is ascribed to the enhanced structural stabilization of the complex or cocatalysts when incorporated with MOFs as well as the protection of cocatalysts from undesirable charge recombination. The component/structural design and optimization of MOFs are needed to enhance the mass and charge carrier transfer along with light penetration for high-performance photocatalysis, in particular for hydrogen production and water splitting. The critical issues, including bandgap engineering, photosensitization, active site/cocatalyst optimization, and coupling with other functional materials are listed next for further research toward industrial application.

Further efforts should be paid on the controlled synthesis, effective surface/interface modification, water molecule adsorption ability as well as in-depth understanding of structure−performance correlation. The bandgap energy of MOFs can be tailored by changing the cluster and/or linkers. The postsynthetic exchange protocol is crucial as direct solvothermal synthesis fails to produce the functionalized MOFs.

Metal SACs based on MOFs are an ideal platform with great advantage and potential in developing efficient visible light−responsive photocatalysts to utilize solar energy. The incorporation of molecular catalysts with MOFs can have a synergistic effect and show the advantages of both components, that is, high catalytic activity, broad visible-light absorption, and long durability of light harvesters; the MOFs significantly improve the stability of molecular catalysts and the photocatalytic system thereof. In conjunction with photosensitizers and electron donors, MOF-based catalysts can further enhance the photochemical reactions, including hydrogen evolution.

The design of MOF-based composites/hybrids by incorporation of matched semiconductors can enhance charge separation/transfer efficiency, extend light absorption, and provide more active reaction sites, thus for a remarkably improved photocatalytic activity. The adoption of noble metal−-free cocatalysts with competent photocatalytic performance will make the MOF-based composites/hybrids more promising for practical photoconversion.

The development of modified MOF-based photocatalysts (or photoelectrodes for two half reactions) to construct overall water-splitting systems as well as to get rid of sacrificial electron donors/acceptors should be given more attention for prominent progress in the near future. And for the fabrication of overall water-splitting system, suitable thermodynamic band structures and effective bifunctional half-reaction kinetics should be considered. Developing affordable, environmentally benign systems of cocatalysts, photosensitizers, and MOF frameworks with high stability but mitigated separating/recycling problems is of critical importance to achieve economic photocatalysis and finally commercialization.

Acknowledgments

This work was supported by National Natural Science Foundation of China (grant no. 51403193), Opening Project of Sichuan University of Science and Engineering, Material Corrosion and Protection Key Laboratory of Sichuan Province (2019CL19), Vanadium and Titanium Resource Comprehensive Utilization Key Laboratory of Sichuan Province (2019FTSZ01), Municipal Sci-Tech program of Panzhihua (2019ZD-G-3), and Doctoral innovation fund of Panzhihua University (20190106).

Abbreviations

1D/2D/3D	one-/two-/three-dimensional
COF	covalent organic frameworks
e−h	electron−hole
ErB	Erythrosin B
EY	Eosin Y
(R)GO	(reduced) graphene oxide
LCCT	linker-to-cluster charge transition

HER	hydrogen evolution reaction
LUMO	lowest unoccupied molecular orbital
MeCN	acetonitrile
MOF	metal-organic framework
MOC	metal-organic cage
NIR	near-infrared
NPs	nanoparticles
OER	oxygen evolution reaction
OOP	out-of-plane
PMD	photochemical molecular device
POM	polyoxometalate
PSE	postsynthetic exchange
PTC	polyoxo-titanium cluster
SAC	single-atom catalyst
SPR	surface plasmon resonance
TEOA	triethanolamine
TOF	turnover frequency
TON	turnover number
UCNPs	upconversion nanoparticles
UV	ultraviolet

References

[1] Chu S, Majumdar A. Opportunities and challenges for a sustainable energy future. Nature 2012;488(7411):294–303.

[2] Chu S, Cui Y, Liu N. The path towards sustainable energy. Nat Mater 2016;16:16–22.

[3] Wang Q, Astruc D. State of the art and prospects in metal–organic framework (MOF)-based and MOF-derived nanocatalysis. Chem Rev 2020;120(2):1438–511.

[4] Ravelli D, Dondi D, Fagnoni M, Albini A. Photocatalysis. A multi-faceted concept for green chemistry. Chem Soc Rev 2009;38(7):1999–2011.

[5] Xu C, Ravi Anusuyadevi P, Aymonier C, Luque R, Marre S. Nanostructured materials for photocatalysis. Chem Soc Rev 2019;48(14):3868–902.

[6] Djurišić AB, He Y, Ng AMC. Visible-light photocatalysts: prospects and challenges. APL Mater 2020;8(3):030903.

[7] Gao C, Low J, Long R, Kong T, Zhu J, Xiong Y. Heterogeneous single-atom photocatalysts: fundamentals and applications. Chem Rev 2020. Available from: https://doi.org/10.1021/acs.chemrev.9b00840.

[8] Xiao J-D, Jiang H-L. Metal–organic frameworks for photocatalysis and photothermal catalysis. Acc Chem Res 2019;52(2):356–66.

[9] Wang S, Wang X. Multifunctional metal–organic frameworks for photocatalysis. Small 2015;11(26):3097–112.

[10] Wang C-C, Li J-R, Lv X-L, Zhang Y-Q, Guo G. Photocatalytic organic pollutants degradation in metal–organic frameworks. Energy Environ Sci 2014;7(9):2831–67.

[11] Fang Y, Ma Y, Zheng M, Yang P, Asiri AM, Wang X. Metal–organic frameworks for solar energy conversion by photoredox catalysis. Coord Chem Rev 2018;373:83–115.

[12] Dhakshinamoorthy A, Li Z, Garcia H. Catalysis and photocatalysis by metal organic frameworks. Chem Soc Rev 2018;47(22):8134–72.

[13] Hou C-C, Xu Q. Metal−organic frameworks for energy. Adv Energy Mater 2019;9 (23):1801307.
[14] Dhakshinamoorthy A, Asiri AM, García H. Metal−organic framework (MOF) compounds: photocatalysts for redox reactions and solar fuel production. Angew Chem Int Ed 2016;55(18):5414−45.
[15] Zhang T, Lin WB. Metal-organic frameworks for artificial photosynthesis and photocatalysis. Chem Soc Rev 2014;43(16):5982−93.
[16] Wang JL, Wang C, Lin WB. Metal-organic frameworks for light harvesting and photocatalysis. ACS Catal 2012;2(12):2630−40.
[17] Zeng L, Guo XY, He C, Duan CY. Metal-organic frameworks: versatile materials for heterogeneous photocatalysis. ACS Catal 2016;6(11):7935−47.
[18] Qiu J, Zhang X, Feng Y, Zhang X, Wang H, Yao J. Modified metal-organic frameworks as photocatalysts. Appl Catal B 2018;231:317−42.
[19] Li Y, Xu H, Ouyang S, Ye J. Metal−organic frameworks for photocatalysis. Phys Chem Chem Phys 2016;18(11):7563−72.
[20] Zhang TX, Jin YH, Shi YS, Li MC, Li JN, Duan CY. Modulating photoelectronic performance of metal-organic frameworks for premium photocatalysis. Coord Chem Rev 2019;380:201−29.
[21] Zhang HB, Liu GG, Shi L, Liu HM, Wang T, Ye JH. Engineering coordination polymers for photocatalysis. Nano Energy 2016;22:149−68.
[22] Bag PP, Sahoo P. Designing metal-organic frameworks based photocatalyst for specific photocatalytic reactions: a crystal engineering approach. In: Rajendran S, Naushad M, Ponce LC, Lichtfouse E, editors. Green photocatalysts for energy and environmental process. Cham: Springer International Publishing; 2020. p. 141−86.
[23] Horiuchi Y, Toyao T, Saito M, Mochizuki K, Iwata M, Higashimura H, et al. Visible-light-promoted photocatalytic hydrogen production by using an amino-functionalized Ti (IV) metal−organic framework. J Phys Chem C 2012;116(39):20848−53.
[24] Pullen S, Fei H, Orthaber A, Cohen SM, Ott S. Enhanced photochemical hydrogen production by a molecular diiron catalyst incorporated into a metal−organic framework. J Am Chem Soc 2013;135(45):16997−7003.
[25] Furukawa H, Cordova KE, O'Keeffe M, Yaghi OM. The chemistry and applications of metal-organic frameworks. Science 2013;341(6149):1230444.
[26] Dhakshinamoorth A, Asiri AM, Garcia H. 2D metal-organic frameworks as multifunctional materials in heterogeneous catalysis and electro/photocatalysis. Adv Mater 2019;31 (41):1900617.
[27] Ni W, Shi L. Metal-organic-framework composites as proficient cathodes for supercapacitor applications. Mater Res Foundations 2019;58:177−238.
[28] Li D, Xu H-Q, Jiao L, Jiang H-L. Metal-organic frameworks for catalysis: state of the art, challenges, and opportunities. EnergyChem 2019;1(1):100005.
[29] Pattengale B, SantaLucia DJ, Yang S, Hu W, Liu C, Zhang X, et al. Direct observation of node-to-node communication in zeolitic imidazolate frameworks. J Am Chem Soc 2018;140(37):11573−6.
[30] Zhu B, Zou R, Xu Q. Metal−organic framework based catalysts for hydrogen evolution. Adv Energy Mater 2018;8(24):1801193.
[31] Liang W, Babarao R, D'Alessandro DM. Microwave-assisted solvothermal synthesis and optical properties of tagged MIL-140A metal−organic frameworks. Inorg Chem 2013;52 (22):12878−80.

[32] Wang Z, Cohen SM. Postsynthetic modification of metal−organic frameworks. Chem Soc Rev 2009;38(5):1315−29.
[33] Cohen SM. Modifying MOFs: new chemistry, new materials. Chem Sci 2010;1(1):32−6.
[34] Lian X, Yan B. A postsynthetic modified MOF hybrid as heterogeneous photocatalyst for α-phenethyl alcohol and reusable fluorescence sensor. Inorg Chem 2016;55(22):11831−8.
[35] Hendon CH, Tiana D, Fontecave M, Sanchez C, D'arras L, Sassoye C, et al. Engineering the optical response of the titanium-MIL-125 metal−organic framework through ligand functionalization. J Am Chem Soc 2013;135(30):10942−5.
[36] Liu Y, Liu Z, Huang D, Cheng M, Zeng G, Lai C, et al. Metal or metal-containing nanoparticle@MOF nanocomposites as a promising type of photocatalyst. Coord Chem Rev 2019;388:63−78.
[37] Li SX, Luo P, Wu HZ, Wei CH, Hu Y, Qiu GL. Strategies for improving the performance and application of MOFs photocatalysts. ChemCatChem 2019;11(13):2978−93.
[38] Yang SZ, Fan DH, Hu WH, Pattengale B, Liu CM, Zhang XY, et al. Elucidating charge separation dynamics in a hybrid metal-organic framework photocatalyst for light-driven H_2 evolution. J Phys Chem C 2018;122(6):3305−11.
[39] Xiao JD, Han LL, Luo J, Yu SH, Jiang HL. Integration of plasmonic effects and Schottky junctions into metal-organic framework composites: steering charge flow for enhanced visible-light photocatalysis. Angew Chem Int Ed 2018;57(4):1103−7.
[40] Li DD, Yu SH, Jiang HL. From UV to near-infrared light-responsive metal-organic framework composites: plasmon and upconversion enhanced photocatalysis. Adv Mater 2018;30(27):1707377.
[41] Wen LL, Zhao JB, Lv KL, Wu YH, Deng KJ, Leng XK, et al. Visible-light-driven photocatalysts of metal-organic frameworks derived from multi-carboxylic acid and imidazole-based spacer. Cryst Growth Des 2012;12(3):1603−12.
[42] Yu Q, Dong H, Zhang X, Zhu YX, Wang JH, Zhang FM, et al. Novel stable metal-organic framework photocatalyst for light-driven hydrogen production. CrystEngComm 2018;20(23):3228−33.
[43] Li CQ, Xu H, Gao JK, Du WN, Shangguan L, Zhang X, et al. Tunable titanium metal-organic frameworks with infinite 1D Ti-O rods for efficient visible-light-driven photocatalytic H_2 evolution. J Mater Chem A 2019;7(19):11928−33.
[44] Cadiau A, Kolobov N, Srinivasan S, Goesten M, Haspel H, Bavykina A, et al. A new titanium metal organic framework with visible-light responsive photocatalytic activity. Angew Chem Int Ed 2020;59(32):13468−72.
[45] Fu YH, Sun DR, Chen YJ, Huang RK, Ding ZX, Fu XZ, et al. An amine-functionalized titanium metal-organic framework photocatalyst with visible-light-induced activity for CO_2 reduction. Angew Chem Int Ed 2012;51(14):3364−7.
[46] Xu H-Q, Hu J, Wang D, Li Z, Zhang Q, Luo Y, et al. Visible-light photoreduction of CO_2 in a metal−organic framework: boosting electron−hole separation via electron trap states. J Am Chem Soc 2015;137(42):13440−3.
[47] Wang X, Zhang X, Zhou W, Liu L, Ye J, Wang D. An ultrathin porphyrin-based metal-organic framework for efficient photocatalytic hydrogen evolution under visible light. Nano Energy 2019;62:250−8.
[48] Zhang P, Hu J, Liu B, Yang J, Hou H. Recent advances in metalloporphyrins for environmental and energy applications. Chemosphere 2019;219:617−35.
[49] Min Park J, Lee JH, Jang W-D. Applications of porphyrins in emerging energy conversion technologies. Coord Chem Rev 2020;407:213157.

[50] Zhou T, Du Y, Borgna A, Hong J, Wang Y, Han J, et al. Post-synthesis modification of a metal−organic framework to construct a bifunctional photocatalyst for hydrogen production. Energy Environ Sci 2013;6(11):3229−34.

[51] Nasalevich MA, Becker R, Ramos-Fernandez EV, Castellanos S, Veber SL, Fedin MV, et al. Co@NH_2-MIL-125(Ti): cobaloxime-derived metal-organic framework-based composite for light-driven H_2 production. Energy Environ Sci 2015;8(1):364−75.

[52] Xia ZQ, He C, Wang XG, Duan CY. Modifying electron transfer between photoredox and organocatalytic units via framework interpenetration for beta-carbonyl functionalization. Nat Commun 2017;8:361.

[53] Li Z, Xiao JD, Jiang HL. Encapsulating a Co(II) molecular photocatalyst in metal-organic framework for visible-light-driven H_2 production: boosting catalytic efficiency via spatial charge separation. ACS Catal 2016;6(8):5359−65.

[54] An Y, Xu B, Liu Y, Wang Z, Wang P, Dai Y, et al. Photocatalytic overall water splitting over MIL-125(Ti) upon CoPi and Pt co-catalyst deposition. ChemistryOpen 2017;6(6):701−5.

[55] Mancuso JL, Hendon CH. Titanium(IV) inclusion as a versatile route to photoactivity in metal-organic frameworks. Adv Theory Simul 2019;2(11):1900126.

[56] De Vos A, Hendrickx K, Van Der Voort P, Van Speybroeck V, Lejaeghere K. Missing linkers: an alternative pathway to UiO-66 electronic structure engineering. Chem Mater 2017;29(7):3006−19.

[57] Feng Y, Chen Q, Jiang MQ, Yao JF. Tailoring the properties of UiO-66 through defect engineering: a review. Ind Eng Chem Res 2019;58(38):17646−59.

[58] Liu Y, Huang D, Cheng M, Liu Z, Lai C, Zhang C, et al. Metal sulfide/MOF-based composites as visible-light-driven photocatalysts for enhanced hydrogen production from water splitting. Coord Chem Rev 2020;409:213220.

[59] Li S, Mei HM, Yao SL, Chen ZY, Lu YL, Zhang L, et al. Well-distributed Pt-nanoparticles within confined coordination interspaces of self-sensitized porphyrin metal-organic frameworks: synergistic effect boosting highly efficient photocatalytic hydrogen evolution reaction. Chem Sci 2019;10(45):10577−85.

[60] Jiao L, Wang Y, Jiang H-L, Xu Q. Metal−organic frameworks as platforms for catalytic applications. Adv Mater 2018;30(37):1703663.

[61] Li GD, Zhao SL, Zhang Y, Tang ZY. Metal-organic frameworks encapsulating active nanoparticles as emerging composites for catalysis: recent progress and perspectives. Adv Mater 2018;30(51):1800702.

[62] Wang H, Zhu Q-L, Zou R, Xu Q. Metal-organic frameworks for energy applications. Chem 2017;2(1):52−80.

[63] Qiu T, Liang Z, Guo W, Tabassum H, Gao S, Zou R. Metal−organic framework-based materials for energy conversion and storage. ACS Energy Lett 2020;5(2):520−32.

[64] Han S-Y, Pan D-L, Chen H, Bu X-B, Gao Y-X, Gao H, et al. A methylthio-functionalized-MOF photocatalyst with high performance for visible-light-driven H_2 evolution. Angew Chem Int Ed 2018;57(31):9864−9.

[65] Chen T-F, Han S-Y, Wang Z-P, Gao H, Wang L-Y, Deng Y-H, et al. Modified UiO-66 frameworks with methylthio, thiol and sulfonic acid function groups: the structure and visible-light-driven photocatalytic property study. Appl Catal B 2019;259:118047.

[66] An Y, Liu YY, Bian HT, Wang ZY, Wang P, Zheng ZK, et al. Improving the photocatalytic hydrogen evolution of UiO-67 by incorporating Ce^{4+}-coordinated bipyridinedicarboxylate ligands. Sci Bull 2019;64(20):1502−9.

[67] Wu XP, Gagliardi L, Truhlar DG. Cerium metal-organic framework for photocatalysis. J Am Chem Soc 2018;140(25):7904–12.
[68] Lionet Z, Kim TH, Horiuchi Y, Lee SW, Matsuoka M. Linker engineering of iron-based MOFs for efficient visible-light-driven water oxidation reaction. J Phys Chem C 2019;123 (45):27501–8.
[69] Ma X, Wang L, Zhang Q, Jiang HL. Switching on the photocatalysis of metal-organic frameworks by engineering structural defects. Angew Chem Int Ed 2019;58(35):12175–9.
[70] Lionet Z, Kim TH, Horiuchi Y, Lee SW, Matsuoka M. Facile post-synthetic modification of amine-functionalized metal-organic frameworks to integrate visible-light responsive Pt complexes for hydrogen evolution reaction. ChemNanoMat 2019;5(12):1467–70.
[71] Liao W-M, Zhang J-H, Wang Z, Lu Y-L, Yin S-Y, Wang H-P, et al. Semiconductive amine-functionalized Co(II)-MOF for visible-light-driven hydrogen evolution and CO_2 reduction. Inorg Chem 2018;57(18):11436–42.
[72] Dong Y-J, Liao J-F, Kong Z-C, Xu Y-F, Chen Z-J, Chen H-Y, et al. Conformal coating of ultrathin metal-organic framework on semiconductor electrode for boosted photoelectrochemical water oxidation. Appl Catal B 2018;237:9–17.
[73] de Miguel M, Ragon F, Devic T, Serre C, Horcajada P, García H. Evidence of photoinduced charge separation in the metal–organic framework MIL-125(Ti)-NH_2. ChemPhysChem 2012;13(16):3651–4.
[74] Li Y, Fu YQ, Ni BL, Ding KN, Chen WK, Wu KC, et al. Effects of ligand functionalization on the photocatalytic properties of titanium-based MOF: a density functional theory study. AIP Adv 2018;8(3):035012.
[75] Hendrickx K, Vanpoucke DEP, Leus K, Lejaeghere K, Van Yperen-De Deyne A, Van Speybroeck V, et al. Understanding intrinsic light absorption properties of UiO-66 frameworks: a combined theoretical and experimental study. Inorg Chem 2015;54 (22):10701–10.
[76] Zhang Y, Guo J, Shi L, Zhu YF, Hou K, Zheng YL, et al. Tunable chiral metal organic frameworks toward visible light-driven asymmetric catalysis. Sci Adv 2017;3(8):e1701162.
[77] Kamakura Y, Chinapang P, Masaoka S, Saeki A, Ogasawara K, Nishitani SR, et al. Semiconductive nature of lead-based metal–organic frameworks with three-dimensionally extended sulfur secondary building units. J Am Chem Soc 2020;142(1):27–32.
[78] Otal EH, Kim ML, Calvo ME, Karvonen L, Fabregas IO, Sierra CA, et al. A panchromatic modification of the light absorption spectra of metal–organic frameworks. Chem Commun 2016;52(40):6665–8.
[79] Hamad S, Hernandez NC, Aziz A, Ruiz-Salvador AR, Calero S, Grau-Crespo R. Electronic structure of porphyrin-based metal-organic frameworks and their suitability for solar fuel production photocatalysis. J Mater Chem A 2015;3(46):23458–65.
[80] Zhang FY, Zhang BX, Feng JQ, Tan XN, Liu L, Liu LF, et al. Highly mesoporous Ru-MIL-125-NH_2 produced by supercritical fluid for efficient photocatalytic hydrogen production. ACS Appl Energy Mater 2019;2(7):4964–70.
[81] Zhen WL, Gao HB, Tian B, Ma JT, Lu GX. Fabrication of low adsorption energy Ni-Mo cluster cocatalyst in metal-organic frameworks for visible photocatalytic hydrogen evolution. ACS Appl Mater Interfaces 2016;8(17):10808–19.
[82] Santaclara JG, Olivos-Suarez AI, Gonzalez-Nelson A, Osadchii D, Nasalevich MA, van der Veen MA, et al. Revisiting the incorporation of Ti(IV) in UiO-type metal-organic frameworks: metal exchange versus grafting and their implications on photocatalysis. Chem Mater 2017;29(21):8963–7.

[83] Castells-Gil J, Padial NM, Almora-Barrios N, Albero J, Ruiz-Salvador AR, Gonzalez-Platas J, et al. Chemical engineering of photoactivity in heterometallic titanium-organic frameworks by metal doping. Angew Chem Int Ed 2018;57(28):8453–7.

[84] Wu XP, Gagliardi L, Truhlar DG. Metal doping in cerium metal-organic frameworks for visible-response water splitting photocatalysts. J Chem Phys 2019;150(4):041701.

[85] Aziz A, Ruiz-Salvador AR, Hernandez NC, Calero S, Hamad S, Grau-Crespo R. Porphyrin-based metal-organic frameworks for solar fuel synthesis photocatalysis: band gap tuning via iron substitutions. J Mater Chem A 2017;5(23):11894–904.

[86] Karthik P, Shaheer ARM, Vinu A, Neppolian B. Amine functionalized metal–organic framework coordinated with transition metal ions: d–d transition enhanced optical absorption and role of transition metal sites on solar light driven H_2 production. Small 2020;16(12):1902990.

[87] Chen Y-Z, Zhang R, Jiao L, Jiang H-L. Metal–organic framework-derived porous materials for catalysis. Coord Chem Rev 2018;362:1–23.

[88] Shen L, Luo M, Huang L, Feng P, Wu L. A clean and general strategy to decorate a titanium metal–organic framework with noble-metal nanoparticles for versatile photocatalytic applications. Inorg Chem 2015;54(4):1191–3.

[89] Luo S, Zeng ZT, Zeng GM, Liu ZF, Xiao R, Chen M, et al. Metal organic frameworks as robust host of palladium nanoparticles in heterogeneous catalysis: synthesis, application, and prospect. ACS Appl Mater Interfaces 2019;11(36):32579–98.

[90] Wang M, Tang Y, Jin Y. Modulating catalytic performance of metal–organic framework composites by localized surface plasmon resonance. ACS Catal 2019;9(12):11502–14.

[91] Wen MC, Cui YW, Kuwahara Y, Mori K, Yamashita H. Non-noble-metal nanoparticle supported on metal-organic framework as an efficient and durable catalyst for promoting H_2 production from ammonia borane under visible light irradiation. ACS Appl Mater Interfaces 2016;8(33):21278–84.

[92] Xu H-Q, Yang S, Ma X, Huang J, Jiang H-L. Unveiling charge-separation dynamics in CdS/metal–organic framework composites for enhanced photocatalysis. ACS Catal 2018;8(12):11615–21.

[93] Zhang B, Zhang J, Tan X, Shao D, Shi J, Zheng L, et al. MIL-125-NH_2@TiO_2 core–shell particles produced by a post-solvothermal route for high-performance photocatalytic H_2 production. ACS Appl Mater Interfaces 2018;10(19):16418–23.

[94] Zhang M, Shang Q, Wan Y, Cheng Q, Liao G, Pan Z. Self-template synthesis of double-shell TiO_2@ZIF-8 hollow nanospheres via sonocrystallization with enhanced photocatalytic activities in hydrogen generation. Appl Catal B 2019;241:149–58.

[95] Karthik P, Balaraman E, Neppolian B. Efficient solar light-driven H_2 production: post-synthetic encapsulation of a Cu_2O co-catalyst in a metal-organic framework (MOF) for boosting the effective charge carrier separation. Catal Sci Technol 2018;8(13):3286–94.

[96] Fan K, Jin ZL, Yuan H, Hu HY, Bi YP. Coinstruction of CuO-modified zeolitic imidazolate framework-9 for photocatalytic hydrogen evolution. Chin J Catal 2017;38(12):2056–66.

[97] Zheng J, Jiao Z. Modified Bi_2WO_6 with metal-organic frameworks for enhanced photocatalytic activity under visible light. J Colloid Interface Sci 2017;488:234–9.

[98] He J, Yan Z, Wang J, Xie J, Jiang L, Shi Y, et al. Significantly enhanced photocatalytic hydrogen evolution under visible light over CdS embedded on metal–organic frameworks. Chem Commun 2013;49(60):6761–3.

[99] Ran J, Qu J, Zhang H, Wen T, Wang H, Chen S, et al. 2D metal organic framework nanosheet: a universal platform promoting highly efficient visible-light-induced hydrogen production. Adv Energy Mater 2019;9(11):1803402.

[100] Nguyen TN, Kampouri S, Valizadeh B, Luo W, Ongari D, Planes OM, et al. Photocatalytic hydrogen generation from a visible-light-responsive metal−organic framework system: stability versus activity of molybdenum sulfide cocatalysts. ACS Appl Mater Interfaces 2018;10(36):30035−9.

[101] Su Y, Zhang Z, Liu H, Wang Y. $Cd_{0.2}Zn_{0.8}S$@UiO-66-NH_2 nanocomposites as efficient and stable visible-light-driven photocatalyst for H_2 evolution and CO_2 reduction. Appl Catal B 2017;200(448-57).

[102] Liu H, Zhang J, Ao D. Construction of heterostructured $ZnIn_2S_4$@NH_2-MIL-125(Ti) nanocomposites for visible-light-driven H_2 production. Appl Catal B 2018;221:433−42.

[103] Chen Q, Li J, Cheng L, Liu H. Construction of $CdLa_2S_4$/MIL-88A(Fe) heterojunctions for enhanced photocatalytic H_2-evolution activity via a direct Z-scheme electron transfer. Chem Eng J 2020;379:122389.

[104] Bariki R, Majhi D, Das K, Behera A, Mishra BG. Facile synthesis and photocatalytic efficacy of UiO-66/$CdIn_2S_4$ nanocomposites with flowerlike 3D-microspheres towards aqueous phase decontamination of triclosan and H_2 evolution. Appl Catal B 2020;270:118882.

[105] Shen L, Luo M, Liu Y, Liang R, Jing F, Wu L. Noble-metal-free MoS_2 co-catalyst decorated UiO-66/CdS hybrids for efficient photocatalytic H_2 production. Appl Catal B 2015;166-167:445−53.

[106] Lin R, Shen L, Ren Z, Wu W, Tan Y, Fu H, et al. Enhanced photocatalytic hydrogen production activity via dual modification of MOF and reduced graphene oxide on CdS. Chem Commun 2014;50(62):8533−5.

[107] Zhang YK, Jin ZL. Boosting photocatalytic hydrogen evolution achieved by NiS_x coupled with g-C_3N_4@ZIF-67 heterojunction. J Phys Chem C 2019;123(30):18248−63.

[108] Mu F, Cai Q, Hu H, Wang J, Wang Y, Zhou S, et al. Construction of 3D hierarchical microarchitectures of Z-scheme UiO-66-$(COOH)_2$/$ZnIn_2S_4$ hybrid decorated with non-noble MoS_2 cocatalyst: a highly efficient photocatalyst for hydrogen evolution and Cr (VI) reduction. Chem Eng J 2020;384:123352.

[109] Zhang S, Du M, Xing Z, Li Z, Pan K, Zhou W. Defect-rich and electron-rich mesoporous Ti-MOFs based NH_2-MIL-125(Ti)@$ZnIn_2S_4$/CdS hierarchical tandem heterojunctions with improved charge separation and enhanced solar-driven photocatalytic performance. Appl Catal B 2020;262:118202.

[110] Jiang ZQ, Liu JX, Gao MY, Fan X, Zhang L, Zhang J. Assembling polyoxo-titanium clusters and CdS nanoparticles to a porous matrix for efficient and tunable H_2-evolution activities with visible light. Adv Mater 2017;29(5):1603369.

[111] Wang W, Xu X, Zhou W, Shao Z. Recent progress in metal-organic frameworks for applications in electrocatalytic and photocatalytic water splitting. Adv Sci 2017;4 (4):1600371.

[112] Nasir MS, Yang G, Ayub I, Wang S, Wang L, Wang X, et al. Recent development in graphitic carbon nitride based photocatalysis for hydrogen generation. Appl Catal B 2019;257:117855.

[113] Wang Z, Huang J, Mao J, Guo Q, Chen Z, Lai Y. Metal−organic frameworks and their derivatives with graphene composites: preparation and applications in electrocatalysis and photocatalysis. J Mater Chem A 2020;8(6):2934−61.

[114] Wang R, Gu L, Zhou J, Liu X, Teng F, Li C, et al. Quasi-polymeric metal−organic framework UiO-66/g-C_3N_4 heterojunctions for enhanced photocatalytic hydrogen evolution under visible light irradiation. Adv Mater Interfaces 2015;2(10):1500037.

[115] Tian L, Yang X, Liu Q, Qu F, Tang H. Anchoring metal-organic framework nanoparticles on graphitic carbon nitrides for solar-driven photocatalytic hydrogen evolution. Appl Surf Sci 2018;455:403−9.

[116] Hong J, Chen C, Bedoya FE, Kelsall GH, O'Hare D, Petit C. Carbon nitride nanosheet/metal−organic framework nanocomposites with synergistic photocatalytic activities. Catal Sci Technol 2016;6(13):5042−51.

[117] Xu XX, Lu TT, Liu XX, Wang XL. An efficient p-n heterojunction photocatalyst constructed from a coordination polymer nanoplate and a partically reduced graphene oxide for visible-light hydrogen production. Chem Eur J 2015;21(41):14638−47.

[118] Chen YF, Tan LL, Liu JM, Qin S, Xie ZQ, Huang JF, et al. Calix[4]arene based dye-sensitized Pt@UiO-66-NH_2 metal-organic framework for efficient visible-light photocatalytic hydrogen production. Appl Catal B 2017;206:426−33.

[119] Yang SZ, Pattengale B, Lee S, Huang J. Real-time visualization of active species in a single-site metal-organic framework photocatalyst. ACS Energy Lett 2018;3(3):532−9.

[120] Zhou Y, Hu W, Yang S, Zhang Y, Nyakuchena J, Duisenova K, et al. Site-selective probes of mixed-node metal organic frameworks for photocatalytic hydrogen generation. J Phys Chem C 2020;124(2):1405−12.

[121] Qu LL, Wang J, Xu TY, Chen QY, Chen JH, Shi CJ. Iron(III)-based metal-organic frameworks as oxygen-evolving photocatalysts for water oxidation. Sustain Energy Fuels 2018;2(9):2109−14.

[122] Shi D, Zheng R, Liu C-S, Chen D-M, Zhao J, Du M. Dual-functionalized mixed Keggin- and Lindqvist-type Cu_{24}-based POM@MOF for visible-light-driven H_2 and O_2 evolution. Inorg Chem 2019;58(11):7229−35.

[123] Jin ZL, Zhang YK, Ma QX. Orthorhombic WP co-catalyst coupled with electron transfer bridge UiO-66 for efficient visible-light-driven H_2 evolution. J Colloid Interface Sci 2019;556:689−703.

[124] Yuan Y-P, Yin L-S, Cao S-W, Xu G-S, Li C-H, Xue C. Improving photocatalytic hydrogen production of metal−organic framework UiO-66 octahedrons by dye-sensitization. Appl Catal B 2015;168-169:572−6.

[125] Singh AK, Gonuguntla S, Mahajan B, Pal U. Noble metal-free integrated UiO-66-PANI-Co_3O_4 catalyst for visible-light-induced H_2 production. Chem Commun 2019;55(96):14494−7.

[126] Wang Y, Ling LJ, Zhang W, Ding KJ, Yu Y, Duan WB, et al. A strategy to boost H_2 generation ability of metal-organic frameworks: inside-outside decoration for the separation of electrons and holes. ChemSusChem 2018;11(4):666−71.

[127] Li F, Wang D, Xing Q-J, Zhou G, Liu S-S, Li Y, et al. Design and syntheses of MOF/COF hybrid materials via postsynthetic covalent modification: an efficient strategy to boost the visible-light-driven photocatalytic performance. Appl Catal B 2019;243:621−8.

[128] Zhang FM, Sheng JL, Yang ZD, Sun XJ, Tang HL, Lu M, et al. Rational design of MOF/COF hybrid materials for photocatalytic H_2 evolution in the presence of sacrificial electron donors. Angew Chem Int Ed 2018;57(37):12106−10.

[129] Sun D, Jang S, Yim S-J, Ye L, Kim D-P. Metal doped core−shell metal-organic frameworks@covalent organic frameworks (MOFs@COFs) hybrids as a novel photocatalytic platform. Adv Funct Mater 2018;28(13):1707110.

[130] Luo Y-C, Chu K-L, Shi J-Y, Wu D-J, Wang X-D, Mayor M, et al. Heterogenization of photochemical molecular devices: embedding a metal−organic cage into a ZIF-8-derived matrix to promote proton and electron transfer. J Am Chem Soc 2019;141(33):13057−65.

[131] Guo W, Lv H, Chen Z, Sullivan KP, Lauinger SM, Chi Y, et al. Self-assembly of polyoxometalates, Pt nanoparticles and metal−organic frameworks into a hybrid material for synergistic hydrogen evolution. J Mater Chem A 2016;4(16):5952−7.
[132] Tian P, He X, Zhao L, Li W, Fang W, Chen H, et al. Enhanced charge transfer for efficient photocatalytic H_2 evolution over UiO-66-NH_2 with annealed $Ti_3C_2T_x$ MXenes. Int J Hydrogen Energy 2019;44(2):788−800.
[133] Tian P, He X, Zhao L, Li WX, Fang W, Chen H, et al. Ti_3C_2 nanosheets modified Zr-MOFs with Schottky junction for boosting photocatalytic HER performance. Sol Energy 2019;188:750−9.
[134] Hlophe PV, Dlamini LN. Synthesis of a semi-conductor-like MOF with black phosphorous as a composite for visible light-driven photocatalysis. RSC Adv 2019;9(64):37321−30.
[135] Aguilera-Sigalat J, Bradshaw D. Synthesis and applications of metal-organic framework-quantum dot (QD@MOF) composites. Coord Chem Rev 2016;307:267−91.
[136] Wu T, Liu X, Liu Y, Cheng M, Liu Z, Zeng G, et al. Application of QD-MOF composites for photocatalysis: energy production and environmental remediation. Coord Chem Rev 2020;403:213097.
[137] Wen MC, Mori K, Kuwahara Y, An TC, Yamashita H. Design of single-site photocatalysts by using metal-organic frameworks as a Matrix. Chem Asian J 2018;13(14):1767−79.
[138] Fang XZ, Shang QC, Wang Y, Jiao L, Yao T, Li YF, et al. Single Pt atoms confined into a metal-organic framework for efficient photocatalysis. Adv Mater 2018;30(7):1705112.
[139] Zuo Q, Liu TT, Chen CS, Ji Y, Gong XQ, Mai YY, et al. Ultrathin metal-organic framework nanosheets with ultrahigh loading of single Pt atoms for efficient visible-light-driven photocatalytic H_2 evolution. Angew Chem Int Ed 2019;58(30):10198−203.
[140] He T, Chen S, Ni B, Gong Y, Wu Z, Song L, et al. Zirconium−porphyrin-based metal−organic framework hollow nanotubes for immobilization of noble-metal single atoms. Angew Chem Int Ed 2018;57(13):3493−8.
[141] Wang Y, Yu Y, Li R, Liu H, Zhang W, Ling L, et al. Hydrogen production with ultrahigh efficiency under visible light by graphene well-wrapped UiO-66-NH_2 octahedrons. J Mater Chem A 2017;5(38):20136−40.
[142] Karthik P, Vinoth R, Zhang P, Choi W, Balaraman E, Neppolian B. $\pi-\pi$ interaction between metal−organic framework and reduced graphene oxide for visible-light photocatalytic H_2 production. ACS Appl Energy Mater 2018;1(5):1913−23.
[143] Zhang X, Dong H, Sun X-J, Yang D-D, Sheng J-L, Tang H-L, et al. Step-by-step improving photocatalytic hydrogen evolution activity of NH_2−UiO-66 by constructing heterojunction and encapsulating carbon nanodots. ACS Sustain Chem Eng 2018;6(9):11563−9.
[144] Wen M, Mori K, Kuwahara Y, An T, Yamashita H. Design and architecture of metal organic frameworks for visible light enhanced hydrogen production. Appl Catal B 2017;218:555−69.
[145] Luo HZ, Zeng ZT, Zeng GM, Zhang C, Xiao R, Huang DL, et al. Recent progress on metal-organic frameworks based- and derived-photocatalysts for water splitting. Chem Eng J 2020;383:123196.
[146] Shi Y, Yang AF, Cao CS, Zhao B. Applications of MOFs: recent advances in photocatalytic hydrogen production from water. Coord Chem Rev 2019;390:50−75.

[147] Liu S, Zhang C, Sun Y, Chen Q, He L, Zhang K, et al. Design of metal-organic framework-based photocatalysts for hydrogen generation. Coord Chem Rev 2020;413:213266.
[148] Santaclara JG, Kapteijn F, Gascon J, van der Veen MA. Understanding metal-organic frameworks for photocatalytic solar fuel production. CrystEngComm 2017;19(29):4118–25.
[149] Huang C-W, Nguyen V-H, Zhou S-R, Hsu S-Y, Tan J-X, Wu KCW. Metal–organic frameworks: preparation and applications in highly efficient heterogeneous photocatalysis. Sustain Energy Fuels 2020;4(2):504–21.
[150] Fateeva A, Chater PA, Ireland CP, Tahir AA, Khimyak YZ, Wiper PV, et al. A water-stable porphyrin-based metal-organic framework active for visible-light photocatalysis. Angew Chem Int Ed 2012;51(30):7440–4.
[151] Liu H, Xu C, Li D, Jiang H-L. Photocatalytic hydrogen production coupled with selective benzylamine oxidation over MOF composites. Angew Chem Int Ed 2018;57(19):5379–83.
[152] Sun M, Wang QQ, Qin C, Sun CY, Wang XL, Su ZM. An amine-functionalized zirconium metal-organic polyhedron photocatalyst with high visible-light activity for hydrogen production. Chem Eur J 2019;25(11):2824–30.
[153] Li L, Zhu S, Hao R, Wang JJ, Yang EC, Zhao XJ. Amino group promoted photocatalytic hydrogen evolution activity observed in two copper(II)-based layered complexes. Dalton Trans 2018;47(36):12726–33.
[154] Zhu Y-P, Yin J, Abou-Hamad E, Liu X, Chen W, Yao T, et al. Highly stable phosphonate-based MOFs with engineered bandgaps for efficient photocatalytic hydrogen production. Adv Mater 2020;32(16):1906368.
[155] Mateo D, Santiago-Portillo A, Albero J, Navalon S, Alvaro M, Garcia H. Long-term photostability in terephthalate metal-organic frameworks. Angew Chem Int Ed 2019;58(49):17843–8.
[156] Wang A, Li J, Zhang T. Heterogeneous single-atom catalysis. Nat Rev Chem 2018;2(6):65–81.
[157] Zhang H, Liu G, Shi L, Ye J. Single-atom catalysts: emerging multifunctional materials in heterogeneous catalysis. Adv Energy Mater 2018;8(1):1701343.
[158] Szuromi P. Hot single-atom catalysts. Science 2016;353(6295):133.
[159] Jiao L, Jiang HL. Metal-organic-framework-based single-atom catalysts for energy applications. Chem 2019;5(4):786–804.
[160] Wang M, Han K, Zhang S, Sun L. Integration of organometallic complexes with semiconductors and other nanomaterials for photocatalytic H_2 production. Coord Chem Rev 2015;287:1–14.
[161] Bozal-Ginesta C, Pullen S, Ott S, Hammarström L. Self-recovery of photochemical H_2 evolution with a molecular diiron catalyst incorporated in a UiO-66 metal-organic framework. ChemPhotoChem 2020;4:287–90.
[162] Sasan K, Lin Q, Mao C, Feng P. Incorporation of iron hydrogenase active sites into a highly stable metal–organic framework for photocatalytic hydrogen generation. Chem Commun 2014;50(72):10390–3.
[163] Roy S, Bhunia A, Schuth N, Haumann M, Ott S. Light-driven hydrogen evolution catalyzed by a cobaloxime catalyst incorporated in a MIL-101(Cr) metal-organic framework. Sustain Energy Fuels 2018;2(6):1148–52.
[164] Iglesias-Juez A, Castellanos S, Monte M, Agostini G, Osadchii D, Nasalevich MA, et al. Illuminating the nature and behavior of the active center: the key for photocatalytic H_2 production in Co@NH_2-MIL-125(Ti). J Mater Chem A 2018;6(36):17318–22.

[165] Zhang RQ, Liu YY, Wang JJ, Wang ZY, Wang P, Zheng ZK, et al. Post-synthetic platinum complex modification of a triazine based metal organic frameworks for enhanced photocatalytic H_2 evolution. J Solid State Chem 2019;271:260–5.

[166] Leng F, Liu H, Ding M, Lin Q-P, Jiang H-L. Boosting photocatalytic hydrogen production of porphyrinic MOFs: the metal location in metalloporphyrin matters. ACS Catal 2018;8(5):4583–90.

[167] Liang Y, Shang R, Lu J, An W, Hu J, Liu L, et al. 2D MOFs enriched g-C_3N_4 nanosheets for highly efficient charge separation and photocatalytic hydrogen evolution from water. Int J Hydrogen Energy 2019;44(5):2797–810.

[168] Xia BQ, Ran JR, Chen SM, Song L, Zhang XL, Jing LQ, et al. A two-dimensional metal-organic framework accelerating visible-light-driven H_2 production. Nanoscale 2019;11(17):8304–9.

[169] Jiang Z-Q, Chen X-L, Lu J, Li Y-F, Wen T, Zhang L. Ultrathin Ni(II)-based coordination polymer nanosheets as a co-catalyst for promoting photocatalytic H_2-production. Chem Commun 2019;55(46):6499–502.

[170] Shi X, Zhang J, Cui G, Deng N, Wang W, Wang Q, et al. Photocatalytic H_2 evolution improvement for H free-radical stabilization by electrostatic interaction of a Cu-BTC MOF with ZnO/GO. Nano Res 2018;11(2):979–87.

[171] Wang Z, Jin Z, Wang G, Ma B. Efficient hydrogen production over MOFs (ZIF-67) and g-C_3N_4 boosted with MoS_2 nanoparticles. Int J Hydrogen Energy 2018;43(29):13039–50.

[172] Yoon JW, Kim DH, Kim J-H, Jang HW, Lee J-H. NH_2-MIL-125(Ti)/TiO_2 nanorod heterojunction photoanodes for efficient photoelectrochemical water splitting. Appl Catal B 2019;244:511–18.

[173] Low J, Yu J, Jaroniec M, Wageh S, Al-Ghamdi AA. Heterojunction photocatalysts. Adv Mater 2017;29(20):1601694.

[174] Hao XQ, Cui ZW, Zhou J, Wang YC, Hu Y, Wang Y, et al. Architecture of high efficient zinc vacancy mediated Z-scheme photocatalyst from metal-organic frameworks. Nano Energy 2018;52:105–16.

[175] Subudhi S, Mansingh S, Swain G, Behera A, Rath D, Parida K. HPW-anchored UiO-66 metal-organic framework: a promising photocatalyst effective toward tetracycline hydrochloride degradation and H_2 evolution via Z-scheme charge dynamics. Inorg Chem 2019;58(8):4921–34.

[176] Fang W-H, Zhang L, Zhang J. A 3.6 nm Ti_{52}–oxo nanocluster with precise atomic structure. J Am Chem Soc 2016;138(24):7480–3.

[177] Tian P, He X, Li W, Zhao L, Fang W, Chen H, et al. Zr-MOFs based on Keggin-type polyoxometalates for photocatalytic hydrogen production. J Mater Sci 2018;53(17):12016–29.

[178] Zhao XX, Zhang SW, Yan JQ, Li LD, Wu GJ, Shi W, et al. Polyoxometalate-based metal-organic frameworks as visible-light-induced photocatalysts. Inorg Chem 2018;57(9):5030–7.

[179] Wang YJ, Zhang YN, Jiang ZQ, Jiang GY, Zhao Z, Wu QH, et al. Controlled fabrication and enhanced visible-light photocatalytic hydrogen production of Au@CdS/MIL-101 heterostructure. Appl Catal B 2016;185:307–14.

[180] Tilgner D, Kempe R. A plasmonic colloidal photocatalyst composed of a metal-organic framework core and a gold/anatase shell for visible-light-driven wastewater purification from antibiotics and hydrogen evolution. Chem Eur J 2017;23(13):3184–90.

[181] Zhang YK, Jin ZL. Effective electron-hole separation over a controllably constructed WP/UiO-66/CdS heterojunction to achieve efficiently improved visible-light-driven photocatalytic hydrogen evolution. Phys Chem Chem Phys 2019;21(16):8326–41.

[182] Pan Y, Li D, Jiang H-L. Sodium-doped C_3N_4/MOF heterojunction composites with tunable band structures for photocatalysis: interplay between light harvesting and electron transfer. Chem Eur J 2018;24(69):18403–7.

[183] He J, Wang J, Chen Y, Zhang J, Duan D, Wang Y, et al. A dye-sensitized Pt@UiO-66 (Zr) metal–organic framework for visible-light photocatalytic hydrogen production. Chem Commun 2014;50(53):7063–6.

[184] Li Y, Jin Z, Hao X, Wang G. Insights into the unique role of cobalt phosphide for boosting hydrogen evolution activity based on MIL-125-NH_2. Int J Hydrogen Energy 2019;44 (33):17909–21.

[185] Liu D, Jin Z, Bi Y. Charge transmission channel construction between a MOF and rGO by means of Co–Mo–S modification. Catal Sci Technol 2017;7(19):4478–88.

[186] Xu J, Gao J, Wang C, Yang Y, Wang L. NH_2-MIL-125(Ti)/graphitic carbon nitride heterostructure decorated with NiPd co-catalysts for efficient photocatalytic hydrogen production. Appl Catal B 2017;219:101–8.

[187] Liu XL, Wang R, Zhang MY, Yuan YP, Xue C. Dye-sensitized MIL-101 metal organic frameworks loaded with Ni/NiO_x nanoparticles for efficient visible-light-driven hydrogen generation. APL Mater 2015;3(10):104403.

[188] Wen MC, Mori K, Kamegawa T, Yamashita H. Amine-functionalized MIL-101(Cr) with imbedded platinum nanoparticles as a durable photocatalyst for hydrogen production from water. Chem Commun 2014;50(79):11645–8.

[189] Martis M, Meicheng W, Mori K, Yamashita H. Fabrication of metal nanoparticles in metal organic framework NH_2-MIL-125 by UV photo-assisted methods for optimized catalytic properties. Catal Today 2014;235:98–102.

[190] Cheng J, Gu X, Liu P, Zhang H, Ma L, Su H. Achieving efficient room-temperature catalytic H_2 evolution from formic acid through atomically controlling the chemical environment of bimetallic nanoparticles immobilized by isoreticular amine-functionalized metal-organic frameworks. Appl Catal B 2017;218:460–9.

[191] Xiao Y, Qi Y, Wang X, Wang X, Zhang F, Li C. Visible-light-responsive 2D cadmium–organic framework single crystals with dual functions of water reduction and oxidation. Adv Mater 2018;30(44):1803401.

[192] Horiuchi Y, Toyao T, Miyahara K, Zakary L, Van DD, Kamata Y, et al. Visible-light-driven photocatalytic water oxidation catalysed by iron-based metal–organic frameworks. Chem Commun 2016;52(29):5190–3.

[193] Wang G, Sun Q, Liu Y, Huang B, Dai Y, Zhang X, et al. A bismuth-based metal–organic framework as an efficient visible-light-driven photocatalyst. Chem Eur J 2015;21 (6):2364–7.

[194] Remiro-Buenamañana S, Cabrero-Antonino M, Martínez-Guanter M, Álvaro M, Navalón S, García H. Influence of co-catalysts on the photocatalytic activity of MIL-125(Ti)-NH_2 in the overall water splitting. Appl Catal B 2019;254:677–84.

[195] An Y, Liu Y, An P, Dong J, Xu B, Dai Y, et al. Ni^{II} Coordination to an Al-based metal–organic framework made from 2-aminoterephthalate for photocatalytic overall water splitting. Angew Chem Int Ed 2017;56(11):3036–40.

[196] Han Q, Dong Y, Xu C, Hu Q, Dong C, Liang X, et al. Immobilization of metal–organic framework MIL-100(Fe) on the surface of $BiVO_4$: a new platform for enhanced visible-light-driven water oxidation. ACS Appl Mater Interfaces 2020;12(9):10410–19.

[197] Han J, Wang D, Du Y, Xi S, Hong J, Yin S, et al. Metal−organic framework immobilized cobalt oxide nanoparticles for efficient photocatalytic water oxidation. J Mater Chem A 2015;3(41):20607−13.
[198] Dou Y, Zhou J, Zhou A, Li J-R, Nie Z. Visible-light responsive MOF encapsulation of noble-metal-sensitized semiconductors for high-performance photoelectrochemical water splitting. J Mater Chem A 2017;5(36):19491−8.
[199] Zhang BB, Dong GJ, Wang L, Zhang YJ, Ding Y, Bi YP. Efficient hydrogen production from MIL-53(Fe) catalyst-modified Mo:$BiVO_4$ photoelectrodes. Catal Sci Technol 2017;7(21):4971−6.
[200] Zhang S, Du M, Kuang J, Xing Z, Li Z, Pan K, et al. Surface-defect-rich mesoporous NH_2-MIL-125(Ti)@Bi_2MoO_6 core-shell heterojunction with improved charge separation and enhanced visible-light-driven photocatalytic performance. J Colloid Interface Sci 2019;554:324−34.
[201] Zhou S, Chen K, Huang J, Wang L, Zhang M, Bai B, et al. Preparation of heterometallic CoNi-MOFs-modified $BiVO_4$: a steady photoanode for improved performance in photoelectrochemical water splitting. Appl Catal B 2020;266:118513.
[202] Vu NN, Kaliaguine S, Do TO. Critical aspects and recent advances in structural engineering of photocatalysts for sunlight-driven photocatalytic reduction of CO_2 into fuels. Adv Funct Mater 2019;29(31):1901825.
[203] Tu W, Zhou Y, Zou Z. Photocatalytic conversion of CO_2 into renewable hydrocarbon fuels: state-of-the-art accomplishment, challenges, and prospects. Adv Mater 2014;26(27):4607−26.
[204] Lingampalli SR, Ayyub MM, Rao CNR. Recent progress in the photocatalytic reduction of carbon dioxide. ACS Omega 2017;2(6):2740−8.
[205] Li X, Yu J, Jaroniec M, Chen X. Cocatalysts for selective photoreduction of CO_2 into solar fuels. Chem Rev 2019;119(6):3962−4179.
[206] Hou S-L, Dong J, Zhao B. Formation of C−X bonds in CO_2 chemical fixation catalyzed by metal−organic frameworks. Adv Mater 2020;32(3):1806163.
[207] Li R, Zhang W, Zhou K. Metal−organic-framework-based catalysts for photoreduction of CO_2. Adv Mater 2018;30(35):1705512.
[208] Subudhi S, Rath D, Parida KM. A mechanistic approach towards the photocatalytic organic transformations over functionalised metal organic frameworks: a review. Catal Sci Technol 2018;8(3):679−96.
[209] Alkhatib II, Garlisi C, Pagliaro M, Al-Ali K, Palmisano G. Metal-organic frameworks for photocatalytic CO_2 reduction under visible radiation: a review of strategies and applications. Catal Today 2020;340:209−24.
[210] Wang QQ, Zhang Y, Lin HJ, Zhu JX. Recent advances in metal-organic frameworks for photo-/electrocatalytic CO_2 reduction. Chem Eur J 2019;25(62):14026−35.
[211] Zhang L, Zhang JQ. Metal-organic frameworks for CO_2 photoreduction. Front Energy 2019;13(2):221−50.
[212] Liu C, Wang WZ, Liu B, Qiao J, Lv LF, Gao XP, et al. Recent advances in MOF-based nanocatalysts for photo-promoted CO_2 reduction applications. Catalysts 2019;9(8):658.
[213] Kidanemariam A, Lee J, Park J. Recent innovation of metal-organic frameworks for carbon dioxide photocatalytic reduction. Polymers 2019;11(12):2090.
[214] Lei Z, Xue Y, Chen W, Qiu W, Zhang Y, Horike S, et al. MOFs-based heterogeneous catalysts: new opportunities for energy-related CO_2 conversion. Adv Energy Mater 2018;8(32):1801587.

[215] Zhang HG, Li JZ, Tan Q, Lu LL, Wang ZB, Wu G. Metal-organic frameworks and their derived materials as electrocatalysts and photocatalysts for CO_2 reduction: progress, challenges, and perspectives. Chem Eur J 2018;24(69):18137−57.

[216] Luo YH, Dong LZ, Liu J, Li SL, Lan YQ. From molecular metal complex to metal-organic framework: the CO_2 reduction photocatalysts with clear and tunable structure. Coord Chem Rev 2019;390:86−126.

[217] Deng XY, Li ZH, Garcia H. Visible light induced organic transformations using metal-organic-frameworks (MOFs). Chem Eur J 2017;23(47):11189−209.

[218] Wang Q, Gao QY, Al-Enizi AM, Nafady A, Ma SQ. Recent advances in MOF-based photocatalysis: environmental remediation under visible light. Inorg Chem Front 2020;7 (2):300−39.

[219] Zhu L, Meng L, Shi J, Li J, Zhang X, Feng M. Metal-organic frameworks/carbon-based materials for environmental remediation: a state-of-the-art mini-review. J Environ Manage 2019;232:964−77.

[220] Nadar SS, Varadan ON, Suresh S, Rao P, Ahirrao DJ, Adsare S. Recent progress in nanostructured magnetic framework composites (MFCs): synthesis and applications. J Taiwan Inst Chem Eng 2018;91:653−77.

[221] Jiang D, Xu P, Wang H, Zeng G, Huang D, Chen M, et al. Strategies to improve metal organic frameworks photocatalyst's performance for degradation of organic pollutants. Coord Chem Rev 2018;376:449−66.

[222] Zhang X, Wang J, Dong XX, Lv YK. Functionalized metal-organic frameworks for photocatalytic degradation of organic pollutants in environment. Chemosphere 2020;242:125144.

[223] Feng M, Zhang P, Zhou H-C, Sharma VK. Water-stable metal-organic frameworks for aqueous removal of heavy metals and radionuclides: a review. Chemosphere 2018;209:783−800.

[224] Wang CC, Du XD, Li J, Guo XX, Wang P, Zhang J. Photocatalytic Cr(VI) reduction in metal-organic frameworks: a mini-review. Appl Catal B 2016;193:198−216.

[225] Sharma VK, Feng MB. Water depollution using metal-organic frameworks-catalyzed advanced oxidation processes: a review. J Hazard Mater 2019;372:3−16.

[226] Fang Y, Yang Z, Li H, Liu X. MIL-100(Fe) and its derivatives: from synthesis to application for wastewater decontamination. Environ Sci Pollut Res 2020;27(5):4703−24.

[227] Gao Q, Xu J, Bu X-H. Recent advances about metal−organic frameworks in the removal of pollutants from wastewater. Coord Chem Rev 2019;378:17−31.

[228] Bedia J, Muelas-Ramos V, Penas-Garzon M, Gomez-Aviles A, Rodriguez JJ, Belver C. A review on the synthesis and characterization of metal organic frameworks for photocatalytic water purification. Catalysts 2019;9(1):52.

[229] Pi Y, Li X, Xia Q, Wu J, Li Y, Xiao J, et al. Adsorptive and photocatalytic removal of persistent organic pollutants (POPs) in water by metal-organic frameworks (MOFs). Chem Eng J 2018;337:351−71.

Chapter 11

The sensing applications of metal-organic frameworks and their basic features affecting the fate of detection

Tolga Zorlu[1], Luca Guerrini[1] and Ramon A. Alvarez-Puebla[1,2]
[1]*Department of Physical and Inorganic Chemistry and EMaS, Universitat Rovira I Virgili, Tarragona, Spain,* [2]*ICREA, Barcelona, Spain*

11.1 Introduction

Today, environmental pollution represents one of the major menaces threatening humanity and ecosystems. An important part of pollution consists of metals such as mercury, cadmium, or lead. In addition, molecular species product of the industrial or agricultural processes such as dioxins, polycyclic aromatic hydrocarbons (PAHs), or pesticides/insecticides are also harmful. The high increase of environmental pollution that has been witnessed in recent years has led to an analogous rise of chemical contaminants entering the human body through the food chain or by direct contact. This has been linked to cancer risks [1,2], the development of various neurodegenerative diseases such as Alzheimer's and Parkinson's [3,4], and an overall decrease in the quality of life. Various techniques such as high-performance liquid chromatography (HPLC), gas chromatography, and inductively coupled plasma mass spectrometry are being used for determining the chemicals in question.

Up to now, nanomaterial-based sensors are considered as one of the most powerful approaches to address current limitations of more established techniques. Nanotechnology facilitates novel materials with superior electrical [5], optical [6], thermal [7], and catalytic properties [8] that can be harnessed for sensing purposes over a wide range of applications. This has spurred the scientific research for the development of nano-sensors capable of detecting a very small amount of the target analyte, in a short time and with accuracy comparable or superior to that of conventional techniques [9,10]. Notably, nanomaterials based on Au [11] and Ag [12] nanoparticles (NPs), carbon

Metal-Organic Frameworks for Chemical Reactions. DOI: https://doi.org/10.1016/B978-0-12-822099-3.00011-3

nanotubes [13], and quantum dots [14] have been frequently used in sensing applications to detect of various toxic metal ions, gases, and environmental contaminants. In particular, plasmonic NPs provide significant advantages in terms of ease of production and scalability, as well as tunability of both morphological features and chemical–physical surface properties. In fact, plasmonic NPs can be produced in a large variety of different shapes (sphere, rod, star, etc.) that directly impact the sensing properties of the material [15]. As a result, this material constitutes one of the major components in designing nano-sensor studies [16–18].

Imparting porosity on nanomaterials offers a valuable tool for improving their performance since the consequent increase in surface area can lead to a larger number of binding events with target molecules. Remarkably, such materials may display high interactivity toward low-mass analytes. Therefore there is great interest in the development of engineered porous nanomaterials, and their use in sensing [19], catalysis [20], gas absorption [21], and drug delivery [22]. In this regard, metal-organic frameworks (MOFs), a class of porous coordination polymers, have attracted tremendous interest because of the porous structure, tunability of porous size, ease of production, and versatility. MOF constructs consist of two classes of components: (1) metal ions and (2) organic linkers. Selection of different types of these building elements enables the generation of MOFs with very different chemical and structural properties. In fact, approximately 20,000 different MOF variations have been reported so far [23]. The secondary building unit (SBU) is very important in defining each type of MOF. SBU is the portion that contains the coordination area of the metal ion and linker and was first described by Yaghi et al. [24]. Accordingly, the generation of MOFs with different pore diameters and geometries is related to the coordination numbers and areas of the metal ion and linker in the SBU as well as the length of the linker. Thus the high surface area and the adjustable pore size allow tailoring MOF structures for the selective encapsulation of the desired analyte.

In the synthesis of MOFs, some metal ions such as Zn^{2+}, Al^{3+}, Cu^{2+}, and Cd^{2+} are frequently used. Different ions impart different geometries such as tetrahedral, trigonal bipyramidal square, and pyramidal octahedral, due to their different coordination areas [25]. On the other hand, the chemical and structural diversity of the organic linkers further enhances the customizability of MOF-based substrates. Nonetheless, it is possible to recognize four basic features largely define the traits of MOFs to be used in sensing applications. These characteristics are (1) composition, (2) pore diameter, (3) pore morphology, and (4) combination with different nanomaterials.

11.2 Type of metal-organic frameworks

The feasibility of carefully tuning the structural and chemical properties of MOFs unlocks the application of these materials in variegated examples of

sensing platforms. Among the most common types of MOFs preferably employed in sensing, we can list MOF-5, HKUST-1, UiO, zeolitic imidazolate framework (ZIF), MOF-76, and MIL-101.

11.2.1 MOF-5

MOF-5 or IRMOF-1 is a type of MOF with $Zn_4O(BDC)_3$ (BDC: 1,4-benzodicarboxylate) composition. It was produced for the first time by Yaghi et al. [26]. It contains Zn^{2+} ion as metal and 1,4-benzodicarboxylate organic compound as a linker and is used in various sensing applications due to its high surface area, thermal stability, and extraordinarily large pore volume (Fig. 11.1A). For instance, MOF-5 was used as a sensing material for the detection of aniline [27], an aromatic amine of great relevance due to its carcinogenic nature. In this study, it was reported that Brunauer–Emmett–Teller surface area of MOF-5 was 1330 $m^2\ g^{-1}$ and with mesoporous structure (pore diameter: 20 nm). Thanks to these features, the MOF-5 showed an excellent sensitivity with a detection limit of c. 1.4 ppm. In addition, MOF-5 displays phosphorescence properties that can be also exploited for sensing purposes, as illustrated by Xu et al. in Pb^{2+} ion detection [28]. The results showed that the increasing Pb^{2+} content promotes a proportional intensification of the MOF-5 phosphorescence, which, in turn, enabled the quantification of Pb^{2+} in aqueous solution to 2 nmol L^{-1}. Notably, MOF-5 can be also combined with

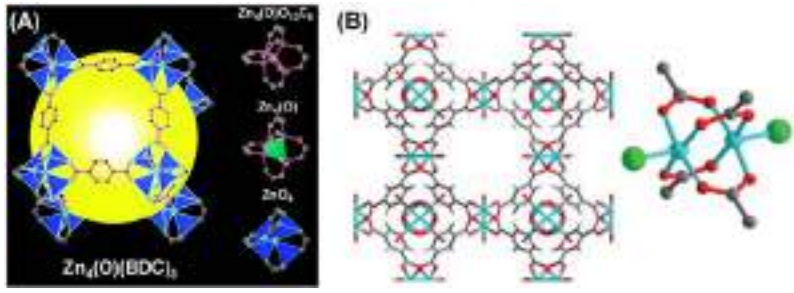

FIGURE 11.1 (A) Schematic representation of MOF-5 structure. $Zn_4(O)(BDC)_3$ represents all structure of MOF-5 framework. Yellow sphere indicates pore with a diameter of 18.5 Å. The $Zn_4(O)O_{12}C_6$ cluster represents as a ball and stick model (Zn, *blue*; O, *green*; C, *gray*). $Zn_4(O)$ tetrahedron indicated in green. On the other hand, ZnO_4 tetrahedra indicated in *blue*. (B) Schematic representation of HKUST-1 MOF structure (left). SBU of HKUST-1 (right). (C, *gray*; H, *light gray*; O, *red*; Cu, *cyan*). *MOF*, Metal-organic framework; *SBU*, secondary building unit. *(A) Adapted with permission from Li H, Eddaoudi M, O'Keeffe M, Yaghi OM. Design and synthesis of an exceptionally stable and highly porous metal–organic framework. Nature 1999;402:276–9. https://doi.org/10.1038/46248. ©1999 Nature and (B) adapted with permission from O'Neill LD, Zhang H, Bradshaw D. Macro-/microporous MOF composite beads. J Mater Chem 2010;20:5720–6. https://doi.org/10.1039/c0jm00515k [31]. ©2010 Royal Society of Chemistry.*

different chemicals or metals to improve, for instance, the thermal stability [29] or trigger fluorescence response to be exploited as a signal readout. In one of these studies, rhodamine B-encapsulated MOF-5 (RhB@MOF-5) was used for the fluorescence detection of β-glucuronidase (β-GCU) [30]. Here, the detection of β-GCU with both inner filter effect and static quenching effect was carried out using 4-nitrophenyl-β-D-glucuronide as substrate. The results showed that the detection limit was as low as 0.03 U L^{-1}.

11.2.2 HKUST-1

HKUST-1 is a class of MOFs combining Cu nodes with 1,3,5-benzenetricarboxylic acid organic linkers (Fig. 11.1B). It is preferred in sensing studies due to its high surface area, large porosity, chemiluminescence, and ease of production. For instance, Zhu et al. engineered chemiluminescence response of HKUST-1 for dopamine detection [32]. Specifically, HKUST-1 was reacted with luminol-H_2O_2 in alkaline medium to yield a new material (luminol-H_2O_2-HKUST-1) with enhanced chemiluminescence intensity (nearly $\times 90$ times). In the presence of dopamine a fast chemical reaction with luminol takes place leading to a decrease of chemiluminescence intensity, which made possible the detection of dopamine down to 2.3 nM.

In another study the trapping performance of HKUST-1-based thin films was tested against molecules with different size (anthracene, methylene blue, rhodamine B, and riboflavin) [33]. The uptake of the selected guest molecules was examined using both fluorescence and brightfield microscopy. Due to the relatively narrow pore size (10 and 14 Å), molecular sequestering was restricted to smaller molecules (anthracene and methylene blue) (Fig. 11.2). However, the high surface area of HKUST-1 can be further increased with different approaches and, in turn, so it can be its detection capability. For instance, HKUST-1 was decorated with graphite nanosheets (GNs) and used for the detection of 8-hydroxy-2′-deoxyguanosine (8-OHdG). 8-OHdG is a biomarker of DNA damage, the high levels of which have been related to cancer, neurodegenerative diseases, and diabetes [34]. HKUST-1/GN hybrids combine excellent electrochemical activity against the electrochemical oxidation of 8-OHdG and increased MOF surface area, which gave rise to a sensing platform with high detection rate ($\sim$240 seconds), sensitivity, and low detection limit ($\sim$2.5 nM).

11.2.3 UiO

UiOs are a family of MOFs that comprise three main classes: UiO-66, UiO-67, and UiO-68. The difference between these MOFs is due to the selected linker. Specifically, UiO-67 is a type of MOF obtained by coordinating the $Zr_6O_4(OH)_4$ metal unit with the 4,4′-biphenyldicarboxylate organic linker.

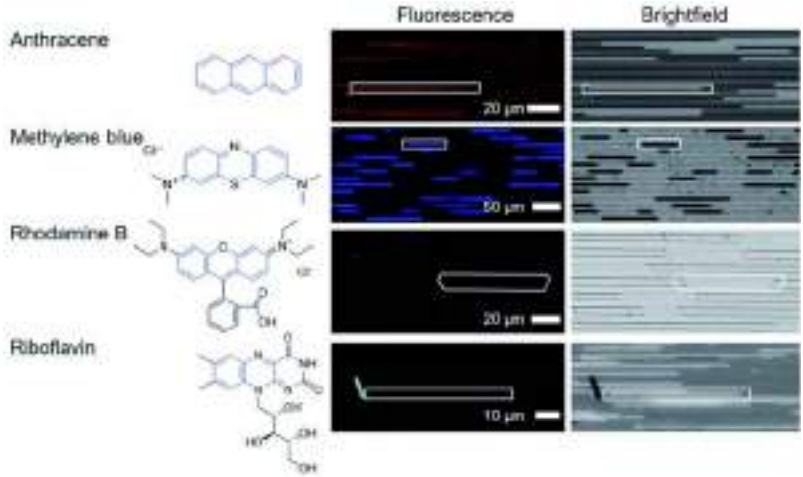

FIGURE 11.2 Monitoring of anthracene, methylene blue, rhodamine B, and riboflavin uptakes in HKUST-1 with fluorescence and brightfield microscopy. *Reprinted with permission from Guthrie S, Huelsenbeck L, Salahi A, Varhue W, Smith N, Yu X, et al. Crystallization of high aspect ratio HKUST-1 thin films in nanoconfined channels for selective small molecule uptake. Nanoscale Adv 2019;1:2946–52. https://doi.org/10.1039/c9na00254e. ©2019 Royal Society of Chemistry.*

On the other hand, UiO-66 and UiO-68 are obtained by coordinating the same metal building block but with different linkers such as 1,4-benzenedicarboxylate and 4,4′,4′-triphenyldicarboxylate, respectively (Fig. 11.3).

UiO MOF family is characterized by very high thermal stability. Thus they are ideal for gas-sensing applications because gas-sensing applications are largely carried out at high temperature. In addition, they also allow electrochemical [36] and fluorescent detection [37]. For instance, He et al. examined the use of UiO-66 in combination with 1,4-naphthalenedicarboxilic acid (NDC) as a fluorescent probe for Fe^{3+} metal ion detection [38]. The results showed a remarkable fluorescence quenching of UiO-66-NDC for upon selective Fe^{3+} binding providing the basis for the design of a sensitive sensing method. In another study, Miao et al. produced a dual-signal sandwich electrochemical immunosensor based on UiO-66, in which amperometric and square wave voltammetric methods were combined to detect Alzheimer's disease biomarker amyloid β (Aβ) protein as low as 3.3 fg mL^{-1} [39]. The sensing platform can be described as follows. First, the authors immobilized a $Cu-Al_2O_3-g\text{-}C_3N_4-Pd$ complex consisting of Al_2O_3, Cu, graphite carbon nitride ($g\text{-}C_3N_4$), and Pd NPs to yield the amperometric component of the sensor. On the other hand, UiO-66 was modified with polyaniline (PANI) providing higher surface area and conductivity. When supplemented with

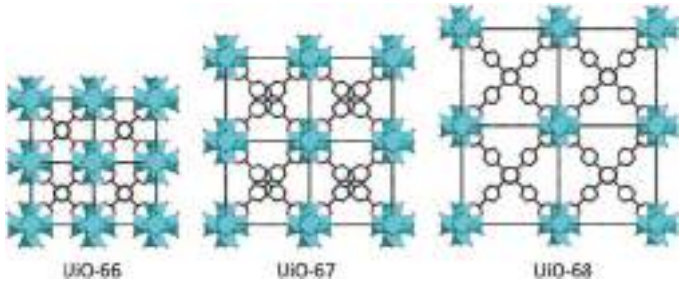

FIGURE 11.3 Schematic representation of UiO-66, UiO-67, and UiO-68. All of them have the same metal node (Zr) but different organic ligands for the structures (1,4-benzene-dicarboxylate; 4,4′-biphenyldicarboxylate; and 4,4′,4′-triphenyldicarboxylate, respectively) which allows obtaining different pore sizes. *Reprinted with permission from Yuan S, Feng L, Wang K, Pang J, Bosch M, Lollar C, et al. Stable metal-organic frameworks: design, synthesis, and applications. Adv Mater 2018;30:1704303. https://doi.org/10.1002/adma.201704303 [35]. ©2018 Wiley VCH.*

methylene blue, the voltammetric component of the system was obtained (Fig. 11.4).

11.2.4 ZIF-8 and ZIF-67

ZIF is an MOF subgroup organized as M−Im−M, where "Im" is the imidazole organic linker and "M" represents Zn^{2+} or Co^{2+} metal ion [40]. In the former case (Zn^{2+} ion), we refer to as ZIF-8, while in the latter case (Co^{2+} ion) the corresponding MOF is termed ZIF-67 (Fig. 11.5). Currently, ZIF-8 is largely preferred over ZIF-67 in both chemical and gas-sensing studies due to its ease of production, higher surface area, and thermal stability. However, there are also some studies that successfully combined the two classes of ZIF to yield more sensitive sensors, as reported for instance by Matatagui et al. [41]. In this study, a gas sensor was developed by combining ZIF-8 and ZIF-67 nanocrystals and tested on multiple analytes such as toluene, ethanol, carbon monoxide, hydrogen, and nitrogen dioxide. The results showed that the sensor obtained by the combination of the two ZIF nanocrystals was more effective than the one solely based on ZIF-67. Notably, ZIFs have found large use as a coating of nanomaterials for devising multifunctional sensors. In one of these works an effective sensing material for NO_2 detection was developed by coating In_2O_3 nanofibers with ZIF-8 [42]. The results showed that the ZIF-8-coated In_2O_3 sensor gives better results in NO_2 detection as compared to bare In_2O_3, pushing the detection limit for NO_2 as low as 10 ppb. In another study, Li et al. developed a necklace-like Ag@ZIF-8 core/shell material for surface-enhanced Raman scattering (SERS) detection [43]. In the study, the crystal violet was selected as a probe

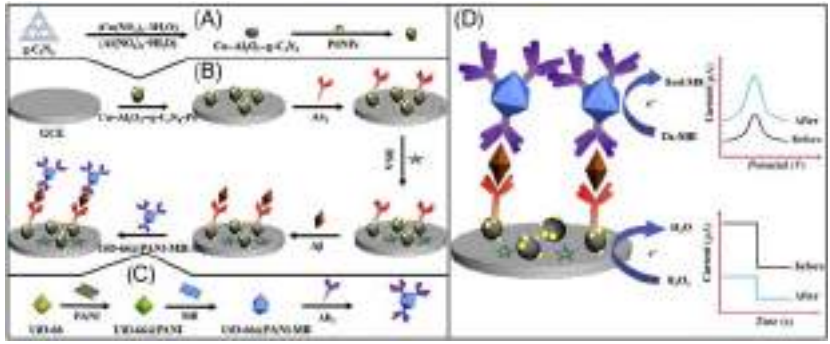

FIGURE 11.4 Outline of the Aβ protein sensing. The system has two parts. In the first part, (A) Cu−Al_2O_3−g-C_3N_4−Pd complex consisting of Al_2O_3, Cu, graphite carbon g-C_3N_4, and Pd NPs was assembled to form the amperometric part. Afterward (B), it was immobilized onto the platform. In the third part, (C) UiO-66 was modified with PANI, having higher surface area and conductivity. It was then supplemented with methylene blue for creating a voltammetric part. (D) The system allowed to dual-detection of Aβ. *Reprinted with permission from Miao J, Li X, Li Y, Dong X, Zhao G, Fang J, et al. Dual-signal sandwich electrochemical immunosensor for amyloid β-protein detection based on Cu−Al_2O_3-g−C_3N_4−Pd and UiO-66@PANI-MB. Anal Chim Acta 2019;1089:48−55. https://doi.org/10.1016/j.aca.2019.09.017.* ©*2019 Elsevier.*

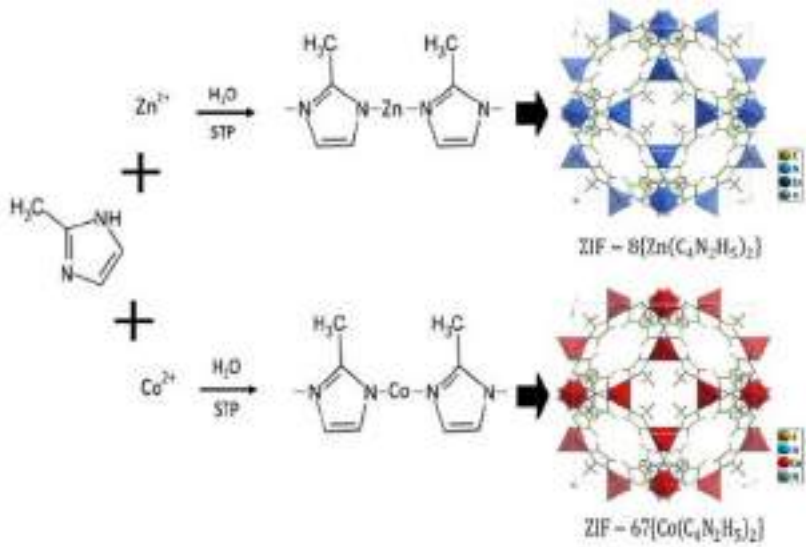

FIGURE 11.5 Schematic representation and synthesis routes for ZIF-8 and ZIF-67. *Reprinted with permission from Bahos F, Sainz-Vidal A, Sánchez-Pérez C, Saniger J, Gràcia I, Saniger-Alba M, et al. ZIF nanocrystal-based surface acoustic wave (SAW) electronic nose to detect diabetes in human breath. Biosensors 2018;9:4. https://doi.org/10.3390/bios9010004 [44].* ©*2018 Multidisciplinary Digital Publishing Institute (MDPI).*

molecule and the material showed high active, robust, and sensitive SERS responses to the target analyte.

11.2.5 MOF-76

MOF-76, belonging to the class of lanthanide MOFs, has the great advantage of high photoluminescence as compared to other MOF varieties that contain transition metals. In the structure of MOF-76, lanthanide metals such as Eu, Tb, Sm, and Dy can be found. In this way, MOF-76 can be used in sensing studies as well as biological imaging [45] and light interactive devices [46]. Li et al. used MOF-76(Tb) coated onto silk fibers for Cu^{2+} metal ion detection [47]. In the study, different methods such as hydrothermal, microwave-assisted, and layer-by-layer were used to cover silk fibers with MOF-76(Tb). The authors reported that layer-by-layer is the most effective method (Fig. 11.6A) and selective Cu^{2+} ion detection has been demonstrated against a broad pool of different metal ions [K^+, Na^+, Ca^{2+}, Al^{3+}, Pb^{2+}, Ni^{2+}, Fe^{3+}, Cu^{2+}, and Cd^{2+}; Cu^{2+} (detection limit: 0.5 mg L^{-1})] (Fig. 11.6B). In another study, MOF-76(Tb) coated with a molecularly imprinted polymer (MIP) MIP@MOF-76(Tb) was used in the fluorometric detection of an antibiotic, cefixime [48]. Here, MIP provided appropriate channels for target molecule diffusion while the fluorometric signal readout arisen from the interaction of cefixime with the Tb-active region of MOF-76. The results showed that cefixime had a great affinity for MIP@MOF-76(Tb) leading to a detection limit in the sub-ng mL^{-1} range.

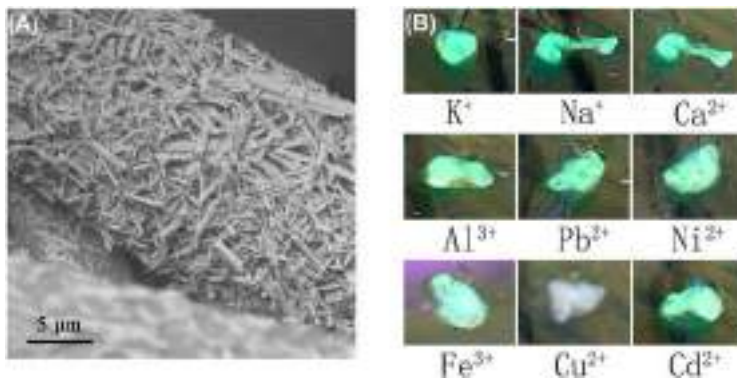

FIGURE 11.6 (A) SEM image of MOF-76(Tb)@silk fiber that was synthesized by layer-by-layer method. (B) Fluorescence images of the MOF-76(Tb)@silk fiber after immersion in equal volumes of solutions containing different metal ions such as K^+, Na^+, Al^{3+}, Fe^{3+}, Ca^{2+}, Pb^{2+}, Ni^{2+}, Cd^{2+}, and Cu^{2+}. *SEM*, Scanning electron microscopy. *Adapted with permission from Li J, Yuan X, Wu Y, Ma X, Li F, Zhang B, et al. From powder to cloth: facile fabrication of dense MOF-76(Tb) coating onto natural silk fiber for feasible detection of copper ions. Chem Eng J 2018;350:637–44. https://doi.org/10.1016/j.cej.2018.05.144.*

11.2.6 MIL-101

MIL-101 is a type of MOF with $C_{24}H_{17}O_{16}Cr_3$ composition that contains Cr^{3+} as its metal ion and terephthalic acid as the organic linker. Thanks to its improved surface area and porous structure, MIL-101 represents a promising material to be used in the place of HKUST-1 and MOF-5 for future energy and environmental applications [49]. In fact, its superior properties have been exploited for the detection of various gases and molecules. For instance, Haghighi and Zeinali used MIL-101 to detect various volatile organic compounds (VOCs) such as methanol, ethanol, isopropanol, *n*-hexane, acetone, dichloromethane, chloroform, tetrahydrofuran, and pyridine [50]. In this study, it was reported that MIL-101 showed VOCs' sensitivity in the range of 0.114−2.793 Hz ppm^{-1}. In addition, due to the π−π interaction of MIL-101 linker moieties, an $\times 24$ times increase in sensitivity was achieved in pyridine detection as compared to other VOCs. In another study, Gan et al. carried out nitrofurazone detection with MIL-101-based hollow cages [51]. Here, it was first produced MIL-101 under the coordination of terephthalic acid and Cr^{3+} metal ion and, then, acquired the form of a hollow cage upon an acid etching process. In this way, more accessible sites and short diffusion distance were obtained (Fig. 11.7). As a result, MIL-101 showed high electrocatalytic activity and excellent voltammetric response enabling the detection of nitrofurazone down to 10 nM. In addition, MIL-101 has been also exploited as a trapping matrix for removal of interferences in the analyzed sample [52,53]. For instance, matrix-assisted laser desorption/ionization time-of-flight mass spectrometry (MALDI-TOF-MS) is an advanced technique commonly used for the identification and detection of large analytes such as polymers and various proteins. Detection of small molecules (e.g., quercetin), on the other hand, poses major challenges as the analyte signals cannot often be detected and suppressed. However, when combined with MIL-101 matrix, background signals were eliminated, and

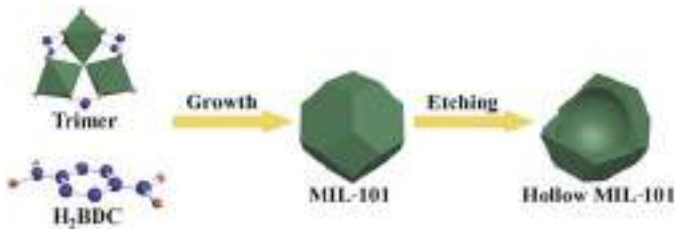

FIGURE 11.7 Schematic representation of the preparation of hollow MIL-101. *Reprinted with permission from Gan T, Li J, Xu L, Yao Y, Liu Y. Construction of a voltammetric sensor based on MIL-101 hollow cages for electrocatalytic oxidation and sensitive determination of nitrofurazone. J Electroanal Chem 2019;848:113287. https://doi.org/10.1016/j.jelechem.2019.113287. ©2019 Elsevier.*

MALDI-TOF-MS detection of quercetin was achieved with a detection limit of 2.11 ng mL^{-1} [54].

11.3 Pore diameter

As mentioned before, the ability to tailor the MOF pore diameters is key to impart size-dependent guest molecule selectivity (i.e., molecules larger than the pore diameter remain outside the MOF). In this regard, a representative study was carried out by Mohan Reddy et al. [55]. The authors synthesized ZIF-8, Zn(NA), and Zn(INA) MOFs by combining linkers such as 2-methylimidazole, nicotinic acid, and isonicotinic acid with Zn^{2+} metal ion, respectively. The results showed that these MOFs had different pore diameters (ZIF-8: 1.8691 nm; Zn(NA): 7.851 nm; and Zn(INA): 4.5415 nm). Gas-sensing results also showed that Zn(NA) had the best ammonia gas-sensing performance (detection limit: 10 ppm) and long-term stability while requiring lower operating temperature. However, pore diameter can also increase sensing capability. Especially in gas-sensing studies, pore diameter is a very important parameter as even minor differences in size can dramatically impact the sensing outcome. Zhou et al. carried out a gas-sensing study by covering their ZnO nanorod with two different pore size ZIF varieties ($\sim$3.4 Å for ZIF-8, $\sim$4.8 Å for ZIF-71) [56]. In the study, gases such as hydrogen, ammonia, ethanol, acetone, and benzene, the molecular size of which varied from 2.89 to 5.85 Å, were used as analytes. The results showed that the ZnO@ZIF-8 material developed a selective response for gases that have a smaller molecular size such as hydrogen and ammonia. On the other hand, ZnO@ZIF-71 was functional in the detection of all other gas molecules except benzene, which has the largest molecular size (Fig. 11.8). As previously pointed out, the MOF's unique features in terms of surface area and pore size can also be used to improve the sensing performances of other nanomaterials. For instance, Lü et al. produced Co_3O_4 concave nanocubes using ZIF-67 as a template and employed these MOF-modified nanoparticles in the detection of gas molecules such as ethanol, acetone, toluene, and benzene [57]. In this approach, ZIF-67 was first produced and, then, calcination at different temperatures (300°C, 350°C, and 400°C) was applied yielding nanostructures with different pore sizes. The results show that the Co_3O_4-300 nanocubes that were obtained at 300°C had the smallest pore size (2−4 nm) (for Co_3O_4-350: 13−15 nm, for Co_3O_4-400: 29−32 nm) and it was reported that it had the highest sensitivity, especially to ethanol (detection limit: 10 ppm).

11.4 Pore morphology

Besides the pore size, another critical parameter to be considered in the design of MOF for sensing purposes is the pore geometry. Kucheryavy et al.

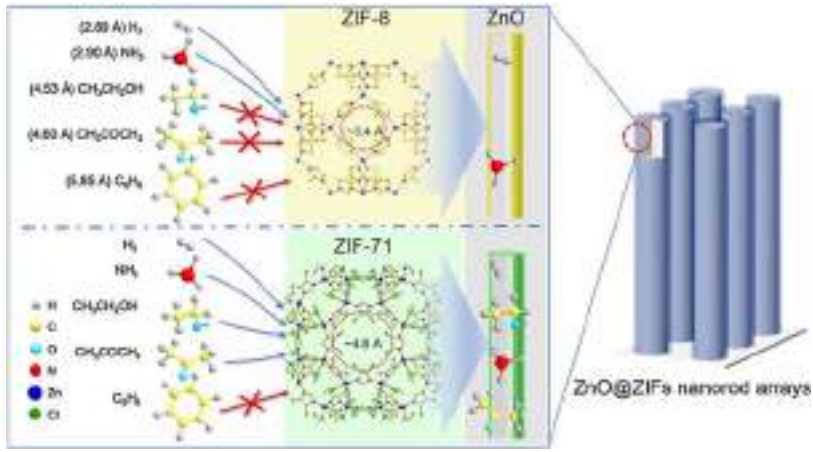

FIGURE 11.8 Illustration of various types of ZIF-8 and ZIF-71 with different pore sizes (c. 3.4 and c. 4.8 Å, respectively). Due to their small dimensions, H_2 and NH_3 easily permeate within both ZIFs, while larger molecules such as CH_3CH_2OH and CH_3COCH_3 can only enter into ZIF-71 pores. Finally, the largest investigated analyte, C_6H_6, can diffuse into neither ZIFs. *ZIFs*, Zeolitic imidazolate framework. *Reprinted with permission from Zhou T, Sang Y, Wang X, Wu C, Zeng D, Xie C. Pore size dependent gas-sensing selectivity based on ZnO@ZIF nanorod arrays. Sens Actuat B: Chem 2018;258:1099–106. https://doi.org/10.1016/j.snb.2017.12.024. ©2018 Elsevier.*

synthesized iron porphyrin–based MOFs with two different pore geometries and examined their interactions with different guest molecules such as imidazole and piperidine [58]. MOFs with the same composition but different pore geometry (PCN222 and PCN224) were selected. Specifically, PCN222 has two types of 1D pores with drastically different shapes and dimensions (hexagonal vs trigonal channels with spans of ~37 and ~10 Å, respectively) while PCN224 only displays cubic pores with intermediate size (~19 Å diameter) (Fig. 11.9). The results show that PCN224, which has a more regular pore geometry, affords superior sensing efficiency than PCN222.

11.5 Combination with different nanoparticles

Hybrid materials comprising metallic NPs and various MOF types have recently emerged as one of the most interesting topics in sensing studies. Combination of these materials typically exploits the high surface area of MOFs to enhance the sensing response originating from the nanomaterials by accumulating a larger number of target analytes at the MOF pores. For instance, Shao et al. used ZIF-8 nanohybrid probes that contain Au nanoclusters and poly(9,9-dioctylfluorenyl-2,7-diol) (PFO) dots for dopamine detection [59]. Au nanoclusters and PFO dots have orange and blue fluorescence,

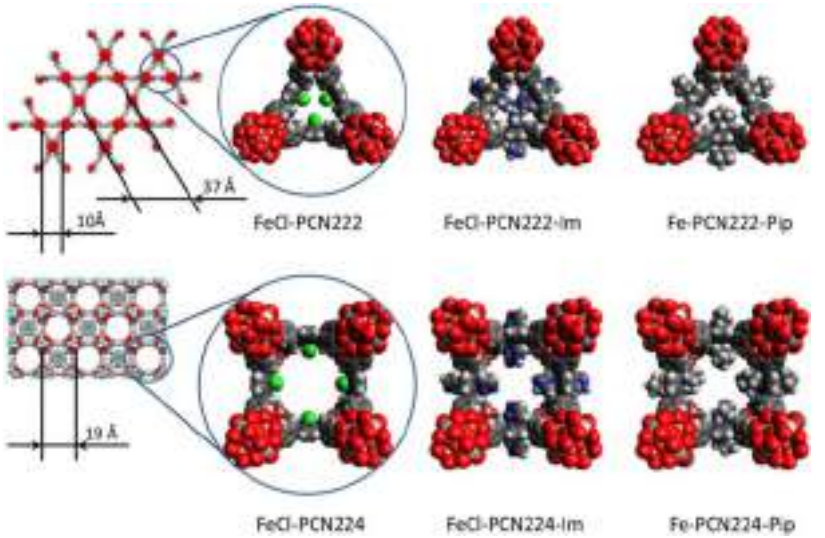

FIGURE 11.9 Pore structure and dimensions of FeCl-PCN222 (top) and FeCl-PCN224 (bottom) MOFs. *MOFs*, Metal-organic frameworks. *Reprinted with permission from Kucheryavy P, Lahanas N, Lockard JV. Spectroscopic evidence of pore geometry effect on axial coordination of guest molecules in metalloporphyrin-based metal organic frameworks. Inorg Chem 2018;57:3339–47. https://doi.org/10.1021/acs.inorgchem.8b00117. ©2018 American Chemical Society.*

respectively. Interaction of dopamine with ZIF-8@AuNCs-PFO probes leads to a sharp quenching of Au nanocluster fluorescence while the PFO dot fluorescence was only slightly affected, thereby enabling ratiometric sensing of dopamine (detection limit: 4.8 nmol L^{-1}). Interestingly, ZIF-8 was reported to enhance Au nanocluster fluorescence, which further increased the sensitivity of the probe. In another study, Ag@ZIF-67 nanocomposites were used for glucose detection [60]. ZIF-67-modified glassy carbon electrode (GCE) showed good activity as an electrochemical sensor, which was significantly improved by loading silver NPs to generate the corresponding Ag@ZIF-67 nanocomposites. Optimum Ag loading (0.5%) provided an $\times 2$ times faster response and an $\times 2.5$ increase in glucose sensitivity (detection limit: 0.66 μM). On the other hand, Cao et al. devised an MOF/Au-based sensor for the detection of the pesticide acetamiprid, where Au NPs were coated with three different MOF types (MOF-199, UiO-66, and UiO-67) [61]. The results showed that the detection limit for Au@MOF-199, Au@UiO-66, and Au@UiO-67 was 0.02, 0.009, and 0.02 μM, respectively.

Despite their overall high thermal stability of MOFs, specific applications require high temperatures that cannot withstand by common MOFs. To tackle this issue, different approaches were pursued. One of these approaches is to obtain metal oxides with high surface area and porous structure that are

resistant to extreme temperatures by using MOFs as templates. For instance, HKUST-1 was used as a template to yield CuO structures with high surface area and porosity upon MOF removal after calcination (in 500°C). Subsequent decoration with Pt NPs further improved the sensing performances in the detection of formaldehyde down to 100 ppb [62]. Notably, as formaldehyde is a highly harmful pollutant that can have a carcinogenic effect, its quick removal from the environment after the detection is desirable. To this end, Wang et al. synthesized dual-mode Janus Au@ZnO@ZIF-8 NPs, via anisotropic growth method, equipped with the ability of simultaneously detecting and eliminating formaldehyde from the air [63]. The results showed that formaldehyde can be selectively detected in a wide range ranging from 0.25 to 100 ppm. At the same time, formaldehyde was partially oxidized to formic acid that is a nontoxic chemical.

11.6 The sensing applications carried out with metal-organic frameworks

The sorption capacity of MOF is key to maximize the diffusion of a higher amount of analytes through the MOF pores. Detection is then achieved upon the interaction of the trapped analytes either with the metal nodes of the MOF structure or with a "secondary" structure within the MOF. These secondary structures can generally be either inorganic NP units or organic groups that recognize the analyte entering the pores. These interactions are finally recorded by various analytical techniques. Among others, SERS, colorimetric, voltammetric, and electrochemical techniques are the most frequently used [64–67]. Overall, three main classes of analytes have been targeted by using MOF-based sensors: gases, metal ions, and hydrophobic small molecules.

11.6.1 Gas-sensing applications

The release of gases from industries and human activities requires environmental monitoring for control and safety. Up to now, photovoltaic technologies are widely used in the sensing of environmentally hazardous, toxic, or flammable gases [68,69]. However, these techniques suffer from major limitations in terms of sensitivity, which hamper the detection of gases in low amounts [70]. An intriguing alternative to these conventional approaches is provided by the design of MOF-based sensors, which profit from the adjustable pore sizes and enormous surface areas to impart enhanced sensitivity and selectivity to the sensing platform. For instance, carbon monoxide (CO) is one of the most harmful and toxic gases. It is also very difficult to perceive because it is colorless, odorless, and tasteless. Lv et al. developed Ni-MOF-74 composite for the CO detection at ppb level [71], exploiting the affinity of the Ni^{2+} metal ion for CO binding to create an MOF construct with high absorption capacity against this gas (detection limit: 10 ppb).

In addition, the Ni-MOF-74 composite offers long-term stability and reusability, thereby representing a promising material in gas-sensing applications. In another study, Wang and Chen developed $Co_3[Co(CN)_6]_2$ MOF, which colorimetrically detects ethanol vapors [72]. This MOF changes its color from pink to purple in the presence of ethanol due to its binding with Co^{2+} centers that leads to the geometrical reorganization from octahedral to tetrahedral coordination. The original structure is restored upon ethanol removal from the environment, thus ensuring the reusability of the material.

Combination of MOFs and metallic NPs can further improve the sensing performance of the detector. With such an approach, the signal readout does not result from the interaction of the gas with metal nodes in the MOF structure. For instance, Surya et al. (2019) loaded three different MOF types [UiO-66(Zr)BDC, UiO-66(Zr)BDC-NO_2, and UiO-66(Zr)BDC-N_3] with Ag_2O NPs and used these constructs for the fast detection of the highly toxic H_2S gas [73]. Hybrid UiO-66(Zr)BDC-NO_2/Ag_2O material showed the highest sensitivity enabling the detection of H_2S gas at room temperature down to 1 ppm detection limit. Such higher sensitivity was related to a higher affinity of H_2S gas for NO_2 and Ag_2O. In another study, NO_2 gas detection was achieved by using the luminescent feature of the MOFs [74]. In this study, Tb(BTC) (BTC = benzene1,3,5-tricarboxilate) MOF was synthesized and deposited in an affordable and easy manner onto a glass surface using polymethyl-methacrylate and polydimethyl-siloxane as fixing materials. Thus fluorescence quenching of the Tb^{3+}-active region of the mixed-matrix membranes was monitored in the presence of NO_2. The results showed that NO_2 can be detected at low concentrations (detection limit: 4 ppm).

11.6.2 Metal ion sensing applications

Heavy metal ions (Pb^{2+}, Cd^{2+}, Cu^{2+}, Fe^{3+}, and Hg^{2+}) are major contaminants determining both environmental and physiological toxic effects even at very small concentrations. MOFs are particularly suited for devising platforms for heavy metal ion detection. For instance, Pournara et al. carried out the voltammetric determination of heavy metal ions such as Pb^{2+}, Cd^{2+}, Ni^{2+}, and Zn^{2+} in an aqueous medium with MOFs (Ca-MOF) combined with Ca^{2+} [75]. The results showed that Ca-MOF substrates are highly selective and effective sorbent, especially for Pb^{2+} and Cd^{2+} metal ions, allowing their quantification in $0.64-1.4\ \mu g\ L^{-1}$ concentration range. In another study, $CH_3NH_3PbBr_3$ perovskite quantum dots were encapsulated into MOF-5 to enhance water resistance, thermal stability, and pH adaptability as compared to $CH_3NH_3PbBr_3$ alone. The sensing performance of the resulting material was tested against metal ions such as Al^{3+}, Bi^{3+}, Ca^{2+}, Cd^{2+}, Co^{2+}, Cu^{2+}, Fe^{3+}, K^+, Na^+, Ni^{2+}, and Sr^{2+} [76].

On the other hand, Ye et al. synthesized ZJU-27, a lanthanide MOF, to be used in the detection of Cd^{2+} and Pb^{2+} metal ions [77]. For this end, the ZJU-27-modified GCE served as an electrochemical sensor for the detection of heavy metal ions. The results showed that the detection limit for Cd^{2+} and Pb^{2+} metal ions is 1.66 and 1.10 nM, respectively. In another study, Liu et al. used four different MOFs based on alkaline metals such as Mg, Ca, Sr, and Ba for the detection of Fe^{3+}, Pb^{2+}, and Cu^{2+} metal ions in the aqueous medium [78]. The results showed Fe^{3+} and Pb^{2+} metal ions are efficiently detected by Mg-based MOF substrates while Ca-based MOFs are better suited for the detection of Fe^{3+} and Cu^{2+} metal ions. Conversely, Sr- and Ba-based MOFs are allowed for the identification of Fe^{3+} metal ions only.

11.6.3 Hydrophobic molecule sensing applications

Hydrophobic pollutants, mainly PAHs and their derivatives, polychlorinated biphenyls, are toxic and environmentally persistent. Their hydrophobic nature makes them highly lipophilic leading to bioaccumulation, and their important biological activity has been demonstrated in many mutagenic and carcinogenic processes. MOFs are very efficient materials for trapping hydrophobic molecules, from small alkanes such as CH_4, C_2H_6, and C_3H_8 to larger compounds such as steroid hormones and PAHs.

For instance, Lian and Yan tested MOF-76(Eu) and MOF-76(Tb) as substrates for fluorescent detection of different monochromatic hydrocarbons (BTEX) such as benzene, toluene, ethylbenzene, *p*-xylene, *o*-xylene, *m*-xylene, anisole, chlorobenzene, benzonitrile, *m*-cresol, diphenyl ether, ethyl benzoate, and acetophenone [79]. The results indicated that both MOF materials display preferential sensitivity toward acetophenone, which has been attributed to the lower volatility of this pollutant among other BTEXs. On the other hand, Phan-Quang et al. fabricated a hybrid substrate comprising Ag nanocubes coated with ZIF-8 (Ag@MOF) for the detection of airborne molecules such as CO_2, naphthalene, and toluene [80]. Intriguingly, they combined standoff Raman spectroscopy, a system that allows long-range detection of chemicals at distant or inaccessible sites, with MOF-based SERS-active materials to monitor the presence of toxic gases and molecules from several meters afar. Real-time detection of hydrophobic molecules was demonstrated at a distance of 2−10 m, at ppb level and under strong daylight background interference (Fig. 11.10).

Ultrasensitive SERS detection of PAHs was also achieved by using HKUST-1(Cu)@Ag NP nanocomposites [81]. In the study, Li et al. [81] prepared such nanocomposites on a screen-printed carbon electrode via in situ electrodeposition. With the electrodeposition technique, the morphology and Ag NP coverage of the nanocomposite were easily controlled (Fig. 11.11).

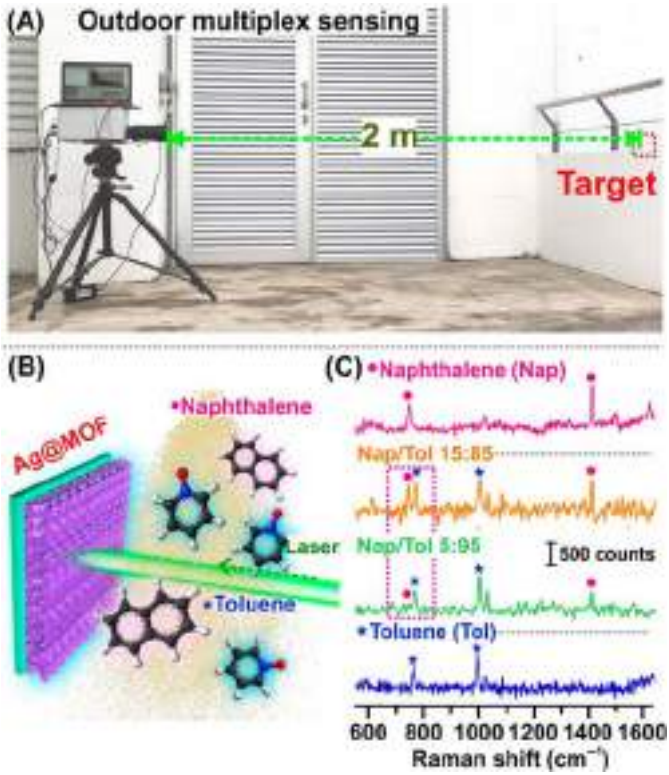

FIGURE 11.10 Outdoor remote sensing of airborne PAH mixture. (A) Outdoor standoff detection setup. (B) Scheme showing the standoff detection of aerosolized toluene and naphthalene. (C) Standoff multiplex spectra obtained in outdoor condition with natural light, for Nap/Tol mixtures (5:95 and 15:85 ratio) and individual naphthalene and toluene SERS spectra. *PAH*, Polycyclic aromatic hydrocarbon. *Adapted with permission from Phan-Quang GC, Yang N, Lee HK, Sim HYF, Koh CSL, Kao YC, et al. Tracking airborne molecules from afar: three-dimensional metal-organic framework-surface-enhanced Raman scattering platform for stand-off and real-time atmospheric monitoring. ACS Nano 2019;13:12090−9. https://doi.org/10.1021/acsnano.9b06486. ©2019 American Chemical Society.*

The results showed that different polyaromatic hydrocarbons such as anthracene, pyrene, perylene, and 4-chlorobiphenyl are detectable down to 20, 0.15, 3 and 5 nM, respectively. Another MOF-based SERS-active substrate was generated by in situ by the synthesis of Ag NPs on the surface of MIL-101(Fe) MOF for dopamine detection [82]. Profiting again for the high affinity of dopamine molecules for MOF binding, a larger number of target molecules are accumulated close to the metallic substrates, thereby enabling high sensitive detection at the sub-pM level.

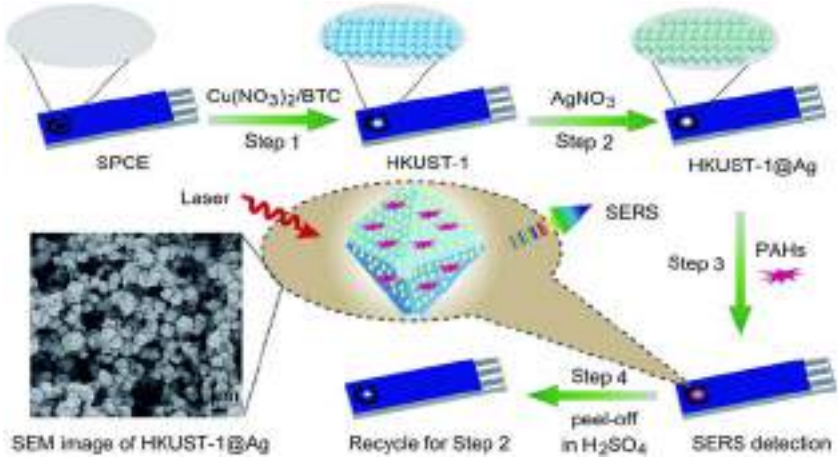

FIGURE 11.11 Schematic representation of the preparation of the HKUST-1 and core−shell HKUST-1@Ag composites. *Reprinted with permission from Li D, Cao X, Zhang Q, Ren X, Jiang L, Li D, et al. Facile: in situ synthesis of core-shell MOF@Ag nanoparticle composites on screen-printed electrodes for ultrasensitive SERS detection of polycyclic aromatic hydrocarbons. J Mater Chem A 2019;7:14108−17. https://doi.org/10.1039/c9ta03690c. ©2019 Royal Society of Chemistry.*

11.7 Conclusion

The unique and customizable properties of MOFs such as thermal stability, porosity, high surface area, large pore volume, surface modification, and reusability convert MOFs as an ideal material to be used in chemical sensing [61]. In addition, an increasing number of studies are paving the way for the synergetic combination of MOFs with other classes of nanomaterials to yield hybrid platforms with advanced properties. Remarkably, integration of MOFs with metallic nanoparticles represents a powerful approach for synergistically enhancing the sensing response of these newly designed materials, as demonstrated in their applications in the detection of three major classes of environmental contaminants (gas, metal ions, and hydrophobic small molecules). We believe that more functional and compact MOF structures will be developed in the near future with the possibility of tailoring their properties for maximizing selectivity, sensitivity, rapidity, and robustness of the sensing platform.

References

[1] Guo H, Chang Z, Wu J, Li W. Air pollution and lung cancer incidence in China: who are faced with a greater effect? Environ Int 2019;132:105077. Available from: https://doi.org/10.1016/j.envint.2019.105077.

[2] Cohen G, Steinberg DM, Yuval, Levy I, Chen S, Kark JD, et al. Cancer and mortality in relation to traffic-related air pollution among coronary patients: using an ensemble of exposure estimates to identify high-risk individuals. Environ Res 2019;176:108560. Available from: https://doi.org/10.1016/j.envres.2019.108560.

[3] Walton EL. Tainted air: the link between pollution and Alzheimer's disease. Biomed J 2018;41:137−40. Available from: https://doi.org/10.1016/j.bj.2018.06.004.

[4] Toro R, Downward GS, van der Mark M, Brouwer M, Huss A, Peters S, et al. Parkinson's disease and long-term exposure to outdoor air pollution: a matched case-control study in the Netherlands. Environ Int 2019;129:28−34. Available from: https://doi.org/10.1016/j.envint.2019.04.069.

[5] Geng Y, Khodadadi H, Karimipour A, Reza Safaei M, Nguyen TK. A comprehensive presentation on nanoparticles electrical conductivity of nanofluids: statistical study concerned effects of temperature, nanoparticles type and solid volume concentration. Physica A 2020;542:123432. Available from: https://doi.org/10.1016/j.physa.2019.123432.

[6] Badán JA, Navarrete-Astorga E, Henríquez R, Martín F, Marotti RE, Ramos-Barrado JR, et al. Optical properties of silver nanoparticles deposited onto silicon substrates by different soft-solution processing techniques. Opt Mater (Amst) 2020;100:109651. Available from: https://doi.org/10.1016/j.optmat.2020.109651.

[7] Ghazvini M, Maddah H, Peymanfar R, Ahmadi MH, Kumar R. Experimental evaluation and artificial neural network modeling of thermal conductivity of water based nanofluid containing magnetic copper nanoparticles. Physica A 2020;551:124127. Available from: https://doi.org/10.1016/j.physa.2019.124127.

[8] Unal IS, Demirbas A, Onal I, Ildiz N, Ocsoy I. One step preparation of stable gold nanoparticle using red cabbage extracts under UV light and its catalytic activity. J Photochem Photobiol B Biol 2020;204:111800. Available from: https://doi.org/10.1016/j.jphotobiol.2020.111800.

[9] Carbone GG, Serra A, Buccolieri A, Manno D. A silver nanoparticle-poly(methyl methacrylate) based colorimetric sensor for the detection of hydrogen peroxide. Heliyon 2019;5:e02887. Available from: https://doi.org/10.1016/j.heliyon.2019.e02887.

[10] Wang Q, Li X, Zhao WM, Jin S. Lossy mode resonance-based fiber optic sensor using layer-by-layer SnO_2 thin film and SnO_2 nanoparticles. Appl Surf Sci 2019;492:374−81. Available from: https://doi.org/10.1016/j.apsusc.2019.06.168.

[11] Lian X, Li Y, Zhu J, Zou Y, An D, Wang Q. Fabrication of Au-decorated SnO_2 nanoparticles with enhanced *n*-buthanol gas sensing properties. Mater Sci Semicond Process 2019;101:198−205. Available from: https://doi.org/10.1016/j.mssp.2019.06.008.

[12] Li X, Dai L, Meng W, Li Y, Wang L, He Z. A novel mixed-potential type NH_3 sensor based on Ag nanoparticles decorated $AgNbO_3$ sensing electrode synthesized by demixing method. Sens Actuat B: Chem 2019;301:127146. Available from: https://doi.org/10.1016/j.snb.2019.127146.

[13] Ni X, Luo J, Liu R, Liu X. A novel flexible UV-cured carbon nanotube composite film for humidity sensing. Sens Actuat B: Chem 2019;297:126785. Available from: https://doi.org/10.1016/j.snb.2019.126785.

[14] Bhanjana G, Toor I, Chaudhary GR, Dilbaghi N, Kim KH, Kumar S. Direct redox sensing of uranium using copper oxide quantum dots. J Mol Liq 2019;292:111455. Available from: https://doi.org/10.1016/j.molliq.2019.111455.

[15] Prasad BB, Singh R, Kumar A. Gold nanorods: vs. gold nanoparticles: application in electrochemical sensing of cytosine β-d-arabinoside using metal ion mediated molecularly imprinted polymer. RSC Adv 2016;6:80679−91. Available from: https://doi.org/10.1039/c6ra14097a.

[16] Ma X, Kou X, Xu Y, Yang D, Miao P. Colorimetric sensing strategy for heparin assay based on PDDA-induced aggregation of gold nanoparticles. Nanoscale Adv 2019;1:486–9. Available from: https://doi.org/10.1039/c8na00162f.

[17] Xu J, Chen T, Qiao X, Sheng Q, Yue T, Zheng J. The hybrid of gold nanoparticles and Ni(OH)2 nanosheet for non-enzymatic glucose sensing in food. Colloids Surf A Physicochem Eng Asp 2019;561:25–31. Available from: https://doi.org/10.1016/j.colsurfa.2018.10.067.

[18] Farmani MR, Peyman H, Roshanfekr H. Blue luminescent graphene quantum dot conjugated cysteamine functionalized-gold nanoparticles (GQD-AuNPs) for sensing hazardous dye erythrosine B. Spectrochim Acta, A: Mol Biomol Spectrosc 2020;229:117960. Available from: https://doi.org/10.1016/j.saa.2019.117960.

[19] Liao N, Zhang M, Zheng B, Xue W. Temperature-dependent gas sensing properties of porous silicon oxycarbide: insight from first principles. Appl Surf Sci 2019;493:1286–90. Available from: https://doi.org/10.1016/j.apsusc.2019.07.133.

[20] Liu MH, Kameoka S, Nishimoto K, Ueda S, Tsai AP. Origins of catalysis for CO oxidation on porous Ag fabricated by leaching of intermetallic compound Mg_3Ag. Appl Catal A: Gen 2019;586:117216. Available from: https://doi.org/10.1016/j.apcata.2019.117216.

[21] Fominykh A, Katra I, Krasovitov B, Levy A. Adsorption of active trace gases by ensemble of ultrafine porous particles with impermeable cores. Process Saf Environ Prot 2019;131:189–96. Available from: https://doi.org/10.1016/j.psep.2019.09.012.

[22] Ali M, Mujtaba-ul-Hassan S, Ahmad J, Khurshid A, Shahzad F, Iqbal Z, et al. Fabrication of PEGylated porous alumina whiskers (PAW) for drug delivery applications. Mater Lett 2019;241:23–6. Available from: https://doi.org/10.1016/j.matlet.2019.01.044.

[23] Sumby CJ. Metal-organic frameworks: a thin film opening. Nat Chem 2016;8:294–6. Available from: https://doi.org/10.1038/nchem.2481.

[24] Yaghi OM, Li H. Hydrothermal synthesis of a metal-organic framework containing large rectangular channels. J Am Chem Soc 1995;117:10401–2. Available from: https://doi.org/10.1021/ja00146a033.

[25] Burnett BJ, Barron PM, Choe W. Recent advances in porphyrinic metal-organic frameworks: materials design, synthetic strategies, and emerging applications. CrystEngComm 2012;14:3839–46. Available from: https://doi.org/10.1039/c2ce06692k.

[26] Li H, Eddaoudi M, O'Keeffe M, Yaghi OM. Design and synthesis of an exceptionally stable and highly porous metal-organic framework. Nature 1999;402:276–9. Available from: https://doi.org/10.1038/46248.

[27] Lv Y, Yu H, Xu P, Xu J, Li X. Metal organic framework of MOF-5 with hierarchical nanopores as micro-gravimetric sensing material for aniline detection. Sens Actuat B: Chem 2018;256:639–47. Available from: https://doi.org/10.1016/j.snb.2017.09.195.

[28] Xu S, Zhan L, Hong C, Chen X, Chen X, Oyama M. Metal–organic framework-5 as a novel phosphorescent probe for the highly selective and sensitive detection of Pb(II) in mussels. Sens Actuat B: Chem 2020;308:127733. Available from: https://doi.org/10.1016/j.snb.2020.127733.

[29] Xia C, Yu C, Cao M, Xia J, Jiang D, Zhou G, et al. A Eu and Tb co-doped MOF-5 compound for ratiometric high temperature sensing. Ceram Int 2018;44:21040–6. Available from: https://doi.org/10.1016/j.ceramint.2018.08.140.

[30] Guo L, Liu Y, Kong R, Chen G, Wang H, Wang X, et al. Turn-on fluorescence detection of β-glucuronidase using RhB@MOF-5 as an ultrasensitive nanoprobe. Sens Actuat B: Chem 2019;295:1–6. Available from: https://doi.org/10.1016/j.snb.2019.05.064.

[31] O'Neill LD, Zhang H, Bradshaw D. Macro-/microporous MOF composite beads. J Mater Chem 2010;20:5720–6. Available from: https://doi.org/10.1039/c0jm00515k.

[32] Zhu Q, Chen Y, Wang W, Zhang H, Ren C, Chen H, et al. A sensitive biosensor for dopamine determination based on the unique catalytic chemiluminescence of metal-organic framework HKUST-1. Sens Actuat B: Chem 2015;210:500−7. Available from: https://doi.org/10.1016/j.snb.2015.01.012.

[33] Guthrie S, Huelsenbeck L, Salahi A, Varhue W, Smith N, Yu X, et al. Crystallization of high aspect ratio HKUST-1 thin films in nanoconfined channels for selective small molecule uptake. Nanoscale Adv 2019;1:2946−52. Available from: https://doi.org/10.1039/c9na00254e.

[34] Cao G, Wu C, Tang Y, Wan C. Ultrasmall HKUST-1 nanoparticles decorated graphite nanosheets for highly sensitive electrochemical sensing of DNA damage biomarker 8-hydroxy-2′-deoxyguanosine. Anal Chim Acta 2019;1058:80−8. Available from: https://doi.org/10.1016/j.aca.2019.01.031.

[35] Yuan S, Feng L, Wang K, Pang J, Bosch M, Lollar C, et al. Stable metal-organic frameworks: design, synthesis, and applications. Adv Mater 2018;30:1704303. Available from: https://doi.org/10.1002/adma.201704303.

[36] Zhang T, Wei JZ, Sun XJ, Zhao XJ, Tang H, Yan H, et al. Rapid synthesis of UiO-66 by means of electrochemical cathode method with electrochemical detection of 2,4,6-TCP. Inorg Chem Commun 2020;111:107671. Available from: https://doi.org/10.1016/j.inoche.2019.107671.

[37] Tang Y, Wu H, Chen J, Jia J, Yu J, Xu W, et al. A highly fluorescent metal organic framework probe for 2,4,6-trinitrophenol detection via post-synthetic modification of UIO-66-NH_2. Dye Pigment 2019;167:10−15. Available from: https://doi.org/10.1016/j.dyepig.2019.03.055.

[38] He Y, Shi L, Wang J, Yan J, Chen Y, Wang X, et al. UiO-66-NDC (1,4-naphthalenedicarboxilic acid) as a novel fluorescent probe for the selective detection of Fe^{3+}. J Solid State Chem 2020;285:121206. Available from: https://doi.org/10.1016/j.jssc.2020.121206.

[39] Miao J, Li X, Li Y, Dong X, Zhao G, Fang J, et al. Dual-signal sandwich electrochemical immunosensor for amyloid β-protein detection based on Cu−Al_2O_3−g-C_3N_4−Pd and UiO-66@PANI-MB. Anal Chim Acta 2019;1089:48−55. Available from: https://doi.org/10.1016/j.aca.2019.09.017.

[40] Huang XC, Lin YY, Zhang JP, Chen XM. Ligand-directed strategy for zeolite-type metal-organic frameworks: zinc(II) imidazolates with unusual zeolitic topologies. Angew Chem—Int Ed 2006;45:1557−9. Available from: https://doi.org/10.1002/anie.200503778.

[41] Matatagui D, Sainz-Vidal A, Gràcia I, Figueras E, Cané C, Saniger JM. Chemoresistive gas sensor based on ZIF-8/ZIF-67 nanocrystals. Sens Actuat B: Chem 2018;274:601−8. Available from: https://doi.org/10.1016/j.snb.2018.07.137.

[42] Liu Y, Wang R, Zhang T, Liu S, Fei T. Zeolitic imidazolate framework-8 (ZIF-8)-coated In_2O_3 nanofibers as an efficient sensing material for ppb-level NO_2 detection. J Colloid Interface Sci 2019;541:249−57. Available from: https://doi.org/10.1016/j.jcis.2019.01.052.

[43] Li Q, Gong S, Zhang H, Huang F, Zhang L, Li S. Tailored necklace-like Ag@ZIF-8 core/shell heterostructure nanowires for high-performance plasmonic SERS detection. Chem Eng J 2019;371:26−33. Available from: https://doi.org/10.1016/j.cej.2019.03.236.

[44] Bahos F, Sainz-Vidal A, Sánchez-Pérez C, Saniger J, Gràcia I, Saniger-Alba M, et al. ZIF nanocrystal-based surface acoustic wave (SAW) electronic nose to detect diabetes in human breath. Biosensors 2018;9:4. Available from: https://doi.org/10.3390/bios9010004.

[45] Shah SSA, Najam T, Cheng D, Hafeez A, Lu Y, Waseem A. Nano-metal organic frame work an excellent tool for biomedical imaging. Curr Med Imaging Rev 2018;14:669–74. Available from: https://doi.org/10.2174/1573405613666170919151454.

[46] Yang W, Bai ZQ, Shi WQ, Yuan LY, Tian T, Chai ZF, et al. MOF-76: from a luminescent probe to highly efficient UVI sorption material. Chem Commun 2013;49:10415–17. Available from: https://doi.org/10.1039/c3cc44983a.

[47] Li J, Yuan X, Wu YN, Ma X, Li F, Zhang B, et al. From powder to cloth: facile fabrication of dense MOF-76(Tb) coating onto natural silk fiber for feasible detection of copper ions. Chem Eng J 2018;350:637–44. Available from: https://doi.org/10.1016/j.cej.2018.05.144.

[48] Eskandari H, Amirzehni M, Asadollahzadeh H, Hassanzadeh J, Eslami PA. MIP-capped terbium MOF-76 for the selective fluorometric detection of cefixime after its preconcentration with magnetic graphene oxide. Sens Actuat B: Chem 2018;275:145–54. Available from: https://doi.org/10.1016/j.snb.2018.08.050.

[49] Bhattacharjee S, Chen C, Ahn WS. Chromium terephthalate metal-organic framework MIL-101: synthesis, functionalization, and applications for adsorption and catalysis. RSC Adv 2014;4:52500–25. Available from: https://doi.org/10.1039/c4ra11259h.

[50] Haghighi E, Zeinali S. Nanoporous MIL-101(Cr) as a sensing layer coated on a quartz crystal microbalance (QCM) nanosensor to detect volatile organic compounds (VOCs). RSC Adv 2019;9:24460–70. Available from: https://doi.org/10.1039/c9ra04152d.

[51] Gan T, Li J, Xu L, Yao Y, Liu Y. Construction of a voltammetric sensor based on MIL-101 hollow cages for electrocatalytic oxidation and sensitive determination of nitrofurazone. J Electroanal Chem 2019;848:113287. Available from: https://doi.org/10.1016/j.jelechem.2019.113287.

[52] Peng S, Wang S, Hao G, Zhu C, Zhang Y, Lv X, et al. Preparation of magnetic flower-like carbon-matrix composites with efficient electromagnetic wave absorption properties by carbonization of MIL-101(Fe). J Magn Magn Mater 2019;487:165306. Available from: https://doi.org/10.1016/j.jmmm.2019.165306.

[53] Khdhayyer M, Bushell AF, Budd PM, Attfield MP, Jiang D, Burrows AD, et al. Mixed matrix membranes based on MIL-101 metal–organic frameworks in polymer of intrinsic microporosity PIM-1. Sep Purif Technol 2019;212:545–54. Available from: https://doi.org/10.1016/j.seppur.2018.11.055.

[54] Han G, Zeng Q, Jiang Z, Xing T, Huang C, Li Y. MIL-101(Cr) as matrix for sensitive detection of quercetin by matrix-assisted laser desorption/ionization mass spectrometry. Talanta 2017;164:355–61. Available from: https://doi.org/10.1016/j.talanta.2016.11.044.

[55] Mohan Reddy AJ, Katari NK, Nagaraju P, Manabolu Surya SB. ZIF-8, Zn(NA) and Zn (INA) MOFs as chemical selective sensors of ammonia, formaldehyde and ethanol gases. Mater Chem Phys 2020;241:122357. Available from: https://doi.org/10.1016/j.matchemphys.2019.122357.

[56] Zhou T, Sang Y, Wang X, Wu C, Zeng D, Xie C. Pore size dependent gas-sensing selectivity based on ZnO@ZIF nanorod arrays. Sens Actuat B: Chem 2018;258:1099–106. Available from: https://doi.org/10.1016/j.snb.2017.12.024.

[57] Lü Y, Zhan W, He Y, Wang Y, Kong X, Kuang Q, et al. MOF-templated synthesis of porous Co_3O_4 concave nanocubes with high specific surface area and their gas sensing properties. ACS Appl Mater Interfaces 2014;6:4186–95. Available from: https://doi.org/10.1021/am405858v.

[58] Kucheryavy P, Lahanas N, Lockard JV. Spectroscopic evidence of pore geometry effect on axial coordination of guest molecules in metalloporphyrin-based metal organic frameworks. Inorg Chem 2018;57:3339−47. Available from: https://doi.org/10.1021/acs.inorgchem.8b00117.

[59] Shao K, You J, Ye S, Gu D, Wang T, Teng Y, et al. Gold nanoclusters-poly(9,9-dioctylfluorenyl-2,7-diyl) dots@zeolitic imidazolate framework-8 (ZIF-8) nanohybrid based probe for ratiometric analysis of dopamine. Anal Chim Acta 2020;1098:102−9. Available from: https://doi.org/10.1016/j.aca.2019.10.065.

[60] Meng W, Wen Y, Dai L, He Z, Wang L. A novel electrochemical sensor for glucose detection based on Ag@ZIF-67 nanocomposite. Sens Actuat B: Chem 2018;260:852−60. Available from: https://doi.org/10.1016/j.snb.2018.01.109.

[61] Cao X, Hong S, Jiang Z, She Y, Wang S, Zhang C, et al. SERS-active metal-organic frameworks with embedded gold nanoparticles. Analyst 2017;142:2640−7. Available from: https://doi.org/10.1039/c7an00534b.

[62] Lee JE, Kim DY, Lee HK, Park HJ, Ma A, Choi SY, et al. Sonochemical synthesis of HKUST-1-based CuO decorated with Pt nanoparticles for formaldehyde gas-sensor applications. Sens Actuat B: Chem 2019;292:289−96. Available from: https://doi.org/10.1016/j.snb.2019.04.062.

[63] Wang D, Li Z, Zhou J, Fang H, He X, Jena P, et al. Simultaneous detection and removal of formaldehyde at room temperature: Janus Au@ZnO@ZIF-8 nanoparticles. Nano-Micro Lett 2018;10:1−11. Available from: https://doi.org/10.1007/s40820-017-0158-0.

[64] Karthick Kannan P, Shankar P, Blackman C, Chung C. Recent advances in 2D inorganic nanomaterials for SERS sensing. Adv Mater 2019;31:1803432. Available from: https://doi.org/10.1002/adma.201803432.

[65] Bamrungsap S, Cherngsuwanwong J, Srisurat P, Chonirat J, Sangsing N, Wiriyachaiporn N. Visual colorimetric sensing system based on the self-assembly of gold nanorods and graphene oxide for heparin detection using a polycationic polymer as a molecular probe. Anal Methods 2019;11:1387−92. Available from: https://doi.org/10.1039/c8ay02129e.

[66] Hay CE, Lee J, Silvester DS. Formation of 3-dimensional gold, copper and palladium microelectrode arrays for enhanced electrochemical sensing applications. Nanomaterials 2019;9. Available from: https://doi.org/10.3390/nano9081170.

[67] Huang Y, Tan Y, Feng C, Wang S, Wu H, Zhang G. Synthesis of CuO/g-C_3N_4 composites, and their application to voltammetric sensing of glucose and dopamine. Microchim Acta 2019;186:10. Available from: https://doi.org/10.1007/s00604-018-3120-z.

[68] Liu XL, Zhao Y, Ma SX, Zhu SW, Ning XJ, Zhao L, et al. Rapid and wide-range detection of NO_x gas by *N*-hyperdoped silicon with the assistance of a photovoltaic self-powered sensing mode. ACS Sens 2019;4:3056−65. Available from: https://doi.org/10.1021/acssensors.9b01704.

[69] Vashpanov Y, Son JY, Heo G, Kwack KD. Photovoltaic intelligent gas sensors for the detection of acetone concentration over a wide range of measurement for biomedical applications and tasks of public safety. IOP Conf Ser Mater Sci Eng 2020;715:012094. Available from: https://doi.org/10.1088/1757-899X/715/1/012094.

[70] Honeycutt WT, Ley MT, Materer NF. Precision and limits of detection for selected commercially available, low-cost carbon dioxide and methane gas sensors. Sensors 2019;19:3157. Available from: https://doi.org/10.3390/s19143157.

[71] Lv Y, Xu P, Yu H, Xu J, Li X. Ni-MOF-74 as sensing material for resonant-gravimetric detection of ppb-level CO. Sens Actuat B: Chem 2018;262:562−9. Available from: https://doi.org/10.1016/j.snb.2018.02.058.

[72] Wang Z, Chen Q. Vapochromic behavior of MOF for selective sensing of ethanol. Spectrochim Acta, A: Mol Biomol Spectrosc 2018;194:158–62. Available from: https://doi.org/10.1016/j.saa.2017.12.072.

[73] Surya SG, Bhanoth S, Majhi SM, More YD, Teja VM, Chappanda KN. A silver nanoparticle-anchored UiO-66(Zr) metal-organic framework (MOF)-based capacitive H_2S gas sensor. CrystEngComm 2019;21:7303–12. Available from: https://doi.org/10.1039/c9ce01323g.

[74] Moscoso G, Almeida F, Sousaraei J, Lopes-Costa A, Silva AMG T, Cabanillas-Gonzalez J, et al. Luminescent MOF crystals embedded in PMMA/PDMS transparent films as effective NO_2 gas sensors. Mol Syst Des Eng 2020;5:1048. Available from: https://doi.org/10.1039/c9me00164f.

[75] Pournara AD, Margariti A, Tarlas GD, Kourtelaris A, Petkov V, Kokkinos C, et al. A Ca^{2+} MOF combining highly efficient sorption and capability for voltammetric determination of heavy metal ions in aqueous media. J Mater Chem A 2019;7:15432–43. Available from: https://doi.org/10.1039/c9ta03337h.

[76] Zhang D, Xu Y, Liu Q, Xia Z. Encapsulation of $CH_3NH_3PbBr_3$ perovskite quantum dots in MOF-5 microcrystals as a stable platform for temperature and aqueous heavy metal ion detection. Inorg Chem 2018;57:4613–19. Available from: https://doi.org/10.1021/acs.inorgchem.8b00355.

[77] Ye W, Li Y, Wang J, Li B, Cui Y, Yang Y, et al. Electrochemical detection of trace heavy metal ions using a Ln-MOF modified glass carbon electrode. J Solid State Chem 2020;281:121032. Available from: https://doi.org/10.1016/j.jssc.2019.121032.

[78] Liu Y, Ma LN, Shi WJ, Lu YK, Hou L, Wang YY. Four alkaline earth metal (Mg, Ca, Sr, Ba)-based MOFs as multiresponsive fluorescent sensors for Fe^{3+}, Pb^{2+} and Cu^{2+} ions in aqueous solution. J Solid State Chem 2019;277:636–47. Available from: https://doi.org/10.1016/j.jssc.2019.07.020.

[79] Lian X, Yan B. A lanthanide metal-organic framework (MOF-76) for adsorbing dyes and fluorescence detecting aromatic pollutants. RSC Adv 2016;6:11570–6. Available from: https://doi.org/10.1039/c5ra23681a.

[80] Phan-Quang GC, Yang N, Lee HK, Sim HYF, Koh CSL, Kao YC, et al. Tracking airborne molecules from afar: three-dimensional metal-organic framework-surface-enhanced Raman scattering platform for stand-off and real-time atmospheric monitoring. ACS Nano 2019;13:12090–9. Available from: https://doi.org/10.1021/acsnano.9b06486.

[81] Li D, Cao X, Zhang Q, Ren X, Jiang L, Li D, et al. Facile: in situ synthesis of core-shell MOF@Ag nanoparticle composites on screen-printed electrodes for ultrasensitive SERS detection of polycyclic aromatic hydrocarbons. J Mater Chem A 2019;7:14108–17. Available from: https://doi.org/10.1039/c9ta03690c.

[82] Jiang Z, Gao P, Yang L, Huang C, Li Y. Facile in situ synthesis of silver nanoparticles on the surface of metal-organic framework for ultrasensitive surface-enhanced Raman scattering detection of dopamine. Anal Chem 2015;87:12177–82. Available from: https://doi.org/10.1021/acs.analchem.5b03058.

This page intentionally left blank

Chapter 12

Thermomechanical and anticorrosion characteristics of metal-organic frameworks

Mohammad Ramezanzadeh and Bahram Ramezanzadeh
Department of Surface Coatings and Corrosion, Institute for Color Science and Technology, Tehran, Iran

12.1 Introduction

The three-dimensional (3D) nanostructure metal-organic frameworks (MOFs) are among the subdivisions of the advanced coordination polymers that have been engrossed thoughts among the researchers in the last few decades due to several unique characteristics. MOFs have high crystallinity and porosity as they have over 6200 $m^2 g^{-1}$ internal surfaces and up to 90% free volume, which can host other molecules [1]. These highly ordered crystalline porous structures can be formed through the donor−acceptor mechanism between metal ions/oxides clusters (such as Zn, Cu, Cr, Al, and Zr) that are coordinated to the polyatomic organic ligands (mostly bivalent/trivalent modes of N-containing aromatics or aromatic carboxylic acids) [2–4]. The formidability of the metallic nodes and organic struts, geometrical arrangements (coordination entities repeating) of the nodes, and linkers beside the connectivity of the whole structure are the three principal prerequisites for the MOFs. Their coordination spaces (for ions exchanges) and pore size are stretchy and elastic, which can be adjusted [5]. These superstructures can be constructed through several approaches such as solvent evaporation and isothermal synthesis [6], ultrasonic- and microwave (MW)-assisted methods [7], hydro(solvo)thermal method [8], electrochemical (EC) synthesis [9], diffusion method [10], and mechanochemical synthesis [11], each of which has their advantages and disadvantages. This makes MOFs versatile in lots of applications. The pores are firm over the guest molecules removal (often solvents); therefore, they have this chance to be reloaded with other substances. Due to this feature, MOFs are favorable candidates in the fields of catalysis [12], high-capacity adsorbents for selective separation [13], and storage containers for gases such as hydrogen and methane [14]. The application in

Metal-Organic Frameworks for Chemical Reactions. DOI: https://doi.org/10.1016/B978-0-12-822099-3.00012-5

biomedical fields such as wound healing [15], anticancer [16,17], antibacterial [18], and drug loading [19] has also been observed. Being nontoxic and bioactive has made MOFs a popular choice. Several review papers regarding the applications, characterizations, and synthesis of these structures have been published [4,6,20–23]. In this chapter, we are going to talk about the engineering aspects of MOFs with an inclination to the field of corrosion and metal protection.

12.2 Design of metal-organic frameworks

The design and synthesis of the functional nanoscale material from the molecular aspect have been a hot spot for a long time, though they are encountering great challenges. Generally, MOFs are fabricated by the coordination of inorganic centers (metal nodes) with polydentate organic ligands, which constructs low-density and highly ordered lattice (Fig. 12.1) [24]. The MOFs manifest solitary chemical and physical characteristics due to the various architectures and molecular functionalities of different inorganic nodes and ligands. On that account, particular doping metal ions and ligands arrangement in the body of the structure became prevalent approaches for the MOFs functionalization [25]. Usually, Ru, Re, and Ir complexes using dicarboxylic acid functional groups have been integrated catalytically into a greatly solid and porous $Zr_6O_4(OH)_4(bpdc)_6$ (UiO-67, bpdc = para-biphenyldicarboxylic acid) lattice utilizing a mix-and-match fabrication approach. These doped MOFs are profoundly efficient catalysts for organic transformations, CO_2 reduction, and water oxidation [26]. Limited loads intercalation of Ru(II) into a fluorescent ultramicroporous Zn(II) coordination polymer led to the production of phosphorescent compounds with great tunable oxygen-quenching performance. This type of MOF was utilized to fabricate oxygen sensors with modest, ratiometric, and color-changing capabilities [27].

Organic struts enlargement also gives the chance of providing diverse functionalities to MOFs. For instance, an anionic chiral MOF has been rationally

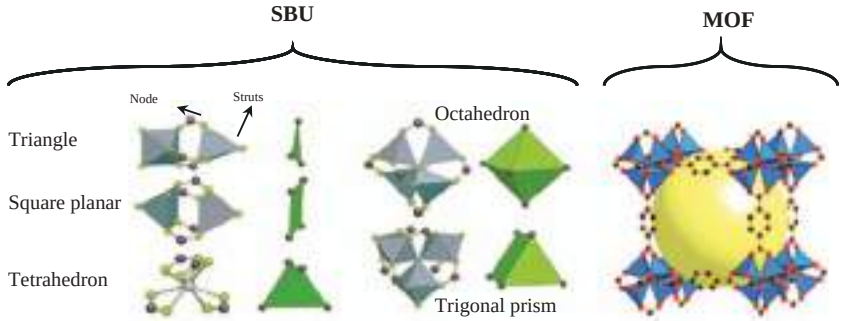

FIGURE 12.1 Schematic illustration of prototypical examples of SBU and the MOF. *MOF*, Metal-organic framework; *SBU*, secondary building unit.

designed with a predesigned hexatopic size-expanded ligand known as 5,5′,5″-(1,3,5-triazine-2,4,6-triyl)tris-(azanediyl)triisophthalate (TATAT). The luminescence power of the constructed framework is substantially improved in benzene and toluene, while quenching impacts are noted in ethanol and acetone, bringing a promising usage for luminescent probes [28].

MMPF-6, which is an Fe-based porous framework, has been synthesized by in situ self-assembly of $Zr_6O_8(CO_2)_8(H_2O)_8$ with iron(III) meso-tetrakis (4-carboxyphenyl)porphyrin chloride developed through the solvothermal method. This MOF demonstrates attractive peroxidase function, which can be compared to that of hemeprotein myoglobin [29].

The colorless, peptide-based $[Zn(Gly-Thr)_2]\cdot CH_3OH$ crystals were constructed through the interactions between the Gly−Thr and zinc nitrate in a methanolic medium successfully [30]. This lattice showed selective-mode adsorption of carbon dioxide rather than methane. Such achievements in studies can lead to a new world of designing high-class biomimetic compounds for bioanalysis usages.

12.2.1 Key structures in metal-organic frameworks

Any shortage in controlling the coherence of conventional solid-based compound structures such as activated carbons and zeolites is ascribed to the case that since there is a low correlation between the products and reactants, the origin substances do not keep their arrangement. On the other hand, these frameworks can be procured by the aid of rigorous molecular structure blocks under reaction situations that preserve the integrity of the building by the synthesis system [27]. The construction of a net-like structure can be characterized as the gathering procedure of rational principal structure blocks to assemble secondary building units (SBUs), which predispose ordered structures supported by solid coordination links (Fig. 12.1). As a summary, using such approaches, the total coordination number control of the organic and inorganic structure units can be feasible, and later the identification of the network, which is believed to be an outcome of topological aspects, gets critical [31].

Generally, MOFs are built of two types of extension points or primary structure units. The multitopic organic ligands are one type. Another one is a finite polyatomic knot or a metal atom (homometallic such as Zr_6O_4, and Zn_4O) or other forms (heterometallic such as polyoxometalates). The two kinds of structural units demonstrate the roles of features in the development of secondary structural units (well known as SBUs) [32]. Eventually, these SBUs reconstruct in larger dimensions to build the body of MOF (Fig. 12.1). The basic topology of a lattice can be detailed by a network, specified using a three-letter code such as abc (rht, soc, pts, etc.). The details of nets are accessible through searching in a directory, namely, as Reticular Chemistry Structure Resource. This database possesses more than 2000 various lattices

[33]. Blatov et al. have developed a computer program named TOPOS that can characterize the origin lattice of the structure. This program is a wide database for around 75,000 lattices [34]. Structures with one kind of head are named uninodal, while the ones with two kinds of heads are called bimodal. During the synthesis the produced structural blocks that contain metallic atoms are typically polyhedral or polygonal. Even though the shape and the geometry of the organic structural units are predetermined, the flexibility of them generally shapes the eventual architecture. Therefore the characterization of all edges and vertices is more important than just identifying the net. All sorts of netted frameworks (inorganic, organic, or organic–inorganic hybrid compounds) have innate nets. Thus the researchers' passion has been engrossed in the field of topological design of MOF structures based on a rational reconstruction of building units in various dimensions [31,32].

12.2.2 Dimensionality of metal-organic frameworks

MOFs are a particular structural type of versatile porous crystalline compounds with various topologies and dimensionalities, which can be acquired through procedures based on bridging ligands binding and metal ion geometry approaches [35,36]. Depending on the dimensionality of the structure, these frameworks can be classified in the presence and absence of the guest's moieties. In single-dimensional MOFs (1D) the coordination links cover the whole structure in only one direction, and the potential vacancies can be incorporated with the low-size molecules. In two-dimensional (2D) frames the sole layers are overlapped over either staggered sort of stacking or edge to edge or where poor interactions occur among the sheets. Ligand treatment can govern the functionality and stacking behavior of the internal parts of the channel. Two hypotheses for the incorporation of the external molecules in 2D lattices have been proposed: (1) the interval space of the sheets and (2) the interval space of the layers struts. Due to the coordination bonds coverage in three orientations in 3D lattices, structures are so stable and porous. The 3D pillared grids and layers can be met in most of the MOFs. The noncovalent $\pi-\pi$ hydrogen and stacking links expedite the building units bonding (1D, 2D, and 3D lattices). These interactions engagement not only turn the framework into a limitless high dimensional lattice but also governs their orientationality and stability [35].

12.2.3 Methods for the construction of metal-organic framework structures

New MOFs can be acquired through designating a couple of determining parameters. While maintaining the SBUs of the whole structure is the most vital task, the construction of novel organic ligands for the struts and optimum circumstances for the bond improvement of the metal-organic ligand

has gained lots of attention and turned into a hot spot for researchers. The typical features of ligand, such as geometries, chirality, angles of links, bulkiness, and ligand length, obtained by the metallic ions, affect the MOFs structure dramatically. While the estimation and testing through trial-and-error mode are yet appropriate in the architecture and fabrication of novel MOF compounds, numbers of efficient and feasible construction methods have been addressed in many studies. Fig. 12.2 demonstrates the most implied procedures in the studies. The most used processes are described in the following sections [10,11,37–39].

12.2.3.1 Hydro(solvo)thermal method

The solvothermal procedure is the most used technique in the fabrication of MOF compounds. Synthesis can be accomplished by heterogeneous reactions occurring between the aqueous solvents and mineralizers placed in sealed nuclear magnetic resonance (NMR) tubes (high temperatures) or glass vials (low temperature), which are heated by electrical current (above solvent boiling temperature). Frequently, methanol, ethanol, acetone, acetonitrile, diethylformamide, dimethylformamide (DMF), etc. are used as organic solvents. High-pressure and -temperature circumstances are critical requirements for the synthesis media. This process has a high throughput and can expedite the production rate [40]. The hydrothermal process has been conventionally utilized during metal extraction. Also, the application for the construction of extensive crystals has been observed [41]. This strategy is effective for two comprehensive reasons. In the first place, solubility issues of the heavy organic compounds under the experimental circumstances can be reduced. Also, under

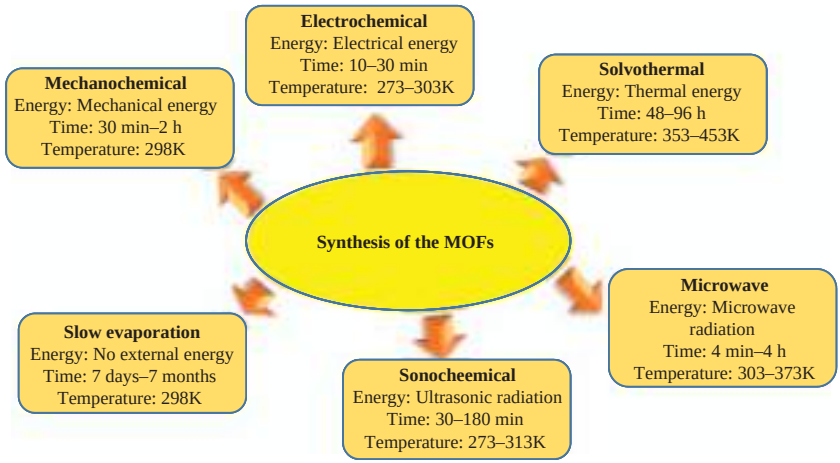

FIGURE 12.2 Different approaches to the synthesis of the MOF compound. *MOF*, Metal-organic framework.

equal empirical circumstances, the nucleation procedure can be triggered immediately for the generation of rare complexes [37]. During the water viscosity reduction under such circumstances, the precursor's mobilization activity is preferred. In these circumstances the thermodynamically low-stable phases of the coordination lattice can be insulated. The growth of crystal can be improved in the steel autoclaves located in adjustable high-temperature laboratory ovens at functioning temperatures lower than 300°C with definite resting time. Nonetheless, this method is restricted by high-temperature requirements, long reaction times, and low product output. The demand for the application of hazardous solvents such as DMF can be considered as another limitation of this process (Fig. 12.3) [8,37,41].

12.2.3.2 Microwave and ultrasonic methods

MW-based synthesis of MOF-structured compounds is the same as the typical hydro/solvothermal strategy. MW radiation has been evolved for the construction of inorganic or organic solid-state compounds with benefits of particle size distribution, phase and microstructure control, and reduction in crystallization times. Indeed, the application of electromagnetic radiation such as MW has been extensively settled in the synthesis of compounds

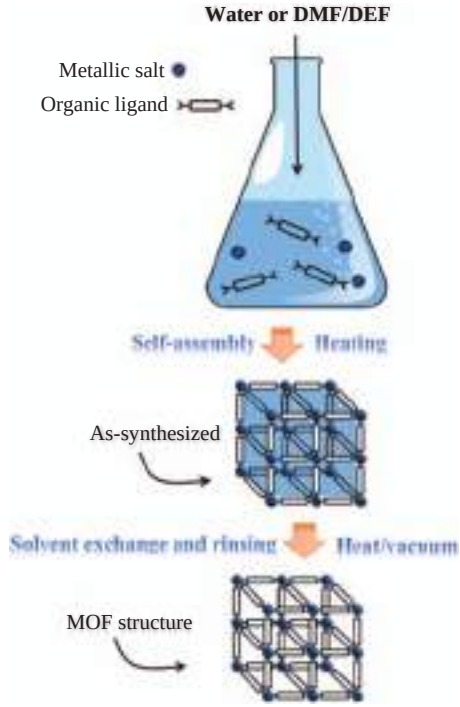

FIGURE 12.3 Schematic illustration of the solvothermal process.

using organic chemistry [40]. The MW-assisted route was also used in synthesizing of the solution and solid−solid-based MOFs and zeolites. The textural and physical characteristics of the acquired crystals from the MW route have desirable similarities with the conventional solvothermal strategy. The first structure, which was fabricated using the MW process, was MIL-100. With the operational temperature of 493K for 4 hours, the obtained X-ray diffraction (XRD) pattern was in good accordance with the one synthesized through a solvothermal approach in the operational temperature of 493K for 4 days. The output rate was also well comparable. The investigation indicated that the construction of an MOF could be accomplished in runs with shorter operational time using the microwave (MW) process. The conventional solvothermal procedure cannot construct coordination polymers that have microporous inherent, but through using the MW-assisted route, this can be achieved, which is a sign of lucrative employment of MW in such frameworks synthesis [40,42]. The fundamental mechanism of the MW-based synthesis is based on the interactions between the electrical charges and electromagnetic irradiation, which may contain the electrons, molecules in solid or solution ions, and ions of the polar solvent (Fig. 12.4). Due to the presence of electrical resistance in solids, the electrical current can be generated. In liquids the increase in the temperature can lead to the augmentation in the kinetic energy of molecules. Consequently, with the aid of frequency in the electromagnetic field, the contacts between the polar molecules will

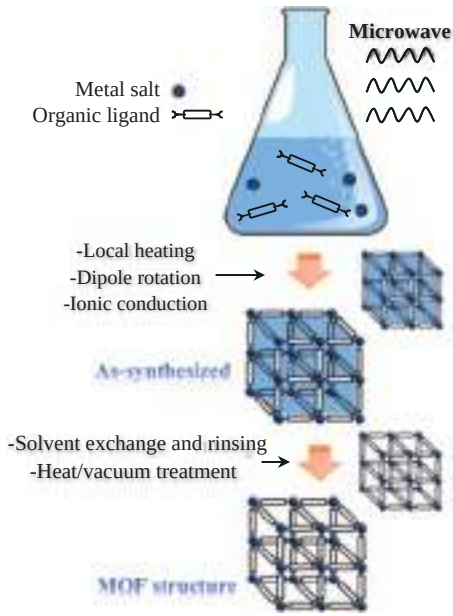

FIGURE 12.4 Schematic illustration of the microwave-assisted technique.

be boosted. MOF-5, Cr-MIL-101, and Fe-MIL-100 can be introduced as typical synthetic MOF compounds using this method. Besides the typical solvents the distinctive features of ionic polarizability and conductivity can induce the ionic liquids (ILs), a desirable agent for MW absorbing. Therefore these liquids have to be considered as appropriate solvent candidates in the MW technique [40,43,44].

The sonochemical method using ultrasonic waves is other eco-friendly, cost-effective, and facile for the construction of MOFs with clean surfaces. Sonochemistry manages the chemical−physical behavior of the molecules that experience vigorous ultrasounds (20 kHz−10 MHz) [45]. It is a hierarchical strategy for the synthesis of nanoscale MOFs. In the direct interaction between the molecules and the ultrasonic waves, no chemical reaction can occur. Ultrasonic waves can create an alternating pressure pattern in the presence of the liquid phase. The pressure alteration will finally lead to the construction of cavities in the solvent (small bubbles, Fig. 12.5). Afterward, the bubbles develop and fall apart. The whole interaction is known as the cavitation phenomenon. As the procedure continues, hot sites will be created in the vicinity of the liquid (5000°C and pressure of around 500 atm). This condition is in the microsecond range [46]. The aforementioned intense

FIGURE 12.5 The schematic presentation of the sonochemical route for the synthesis of MOF compounds. *MOF*, Metal-organic framework.

circumstances can cause the occurrence of chemical reactions. MOF-177, Fe-MIL-53, and MOF-5 can be presented as typical MOFs constructed using this regime [47–49].

12.2.3.3 Electrochemical production

The EC technique is the most feasible, applicable technique among the different strategies for MOFs construction. Procedure control by the aid of this regime is more precise. The high purity and the desired rate of the process as a result of the lack of counter ions such as NO_3^-, ClO_4^-, Cl^- from the metallic salts can be considered as the principal benefits of this strategy. In this technique the metallic ions can be generated in the anode instead of the metallic salts (anodic dissolution) [9,50]. However, the organic strut is located at the cathode, and the EC bath is replete with saline electrolyte. Researchers of the BASF (a German chemical corporation and the second biggest chemical producer in the world) have implemented an innovative study regarding the synthesis of the MOF-structured compounds using the EC technique [51]. Cu-MOF is the first compound constructed using the EC technique. In the designed strategy the EC bath was filled with methanol, and the benzene tricarboxylate and Cu plates were utilized as cathodic and anodic electrodes. With the operational electrical current of 1.3 A and voltage of 12–19 V, a turquoise colored Cu-MOF deposit was produced in 150 minutes (Fig. 12.6) [52]. HKUST-1 and Zn-imidazolate are the typical structures constructed through this technique [53–55].

12.2.3.4 Diffusion method

In most cases the intense agitation of the solutions having organic acid ligands and metallic salts leads to the fabrication of powder samples (microcrystals), which are inappropriate for XRD analysis. Diffusion techniques are generally employed to prevent the generation of polycrystalline powder compounds [56]. This method requires acid ligand and metallic salt to be mixed in a medium such as DMF and conveyed to an open-air dish encircled by chemicals such as triethylamine, ammonia, trimethylamine, dimethylamine that are volatile base. The base slowly diffuses into the reaction blend. Using acid deprotonation, the mixture enhances the MOF construction that induces increment in the amount of conjugate base of the acidic ligand [10]. Large crystals could be fabricated at room temperatures by giving extended reaction time and the diffusion rate of this procedure [57] so that the XRD experiment can be carried out. The growth of crystal takes place by the construction of three individual layers within the liquid-solvent diffusion. Although the precipitant solvent is held in the first layer, the second layer has a product solvent, and the third layer detaches these two sheets and enables a low-speed diffusion. At the same time, as the solvents shift from one layer to another one, the certain crystals' growth ensues at the layers interface. One more technique is the reactant's gradual diffusion using gels [58,59].

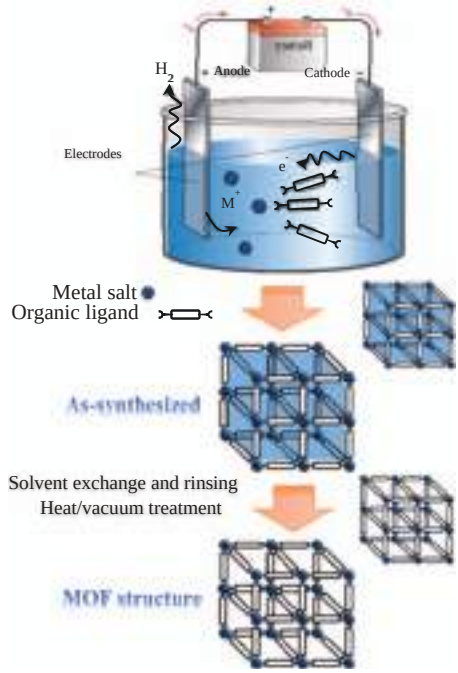

FIGURE 12.6 The schematic demonstration of the EC technique for the fabrication of the MOF structure. *EC*, Electrochemical; *MOF*, metal-organic framework.

12.2.3.5 Mechanochemical synthesis

Most of the volatile organic solvents are classified as hazardous chemicals that harm the environment [11]. To lower the issues concerned with such toxic compounds, the mechanochemical synthesis was designed and recommended for the fabrication of MOF materials (Fig. 12.7). Construction under solvent-free processes, to prevent the employment of organic solvents and shortened reaction periods (around 10−60 minutes) with a desirable output rate, can be considered as the advantages of this technique [60]. Using mechanical force can bring about changes in the physical properties and also trigger the chemical reactions [61], which originate the solvent-free synthesis or mechanochemical inception. Employing the bridging organic ligands and metallic precursors, the mechanochemical process (grinding) synthesizes distinct coordination complexes with intramolecular links reorientation that engenders the chemical reaction. Braga et al. have introduced several 1D coordination polymers using this regime [62]. They corroborated the crystalline inherent employing powder XRD patterns and also confirmed the structural characteristics by the aid of simulation investigations. Mainly metallic oxides have a lower solubility in solvent-based reactions; nevertheless, in the mechanochemical processes the metallic oxides can be supplanted, which

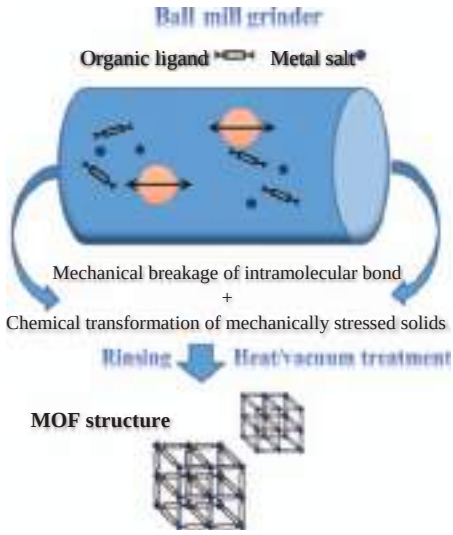

FIGURE 12.7 The schematic illustration of mechanochemical synthesis.

replace the metallic salts as the primary substances. In this case the by-product will be just water. The first 3D synthetic coordination polymer was $[Cu(INA)_2]$. This structure was synthesized employing ball mill as crushing equipment for the grinding of primary compounds such as isonicotinic acid and copper acetate. The operational conditions were set as follows: a steel ball in combination with around 0.5 g of metallic precursors at a vibration frequency of 25 Hz kept for 10 minutes [60]. Researchers have found that a minute of solvent addition can enhance the architecture of the pillared-layered MOFs in the liquid-assisted grinding [61,63,64]. The liquid attendance boosts the mechanochemical reactions by the precursors' mobility improvement.

12.2.3.6 Solvent evaporation and isothermal synthesis

Solvent evaporation is another strategy for the construction of MOFs. Crystals are assembled by the gradual enhancement in the concentration of the leftover solution in this method. Originally, reactants are combined in a proper solvent with steady agitation until the lucid solution is realized. Conveying the reaction blend into the beaker, the glass was isolated using a parafilm. The growth of crystals is triggered by solution saturation or by solution cooling or surplus solvent removal [65–67].

Ionothermal is a lucrative and applicable strategy that was also employed for the construction of MOFs [68,69]. This process is similar to the solvothermal regime, where the solvent of the process is water. Due to the strange and also exciting properties such as high ionic conductivity, good

dissolving capability, high thermal stability, poor coordination ability, and extremely low volatility, ILs are classified as suitable and unique reaction solvents [69]. Performing as solvents, they function as a template guiding agents in the crystalline solids synthesis. The application of ILs as solvents in the synthesis process may result in the presentation of new parameters in the MOF architecture such as anion control, chiral induction impacts, and structural directing [70]. In addition, using the chiral IL, the ionothermal method expedites the chiral MOFs preparation. In the reactive container the ionic situation carries the acentric or chiral data from solution to solid products. Lin et al. [71] and Zhang et al. [72] have detailed the series construction of chiral MOFs using ionothermal strategy. Hydrogen bonding is a dominant directional power in the fabrication of the solid, but the lack of efficient hydrogen bonds of the donor−acceptor species in the ionothermal process may harm the controlled construction of the MOF structure, except the powerful hydrogen bond addition constructs effective auxiliary ligands in the environment [70,71,73].

ILs as a synthesis medium, microfluidic MOF synthesis system, and drygel conversion MOF synthesis have been proposed by researchers as further new approaches in the construction of MOFs, but more investigations to enhance and develop such procedures are required.

12.3 Stability of metal-organic frameworks

"Stability" or "robustness" cannot be regarded as a certain quality, and one shall look at it as several parameters that have been defined in advance. These count on intended usages where the porous compound will be subjected to specific environments at a determined amount and duration (such as corrosive solutions, water, and organic solvents) [74]. Therefore based on the reviewed principles, stability can be studied in three genres that are mechanical stability, thermal stability, chemical stability, and water stability. Hereafter, the MOF stability indicates the structural resistance to deterioration when the framework is in the exposure to the operational circumstances [75]. However, it is noteworthy that the thermal stability (other than melting and amorphization) is linked up with chemical stability since the heat may change the chemical structure of the frame by triggering and/or expediting the chemical reaction, which activates the deterioration of the crystalline lattice [76]. Owing to the coordination bonds interruption between the organic ligands and inorganic nodes (such as redox activity and hydrolysis), this mainly influences the coordination sphere of the metallic cation. Even sometimes, it can influence the organic strut itself (such as alkyne oxidation and decarboxylation). Metal-organic structures must have several genres of stabilities. For instance, chemical stability is vital for the usages in aqueous environments that have different pHs. Drug delivery or molecular separation are typical examples of such environments [75,77]. Both thermal and

chemical stabilities are vital for the catalytic procedures carried out under rough circumstances such as applications in fuel production and chemical feedstock [32,74,77]. The mechanical stability is primarily studied in the shaping of such frameworks (i.e., pellets fabrication or other compact types that can be used in industrial procedures) [76,78].

12.3.1 Various aspects regarding the stability of metal-organic frameworks

The mechanical, hydrothermal, thermal, and chemical stabilities (structural resistance to degradation and deterioration) of MOFs have been frequently considered as an ambiguous case of study, but it is not anymore [32,75,78]. A wide range of thermally−chemically stable MOFs that have interesting applications were synthesized in recent years. The following sections will discuss the various aspects of stability.

12.3.1.1 Thermal stability of metal-organic frameworks

Thermally stable compounds are among the most vital materials that have wide applications in industry. The thermal stability of a metal-organic lattice can be described generally as the capability of the structure to eschew irreversible changes (from the physical and chemical points of view) when the compound is subjected to a high-temperature environment. Throughout the thermal treatment procedures, the structural deterioration results in either linker dehydrogenation, metal-oxo-cluster dehydration, amorphization, and melting or graphitization [78,79]. These phenomena occur gradually over the heating level. Otherwise, they take place only in the temperatures higher than the decomposition point. This condition typically occurs with the combustion and/or releasement of the guest molecules besides the ligand−metal links failure and the subsequent ignition of the organic spacer [80].

The analyses for evaluating the thermal stability of a structure are yet restricted. The thermogravimetric analysis (TGA) data can be obtained for most of such frameworks showing the accessibility of the test. Variable temperature powder X-ray diffraction (VT-PXRD) analysis is a highly detailed method for studying thermal stability. Nonetheless, diverse assessment conditions are assumed for each specimen (specific temperature period for data collection, scanning speeds, etc.), which causes the thermal stabilities comparison more difficult by employing this technique. Besides and in most cases, VT-PXRD patterns are acquired under inert terms. Such conditions do not show the real behavior of the lattice when the structure is simultaneously subjected to heat and an environment containing oxygen and/or moisture [81,82].

The elements of rare-earth, alkaline-earth, alkali, main-group, and transition classes can be employed as the metallic nodes of the MOFs. Inside the

frame, these moieties are in the form of either metal-oxo-cluster with multinuclearity, layers, and chains or even single metallic sites. Principally, the inherent of a metallic ion, such as the coordination number, and its interaction with a strut by ligand−metal coordination, ion radius, and the oxidation state perform an important function in the thermal stability determination of the MOF [83,84].

The inherent of organic strut is the second fundamental vital factor in the thermal stability determination of MOF structures. Considering the nitrogenated and oxygenated linkers besides the donor heteroatoms, linkers can be classified into two main groups. Based on their chemical structures, linkers can be further separated into aliphatic and aromatic types. A linker molecule has this ability to simultaneously comprise a number or all of these kinds together, which in this case, are normally invoked as a "multifunctional" spacer [80]. So here, the thermal stability of the MOF-based compound grows into a very unpredictable case of study. Luckily, a remarkable number of the studied frameworks contain only a single form of the organic spacer with a homogeneous functional group or occasionally two forms of distinct organic ligands for coordination [85].

As abstracted from the previous discussions, a framework that features a dense and defect-free packing beside a robust ligand−metal interaction, metallic ions with steady oxidation state, and short aromatic linker is an excellent choice for high thermal stability. However, the employment of MOF-based compounds does not solely require high thermal stability but also needs other characteristics counting on the particular applications area. Hence, there should always be a compromise between the stability, functionality, and porosity of the structure [84,86].

12.3.1.2 Mechanical stability

The mechanical stability of the MOF under pressure or vacuum is an additional significant parameter for the practical and industrial utilization of MOF-based materials from the engineering aspects. Occasionally, the instability of porous lattice under vacuumed conditions can result in partial failure of the structure or severe phase changes [87]. The solvent evacuation and solvent exchange are the common approaches for the full activation of MOFs besides the structural collapse inhibition. The replacement of greater surface tension solvents with the lower solvents containing liquid CO_2, *n*-hexane, and CH_2Cl_2 and subsequent solvent evacuation can aid the effective MOFs activation. In addition, MOFs also have rather low stability under mechanical pressure in comparison with zeolites [88].

There is not any useful technique to assess the structural stability of an MOF. Counting on the operational environments, distinct standards should be to be considered. For instance, few catalysis procedures need oxidizing/reducing conditions or acidic/basic environments. Industrial catalysis demands stability in

front of hydrothermal steaming. From an engineering outlook the mechanical stability of an MOF desires to be adopted for the industrial treatments. These structures may present completely different behavior under diverse conditions. For instance, MOFs with carboxylate-type struts and high-valency metallic ions exhibit durable stability in acidic environments but are likely to be degraded by coordination anions such as Co_3^{2-} and basic environments. Correspondingly, the $C_5H_4NO_2$-based structures besides low-valency metallic ions possess robust resistance in alkaline solutions but can be readily degraded in front of acidic solutions. MIL-53 (iron or chromium) and MIL-88 (iron or chromium) symbolize a novel genre of chemically stable MOFs with poor mechanical stability as expressed by their pliable performance when facing the guest molecule adsorption/desorption. Accordingly, depending on the operational environments for specific uses, diverse criteria are required to be viewed [89–93].

12.3.1.3 Chemical stability

While lots of different MOF designs have been announced until now, only a few of them have nearly demonstrated successful performance in noninert environments so that their structure can be shaped without any change in their porous network. The synthesized MOFs from carboxylate-based struts and divalent cations (M^{2+}) are common frail structures [94,95]. For example, Cu^{2+} trimesate HKUST-1 decomposes by time in the water at ambient temperature, but Zn^{2+} terephthalate MOF-5 decomposes quickly in water [96]. The stability deficiency of water is a serious restriction on the MOFs consumption, not only for practical uses demanding a nonstop interaction with water (e.g., separation procedures from gases exited from industrial flues, which may encompass great volumes of H_2O, or water splitting catalysis [77,97]) but also for clean uses such as H_2 storage for fuel cells wherein H_2O is itself a by-product of the reaction or could be a contaminant throughout the refilling course. In general, the chemical stability is one of the supreme fundamental standards and has to be considered to produce an atmosphere-resistant MOF wherein moisture or water may be taken into account as a sizable decomposition risk [77,95,98].

The influence of water (and steam) on several MOFs was evaluated using dual experimental and computational types of investigations in 2009 [99]. They have emphasized that the hydrolysis possibility of the ligand–metal bond is related in reverse with the bond strength between the organic strut and the metallic cations of the framework. This connection can also be employed to all molecules (specifically $C_6H_5O^-$, NH_3, NO_x, SO_x, H_2S, PO_4^{3-}, and so on), which can theoretically contend with the organic strut and disrupt the ligand–cation bond. Therefore on the topic of the potential competing agent (or reactive moieties), the chemical stability can be divided into various classes such as stability under severe circumstances (such as physiological environments that contain NH_3 or H_2S), stability against acidic

or basic environments, water, and moisture stability. Hence, to enhance the chemical stability of such frameworks, the interaction reinforcement between the organic and inorganic species has to be the main approach. Stability promotion can also be accomplished by avoiding or restricting any competing agent entrance to the ligand−cation bond. To evaluate the chemical stability of the lattice structures, a sequence of issues has to be taken into consideration. The main subfactors are intra- and intermolecular interaction, framework catenation, hydrophobic inherent of the structure, the attendance of defects or open metallic sites, linker rigidity, the connectivity, and the nuclearity of the inorganic building unit, the coordination geometry of the cation, redox behavior, etc. [95−97].

The PXRD technique is the common technique for the chemical stability evaluation of a metal-organic lattice. A simple comparison between the sample patterns before and after the structure subjection to a specific environment can reveal the chemical stability. However, this technique cannot perform a comprehensive and accurate assessment from the stability even if both patterns would be thoroughly similar. Since such a technique is not quantitative and cannot show what has released (solution) or cannot prove the development of amorphous phases, an incomplete decomposition can still take place. An integral and more precise investigation can be accomplished before and after the treatment by measuring the supplementary inert gas adsorption isotherm. The porosity reduction reveals partial decomposition of the crystalline lattice. However, up to date, there are not any standard experimental approaches designed for the evaluation of the chemical stability (number of cycles, exposure time, concentration, and so on). Moreover, in most of the cases, pH confirmation of the solution after MOF addition is not performed when assessing the stability as a function of pH. Nonetheless, for example, in most cases reporting the chemical stability in the case of $RCOO^-$-based frameworks at high pH values would not be precise. Partial decomposition of the framework can take place, bringing partial linker unleashment in the solution. Consequently, these interactions can cause a substantial reduction in the initial pH of the environment [77,82,98].

12.3.1.4 Water stability

The highest concern regarding the chemical stability enhancement of MOF compounds is mainly associated with water vapor. A ligand−metal coordination link is a fragile site in the framework. Hydrolysis generates −OH (or H_2O) or even a protonated linker. Bond strength can be a clear gauge of water stability [100,101].

Researchers have allocated a stability category for the MOFs after subjection to water: (1) unstable, (2) low-kinetic stable MOFs, (3) high-kinetic stable MOFs, and (4) thermodynamically stable MOFs. The compounds of

group iv are stable after durable contact with the aqueous mediums and have the active potential for a wider variety of applications. For instance, NOTT-300, zeolitic imidazole framework-8 (ZIF-8), MIL-101(Cr), MIL-96(Al), $Ni_3(BTP)_2$, and JUC-110 fit in this group, which represents stability in boiling water and under steaming circumstances [102,103].

The third group is stable after a high-humid exposure and shows active potential for high-humid industrial demands. There is a wide variety of MOFs in this set, as well as DUT-67, UiO-66, and numerous members of the MIL-group substances. Low-kinetic stable MOFs [for instance, CPO-27, MIL-125(Ti), and MIL-110(Al)] are stable only at low-humid conditions and can be used in predried gas applications [79,104].

Certain frameworks are not only highly hydrolytically stable but also able to hold the integrity of their structure on the frequent subjection to successive steam adsorption/desorption sets. For instance, amine-modified H_2N-MIL-125-Ti stays almost unchanged throughout the short nonequilibrium multicycle adsorption/desorption tests [76,105].

12.4 Application

The greatly engineered and crystalline inherent of MOFs can be easily discovered by their crystal design, which is a convenient assessment in the characterization of property−structure relations. The removal of the incorporated guest molecules (into the structure of any framework) may result in structural failure because of fragile coordination bonds. The structure of MOF deforms upon introduction to heat and guest molecules exhaustion, which proves that such structures are not indeed crystalline. Knowing the fact that in such conditions, an inflexible and highly thermostable structure can be a good choice [25,43], several metal-organic structures, stable up to 300°C or 400°C (and even 500°C), have been advanced, which are appropriate for the most demands. Despite heat resistance, these structures have other restrictions, such as low chemical stability in front of the water. Therefore MOFs can be recognized as an appropriate choice for new practical uses thanks to the diverse and remarkable structural properties [35,99].

Due to the fascinating structural features of MOF-based materials, they can be employed in numerous substantial grounds (Fig. 12.8). Modified detailed applications of MOFs can be realized by changing the structure architecture properly. It has been stated that MOF properties associate with the variations in the matrix and chemical functionality. Numerous design approaches can be utilized to having the anticipated performance of the material for any application [30,78]. Here in this section, the novel employment of MOFs in corrosion protection of metals will be discussed.

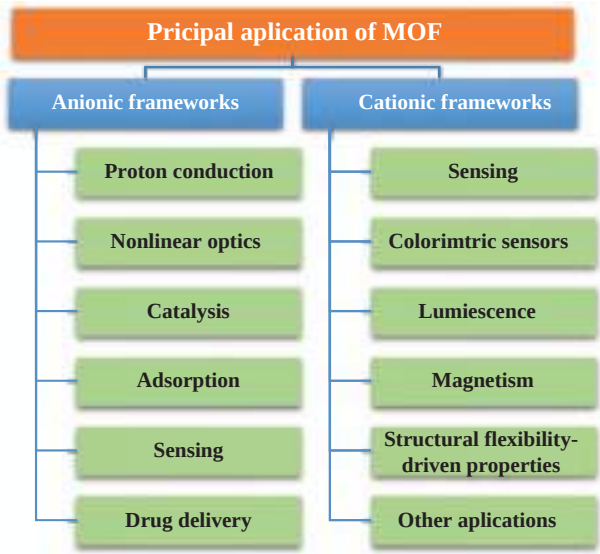

FIGURE 12.8 The various application for MOFs. *MOF*, Metal-organic framework.

12.4.1 Anticorrosion properties of metal-organic frameworks

Corrosion is one of the detrimental phenomena that cause severe damages (from both physical and economical aspects) [106–108]. Different strategies have been proposed over the years to avoid or at least lower the impact of chemical attacks. Applications of inhibitors, anodic/cathodic protection, organic/inorganic coatings, etc. are among the main approaches. According to the aforementioned properties and performance of the MOFs, these compounds have this capability to be employed as corrosion protective agents in the chemicals, surficial films, and organic coatings. They can also be utilized as nanocontainers for carrying the protective compounds and release them if needed [109–111].

Stability is a crucial parameter in studying the efficiency of an MOF in corrosion protection applications. Each aspect of the stability (chemical, hydrolytic, thermal, and mechanical) can be reviewed in the case of MOF applications for corrosion control. For example, in the inhibitors, the added compounds must have high water solubility to prevent sludge production. The high water solubility of MOFs in polymeric nanocomposites can undermine the barrier function of the coating in longer exposure times. In such a way, they can be leached/dissolved before the on-demand release mechanism. MOFs should have good chemical stability to endure in alkaline, acidic, and saline corrosive environments. Thermal stability is also vital in these applications. Sometimes, corrosion inhibitors are applied in environments with elevated temperatures. As mentioned earlier, MOFs can be utilized as the nanocontainers of protective compounds

and incorporated into the polymeric matrix. These coatings must experience a curing stage to be stiffened (normally around 100°C). Hence, they have to show desirable thermal stability in order not to decompose and collapse.

12.4.1.1 Metal-organic frameworks as a corrosion inhibitors

The application of protective chemicals known as "inhibitors" is the most feasible and cost-effective way to prevent chemical attacks toward the metallic substrates. These compounds can protect the surfaces through three general mechanisms: (1) construction of barrier films on the metallic surface, (2) elimination of the corrosive species of the environment, and (3) blocking the active cathodic and anodic sites of the surface. Generally, these compounds can be categorized into three classes of organic (e.g., azoles), inorganic (e.g., chromates and phosphates), and green compounds (herbal extracts). They can be adsorbed on the surface through chemisorption, physisorption, or a condition combined from both [107,108,112–114].

Recently researchers have come to this idea to utilize MOF as hybrid organic–inorganic corrosion inhibitors. The employment of these structures as corrosion inhibitors is fascinating thanks to their supramolecular inherent and abundance of the heteroaromatic and π-systems species. These substances can be adsorbed on the metal surfaces and construct new protective complexes. Mesbah et al. have employed $Mg(C7)_2$ and $Mg(C10)_2$ as two types of MOFs for the corrosion retardation of magnesium in a neutral environment. However, both structures were very similar, and they noted that $Mg(C10)_2$ structure discloses improved inhibition efficiency owing to its lower solubility in comparison with $Mg(C7)_2$ framework [115]. Fouda et al. have constructed two novel metal-organic lattices based on nitrogen donors and Au(I) to explore the corrosion inhibition of copper in HCl medium. They have concluded that the physisorption of both compounds is based on the Langmuir adsorption isotherm [116]. Zafari et al. have synthesized zeolitic imidazolate framework-8@$\{Mo_{132}\}$ (ZIF-8@$\{Mo_{132}\}$) as an effective and eco-friendly type of inhibitor for the corrosion protection in HCl solution. The results of the ANOVA analyses specified that the temperature is not a highly important and active factor in the protection of the corroding samples immersed in solutions containing blank and modified ZIF-8 compounds. It was proved that the chemisorption takes place during adsorption of modified MOF on the surface, and it was attributed to the high tendency of the anionic nature of the inhibitor [117]. Several other studies were conducted over the years to investigate the performance of MOFs in the corrosion inhibition approaches [111,118–120].

The smart delivery of the protective compounds is an advanced method to adjust the growth kinetics of protective film [111,121]. The constant release based on the incorporation of chemicals into the galleries of nanoreservoirs can induce long-term protection by prolonging the film growth in a

continuous way [117]. Tian et al. have loaded a series of inhibitors into the galleries of MOF for the corrosion retardation of mild steel in 0.5 M NaCl solution. The electrochemical impedance spectroscopy (EIS) results indicated that the inhibitor blocked both the anodic and cathodic reactions efficiently by developing a barrier film, resulting in an inhibition performance around 98%. The outcome of surface characterization and EC quartz crystal microbalance measurement has shown that controlled delivery has greatly improved the protection performance by making the protective film more compact [122].

12.4.1.2 Metal-organic framework–based thin films

The surface/interface functionalization is of great interest, which has attracted attention. Changing, enhancing, increasing, or adjusting the surface properties by concerning the biological, wetting, tribological, electrical, and optical or properties are key factors in giving a preferred functionality to a body. The porous structures were concerned as reservoirs that have decent control capability of the inhibitor immobilization. Nonetheless, the selected containers have to exhibit decent compatibility and adhesion between the metal surface and containers, together with incorporating appropriate amounts of the corrosion inhibitors. Therefore the carrier design is relatively significant. Most efforts have been made on utilizing polyelectrolytes shells, nanotube, oxide nanoparticles, layered double hydroxides, and mesoporous inorganic compounds (such as mesoporous silica nanostructures) as containers for incorporating inhibitors [10,123,124].

The application of MOFs as thin films has been surveyed in recent years owing to the presence of accessible metal sites, huge capacity for guests (such as dye molecules, gases, and drugs), easy functionalization, and long-lasting pores. MOFs that are added on solid surfaces as thin films or coatings can keep the benefits of the bulk MOF, which induce them to be a favorable choice for hosting and encapsulating inhibitors. As a result of the trouble of adjusting the discipline of inhibitor molecules in MOF galleries, the advancement of networked film for the smart encapsulation of the inhibitors in the corrosion prevention applications is a considerable contest. Meanwhile, most MOF resources show great affinity interactions with both organic and inorganic composites, and they can effortlessly fabricate MOF-inorganic/polymer protective coatings to enhance protective performance. Some methods for the construction of compact MOF films have been proposed through years, including in situ growth, seeded growth, EC deposition, layer-by-layer deposition, liquid-phase epitaxy, and Langmuir–Blodgett, each of which has their advantages and restrictions and can be applied by other coating technologies such as physical vapor deposition (PVD) and chemical vapor deposition (CVD) [125–127]. Li et al. have intercalated the cetyltrimethylammonium bromide (CTAB) into the classic HKUST-1 framework through a one-pot

preparation method. The substrate was coated with the modified MOF through an electrophoretic deposition process. The outcome indicated that the assembled CTAB@HKUST-1 film demonstrated noble protective behavior through the active type of corrosion inhibition [121]. Zhang et al. have converted a surficial layered double hydroxide (LDH) structure into MOF one on the metal surface using a simple ligand-assisted conversion approach. In this study the $ZnAl-CO_3$ LDH sheets were modified to realize intergrown ZIF-8 coatings. The polarization curves specified that the constructed ZIF-8 coatings could lower the corrosion current density four orders of magnitude in comparison with the blank substrate. The results revealed the fantastic capability of MOF structures in providing corrosion protection function [128]. Liu et al. have fashioned a novel system based on Mg-MOF-74/MgF_2 and applied on the AZ31B Mg alloy using in situ solvothermal synthesis methods. Surface characterizations revealed a compact and uniform topography besides desirable crystallinity. The anticorrosion analysis accomplished in the simulated body fluid at 37°C decreased the corrosion rate of the corroding substrate. The superhydrophilicity behavior of the thin film is attributed to the rough topology of the substrate surface, the great specific surface area of Mg-MOF-74, and the high presence of hydroxyl groups [129]. Several other thin-film studies were also conducted [130,131].

12.4.1.3 Metal-organic framework–based polymer composite coatings

The uniform distribution of organic, inorganic, or hybrid nanoparticles inside a polymeric matrix leads to a system with chemically and/or physically diverse phases known as polymer nanocomposites. These composites have exceptional and enhanced characteristics in comparison to the blank polymers or traditional composites, which can be readily altered by functionalizing the additives surface, choosing a detailed production process, adjusting additives concentration, etc. The polymeric nanocomposites are employed in diverse fields in most research and industrial applications thanks to the superb features and the products range of nanocomposites [132,133].

Several kinds of nanostructured compounds (magnetic nanoparticles, porous nanomaterials, metal oxides, graphene, carbon nanotubes, clays, etc.) have been incorporated into the biocompatible polymers to construct nanocomposites for industrial applications. These coatings may demonstrate different performances. For instance, they can govern the transport phenomena over the polymeric matrix, they can interact with a surface or a compound when it would not be feasible for the coating, and they can strengthen the coating matrix or give particular features to it [134–136].

MOF-based polymeric nanocomposites have engrossed the attention since they cover the benefits of flexible polymeric structures and highly porous MOFs simultaneously. The application of MOFs with organic coatings has

been surveyed through some studies. For the mixed-matrix membranes, polymers are frequently coblended with the MOFs. In composite-based structures the particles of MOF are cross-linked through polymer chains, where certain recurrent units in the polymer chain perform as ligands of the MOF structure. To form a core−shell-like structure in the biomedical fields, the MOF nanocontainers can be coated with a polymeric film. An ideal coating must (1) improve the MOF function by improving their colloidal stability, degradation hindering, and permitting targeting; (2) not interfere with the incorporated chemicals; (3) be selectively adhered on the external surface, circumventing intrusion inside the porous framework, etc.; (4) be achieved in one phase (or few phases), under mild circumstances; and (5) exhibition appropriate stability under physiological situations [125,137].

The polymeric coating can be usually fabricated through postsynthetic strategies. The coating processes of MOF nanocarriers can be branded into two comprehensive sets of covalent and noncovalent methods. Noncovalent processes are mainly based on hydrogen bonds or electrostatic interactions, while the covalent ones can be classified into "grafting from" or "grafting to" approaches. The "grafting from" techniques encompasses polymerization from active sites on the framework while the "grafting to" includes the reaction of end-functionalized polymers with the groups on the ligands, the coordinatively unsaturated metal sites or functional groups positioned on the MOF [138,139].

12.4.1.3.1 Metal-organic framework−based anticorrosion polymer composite coatings

Currently, protective organic coatings are the most efficient approach to inhibit metallic surfaces from severe corrosion in corrosive environments [140−142]. Unfortunately, the performance of these coating is so vulnerable when facing defects or scratches, allowing the corrosion to take place. The presence of microcracks and cavities due to the solvent evaporation of the polymer coating can decrease the inhibition function of the coating during the time. This inhibition reduction is attributed to the transmission of corrosive moieties into the body of the organic coating, which can be reached to the polymer/interface. A category of new dynamic coatings encompassing inorganic micro- and nanoreservoirs loaded with corrosion inhibitors, polyelectrolytes, organic polymers, etc. have been advanced. Supramolecular chemistry has been employed to produce active self-healing protective coatings using reversible bond recombination [133,143−147]. Furthermore, an efficient active-protective coating should have some properties such as prevention of unwanted leaching earlier than the effective carriage of protective compounds to the addressed points, the stable and on-demand releasement of the functional compounds, and a sustained passive matrix. One of the main reasons for incorporating the inhibitor in inert nanoreservoirs is to prevent the unwanted interactions between the inhibitor molecules and the polar tails of the organic coating, which leads to a reduction in structural integrity [148−150].

Thanks to the fascinating properties of MOFs, which were thoroughly discussed in previous sections, these structures can be utilized as nanocarriers for the protective compound to conferring self-healing property to the polymer coating [109,110,129,151]. Ramezanzadeh et al. have proposed an innovative protective coating with an admirable active anticorrosion and barrier properties. They have prepared ZIF-8 MOF particles via a one-pot synthesis technique on the graphene oxide (GO) layers. The surface characterizations have shown the effective construction of GO@ZIF-8 units with a 79% advance of the specific surface area in comparison with the neat GO. The polarization investigations in the liquid phase have revealed corrosion inhibition efficiency of around 79% for the steel sample dipped in the saline environment containing GO@ZIF-8 particles, which illustrates the active inhibition action of the added modified MOF. Excellent barrier performance and also smart inhibition of the GO@ZIF-8/epoxy coating were also observed. Comparing the GO@ZIF-8/epoxy sample with the neat epoxy one, around 60% and 73% improvements in the wet adhesion strength and the cathodic delamination resistance of the epoxy coating were recorded, respectively [152]. Guo et al. have fabricated ZIF-7@BTA particles were fashioned through a ligand-exchange technique. According to the anticorrosion evaluation of the entire system, prepared ZIF-7@BTA nanoparticles have provided 99.4% inhibition efficiency in the liquid phase under an acidic environment, which was attributed to the rapid and decent release of the BTA molecules on the active sites of the corroding metal. Furthermore, the measurements in the neutral environment proved that a limited amount of BTA molecules were leached out ($<4\%$). The self-healing impact of the nanoparticle dispersion in the epoxy coating was assigned to the pH-sensitive nature of the loaded MOFs [144]. Cao et al. have designed an interesting protective system with passive and active-protective behaviors. The synthesized MOFs were loaded with BTA and coated and wrapped with tetraethyl orthosilicate (TEOS). The addition of TEOS has given a pH-responsive releasement property of the protective compounds and active inhibition abilities since such film would breakdown in alkaline or acidic environments. Furthermore, the modified−coated MOF was integrated with GO and added to the organic coating. GO had a great impermeability and barrier property. The results of EIS analysis confirmed that the incorporated BTA−MOF−TEOS−GO particles into the polymer coatings presented the highest $|Z|$ values up to $8.6 \times 10^8\ \Omega\ cm^2$, showing outstanding and stable protective function [110]. Also, several other studies have been conducted in the last years [38,109,151−158].

12.4.1.3.2 Thermomechanical properties

Chemical cross-linking and physical blending are major employed procedures to modify the architecture−property relations of the polymeric coatings. These approaches have demonstrated to be operative in augmenting the

fracture toughness of the organic coatings by altering their "brittle" mechanical behavior to a "ductile" one. Polymeric coatings are reputed for their outstanding mechanical properties, which are mainly low thermal stability and creep, large modulus, and high strength. Nonetheless, under impact-induced dynamic loadings, their naturally cross-linked structure ends with brittle failure [159–161]. Several approaches have been implemented to modify the toughening of such coatings. Among them, the addition of fillers into the polymeric matrix is the most feasible method. Nevertheless, the major challenge in the production of these coatings is the low compatibility between the inorganic and organic parts, which can lead to nanofillers particle agglomeration and substantial disruption in system function. On account of higher specific surface activity/surface area as well as lower usage percent and smaller dimensions of nanoparticles in comparison with the macro/micro-sized materials, the nanoparticle-containing polymeric coatings have engrossed huge attention thanks to their pronounced impact on the enhancement of the physical, mechanical, thermal, and barrier corrosion prevention characteristics of the polymeric coatings [132,136,159,160,162–164].

The integration of micro/nano-MOFs into polymeric coatings is an interesting and viable technique to enhance the thermomechanical of the coating. MOFs are usually well matched with a matrix of the organic coatings than other nanofillers such as carbon black, alumina, and silica since the organic struts can interact with the polymeric matrix utilizing the molecular design. These structures can also be employed due to their ability for the dissipation of the applied stresses energies. The fabricated MOF–containing organic composites not only merge the polymer toughness with the great thermal stability of MOFs but also effectively compensate for the brittleness and restricted mechanical strength of the polymers. The dimensionality besides the architecture of these compounds is prone to experience elastic transformations under determining directions, which sequentially can influence their physical properties [109,110,129]. The organic ligands of MOFs can efficiently interact with the polymers matrix and mend their thermal–mechanical properties. The linkers of a framework can also reinforce the cross-linking density, enhance the mechanical properties, and lower the dielectric constant of polymeric resins [165,166].

One of the applications of organic coating is to use as neutron shielding substances for spent nuclear fuel casks. Hu et al. have amended the mechanical characteristics of the epoxy coating through the incorporation of the nanosized UiO-66 and UiO-66-NH_2 MOFs using a solution casting process. The outcome disclosed that the UiO-66 addition had a vigorous impact on the toughness of the coating, and this is while the functionalized MOF indicated a higher effect [167]. Roy et al. have studied the incorporation impact of MOF-5 into the epoxy coating on the toughness of the composite. The addition of MOF-5 has stiffened the whole composite significantly so that a 230% growth in fracture energy besides a 68% increment in impact strength

at an optimum loading of 0.3% w/w were was observed [168]. Liu et al. have used ZIF-8 as the curing agent and functional filler in the production of epoxy coating. The presence of the $C_3H_4N_2$ group on the MOF surface triggers the curing epoxy group, causing covalent forces between the polymer matrix and MOF crystals, and a considerable rise in the tensile modulus and a decrease in dielectric constant were detected. Several previous studies have proposed that the incorporation of nanoparticles may induce a reduction in the thermal resistance of the polymeric composite due to augmentation in the free volume fractions. But here it can be realized that the total weight loss of the first degradation procedure reduces with the raise in the loading of ZIF-8 nanoparticles, which can be ascribed to the great thermal resistance of ZIF-8 particles and their covalent bondings to the polymer matrix that hampers the discharge of decomposed low molecular moieties throughout TGA analysis. Moreover, the dynamic mechanical analysis (DMA) revealed that the polymer pigmentation did not alter the thermal properties of the composite. At the same time, the coating must have an analogous cross-linked arrangement with neat epoxy cured by 2-methyl-1*H*-imidazole. Consequently, the substantial surge in E' and constant T_g prove the efficiency of the added MOF as an enhancing and curing agent [165]. Some MOFs such as ZIF-8 can be highly dissolute in an uncontrolled way in the aqueous environments during the time, resulting in the free volumes and defects within the polymeric matrix. These occurrences can consequently weaken the thermomechanical properties of the coating in the long term. MOF modification can solve such problems. Motamedi et al. have synthesized MOF-based nanopigment for the assembly of an effective epoxy coating with superb anticorrosion and thermomechanical features. The nanoscale cerium(III)-imidazole network was constructed through a one-pot coprecipitation process. The structural characterizations have proved the thermal stability of the MOF structure. The results of function evaluations of the nanocomposite indicated the self-healing properties besides the barrier behavior of the polymer coating. Furthermore, the considerable increment in the cross-linking density (more than four times), toughness, and ductility (four times) of the polymeric composite was established, which were attributed to the plausible chemical interactions between the functional groups of the synthesized MOF and the epoxy matrix [154].

The intense chemical interaction between the functional groups of the framework and the polymer matrix (for instance epoxide) results in the ring openings of the functional group of the epoxide by the MOF in preference to those by the hardener as a common reaction of the dual epoxy hardener. Consequently, the focused stresses can be conveyed from the polymer matrix to the MOF. From these actions the construction of the linear flexible cross-linked lattice at the MOF/polymer interface can be figured out. In addition, this brings about a reduction in the brittleness performance by a huge improvement in the toughness characteristics of the polymer structure along

with the resistance in front of crack propagation. Hence, strengthening in the mechanical performance altered the coating ductility through a decent affinity between the coating matrix and MOF.

12.5 Conclusion

In this chapter, different aspects of MOFs have been reviewed. MOFs have high crystallinity and porosity as they have over 6200 $m^2 g^{-1}$ internal surfaces and up to 90% free volume, which can host other molecules. These superstructures can be constructed through several approaches such as hydro(solvo)thermal method, MW-assisted and ultrasonic methods, solvent evaporation and isothermal synthesis, EC synthesis, diffusion method, and mechanochemical synthesis, each of which has their advantages and disadvantages. This makes MOFs versatile in lots of applications. Due to the unique characteristics of MOFs, these materials can be employed in various applications such as proton conduction, nonlinear optics, catalysis, adsorption, sensing, drug delivery, colorimetric sensors, luminescence, magnetism, structural flexibility driven properties, and other applications. Generally, MOFs are fabricated by the coordination of inorganic centers (metal nodes) with polydentate organic ligands, which constructs low-density and highly ordered lattice. The MOF stability indicates the structural resistance to deterioration when the framework is in the exposure to the operational circumstances. Metal-organic structures must have several types of stabilities. Both thermal and chemical stabilities are vital for the catalytic procedures carried out under rough circumstances such as applications in fuel production and chemical feedstock. The mechanical and hydrolytic stabilities have also been studied. Nevertheless, MOFs have shown excellent potential to be used in the field of corrosion protection. These compounds can be used as corrosion inhibitors, thin films, or nanocontainers of the protective compounds in the polymeric nanocomposites. The employment of these structures as corrosion inhibitors is fascinating due to their supramolecular inherent and abundance of the heteroaromatic and π-systems species. The application of MOFs as thin films has been surveyed in recent years due to the presence of accessible metal sites, huge capacity for guests, easy functionalization, and long-lasting pores. In the composite-based structures the particles of MOF are cross-linked through polymer chains, where certain recurrent units in the polymer chain perform as ligands of the MOF structure. As a future remark, using MOFs in combination with the other types of nanomaterials, that is, GO, or its application for the modification of the nanomaterials would be promising strategies for development of the high-performance polymer composites with outstanding anticorrosion and thermal−mechanical properties.

References

[1] Lu K, Aung T, Guo N, Weichselbaum R, Lin W. Nanoscale metal–organic frameworks for therapeutic, imaging, and sensing applications. Adv Mater 2018;30(37):1707634.

[2] Long JR, Yaghi OM. The pervasive chemistry of metal–organic frameworks. Chem Soc Rev 2009;38(5):1213–14.

[3] Eddaoudi M, Moler DB, Li H, Chen B, Reineke TM, O'Keeffe M, et al. Modular chemistry: secondary building units as a basis for the design of highly porous and robust metal–organic carboxylate frameworks. Acc Chem Res 2001;34(4):319–30.

[4] Tranchemontagne DJ, Mendoza-Cortés JL, O'Keeffe M, Yaghi OM. Secondary building units, nets and bonding in the chemistry of metal–organic frameworks. Chem Soc Rev 2009;38(5):1257–83.

[5] Zhao P, Fang H, Mukhopadhyay S, Li A, Rudić S, McPherson IJ, et al. Structural dynamics of a metal–organic framework induced by CO_2 migration in its non-uniform porous structure. Nat Commun 2019;10(1):1–8.

[6] Stock N, Biswas S. Synthesis of metal-organic frameworks (MOFs): routes to various MOF topologies, morphologies, and composites. Chem Rev 2012;112(2):933–69.

[7] Haque E, Khan NA, Park JH, Jhung SH. Synthesis of a metal–organic framework material, iron terephthalate, by ultrasound, microwave, and conventional electric heating: a kinetic study. Chem Eur J 2010;16(3):1046–52.

[8] Liu W, Ye L, Liu X, Yuan L, Lu X, Jiang J. Rapid synthesis of a novel cadmium imidazole-4,5-dicarboxylate metal–organic framework under microwave-assisted solvothermal condition. Inorg Chem Commun 2008;11(10):1250–2.

[9] Ameloot R, Stappers L, Fransaer J, Alaerts L, Sels BF, De Vos DE. Patterned growth of metal-organic framework coatings by electrochemical synthesis. Chem Mater 2009;21(13):2580–2.

[10] Wei Y, Han S, Walker DA, Fuller PE, Grzybowski BA. Nanoparticle core/shell architectures within MOF crystals synthesized by reaction diffusion. Angew Chem Int Ed 2012;51(30):7435–9.

[11] Lv D, Chen Y, Li Y, Shi R, Wu H, Sun X, et al. Efficient mechanochemical synthesis of MOF-5 for linear alkanes adsorption. J Chem Eng Data 2017;62(7):2030–6.

[12] Müller M, Hermes S, Kä hler K, van den Berg MW, Muhler M, Fischer RA. Loading of MOF-5 with Cu and ZnO nanoparticles by gas-phase infiltration with organometallic precursors: properties of Cu/ZnO@MOF-5 as catalyst for methanol synthesis. Chem Mater 2008;20(14):4576–87.

[13] Song Q, Nataraj S, Roussenova MV, Tan JC, Hughes DJ, Li W, et al. Zeolitic imidazolate framework (ZIF-8) based polymer nanocomposite membranes for gas separation. Energy Environ Sci 2012;5(8):8359–69.

[14] Frameworks M-O. Applications from catalysis to gas storage. Weinheim: Wiley-VCH Verlag GmbH & Co KGaA; 2011.

[15] Xiao J, Chen S, Yi J, Zhang HF, Ameer GA. A cooperative copper metal–organic framework-hydrogel system improves wound healing in diabetes. Adv Funct Mater 2017;27(1):1604872.

[16] Dong K, Wang Z, Zhang Y, Ren J, Qu X. Metal–organic framework-based nanoplatform for intracellular environment-responsive endo/lysosomal escape and enhanced cancer therapy. ACS Appl Mater Interfaces 2018;10(38):31998–2005.

[17] Zhang H, Li Q, Liu R, Zhang X, Li Z, Luan Y. A versatile prodrug strategy to in situ encapsulate drugs in MOF nanocarriers: a case of cytarabine-IR820 prodrug encapsulated ZIF-8 toward chemo-photothermal therapy. Adv Funct Mater 2018;28(35):1802830.

[18] Lin S, Liu X, Tan L, Cui Z, Yang X, Yeung KW, et al. Porous iron-carboxylate metal–organic framework: a novel bioplatform with sustained antibacterial efficacy and nontoxicity. ACS Appl Mater Interfaces 2017;9(22):19248–57.
[19] Wu MX, Yang YW. Metal–organic framework (MOF)-based drug/cargo delivery and cancer therapy. Adv Mater 2017;29(23):1606134.
[20] Li J-R, Kuppler RJ, Zhou H-C. Selective gas adsorption and separation in metal–organic frameworks. Chem Soc Rev 2009;38(5):1477–504.
[21] Czaja AU, Trukhan N, Müller U. Industrial applications of metal–organic frameworks. Chem Soc Rev 2009;38(5):1284–93.
[22] Lee J, Farha OK, Roberts J, Scheidt KA, Nguyen ST, Hupp JT. Metal–organic framework materials as catalysts. Chem Soc Rev 2009;38(5):1450–9.
[23] Jhung SH, Khan NA, Hasan Z. Analogous porous metal–organic frameworks: synthesis, stability and application in adsorption. CrystEngComm 2012;14(21):7099–109.
[24] O'Keeffe M. Design of MOFs and intellectual content in reticular chemistry: a personal view. Chem Soc Rev 2009;38(5):1215–17.
[25] Eddaoudi M, Kim J, Rosi N, Vodak D, Wachter J, O'Keeffe M, et al. Systematic design of pore size and functionality in isoreticular MOFs and their application in methane storage. Science 2002;295(5554):469–72.
[26] Qi X-L, Liu S-Y, Lin R-B, Liao P-Q, Ye J-W, Lai Z, et al. Phosphorescence doping in a flexible ultramicroporous framework for high and tunable oxygen sensing efficiency. Chem Commun 2013;49(61):6864–6.
[27] Xie Y, Yu Z, Huang X, Wang Z, Niu L, Teng M, et al. Rational design of MOFs constructed from modified aromatic amino acids. Chem Eur J 2007;13(33):9399–405.
[28] Sun C-Y, Wang X-L, Qin C, Jin J-L, Su Z-M, Huang P, et al. Solvatochromic behavior of chiral mesoporous metal–organic frameworks and their applications for sensing small molecules and separating cationic dyes. Chem Eur J 2013;19(11):3639–45.
[29] Chen Y, Hoang T, Ma S. Biomimetic catalysis of a porous iron-based metal–metalloporphyrin framework. Inorg Chem 2012;51(23):12600–2.
[30] Lin Z-J, Lü J, Hong M, Cao R. Metal–organic frameworks based on flexible ligands (FL-MOFs): structures and applications. Chem Soc Rev 2014;43(16):5867–95.
[31] Du M, Zhang ZH, Tang LF, Wang XG, Zhao XJ, Batten SR. Molecular tectonics of metal–organic frameworks (MOFs): a rational design strategy for unusual mixed-connected network topologies. Chem Eur J 2007;13(9):2578–86.
[32] Qu C, Jiao Y, Zhao B, Chen D, Zou R, Walton KS, et al. Nickel-based pillared MOFs for high-performance supercapacitors: design, synthesis and stability study. Nano Energy 2016;26:66–73.
[33] O'Keeffe M, Peskov MA, Ramsden SJ, Yaghi OM. The Reticular Chemistry Structure Resource (RCSR) database of, and symbols for, crystal nets. Acc Chem Res 2008;41(12):1782–9.
[34] (a) Blatov V. Multipurpose crystallochemical analysis with the program package TOPOS. IUCr CompComm Newsletter 2006;7:4.
(b) Blatov VA, Shevchenko AP, Serezhkin VN. TOPOS3. 2: a new version of the program package for multipurpose crystal-chemical analysis. J Appl Crystallogr 2000;33:1193.
[35] Haldar R, Maji TK. Metal–organic frameworks (MOFs) based on mixed linker systems: structural diversities towards functional materials. CrystEngComm 2013;15(45):9276–95.
[36] Uemura K, Matsuda R, Kitagawa S. Flexible microporous coordination polymers. J Solid State Chem 2005;178(8):2420–9.

[37] Bhattacharjee S, Choi J-S, Yang S-T, Choi SB, Kim J, Ahn W-S. Solvothermal synthesis of Fe-MOF-74 and its catalytic properties in phenol hydroxylation. J Nanosci Nanotechnol 2010;10(1):135–41.
[38] Jouyandeh M, Tikhani F, Shabanian M, Movahedi F, Moghari S, Akbari V, et al. Synthesis, characterization, and high potential of 3D metal–organic framework (MOF) nanoparticles for curing with epoxy. J Alloy Compd 2020;829:154547.
[39] Luebke R, Belmabkhout Y, Weseliński ŁJ, Cairns AJ, Alkordi M, Norton G, et al. Versatile rare earth hexanuclear clusters for the design and synthesis of highly-connected ftw-MOFs. Chem Sci 2015;6(7):4095–102.
[40] Yoo Y, Lai Z, Jeong H-K. Fabrication of MOF-5 membranes using microwave-induced rapid seeding and solvothermal secondary growth. Microporous Mesoporous Mater 2009;123(1–3):100–6.
[41] Marthala VR, Hunger M, Kettner F, Krautscheid H, Chmelik C, Kaŕger J, et al. Solvothermal synthesis and characterization of large-crystal all-silica, aluminum-, and boron-containing ferrierite zeolites. Chem Mater 2011;23(10):2521–8.
[42] Choi J-S, Son W-J, Kim J, Ahn W-S. Metal–organic framework MOF-5 prepared by microwave heating: factors to be considered. Microporous Mesoporous Mater 2008;116 (1–3):727–31.
[43] Cho H-Y, Yang D-A, Kim J, Jeong S-Y, Ahn W-S. CO_2 adsorption and catalytic application of Co-MOF-74 synthesized by microwave heating. Catal Today 2012;185(1):35–40.
[44] Choi JY, Kim J, Jhung S-H, Kim H, Chang J, Chae HK. Microwave synthesis of a porous metal-organic framework, zinc terephthalate MOF-5. Bull Korean Chem Soc 2006;27 (10):1523.
[45] Son W-J, Kim J, Kim J, Ahn W-S. Sonochemical synthesis of MOF-5. Chem Commun 2008;47:6336–8.
[46] Yang D-A, Cho H-Y, Kim J, Yang S-T, Ahn W-S. CO_2 capture and conversion using Mg-MOF-74 prepared by a sonochemical method. Energy Environ Sci 2012;5 (4):6465–73.
[47] Jung D-W, Yang D-A, Kim J, Kim J, Ahn W-S. Facile synthesis of MOF-177 by a sonochemical method using 1-methyl-2-pyrrolidinone as a solvent. Dalton Trans 2010;39 (11):2883–7.
[48] Kim J, Yang S-T, Choi SB, Sim J, Kim J, Ahn W-S. Control of catenation in CuTATB-n metal–organic frameworks by sonochemical synthesis and its effect on CO_2 adsorption. J Mater Chem 2011;21(9):3070–6.
[49] Tanhaei M, Mahjoub AR, Safarifard V. Sonochemical synthesis of amide-functionalized metal-organic framework/graphene oxide nanocomposite for the adsorption of methylene blue from aqueous solution. Ultrason Sonochem 2018;41:189–95.
[50] Van Assche TR, Desmet G, Ameloot R, De Vos DE, Terryn H, Denayer JF. Electrochemical synthesis of thin HKUST-1 layers on copper mesh. Microporous Mesoporous Mater 2012;158:209–13.
[51] Campagnol N, Souza ER, De Vos DE, Binnemans K, Fransaer J. Luminescent terbium-containing metal–organic framework films: new approaches for the electrochemical synthesis and application as detectors for explosives. Chem Commun 2014;50(83):12545–7.
[52] Campagnol N, Van Assche T, Boudewijns T, Denayer J, Binnemans K, De Vos D, et al. High pressure, high temperature electrochemical synthesis of metal–organic frameworks: films of MIL-100 (Fe) and HKUST-1 in different morphologies. J Mater Chem A 2013;1 (19):5827–30.

[53] Yang H-M, Xian L, Song X-L, Yang T-L, Liang Z-H, Fan C-M. In situ electrochemical synthesis of MOF-5 and its application in improving photocatalytic activity of BiOBr. Trans Nonferrous Met Soc China 2015;25(12):3987–94.

[54] Yang H, Song X, Yang T, Liang Z, Fan C, Hao X. Electrochemical synthesis of flower shaped morphology MOFs in an ionic liquid system and their electrocatalytic application to the hydrogen evolution reaction. RSC Adv 2014;4(30):15720–6.

[55] Martinez Joaristi A, Juan-Alcañiz J, Serra-Crespo P, Kapteijn F, Gascon J. Electrochemical synthesis of some archetypical Zn^{2+}, Cu^{2+}, and Al^{3+} metal organic frameworks. Cryst Growth Des 2012;12(7):3489–98.

[56] Yao J, Dong D, Li D, He L, Xu G, Wang H. Contra-diffusion synthesis of ZIF-8 films on a polymer substrate. Chem Commun 2011;47(9):2559–61.

[57] Zhao Z, Li Z, Lin Y. Adsorption and diffusion of carbon dioxide on metal–organic framework (MOF-5). Ind Eng Chem Res 2009;48(22):10015–20.

[58] Xiao J-D, Qiu L-G, Ke F, Yuan Y-P, Xu G-S, Wang Y-M, et al. Rapid synthesis of nanoscale terbium-based metal–organic frameworks by a combined ultrasound-vapour phase diffusion method for highly selective sensing of picric acid. J Mater Chem A 2013;1(31):8745–52.

[59] Chen Y, Yang C, Wang X, Yang J, Ouyang K, Li J. Kinetically controlled ammonia vapor diffusion synthesis of a Zn(ii) MOF and its H_2O/NH_3 adsorption properties. J Mater Chem A 2016;4(26):10345–51.

[60] Yan D, Gao R, Wei M, Li S, Lu J, Evans DG, et al. Mechanochemical synthesis of a fluorenone-based metal organic framework with polarized fluorescence: an experimental and computational study. J Mater Chem C 2013;1(5):997–1004.

[61] Pilloni M, Padella F, Ennas G, Lai S, Bellusci M, Rombi E, et al. Liquid-assisted mechanochemical synthesis of an iron carboxylate metal organic framework and its evaluation in diesel fuel desulfurization. Microporous Mesoporous Mater 2015;213:14–21.

[62] Braga D, Maini L, Mazzeo PP, Ventura B. Reversible interconversion between luminescent isomeric metal–organic frameworks of [Cu4I4(DABCO)2] (DABCO = 1,4-diazabicyclo[2.2.2]octane). Chem Eur J 2010;16(5):1553–9.

[63] Chen Y, Wu H, Liu Z, Sun X, Xia Q, Li Z. Liquid-assisted mechanochemical synthesis of copper based MOF-505 for the separation of CO_2 over CH_4 or N_2. Ind Eng Chem Res 2018;57(2):703–9.

[64] Yuan W, Garay AL, Pichon A, Clowes R, Wood CD, Cooper AI, et al. Study of the mechanochemical formation and resulting properties of an archetypal MOF: Cu3(BTC)2 (BTC = 1,3,5-benzenetricarboxylate). CrystEngComm 2010;12(12):4063–5.

[65] Bruinsma PJ, Kim AY, Liu J, Baskaran S. Mesoporous silica synthesized by solvent evaporation: spun fibers and spray-dried hollow spheres. Chem Mater 1997;9(11):2507–12.

[66] Sau TK, Murphy CJ. Self-assembly patterns formed upon solvent evaporation of aqueous cetyltrimethylammonium bromide-coated gold nanoparticles of various shapes. Langmuir 2005;21(7):2923–9.

[67] Yang SJ, Kim T, Lee K, Kim YS, Yoon J, Park CR. Solvent evaporation mediated preparation of hierarchically porous metal organic framework-derived carbon with controllable and accessible large-scale porosity. Carbon 2014;71:294–302.

[68] Parnham ER, Morris RE. Ionothermal synthesis of zeolites, metal–organic frameworks, and inorganic–organic hybrids. Acc Chem Res 2007;40(10):1005–13.

[69] Bojdys MJ, Müller JO, Antonietti M, Thomas A. Ionothermal synthesis of crystalline, condensed, graphitic carbon nitride. Chem Eur J 2008;14(27):8177–82.

[70] Kuhn P, Antonietti M, Thomas A. Porous, covalent triazine-based frameworks prepared by ionothermal synthesis. Angew Chem Int Ed 2008;47(18):3450–3.
[71] Lin Z, Slawin AM, Morris RE. Chiral induction in the ionothermal synthesis of a 3-D coordination polymer. J Am Chem Soc 2007;129(16):4880–1.
[72] Zhang G, Lin L, Li G, Zhang Y, Savateev A, Zafeiratos S, et al. Ionothermal synthesis of triazine–heptazine-based copolymers with apparent quantum yields of 60% at 420 nm for solar hydrogen production from "sea water". Angew Chem Int Ed 2018;57(30):9372–6.
[73] Parnham ER, Morris RE. The ionothermal synthesis of cobalt aluminophosphate zeolite frameworks. J Am Chem Soc 2006;128(7):2204–5.
[74] Tan Y-X, He Y-P, Zhang J. Tuning MOF stability and porosity via adding rigid pillars. Inorg Chem 2012;51(18):9649–54.
[75] Saha D, Deng S. Ammonia adsorption and its effects on framework stability of MOF-5 and MOF-177. J Colloid Interface Sci 2010;348(2):615–20.
[76] Han S, Huang Y, Watanabe T, Nair S, Walton KS, Sholl DS, et al. MOF stability and gas adsorption as a function of exposure to water, humid air, SO_2, and NO_2. Microporous Mesoporous Mater 2013;173:86–91.
[77] Decoste JB, Peterson GW, Smith MW, Stone CA, Willis CR. Enhanced stability of Cu-BTC MOF via perfluorohexane plasma-enhanced chemical vapor deposition. J Am Chem Soc 2012;134(3):1486–9.
[78] Kleist W, Maciejewski M, Baiker A. MOF-5 based mixed-linker metal–organic frameworks: synthesis, thermal stability and catalytic application. Thermochim Acta 2010;499(1–2):71–8.
[79] Yang J, Grzech A, Mulder FM, Dingemans TJ. Methyl modified MOF-5: a water stable hydrogen storage material. Chem Commun 2011;47(18):5244–6.
[80] Nguyen HGT, Schweitzer NM, Chang C-Y, Drake TL, So MC, Stair PC, et al. Vanadium-node-functionalized UiO-66: a thermally stable MOF-supported catalyst for the gas-phase oxidative dehydrogenation of cyclohexene. ACS Catal 2014;4(8):2496–500.
[81] Perles J, Snejko N, Iglesias M, Monge MÁ. 3D scandium and yttrium arenedisulfonate MOF materials as highly thermally stable bifunctional heterogeneous catalysts. J Mater Chem 2009;19(36):6504–11.
[82] Han Y-H, Tian C-B, Li Q-H, Du S-W. Highly chemical and thermally stable luminescent EuxTb1 − x MOF materials for broad-range pH and temperature sensors. J Mater Chem C 2014;2(38):8065–70.
[83] Zeng Y, Fu Z, Chen H, Liu C, Liao S, Dai J. Photo- and thermally induced coloration of a crystalline MOF accompanying electron transfer and long-lived charge separation in a stable host–guest system. Chem Commun 2012;48(65):8114–16.
[84] Calleja G, Botas J, Sánchez-Sánchez M, Orcajo M. Hydrogen adsorption over zeolite-like MOF materials modified by ion exchange. Int J Hydrogen Energ 2010;35(18):9916–23.
[85] Nadar SS, Rathod VK. Facile synthesis of glucoamylase embedded metal-organic frameworks (glucoamylase-MOF) with enhanced stability. Int J Biol Macromol 2017;95:511–19.
[86] Perez EV, Balkus Jr KJ, Ferraris JP, Musselman IH. Mixed-matrix membranes containing MOF-5 for gas separations. J Membr Sci 2009;328(1–2):165–73.
[87] Wu H, Yildirim T, Zhou W. Exceptional mechanical stability of highly porous zirconium metal–organic framework UiO-66 and its important implications. J Phys Chem Lett 2013;4(6):925–30.
[88] O'Neill LD, Zhang H, Bradshaw D. Macro-/microporous MOF composite beads. J Mater Chem 2010;20(27):5720–6.

[89] Van de Voorde B, Stassen I, Bueken B, Vermoortele F, De Vos D, Ameloot R, et al. Improving the mechanical stability of zirconium-based metal−organic frameworks by incorporation of acidic modulators. J Mater Chem A 2015;3(4):1737−42.
[90] Hönicke IM, Senkovska I, Bon V, Baburin IA, Bönisch N, Raschke S, et al. Balancing mechanical stability and ultrahigh porosity in crystalline framework materials. Angew Chem Int Ed 2018;57(42):13780−3.
[91] Vanstreels K, Wu C, Baklanov M. Mechanical stability of porous low-k dielectrics. ECS J Solid State Sci Technol 2014;4(1):N3058.
[92] Casco ME, Fernández-Catalá J, Martinez-Escandell M, Rodríguez-Reinoso F, Ramos-Fernández EV, Silvestre-Albero J. Improved mechanical stability of HKUST-1 in confined nanospace. Chem Commun 2015;51(75):14191−4.
[93] Basu S, Cano-Odena A, Vankelecom IF. MOF-containing mixed-matrix membranes for CO_2/CH_4 and CO_2/N_2 binary gas mixture separations. Sep Purif Technol 2011;81(1):31−40.
[94] Zhai F, Zheng Q, Chen Z, Ling Y, Liu X, Weng L, et al. Crystal transformation synthesis of a highly stable phosphonate MOF for selective adsorption of CO_2. CrystEngComm 2013;15(11):2040−3.
[95] Aguilera-Sigalat J, Bradshaw D. A colloidal water-stable MOF as a broad-range fluorescent pH sensor via post-synthetic modification. Chem Commun 2014;50(36):4711−13.
[96] Howarth AJ, Liu Y, Li P, Li Z, Wang TC, Hupp JT, et al. Chemical, thermal and mechanical stabilities of metal−organic frameworks. Nat Rev Mater 2016;1(3):1−15.
[97] Abtab SMT, Alezi D, Bhatt PM, Shkurenko A, Belmabkhout Y, Aggarwal H, et al. Reticular chemistry in action: a hydrolytically stable MOF capturing twice its weight in adsorbed water. Chemistry 2018;4(1):94−105.
[98] Sabo M, Henschel A, Fröde H, Klemm E, Kaskel S. Solution infiltration of palladium into MOF-5: synthesis, physisorption and catalytic properties. J Mater Chem 2007;17(36):3827−32.
[99] Karmakar A, Desai AV, Ghosh SK. Ionic metal-organic frameworks (iMOFs): design principles and applications. Coord Chem Rev 2016;307:313−41.
[100] Li T, Chen D-L, Sullivan JE, Kozlowski MT, Johnson JK, Rosi NL. Systematic modulation and enhancement of CO_2:N_2 selectivity and water stability in an isoreticular series of bio-MOF-11 analogues. Chem Sci 2013;4(4):1746−55.
[101] Zuluaga S, Fuentes-Fernandez EM, Tan K, Xu F, Li J, Chabal YJ, et al. Understanding and controlling water stability of MOF-74. J Mater Chem A 2016;4(14):5176−83.
[102] Jiao Y, Morelock CR, Burtch NC, Mounfield III WP, Hungerford JT, Walton KS. Tuning the kinetic water stability and adsorption interactions of Mg-MOF-74 by partial substitution with Co or Ni. Ind Eng Chem Res 2015;54(49):12408−14.
[103] Fröhlich D, Henninger SK, Janiak C. Multicycle water vapour stability of microporous breathing MOF aluminium isophthalate CAU-10-H. Dalton Trans 2014;43(41):15300−4.
[104] Jasuja H, Walton KS. Effect of catenation and basicity of pillared ligands on the water stability of MOFs. Dalton Trans 2013;42(43):15421−6.
[105] DeCoste JB, Peterson GW, Schindler BJ, Killops KL, Browe MA, Mahle JJ. The effect of water adsorption on the structure of the carboxylate containing metal−organic frameworks Cu-BTC, Mg-MOF-74, and UiO-66. J Mater Chem A 2013;1(38):11922−32.
[106] Akbarzadeh S, Ramezanzadeh M, Bahlakeh G, Ramezanzadeh B. A detailed investigation of the chloride-induced corrosion of mild steel in the presence of combined green organic molecules of primrose flower and zinc cations. J Mol Liq 2020;297:111862.

[107] Tabatabaeimajd M, Ramezanzadeh M, Bahlakeh G, Ramezanzadeh B. Probing molecular adsorption/interactions and anti-corrosion performance of poppy extract in acidic environments. J Mol Liq 2020;304:112750.
[108] Tabatabaeimajd M, Naderi R, Ramezanzadeh B. Promotion of the active/barrier protection function of epoxy ester coating/steel system utilizing differently synthesized hybrid pigment through zinc acetylacetonate tailored with green inhibitor molecules. Prog Org Coat 2020;138:105380.
[109] Cao K, Yu Z, Yin D. Preparation of Ce-MOF@TEOS to enhance the anti-corrosion properties of epoxy coatings. Prog Org Coat 2019;135:613–21.
[110] Cao K, Yu Z, Yin D, Chen L, Jiang Y, Zhu L. Fabrication of BTA-MOF-TEOS-GO nanocomposite to endow coating systems with active inhibition and durable anticorrosion performances. Prog Org Coat 2020;143:105629.
[111] Etaiw SEH, Fouda AS, El-bendary M, et al. Cluster type molecule as novel corrosion inhibitor for steel in HCl solution. Prot Met Phys Chem Surf 2013;49(1):113–23.
[112] Tabatabaeimajd M, Akbarzadeh S, Ramezanzadeh M, Bahlakeh G, Ramezanzadeh B. A detailed investigation of the chloride-induced corrosion of mild steel in the presence of combined green organic molecules of primrose flower and zinc cations. J Mol Liq 2019;297:111862.
[113] Tabatabaeimajd M, Davoudi M, Ramezanzadeh M, Ghasemi E, Ramezanzadeh B, Mahdavian M. Construction of a smart active/barrier anti-corrosion system based on epoxy-ester/zinc intercalated kaolin nanocontainer for steel substrate. Constr Build Mater 2020;247:118555.
[114] Tabatabaeimajd M, Ramezanzadeh M, Bahlakeh G, Ramezanzadeh B. Steel corrosion lowering in front of the saline solution by a nitrogen-rich source of green inhibitors: detailed surface, electrochemical and computational studies. Constr Build Mater 2020;254:119266.
[115] Mesbah A, Juers C, Lacouture F, Mathieu S, Rocca E, François M, et al. Inhibitors for magnesium corrosion: metal organic frameworks. Solid State Sci 2007;9(3–4):322–8.
[116] Fouda AS, Etaiw SEH, El-bendary MM, Maher MM. Metal-organic frameworks based on silver(I) and nitrogen donors as new corrosion inhibitors for copper in HCl solution. J Mol Liq 2016;213:228–34.
[117] Zafari S, Shahrak MN, Ghahramaninezhad M. New MOF-based corrosion inhibitor for carbon steel in acidic media. Met Mater Int 2020;26(1):25–38.
[118] Etaiw SEH, Fouda AS, Amer SA, El-bendary MM. Structure, characterization and anti-corrosion activity of the new metal–organic framework [Ag(qox)(4-ab)]. J Inorg Organomet Polym Mater 2011;21(2):327–35.
[119] Etaiw SEH, Fouda AS, Abdou SN, El-bendary MM. Structure, characterization and inhibition activity of new metal–organic framework. Corros Sci 2011;53(11):3657–65.
[120] Etaiw SEH, El-bendary MM, Fouda AS, Maher MM. A new metal-organic framework based on cadmium thiocyanate and 6-methylequinoline as corrosion inhibitor for copper in 1 M HCl solution. Prot Met Phys Chem Surf 2017;53(5):937–49.
[121] Li W, Ren B, Chen Y, Wang X, Cao R. Excellent efficacy of MOF films for bronze artwork conservation: the key role of HKUST-1 film nanocontainers in selectively positioning and protecting inhibitors. ACS Appl Mater Interfaces 2018;10(43):37529–34.
[122] Tian H, Li W, Liu A, Gao X, Han P, Ding R, et al. Controlled delivery of multi-substituted triazole by metal-organic framework for efficient inhibition of mild steel corrosion in neutral chloride solution. Corros Sci 2018;131:1–16.

[123] Shekhah O, Fu L, Sougrat R, Belmabkhout Y, Cairns AJ, Giannelis EP, et al. Successful implementation of the stepwise layer-by-layer growth of MOF thin films on confined surfaces: mesoporous silica foam as a first case study. Chem Commun 2012;48 (93):11434–6.

[124] Shekhah O, Hirai K, Wang H, Uehara H, Kondo M, Diring S, et al. MOF-on-MOF heteroepitaxy: perfectly oriented [Zn2(ndc)2(dabco)]n grown on [Cu2(ndc)2(dabco)]n thin films. Dalton Trans 2011;40(18):4954–8.

[125] Campbell J, Davies R, Braddock DC, Livingston A. Improving the permeance of hybrid polymer/metal–organic framework (MOF) membranes for organic solvent nanofiltration (OSN)–development of MOF thin films via interfacial synthesis. J Mater Chem A 2015;3(18):9668–74.

[126] Liu J, Zhou W, Liu J, Howard I, Kilibarda G, Schlabach S, et al. Photoinduced charge-carrier generation in epitaxial MOF thin films: high efficiency as a result of an indirect electronic band gap? Angew Chem Int Ed 2015;54(25):7441–5.

[127] Shekhah O, Liu J, Fischer R, Wöll C. MOF thin films: existing and future applications. Chem Soc Rev 2011;40(2):1081–106.

[128] Zhang M, Ma L, Wang L, Sun Y, Liu Y. Insights into the use of metal–organic framework as high-performance anticorrosion coatings. ACS Appl Mater Interfaces 2018;10 (3):2259–63.

[129] Liu W, Yan Z, Ma X, Geng T, Wu H, Li Z. Mg-MOF-74/MgF2 composite coating for improving the properties of magnesium alloy implants: hydrophilicity and corrosion resistance. Materials 2018;11(3):396.

[130] Wu C, Liu Q, Chen R, Liu J, Zhang H, Li R, et al. Fabrication of ZIF-8@SiO_2 micro/nano hierarchical superhydrophobic surface on AZ31 magnesium alloy with impressive corrosion resistance and abrasion resistance. ACS Appl Mater Interfaces 2017;9 (12):11106–15.

[131] Mesbah A, Jacques S, Rocca E, François M, Steinmetz J. Compact metal–organic frameworks for anti-corrosion applications: new binary linear saturated carboxylates of zinc. Eur J Inorg Chem 2011;2011(8):1315–21.

[132] Lin Y-T, Don T-M, Wong C-J, Meng F-C, Lin Y-J, Lee S-Y, et al. Improvement of mechanical properties and anticorrosion performance of epoxy coatings by the introduction of polyaniline/graphene composite. Surf Coat Technol 2019;374:1128–38.

[133] Cui L-Y, Gao S-D, Li P-P, Zeng R-C, Zhang F, Li S-Q, et al. Corrosion resistance of a self-healing micro-arc oxidation/polymethyltrimethoxysilane composite coating on magnesium alloy AZ31. Corros Sci 2017;118:84–95.

[134] Ahmed NM, Abd El-Gawad WM, Souaya ER. Study on the corrosion protection performance of new ferrite/kaolin core-shell pigments in epoxy-based paints. Anti-Corros Methods Mater 2016;63(1):36–46.

[135] Ahmed NM. Comparative study on the role of kaolin, calcined kaolin and chemically treated kaolin in alkyd-based paints for protection of steel. Pigm Resin Technol 2013;42 (1):3–14.

[136] Ahmed NM, Selim MM. Modified properties of Egyptian kaolin-phosphate core-shell pigments in solvent-based paints for protection of cold-rolled steel surfaces. Pigm Resin Technol 2010;39(1):15–26.

[137] Robson R. Design and its limitations in the construction of bi-and poly-nuclear coordination complexes and coordination polymers (aka MOFs): a personal view. Dalton Trans 2008;38:5113–31.

[138] Xie K, Fu Q, He Y, Kim J, Goh SJ, Nam E, et al. Synthesis of well dispersed polymer grafted metal−organic framework nanoparticles. Chem Commun 2015;51(85):15566−9.
[139] McDonald KA, Feldblyum JI, Koh K, Wong-Foy AG, Matzger AJ. Polymer@MOF@MOF: "grafting from" atom transfer radical polymerization for the synthesis of hybrid porous solids. Chem Commun 2015;51(60):11994−6.
[140] Živković LS, Bajat JB, Popić JP, Jegdić BV, Stevanović S, Mišković-Stanković VB. Protective properties of cataphoretic epoxy coating on aluminium alloy AA6060 modified with electrodeposited Ce-based coatings: effect of post-treatment. Prog Org Coat 2015;79:43−52.
[141] Jamali SS, Mills DJ. Steel surface preparation prior to painting and its impact on protective performance of organic coating. Prog Org Coat 2014;77(12, Part B):2091−9.
[142] Snihirova D, Lamaka SV, Montemor MF. "SMART" protective ability of water based epoxy coatings loaded with $CaCO_3$ microbeads impregnated with corrosion inhibitors applied on AA2024 substrates. Electrochim Acta 2012;83:439−47.
[143] Montemor MF, Snihirova DV, Taryba MG, Lamaka SV, Kartsonakis IA, Balaskas AC, et al. Evaluation of self-healing ability in protective coatings modified with combinations of layered double hydroxides and cerium molybdate nanocontainers filled with corrosion inhibitors. Electrochim Acta 2012;60:31−40.
[144] Guo Y, Wang J, Zhang D, Qi T, Li GL. pH-responsive self-healing anticorrosion coatings based on benzotriazole-containing zeolitic imidazole framework. Colloids Surf A Physicochem Eng Asp 2019;561:1−8.
[145] Yarmohammadi M, Shahidzadeh M, Ramezanzadeh B. Designing an elastomeric polyurethane coating with enhanced mechanical and self-healing properties: the influence of disulfide chain extender. Prog Org Coat 2018;121:45−52.
[146] Song J, Cui X, Liu Z, Jin G, Liu E, Zhang D, et al. Advanced microcapsules for self-healing conversion coating on magnesium alloy in $Ce(NO_3)_3$ solution with microcapsules containing $La(NO_3)_3$. Surf Coat Technol 2016;307:500−5.
[147] Li K, Liu J, Lei T, Xiao T. Optimization of process factors for self-healing vanadium-based conversion coating on AZ31 magnesium alloy. Appl Surf Sci 2015;353:811−19.
[148] Yeganeh M, Keyvani A. The effect of mesoporous silica nanocontainers incorporation on the corrosion behavior of scratched polymer coatings. Prog Org Coat 2016;90:296−303.
[149] Bhanvase BA, Patel MA, Sonawane SH. Kinetic properties of layer-by-layer assembled cerium zinc molybdate nanocontainers during corrosion inhibition. Corros Sci 2014;88:170−7.
[150] Tyagi M, Bhanvase BA, Pandharipande SL. Computational studies on release of corrosion inhibitor from layer-by-layer assembled silica nanocontainer. Ind Eng Chem Res 2014;53(23):9764−71.
[151] Tarzanagh YJ, Seifzadeh D, Rajabalizadeh Z, Habibi-Yangjeh A, Khodayari A, Sohrabnezhad S. Sol-gel/MOF nanocomposite for effective protection of 2024 aluminum alloy against corrosion. Surf Coat Technol 2019;380:125038.
[152] Ramezanzadeh M, Ramezanzadeh B, Mahdavian M, Bahlakeh G. Development of metal-organic framework (MOF) decorated graphene oxide nanoplatforms for anti-corrosion epoxy coatings. Carbon 2020;161.
[153] Ren B, Chen Y, Li Y, Li W, Gao S, Li H, et al. Rational design of metallic anti-corrosion coatings based on zinc gluconate@ZIF-8. Chem Eng J 2020;384:123389.
[154] Motamedi M, Ramezanzadeh M, Ramezanzadeh B, Mahdavian M. One-pot synthesis and construction of a high performance metal-organic structured nano pigment based on nanoceria decorated cerium(III)-imidazole network (NC/CIN) for effective epoxy composite coating anti-corrosion and thermo-mechanical properties improvement. Chem Eng J 2020;382:122820.

[155] Yin D, Yu Z, Chen L, Cao K. Enhancement of the anti-corrosion performance of composite epoxy coatings in presence of BTA-loaded copper-based metal-organic frameworks. Int J Electrochem Sci 2019;14(5):4240–53.
[156] Zheng Q, Li J, Yuan W, Liu X, Tan L, Zheng Y, et al. Metal–organic frameworks incorporated polycaprolactone film for enhanced corrosion resistance and biocompatibility of Mg alloy. ACS Sustain Chem Eng 2019;7(21):18114–24.
[157] Wang N, Zhang Y, Chen J, Zhang J, Fang Q. Dopamine modified metal-organic frameworks on anti-corrosion properties of waterborne epoxy coatings. Prog Org Coat 2017;109:126–34.
[158] Xiong L, Liu J, Yu M, Li S. Improving the corrosion protection properties of PVB coating by using salicylaldehyde@ZIF-8/graphene oxide two-dimensional nanocomposites. Corros Sci 2019;146:70–9.
[159] Emira HSA. High performance alkyd paints based on platy kaolin for corrosion protection of steel. J Coat Technol Res 2013;10(2):199–208.
[160] Ferchichi A, Calas-Etienne S, Smaïhi M, Prévot G, Solignac P, Etienne P. Relation between structure and mechanical properties (elastoplastic and fracture behavior) of hybrid organic-inorganic coating. J Mater Sci 2009;44(11):2752–8.
[161] Nichols ME, Gerlock JL, Smith CA, Darr CA. Effects of weathering on the mechanical performance of automotive paint systems. Prog Org Coat 1999;35(1–4):153–9.
[162] Alam MA, Sherif ESM, Al-Zahrani SM. Fabrication of various epoxy coatings for offshore applications and evaluating their mechanical properties and corrosion behavior. Int J Electrochem Sci 2013;8(3):3121–31.
[163] Ballarre J, Jimenez-Pique E, Anglada M, Pellice SA, Cavalieri AL. Mechanical characterization of nano-reinforced silica based sol-gel hybrid coatings on AISI 316L stainless steel using nanoindentation techniques. Surf Coat Technol 2009;203(20–21):3325–31.
[164] Shi X, Nguyen TA, Suo Z, Liu Y, Avci R. Effect of nanoparticles on the anticorrosion and mechanical properties of epoxy coating. Surf Coat Technol 2009;204(3):237–45.
[165] Liu C, Mullins M, Hawkins S, Kotaki M, Sue H-J. Epoxy nanocomposites containing zeolitic imidazolate framework-8. ACS Appl Mater Interfaces 2018;10(1):1250–7.
[166] Lee SH, Seo HY, Yeom YS, Kim JE, An H, Lee J-S, et al. Rational design of epoxy/ZIF-8 nanocomposites for enhanced suppression of copper ion migration. Polymer 2018;150:159–68.
[167] Hu C, Xiao J-D, Mao X-D, Song L-L, Yang X-Y, Liu S-J. Toughening mechanisms of epoxy resin using aminated metal-organic framework as additive. Mater Lett 2019;240:113–16.
[168] Roy PK, Ramanan A. Toughening of epoxy resin using Zn_4O (1,4-benzenedicarboxylate) 3 metal–organic frameworks. RSC Adv 2014;4(94):52338–45.

Chapter 13

Metal-organic frameworks: preparation and application in electrocatalytic CO_2 reduction reaction

Rajasekaran Elakkiya and Govindhan Maduraiveeran
Materials Electrochemistry Laboratory, Department of Chemistry, SRM Institute of Science and Technology, Kattankulathur, Chennai, India

13.1 Introduction

Metal-organic frameworks (MOFs) have perilous growth in the synthesis, properties, and electrochemical applications. The major contribution of the MOF is generated by small and uniform nanostructures. Due to postsynthesis and modification of the morphology, MOFs are more flexible and adjustable, meanwhile the organic struts might have the significant potential for catalytic activities, and the massy frameworks from thermodynamics are more stable [1]. The enhancement of activity and selectivity of the catalyst might be ascribed to the synergistic effect between the nanoparticles and MOF, furthermore, synergy amidst the two metals. One of the most desired properties of MOFs is to permit the place of chemical species to include the field of storage of energy-relevant gases such as H_2 and CH_4, CO_2 capture, elimination of toxic gaseous species, and embedding of biological molecules. In this situation a prodigious development has been perceived regarding the pore/cage dimensions, which led to the isolation of some of highly porous MOFs over recent years (Fig. 13.1) [2].

The essential pathways to form the functionalized MOFs for coordination vacancies are postsynthetic modification of MOFs, and the organic linker should necessarily have the functionalized group. For instance, Irabien coworkers proposed the copper-based metal organic porous materials such as HKUST-1, and CuAdeAce are MOFs and metal organic aerogels of CuDTA and CuZnDTA for the production of alcohols from hydrogenation of CO_2

Metal-Organic Frameworks for Chemical Reactions. DOI: https://doi.org/10.1016/B978-0-12-822099-3.00013-7

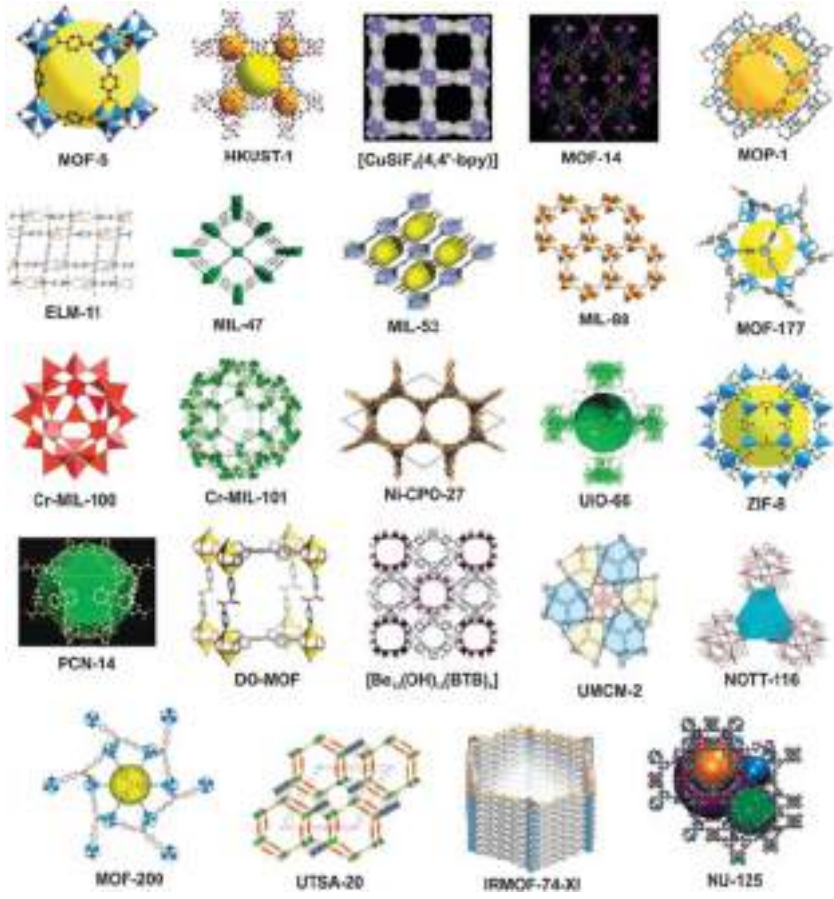

FIGURE 13.1 Numerous MOFs with porous nature were synthesized by various research teams directing the accommodation or retention of chemical molecules in their pores or channels [2]. *MOFs*, Metal organic frameworks.

with the saturated electrolyte of $KHCO_3$ [3]. The metal center with two small crystal-sized amine groups is synthesized by the postsynthetic method for the CO_2 gas adsorption property, which was demonstrated by Moon coworkers [4]. The textural property of the MOF exhibited the interaction between the substrate and catalyst, and it must be superior wherefore it increases the active sites and promotes the charge transfer process. In some cases, MOF has the ability to resist the crack and fractures of the crystal structures. Jeong coworkers fabricated the IRMOF-3 material for the application of resistivity of the cracks in the crystals [5]. Fig. 13.2 demonstrates the prevention of cracks morphology using IRMOF-3 [5]. The membrane thickness was calculated to be $\sim 10.0\,\mu m$.

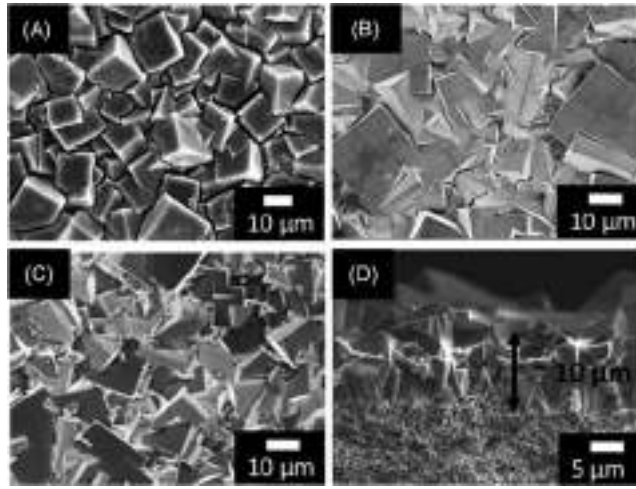

FIGURE 13.2 SEM images obtained from IRMOF-3 membranes after drying without surfactant (A), with a triblock copolymer, P-123 (B), and Span 80 (C). The cross-sectional view is from the membrane with Span 80 (D) [5].

A lot of MOFs have been developed and successfully tested toward the electrocatalytic applications of carbon dioxide (CO_2) reduction reaction (CO_2RR). An enormous amount of CO_2 evolution affects the environment, facilitating the global warming issues. To avoid the adverse effects the conversion of CO_2 into fuels or value-added chemicals becomes a valuable solution for an energy transition, which will lead to the growth of a sustainable CO_2 economy from fossil fuel economy [6]. The conversion of CO_2 to fuels and chemicals can be conducted via diverse methodologies, including reverse water gas shift [7–9], methanation [10,11], electrochemical [12–18], and photochemical reduction [19–22]. The direct electrochemical reduction of CO_2 to hydrocarbons is an interesting strategy among other methods due to its attribution of environmental compatibility, operating under ambient temperature and pressure, ease of control of reactions, and engineering and low-cost feasibility [23]. Furthermore, the transformation of CO_2 into a precious product is a solid approach using the electrocatalytic process for the renewable energy by water and sunlight.

However, the electrocatalytic reduction of CO_2 quiet expressions some challenges, including large overpotential and stumpy electron-transfer kinetics [24]. Due to these reasons, the practical applicability and electrochemical technological commercialization are still limited. A variety of MOF-based materials have been reported as a potential catalyst toward the numerous electrochemical reactions, in particular, CO_2RR. Moreover, the physical, chemical, and electrochemical characteristics of the MOFs may be meritoriously altered in different methods [25]. In this chapter, we focus on recent advances of MOFs in electrocatalytic CO_2RR. The correlation among the

synthetic approaches, surface structures, physicochemical properties, and catalytic activities is systematically described. In addition, the electrocatalytic CO_2RR and likely reaction mechanism are highlighted at the MOFs.

13.2 Synthesis and properties of metal-organic frameworks

Controlled pore-size distribution, distinct morphologies such as one-dimensional, two-dimensional, and three-dimensional structures can easily be prepared for numerous electrochemical applications [26]. Template method [27], microemulsion [28], recrystallization [29], modulation [30], interfacial growth [31], chemical etching process [32], and lab on a chip approach [33] are considered the major controlled synthetic processes for MOFs. Based on the specific requirements, the structure and properties of MOFs may be engineered due to their tunable pore dimension and shape, network morphology, and surface functionality via the selection of appropriate chemical modification and strategy. For instance, Donbebe coworkers [34] shortly reviewed the application of MOFs in the field of adsorption process in diverse industrial processes, including removal of noxious and harmful substances from liquid/gaseous media, gas storage, separation, and catalysis. Fig. 13.3 shows the gas storage properties of some major MOFs [34]. The functionalized MOFs may offer remarkable properties because of the

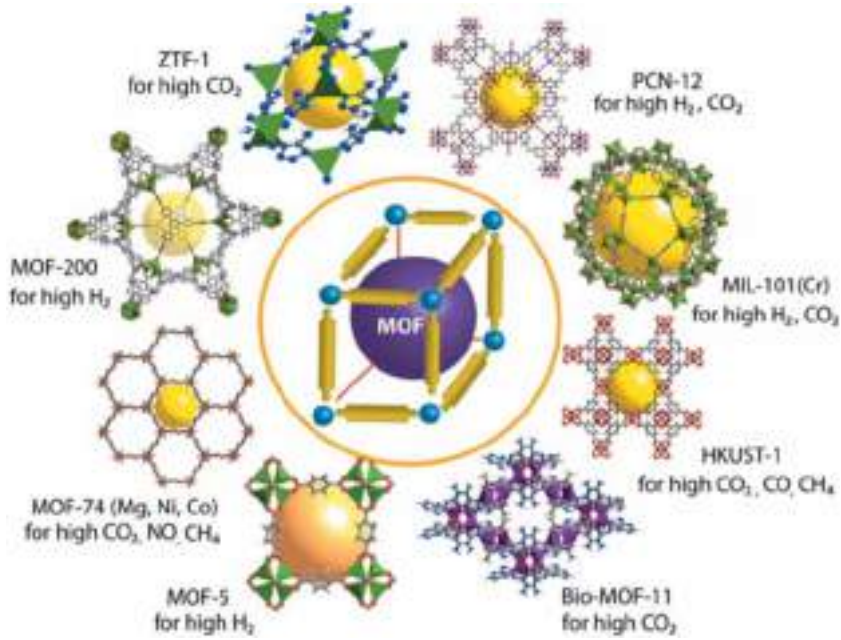

FIGURE 13.3 Pictorial illustration of some MOFs with high gas storage properties [34]. *MOFs*, Metal organic frameworks.

introduction of active functional groups. Thus the properties and high sorbent performance of MOFs in industrial processes are contingent on functionality, surface area, and nature of porosity.

Research reports have shown that MOFs are one of the most encouraging adsorbents due to their novel structure, composition, surface area, tunable pore size, and active sites. Bottom-up strategy of interfacial growth approach is one of the synthesis methods for the production of two-dimensional MOFs. It is so-formed during the process of the growth of the 2D material, which exhibits in between the two different kinds of solvents such as metal precursors and organic linker. The formation of square-layered structure of CuBDC nanosheets fabricated using interfacial growth method was developed [35]. In this study, there was no surfactant or tensio-active additives used to alter the crystal growth pattern. Hence, use of the three-layer synthesis approach to MOFs with a propensity for isotropic progress modes principally conserved their crystal morphology. Jointly, the established method may be considered the versatile route for the synthesis of 2D nanocrystals of many MOFs. MOFs can be synthesized by numerous approaches, including hydro/solvothermal [36,37], sonochemical, slow diffusion [38], atomic layer deposition (ALD) [39], electrochemical [40], microwave [41], and mechanochemical [42].

13.2.1 Hydrothermal method

MOFs are prepared under hydro/solvothermal conditions using of metal cation center tethered with polydentate organic ligand in relevant solvents. Entropy-driven dehydration process possesses the compounds of M−O−M clusters and linkages, which are employed for the formation. It depends on the temperature in a thermodynamically controlled experiment. A variety of micro/nanostructures of MOFs with controlled shape, dimension, and composition were developed using a hydrothermal method [43]. For example, Wang et al. developed a glucose-assisted hydrothermal strategy for the direct transformation of MOFs into hollow carbonaceous materials [44]. The MOF particles (zeolitic imidazolate frameworks-8, ZIF-8) were decomposed through the hydrothermal reaction by the acid generation from the hydrolysis of glucose. Besides, the decomposed MOF incessantly diffuses out and reacts with the glucose-derived polymers, forming hollow Zn-containing carbonaceous composites. The as-prepared Zn-based MOFs showed extraordinary electrochemical properties toward the supercapacitor concerns. Moreover, hydrothermal-based synthesis approach delivers a lot of multicompositional inorganic MOFs with the advancement of this research area.

13.2.2 Sonochemical method

Sonochemical strategy stimulates homogeneous nucleation and fast kinetics; consequently, it forms remarkable reduction of particle size due to that

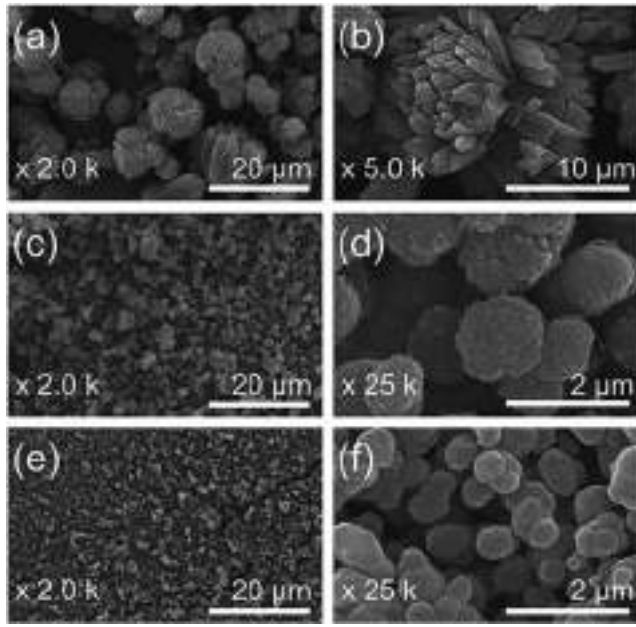

FIGURE 13.4 SEM images obtained for Mg-MOF-74(C) (A and B), Mg-MOF-74(C)−TEA (C and D), and Mg-MOF-74(S) (E and F) [45].

acoustic cavitation by ultrasound waves [1,45]. Ahn coworkers demonstrated that the synthesis of Mg-MOF-74 by sonochemical method in the helium atmosphere for the deprotonating agent for CO_2 capture and sequestration. Fig. 13.4 shows the SEM images of the various particles of Mg-MOF-74. The cauliflower-shaped Mg-MOF-74 was found with a diameter of $\sim$14 μm, containing agglomerated needle-type crystals, whereas the others were in spherical shape with a uniform particle size of $\sim$0.6 mm. It is found that the accelerated nucleation and short preparation time appear to make particles more uniform and smaller. The MOF-based thin film exhibited improved charge transport process, preserving the framework durability in the electrolyte solution.

13.2.3 Atomic layer deposition

ALD in MOFs (AIM) has been used as a postsynthetic modification technique for depositing thin films. This transfer of ALD technique has significant application of engineered materials, and more functionalized mesoporous crystalline compounds from flat surface are performed. It is the key to enable the performance of functional groups in coordinative unsaturated metal ions. AIM, having the major application part of to be highly functional, construct diverse and few atom clusters [46]. The design of

emergent catalytic materials in the electrochemical carbon dioxide reduction is a key, highlighting product selectivity, durability, and a chemical composition of Earth-abundant elements. Yang coworkers reported a strategy to enhance the carbon monoxide production by the fabrication of cobalt porphyrin MOF ($Al_2(OH)_2$TCPP-Co), which synthesized through home-built thermal ALD system the alumina and tin oxide carried out with the temperature of 150°C and 200°C, respectively [47]. In this MOF, thin film of nanoscale MOFs is atomically defined and is employed as an efficient catalyst for the improved and selective catalytic reduction of carbon dioxide to carbon monoxide. The huge amount of catalytic active sites, inorganic backbone, and thickness or homogeneous loading onto a conductive support are vital for enhanced CO_2RR, leading to a new route in electrocatalysis.

13.2.4 Electrochemical method

Electrochemical approach is one of the finest synthesis protocols for the production of MOF. It can be achieved in continuous flow operation or batch mode. A common advantage of this synthesis is that it works under mild conditions than ordinary microwave and hydrothermal synthesis. In addition, it can yield a product within a minute or hour by using chronopotentiometry and amperometry [48]. Especially it is able to control the oxidation state of the metal using the applied potential/current. The major advantage of this synthesis is low temperature with rapid reaction, high faradaic efficiency, and no anionic residues, which end up in the MOFs [49]. The organic linker does not dissolve easily, which is the major drawback of this method. However, electrochemical strategy is a promising technique because of its simple operation procedure, operating under ambient conditions. The electrocatalytic CO_2RR was studied at Cu-based MOF film surface in *N*,*N*-dimethylformamide containing tetrabutylammonium tetrafluoroborate with saturated CO_2 [50]. Fig. 13.5 depicts the physical, electrochemical, and electrocatalytic characteristics of the developed $Cu_3(BTC)_2$ electrode. The developed electrocatalysts reduce the CO_2 to oxalic acid, which was established via bulk electrolysis and using gas chromatography mass spectrometry analysis.

13.2.5 Other synthesis methods

Slow diffusion strategy is effectively used for the preparation of MOFs. In this method, liquid phase metal precursor with organic linker blended enhances the slow evaporation method where there is no external energy supply at a room temperature. It forms an extremely stable configuration of structures. The major drawback of this method is that it is a very slow process and takes a few days or months to prepare the MOFs. To overcome this complication the mixture of solvents can be used to induce evaporation at a low boiling temperature, leading to faster reaction [51]. Moreover, crystal growth formation also

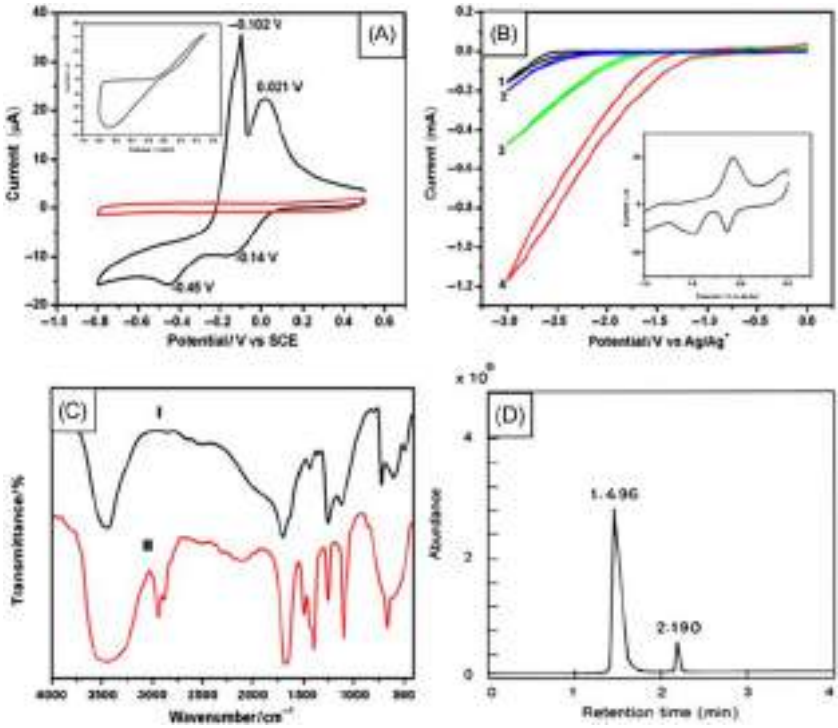

FIGURE 13.5 CV curves of the GC/$Cu_3(BTC)_2$-coated GC (A), bare GC, and bare GC in presence of CO_2, GC/$Cu_3(BTC)_2$, and GC/$Cu_3(BTC)_2$ in presence of CO_2, in a solution containing 0.01 M TBATFB/DMF, scan rate 50 mV s^{-1} (B), FT-IR spectra of (I) oxalic acid (authentic) and (II) oxalic acid (synthesized) (C), and spectrum of the bulk electrolysis (D) [50]. *GC–MS*, Gas chromatography mass spectrometry.

happened in the slow diffusion method, fabricating the bimetallic MOF with five-membered aromatic ring compound [52]. *Microwave synthesis* method is the transfer of radiation (300−300,000 MHz) into heat (interaction of electromagnetic waves with mobile electric charges); the volume of the container is independent. It has benefitted from fast synthetic kinetics without disturbing the yield. The synthesis of inorganic materials promotes phase purity and morphology of the particle. Due to higher nucleation rate, it accomplishes fast crystallization. Microwave facilitates technique traditionally used for the synthesis of the high purity of nanoscale MOFs [53]. *Mechanochemical synthesis* enables to escape from high temperature, bulk solvents, and corrosive reagents using the ball milling method. For example, Emmerling coworkers reported the mechanochemical synthesis of Ni-MOF. Mechanochemical synthesis is one such destination path of using mechanical force, solvent free, and, to be easy, rapid process [54]. The specific techniques of mechanochemical

synthesis are neat grinding [55], liquid-assisted grinding [56], ion- and liquid-assisted grinding [57], and neat grinding followed by calcination [58]. To overcome the challenges in the catalyst design the development of catalyst must have the following features: (1) high selectivity toward the CO_2RR in water with minimum H_2 evolution, (2) long-term durability and minimum adsorbed intermediates, (3) high catalytic and faradaic efficiency at low electrochemical overpotential, and (4) employment of Earth-abundant catalytic materials. The electrochemical applications of MOFs in the field of CO_2RR will be described in the following section.

13.3 Electrocatalytic CO_2 reduction reaction

One of the most promising strategies is the electrochemical transformation of atmospheric carbon dioxide (CO_2) into highly energy-dense carbon compounds that may be employed as fuels and chemical feedstock, leading to "carbon-neutral energy" [59]. Fig. 13.6 clearly shows the utilization of CO_2 for the production of methanol from electrochemical reduction [60]. Enormous research efforts have been dedicated to the design and the development of homogeneous and heterogeneous catalysts for CO_2RR under alkaline and organic electrolytes [24]. The major advantages of the electrocatalytic conversion of CO_2 to value-added products are as follows: (1) reduce the CO_2 emission, (2) possibility to reuse the supporting electrolyte, (3) accessible changes in the electrochemical cell, and (4) control the process by temperature and potential. The design of low-cost, highly catalytic active, and earth abundant is

FIGURE 13.6 Pictorial representation of electrochemical reduction of CO_2 and probable of fuel product or chemicals [60].

a major key in CO_2RR. Due to the tunable nature of MOFs, the nanoscale MOFs encounter these standards and also existing additional prospects such as integrated organic and inorganic components, ease of functionalization, and highly arranged crystalline structure.

The rate and selectivity of the electrochemical reduction of carbon dioxide mainly depend on the concentration of the carbon dioxide in the electrolyte, nature of electrolyte and electrode, applied potential or current, etc. [61]. In particular, MOF carries the pores of significant shape and size, enhancing more selective catalysts for the CO_2RR. It possessed the higher standard potential of -1.9 V versus standard hydrogen electrode at the intermediate state of $-CO_2^-$, where the overpotential can be enhanced by stabilizing the intermediate. Initially, the major output from CO_2RR forms C1 products using the electrocatalysts of MOFs where MOFs were prepared using pyrolyzed and hybrid strategy. Generally, Cu-based catalysts exhibit the selective production of valuable-added chemicals (methane, alcohols, etc.) from carbon dioxide reduction [62,63]. On the other hand, gold and silver-based catalysts showed the selective production for carbon monoxide, although poisonous and economically prohibited [64].

Gascon coworkers reported the incorporation of heteroatom into carbon material, which enhances the functional properties of carbon nanotube as mediated by MOF for the production of carbon monoxide [65]. The MOF-possessed nitrogen contained organic struts, and it was prepared by the pyrolysis method with the template of ZIF-8. In numerous cases the synergistic effect plays a vital role for the enhanced catalytic activity and selectivity of products. For example, copper- and carbon-incorporated nitrogen MOF exhibited a better CO_2RR performance [66]. The Cu-based MOFs were prepared at various temperatures of the BEN-Cu-BTC for the hydrogenation of CO_2 into multiple carbon products. Fig. 13.7 demonstrates the CO_2 reduction of the different MOFs [14,61,67,68].

Generally, copper-based materials show high faradaic efficiency and selectivity toward carbon dioxide reduction and great reaction rate for the C1 carbon, methanol, and ethanol products [70–72]. Perez-Yanez et al. prepared a HKUST-1 (Cu, dopant metal) material of hetero metallic MOF by solvent-free synthesis method. The electrochemical condition possesses the gas–liquid–solid interfaces toward the reduction of CO_2, which takes place in the gas phase [73]. The developed MOF-based electrode showed improved CO_2RR activity with the total faradic efficiency of 45.2%–71.2% at -0.1 to -0.7 V versus RHE. Zhang et al. developed a Cu-based MOF [$Cu_3(BTC)_2$ (Cu-MOF)] for the improved reduction of CO_2 and CO_2 capture using the carbon paper–derived gas diffusion electrode (GDE) [61]. The faradaic efficiencies of CH_4 on Cu-MOF weight ratio in the range of 7.5% − 10% were two- to threefold larger in comparison to bare GDE under the applied potentials, starting from -2.3 to -2.5 V versus SCE. It is interesting to note that the faradaic efficiency of the competitive hydrogen evolution reaction (HER)

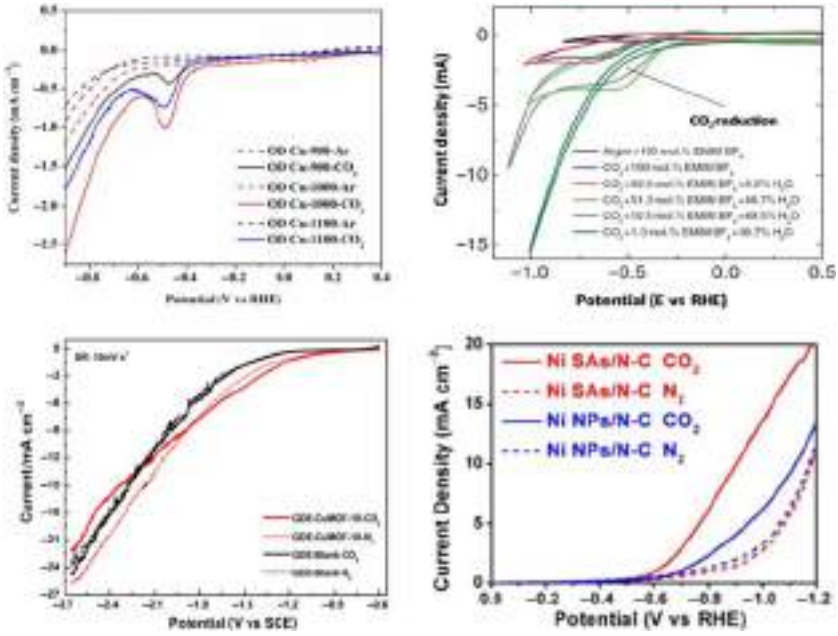

FIGURE 13.7 Electrocatalytic reduction of CO_2RR at the various MOF-based electrode materials [14,67–69]. *CO_2RR*, CO_2 reduction reaction; *MOFs*, metal organic frameworks.

was reduced to 30%. The copper-based electrode often yields a lot of hydrocarbon and oxygenated products at an intermediate potential of −1.04 V versus RHE (for instance, at an overpotential of 0.9 V for CO_2RR to CO and at an overpotential of 1.2 V for CO_2RR to methane). It is understood that the selectivity of CO_2RR may effect with experimental conditions and electrode potential for analyzing the CO_2RR. The excruciation of the metals into these four major divisions based on their selectivity toward CO_2RR may be described based on the result of their binding energy to CO_2RR and HER intermediates such as $^{\bullet}H$, $^{\bullet}OCHO$, $^{\bullet}COOH$, and $^{\bullet}CO$. The formed products are based on the ability of Cu to reduce CO_2 to $>2e^-$ due to the fact that it is the only metal with a negative adsorption energy for $^{\bullet}CO$ but a positive adsorption energy for $^{\bullet}H$ (Fig. 13.8) [74].

13.4 Conclusion

In summary the recent advances in synthesis and electrocatalytic reduction of CO_2 reaction of MOFs were described in this chapter. The electrochemical conversion of CO_2 into hydrocarbons and alcohols devours the great potential in carbon-neutral energy sector. It is understood that a variety of prime factors impact CO_2RR activity and selective formation of products,

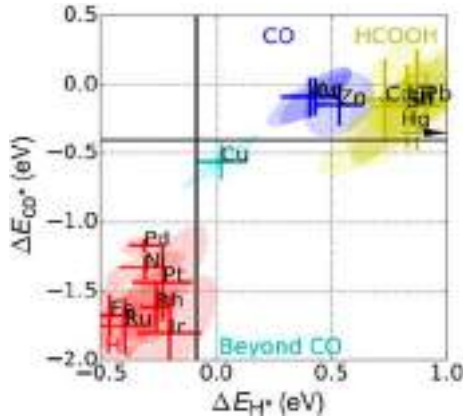

FIGURE 13.8 The metal classification based on the CO_2 reduction potential [74].

counting the nature of catalyst, surface structure and energy, surface morphology, chemical composition, electrolyte ions and pH, etc. The discovery of novel catalyst design is a very complicated strategy and even several of other factors often intertwined. In the present chapter a broad view of many preparation strategies and their complex relationship in the design of dimension, pore size−controlled synthesis of MOF-based electrocatalysts, new insights on preparation methods, and suitable guide for the designing catalyst toward the CO_2RR is systematically discussed.

Owing to the huge surface area, high porosity, functional groups of the organic linkers, unsaturated metal sites and structure of the compounds, etc., MOFs are often exhibited as a suitable material candidate toward CO_2RR. The fabrication method of MOF enhances the structural and surface property for the activity dependent on the electrocatalysts. As we have mentioned earlier, trends in the area of electrochemical CO_2RR may interestingly put effort on the novel synthesis of micro-/nanostructured MOFs catalysts with a facile route, low cost, less time consumption, high active sites, maintain ordered crystalline layers, high surface energy, high selectivity, and high faradaic efficiency. The basic deep-understanding of the CO_2RR mechanisms may offer applied information for the sensible electrocatalysts design. Further, the allowance of this emergent field from academic studies to industrial production is a significant task as well for the successful employment of the catalysts, although the current developments in the area of solid-state catalysts for heterogeneous transformation of CO_2 to chemicals and fuels through electrochemical strategy are still distant from large-scale uses.

It is believed that the prime factors for the yield of many products may be exposed, and a succession of solid-state catalysts with high selectivity may be realistically intended through advances in synthetic strategies and the appropriate theoretical guidance. Moreover, the optimization of the

fabrication of the working electrode (cathode) and significant reduction of catalyst cost may be paid more devotion. We believe that systematic MOFs design and application in CO_2RR yield numerous opportunities to advance catalytic performance and unlock new ways in electrocatalysis.

Acknowledgment

Authors acknowledge the financial support from the SERB-Start-up Research Grant (SRG) (ref. no.: SERB-SRG/2019/000123), Department of Science & Technology, Government of India.

References

[1] Butova VV, Soldatov MA, Guda AA, Lomachenko KA, Lamberti C. Metal-organic frameworks: structure, properties, methods of synthesis and characterization. Russ Chem Rev 2016;85(3):280–307.

[2] Silva P, Vilela SMF, Tomé JPC, Almeida Paz FA. Multifunctional metal-organic frameworks: from academia to industrial applications. Chem Soc Rev 2015;44(19):6774–803.

[3] Albo J, Vallejo D, Beobide G, Castillo O, Castaño P, Irabien A. Copper-based metal–organic porous materials for CO_2 electrocatalytic reduction to alcohols. ChemSusChem 2017;10:1100–9.

[4] Kim YK, Hyun SM, Lee JH, Kim TK, Moon D, Moon HR. Crystal-size effects on carbon dioxide capture of a covalently alkylamine-tethered metal-organic framework constructed by a one-step self-assembly. Sci Rep 2016;6:1–8 [Internet] Available from: http://doi.org/10.1038/srep19337.

[5] Yoo Y, Varela-Guerrero V, Jeong HK. Isoreticular metal-organic frameworks and their membranes with enhanced crack resistance and moisture stability by surfactant-assisted drying. Langmuir 2011;27(6):2652–7.

[6] Jia C, Dastafkan K, Ren W, Yang W, Zhao C. Carbon-based catalysts for electrochemical CO_2 reduction. Sustain. Energy Fuels 2019;3(11):2890–906.

[7] Chen CC, Tseng HH, Lin YL, Chen WH. Hydrogen production and carbon dioxide enrichment from ethanol steam reforming followed by water gas shift reaction. J Clean Prod 2017;162:1430–41 [Internet] Available from: http://doi.org/10.1016/j.jclepro.2017.06.149.

[8] Ghosh S, Uday V, Giri A, Srinivas S. Biogas to methanol: a comparison of conversion processes involving direct carbon dioxide hydrogenation and via reverse water gas shift reaction. J Clean Prod 2019;217:615–26 [Internet] Available from: https://doi.org/10.1016/j.jclepro.2019.01.171.

[9] Chen WH, Chen CY. Water gas shift reaction for hydrogen production and carbon dioxide capture: a review. Appl Energy 2020;258:114078 [Internet] Available from: https://doi.org/10.1016/j.apenergy.2019.114078.

[10] Shin HH, Lu L, Yang Z, Kiely CJ, McIntosh S. Cobalt catalysts decorated with platinum atoms supported on barium zirconate provide enhanced activity and selectivity for CO_2 methanation. ACS Catal 2016;6(5):2811–18.

[11] Wang F, He S, Chen H, Wang B, Zheng L, Wei M, et al. Active site dependent reaction mechanism over Ru/CeO_2 catalyst toward CO_2 methanation. J Am Chem Soc 2016;138(19):6298–305.

[12] Lu Q, Jiao F. Electrochemical CO_2 reduction: electrocatalyst, reaction mechanism, and process engineering. Nano Energy 2016;29:439–56.

[13] Sastre F, Muñoz-Batista MJ, Kubacka A, Fernández-García M, Smith WA, Kapteijn F, et al. Efficient electrochemical production of syngas from CO_2 and H_2O by using a nanostructured Ag/g-C_3N_4 catalyst. ChemElectroChem 2016;3(9):1497–502 [Internet] Available from: http://doi.wiley.com/10.1002/celc.201600392.

[14] Zhao C, Dai X, Yao T, Chen W, Wang X, Wang J, et al. Ionic exchange of metal-organic frameworks to access single nickel sites for efficient electroreduction of CO_2. J Am Chem Soc 2017;139(24):8078–81.

[15] Lu X, Liu Y, He Y, Kuhn AN, Shih P-C, Sun C-J, et al. Cobalt-based nonprecious metal catalysts derived from metal–organic frameworks for high-rate hydrogenation of carbon dioxide. ACS Appl Mater Interfaces 2019;11(31):27717–26.

[16] Zhang XD, Hou SZ, Wu JX, Gu ZY. Two-dimensional metal-organic framework nanosheets with cobalt-porphyrins for high-performance CO2 electroreduction. Chemistry 2020;26:1604–11.

[17] Wang YR, Huang Q, He CT, Chen Y, Liu J, Shen FC, et al. Oriented electron transmission in polyoxometalate-metalloporphyrin organic framework for highly selective electroreduction of CO_2. Nat Commun 2018;9(1):1–8 [Internet] Available from: http://doi.org/10.1038/s41467-018-06938-z.

[18] Qiao J, Liu Y, Hong F, Zhang J. A review of catalysts for the electroreduction of carbon dioxide to produce low-carbon fuels. Chem Soc Rev 2014;43:631–75.

[19] Viswanathan B. Active materials for photocatalytic reduction of carbon dioxide. 2019. p. 343–372.

[20] Yang P, Guo S, Yu X, Zhang F, Yu B, Zhang H, et al. Photocatalytic reduction of carbon dioxide over quinacridone nanoparticles supported on reduced graphene oxide. Ind Eng Chem Res 2019;58(22):9636–43.

[21] Zhang H, Li J, Tan Q, Lu L, Wang Z, Wu G. Metal–organic frameworks and their derived materials as electrocatalysts and photocatalysts for CO_2 reduction: progress, challenges, and perspectives. Chemistry 2018;24(69):18137–57.

[22] Shen L, Wu W, Liang R, Lin R, Wu L. Highly dispersed palladium nanoparticles anchored on UiO-66(NH_2) metal-organic framework as a reusable and dual functional visible-light- driven photocatalyst. Nanoscale 2013;3(207890):10715–22 [Internet] Available from: http://xlink.rsc.org/?DOI = C5TC02043C.

[23] Takht Ravanchi M, Sahebdelfar S. Carbon dioxide capture and utilization in petrochemical industry: potentials and challenges. Appl Petrochem Res 2014;4(1):63–77.

[24] Kumar B, Brian JP, Atla V, Kumari S, Bertram KA, White RT, et al. New trends in the development of heterogeneous catalysts for electrochemical CO_2 reduction. Catal Today 2016;270:19–30 [Internet] Available from: http://doi.org/10.1016/j.cattod.2016.02.006.

[25] Xue Y, Zheng S, Xue H, Pang H. Metal-organic framework composites and their electrochemical applications. J Mater Chem A 2019;7(13):7301–27.

[26] Xiao X, Zou L, Pang H, Xu Q. Synthesis of micro/nanoscaled metal-organic frameworks and their direct electrochemical applications. Chem Soc Rev 2020;49(1):301–31.

[27] Fan X, Wang W, Li W, Zhou J, Wang B, Zheng J, et al. Highly porous ZIF-8 nanocrystals prepared by a surfactant mediated method in aqueous solution with enhanced adsorption kinetics. ACS Appl Mater Interfaces 2014;6:14994–9.

[28] Rieter WJ, Taylor KML, An H, Lin W, Lin W. Nanoscale metal–organic frameworks as potential multimodal contrast enhancing agents. J Am Chem Soc 2006;128(28):9024–5.

[29] Zou L, Hou CC, Liu Z, Pang H, Xu Q. Super-long single-crystal metal-organic framework nanotubes. J. Am. Chem. Soc. 140, 2018, 15393−15401.
[30] Zhan G, Zeng HC. Synthesis and functionalization of oriented metal−organic-framework nanosheets: toward a series of 2D catalysts. 2016.
[31] Clough AJ, Skelton JM, Downes CA, De Rosa AA, Yoo JW, Walsh A, et al. Metallic conductivity in a two-dimensional cobalt dithiolene metal − organic framework. 2017.
[32] Liu W, Huang J, Yang Q, Wang S, Sun X, Zhang W, et al. Multi-shelled hollow metal−organic frameworks. Angew Chem Int Ed 2017;56:5512−16.
[33] Puigmartí-luis J, Rubio-martínez M, Hartfelder U, Imaz I, Maspoch D, Dittrich PS. Coord Polym Nanofibers Generated Microfluidic 2011;133:4216−19.
[34] Ebelegi A, Nimibofa A, Inengite AK, Donbebe W. Metal-organic frameworks as novel adsorbents: a preview metal-organic frameworks as novel adsorbents: a preview. 2017.
[35] Rodenas T, Luz I, Prieto G, Seoane B, Miro H, Corma A, et al. Metal-organic framework nanosheets in polymer composite materials for gas separation. Nat Mater 2015;14 (1):48−55.
[36] Nozohour Yazdi M, Yamini Y, Asiabi H, Alizadeh A. A metal organic framework prepared from benzene-1,3,5-tricarboxylic acid and copper(II), and functionalized with various polysulfides as a sorbent for selective sorption of trace amounts of heavy metal ions. Microchim Acta 2018;185(11):1−8.
[37] Zhang Y, Bo X, Nsabimana A, Han C, Li M, Guo L. Electrocatalytically active cobalt-based metal-organic framework with incorporated macroporous carbon composite for electrochemical applications. J Mater Chem A 2015;3(2):732−8.
[38] Chen XY, Zhao B, Shi W, Xia J, Cheng P, Liao DZ, et al. Microporous metal-organic frameworks built on a Ln_3 cluster as a six-connecting node Xiao-Yan. 2005. p. 2866−74.
[39] Kim IS, Borycz J, Platero-Prats AE, Tussupbayev S, Wang TC, Farha OK, et al. Targeted single-site MOF node modification: trivalent metal loading via atomic layer deposition. Chem Mater 2015;27(13):4772−8.
[40] Van Assche TRC, Desmet G, Ameloot R, De Vos DE, Terryn H, Denayer JFM. Electrochemical synthesis of thin HKUST-1 layers on copper mesh. Microporous Mesoporous Mater 2012;158:209−13 [Internet] Available from: http://doi.org/10.1016/j.micromeso.2012.03.029.
[41] Haque E, Khan NA, Kim CM, Jhung SH. Syntheses of metal-organic frameworks and aluminophosphates under microwave heating: quantitative analysis of accelerations. Cryst Growth Des 2011;11(10):4413−21.
[42] Masoomi MY, Morsali A, Junk PC. Rapid mechanochemical synthesis of two new Cd(II)-based metal-organic frameworks with high removal efficiency of Congo red. CrystEngComm 2015;17(3):686−92 [Internet] Available from: http://doi.org/10.1039/C4CE01783H.
[43] Nimbalkar MN, Bhat BR. Facile green synthesis of zirconium based metal-organic framework having carboxylic anchors. Mater Today Proc 2019;9:522−7 [Internet] Available from: https://doi.org/10.1016/j.matpr.2018.10.371.
[44] Wang J, Luo X, Young C, Kim J, Kaneti YV, You J, et al. A glucose-assisted hydrothermal reaction for directly transforming metal-organic frameworks into hollow carbonaceous materials. Chem Mater 2018;30(13):4401−8.
[45] Yang DA, Cho HY, Kim J, Yang ST, Ahn WS. CO_2 capture and conversion using Mg-MOF-74 prepared by a sonochemical method. Energy Environ Sci 2012;5(4):6465−73.
[46] Mondloch JE, Bury W, Fairen-Jimenez D, Kwon S, Demarco EJ, Weston MH, et al. Vapor-phase metalation by atomic layer deposition in a metal-organic framework. J Am Chem Soc 2013;135(28):10294−7.

[47] Kornienko N, Zhao Y, Kley CS, Zhu C, Kim D, Lin S, et al. Metal-organic frameworks for electrocatalytic reduction of carbon dioxide. J Am Chem Soc 2015;137(44):14129–35.

[48] Martinez Joaristi A, Juan-Alcañiz J, Serra-Crespo P, Kapteijn F, Gascon J. Electrochemical synthesis of some archetypical Zn^{2+}, Cu^{2+}, and Al^{3+} metal organic frameworks. Cryst Growth Des 2012;12(7):3489–98.

[49] Lee YR, Kim J, Ahn WS. Synthesis of metal-organic frameworks: a mini review. Korean J Chem Eng 2013;30(9):1667–80.

[50] Senthil Kumar R, Senthil Kumar S, Anbu Kulandainathan M. Highly selective electrochemical reduction of carbon dioxide using Cu based metal organic framework as an electrocatalyst. Electrochem Commun 2012;25(1):70–3 [Internet] Available from: http://doi.org/10.1016/j.elecom.2012.09.018.

[51] Seetharaj R, Vandana PV, Arya P, Mathew S. Dependence of solvents, pH, molar ratio and temperature in tuning metal organic framework architecture. Arab J Chem 2019;12(3):295–315 [Internet] Available from: http://doi.org/10.1016/j.arabjc.2016.01.003.

[52] Piñeiro-López L, Arcís-Castillo Z, Muñoz MC, Real JA. Clathration of five-membered aromatic rings in the bimetallic spin crossover metal-organic framework $[Fe(TPT)_{2/3}\{MI(CN)_2\}_2]\cdot G$ (MI = Ag, Au). Cryst Growth Des 2014;14(12):6311–19.

[53] Taddei M, Steitz DA, van Bokhoven JA, Ranocchiari M. Continuous-flow microwave synthesis of metal-organic frameworks: a highly efficient method for large-scale production. Chemistry 2016;22(10):3245–9 [Internet] Available from: http://doi.wiley.com/10.1002/chem.201505139.

[54] Zhang R, Tao CA, Chen R, Wu L, Zou X, Wang J. Ultrafast synthesis of Ni-MOF in one minute by ball milling. Nanomaterials 2018;8(12):1–11.

[55] Friščić T. Metal-organic frameworks: mechanochemical synthesis strategies. Encycl Inorg Bioinorg Chem 2014;1–19.

[56] Shan N, Toda F, Jones W. Mechanochemistry and co-crystal formation: effect of solvent on reaction kinetics. Chem Commun 2002;2(20):2372–3.

[57] Friščić T, Reid DG, Halasz I, Stein RS, Dinnebier RE, Duer MJ. Ion- and liquid-assisted grinding: improved mechanochemical synthesis of metal-organic frameworks reveals salt inclusion and anion templating. Angew Chem Int Ed 2010;49(4):712–15.

[58] James SL, Adams CJ, Bolm C, Braga D, Collier P, Friščić T, et al. Mechanochemistry: opportunities for new and cleaner synthesis. Chem Soc Rev 2012;41(1):413–47 [Internet] Available from: http://xlink.rsc.org/?DOI = C1CS15171A.

[59] Pearson BRJ, Eisaman MD, Turner JWG, Edwards PP, Jiang Z, Kuznetsov VL, et al. Energy storage via carbon-neutral fuels made from CO_2, water, and renewable energy. This paper highlights how a versatile energy carrier can be produced by recycling. 2012;100(2).

[60] Al-Rowaili FN, Jamal A, Ba Shammakh MS, Rana A. A review on recent advances for electrochemical reduction of carbon dioxide to methanol using metal-organic framework (MOF) and non-MOF catalysts: challenges and future prospects. ACS Sustain Chem Eng 2018;6(12):15895–914.

[61] Qiu YL, Zhong HX, Zhang TT, Xu WB, Su PP, Li XF, et al. Selective electrochemical reduction of carbon dioxide using cu based metal organic framework for CO_2 capture. ACS Appl Mater Interfaces 2018;10(3):2480–9.

[62] Kim MK, Kim HJ, Lim H, Kwon Y, Jeong HM. Metal–organic framework-mediated strategy for enhanced methane production on copper nanoparticles in electrochemical CO_2 reduction. Electrochim Acta 2019;306:28–34 [Internet] Available from: https://doi.org/10.1016/j.electacta.2019.03.101.

[63] Albo J, Perfecto-Irigaray M, Beobide G, Irabien A. Cu/Bi metal-organic framework-based systems for an enhanced electrochemical transformation of CO_2 to alcohols. J CO_2 Util 2019;33:157–65 [Internet] Available from: https://doi.org/10.1016/j.jcou.2019.05.025.

[64] Wang R, Sun X, Ould-Chikh S, Osadchii D, Bai F, Kapteijn F, et al. Metal-organic-framework-mediated nitrogen-doped carbon for CO_2 electrochemical reduction. ACS Appl Mater Interfaces 2018;10(17):14751–8.

[65] Wang R, Kapteijn F, Gascon J. Engineering metal–organic frameworks for the electrochemical reduction of CO_2: a minireview. Chemistry 2019;14(20):3452–61.

[66] Cheng YS, Chu XP, Ling M, Li N, Wu KL, Wu FH, et al. An MOF-derived copper@nitrogen-doped carbon composite: the synergistic effects of N-types and copper on selective CO_2 electroreduction. Catal Sci Technol 2019;9(20):5668–75.

[67] Albo J, Alvarez-Guerra M, Castaño P, Irabien A. Towards the electrochemical conversion of carbon dioxide into methanol. Green Chem 2015;17(4):2304–24 [Internet] Available from: http://xlink.rsc.org/?DOI = C4GC02453B.

[68] Zhao K, Liu Y, Quan X, Chen S, Yu H. CO_2 electroreduction at low overpotential on oxide-derived Cu/carbons fabricated from metal organic framework. ACS Appl Mater Interfaces 2017;9(6):5302–11.

[69] Chen C, Bloomfield AJ, Sheehan SW. Selective electrochemical oxidation of lactic acid using iridium-based catalysts. Ind Eng Chem Res 2017;56(13):3560–7.

[70] Kung CW, Audu CO, Peters AW, Noh H, Farha OK, Hupp JT. Copper nanoparticles installed in metal-organic framework thin films are electrocatalytically competent for CO_2 reduction. ACS Energy Lett 2017;2(10):2394–401.

[71] Yang H, Wu Y, Li G, Lin Q, Hu Q, Zhang Q, et al. Scalable production of efficient single-atom copper decorated carbon membranes for CO_2 electroreduction to methanol. J Am Chem Soc 2019;141(32):12717–23.

[72] Weng Z, Wu Y, Wang M, Jiang J, Yang K, Huo S, et al. Active sites of copper-complex catalytic materials for electrochemical carbon dioxide reduction. Nat Commun 2018;9(1):1–9 [Internet] Available from: http://doi.org/10.1038/s41467-018-02819-7.

[73] Perfecto-Irigaray M, Albo J, Beobide G, Castillo O, Irabien A, Pérez-Yáñez S. Synthesis of heterometallic metal-organic frameworks and their performance as electrocatalyst for CO_2 reduction. RSC Adv 2018;8(38):21092–9.

[74] Bagger A, Ju W, Varela AS, Strasser P, Rossmeisl J. Electrochemical CO_2 reduction: a classification problem. ChemPhysChem 2017;18(22):3266–73.

This page intentionally left blank

Chapter 14

Metal-organic frameworks as diverse chemical applications

Shahid Pervez Ansari[1], Ahmad Husain[1], Mohd Urooj Shariq[2] and Anish Khan[3,4]

[1]Department of Applied Chemistry, Zakir Husain College of Engineering and Technology, Aligarh Muslim University, Aligarh, India, [2]Department of Chemistry, Aligarh Muslim University, Aligarh, India, [3]Chemistry Department, Faculty of Science, King Abdulaziz University, Jeddah, Saudi Arabia, [4]Center of Excellence for Advanced Materials Research, King Abdulaziz University, Jeddah, Saudi Arabia

14.1 Introduction

The first publication of Tomic in 1965 relating to porous materials and MOF (metal-organic framework) fascinated the researchers at that time. Then it was put forward as an infinite framework of polymers that comprise rod-like segments linked three-dimensionally by Hoskins and Robson [1]. Later, in 1995 a 2D coordination compound was synthesized using trimesic acid (BTC), a rigid organic ligand, and metal Co by Yaghi et al. [2] and was named MOF. This was the first time idea of MOF, which was first formally proposed. Ever since there has been a field that has seen a swift growth, and an array of MOF families (as known as MOF series) come into existence.

MOFs have special characteristics such as huge specific area and porosity, and their pore size can be adjusted adjustable pore size. These properties enable MOFs to be used widely in various application fields such as storage of gas and its separation [3−7], medical transportation [8−11], for preparation of electrode material [12−15], catalysis [16−19], and storage of energy and conversion technologies [such as fuel cells, metal−air batteries, and supercapacitors (SCs)] [20−24].

Up to now, greater than 20,000 MOFs with varying compositions, morphology, and crystal structures have been published [25,26]. There are several MOF series, the nomenclature of which does not follow a standard rule. There are four main aspects involved in the naming of MOFs: (1) the composition of the material, (2) structure, (3) function, and (4) institution/laboratory in which it is synthesized. The MOFs belonging to the same family are

Metal-Organic Frameworks for Chemical Reactions. DOI: https://doi.org/10.1016/B978-0-12-822099-3.00014-9

named in the same way with the members being named with the same letters. Generally, a similar synthetic procedure is adopted to prepare the same MOF families, and naming is done by using the same letters in the front, while different in the last numbers for distinguishing between the dissimilar individuals of the same family. Such as, the "MIL" in "MIL-n" stands for the "Materials of Institute Lavoisier," which is followed and adopted by some followers. Mostly "n" is representative of the serial number of preparation, whereas in some cases, it is arbitrary. For commemorating the classic zeolite structure of ZSM-5, MOF-5 is used.

14.2 Electrochemical applications

Lithium batteries having long cyclic life, high energy density, and being environment-friendly are used widely in several portable electronic devices [27–29]. As they are flexible, cheap, and display redox activity, MOFs are suitable for fabricating electrode materials [30]. The practical application of MOFs is held back by its poor conductivity, which results in the cycle performance of the battery to decrease. Consequently, researchers are trying to synthesize MOFs and its composites with superior properties (Fig. 14.1).

14.2.1 Metal-organic frameworks for Li-ion batteries

Rechargeable Li-ion batteries (LIBs) exhibiting high energy density and good cyclic performance have become promising candidates for usage in energy storage devices [32–35]. They have been used as an electrode

FIGURE 14.1 Schematic diagram of MOFs and MOF composites for electrochemical applications [31]. *MOF*, Metal-organic framework.

material as they show tremendous potential and exhibit unique properties owing to the diversity in their structure, ease of synthesis, economic preparation, and redox properties that could be adjusted easily [36,37].

Interfacial transfer of charge is favored as they are highly porous and possess high surface area, which helps in adapting to the Li insertion/extraction strain. Besides, MOFs are more thermally stable as compared to pure organic materials, thereby using metal ions more effectively. MOFs have become a new alternative for crystalline porous materials and have been studied as positive, negative, and electrolyte materials for LIBs.

As the Fe-based MOFs possess excellent electrochemical properties, they have been reported by several researchers [38]. The redox phenomenon of MIL-53(Fe), when employed as LIBs electrode, was explained by the combination of calculations of local chemical bond as well as those based upon the density functional theory by Combelles et al. They showed that the MOF showed good rate capability as well as cycle life [39]. In recent times, some other metal-based MOFs, for example, Cu-based MOFs [40−43], Mn-based MOFs [30,44−46], Ni-based MOFs [47,48], in addition to Fe- and Co-based MOFs, have also been studied by researchers as electrodes for LIBs. For improving the capacity of MOFs, Maiti et al. [30] designed and synthesized an Mn-1,3,5-benzenetricarboxylate MOF (Mn-BTC MOF). When employed in Li-ion button batteries, the as-prepared Mn-BTC MOF anode exhibited superior electrochemical performance. In addition, in the conjugated carboxylates, an aromatic core may have a strong p−p interaction that leads to the stabilization of the 3D structure of the MOF. When Li is inserted into the MOF electrode, the framework structure is preserved, and the volumetric strain is minimized, which facilitates for the electrons and Li^+ to self-assemble, resulting in greater cycling ability. Even though immense advancement has been made in the field of MOFs, they are not suitable for intercalation electrochemically owing to their insulating properties. There is still plenty of room available for understanding the mechanism of Li storage and designing MOFs and its composites exhibiting better electrochemical performance.

14.3 Metal-organic frameworks in supercapacitor applications

SCs have aroused a great amount of interest as a new form of device for storing energy as they have higher power density, rate of charging and discharging, and their cycle life is longer than conventional rechargeable batteries [49−52]. As MOFs possess higher surface area and adjustable pore size, they have grabbed eyeballs as potential electrodes in SCs [53]. As they have poor chemical/mechanical stability and conductivity, they face major challenges when directly used as potential electrode material in SCs. Recently, there has been a wide report on the usage of MOFs as an electrode in SCs

by researchers. Some regular superior organic linkers upon reaction with transition element metal salts (Co, Ni, Mn, Cu, Zn, etc.) form MOF materials with enhanced electrochemical properties. Some of the conventional good organic linkers are 1,4-benzenedicarboxylic acid (1,4-H_2bdc), 2-methylimidazole, 2,3,6,7,10,11-hexahydroxytriphenylene (HHTP), etc., as shown in Fig. 14.2.

For instance, 1,4-H_2bdc, when used as a ligand, leads to layered structures being formed with a network of conducting frameworks in MOFs, which leads to their enhanced electrochemical performance. Coordination of transition metals with HHTP leads to the formation of conductive MOFs that resemble honeycomb structure, thereby displaying good transport properties as well as enhanced electrical conductivity.

MOFs may be employed as novel electrode materials as they possess a different structure and redox centers that are pseudocapacitive. Fewer reports have been published on the usage of MOFs as SC electrodes because their pore size offers steric hindrance to the insertion of ions. Still, their usage in SCs faces a lot of difficulties and challenges [54–57]. For instance, a hierarchical 2D structure of Ni-based MOF was synthesized by Yang et al. [54], which was used in an alkaline electrolyte as an electrode material of SCs. The relation between the electrochemical performance and the inherent properties of Ni-based MOFs was evaluated. Similarly, Jiao et al. reported an exclusive 2D-layered structure of the Ni-MOF, which function as an electrode in alkaline battery–SC hybrid devices [58].

Yan et al. synthesized a new form of solid accordion-like Ni-MOF ($[Ni_3(OH)_2(C_8H_4O_4)_2(H_2O)_4]_2H_2O$) activated carbon device [53]. The SEM and TEM images of the synthesized MOF showed that it is made up of

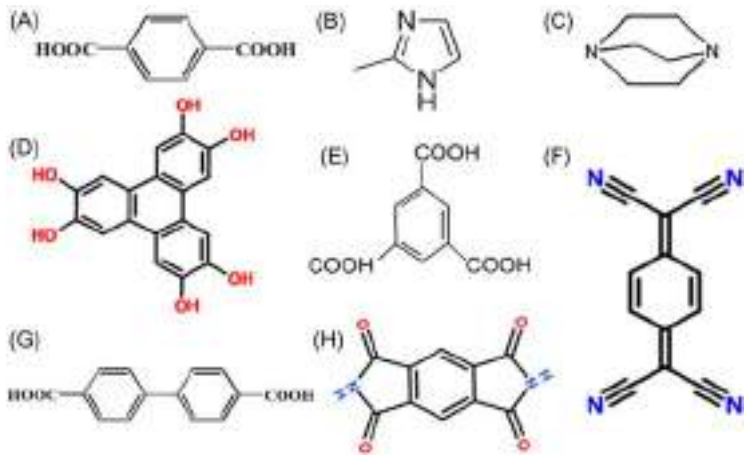

FIGURE 14.2 Schematic representation of 1,4-H_2bdc (A), $C_4H_6N_2$ (B), $C_6H_{12}N_2$ (C), $C_{18}H_{12}O_6$ (D), H_3BTC (E), $C_{12}H_4N_4$ (F), 4,40-H_2bpc (G), and $C_{10}H_4O_4N_2$ (H) [31].

substructures that resembled nanosheets. The results from the electrochemical measurements displayed good cycling stability and asymmetric capacitance behavior (retaining 92.8% after 5000 cycles). The unique structure of the synthesized Ni-MOF attributes to the excellent SC performance. The structure comprises microplates that are many layered. The diffusion of ions and electrolytes is greatly improved as the layered structure contains thousands of nanochannels.

14.3.1 CO_2 fixation

CO_2 is one of the naturally plentiful C1 feedstocks. The capture of CO_2 and its transformation into precious chemicals [cyclic carbonates (CCs), formic acid, substituted urea, dimethyl carbonate, etc.] have aroused much attention in recent times [59,60].

The CCs are vital reactants for the manufacture of ethylene glycol, as intermediates for synthesizing polymeric materials and precursor of polycarbonates in various industries such as pharmaceuticals, dye [61]. It also helps in reducing the quantity of CO_2 present in the environment. Consequently, it is very important to synthesize catalysts for converting CO_2 into CCs. Therefore synthesizing heterogeneous catalysts based on MOFs should be pursued with vigor. MOFs offer some versatile structural features such as crystalline, porous, flexible, and composition can be tuned, thereby offering an important platform for the further investigation on interaction existing between the MOFs and reactants as well as the dynamics of the catalytic reaction.

MOFs have been used in various catalytic applications [62] and proved to be outstanding heterogeneous catalysts in several organic transformations [63]. In recent times, synthesis of CC using MOFs that act as an excellent catalyst (Fig. 14.3) and capture of CO_2 and sequestration (CCS) has been widely reported in a large number of published reports [64].

The adsorption studies showed that the capacity can be enhanced through (1) the proper design of the link (amino-functionalized MOFs, those containing N and F in the linker), (2) hybrid composition (MOF-CNF and MOF-templated carbon), and in some cases (3) by the creation of open metal sites [65]. Han et al. in 2009 employed a two-phase catalytic system MOF-5/n-Bu_4NBr at 323K to synthesize CC. The catalyst exhibited stability for three cycles, and it took 6 hours for the reaction to reach completion with a high degree of selectivity [66]. Ever since a number of MOFs and their derivatives have been employed by researchers to synthesize CCs by the reacting epoxides with CO_2. Zhao and fellow researchers used the solvothermal method to synthesize a Cu(II)-MOF by a tetracarboxylate ligand in which acrylamide is incorporated along with Cu(II) ions [67].

The synthesized MOF (Fig. 14.4) contains nitrogen groups that can be easily accessed as well as unsaturated metal coordination sites making it a

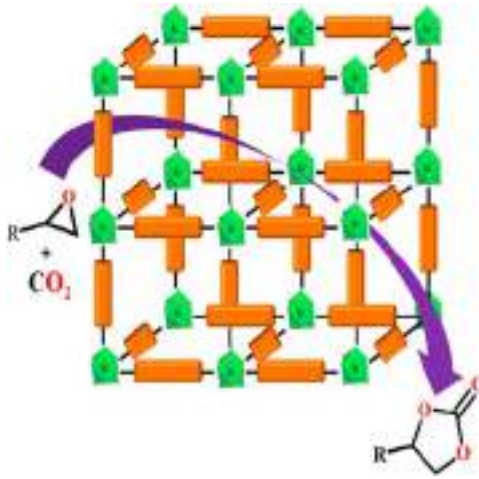

FIGURE 14.3 Schematic representation for cycloaddition reaction between CO_2 and epoxide to cyclic by MOF [64]. *MOF*, Metal-organic framework.

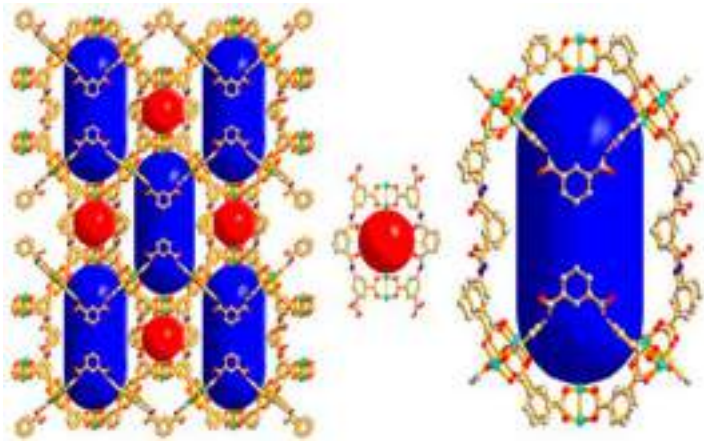

FIGURE 14.4 Perspective views of the Cu(II)-MOF having two types of pores (*blue* and *red*) and are decorated with unsaturated copper metal sites and acylamide groups. *MOF*, Metal-organic framework. *Reproduced with permission from Li P-Z, Wang X-J, Liu J, Phang HS, Li Y, Zhao Y. Highly effective carbon fixation via catalytic conversion of CO_2 by an acylamide-containing metal organic framework. Chem Mater 2017;29:9256−61, Copyright 2017 American Chemical Society.*

suitable contender for selectively adsorbing CO_2. A Schlenk tube was used for the conversion to CC under 1 bar pressure of CO_2 at ambient temperatures for 48 hours utilizing 20 mmol of epoxide and 0.5 g of the cocatalyst, TBAB, and the activated MOF catalyst without the usage of any solvent.

14.4 Wastewater treatment

As the diameter of the pores of the MOF membrane can be adjusted, it displays very good applicability in water treatment technologies. Apart from MOF composite membranes, bare or modified MOF membranes have been widely used in the treatment of wastewater and its regeneration.

14.4.1 Microfiltration

In microfiltration (MF), the driving force that filters and separates by the use of membrane sieving is the differential pressure created across the membrane. Particles, the size ranges of which between 0.1 and 1 mm (e.g., suspended solids, bacteria, some viruses, and large colloids), are retained by MF. At the same time, the macromolecular organic matters and inorganic salts are allowed to penetrate through. The MOF incorporated into the MF membrane is widely employed for membrane MF as the MOF improves the properties of the membrane. For example, Ragab et al. used ZIF-8 to modify the polytetrafluoroethylene double-layer MF membrane and obtained the ZIF-8/PTEE composite membrane, which removed the micropollutants from water [68]. It was displayed by the results that the adsorption capacity rose by nearly 40% results, and water permeability roughly doubled.

14.4.2 Ultrafiltration

As it displays excellent performance in removing the suspended nanoparticles, bacteria, and macromolecules, ultrafiltration membrane has been extensively studied and finds application in the industry, etc. [69]. Owing to this, its modification of ultrafiltration membranes has also aroused a lot of attention. Before combination with polymeric ultrafiltration membrane, other materials can combine with the MOF (e.g., silica, titania, and graphene oxide) to alter significant properties [70,71]. Sun et al. synthesized a novel hollow zeolite imidazole ester skeleton-8/ultrafiltration polysulfone (PSF) (hZIF-8/PSF) membrane by the amalgamation of water-loving zeolitic imidazolate framework-8 (hZIF-8) functionalized by tannic acid with PSF [72]. The results obtained showed that the water permeability of the hZIF-8/PSF UF membrane was 2.8-fold of the PSF membrane, along with maintaining antifouling properties along with good rejection.

14.4.3 Nanofiltration and organic solvent nanofiltration

One of the budding fields in the membrane separation technology is nanofiltration (NF), which is reverse osmosis (RO) carried out at low pressure. Its performance to separate particles lies in between ultrafiltration and RO as it permits only some inorganic salts and some solvents to pass through the membrane to attain

separation. As this process is efficient in environmental applications, it has been used to a great extent for water treatment. Furthermore, organic solvent NF has emerged as an NF separation technology that has extended the application of membranes, that is, it has been used not only for the treatment of water but also for concentrating and filtering organic solutions.

A new kind of MOF membrane was synthesized by Golpour and Pakizeh for the treatment of kinetic hydrate inhibitor [73]. The results showed that there was an enhancement in the antifouling properties as well as the hydrophilic nature of the MOF composite membrane. The MOF composite membrane that performed the best exhibited 50% greater permeation flux than the pristine polymeric membrane, whereas the rejection remained almost the same at 96. Yuan et al. were the first ones to synthesize a new pure ZIF-300 MOF membrane for removing heavy metal ions from wastewater [74]. The prepared ZIF-300 membrane showed high stability energy and water permeability was 39.2 L m^{-2} h^{-1}, while it exhibited a rejection rate of 99.21% for $CuSO_4$. It is expected that in the near future, these pure ZIF-300 membranes shall be used for the removing heavy metals from wastewater.

14.4.4 Reverse osmosis and forward osmosis

The most dominant technique based on the membrane for desalinization is RO. In this technique a pressure greater than that of the osmotic pressure is added, which causes the water to permeate against the osmotic gradient. Conversely, in the process of forward osmosis (FO), which is a considerably newer separation technology based on a membrane, there is diffusion down the osmotic gradient. Zr-MOF (i.e., UiO-66) polycrystalline membranes on alumina hollow fiber were first synthesized by Li group in situ solvothermal to produce the pure phase for desalination in 2015. To assess the performance of desalination of the membranes, five dissimilar aqueous brine solutions (containing KCl, NaCl, $CaCl_2$, $MgCl_2$, or $AlCl_3$) having the same concentration (0.20 wt.%) were employed as feeds in order to assess the desalinization performance of the membranes. It was evident from the results that the membrane showed outstanding multivalent ion repulsion (e.g., Ca^{2+} was 86.3%, Mg^{2+} was 98.0%, and Al^{3+} was 99.3%) and superior permeability (0.28 L m^{-2} h^{-1} bar^{-1} lm) [75]. An ultrathin and pure UiO-66-NH_2 film on the alumina surface was synthesized by Xu et al., which was effective in modulating the cation selectivity, and the cation separation performance was the highest to be reported that ever was achieved ($Na^+/Mg^{2+} > 200$ and $Li^+/Mg^{2+} > 60$). For desalinization applications, this is projected to become an extremely efficient RO membrane [76]. Recently, MOF membranes having a pore size that can be adjusted as well as good compatibility have been used widely in many applications.

The high selective and permeable nature of water-stable MOF membranes plays a vital role especially in wastewater treatment and water regeneration applications, which are membrane-based liquid-phase separation techniques.

14.5 Drug delivery

Recently, there has been a rapid development in the area of nanotechnology and nanomedicine, and a lot of labor has been made to build up a platform that can release a drug in a controlled manner to decrease the side effects as well as improve the therapeutic efficiency [77,78]. MOFs have many unique properties that make it a good contender for use in drug delivery systems. Their high porosity and large surface area are advantageous for improving the efficiency to load the drugs or guest molecules. The MOFs are easy to be functionalized, have good biocompatibility, and are soluble in water and biodegradable. This can lead to an improvement in the bioavailability and effectiveness of the drug in the body. Various interactions such as hydrogen bonds, van der Waals forces, π−π effect between aromatic rings, electrostatic interactions, coordination bonds, and covalent bonds, cause the drugs to chemically conjugate or physically encapsulate within the carriers [79−81]. There are several methods by which the biomolecules can be incorporated within the MOFs, including surface attachment, covalent linkage, pore encapsulation [82], and in situ encapsulation, which lead to the formation of bio-MOF (metal−biomolecule frameworks).

As the MOF is exceptional in encapsulating, it becomes an exclusive platform for loading drugs. A number of drugs have been incorporated into MOFs such as DOX, 5-Fu (5-fluorouracil) [83], β-estradiol [84], I_2 [85], and NO [86,87]. The major challenges, which are faced when used in biomedical applications, are the in vivo retention and the ineffective release of the drug by the MOF at the tumor site. To triumph over these challenges, various types of stimuli, including pH, GSH, glucose, ATP, ion, light, H_2S, magnetic, and thermal, pressure, have been published [88,89].

A pH-sensitive 3-MA@ZIF-8 for delivering 3-methyladenine (3-MA) with a high loading efficiency (19.798 wt.%) was prepared by Chen et al. [90]. In the initial 4 hours, it was observed by them that 3-MA (40%) was released rapidly in PBS at a pH 6.0, which was closely attributed to the proton-initiated degradation of ZIF-8 NPs. Concurrently, it was revealed by the research that the ZIF-8 strengthened the inhibition of 3-MA, thus preventing the autophagosome from forming. In another study conducted a biomimetic nanoreactor (TPZ-GOx-ZIF-8@erythrocyte membrane (TGZ@eM)) was synthesized by Zhang et al. [91], the basis of which was ZIF-8 employed for starvation activated cancer therapy. It displayed “burst release” behavior along with a high drug-releasing output of 70% within 2 hours at a pH 5.0.

14.5.1 Fuel cells

The central part of energy conversion and storage devices such as fuel cells and metal−air batteries is the oxygen reduction reaction (ORR). To fabricate electrocatalysts with high activity and stability (e.g., metal-free carbonous

materials, single-atom catalysts, and nanocomposites) has been a painstaking challenge for cleaner energy technologies. Recently, MOFs possessing a distinctive flexible structure and active sites that are evenly dispersed have become new precursors that have attracted a lot of attention for synthesizing composite materials based on carbon, finding applicability in several fields, especially in electrochemistry.

In 2012 iron porphyrin on pyridine-functionalized graphene was loaded by Loh's research group to synthesize graphene−metal porphyrin MOF exhibiting high catalytic activity [92]. The results displayed that the prepared material was highly porous and could transfer charge at a fast pace thereby showing an easy $4e^-$ oxygen reduction reaction and thus could be employed directly as a potential cathode free from platinum in alkaline methanol fuel cells. Recently, MOFs and their derivatives have been used as catalysts in electrolytic ORR [93−95].

Guo and his coworkers reported the synthesis of an effective nonprecious metal electrocatalyst $Co@Co_3O_4@C-CM$, the carbon matrix of which was highly ordered on MOF materials. [96]. It could provide better pathways for transport of electrons than pure materials derived from MOF. Wang et al. used synthesized an N-doped MOF material for the preparation of hollow skeleton composites. It was more stable and showed better electrocatalytic activity than the commercial Pt/C catalysts [97].

14.6 Conclusion

In this chapter, we have seen the various MOF families and the numerous applications that they could be used in. The unique properties of MOFs are a result of their large surface area, high porosity, and their adjustable pore size. These properties enable MOFs to be used widely in various application fields such as storage of gas and its separation, drug delivery, catalytic conversion of CO_2 to CCs, medical transportation, wastewater treatment, and energy storage of energy and conversion technologies (such as fuel cells, metal−air batteries, and SCs). We conclude, therefore, that the discovery of MOF has proved to be beneficial to every aspect of our lives today, and it continues to attract the eyeballs of the researchers of our times. There is still a lot of research that has to be undertaken in the area of MOFs in order to improve their applicability in the various fields.

References

[1] Hoskins BF, Robson R. Infinite polymeric frameworks consisting of three dimensionally linked rod-like segments. J Am Chem Soc 1989;111(15):5962−4. Available from: https://doi.org/10.1021/ja00197a079.

[2] Yaghi OM, Li G, Li H. Selective binding and removal of guests in a microporous metal-organic framework. Nature 1995;378(6558):703−6. Available from: https://doi.org/10.1038/378703a0.

[3] Li B, Wen H-M, Zhou W, Chen B. Porous metal-organic frameworks for gas storage and separation: what, how, and why? J Phys Chem Lett 2014;5:3468–79.
[4] Ma S, Zhou H-C. Gas storage in porous metal–organic frameworks for clean energy applications. Chem Commun 2010;46:44–53.
[5] Rodenas T, Luz I, Prieto G, Seoane B, Miro H, Corma A, et al. metal–organic framework nanosheets in polymer composite materials for gas separation. Nat Mater 2014;14:48.
[6] Alezi D, Belmabkhout Y, Suyetin M, Bhatt PM, Weseliński ŁJ, Solovyeva V, et al. MOF crystal chemistry paving the way to gas storage needs: aluminum-based SOC-MOF for CH_4, O_2, and CO_2 storage. J Am Chem Soc 2015;137:13308–18.
[7] Chaikittisilp W, Ariga K, Yamauchi Y. A new family of carbon materials: synthesis of MOF-derived nanoporous carbons and their promising applications. J Mater Chem A 2013;1:14–19.
[8] Rojas S, Carmona FJ, Maldonado CR, Horcajada P, Hidalgo T, Serre C, et al. Nanoscaled zinc pyrazolate metal-organic frameworks as drug-delivery systems. Inorg Chem 2016;55:2650–63.
[9] Orellana-Tavra C, Baxter EF, Tian T, Bennett TD, Slater NKH, Cheetham AK, et al. Amorphous metal–organic frameworks for drug delivery. Chem Commun 2015;51:13878–81.
[10] Horcajada P, Serre C, Maurin G, Ramsahye NA, Balas F, Vallet-Regí M, et al. Flexible porous metal-organic frameworks for a controlled drug delivery. J Am Chem Soc 2008;130:6774–80.
[11] Horcajada P, Chalati T, Serre C, Gillet B, Sebrie C, Baati T, et al. Porous metal–organic framework nanoscale carriers as a potential platform for drug delivery and imaging. Nat Mater 2009;9:172–8.
[12] Yu L, Yang JF, Lou XW. Formation of CoS_2 nanobubble hollow prisms for highly reversible lithium storage. Angew Chem Int Ed 2016;55:13422–6.
[13] Zhang G, Hou S, Zhang H, Zeng W, Yan F, Li CC, et al. High-performance and ultra-stable lithium-ion batteries based on MOF-derived ZnO@ZnO quantum dots/C core-shell nanorod arrays on a carbon cloth anode. Adv Mater 2015;27:2400–5.
[14] Wu D, Guo Z, Yin X, Pang Q, Tu B, Zhang L, et al. Metal-organic frameworks as cathode materials for Li–O_2 batteries. Adv Mater 2014;26:3258–62.
[15] Sun T, Tian B, Lu J, Su C. Recent advances in Fe (or Co)/N/C electrocatalysts for the oxygen reduction reaction in polymer electrolyte membrane fuel cells. J Mater Chem A 2017;5:18933–50.
[16] Yang J, Zhang F, Lu H, Hong X, Jiang H, Wu Y, et al. Hollow Zn/Co ZIF particles derived from core-shell ZIF-67@ZIF-8 as selective catalyst for the semi-hydrogenation of acetylene. Angew Chem Int Ed 2015;54:10889–93.
[17] Ma TY, Dai S, Jaroniec M, Qiao SZ. Metal–organic framework derived hybrid Co_3O_4-carbon porous nanowire arrays as reversible oxygen evolution electrodes. J Am Chem Soc 2014;136:13925–31.
[18] Wang C, deKrafft KE, Lin W. Pt nanoparticles@photoactive metal-organic frameworks: efficient hydrogen evolution via synergistic photoexcitation and electron injection. J Am Chem Soc 2012;134:7211–14.
[19] Wang C, Wang J-L, Lin W. Elucidating molecular iridium water oxidation catalysts using metal-organic frameworks: a comprehensive structural, catalytic, spectroscopic, and kinetic study. J Am Chem Soc 2012;134:19895–908.
[20] Choi KM, Jeong HM, Park JH, Zhang Y-B, Kang JK, Yaghi OM. Supercapacitors of nanocrystalline metal-organic frameworks. ACS Nano 2014;8:7451–7.

[21] Xia W, Mahmood A, Zou R, Xu Q. Metal−organic frameworks and their derived nanostructures for electrochemical energy storage and conversion. Energy Environ Sci 2015;8:1837−66.

[22] Bendi R, Kumar V, Bhavanasi V, Parida K, Lee PS. Metal organic framework derived metal phosphates as electrode materials for supercapacitors. Adv Energy Mater 2016;6:1501833.

[23] Wang L, Feng X, Ren L, Piao Q, Zhong J, Wang Y, et al. Flexible solid-state supercapacitor based on a metal-organic framework interwoven by electrochemically-deposited PANI. J Am Chem Soc 2015;137:4920−3.

[24] Liang Z, Zhao R, Qiu T, Zou R, Xu Q. Metal-organic framework-derived materials for electrochemical energy applications. Energy Chem 2019;1:100001.

[25] Cao XH, Tan CL, Sindoro M, Zhang H. Hybrid micro-/nano-structures derived from metal−organic frameworks: preparation and applications in energy storage and conversion. Chem Soc Rev 2017;46:2660−77.

[26] Mehta J, Bhardwaj N, Bhardwaj SK, Kim KH, Deep A, (Eds.), Recent advances in enzyme immobilization techniques: Metal-organic frameworks as novel substrates. Coord Chem Rev 2016;322:30−40.

[27] Shi C, Wang X, Gao Y, Rong H, Song Y, Liu HJ, et al. Nickel metal-organic framework nanoparticles as electrode materials for Li-ion batteries and supercapacitors. J Solid State Electrochem 2017;21:2415−23.

[28] Wei T, Zhang M, Wu P, Tang Y, Li S, Shen F, et al. POM-based metal-organic framework/reduced graphene oxide nanocomposites with hybrid behavior of battery-supercapacitor for superior lithium storage. Nano Energy 2017;34:205−14.

[29] Lu Y, Li B, Zheng S, Xu Y, Xue H, Pang H. Syntheses and energy storage applications of M_xS_y (M = Cu, Ag, Au) and their composites: rechargeable batteries and supercapacitors. Adv Funct Mater 2017;27:1703949.

[30] Maiti S, Pramanik A, Manju U, Mahanty S. Reversible lithium storage in manganese 1,3,5-benzenetricarboxylate metal−organic framework with high capacity and rate performance. ACS Appl Mater Interfaces 2015;7:16357−63.

[31] Xu Y, Li Q, Xue H, Pang H. Metal-organic frameworks for direct electrochemical applications. Coord Chem Rev 2018;376:292−318.

[32] Ge D, Peng J, Qu G, Geng H, Deng Y, Wu J, et al. Nanostructured Co(ii)-based MOFs as promising anodes for advanced lithium storage. N J Chem 2016;40:9238−44.

[33] Yoon T, Bok T, Kim C, Na Y, Park S, Kim KS. Mesoporous silicon hollow nanocubes derived from metal−organic framework template for advanced lithium-ion battery anode. ACS Nano 2017;11:4808−15.

[34] Liu W, Mi Y, Weng Z, Zhong Y, Wu Z, Wang H. Functional metal−organic framework boosting lithium metal anode performance via chemical interactions. Chem Sci 2017;8:4285−91.

[35] Xu Y, Zheng S, Tang H, Guo X, Xue H, Pang H. Prussian blue and its derivatives as electrode materials for electrochemical energy storage. Energy Storage Mater 2017;9:11−30.

[36] Férey G, Millange F, Morcrette M, Serre C, Doublet M, Grenèche JM, et al. Mixed-valence Li/Fe-based metal−organic frameworks with both reversible redox and sorption properties. Angew Chem Int Ed 2007;46:3259−63.

[37] Zhang L, Zheng S, Wang L, Tang H, Xue H, Wang G, et al. Fabrication of metal molybdate micro/nanomaterials for electrochemical energy storage. Small 2017;13:1700917.

[38] de Combarieu G, Morcrette M, Millange F, Guillou N, Cabana J, Grey CP, et al. Influence of the benzoquinone sorption on the structure and electrochemical performance

of the MIL-53(Fe) hybrid porous material in a lithium-ion battery Chem Mater 2009;21:1602–11.

[39] Combelles C, Ben Yahia M, Pedesseau L, Doublet ML. FeII/FeIII mixed-valence state induced by Li-insertion into the metal-organic-framework Mil53 (Fe): A DFT + U study. J Power Sources 2011;196:3426–32.

[40] Zhang Z, Yoshikawa H, Awaga K. Monitoring the solid-state electrochemistry of Cu (2,7-AQDC) (AQDC = anthraquinone dicarboxylate) in a lithium battery: coexistence of metal and ligand redox activities in a metal–organic framework. J Am Chem Soc 2014;136:16112–15.

[41] Maiti S, Pramanik A, Manju U, Mahanty S. Cu_3 (1,3,5 benzenetricarboxylate)$_2$ metal-organic framework: A promising anode material for lithium-ion battery. Microporous Mesoporous Mater 2016;226:353–9.

[42] Peng Z, Yi X, Liu Z, Shang J, Wang D. Triphenylamine-based metal–organic frameworks as cathode materials in lithium-ion batteries with coexistence of redox active sites, high working voltage, and high rate stability. ACS Appl Mater Interfaces 2016;8:14578–85.

[43] Senthil Kumar R, Raja M, Anbu Kulandainathan M, Manuel Stephan A. Metal organic framework-laden composite polymer electrolytes for efficient and durable all-solid-state-lithium batteries. RSC Adv 2014;4:26171–5.

[44] Liu Q, Yu L, Wang Y, Ji Y, Horvat J, Cheng M, et al. Manganese-based layered coordination polymer: synthesis, structural characterization, magnetic property, and electrochemical performance in lithium-ion batteries. Inorg Chem 2013;52:2817–22.

[45] Zhang Z, Yoshikawa H, Awaga K. Discovery of a "bipolar charging" mechanism in the solid-state electrochemical process of a flexible metal–organic framework. Chem Mater 2016;28:1298–303.

[46] Zhang L, Cheng F, Shi W, Chen J, Cheng P. Transition-metal-triggered high-efficiency lithium ion storage via coordination interactions with redox-active croconate in one-dimensional metal–organic anode materials. ACS Appl Mater Interfaces 2018;10:6398–406.

[47] An T, Wang Y, Tang J, Wang Y, Zhang L, Zheng G. A flexible ligand-based wavy layered metal–organic framework for lithium-ion storage. J Colloid Interface Sci 2015;445:320–5.

[48] Zhang Y, Niu Y, Liu T, Li Y, Wang M, Hou J, et al. A nickel-based metal-organic framework: A novel optimized anode material for Li-ion batteries. Mater Lett 2015;161:712–15.

[49] Liang Z, Qu C, Guo W, Zou R, Xu Q. Pristine metal–organic frameworks and their composites for energy storage and conversion. Adv Mater 2017;1702891.

[50] Qu C, Jiao Y, Zhao B, Chen D, Zou R, Walton KS, et al. Nickel-based pillared MOFs for high-performance supercapacitors: Design, synthesis and stability study. Nano Energy 2016;26:66–73.

[51] Li Q, Zheng S, Xu Y, Xue H, Pang H. Ruthenium based materials as electrode materials for supercapacitors. Chem Eng J 2018;333:505–18.

[52] Li X, Ding S, Xiao X, Shao J, Wei J, Pang H, et al. N,S co-doped 3D mesoporous carbon–$Co_3Si_2O_5(OH)_4$ architectures for high-performance flexible pseudo-solid-state supercapacitors. J Mater Chem A 2017;5:12774–81.

[53] Yan Y, Gu P, Zheng S, Zheng M, Pang H, Xue H. Facile synthesis of an accordion-like Ni-MOF superstructure for high-performance flexible supercapacitors. J Mater Chem A 2016;4:19078–85.

[54] Yang J, Xiong P, Zheng C, et al. Metal–organic frameworks: a new promising class of materials for a high performance supercapacitor electrode. J Mater Chem A 2014;2:16640–4.

[55] Xiong X, Zhou L, Cao W, Liang J, Wang Y, Hu S, et al. Metal−organic frameworks based on halogen-bridged dinuclear-Cu-nodes as promising materials for high performance supercapacitor electrodes. Cryst Eng Commun 2017;19:7177−84.
[56] Yang F, Li W, Tang B. Facile synthesis of amorphous UiO-66 (Zr-MOF) for supercapacitor application. J Alloy Compd 2018;733:8−14.
[57] Gao Y, Wu J, Zhang W, Tan Y, Zhao J, Tang B. The electrochemical performance of SnO_2 quantum dots@zeolitic imidazolate frameworks-8 (ZIF-8) composite material for supercapacitors. Mater Lett 2014;128:208−11.
[58] Jiao Y, Pei J, Yan C, Chen D, Hu Y, Chen G. Layered nickel metal−organic framework for high performance alkaline battery-supercapacitor hybrid devices. J Mater Chem A 2016;4:13344−51.
[59] Sakakura T, Saito Y, Okano M, Choi JC, Sako T. Selective conversion of carbon dioxide to dimethyl carbonate by molecular catalysis. J Org Chem 1998;63:7095−6.
[60] Darensbourg DJ, Holtcamp MW. Catalysts for the reactions of epoxides and carbon dioxide. Coord Chem Rev 1996;153:155−74.
[61] Clements JH. Reactive applications of cyclic alkylene carbonates. Ind Eng Chem Res 2003;42:663−74.
[62] Fujita M, Kwon YJ, Washizu S, Ogura K. Preparation, clathration ability, and catalysis of a two-dimensional square network material composed of cadmium(II) and 4,40-bipyridine. J Am Chem Soc 1994;116:1151−2.
[63] Farrusseng D, Aguado S, Pinel C. Metal-organic frameworks: opportunities for catalysis. Angew Chem Int Ed 2009;48:7502−13.
[64] Kathalikkattil AC, Babu R, Tharun J, Roshan R, Park D-W. Advancements in the conversion of carbon dioxide to cyclic carbonates using metal organic frameworks as catalysts. Catal Surv Asia 2015;19:223.
[65] Sumida K, Rogow DL, Mason JA, McDonald TM, Bloch ED, Herm ZR, et al. Carbon dioxide capture in metal-organic frameworks. Chem Rev 2012;112:724−81.
[66] Song J, Zhang Z, Hu S, Wu T, Jiang T, Han B. MOF-5/n-Bu4NBr: an efficient catalyst system for the synthesis of cyclic carbonates from epoxides and CO_2 under mild conditions. Green Chem 2009;11:1031−6.
[67] Li P-Z, Wang X-J, Liu J, Phang HS, Li Y, Zhao Y. Highly effective carbon fixation via catalytic conversion of CO_2 by an acylamide-containing metal organic framework. Chem Mater 2017;29:9256−61.
[68] Ragab D, Gomaa HG, Sabouni R, Salem M, Ren M, Zhu J. Micropollutants removal from water using microfiltration membrane modified with ZIF-8 metal organic frameworks (MOFs). Chem Eng J 2016;300:273−9.
[69] Wang Q, Samitsu S, Ichinose I. Ultrafiltration membranes composed of highly cross-linked cationic polymer gel: the network structure and superior separation performance. Adv Mater 2011;23:2004−8.
[70] Yang S, Zou Q, Wang T, Zhang L. Effects of GO and MOF@GO on the permeation and antifouling properties of cellulose acetate ultrafiltration membrane. J Membr Sci 2019;569:48−59.
[71] Campbell J, Burgal JDS, Szekely G, Davies RP, Braddock DC, Livingston A. Hybrid polymer/MOF membranes for Organic Solvent Nanofiltration (OSN): Chemical modification and the quest for perfection. J Membr Sci 2016;503:166−76.
[72] Sun HZ, Tang BB, Wu PY. Hydrophilic hollow zeolitic imidazolate framework-8 modified ultrafiltration membranes with significantly enhanced water separation properties. J Membr Sci 2018;551:283−93.

[73] Golpour M, Pakizeh M. Preparation and characterization of new PA-MOF/PPSU-GO membrane for the separation of KHI from water. Chem Eng J 2018;345:221–32.
[74] Yuan J, Hung W-S, Zhu H, Guan K, Ji Y, Mao Y, et al. Fabrication of ZIF-300 membrane and its application for efficient removal of heavy metal ions from wastewater. J Membr Sci 2019;572:20–7.
[75] Liu XL, Demir NK, Wu ZT, Li K. Highly water-stable zirconium metal–organic framework UiO-66 membranes supported on alumina hollow fibers for desalination. J Am Chem Soc 2015;137:6999–7002.
[76] Xu TT, Shehzad MA, Yu DB, Li QH, Wu B, Ren XM, et al. Highly cation permselective metal–organic framework membranes with leaf-like morphology. Chem Sus Chem 2019;12:2593–7.
[77] Lou XY, Li YP, Yang YW. Gated materials: installing macrocyclic arenes-based supramolecular nanovalves on porous nanomaterials for controlled cargo release. Biotechnol. J. 2019;14(1):e1800354. Available from: https://doi.org/10.1002/biot.201800354.
[78] Li Z, Song N, Yang Y-W. Stimuli-responsive drug-delivery systems based on supramolecular nanovalves. Matter 2019;1(2):345–68. Available from: https://doi.org/10.1016/j.matt.2019.05.019.
[79] Lin SX, Pan WL, Niu RJ, Liu Y, Chen JX, Zhang WH, et al. Effective loading of cisplatin into a nanoscale UiO-66 metal-organic framework with preformed defects. Dalton Trans 2019;48(16):5308–14. Available from: https://doi.org/10.1039/c9dt00719a.
[80] Nezhad-Mokhtari P, Arsalani N, Javanbakht S, Shaabani A. Development of gelatin microsphere encapsulated Cu-based metal-organic framework nanohybrid for the methotrexate delivery. J Drug Deliv Sci Technol 2019;50:174–80. Available from: https://doi.org/10.1016/j.jddst.2019.01.020.
[81] Xue Z, Zhu M, Dong Y, Feng T, Chen Z, Feng Y, et al. An integrated targeting drug delivery system based on the hybridization of graphdiyne and MOFs for visualized cancer therapy. Nanoscale 2019;11(24):11709–18. Available from: https://doi.org/10.1039/c9nr02017a.
[82] Ke X, Song XQ, Qin NQ, Cai YR, Ke F. Rational synthesis of magnetic Fe_3O_4@MOF nanoparticles for sustained drug delivery. J Porous Mater 2019;26(3):813–18. Available from: https://doi.org/10.1007/s10934-018-0682-4.
[83] Zhang W, Ma YB, Li YA, Wang HP. A low cytotoxic porous zinc-adeninate metal-organic framework carrier: pH-triggered drug release and anti-breast cancer study. J Iran Chem Soc 2019;16(1):65–71. Available from: https://doi.org/10.1007/s13738-018-1481-1.
[84] Ranjbar M, Pardakhty A, Amanatfard A, Asadipour A. Efficient drug delivery of beta-estradiol encapsulated in Zn-metal-organic framework nanostructures by microwave-assisted coprecipitation method. Drug Des Dev Ther 2018;12:2635–43. Available from: https://doi.org/10.2147/DDDT.S173324.
[85] Au-Duong AN, Lee CK. Iodine-loaded metal organic framework as growth triggered antimicrobial agent. Mater Sci Eng C—Mater Biol Appl 2017;76:477–82. Available from: https://doi.org/10.1016/j.msec.2017.03.114.
[86] Pinto RV, Antunes F, Pires J, Graca V, Brandao P, Pinto ML. Vitamin B3 metal-organic frameworks as potential delivery vehicles for therapeutic nitric oxide. Acta Biomater. 2017;51:66–74. Available from: https://doi.org/10.1016/j.actbio.2017.01.039.
[87] Wan SS, Zeng JY, Cheng H, Zhang XZ. ROS-induced NO generation for gas therapy and sensitizing photodynamic therapy of tumor. Biomaterials 2018;185:51–62. Available from: https://doi.org/10.1016/j.biomaterials.2018.09.004.
[88] Cai W, Wang J, Chu C, Chen W, Wu C, Liu G. Metal-organic framework-based stimuli-responsive systems for drug delivery. Adv Sci 2019;6(1):1801526. Available from: https://doi.org/10.1002/advs.201801526.

[89] Yao J, Liu Y, Wang J, Jiang Q, She D, Guo H, et al. On-demand CO release for amplification of chemotherapy by MOF functionalized magnetic carbon nanoparticles with NIR irradiation. Biomaterials 2019;195:51–62. Available from: https://doi.org/10.1016/j.biomaterials.2018.12.029.

[90] Chen X, Tong R, Shi Z, Yang B, Liu H, Ding S, et al. MOF nanoparticles with encapsulated autophagy inhibitor in controlled drug delivery system for antitumor. ACS Appl Mater Interfaces 2018;10(3):2328–37. Available from: https://doi.org/10.1021/acsami.7b16522.

[91] Zhang L, Wang Z, Zhang Y, Cao F, Dong K, Ren J, et al. Erythrocyte membrane cloaked metal-organic framework nanoparticle as biomimetic nanoreactor for starvation-activated colon cancer therapy. ACS Nano 2018;12(10):10201–11. Available from: https://doi.org/10.1021/acsnano.8b05200.

[92] Jahan M, Bao Q, Loh KP. Electrocatalytically active graphene-porphyrin MOF composite for oxygen reduction reaction. J Am Chem Soc 2012;134:6707–13.

[93] Xia W, Li J, Wang T, Song L, Guo H, Gong H, et al. The synergistic effect of Ceria and Co in N-doped leaf-like carbon nanosheets derived from a 2D MOF and their enhanced performance in the oxygen reduction reaction. Chem Commun 2018;54:1623–6.

[94] Ye L, Chai G, Wen Z. Zn-MOF-74 derived N-doped mesoporous carbon as pH-universal electrocatalyst for oxygen reduction reaction. Adv Funct Mater 2017;27:1606190.

[95] Pandiaraj S, Aiyappa HB, Banerjee R, Kurungot S. Post modification of MOF derived carbon via g-C_3N_4 entrapment for an efficient metal-free oxygen reduction reaction. Chem Commun 2014;50:3363–6.

[96] Xia W, Zou R, An L, Xia D, Guo S. A metal–organic framework route to in situ encapsulation of Co@Co_3O_4@C core@bishell nanoparticles into a highly ordered porous carbon matrix for oxygen reduction. Energy Environ Sci 2015;8:568–76.

[97] Xia BY, Yan Y, Li N, Wu HB, Lou XW, Wang X. A metal–organic framework-derived bifunctional oxygen electrocatalyst. Nat Energy 2016;1:15006.

Chapter 15

Metal-organic frameworks as chemical reaction flask

Rakesh Kumar Ameta[1] **and Parth Malik**[2]

[1]*Department of Chemistry, Sri M M Patel Institute of Sciences and Research, Kadi Sarva Vishwavidhyalaya, Gandhinagar, Gujarat, India,* [2]*School of Chemical Sciences, Central University of Gujarat, Gandhinagar, India*

15.1 Introduction to metal-organic frameworks

Metal-organic frameworks (MOFs) are the structural combination of organic and inorganic moieties produced by various synthetic methods and approaches. These hybrid products are fabricated by connecting metallic units that are often called secondary building units (SBUs) and organic moiety via covalent approaches, crystalline framework having specific porosity and varying dimensional tenability (Fig. 15.1) [1].

MOFs consist of SBUs in a regular array, binding the linker arms to form a repeating, cage-like structure [2,3]. Fundamental constitution is based on SBU's joining with stiff forms such as square and octahedral instead of the simpler lump with spacer assembly leading to having permanent porosity [4]. The reticular synthesis mechanism is used for preparation, wherein the size and nature of repetitions are varied to manifest larger porosity and unusually ultrahigh openings of pores [5]. After the combining and chemical

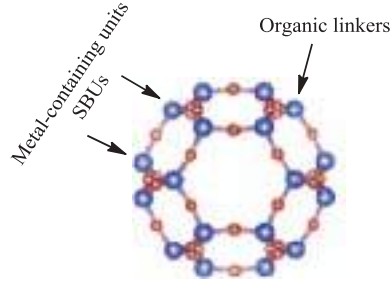

FIGURE 15.1 A metal-organic framework consisting SBUs and organic linkers. *SBUs*, Secondary building units.

Metal-Organic Frameworks for Chemical Reactions. DOI: https://doi.org/10.1016/B978-0-12-822099-3.00015-0

functionalizing of both the moieties, MOFs uphold their fundamental structural and crystalline properties [6–9]. Some eminent MOF assemblies include $Zn_4O(BTE)(BPDC)$, where BTE^{3-} as 4,4-[benzene-1,3,5-triyl-tris (ethyne-2,1-diyl)]tribenzoate and $BPDC^{2-}$ being biphenyl-4,4-dicarboxylate (MOF-210); $Zn_4O(BBC)_2$, with BBC^{3-} being 4,4,4-[benzene-1,3,5-triyl-tris (benzene-4,1-diyl)]tribenzoate (MOF-200); $Zn_4O(BTB)_2$, where BTB^{3-} is 1,3,5-benzenetribenzoate (MOF-177); $Zn_4O(BDC)_3$, where BDC^{2-} is 1,4-benzenedicarboxylate (MOF-5); $Mn_3[(Mn_4Cl)_3(BTT)_8]_2$, where H_3BTT is benzene-1,3,5-tris(1*H*-tetrazole); and $Cu_3(BTC)_2(H_2O)_3$, where H_3BTC is 1,3,5-benzenetricarboxylic acid [10–15]. A porous MOF comprises open channels from where the guest species are able to be removed and reintroduced reversibly, and framework does not tempered. Guest molecules such as lattice and coordinated H_2O or used solvent molecules can be eliminated from these pores without destroying the framework [16]. These steady pores can be used for storing of H_2, CO_2, and similar gases. The study of MOFs has witnessed a considerable growth in research field owing to their broad importance in storing and separation of gases, luminescence, catalysis, nonlinear optics, as well as magnetic attuning [17]. Besides the chemical structure of organic ligand, the architecture of MOFs is greatly influenced by coordination geometries with variable metal ions. The huge majority of reported MOFs' characteristic frameworks comprise transition metal ions containing ligands bound via tetrahedral, square planar, octahedral, or linear, coordination geometries, while higher degrees of coordination are noted for MOFs derived from lanthanide metal ions having up to nine bound ligands [18]. The combinations of metal ion and ligands in MOF build up the new properties providing noteworthy advantage with an infinite number of variations derivable from the framework structures that is unlikely interesting. There are many other advantages such as the surface possessions of channels that can be altered by appending distinct organic substituent onto the organic ligand without changing the framed structure architecture [19]. Primitive research in the "open framework" was concentrated on aluminosilicates and -phosphates [20]. However, present observations suggest that synthetic MOFs are offering strong thermal constancy, comfortably superseding zeolites in terms of surface area and ability of adsorption and storage of small guest molecules [21]. MOFs are also important as sensors and storage cum separation devices, wherein structural constitution confers the specific attributes designated for stimulus specific responses [22]. Major distinctions propelling MOFs better than conventionally employed zeolites (constructed from the organic ligands present in framework backbone) include dimensions, hydrophobicity, exposed functionality; channel reactivity that could be controlled at nano level through synthetic variation of ligand and metal ions during MOF inclusion. Structural and thermal studies of MOFs are swiftly emerging as key research areas nowadays because of their promising multi- and cross-disciplinary applications [23].

15.2 Versatility of metal-organic frameworks

Dynamic modulation of performance attributes has conferred MOFs with manifold robust as well as energy in form of electrochemical and different catalytic processes (Fig. 15.2) [24]. Apart from straight applications, MOFs are swiftly being preferred as exclusive precursors for developing functionalized inorganic materials and their composites providing higher flexibility [25,26].

Researchers are keenly exploring the MOFs' development mechanism through distinctive metal atoms and organic linkers, capable of selective absorption of specific gases over the tailor-made pockets. The larger surface area imparts special suitability prospects to MOFs for gas sensors having high performance, with tunable adsorption being conferred through varying binding molecular coordinates.

15.3 Metal-organic frameworks as chemical reaction flask

MOFs bear several properties equivalent to those of reaction flask, without disturbing their frameworks where they can be removed and reintroduced reversibly. MOFs are the molecular frameworks with high accuracy to reciprocate the porosity even at the nanoscale extent. These molecular segments have caught attention for the past several years as a consequence of their selective accommodation of guest moieties into cavities as per the matched properties, holding a tempting consideration for heterogeneous catalysis [15]. We may imagine surface of MOFs as being constituted of functional centers limited inside a porous network, which diffuses reagents and products without any constraint. Emergence of MOFs enfolds significant research advancements, vis-a-vis, productive supports in the catalytic processes (as heterogeneous catalysis), well proven by the depth of past decade publications. The outstanding porosity and supreme grade tenability create a

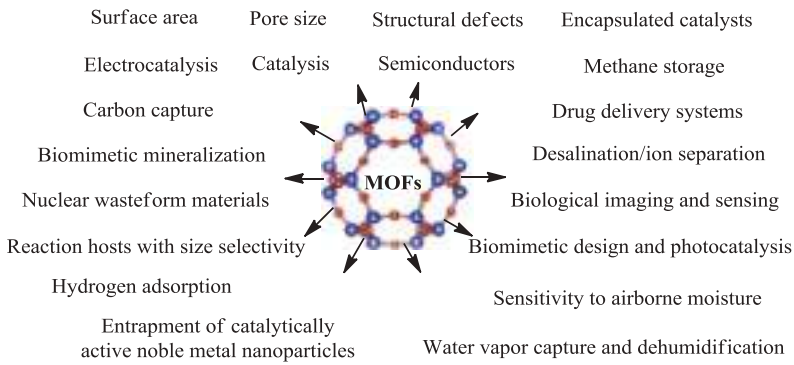

FIGURE 15.2 Versatile applicability of MOFs. *MOFs*, Metal-organic frameworks.

possibility for molecular control of functions through design modulations. With the crystalline property, MOFs facilitate the investigation of functional sites distribution within the structure. MOFs exhibit a balanced mix of porosity and crystallinity, resulting in the ability to fill the gap between micro- and mesoporous compounds [21–25]. There are immense possibilities for profitable uses of such resources in heterogeneous catalysis process. At present, the MOFs have reduced the time for catalytic processes and it is sensible that MOFs can provide even more well-organized solutions for problems being encountered in organic chemistry and modern organometallic catalytical processes. Heterogeneous catalysis processes depending on MOFs are rapidly emerging where the distinct structure of MOFs enables a significant design of catalytic or functional centers. Due to this MOFs are being discovered for solid–gas-phase catalysis to manufacture commodity-based chemicals.

15.4 Utility of metal-organic framework as chemical reaction flask

The micro–mesoporous crystalline nature of MOFs depends on the nature of linking moieties such as organic and inorganic nodes. The constitutive metal nodes and linkers act as hosts to hold guests for performing catalytic activities [27,28]. MOFs act as chemical reaction flask (CRF) due to coordinative unsaturated metal centers and functional linkers having functional groups associated with metal centers or linkers by direct synthetic roots. These can also be attached to the active invitee species such as complexes, metal nanoparticles, and polyoxometalates encapsulated in the pores (Fig. 15.3) [28].

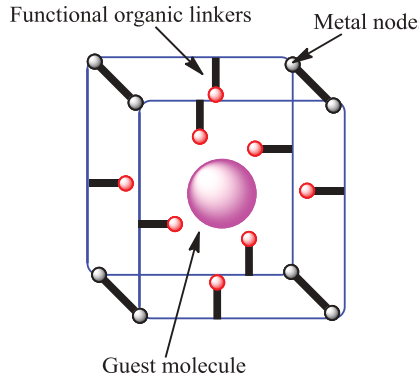

FIGURE 15.3 Features describing MOFs a chemical reaction flask. *MOFs*, Metal-organic frameworks.

15.4.1 Metal-organic framework as chemical reaction flask for the conversion of syngas to hydrocarbons

MOFs of Fe, Co, and Ru have been demonstrated significant for syngas conversion into hydrocarbons, an alternative to meet mounting gasoline demands [29]. Co-based MOFs are suitable as CRF for synthesizing long-chain hydrocarbons (Fig. 15.4) [30].

15.4.2 Metal-organic framework as chemical reaction flask for CO_2 hydrogenation

The CO_2 is used as a new source of carbon, which is an attractive point of view from economic and environmental impact considerations. Many heterogeneous catalysts of MOFs based on Ru, Ir, Co, Fe, and Mn complexes [31–36] hydrogenate CO_2 into formate under alkaline environment, subsequent to immobilization of CO_2 sources on MOFs. For instance, the entrapping of a (tBuPNP)Ru(CO)HCl complex [tBuPNPis 2,6-bis((ditertbutylphosphino)methyl)pyridine] into a Zr-MOF enables CO_2 hydrogenation to formate (Fig. 15.5) [37].

15.4.3 Metal-organic framework as chemical reaction flask for CO_2 cycloaddition

Numerous reactions that conventionally carried out with homogeneous catalysis process can be enthused for solid–gas-phase and evolves a green solvent-free mechanism. The formation of cyclic organic carbonates via epoxide rearrangement and concurrent CO_2 cycloaddition is a potential approach to exploit CO_2 feedstock ability [38]. Commercially such reaction is carried out using a catalyst such as quaternary ammonium halides that yields cyclic carbonate as a solvated product [39]. For instance, the activation of nucleophilic sites or epoxide is carried out by the Lewis acids such as *metallo-salen* complexes as reaction catalysts [40]. A halide anion is generally concerned and replaced by oxygen on carbonate for ring-closing before adding to epoxide for ring-opening. Therefore, with the halide salt (as a

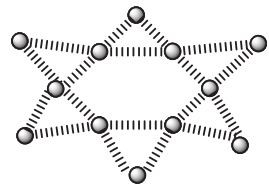

MIL-68

FIGURE 15.4 MOFs (MIL-68 [29]) for the conversion of syngas to hydrocarbons. *MOFs*, Metal-organic frameworks.

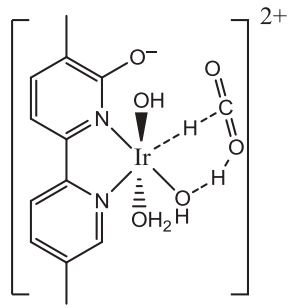

FIGURE 15.5 MOFs as CRF for CO_2 hydrogenation. *CRF*, Chemical reaction flask; *MOFs*, metal-organic frameworks.

cocatalyst), metal-centered MOFs are required to facilitate CO_2 cycloaddition, also known as an MOF-catalyzed cycloaddition [41]. Such MOFs as catalysts are highly active to form cyclic carbonates through catalytic process [42]. It is highly needed to develop both CO_2 activation and epoxide activation centers within the same nano-cavity of such MOFs to associate separate catalytic components within one system [43]. For CO_2 activation the MOFs of derivatives of Lewis base as linkers with $-NH_2$, $-OH$, or $-S=O$ as active sites were reported by Cao and colleagues. Apart from this, for epoxide activation the MOFs, including acidic site associated with the SBU and metallo-ligand, were reported by the same research group [44]. Such MOFs were found to be efficient up to 100% CO_2 cycloaddition as well as epoxidation. Such cycloaddition and epoxidation can be possibly moved to solid−gas-phase for incessant operation because in such reaction there is no need of cocatalyst. A high epoxide yield more than >99% was found using immobilized ionic polymer into cavity of MOF reported by Meili and associates [45]. Reaction between epoxide and CO also inculcates interest for designing cyclic compounds. The In(III) MOFs with N-donor ligands and carboxylic acids are employed as solid catalyst in CO_2-epoxide cycloaddition, where one-dimensional MOFs having unsaturated metal centers promise better catalytic efficiency than the two-dimensional (2D) and three-dimensional (3D) MOFs [46] (Fig. 15.6).

15.4.4 Metal-organic framework as chemical reaction flask for methane conversion

Methane (CH_4) is a cost-effective, plentiful C source, existing as a naturally available gas. Presently, the usefulness of CH_4 endows significance in chemical synthesis because it has ability to convert itself into syngas. Direct incomplete CH_4 oxidation to chemical compounds such as CH_3OH is one of the very useful organic compounds for carrying several organic reactions and also used as fuel [37]. The functionalization of CH_4 through catalytical

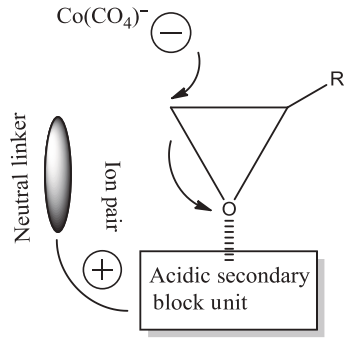

FIGURE 15.6 MOFs as cooperative ion pair for CO_2 cycloadditions. *MOFs*, Metal-organic frameworks.

process is one of the great interests of researchers as partially oxidized product of methane has the higher reactivity and less intrinsic reactivity. In biological processes the partial CH_4 oxidation to CH_3OH is carried out by methane monooxygenases using Cu or Fe clusters as active centers [37]. Similarly the Fe and Cu centers steadied in zeolites are widely used for the oxidation of CH_4 to CH_3OH [36,47]. Such clustering of Cu in zeolites has attracted the scientists to pay attention because the manufacturing of methanol has been carried out using water as an oxidant, though the active Cu site is not completely defined to find out the mechanism of such reaction or oxidation [48,49]. Because of having better structural control and greater diversity than zeolites, MOFs are conferred with an ability to resolve active catalytic sites, ambiguities. In addition, modulation of catalytic site microenvironment decisively facilitates easier and efficient methanol desorption, providing relief from concurrent risks of overoxidation alongside enabling desired mimicking of natural enzymes. For instance, Long and colleagues have used N_2O as an oxidant and MOF such as $Fe_{0.1}Mg$(dobdc), which is a mixed assembly of Fe/Mg for oxidizing ethane to ethanol [50]. Interestingly, here the diluted Fe centers are with another metal that is redox inactive used to gain high selectivity in both systems. This is quite understandable that active sites with high density are needed for avoiding and getting rid of overoxidation before product desorption. To overcome such thing a specific spin state of isolated non-heme Fe can be applied, an alternative clarification for selectivity [50]. In a notable effort, Xiao and associates have made an assembly by immobilizing Cu clusters into an MOF for the interconversion of methane to methanol [50]. Such clustering of the Cu was noted for viaduct neighboring SBUs, via ensuring a need of proposed local structure. In this context, the catalytic functionalization of methane has recently been studied via borylation [51]. For the same purpose an MOF-immobilized Ir catalyst was developed by Lin and colleagues, used previously for CH_4 borylation, reported by Cook et al. [52]. The retrieval of mono-borylated product was

possible substantially because of the shape selectivity of the MOF channel [53]. In natural gas, besides CH_4, C_2H_6 and propane are abundant. Owing to this, the synthesis of olefins from light alkanes was done as the light alkanes were having good feedstock of carbon, and the process is known as alkene dehydrogenation [54]. The oxidative dehydrogenation is enabled via anaerobic process alongside attendant release of H_2, besides being an aerobic process with formation of H_2O [55].

15.4.5 Metal-organic framework as chemical reaction flask for arene oxidative coupling using C−H/C−H activation

The activation reactions of C−H bond are usually provide low turnover numbers and greater catalyst concentrations, owing to an association of less stable catalyst and its activity, projecting a requirement for reusable catalysts specially heterogeneous having stable single-atom-active centers. Significant advances have been made in making Pd-loaded MOFs for this purpose, wherein Pd-loaded Zr-MOFs can be efficient single-site solid hybrid CRF for oxidative coupling of arenes via C−H/C−H activation (Fig. 15.7) [56].

15.4.6 Metal-organic framework as chemical reaction flask for cyanosilylation

As per versatility of MOFs, the 2D square MOF such as $[Cd(bpy)_2](NO_3)_2]$ network is used for catalytic processes, such as shape-dependent aldehyde cyanosilylation [57]. The reaction is carried out in pores depending on the

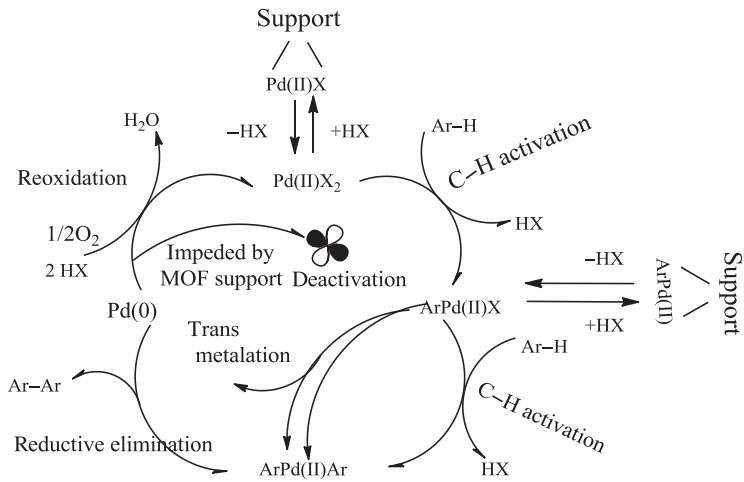

FIGURE 15.7 MOFs as CRF for oxidative coupling of arenes via C−H/C−H activation (X = acetate or 1-propanesulfonate, [56]). *CRF*, Chemical reaction flask; *MOFs*, metal-organic frameworks.

framework cavity size, where b-naphthaldehyde enables preferred products more sterically [57] (Fig. 15.8).

15.4.7 Metal-organic framework as chemical reaction flask for transesterification

The homochiral MOFs with (4*R*,5*R*)-2,2-dimethyl-5-[(4-pyridinylamino)carbonyl]-1,3-dioxolane-4-carboxylic acid ligand having Zn as metal ion are used as CRF for the enantioselective presence of metal complexes in MOF's pores for transesterification [58].

15.4.8 Metal-organic framework as chemical reaction flask for condensation reactions

The Claisen–Schmidt condensation is also carried out via MOFs as CRF; for example, this reaction in toluene between the acetophenone and benzaldehyde has been selectively performed with Fe-based MOFs for the high-yield chalcone [59]. In comparison to other MOFs analogs, the enhanced property of Fe-based MOFs developed from the acidic iron ions is having larger surface areas with high coordination ability (Fig. 15.9).

15.4.9 Metal-organic framework as chemical reaction flask for ring-opening reactions

For the asymmetric ring-opening of an epoxide with amine under solvent-free conditions, the Cu-based chiral MOF with 2,20-dihydroxy-1,10-binaphthalene-5,50-dicarboxylic acid is used [60].

15.4.10 Metal-organic frameworks as chemical reaction flask for Friedel–Crafts reactions

The MOFs as CRF present significant potential in Friedel–Crafts processes for economic and environmental considerations. The Cu-MOFs are being

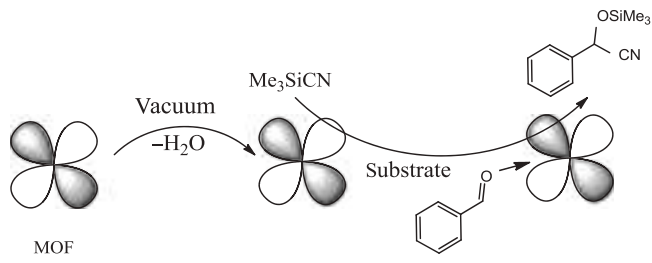

FIGURE 15.8 MOFs as CRF for cyanosilylation [57]. *CRF*, Chemical reaction flask; *MOFs*, metal-organic frameworks.

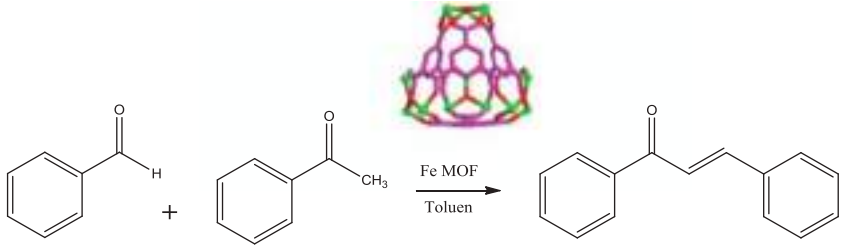

FIGURE 15.9 MOFs as CRF for condensation reactions. *CRF*, Chemical reaction flask; *MOFs*, metal-organic frameworks.

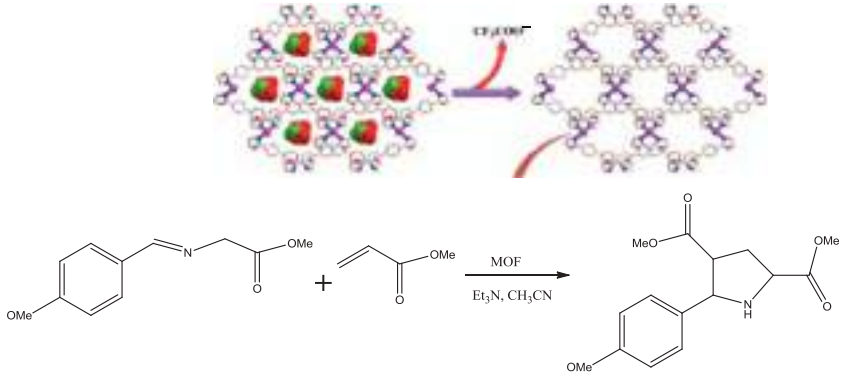

FIGURE 15.10 MOFs as CRF for cycloaddition. *CRF*, Chemical reaction flask; *MOFs*, metal-organic frameworks.

investigated for last decades with unsaturated and available metal centers acting as Lewis acid catalysts in the Friedel–Crafts process like acylation of anisole [61]. Similarly, the sulfonated Zr-terephthalate MOF is also used for the Friedel–Crafts acylation of *p*-xylene [62].

15.4.11 Metal-organic frameworks as chemical reaction flask for cycloaddition

Silver-based MOFs with 4,40-di(2-oxazolinyl)biphenyl ligand have been used as CRF to catalyze imino esters and methyl acrylate, cycloaddition [63] (Fig. 15.10).

15.4.12 Metal-organic frameworks as chemical reaction flask for cross-coupling reactions

CCRs are used to form new C–C and C–heteroatom bonds where the MOFs have shown their applicability as significant interest in the field of

pharmaceutical/medical industry and for obtaining a variety of useful organic materials. MOFs based on Pd, Ni, Ag, and Cu are of great interest because they are relatively stable toward water and air; however, the applicability of such MOFs is limited in industrial area, because their proneness is likely to be aggregated and cumbersome recycling. Using MOFs as entities enabling easier catalyst recovery, several studies have used them in such organic transformations. Pd-, Cu-, Ag-, Eu-, and Nd-based MOFs are being used for cross-coupling reactions [64–66].

15.4.13 Metal-organic frameworks as chemical reaction flasks for Grignard reactions

With the applications of MOFs in various fields, these are also being used in Grignard reactions for the formation of carbon–carbon bonds. For example, in addition, reactions of MOFs of $ZnEt_2$ are providing aromatic aldehydes to develop secondary alcohols with chirality as well as activity, and stereoselectivity exceeding their homogeneous complements. On the basis of XRD predicted structure, it is recommended that merely one-third of binaphthol sites are modified with $Ti(OiPr)_4$, with remaining two-thirds may even render inaccessible [67] (Fig. 15.11).

15.4.14 Metal-organic frameworks as chemical reaction flasks for catalytic reactions

MOFs as CRFs offer acid–base centers for synthesizing catalysts with specific site and multifunctions via procedure tandem catalysis in the pores without self-destruction or intermediate isolation [68,69]. Apart from this,

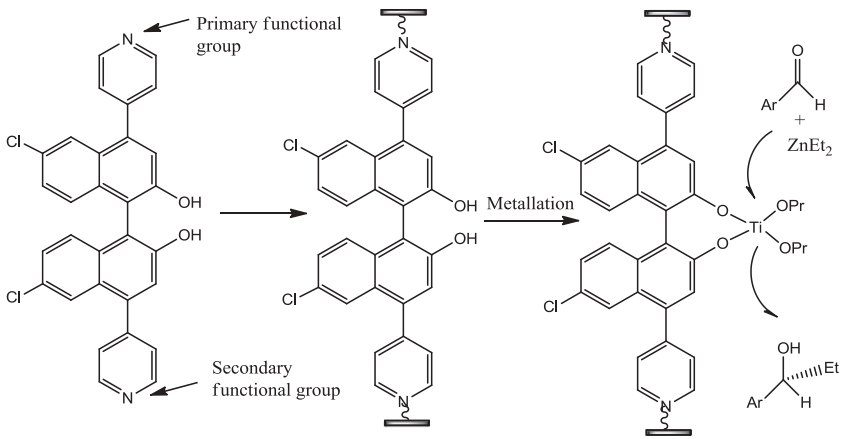

FIGURE 15.11 MOFs as CRF for Grignard reactions. *CRF*, Chemical reaction flask; *MOFs*, metal-organic frameworks.

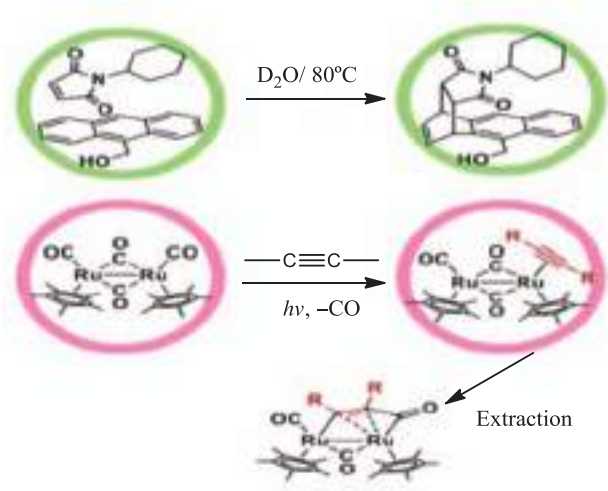

FIGURE 15.12 MOFs as CRF for catalytic reactions. *CRF*, Chemical reaction flask; *MOFs*, metal-organic frameworks.

another advantage of MOFs is their capability of being able to be anchored into countless filters since the functional groups (such as amino, carboxylic, and carbonyl) allow covalent attachment to solid surfaces of the MOFs (Fig. 15.12).

15.4.15 Metal-organic frameworks as chemical reaction flasks for porphyrins

MOFs based on $In(NO_3)_3$ and 4,5-imidazole dicarboxylic acids having large-sized cavities, sufficient to encapsulate porphyrins (Fig. 15.13), are used as network-oriented porphyrin frameworks for adsorption. Such MOF encapsulation makes a contrast with previously reported works of zeolite-encapsulated oxidative catalysis [70–72] as well as Mn (porphyrin) systems [73,74].

15.4.16 Metal-organic frameworks' utilization toward the growth of catalytic clusters or nanoparticles

Recently, MOFs are being used for controlled growth of nanoparticles or catalytic clusters due to their cavities [75–78] and a number of fascinating initial results, chiefly based on metal oxides or metals, have been obtained. It has usually been rather problematic to show that nanoparticles/clusters are actually entrapped in the cavity of well-designed MOFs. Nevertheless, in some instances the conflicting aspect exceeding particle sizes compared to cavities of the single MOF is dimensions. The only clear-cut examples of

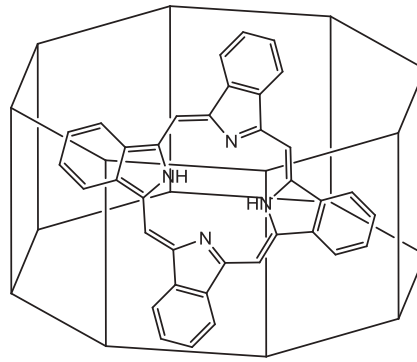

FIGURE 15.13 MOFs as CRF for porphyrins [70–74]. *CRF*, Chemical reaction flask; *MOFs*, metal-organic frameworks.

(exclusively) single cavity encapsulation of well-defined clusters are Keggin-type polyoxometallates inside the rather large MOF cavities [79]. The encapsulation is electrostatic, entailing dislocation of formerly residing fluoride ions.

15.4.17 Metal-organic frameworks as chemical reaction flasks for C–N coupling reactions

A highly porous MOF (Cu-TDPAT) has been developed from a 2,4,6-tris (3,5-dicarboxylphenylamino)-1,3,5-triazine and di-nuclear Cu cluster that is a paddle wheel type is used in conduct of C–N coupling of a broad range of primary and secondary amines with halobenzenes, affording corresponding *N*-arylation compounds in reasonable to excellent extents such as *Ullmann- and Goldberg*-type couplings [80].

15.4.18 Metal-organic frameworks as chemical reaction flasks for self-assembled peptides at interfaces

The artificial motors are the unique innovations, where the cells of oil droplets and camphor are surrounded by surfactants that fuel their motion through Marangoni effect [81–84]. In such motors the release of organic entities makes way for an anisotropic STG (surface tension gradient) around the cells, as a consequence of which, these are accessed within the cells from a low-to-high cohesive energy region. A significant demerit of this is the randomly discharging of organic molecules, which makes them comparatively less efficient for energy transfer. To overcome such hurdles, MOFs are used where a new hybrid-biomimetic motor system was constructing with a diphenylalanine (DPA) peptide and MOF. The peptide loading to MOF assembly

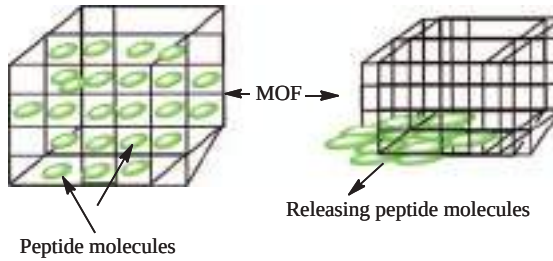

FIGURE 15.14 MOF as an autonomous motor. *MOFs*, Metal-organic frameworks.

ensures simultaneous activities of multiple smaller entities by bringing them together in a specifically defined manner of the coordination assembly, via concurrent bond-breaking rather than being confined within prevailing porous ensembles. Such a provision makes way for isotropic release of guest molecules [85]. Thereby, self-assembling nature of peptides makes way for arranging and releasing guest molecules so as to empower the MOF motors as the released peptides gradually reassemble along the MOF−water interface with much lower entropy. This self-attained ordered texture is driven out of a large STG conferring a vigilant Marangoni effect [86,87] and comparatively higher force toward greater cohesive energy MOF domain (Fig. 15.14).

15.4.19 Metal-organic ionic frameworks as different class of metal-organic frameworks

Not much late, the metal-organic ionic frameworks (MOIF) have established themselves as a significantly distinct domain of MOFs, wherein a combination of surfactants (having cationic quaternary nitrogen as counterion) and anionic inorganic complex is produced through aqueous ion-exchange reaction. MOIF have resilient texture material and biological properties, thereby making them suitable as robust multifunctional molecule [88−91].

15.5 Conclusion

MOFs have rightly emerged as need based on structurally varied entities having significance in multiple domains of chemistry; some exclusive of which are summarized in Table 15.1. The efficient conduct of catalysis by MOFs is due to their manifested exceeding internal surface area, intensive and ordered catalytic sites, and a high adsorption affinity. Homogeneity of channel sizes and functionality of internal channels enable reagent and product size and enantioselectivity. The crucial attributes for MOFs enabled usefulness in driving distinct chemical reactions are the characteristic outcomes of increasing activity (owing to high pore size and surface area), selectivity (making

TABLE 15.1 Reactions for which metal-organic frameworks (MOFs) as chemical reaction flasks.

Sr. no.	MOF	Type of reaction	Ref.
1	Chiral (salen)Mn MOF	Olefin epoxidation	[92]
2	$Cu_3(btc)_2$rearrangement of α-pinene oxide	Cyclization of citronellal	[93]
3	$[Cu_2(BTC)_{4/3}(H_2O)_2]_6[H_nXM_{12}O_{40}] \cdot (C_4H_{12}N)_2$	Hydrolysis of esters	[94]
4	$[Cd(\mu\text{-}Cl)_2]_n$ MOF	Asymmetric catalysis	[95]
5	Zr-terephthalate MOF	Cross-aldol condensation	[96]
6	Zr-metalloporphyrin PCN-222	Oxidation of pyrogallol	[97]
7	Basolite C 300	Friedländer reaction	[98]
8	$[Cu_3(C_9H_3O_6)_2]_4$ $[\{(CH_3)_4N\}_4CuPW_{11}O_{39}H]$	Oxidation of thiols	[99]
9	$Zn_5Cl_4(BTDD)_3$	Olefin polymerization	[100]
10	Fe- and Co-functionalized MOFs	CO_2 reduction	[101]
11	PCN-222/MOF-545	Photooxidation of 2-chloroethyl ethyl sulfide	[102]
12	Porphyrin-based Zr-MOF	Etoxification	[103]
13	Lithium-alkoxide doped Zr-MOF	Self-detoxifying filters	[104]
14	Ni-S electrocatalyst on MOF	Scaffolds' electrochemical hydrogen evolution	[105]
15	InPF-110	Strecker reaction of ketones	[106]
16	$Zr_6O_4(OH)_4(bpydc)_6$	Arene C−H borylation	[107]
17	Hf-NU-1000	1-Hexene polymerization	[108]
18	Hf MOF	Tandem oxidation and functionalization of styrene	[109]
19	Co@NH_2-MIL-125(Ti)	H_2 production	[110]
20	MOOF-based CoP/reduced graphene oxide	Water splitting	[111]
21	Core−shell Pd@IRMOF-3	Nanostructures cascade reactions	[112]

(*Continued*)

TABLE 15.1 (Continued)

Sr. no.	MOF	Type of reaction	Ref.
22	MOF-confined Pd@Co NPs	Hydrolytic dehydrogenation of ammonia borane	[113]
23	$Cu_3(BTC)_2$ aerobic epoxidation of olefins	Oxidation of alcohols	[114]
24	Mo-NU-1000	Cyclohexene epoxidation	[115]
25	Homochiral MOF	Cyanohydrin synthesis	[116]
26	Zr-MOF with Me_2Mg	Hydroboration and hydroamination	[117]
27	Co nanoparticle−embedded carbon@Co_9S_8	Oxygen reduction	[118]
28	N-doped CNT-derived MOF	Oxygen electrocatalyst	[119]
29	Ni−Zr-NU-1000	Gas-phase hydrogenation	[120]
30	Fe-porphyrin MOF	Electrochemical reduction of CO_2	[121]
31	Pd nanocubes@ZIF-8	Hydrogenation of olefins	[122]
32	Hf-NU-1000 CO_2 fixation	Enantioretentive epoxide activation	[123]
33	MIL-101-Cr-$SO_3H \cdot$ Al(III)	Fixed-bed reactions	[124]
34	Mn−Zr MOF	Photocatalytic CO_2 reduction	[125]
35	BINAP-based MOFs	Pauson−Khand reaction between 1,6-enynes and carbon monoxide	[126]

way for need based functionalization), and stability. At present, some major concerns being worked out to improve MOFs' functional performance include the following: (1) diffusion of reagents and products hindering the reaction rates provided the channels are not adequately large, (2) limiting the range of catalyzed reactions in lieu of size-selective working of channels, (3) −3D MOFs attract less usage faithfulness toward catalysis happening on the outer surface owing to the fact that channel catalytic sites are not available for reactions; and (4) the catalysts are seldom recovered due to too small size of MOF particles. Efforts are still in progress to predict the catalytic progress with respect to happening locus alongside using low-energy methods to create assemblies that could, in turn, ensure higher working stability.

Acknowledgment

Authors are highly obliged to suitable working environment and round the clock Internet facility provided by the Central University of Gujarat, India.

References

[1] Yaghi OM, O'Keeffe M, Ockwig NW, Chae HK, Eddaoudi M, Kim J. Reticular synthesis and the design of new materials. Nature 2003;423:705–14.

[2] Hong-Cai Z, Jeffrey Long R, Yaghi OM. Introduction to metal–organic frameworks. Chem Rev 2012;112:673–4.

[3] Mueller U, Schubert M, Teich F, Puetter H, Schierle-Arndta, Pastréa Mueller JU, et al. Metal–organic frameworks—prospective industrial applications. J Mater Chem 2006;16:626–36.

[4] Jacoby M. Metal-organic frameworks for biomedical applications. Chem Eng N 2008;86:13–23.

[5] Eddaoudi M, Kim J, Rosi N, Vodak D, Wachter J, O'Keeffe M, et al. Systematic design of pore size and functionality in isoreticular MOFs and their application in methane storage. Science 2002;295:469–72.

[6] Wang Z, Cohen SM. Postsynthetic covalent modification of a neutral metal–organic framework. J Am Chem Soc 2007;129:12368–9.

[7] Hexiang D, Christian JD, Hiroyasu F, Ricardo BF, John T, Carolyn BK, et al. Multiple functional groups of varying ratios in metal-organic frameworks. Science 2010;327:846–50.

[8] Kinoshita Y, Matsubara I, Higuchi T, Saito Y. The crystal structure of bis(adiponitrilo) copper(I) nitrate. Bull Chem Soc Jpn 1959;32:1221–6.

[9] Yaghi OM, Li H. Hydrothermal synthesis of a metal-organic framework containing large rectangular channels. J Am Chem Soc 1995;117:10401–2.

[10] Furukawa H, Ko N, Go YB, Aratani N, Choi SB, Choi E, et al. Ultra-high porosity in metal-organic frameworks. Science 2010;329:424–8.

[11] Mendoza Cortes JL, Han SS, Goddard WA. High H_2 uptake in Li-, Na-, K-metalated covalent organic frameworks and metal organic frameworks at 298 K. J Phys Chem A 2012;116(6):1621–31.

[12] Rowsell JL, MillwardA R, Park KS, Yaghi OM. Hydrogen sorption in functionalized metal–organic frameworks. J Am Chem Soc 2004;126(18):5666–73.

[13] Rosi NL, Eckert J, Eddaoudi M, Vodak DT, Kim J, OKeeffe M, et al. Hydrogen storage in microporous metal-organic frameworks. Science 2003;300:1127–9.

[14] Dinca M, Dailly A, Liu Y, Brown CM, Neumann DA, Long JR. Hydrogen storage in microporous metal-organic frameworks. J Am Chem Soc 2006;128(51):16876–83.

[15] Cheng ST, Ming SY, Tsui YC, Hsiu CW, Cheng YW, Kuei SC, et al. Characterization of pore structure in metal–organic framework by small-angle x-ray scattering. J Am Chem Soc 2007;129(51):15997–6004.

[16] Batten SR, Champness NR, Chen XM, Garcia Martinez J, Kitagawa S, Hrstrçm L, et al. Terminology of metal–organic frameworks and coordination polymers. Pure Appl Chem 2013;85:1715–24.

[17] Antje H, Irena S, Stefan K. Liquid-phase adsorption on metal-organic frameworks. Adsorption 2011;17:219–26.

[18] Stefan E. Zeolites and catalysis. Synthesis React Appl Angew Chem 2011;50:5425–6.

[19] Rosi NL, Eddaoudi M, Kim J, O'Keeffe M, Yaghi OM. Advances in the chemistry of metal−organic frameworks. CrystEngComm 2002;4:401−4.
[20] Lee J, Farha OK, Roberts J, Scheidt KA, Nguyen ST, Hupp JT. Metal-organic framework materials as catalysts. Chem Soc Rev 2009;38:1450−9.
[21] Furukawa H, Cordova KE, O'Keeffe M, Yaghi OM. The chemistry and applications of metal-organic frameworks. Science 2013;341:1230444.
[22] Cui Y, Li B, He H, Zhou W, Chen B, Qian G. Metal−organic frameworks as platforms for functional materials. Acc Chem Res 2016;49:483−93.
[23] Hendon CH, Rieth AJ, Korzynski MD, Dinca M. Grand challenges and future opportunities for metal-organic frameworks. ACS Cent Sci 2017;3:554−63.
[24] Li M, Eddaoudi M, Keeffe O, Yaghi OM. Design and synthesis of an exceptionally stable and highly porous metal-organic framework. Nature 1999;402:276.
[25] Tranchemontagne DJ, Mendoza-Cortes JL, O'Keeffe M, Yaghi OM. Secondary building units, nets and bonding in the chemistry of metal-organic frameworks. Chem Soc Rev 2009;38:1257−83.
[26] Kitagawa S, Kitaura R, Noro SI. Functional porous coordination polymers. Angew Chem Int Ed 2004;43:2334−75.
[27] Dhakshinamoorthy A, Li Z, Garcia H. Catalysis and photocatalysis by metal organic frameworks. Chem Soc Rev 2018;47:8134−72.
[28] Yuan-Biao H, Jun L, Xu-Sheng W, Rong C. Multifunctional metal−organic framework catalysts: synergistic catalysis and tandem reactions. Chem Soc Rev 2017;46:126−57.
[29] Dugulan M, de Jong AI. Supported iron nanoparticles as catalysts for sustainable production of lower olefins. Science 2012;335:835−43.
[30] Rasmus YB, Unni O. Ethene oligomerization in Ni-containing zeolites: theoretical discrimination of reaction mechanisms. ACS Catal 2016;6:1205−14.
[31] Nicholas Jaegers R, Konstantin K, Libor K, Daniel WK, Jian ZH, Yong W, et al. Catalytic activation of ethylene C−H bonds on uniform d8 Ir(I) and Ni(II) cations in zeolites: toward molecular level understanding of ethylene polymerization on heterogeneous catalysts. Catal Sci Technol 2019;9:6570−6.
[32] Himeda Y, Miyazawa S, Hirose T. Interconversion between formic acid and H(2)/CO(2) using rhodium and ruthenium catalysts for CO(2) fixation and H(2) storage. ChemSus Chem 2011;4:487−93.
[33] Hull JF, Himeda Y, Wang WH, Hashiguchi B, Periana R, Szalda DJ, et al. Reversible hydrogen storage using CO_2 and a proton-switchable iridium catalyst in aqueous media under mild temperatures and pressures. Nat Chem 2012;4:383−8.
[34] Jeletic MS, Mock MT, Appel AM, Linehan JC. A cobalt-based catalyst for the hydrogenation of CO_2 under ambient conditions. J Am Chem Soc 2013;135:11533−9.
[35] Albert B, Björn L, Felix G, Christian T, Koichi F, Henrik J, et al. Iron-catalyzed hydrogen production from formic acid. J Am Chem Soc 2010;132:8924−34.
[36] Grant JT, Carrero CA, Goeltl F, Venegas J, Mueller P, Burt SP, et al. Selective oxidative dehydrogenation of propane to propene using boron nitride catalysts. Science 2016;354:1570−3.
[37] Sirajuddin S, Rosenzweig AC. Enzymatic oxidation of methane. Biochemistry 2015;54:2283−94.
[38] North M, Pasquale R. Mechanism of cyclic carbonate synthesis from epoxides and CO_2. Angew Chem 2009;121:2946−54.
[39] Peppel W. Preparation and properties of the alkylene carbonates. J Ind Eng Chem 1958;50:767−70.

[40] Antonio B, Assunta DN, Alfonso G, Stefano M, Carmine C, Sergei V, et al. Novel iron (III) catalyst for the efficient and selective coupling of carbon dioxide and epoxides to form cyclic carbonates. Catal Sci Technol 2015;5:118–23.
[41] Maina JW, Pozo CG, Kong L, Schuutz J, Hill M, Dumeee LF. Metal organic framework based catalysts for CO_2 conversion. Mater Horiz 2017;4:345–61.
[42] Yang DA, Cho HY, Kim J, Yang ST, Ahn WS. CO_2 capture and conversion using Mg-MOF-74 prepared by a sonochemical method. Energy Environ Sci 2012;5:6465–73.
[43] Kuruppathparambil RR, Babu R, Jeong HM, Hwang GY, Jeong GS, Kim MI, et al. A solid solution zeolitic imidazolate framework as a room temperature efficient catalyst for the chemical fixation of CO_2. Green Chem 2016;18:6349–56.
[44] Liang J, Chen RP, Wang XY, Liu TT, Wang XS, Huang YB, et al. Postsynthetic ionization of an imidazole-containing metal–organic framework for the cycloaddition of carbon dioxide and epoxides. Chem Sci 2017;8:1570–5.
[45] Meili D, Robinson WF, Hai-Long J, Omar MY. Carbon capture and conversion using metal–organic frameworks and MOF-based materials. Chem Soc Rev 2019;48:2783–828.
[46] Babu R, Roshan R, Gim Y, Jang YH, Kurisingal JF, Kim DW, et al. Inverse relationship of dimensionality and catalytic activity in CO_2 transformation: a systematic investigation by comparing multidimensional metal–organic frameworks. J Mater Chem A 2017;5:15961–9.
[47] Min BP, Eun DP, Wha-Seung A. Recent progress in direct conversion of methane to methanol over copper-exchanged zeolites. Front Chem 2019;7. Available from: https://doi.org/10.3389/fchem.2019.00514.
[48] Narsimhan K, Iyoki K, Dinh K, Román-Leshkov Y. Catalytic oxidation of methane into methanol over copper-exchanged zeolites with oxygen at low temperature. ACS Cent Sci 2016;2:424–9.
[49] Sushkevich VL, Palagin D, van Bokhoven JA. The effect of the active-site structure on the activity of copper mordenite in the aerobic and anaerobic conversion of methane into methanol. Angew Chem Int Ed 2018;57:8906–10.
[50] Xiao DJ, Bloch ED, Mason JA, Queen WL, Hudson MR, Planas N, et al. Oxidation of ethane to ethanol by N_2O in a metal-organic framework with coordinatively unsaturated iron(II) sites. Net Chem 2014;6:590–5.
[51] Verma P, Vogiatzis KD, Planas N, Borycz J, Xiao DJ, Long JR, et al. Mechanism of oxidation of ethane to ethanol at iron(IV)–oxo sites in magnesium-diluted Fe^2(dobdc). J Am Chem Soc 2015;137:5770–81.
[52] Cook AK, Schimler SD, Matzger AJ, Sanford MS. Catalyst-controlled selectivity in the C-H borylation of methane and ethane. Science 2016;351:1421–4.
[53] Manna K, Zhang T, Lin W. Postsynthetic metalation of bipyridyl-containing metal–organic frameworks for highly efficient catalytic organic transformations. J Am Chem Soc 2014;136:6566–9.
[54] Zhang X, Huang Z, Ferrandon M, Yang D, Robison L, Li P, et al. Catalytic chemoselective functionalization of methane in a metal-organic framework. Nat Catal 2018;1:356–62.
[55] Searles K, Chan KW, Mendes Burak JA, Zemlyanov D, Safonova O, Copéret C. Highly productive propane dehydrogenation catalyst using silica-supported Ga–Pt nanoparticles generated from single-sites. J Am Chem Soc 2018;140:11674–9.
[56] Niels Van V, Steve W, Sachin MC, Pei L, Simon S, Jannick V, et al. Single-site metal–organic framework catalysts for the oxidative coupling of arenes via C–H/C–H activation. Chem Sci 2019;10:3616–22.

[57] Fujita M, Kwon YJ, Washizu S, Ogura K. Preparation, clathration ability, and catalysis of a two-dimensional square network material composed of cadmium(II) and 4,4′-bipyridine. J Am Chem Soc 1994;116:1151–2.
[58] Seo JS, Whang D, Lee H, Jun SI, Oh J, Jeon YJ, et al. A homochiral metal-organic porous material for enantioselective separation and catalysis. Nature 2000;404:982–6.
[59] Dhakshinamoorthy A, Alvaro M, Garcia H. Claisen–Schmidt condensation catalyzed by metal-organic frameworks. Adv Synth Catal 2010;352:711–17.
[60] Tanaka K, Oda S, Shiro M. A novel chiral porous metal–organic framework: asymmetric ring opening reaction of epoxide with amine in the chiral open space. Chem Commun 2008;45:820–2.
[61] Doan HA, Li Z, Farha OK, Hupp JT, Snurr RQ. Theoretical insights into direct methane to methanol conversion over supported dicopperoxonanoclusters. Catal Today 2018;312:2–9.
[62] Dyballa M, Pappas DK, Kvande K, Borfecchia E, Arstad B, Beato P, et al. On how copper mordenite properties govern the framework stability and activity in the methane-to-methanol conversion. ACS Catal 2019;9:365–75.
[63] Elwell CE, Gagnon NL, Neisen BD, Dhar D, Spaeth AD, Yee GM, et al. Copper-oxygen complexes revisited: structures, spectroscopy, and reactivity. Chem Rev 2017;117:2059–107.
[64] Yong-Qing H, Wei-Yin S. Coordination supramolecules with oxazoline-containing ligands. CrystEngComm 2018;20:6109–21.
[65] Groothaert MH, Smeets PJ, Sels BF, Jacobs PA, Schoonheydt RA. Selective oxidation of methane by the bis(μ-oxo)dicopper core stabilized on ZSM-5 and mordenite zeolites. J Am Chem Soc 2005;127:1394–5.
[66] Thacker NC, Lin Z, Zhang T, Gilhula JC, Abney CW, Lin W. Robust and porous β-diketiminate-functionalized metal–organic frameworks for earth-abundant-metal-catalyzed C–H amination and hydrogenation. J Am Chem Soc 2016;138:3501–9.
[67] Wu CD, Lin WB. Heterogeneous asymmetric catalysis with homochiral metal–organic frameworks: network-structure-dependent catalytic activity. Angew Chem Int Ed 2007;46:1075–8.
[68] Shylesh S, Wagener A, Seifert A, Ernst S, Thiel WR. Mesoporous organosilicas with acidic frameworks and basic sites in the pores: an approach to cooperative catalytic reactions. Angew Chem Int Ed 2010;49:184–7.
[69] Grundner S, Luo W, Sanchez-Sanchez M, Lercher JA. Synthesis of single-site copper catalysts for methane partial oxidation. Chem Commun 2016;52:2553–6.
[70] Grundner S, Markovits MAC, Li G, Tromp M, Pidko EA, Hensen EJM, et al. Single-site trinuclear copper-oxygen clusters in mordenite for selective conversion of methane to methanol. Nat Commun 2015;6:7546–54.
[71] Ipek B, Lobo RF. Catalytic conversion of methane to methanol on Cu-SSZ-13 using N_2O as oxidant. Chem Commun 2016;52:13401–4.
[72] Heidari-Golafzani M, Mahboubeh R, Rahmatollah R, Alireza A. Catalytic oxidation of primary and secondary alcohols over a novel TCPP/Zn–Fe2O4@ZnO catalyst. RSC Adv 2015;5:99640–5.
[73] Ipek B, Wulfers MJ, Kim H, Göltl F, Hermans I, Smith JP, et al. Formation of $[Cu_2O_2]^{2+}$ and $[Cu_2O]^{2+}$ toward C-H bond activation in Cu-SSZ-13 and Cu-SSZ-39. ACS Catal 2017;7:4291–303.
[74] Kim Y, Kim TY, Lee H, Yi J. Distinct activation of Cu-MOR for direct oxidation of methane to methanol. Chem Commun 2017;53:4116–19.

[75] Hermes S, Schrter MK, Schmid R, Khodeir L, Muhler M, Tissler A, et al. Metal@MOF: loading of highly porous coordination polymers host lattices by metal organic chemical vapor deposition. Angew Chem Int Ed 2005;44:6237–41.
[76] Muller M, Hermes S, Kahler K, Berg M, Muhler M, Fischer RA. Loading of MOF-5 with Cu and ZnO nanoparticles by gas-phase infiltration with organometallic precursors: properties of Cu/ZnO@MOF-5 as catalyst for methanol synthesis. Chem Mater 2008;20:4576–87.
[77] Sabo M, Henschel A, Frode H, Klemm E, Kaskel S. Solution infiltration of palladium into MOF-5: synthesis, physisorption and catalytic properties. J Mater Chem 2007;17:3827–32.
[78] Schroder F, Esken D, Cokoja M, Berg M, Lebedev OI, Tendeloo GV, et al. Ruthenium nanoparticles inside porous $[Zn_4O(bdc)_3]$ by hydrogenolysis of adsorbed [Ru(cod)(cot)]: a solid-state reference system for surfactant-stabilized ruthenium colloids. J Am Chem Soc 2008;130:6119–30.
[79] Ferey G, Mellot-Draznieks C, Serre C, Millange F, Dutour J, Surble S, et al. A chromium terephthalate-based solid with unusually large pore volumes and surface area. Science 2005;309:2040–2.
[80] Wei L, Wenge Q, Chongwei G, Chuanqiang L, Liyun S, Guangmei B, et al. A copper-based metal-organic framework as an efficient and reusable heterogeneous catalyst for Ullmann and Goldberg type C-N coupling reactions. Molecules 2015;20:21178–92.
[81] Toyota T, Maru N, Hanczyc MM, Ikegami T, Sugawara TJ. Self-propelled oil droplets consuming "fuel" surfactant. J Am Chem Soc 2009;15:5012–15.
[82] Sumino Y, Magome N, Hamada T, Yoshikawa K. Self-running droplet: emergence of regular motion from nonequilibrium noise. Langmuir 2005;21:982–4.
[83] Satoshi N, Masaharu N, Hiroyuki K, Nobuhiko JS, Takeshi H. Physicochemical design and analysis of self-propelled objects that are characteristically sensitive to environments. Phys Chem Chem Phys 2015;17:10326–38.
[84] Arveson SM, Deng J, Karki BB, Lee KKM. Evidence for Fe-Si-O liquid immiscibility at deep Earth pressures. Proc Natl Acad Sci USA 2019;116(21):10238–43.
[85] Uemura T, Yanai N, Kitagawa S. Polymerization reactions in porous coordination polymers. Chem Soc Rev 2009;38:1228–36.
[86] Hartgerink JD, Beniash E, Stupp SI. Self-assembly and mineralization of peptide-amphiphile nanofibers. Science 2001;294:1684–92.
[87] Gong JP, Matsumoto S, Uchida M, Isogai N, Osada Y. Motion of polymer gels by spreading organic fluid on water. J Phys Chem 1996;100:11092–7.
[88] Ameta RK, Rohit RK, Akshay V, Chirag R, Nitin KS, Man S. $[Fe(CN)_6]_4$-/$[Fe(CN)_6]_3$-based metal organic ionic frameworks and impact of Fe^{2+}/Fe^{3+} on material-medicinal-properties. J Mol Liq 2018;268:677–84.
[89] Yong-Tao D, Chetan BS, Ameta RK. Thermal, SEM, AFM, BET and biological analysis of newly synthesized Fe^{2+}/Fe^{3+} based MOIFs. J Mol Liq 2019;295:111709.
[90] Rakesh KA, Man S. Co(III) based surfactant complexes and their dye, BSA and free radical activities. Heliyon 2019;5(4):e01568.
[91] Rakesh KA, Man S. –NO and –CN directed metal organic ionic framework used for concentration responsive adsorption of organic pollutant, bovine serum albumin and 2,2-diphenyl-1-picrylhydrazyl. Chem Sel 2019;4:1922–9.
[92] Cho S, Ma B, Nguyen ST, Hupp JT, Albrecht-Schmitt TE. A metal–organic framework material that functions as an enantioselective catalyst for olefin epoxidation. Chem Commun 2006;24:2563–5.

[93] Andrei NP, Pierre AJ, Dirk EDV. Palladium catalysts on alkaline-earth supports for racemization and dynamic kinetic resolution of benzylic amines. Chemistry 2007;13:2034–43.
[94] Sun C, Liu S, Liang D, Shao K, Ren Y, Su Z. Highly stable crystalline catalysts based on a microporous metal–organic framework and polyoxometalates. J Am Chem Soc 2009;131(5):1883–8.
[95] Wu C, Hu A, Zhang L, Lin W. A homochiral porous metal–organic framework for highly enantioselective heterogeneous asymmetric catalysis. J Am Chem Soc 2005;127(25):8940–1.
[96] Vermoortele F, Ameloot R, Vimont A, Serrec C, De VD. An amino-modified Zr-terephthalate metal–organic framework as an acid–base catalyst for cross-aldol condensation. Chem Commun 2011;47(5):1521–3.
[97] Feng D, Gu Z, Li J, Jiang H, Wei Z, Zhou H. Zirconium-metalloporphyrin PCN-222: mesoporous metal-organic frameworks with ultrahigh stability as biomimetic catalysts. Angew Chem Int Ed 2012;51:10307–10.
[98] Perez-Mayoral E, Cejka J. [$Cu_3(BTC)_2$]: a metal–organic framework catalyst for the Friedländer reaction. Chem Cat Chem 2011;3(1):157–9.
[99] Xiaoxiao Z, Yunpeng D, Fei Y, Wei W, Yanqing X, Changwen H. Efficient mechanochemical synthesis of polyoxometalate⊂ZIF complexes as reusable catalysts for highly selective oxidation. Inorg Chem 2017;5:14506–12.
[100] Comito RJ, Fritzsching KJ, Sundell BJ, Schmidt-Rohr K, Dinca M. Single-site heterogeneous catalysts for olefin polymerization enabled by cation exchange in a metal-organic framework. J Am Chem Soc 2016;138:10232–7.
[101] Lin S, Diercks CS, Zhang Y, Kornienko N, Nichols EM, Zhao Y, et al. Covalent organic frameworks comprising cobalt porphyrins for catalytic CO_2 reduction in water. Science 2015;349(6253):1208–13.
[102] Liu Y, Howarth AJ, Hupp JT, Farha OK. Selective photooxidation of a mustard-gas simulant catalyzed by a porphyrinic metal–organic framework. Angew Chem Int Ed 2015;54(31):9001–5.
[103] Liu Y, Moon S, Hupp JT, Farha OK. Dual-function metal-organic framework as a versatile catalyst for detoxifying chemical warfare agent simulants. ACS Nano 2015;9(12):12358–64.
[104] López-Maya E, Montoro C, Rodríguez-Albelo LM, Aznar Cervantes SD, Cenís JL. Textile/metal–organic-framework composites as self-detoxifying filters for chemical-warfare agents. Angew Chem Int Ed 2015;54(23):6790–4.
[105] Marek MB, Aaron WP, Michael RW, Joseph TH, Omar KF. Metal–organic frameworks as platform materials for solar fuels catalysis. ACS Energy Lett 2018;3:598–611.
[106] Zhigang H, Dan Z. Metal–organic frameworks with Lewis acidity: synthesis, characterization, and catalytic applications. CrystEngComm 2017;19:4066–81.
[107] Gonzalez MI, Bloch ED, Mason JA, Teat SJ, Long JR. Single-crystal-to-single-crystal metalation of a metal–organic framework: a route toward structurally well-defined catalysts. Inorg Chem 2015;54:2995–3005.
[108] Dong Y, Varinia B, Timur I, Omar KF, Joseph TH, Christopher JC, et al. Tuning the surface chemistry of metal organic framework nodes: proton topology of the metal-oxide-like Zr6 nodes of UiO-66 and NU-1000. J Am Chem Soc 2016;138(46):15189–96.
[109] Varinia B, Manuel AO, Donald GT, Christopher JC, Laura G. Computational design of functionalized metal–organic framework nodes for catalysis. ACS Cent Sci 2018;4:5–19.
[110] Yibo D, Jian Z, Awu Z, Jian-Rong L, Zuoren N. Visible-light responsive MOF encapsulation of noble-metal-sensitized semiconductors for high-performance photoelectrochemical water splitting. J Mater Chem A 2017;5:19491–8.

[111] Jiao L, Zhou Y, Jiang H. Metal−organic framework-based CoP/reduced graphene oxide: high-performance bifunctional electrocatalyst for overall water splitting. Chem Sci 2016;7:1690−5.
[112] Zhao M, Deng K, He L, Liu Y, Li G, Zhao H, et al. Core-shell palladium nanoparticle@-metal-organic frameworks as multifunctional catalysts for cascade reactions. J Am Chem Soc 2014;136(5):1738−41.
[113] Chen Y, Xu Q, Yu S, Jiang H. A seed-mediated approach to the general and mild synthesis of non-noble metal nanoparticles stabilized by a metal−organic framework for highly efficient catalysis. Mater Horiz 2015;2:606−12.
[114] Qi Y, Luan Y, Yu J, Peng X, Wang G. Nanoscaled copper metal−organic framework (MOF) based on carboxylate ligands as an efficient heterogeneous catalyst for aerobic epoxidation of olefins and oxidation of benzylic and allylic alcohols. Chem A Eur J 2015;21(4):1589−97.
[115] Noh H, Cui Y, Peters AW, Pahls DR, Ortuño MA, Vermeulen NA, et al. An exceptionally stable metal−organic framework supported molybdenum(VI) oxide catalyst for cyclohexene epoxidation. J Am Chem Soc 2016;138(44):14720−6.
[116] Chunxia T, Xing H, Zijian L, Yan L, Yong C. Controlled exchange of achiral linkers with chiral linkers in Zr-based UiO-68 metal−organic framework. J Am Chem Soc 2018;140:16229−36.
[117] Manna K, Ji P, Greene FX, Lin W. Metal−organic framework nodes support single-site magnesium−alkyl catalysts for hydroboration and hydroamination reactions. J Am Chem Soc 2016;138(24):7488−749.
[118] Hu H, Han L, Yu M, Wang Z, Lou X. Metal−organic-framework-engaged formation of Co nanoparticle-embedded carbon@Co9S8 double-shelled nanocages for efficient oxygen reduction. Energy Environ Sci 2016;9:107−11.
[119] Bu YG, Le Y, Xiong WL. A dual-metal−organic-framework derived electrocatalyst for oxygen reduction. Energy Environ Sci 2016;9:3092−6.
[120] Hyunho N, Yuexing C, Aaron WP, Dale RP, Manuel AO, Nicolaas AV, et al. An exceptionally stable metal−organic framework supported molybdenum(VI) oxide catalyst for cyclohexene epoxidation. J Am Chem Soc 2016;138:14720−6.
[121] Hod I, Sampson MD, Deria P, Kubiak CP, Farha OK, Hupp JT. Fe-porphyrin-based metal−organic framework films as high surface concentration, heterogeneous catalysts for electrochemical reduction of CO_2. ACS Catal 2015;5(11):6302−9.
[122] Wenlong X, Yueping Z, Hongfei L, Chang-jun L. Nanoparticle/metal−organic framework composites for catalytic applications: current status and perspective. Molecules 2017;22(12):2103.
[123] Rachel CK, Samat T, Joshua B, James RG, Madelyn MS, Jeffrey TM, et al. Single-site organozirconium catalyst embedded in a metal−organic framework. J Am Chem Soc 2015;137:15680−3.
[124] Zhigang H, Ezwan MM, Yongwu P, Yuhong Q, Bin Z, Ning Y, et al. Kinetically controlled synthesis of two-dimensional Zr/Hf metal−organic framework nanosheets via a modulated hydrothermal approach. J Mater Chem A 2017;5:8954−63.
[125] Eirik MT, Sigurd O, Gurpreet K, Mats T, Karl PL, Mohamed A. Strongly visible light-absorbing metal−organic frameworks functionalized by cyclometalatedruthenium(II) complexes. RSC Adv 2020;10:9052−62.
[126] Jun-Sheng Q, Shuai Y, Christina L, Jiandong P, Ali Al, Hong-Cai Z. Stable metal−organic frameworks as a host platform for catalysis and biomimetics. Chem Commun 2018;54:4231−49.

This page intentionally left blank

Chapter 16

Unique attributes of metal-organic frameworks in drug delivery

Parth Malik[1], **Rachna Gupta**[1,2] **and Rakesh Kumar Ameta**[1,3]
[1]*School of Chemical Sciences, Central University of Gujarat, Gandhinagar, India,* [2]*Department of Biotechnology, Visva-Bharati, Santiniketan, Bolpur, India,* [3]*Department of Chemistry, Sri M M Patel Institute of Sciences and Research, Kadi Sarva Vishwavidhyalaya, Gandhinagar, Gujarat, India*

16.1 Introduction

Metal-organic frameworks (MOFs) are characterized by strong covalent linkage of inorganic and organic units. The past decade has seen tremendous developments (>20,000 different MOFs being reported and studied) in this domain, thanks to constituent flexible geometry, size, and functionality. The organic moieties in these materials could be di- or poly-topic organic carboxylates or similar negatively charged molecules, linked to metal comprising units. Such a linkage forms the basis of robust crystalline structures with porosity greater than even 50% of total crystal volume [1,2]. Ranging $1000-10{,}000\ m^2\ g^{-1}$ in surface area (SA), these materials easily exceed the abilities of traditional porous counterparts such as zeolites and carbons. Till date, MOFs with undying porosity have been more explored with respect to their variety of configurations and multiplicity compared to other porous materials, making them favorable for fuel storage, CO_2 capture, and catalysis.

Fascinating aspects of these materials involve the ability to vary the size and structural composition with practically no variation in the underlying topology, thereby consolidating the isoreticular principle with largest pore aperture (98 Å) and as low as $0.13\ g\ cm^{-3}$ density. Such attributes have facilitated the encapsulation of several large biomolecules such as vitamin B12, proteins, and even chemical modification of pores as reaction vessels. A notable aspect in the structural chemistry of these materials is their thermal and chemical stability, making them acquiescent toward photosynthetic

Metal-Organic Frameworks for Chemical Reactions. DOI: https://doi.org/10.1016/B978-0-12-822099-3.00016-2

covalent organic and metal complex functionalization. Several methods are available to prepare MOFs, could be either traditional or specific like microwave treatment, ultrasonic, mechanochemical, and electrochemical processing. Large SA is the most distinctive feature of these entities, flanked by secondary building units (could be nitrogen or oxygen coordinated metal ions or clusters) connected through organic linkers. The flexibility in choosing the initial building units makes it feasible to vary select fundamental parameters, such as pore size, density, and specific SA. This ability forms the most crucial incentive of MOFs applications, providing several tailorable options to modify the physicochemical properties (PCPs).

Design of safer and efficient drug carriers is one of the most promising aspects of human health care and comprises an ever evolving filed for biomedical material sciences [3–5]. Though advances in surface engineering techniques have enabled multiple nanocarriers capable of efficient targeted delivery, yet there remains a consistent concern pertaining to their elimination from the physiological environment after the delivery of drug. So, adequate mechanisms have to be ensured for safer removal of carriers once they complete their job in order to minimize the chances of risk of nonspecific interaction-driven toxicity. Till date, extensive efforts have optimized the design of biocompatible organic polymers and inorganic porous materials for better drug delivery. Though these carriers ensure structural protection of drugs before being delivered, still their unanimous applications are hindered, either due to low drug loading capacity or as the difficulty to control the released drug extents. MOFs address these hurdles quite comprehensively, through their spontaneous self-assembly (between metals and organic linkers)-driven formation methods. Pertaining to specific domain of drug delivery, MOFs are characterized by highly tunable physical texture and properties (allowing need-based variations in pore size, shape, and structure as well as interaction affinity with the specific drug to be encapsulated), high SA encompassed larger drug loading extents, and large pore sizes (up to 6 nm) supporting the encapsulation of different kinds of pharmaceuticals. The flexibility of modifying chemical compositions by the choice of metal and organic linkers lends simplicity in choosing suitable biocompatible material for medicinal applications. These unmatched MOFs' traits imbibe them as distinctive and drug carriers. In general, the expected attributes of a good drug delivery system (DDS) include the following aspects, in order to ensure its effective performance:

1. acceptable toxicology of basal platform for use in health-care applications,
2. controllable degradation of the solids,
3. efficient encapsulation of therapeutic drugs,
4. controllable release of encapsulated cargos, and
5. easier surface engineering of the carriers to control their in vivo fate.

16.2 Synthesis of metal-organic frameworks

The structural platform for a specific MOF preparation involves a chemical reaction between inorganic ion and organic molecule (Scheme 16.1). The fundamental sequence of events for MOF synthesis (involving basal solvent participation, crystal formation, filtering, and recovery in dried form) is depicted in Fig. 16.1. The choice of metal ion could be exercised from either a metal salt or a cluster of metal ions, exhibiting a mandatory capacity to accept the lone pair of electrons (LPEs) in their vacant orbitals or shells. Contrary to this, the organic molecule may be a linker or bridging ligands capable of LPE donation. This combination of metal ion and organic unit constitutes MOFs. Chemical structures of select organic linkers implicated in MOFs are depicted in Fig. 16.2. Many MOFs are or have been synthesized using diverse methods, ranging from hydro- or solvothermal synthesis, microwave treatment, mechanochemical synthesis, sonochemical synthesis, electrochemical synthesis, spray-drying, inverse emulsion, and microfulidic-based approaches.

Each of these methods has specific benefits with definitive PCPs, functionalization, and scale-up ability. On a broader scale, however, these techniques are grouped into conventional and unconventional methods.

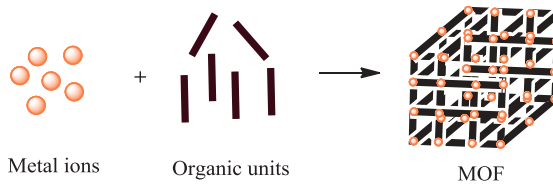

SCHEME 16.1 The structural platform for an MOF preparation. Two major entities are involved, that is, metal ions and organic linkers. *MOF*, Metal-organic framework.

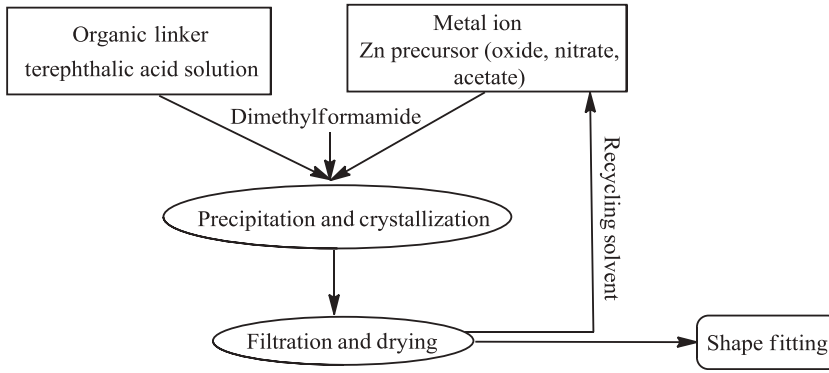

FIGURE 16.1 A flow diagram indicating the sequence of MOF synthesis, using conventional method. *MOF*, Metal-organic framework.

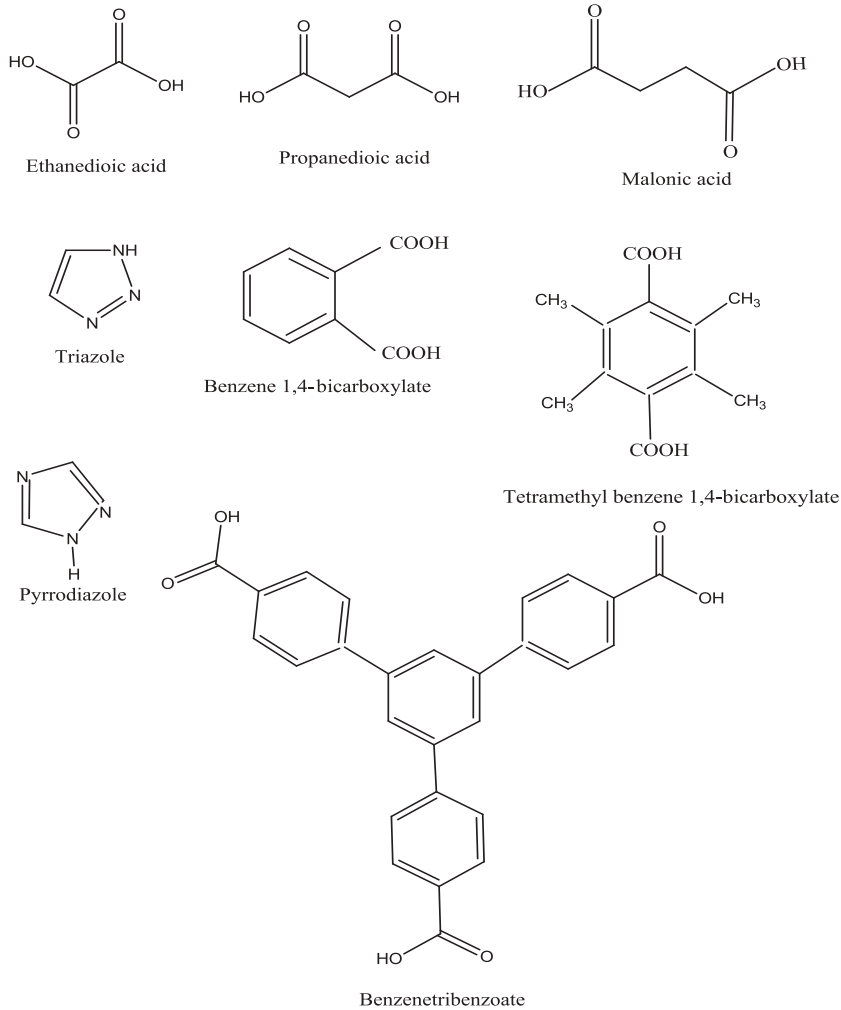

FIGURE 16.2 The chemical structures of select organic linkers implicated in MOFs. *MOF*, Metal-organic framework.

16.2.1 Conventional synthesis methods

This mode of synthesis is usually performed using solvothermal methods, specifically used for preparing readily water-soluble crystalline MOFs. Briefly, a mixture of organic linker and metal salt is heated in a solvent environment that usually comprises the formamide functionality in a ball mill followed by crystal precipitation through salting-out mechanism. Immediately after heating, the mixture contents undergo precipitation, forming crystals in the solvent environment itself. Following crystallization, the

crystals are filtered and dried. Slow growth of a crystal allows the defects to be redissolved, forming an assembly with millimeter-scale crystals and equilibrium products [6]. MOFs produced using conventional approach are generally thermally unstable and also react with solvent. The method facilitates creation of metal sites, accessible to the analyzed as molecules/moieties. Microwave-mediated synthesis has the advantage of shorter reaction time and enabling a high product monodispersity [7,8]. This method is generally preferred for a large-scale (industrial) synthesis requirement. One illustration of MOFs' synthesis using conventional synthesis approach could be the metal ion Zn (enabled from zinc acetate) and organic linker, 2,5-dihydroxylerepthalic acid (DT) using dimethylformamide (DMF) as solvent [9].

16.2.2 Unconventional synthesis

This approach utilizes mechanochemical method, wherein, metal salt and organic linker are initially mixed together, subsequent to being ground by a pestle−mortar. On many instances, a ball mill could also be used for this purpose (Scheme 16.2).

Upon gentle heating of mixture, metal sites are exposed, which tenders hydrogen to get trapped within these locations. This type of mechanochemically initiated reaction is considered as eco-friendly, similar to those of solvent reactions, and provides a better yield of formed products [10,11]. One illustration of MOFs' synthesis using unconventional synthesis methods has been reported by Pichon and associates, wherein copper isonicotinate MOFs were prepared using ball mill, in a solvent-free environment, via grinding copper acetate and isonicotinic acid (INA) [12] (Scheme 16.3).

Fig. 16.3 summarizes some unconventional methods for MOFs synthesis along with their special features and characteristic attributes. A number of variations are available for obtaining the products with desired morphology, response behavior, and drug encapsulating attributes [13−21]. Most of the

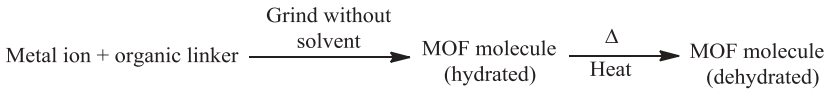

SCHEME 16.2 The MOF preparation through unconventional mode of synthesis. *MOF*, Metal-organic framework.

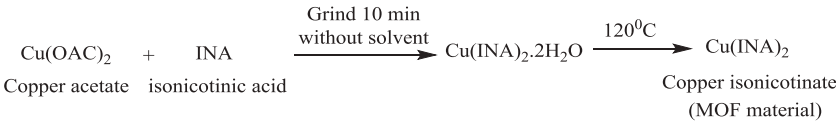

SCHEME 16.3 Formation mechanism of copper isonicotinate.

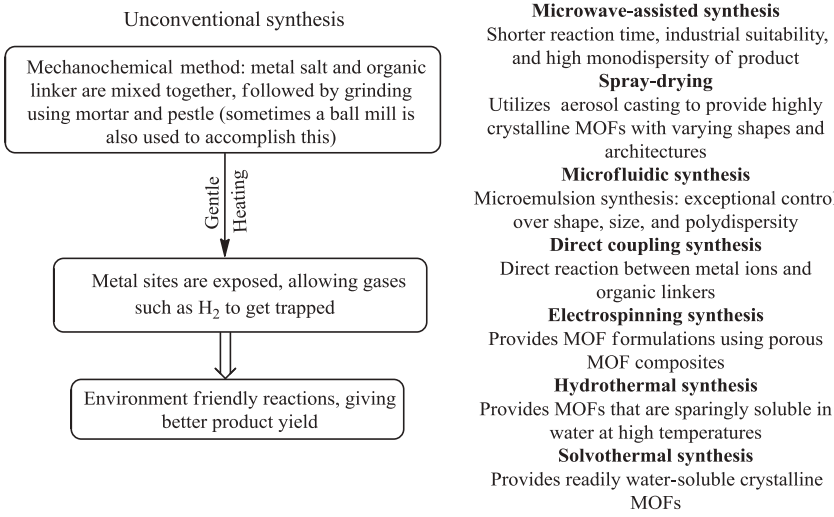

FIGURE 16.3 Schematic representation of unconventional synthesis methodology for MOFs. The different methods allow flexibility of varying the process parameters to have need-based optimized product quality. *MOF*, Metal-organic framework.

formation approaches are green methods, utilizing less external energy and producing low residual wastes, making them robustly operable and compatible handling. The working operations of many unconventional methods, such as microwave treatment, hydrothermal and solvothermal approaches are quite simpler. Some procedures like microfluidic assembly and electrospinning do pose a hindrance on their implementation (through their specific operational suitability). Similarly, in direct coupling method, caution needs to be exercised for controlling reaction process and progress. So, unconventional methods confer an additional benefit of choosing the right option as per the specialty design and performance optimizing product features.

16.3 Aspiring features for metal-organic frameworks' application in drug delivery: toxicological compatibility, stability, and biodegradation

Any moiety intended to be used for pharmaceutical purpose must be toxicologically compatible, necessitating being constituted of nontoxic individual domains. Owing to flexibility in choosing the metal ions and organic linkers, such toxicity modulations could be easily exercised in MOFs. While chromium, cadmium, nickel, cobalt, and several other metals are unsuitable (owing to their high toxicity), metals existing inside the physiological environment present a higher suitability in this regard. Some of these include iron (with nearly 22 μM hemoglobin in the blood plasma), calcium, copper,

manganese, magnesium, zinc, and zirconium. However, thorough studies on terminal biological fates of these metals are yet not reported. The supposed toxicities of these are estimated through oral lethal dose in the extents per kg body weight, could be traced in more specific literature sources [22,23]. To optimize the selection of organic linkers (pertaining to toxicity constraints), exogenous linkers and endogenous organic spacers are the two feasibilities. The former of these are synthesized from natural compounds without interfering in the body cycles, wherein those deemed fit for drug delivery include polycarboxylates, imidazolates, pyridyl, and amines. Several other organic linkers for which toxicity data infer their bioapplication suitability include terephthalic acid, trimesic acid, naphthalenedicarboxylic acid, isonicotinic acid, 5-aminoisophthalic acid, 2-methylimidazole, and 1-methylimidazole. The evaluation of iron trimesic acid deserves mention here, wherein the administration to rat models revealed normal behavior and weight evolution (compared to normal organisms). Second feasible option involves endogenous organic spacers as linkers, wherein molecules comprise ingredients of body composition. Use of organic spacers seems most ideal for the drug delivery ability of MOFs, as the chemical nature of these moieties being organic infers their reuse within the body, substantially reducing the risk of any inadvertent toxicity induction. Numerous endogenous MOFs have been proposed and studied till date, such as amino acid–based MOFs, nucleoabase-based 3D permanently porous MOFs, having a BET estimated SA up to 1700 $m^2\,g^{-1}$ [24]. While studies on saccharide MOFs are not yet extensively reported, except the recent findings of a symmetric cyclic oligosaccharide, γ-cyclodextrin being recruited as a ligand to synthesize two MOFs, [(g-CD)$(KOH)_2$] and [(g-CD)$(RbOH)_2$], having 1.7 nm spherical voids with 0.78 nm apertures and BET SA of 1220 and 1030 cm^3 for K^+ and Rb^+, respectively [25].

Apart from toxicity, another sensitive property affecting the MOF drug delivery suitability is the physiological stability. Carrier chemical composition contributes significantly in this regard, wherein some studies even advocate the possession of a certain minimum degrading activity that would aid in the required drug release extent. This ability, however, is also controlled by the respective host–guest interactions, pore size, and hydrophilic to hydrophobic moderation [26,27]. For instance, carrier of an anticancer drug is expected to preserve the native drug configuration before it reaches the tumor tissue. Nevertheless, till date, not much information is available regarding the MOFs' stability in the physiological environment with most reliable studies only illustrating the performance under the simulated physiological conditions. Some MOFs for which stabilities have been proposed include MIL-100(Cr), MIL-101(Cr), MIL-53 (Cr), and zeolite imidazolate framework-8 (ZIF-8). MIL-11(Cr) has a 3D mesoporous structure carrying trivalent metal in an octahedral regime and 1,3,5-tricarboxybenzene (BTC). This moiety encountered significant degradation after 3 days of

administration to the simulated body fluid (SBF). Similarly, MIL-101(Cr), obtained from identical Cr trimeric and terephthalic acid, having cubical structure, degraded after 7 days of administration to the SBF at 37°C [28]. MIL-53 (Cr), existing as three-dimensional framework comprising terephthalate (BDC) and octahedral trans-chains possessing one-dimensional pore channel system, degraded after 21 days in the SBF [29]. Interestingly, ZIF-8, composed of tetrahedral-oriented imidazolate anions, exhibited significant hydrothermal stability and remained in its native form even after 7 days, existing as suspended within PBS buffer at 37°C [30]. This stability vanished in acetate buffer (pH = 5), in the simulated physiological conditions of tumor tissue, and a quick degradation was observed within a few minutes. Such a pH-dependent functional response attributed to the sensitivity of imidazolate linker, which underwent protonation much easily in acetate buffer and subsequently reduced the binding strength of linker with metals. These observations suggested MOFs' stability as drug carriers to be critically dependent on their composition, crystalline structure, and specific biological environment. Though these studies elucidate a supposed improved MOFs' performance through controlling their structural composition and modulating the biological environment where they are being administered, still no conclusive affirmation can be made without conducting thorough in vivo studies.

16.4 Surface modification of metal-organic frameworks

The chief characteristic of any drug transport system lies in its ability to prolong the therapeutic response, wherein it is highly required to facilitate the stealth delivery. This is needed in order to prevent a prompt recognition of drug molecule by the immune cells (on being perceived as foreign entity), accomplishing this requires a delivery vehicle to be engineered along its surface with a biocompatible coating, which aids in delaying its frequent metabolism and prolonging its physiological residence. Furthermore, surface engineering also aids in minimizing the undesired interactions within the living system, which ensures its efficient expression at the targeted site only. Modification of surface is sometimes deliberately undertaken, so that the drug-loaded carrier could invade the plasma membrane of the cells and achieve a desired extent of cell internalization. This is one of the frequently encountered hurdles in the conventional drug delivery, where even high dosages are rendered ineffective and rather give rise to inadvertent nonspecific responses or side effects. This is primarily caused due to inadequate access of the drug with the targeted location, which results in a rather inadequate proportion of drugs within the tumor cells. Studies inspecting the impact of surface modification on the drug delivery efficacy of MOFs are rare, owing to which there remains a suspicion regarding their in vivo stability. Few results are however interesting to discuss here, wherein, one study

by Lin et al. reported the impact of silica coating on in vivo degradation of manganese-based MOF, inherently prepared for magnetic resonance imaging. The as-prepared MOF disappointedly had a short half-life in water (3.5 hours) and PBS (18 minutes), but the silica coating [conferred through base-catalyzed condensation of tetraethyl orthosilicate on polyvinylpyrrolidone (PVP)-modified solid particles in ethanol] elongated this degradation extent to 7.5 hours in water and 1.44 hours in PBS buffer [31].

Similar to above, the MIL-101 MOF comprising iron on being coated with silica particles revealed a stability of nearly 14 hours in PBS buffer, whereas the uncoated ones decomposed readily ($t_{1/2} = 1.2$ hours) [32]. A number of studies have also utilized biocompatible polymers to incorporate the surface protection, wherein one needs to be careful that coated material should not cross-react within the physiological environment. At the same time, it is essential that its corresponding interactions with encapsulated drugs are not too strong and are controlled through noncovalent forces. This would allow a retainment of native drug structures' failing, it is much likely that their intended functional expression becomes impaired. Most used polymeric material for surface coating of the drug delivering MOFs is polyethylene glycol (PEG), the hydrophilic molecules conferring significant compatibility with physiological conditions. Results of one study are worth discussing in this regard, wherein amino or carboxyl groups were administered to terminal reactive groups of PEG chains into MIL-88 and MIL-100 at 13.6 and 13.3 wt.%. This administration yielded superficial PEG brush-like structures, facilitating the arrest of particle aggregation through requisite induction of steric forces (mediating adequate interparticle repulsion). Upon being modified along the terminals with nonreactive mono-methoxy functionality, a weight content of nearly 17% was achieved, optimizing the stealth delivery [33].

16.5 Synthesis of nanoscale metal-organic frameworks

In the present scenario, it has almost become possible to talk about drug delivery studies and attempts without including distinctive nanomaterials as carriers. Indeed, flexible nanostructures capable of self-assembly-driven molecular rearrangements are fascinating, but there are multiple concerns regarding their efficient removal from the cellular environment, subsequent to the delivery of drug. Even though the moderation of conventional therapeutic payloads has been optimized through this strategy, still many studies claim a possible induction of inflammatory response and the concurrent generation of free radicals. The need for delivery of drugs using nanocarriers stems from the requirement of small particle sizes (lesser than 200 nm) so as to ensure the formation of highly stable solid suspensions in aqueous environment that could enter in the smallest capillaries without the risk of instantaneous or abrupt aggregation [23]. The befitting advantages of using

nanocarriers as delivery vehicles emanate from the ability of controllable sizes and shapes, high SA to volume ratios, and robust surface functionalization. Though limited, yet studies reporting the shape-dependent drug delivery efficacy of nanoparticles have revealed a greater potency of nonspherical shapes for drug encapsulation as well as site-specific delivery. Though it seems easier said than done, controlling the particle size (of the drug encapsulated nanocarrier) after being delivered inside the body is not an easy task and requires serious inputs on the structurally relevant passivation strategies. This is because the environment within the living systems is quite heterogeneous in terms of chemical composition and biochemical nature, wherein each specific organelle has an optimum functional pH. So, it is quite possible that carriers stable in one particular environment may get collapsed in different conditions or vice-versa. Nowadays, computational techniques are being used with great interest to mitigate the possible accidental interactions of delivered drugs and carriers, wherein the strength of drug−carrier binding is studied in terms of its binding energy (through simulation models). In case, the required stability is not feasible, we can also screen the potential mechanisms to achieve so via selective docking attempts (providing site-specific performance effects). Regulation of peculiar shapes and sizes has been demonstrated as critical factors in the final texture of drug preparations, encompassing patches, pellets, and tablets [34].

It is dire essential that the chosen carrier facilitates a monodispersed drug distribution, thanks to several green approaches for making so feasible. Processes such as solvothermal treatment, reverse microemulsion, ultrasonication, and microwave irradiation are some of the green approaches (although not independent of external energy requirements) enabling the preparation of uniform nanoparticles and nanoassemblies. One should try to use the bottom-up approach for this synthesis as these methods enable controlling the growing architecture (wherever needed) with a much lower energy usage and material wastage. Conventional solvothermal process, in this regard, harbors an implicit dependence on reaction time, temperature, pressure, precursor to stabilizing agent stoichiometry, pH, the net hydrophilic−hydrophobic equilibration, and several others. The mechanism of synthesis process renders it feasible to independently control these functional parameters so that the reaction kinetics can be paced suitably for obtaining different nanoscale MOFs' sizes [35,36]. In one such attempt, pyridine has been demonstrated as the inhibitor in the synthesis of benzene 1,4-dicarboxylate (BDC) and $In(NO_3)_3$. Varying extents of pyridine enabled the tuning of BDC particle size from 4 μm to 900 nm [37]. Likewise, gadolinium nanorods (NRs), prepared through stirring a transparent $GdCl_3$ and $[NMeH_3]_2[BDC]$ microemulsion using cetyltrimethylammonium bromide (CTAB) with isooctane and hexanol as stabilizers (for 2 hours), exhibited modifiable morphologies and sizes through varying the water to surfactant molar proportions. Keeping this ratio as 5, the NRs of 100- to-125-nm length

and 40 nm diameter were produced, whereas upon being increased to 10, the length also increased to 1−2 μm while the corresponding diameter was 100 nm [38]. Extending this possibility to ultrasonication, Qiu and coworkers reported the preparation of differently sized MOFs nanocrystals (NCs), $Zn_3(BTC)_2 \cdot 12H_2O$, via controlling the reaction time. Maintaining the time for 5−10 minutes, the size range of NCs retrieved was 50−100 nm, while increasing the reaction time to 30 minutes, it enabled a size of 100−200 nm. It was surprising to note that for 90 minutes reaction duration, the diameter of NCs increased to be within 700−900 nm. Thus the study deduced ultrasonication as the primitive approach to control the diameter, having tunable size and shape through varying reaction times [39].

One approach gathering significant interest in the recent time is microwave irradiation, allowing fast crystallization, phase selectivity, narrow particle sizes, facile structural control, and an accurate analysis of process parameters. Control of working temperature and corresponding heating rates enables efficient tapping of still higher process variables, in order to arrest the particle nucleation and growth. For instance, different MIL-101(Cd) MOF sizes could be obtained through a variation in reaction times. Subjecting an equimolar $Cr(NO_2)_3$ and BDC solution to microwave treatment at 210°C for 1−40 minutes enabled 40−90 nm MIL-101 particles. This method allows a significant reduction in the reaction time, so it presents suitability for being scaled up to a pilot level. In general too, microwave irradiation approach to make metallic NPs has been reported as facile, energy intensive, simpler in operation, and environmentally benign, allowing considerable enhancement in yields and particle size arrest [40].

16.6 Therapeutic efficacy of metal-organic frameworks

Versatile surface morphology and compositional hierarchy of MOFs enable multiple loading modes of drugs, wherein most common provisions include their introduction as organic spacers or active metal as metal nodes. Apart from functioning as drug carriers, native therapeutic essence of MOFs is also needed in their curative efficacy, which could provide contributory impact to the protective functioning of encapsulated compounds. One investigation deems mention over here, wherein Serre and coworkers fabricated a therapeutically active MOF through simultaneous inclusion of iron and nicotinic acid, having pellagra curative, vasodilating, and antilipemic properties [28]. The loading of drugs in this complex carried a high nicotinic acid content (as much as 71.5 wt.%), quite larger compared to total drug content (as 1.4 g of IBU loaded by MIL-101) [41]. A faster release of nicotinic acid here argued for the instability of encapsulated drug in the PBS. Several metals could also be incorporated as therapeutic agents within MOFs, such as silver that is well known for its antimicrobial characteristics, being suitable for biological and pharmacological applications. Silver in its bulk as well as

nanoscale form could enable significant antibacterial response, reports of which are already surfaced for *Staphylococcus aureus* (Gram-positive), *Escherichia coli*, and *Pseudomonas aeruginosa* (Gram-negative) pathogenic stains [42]. Besides silver, other metals investigated for such applications include gold, zinc, vanadium, and bismuth, promising augmented toxic response without any inhibiting activity on the encapsulated drugs.

Another factor affecting the therapeutic activity modulation of MOFs is the extent of encapsulated drug, critically depending on the pore size and fraction on the entire surface. Pore size, architecture, and its geometrical placements are highly crucial factors determining the efficacy of drug release. Ideally, the encapsulation of drugs should be through adsorption (no chemical reaction) and not absorption. At the same time, it is also worth noting that a too high amount of loaded drugs is not always beneficial and could also lead to multiple nonspecific chemical responses.

16.7 How metal-organic frameworks can advance the present success of drug delivery?

Owing to large SA, pore size, and controlled drug release, the MOFs are efficient drug carriers in contrast to other conventional porous materials. A variety of drug molecules having hydrophilic, hydrophobic, and amphiphilic features can be loaded over the MOFs' void spaces via covalent and noncovalent linkages [43–45]. Depending on the placement-driven drug and drug–carrier interactions, the MOF-based cargo-loading methods are classified into three different approaches: encapsulation, direct assembly, and postsynthesis modification (Fig. 16.4) [46].

In encapsulation approach, size matching of chosen drug and MOF pore structure plays a vital role for an effective incorporation of drug within MOF

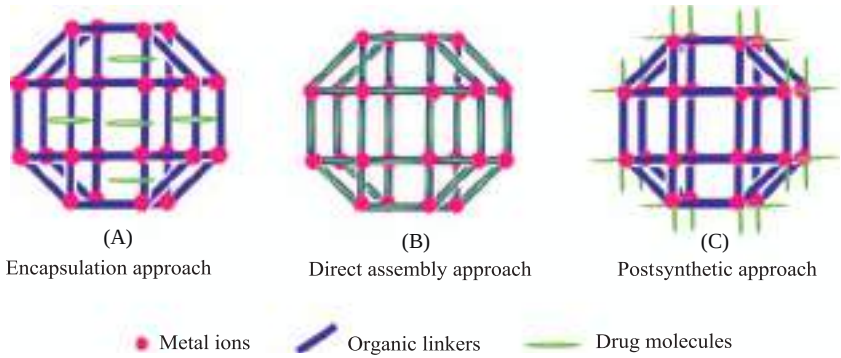

FIGURE 16.4 The MOF-based cargo-loading methods are classified into three different approaches. (A) Encapsulation, (B) direct assembly, and (C) postsynthetic approaches. *MOF*, Metal-organic framework.

cavity. Thereby, in this regard, it seems that amorphous MOFs are much better drug carrier than microporous MOFs owing to capture ability of interested cargo within their cavity areas without any burst release effect. For instance, Orellana-Tavra and colleagues have efficiently incorporated the drug calcein (cal) into nanosized Zr-UiO-66, having 4.9 wt.% loading capacity, along with exhibited an enhanced drug release from 2 to above 30 days in PBS (pH = 7.4) [46]. Likewise, Li and co-workers developed Zn-based MOF (ZiF), where 5-Fu (fluorouracil) having 21.2 wt.% loading content was encapsulated within MOF void spaces via noncovalent interactions [47]. Contrary to encapsulation strategy, few drug molecules such as pamidronate, zoledronate, methotrexate, and other platinum-based anticancer drugs are acted as ligands in the case of direct assembly approach. These ligands are directly involved in the development of framework structures through coordination bonds among the available cargo and chosen metal nodes. Lin and colleagues used cisplatin prodrug, c,c,t-$Pt(NH_3)_2Cl_2$(succinate) as a ligand to bind with Tb^{3+} for a stable amorphous MOF (Tb-DSCP) preparation [48]. This Tb-DSCP significantly controlled the Pt release in tumor cells. Similarly, Yang and colleagues developed amorphous Mn-IR825@PDA-PEG MOF consisting Mn^{2+} and IR825 dye (indocyanine green derivative) via direct assembly strategy. This MOF was coated and functionalized with polydopamine (PDA) and polyethylene glycol (PEG), respectively, conferring significant biocompatibility and efficient photothermal conversion to kill cancer cells [49].

Apart from abovementioned two approaches, the introduction of cargo into MOF carrier via postsynthesis involves the formation of either coordination bond with metal nodes or covalent bond with the functional coordinates of the linkers. The three different postsynthesis sites include functional linker vicinity, coordinately open metal sites, and ligand imperfect domains in the metal nodes. Among these sites, open metal sites serve as exceptional characteristic of MOFs exhibiting efficient control on drug binding so as to minimize the concurrent premature drug release risk. One attempt by Taylor-Pashow and colleagues examined the cisplatin loading in Fe-based MOF (MIL-101) via postsynthetic covalent interactions [32].

Another study established the multifunctional systems through binding oligohistidine-tags (His-tags) on MOF surfaces by means of M−N interactions [50]. Besides this, Mirkin and coworkers together reported the DNA loading MOF using postsynthetic strategy based on open metal sites [51]. In this work, Zr-phosphate coordination bonds are formed on the surface of UiO-66 MOF having terminal phosphate altered DNA. Erstwhile of the above, pulsating efforts are in pursuit for designing synergistic DDS via combining the three approaches in order to enhance therapeutic efficacy of a single drug-loaded MOF, usually rendered ineffective [52]. For instance, Lu and colleagues reported the combined effect of both local PDT therapy and checkpoint blockade immunotherapy in treatment of colorectal cancer using

mixed approach [53]. In this work the investigators reported enhanced immunotherapy in MC38 cells using TBC-HF NMOFs, wherein inhibitors of indoleamine 2,3-dioxygenase (IDOi) with 4.7% loading content were encapsulated. Similarly, Levine and coworkers described Mg_2(olz) (PEA) via encapsulating two different drugs, olsalazine (H_4olz) and phenethylamine (PEA), with olsalazine as a single bridging ligand. The results of this study showed a faster PEA release than olz from Mg_2(olz) (PEA), signifying high potential of synergistic strategy in modifying MOF DDS controllable aspects [54]. Table 16.1 comprises several other MOF DDS working on similar mechanism, signifying that specific and threshold cargo molecules and MOFs interactions are necessary requirements, not only for an improved loading ability but also for tunable release behavior.

16.8 Drug release mechanisms of metal-organic frameworks

MOF-based DDS are influenced by various exogenous and endogenous factors such as light, temperature, pressure, pH, glutathione (GSH), H_2S, ATP, glucose, ion, and enzyme [61,62]. These factors play a crucial role in triggering the drug release from MOFs at the specific desired site of tumor in a slow and gradual manner. Consequently, it is pertinent to understand the drug release mechanisms under the influence of these factors for improvement in constructing MOF-based DDS. The constituents or groups of MOFs that respond to such factors undergo conformational changes, hydrolytic cleavage, and protonation to trigger the release of drugs [63]. These constituents include imidazole (pH), disulfide bond (GSH), and porphyrin (light). Since the substantial tumor microenvironment occupied by lysosomes and endosomes is acidic, several acid-sensitive MOF-based DDS have been designed wherein coordination bonds are broken on exposure to low pH, resulting in drug release (Fig. 16.5). For instance, Zheng and colleagues developed 2-methylimidazole and Zn^{2+} ZIF-8-constituted MOFs, which exhibited negligible drug release at neutral pH, got distorted under acidic conditions [64].

At <7 pH the 2-methylimidazole underwent protonation that weakened its coordination bonds with Zn^{2+} and accelerated the drug release by portioning the structural linkages with ZIF-8. In another study, *Chen and team* synthesized 3-MA@ZIF-8 where 40% of 3-methyladenine (3-MA) was released in PBS at pH = 6 [65].

Likewise pH- and GSH (glutathione)-sensitive MOF DDS are also receiving great interest among researchers. In tumor cells, GSH concentration is 1000 times higher than normal cells, which can be oxidized, including disulfide bonds and redox-active groups. Therefore, based on these reasons, DDS were designed via introducing disulfide linkages between drug and carrier that are sensitive to high GSH and release drug by means of redox reaction [58]. The MOF-Zr (DTAB) was prepared by Lei and coworkers utilized Zr

TABLE 16.1 Summary of metal-organic frameworks (MOFs)–based drug delivery systems (DDS) explored as per three different strategies.

S. no.	MOFs DDS	Constituents	Size (nm)	Drugs	Loading capacity (wt.%)	Characteristics	Ref.
Encapsulation approach							
1	MIL-100(Fe)	(Fe_3O) trimer; BTC	200	DOX, CDV, AZT-TP	9.1 (DOX), 16.1 (CDV), 21.2 (AZT-TP)	Noncovalent bonds, releases drug after 5 days in PBS	[55]
2 (a) 2 (b)	NU-901 NU-1000	(Zr6O8) clusters H_4TBAPy	200 150	α-CHC	54.6 68.5	Noncovalent bonds, heating at 180°C controlled drug release	[56]
3	CP5-capped UMCM-1-NH-Py	(Zn_4) clusters NH_2-BDC, BTB, CP5, Py	102.9	DOX	3.4	pH-activated drug release	[57]
4	CP5-capped UiO-66-NH_2	(Zr_6O_8) clusters NH_2-BDC, CP5 Quaternary ammonium salt	326	5-Fu	1.5	Zn^{2+} and thermo-elicited drug release	[58]
Direct assembly approach							
5	DBC-UiO	(Zr_6O_8) clusters, H_2DBC	100–200	PDT	64	Coordination interactions	[59]

(*Continued*)

TABLE 16.1 (Continued)

S. no.	MOFs DDS	Constituents	Size (nm)	Drugs	Loading capacity (wt.%)	Characteristics	Ref.
6 (a) 6 (b)	Ca-Pam Ca-Zol	Ca^{2+}, Pam, Zol	6.4×10^6	Pam, Zol	75.1 (Pam), 75.7 (Zol)	Coordination interactions	[60]
7	Tb-DSCP	Tb^{3+}, DSCP	58–70	DSCP	72	Coordination interactions	[61]
8	Mn-IR-825	Mn^{2+}, IR-825	40	PTT	>57.5	Coordination interactions	[62]
Post synthesis approach							
9	UiO-MIL	(M_3O) trimer (Zr_xO_y) cluster SBU	Dimensions varied	P-modified DNA	–	Open metal sites, metal-phosphate interactions, surface modification	[63]
10	MIL-88A, HKUST-1, Zr-fum	(Fe_3O) trimer, BDC, (Cu_2) dimer, BTC, (Zr_6O_8) clusters, fumaric acid	68 (MIL-88A), 177 (HKUST-1), and 89 (Zr-fum)	His-tags proteins	22.7 (MIL-88A), 2.2 (HKUST-1), 3.5 (Zr-fum)	Open metal sites, M–N interactions, surface modification, pH-sensitive drug release	[64]

5-Fu, 5-Fluorouracil; *AZT-TP*, azidothymidine triphosphate; *BDC*, 1,4-benzenedicarboxylate; *BTB*, 1,3,5-benzene-tri-*p*-benzoate; *BTC*, 1,3,5-benzenetricarboxylic acid; *CDV*, cidofovir; *CP5*, carboxylatopillar-5-arene; *DOX*, doxorubicin hydrochloride; *DSCP*, *c,c,t*-(diamminedichlorodisuccinato) Pt(IV); *H_2DBC*, 5,15-di(*p*-benzoato)chlorin; *H_4TBAPy*, 1,3,6,8-tetrakis(*p*-benzoic acid)pyrene; *Pam*, pamidronate; *Zol*, zoledronate; *α-CHC*, α-cyano-4-hydroxycinnamic acid.

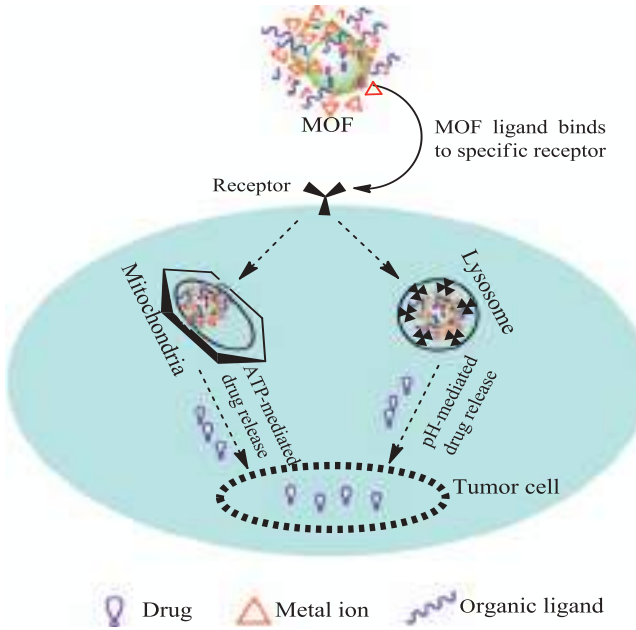

FIGURE 16.5 Schematic representation of MOF-based stimulating response drug delivery system. *MOF*, Metal-organic framework.

as metal nodes and 4,4-dithiobisbenzoic acid (4,4-DTAB) containing disulfide bonds as organic ligand [66]. Similarly, Xue and team developed DOX@FITC-ssCGP through cross-linking cyclodextrin-based MOF (CD-MOFs) with linker [3,30-dithiobis (propanoyl chloride) (DTPC)] having disulfide bonds. In this case, linker is likely to undergo a higher structural distortion than the framework. Apart from this, destruction of redox-active metals (Cu^{2+}, Mn^{4+}, and so on) also aids in releasing drug via glutathione oxidation [67]. In general, MOFs having drugs loaded through covalent conjugation exhibit better release control compared to the ones that are directly adsorbed within the cavity [55,68]. Apart from this basic distinction, the drug release attributes of MOFs are critically influenced by the PCPs of the interacted states of chemical constituents and loaded drugs. These factors include pore size and three-dimensional arrangements modulating characteristic fitting of drug molecules within the carrier molecules for efficient delivery. Release of drugs from MOFs occurs in a slow and controlled regime involving matrix degradation [69]. A befitting example in this regard is the study showing higher nicotinic acid loading ($\sim$75%) in the iron-containing BioMIL-1 MOFs compared to the native MOF structures, which facilitated its controlled delivery [70].

Applications of MOFs for drug delivery have been reported through manifold formulations in the configurations of tablets, pills, films, patches, etc. besides direct drug delivery. Such formulations significantly arrested the persistent risk of elaborate and restrictive patient compliance [23]. A prospective area where attempts are being made with significant interest is the nanoparticle-driven MOF formulations wherein the drug loading can be made wither during the synthesis (in situ mechanism) or postsynthesis phase. The encapsulation of drugs generally involves noncovalent interaction, contrary to that of functionalization that is mediated via covalent binding with the MOFs surface. Thereby the structural flexibility of MOFs is an incentive to make use of covalent as well as noncovalent approaches for attaining multimodal drug delivery and imaging [71]. Interestingly, the noncovalent approach allows a greater release control for the encapsulated drugs, having been reported for ibuprofen and cisplatin, wherein, there is no burst effect controlling the initiation of release [72]. Table 16.2 in this regard comprises the structural makeup of the specific MOF configurations alongside the drug release regulating physical parameters. Extending the generalization of these concepts is the approach involving mesoporous silica and zeolites in propelling the MOF-based structures, where the flexibility of robust internal frameworks confer the advantage of drug release, without any burst release effect [73].

16.8.1 Commercialized research on metal-organic framework–enabled drug delivery

Here we specifically discuss two recent studies focused on MOF-facilitated drug delivery. While efforts to better the delivery optimization continue to improve, a strikingly distinct domain of MOFs for drug delivery has been the control of their in vivo stability and efficient removal from within the body. The first study we are going to discuss here is a 2018 research attempt from collaborative efforts of both France and Spain, wherein MIL-100(Fe), UiO-66(Zr), and MIL-127(Fe) were evaluated for the adsorption/desorption kinetics study of aspirin and ibuprofen. The study involved experimental and computational investigation of major structural and physicochemical parameters affecting the drug binding capabilities. The chosen MOFs were water-soluble and their evaluation provided a variety of drug–matrix couples having distinct structural and physicochemical properties. It was found that drug loading and delivery efficacy of the MOFs were affected by the structural aspects (availability of framework for drug volume) apart from the MOF and drug philicphobic equilibration. The delivery of adsorbed drugs was screened under simulated cutaneous environment (corresponding to aqueous media at 37°C), wherein it was found that these systems fulfilled the need of topical delivery systems, reaching the designated payload extent within 1–7 days. It was interesting to note that all drug-loaded matrixes

TABLE 16.2 Stimuli sensitive metal-organic framework (MOF)–based drug delivery systems with their drug release mechanisms.

Sr. no.	MOFs	Factors	Groups	Mechanism	Ref.
1	(UCNPs/TAPP@ZIF-8)	Glucose	Glucose oxidase–functionalized ZIF-8	Glucose-sensitive materials	[66]
2	UiO-68/hydrogel	ATP	Hydrogel	Production of ATP-aptamer complexes	[67]
3	PPy@UiO66@WP6@PEI-Fa	Temperature	WP6 and Py stalk	Host–guest interactions	[74]
4	MTX@Zn-GA (bio-MOF)	Temperature	Zn-GA	Structural damage	[75]
5	HA-Dox-PCN	Enzyme	HA/HAase	Enzyme-activated mechanism	[76]
6	UiO-66-NH2 MOFs	Ion	Zn^{2+}	Competitive binding	[77]
7	Poly(DH-Se/PEG/PPG urethane) @PCN-224	Light	Porphyrin	Generation of O_2	[78]
8	Zirconium-based MOF (ZJU-800)	Pressure	(2*E*,2*E*′)-3,3′-(2-fluoro-1,4-phenylene) diacrylic acid	Pressure-triggered release mechanism	[79]

HA, Hyaluronicacid; *HAase*, hyaluronidase; *ZIF-8*, zeolite imidazolate framework-8.

(MIL-100, MIL-127, and UiO-66) reached a maximum loading capacity for aspirin and ibuprofen, and inspection through X-ray powder diffraction revealed that loading of drugs did not alter the crystalline structure of native MOF assemblies. No drug loss inferred by missing Bragg peaks corresponding to free aspirin or ibuprofen delivery, was noticed. Drug loading extent was determined through thermogravimetric analysis and high-performance liquid chromatography, with UiO-66 exhibiting 35.5 and 25.5 (the highest, both on weight percent basis) for ibuprofen and aspirin, respectively. Such a high loading efficacy of UiO-66 over MIL-100 and MiL-127 was reasoned for a larger pore volume of UiO 66. Apart from this, significant contribution of geometrical and chemical parameters was noticed to regulate the specific binding mechanism of drug on the MOF, subsequently emerging as significant controller of adsorption and release.

Studying the adsorption mechanism of each drug into MOF cavities through N_2 sorption capacity, the researchers determined the volume occupied by one drug molecule inside the MOF, through evaluating the variation in pore volume after the drug encapsulation and total content of loaded drug. It was found that both MIL-100 and MIL-127 exhibited a larger pore volume, due to the partial occupancy of porosity. This observation was concluded following the ascertainment of postdrug insertion porosity, which inferred a selective drug adsorption only within the larger MIL-100 cages that remained accessible via 8.6 Å hexagonal windows and the 6 Å MIL-127 channels. Compared to this, the smaller MIL-100 cages were exclusively reachable through pentagonal windows of 4.8−5.8 Å, and the $11.0 \times 5.0 \times 4.3$ and $7.8 \times 5.8 \times 2.3$ $Å^3$ as dimensions of ibuprofen and aspirin prevented their loading. Similar was the complicacy for MIL-127 hydrophilic cages that remained accessible through 3 Å apertures. Besides, the ethanol impregnation in MIL-100 played a key role of inducing coordinate binding of unsaturated iron (+3 oxidation state) metal, considerably reducing the free diameters of hexagonal and pentagonal windows. This was the major reason for reduced drug diffusion within the pores, especially within the smaller cages [80]. These observations corroborated the earlier conclusions of chromium-based MIL-100, wherein ibuprofen bound exclusively within the larger cages [28]. Furthermore, high ibuprofen loading of UiO-66 also complemented the observations of recent reports, wherein, CD-MOF-1 and the porous carbon derived from MOF PCDM-1000 exhibited a higher release (35.5 against 26 and 32 wt.%) [81]. These observations reflected the significance of MOFs' rotational selection, wherein geometrical and chemical parameters of both the MOF and drug affected the drug adsorption and release attributes [82].

Second study evaluated the intraocular drug delivery efficacy of UiO-67 and MIL-100 (Fe) MOFs for brimonidine tartrate in the course of chronic glaucoma treatment. Analysis of drug loading efficacies inferred both these MOFs exhibiting a highest loading capacity with 50%−60% extents.

Contrary to this, poor efficacy was noted for MOFs having narrow cavities (below 0.8 nm, such as UiO-66 and HKUST-1). Higher drug loading capacity of UiO-67 was found to be due to its irreversible amorphous structural rearrangement in aqueous and physiological environments, facilitating the extended release kinetics lasting for more than 12 days. Drug adsorption was accomplished through the exposure of 100 mg of each MOF with 50 mL varying brimonidine tartrate concentrations, after being left for stirring till the attainment of equilibrium. The study of kinetic behavior of each MOF was done using aliquot selections at varying time intervals, where all samples reached equilibrium after 7 hours. Quantification of brimonidine tartrate was made using UV−vis spectrophotometry, each being subjected to 1:100 dilutions. For comparison an MOF-loaded blank experiment was done to determine the possible interferences in UV−vis signal, because of a possible degradation. All the evaluated MOFs revealed no interferences for brimonifine at the studied wavelengths. The release experiments were conducted by subjecting the drug-loaded MOFs (after providing proper stirring times) to filtration, in the meanwhile of which, an aliquot was saved to ascertain the maximum loading. Drug-loaded MOF was subsequently washed several times with ultrapure water, followed by vacuum drying at 333K for 6 hours. The dried brimonidine-loaded MOF was thereafter immersed in 50 mL physiological solution and the aliquots were taken on varying time intervals up to 12 days. Matching with calibration curve (with known concentration of loaded drugs) enabled the determination of loaded drug extents, wherein the dilutions were made using PBS as solvent. To examine the cytotoxicity the drug-loaded MOFs were administered to 661 W cell lines (mouse retinoblastoma) at different concentrations for 24−48 hours. A death control was also included so as to ensure the toxicity emanated from the affected cells only. Drug-loaded MOFs having drug at 0, 10, 20, 30, 40, and 50 $\mu g\ mL^{-1}$ were used in DMEM. Maintaining MOFs and their respective components within the medium, the cell viability was assessed at 24 and 48 hours using the XTT assay (Cell Proliferation Kit II, a colorimeteric assay for nonradioactive quantification of cellular proliferation, viability and cytotoxicity). The absorbance was assumed as viability extent considering the value of null concentration (positive control) as 100% cell viability. Except for HKUST-1 MOFs, UiO-66 and UiO-67 did not affect the retinal photoreceptor cell viability, with the 48 hour viability remaining close to 100%. These results were complemented by the textural and morphological investigations, where UiO-66 and UiO-67 retained their nanoscale features (120 and 140 nm in sizes) contrary to the micrometer ranged HKUST-1 (after a 30-day incubation). The studied IC50 values were highest for HKUST-1 (940 $mg\ kg^{-1}$) contrary to MIL-100 (3250 $mg\ kg^{-1}$) and UiO-66, UiO-67 (3500 $mg\ kg^{-1}$). Thereby this study potentiated MOFs as drug delivery carriers wherein retainment of nanoscale dimensions allowed an optimum expression of their therapeutic effect [83].

16.9 Conclusion and future directions

We have presented a comprehensive account of MOF-enabled drug delivery response through their flexible compositional makeup and high SA-enabled efficient drug loading capabilities. The chief attributes of MOFs advocating their drug delivery potential comprises their large SA, structural flexibility with a wide range of pore size and the ability of being stabilized through self-assembly in the physiological environment. Though potential seems significant but not much details are known regarding the mechanisms and in vivo fates subsequent to the drug delivery.

Ideal present-day substitutes of MOFs could be the dendrimers, having significant advantage through manifold low-energy preparation mechanisms/methods. With the amalgamation of nanoscale features as well as noncovalent binding mechanisms, the challenge of adequate drug release (without any external stimulus) seems resolved now. Such features provide much needed incentives to augment the site-directed drug release and expression, concurrently minimizing the risk of wrongful drug expression and elaborating patient sensitization. The observation of investigation revealing reduced resistant response for cisplatin encapsulated within MOFs together with siRNA to the resistant ovarian cancer cells is indeed an inspiration. In this study, MOFs not only protected the siRNA from ribonuclease degradation once these were within the living environment but also enhanced their cellular uptake as well as escape from endosomal enzymes (intended to silent the MDR genes) [84]. Though this enhanced the chemotherapeutic efficacy, still much needs to be done (repetitive and reproducible responses of such kind) for which, there is an urgent need to expedite the studies on animal models and associated clinical trials. Anticipations at present do argue a bright future for MOF-enabled drug delivery, especially considering the results of studies published till date. Nevertheless, transforming ideas into reality is a herculean task (always) since in vitro environment is very different from that of in vivo conditions, time and again revealing distinct responses and creating obstruction in successful completion of clinical trials. Since it is the inceptive stage of MOFs in developing economies, the joint efforts of academia and industry could be crucial to propel the MOFs' science and working efficacy as a remarkable biomaterial.

References

[1] McGuire CV, Forgan RS. The surface chemistry of metal-organic frameworks. Chem Comm 2015;51:5199–217.

[2] Yaghi OM, Kim J, Ko N, Choi SB, Furukawa H. Open metal organic frameworks with exceptional surface area and high gas storage capacity. US8841471B2 (US patent).

[3] Li C, Wang J, Wang Y, Gao H, Wei G, Huang Y, et al. Recent progress in drug delivery. Acta Pharm Sin B 2019;9:1145–62.

[4] Safari J, Zarnegar Z. Advanced drug delivery systems: nanotechnology of health design: a review. J Saudi Chem Soc 2014;18:85–99.
[5] Patra JK, Das G, Fraceto LF, Campos EVR, Rodriguez-Torres MDP, Acosta-Torres LS, et al. Nano based drug delivery systems: recent developments and future prospects. J Nanobiotechnol 2018;16:71.
[6] Yaghi OM, Long JR. The pervasive chemistry of metal organic frameworks. Chem Soc Rev 2009;38:1213–14.
[7] Jhung SH, Lee JH, Chang JS. Microwave synthesis of a nanoporous hybrid material, chromium trimesate. Bull Korean Chem Soc 2005;26:880–1.
[8] Klinowski J, Paz FAA, Silva P, Rocha J. Microwave-assisted synthesis of metal-organic frameworks. Dalton Trans 2011;40:321–30.
[9] Dinca M, Long JR. Hydrogen storage in microporous metal-organic frameworks with exposed metal sites. Angew Chem Int Ed 2009;47:6766–79.
[10] Braga D, Giaffreda SL, Grepioni F, Chierotti MR, Gobetto R, Palladino G, et al. Solvent effect in a "solvent free" reaction. CrystEngComm 2007;9:879–81.
[11] James SL, Pichon A. An array-based study of reactivity under solvent-free mechanochemical conditions-insights and trends. CrystEngComm 2008;10:1839–47.
[12] Pichon A, James SL. An array-based study of reactivity under solvent free mechanochemical conditions insights and trends. CrystEngComm 2008;10:1839–47.
[13] Ni Z, Masel RI. Rapid production of metal-organic frameworks via microwave-associated solvothermal synthesis. J Am Chem Soc 2006;128:12394–5.
[14] Sanchez AC, Imaz I, Sarab MC, Maspoch D. A spray-drying strategy for synthesis of nanoscale metal-organic frameworks and their assembly into hollow superstructures. Nat Chem 2013;5:203–11.
[15] Faustini M, Kim J, Jeong GY, Kim JY, Moon HR, Ahn WS, et al. Microfluidic approach towards continuous and ultrafast synthesis of metal-organic framework crystals and heterostructures in confined microdroplets. J Am Chem Soc 2013;135:14619–26.
[16] Shang W, Kang X, Ning H, Zhang J, Zhnag X, Wu Z, et al. Shape and size controlled synthesis of MOF nanocrystals with the assistance of ionic liquid microemulsions. Langmuir 2013;29:13168–74.
[17] Dang GH, Lam HQ, Nguyen AT, Le DT, Truong T, Phan NTS. Synthesis of indolizines through aldehyde-amine-alkyne couplings using metal-organic framework Cu-MOF-74 as an efficient heterogeneous catalyst. J Catal 2016;337:167–76.
[18] Bechelany M, Drobek M, Vallicari C, Chaaya AA, Julbe A, Miele P. Highly crystalline MOF-based materials grown on electrospun nanofibers. Nanoscale 2015;7:5794–802.
[19] Pachfule P, Das R, Poddar P, Banarjee R. Solvothermal synthesis, structure and properties of metal organic framework isomers derived from a partially fluorinated link. Cryst Growth Des 2011;11:1215–22.
[20] Singh R, Geetanjali. Chapter 25: Metal–organic frameworks for drug delivery. Applications of nanocomposite materials in drug delivery. Elsevier Inc.; 2018.
[21] Haque E, Khan NA, Park JH, Jhung SH. Synthesis of a metal-organic framework material, iron terephthalate, by ultrasound, microwave and conventional electrical heating: a kinetic study. Chemistry 2010;16:1046–52.
[22] Bertini I. Biological inorganic chemistry: structure and reactivity. Sausalito, CA: University Science Books; 2007.
[23] Horcajada P, Gref R, Baati T, Allan PK, Maurin G, Couvreur P, et al. Metal-organic frameworks in biomedicine. Chem Rev 2012;112:1232–68.

[24] An J, Geib SJ, Rosi NL. Cation-triggered drug release from a porous zinc-adeninate metal-organic framework. J Am Chem Soc 2009;131:8376–7.
[25] Smaldone RA, Forgan RS, Furukawa H, Gassensmith JJ, Slawin AM, Yaghi OM, et al. Metal organic frameworks from edible natural products. Angew Chem Int Ed 2010;49:8630–4.
[26] Li X, Lachmanski L, Safi S, Sene S, Serre C, Grenèche JM, et al. New insights into the degradation mechanism of metal-organic frameworks drug carriers. Sci Rep 2017;7:13142.
[27] Liechty WB, Kryscio DR, Slaughter BV, Peppas NA. Polymers for drug delivery systems. Annu Rev Chem Biomol Eng 2010;1:149–73.
[28] Horcajada P, Serre C, Vallet-Reg M, Sebban M, Taulelle F, Férey G, et al. Metal-organic frameworks as efficient materials for drug delivery. Angew Chem Int Ed 2006;45:5974–8.
[29] Shi Q, Chen ZF, Song Z, Li J, Dong J. Synthesis of ZIF-8 and ZIF-67 by steam-assisted conversion and an investigation of their tribological behaviors. Angew Chem Int Ed 2011;50:672–5.
[30] Sun CY, Qin C, Wang XL, Yang GS, Shao KZ, Lan YQ, et al. Zeolitic imidazolate framework-8 as efficient pH-sensitive drug delivery vehicle. Dalton Trans 2012;41:6906–9.
[31] Taylor KML, Rieter WJ, Lin W. Manganese-based nanoscale metal-organic frameworks for magnetic resonance imaging. J Am Chem Soc 2008;130:14358–9.
[32] Taylor-Pashow KML, Rocca JD, Xie Z, Tran S, Lin W. Post-synthetic modifications of iron-carboxylate nanoscale metal-organic frameworks for imaging and drug delivery. J Am Chem Soc 2009;131:14261–3.
[33] Gref R, Domb A, Quellec P, Blunk T, Müller RH, Verbavatz JM, et al. The controlled intravenous delivery of drugs using PEG-coated sterically stabilized nanospheres. Adv Drug Deliv Rev 1995;16:215–33.
[34] McKinlay AC, Morris RE, Horcajada P, Férey G, Gref R, Couvreur P, et al. BioMOFs: metal-organic frameworks for biological and medical applications. Angew Chem Int Ed 2010;49:6260–6.
[35] Chalati T, Horcajada P, Gref R, Couvreur P, Serre C. Optimisation of the synthesis of MOF nanoparticles made of flexible porous iron fumarate MIL-88A. J Mater Chem 2011;21:2220–7.
[36] Horcajada P, Serre C, Grosso D, Boissière C, Perruchas S, Sanchez C, et al. Colloidal route for preparing optical thin films of nanoporous metal-organic frameworks. Adv Mater 2009;21:1931–5.
[37] Cho W, Lee HJ, Oh MJ. Growth-controlled formation of porous coordination polymer particles. J Am Chem Soc 2008;130:16943–6.
[38] Rieter WJ, Taylor KML, An H, Lin W, Lin W. Nanoscale metal organic frameworks as potential multimodal contrast enhancing agents. J Am Chem Soc 2006;128:9024–5.
[39] Qiu LG, Li ZQ, Wu Y, Wang W, Xu T, Jiang X. Facile synthesis of nanocrystals of a microporous metal-organic framework by an ultrasonic method and selective sensing of organoamines. Chem Comm 2008;3642–4.
[40] Vollmer C, Redel E, Abu-Shandi KH, Thomsan R. Microwave irradiation for the facile synthesis of transition-metal nanoparticles (NPs) in ionic liquids (ILs) from metal-carbonyl precursors and Ru-, Rh-, and Ir-NP/IL dispersions as biphasic liquid–liquid hydrogenation nanocatalysts for cyclohexene. Chemistry 2010;16:3849–58.

[41] Ahmad S, Isab AA, Ali S, Al-Arfaj AR. Perspectives in bioinorganic chemistry of some metal based therapeutic agents. Polyhedron 2006;25:1633–45.
[42] Lin SX, Pan WL, Niu RJ, Liu Y, Chen JX, Zhang WH, et al. Effective loading of cisplatin into a nanoscale UiO-66 metal-organic framework with preformed defects. Dalton Trans 2019;48:5308–14.
[43] Nezhad-Mokhtari P, Arsalani N, Javanbakht S, Shaabani A. Development of gelatin microsphere encapsulated Cu-based metal-organic framework nanohybrid for the methotrexate delivery. J Drug Deliv Sci Tec 2019;50:174–80.
[44] Xue Z, Zhu M, Dong Y, Feng T, Chen Z, Feng Y, et al. An integrated targeting drug delivery system based on the hybridization of graphdiyne and MOFs for visualized cancer therapy. Nanoscale 2019;11:11709–18.
[45] Wang L, Zheng M, Xie Z. Nanoscale metal-organic frameworks for drug delivery: a conventional platform with new promise. J Mater Chem B 2018;6:707–17.
[46] Orellana-Tavra C, Baxter EF, Tian T, Bennett TD, Slater NK, Cheetham AK, et al. Amorphous metal-organic frameworks for drug delivery. Chem Commun 2015;51:13878–81.
[47] Li S, Wang K, Shi Y, Cui Y, Chen B, He B, et al. Novel biological functions of ZIF-NP as a delivery vehicle: high pulmonary accumulation, favorable biocompatibility, and improved therapeutic outcome. Adv Funct Mater 2016;26:2715–27.
[48] Rieter WJ, Pott KM, Taylor KML, Lin W. Nanoscale coordination polymers for platinum-based anticancer drug delivery. J Am Chem Soc 2008;130:11584–5.
[49] Yang Y, Liu J, Liang C, Feng L, Fu T, Dong Z, et al. Nanoscale metal-organic particles with rapid clearance for magnetic resonance imaging-guided photothermal therapy. ACS Nano 2016;10:2774–81.
[50] Roder R, Preiss T, Hirschle P, Steinborn B, Zimpel A, Hohn M, et al. Multifunctional nanoparticles by coordinative self-assembly of his-tagged units with metal-organic frameworks. J Am Chem Soc 2017;139:2359–68.
[51] Wang S, McGuirk CM, Ross MB, Wang S, Chen P, Xing H, et al. General and direct method for preparing oligonucleotide-functionalized metal-organic framework nanoparticles. J Am Chem Soc 2017;139:9827–30.
[52] Fan W, Yung B, Huang P, Chen X. Nanotechnology for multimodal synergistic cancer therapy. Chem Rev 2017;117:13566–638.
[53] Lu K, He C, Guo N, Chan C, Ni K, Weichselbaum RR, et al. Chlorin-based nanoscale metal-organic framework systemically rejects colorectal cancers via synergistic photodynamic therapy and checkpoint blockade immunotherapy. J Am Chem Soc 2016;138:12502–10.
[54] Levine DJ, Runcevski T, Kapelewski MT, Keitz BK, Oktawiec J, Reed DA, et al. Olsalazine-based metal-organic frameworks as biocompatible platforms for H_2 adsorption and drug delivery. J Am Chem Soc 2016;138:10143–50.
[55] Horcajada P, Chalati T, Serre C, Gillet B, Sebrie C, Baati T, et al. Porous metal-organic-framework nanoscale carriers as a potential platform for drug delivery and imaging. Nat Mater 2010;9:172–8.
[56] Teplensky MH, Fantham M, Li P, Wang TC, Mehta JP, Young LJ, et al. Temperature treatment of highly porous zirconium-containing metal-organic frameworks extends drug delivery release. J Am Chem Soc 2017;139:7522–32.
[57] Tan LL, Li H, Qiu YC, Chen DX, Wang X, Pan RY, et al. Stimuli-responsive metal-organic frameworks gated by pillar[5]arene supramolecular switches. Chem Sci 2015;6:1640–4.

[58] Tan LL, Li H, Zhou Y, Zhang Y, Feng X, Wang B, et al. Zn(2 +)-triggered drug release from biocompatible zirconium MOFs equipped with supramolecular gates. Small 2015;11:3807–13.
[59] Lu K, He C, Lin W. A chlorin-based nanoscale metal-organic framework for photodynamic therapy of colon cancers. J Am Chem Soc 2015;137:7600–3.
[60] Liu D, Kramer SA, Huxford-Phillips RC, Wang S, Della Rocca J, Lin W. Coercing bisphosphonates to kill cancer cells with nanoscale coordination polymers. Chem Commun 2012;48:2668–70.
[61] Cai W, Wang J, Chu C, Chen W, Wu C, Liu G. Metal-organic framework-based stimuli-responsive systems for drug delivery. Adv Sci 2019;6:1801526.
[62] Yao J, Liu Y, Wang J, Jiang Q, She D, Guo H, et al. On-demand CO release for amplification of chemotherapy by MOF functionalized magnetic carbon nanoparticles with NIR irradiation. Biomaterials 2019;195:51–62.
[63] Mura S, Nicolas J, Couvreur P. Stimuli-responsive nanocarriers for drug delivery. Nat Mater 2013;12:991–1003.
[64] Zheng H, Zhang Y, Liu L, Wan W, Guo P, Nystrom AM, et al. One-pot synthesis of metal-organic frameworks with encapsulated target molecules and their applications for controlled drug delivery. J Am Chem Soc 2016;138:962–8.
[65] Chen X, Tong R, Shi Z, Yang B, Liu H, Ding S, et al. MOF nanoparticles with encapsulated autophagy inhibitor in controlled drug delivery system for antitumor. ACS Appl Mater Interfaces 2018;10:2328–37.
[66] Lei B, Wang M, Jiang Z, Qi W, Su R, He Z. Constructing redox-responsive metal-organic framework nanocarriers for anticancer drug delivery. ACS Appl Mater Interfaces 2018;10:16698–706.
[67] Xue Q, Ye C, Zhang M, Hu X, Cai T. Glutathione responsive cubic gel particles cyclodextrin metal-organic frameworks for intracellular drug delivery. J Colloid Interface Sci 2019;551:39–46.
[68] Cohen SM. Postsynthetic methods for the functionalization of metal-organic frameworks. Chem Rev 2012;112:970–1000.
[69] Sun CY, Qin C, Wang XL, Su ZM. Metal-organic frameworks as potential drug delivery systems. Expert Opin Drug Deliv 2013;10:89–101.
[70] Miller SR, Heurtaux D, Baati T, Horcajada P, Greneche JM, Seere C. Biodegradable therapeutic MOFs for the delivery of bioactive molecules. Chem Comm 2010;46:4526–8.
[71] Rocca JD, Liu D, Lin W. Nanoscale metal-organic frameworks for biomedical imaging and drug delivery. Acc Chem Res 2011;44:957–68.
[72] Morris W, Briley WE, Auyeung E, Cabezas MD, Mirkin CA. Nucleic acid-metal organic framework (MOF) nanoparticle conjugates. J Am Chem Soc 2014;136:7261–4.
[73] Davis ME. Ordered porous materials for emerging application. Nature 2002;417:813–21.
[74] Min H, Wang J, Qi Y, Zhang Y, Han X, Xu Y, et al. Biomimetic metal-organic framework nanoparticles for cooperative combination of antiangiogenesis and photodynamic therapy for enhanced efficacy. Adv Mater 2019;31:e1808200.
[75] You YQ, Xu DD, Pan X, Ma X. Self-propelled enzymatic nanomotors for enhancing synergetic photodynamic and starvation therapy by self-accelerated cascade reactions. Appl Mater Today 2019;16:508–17.
[76] Chen WH, Liao WC, Sohn YS, Fadeev M, Cecconello A, Nechushtai R, et al. Stimuli-responsive nucleic acid-based polyacrylamide hydrogel-coated metal-organic framework nanoparticles for controlled drug release. Adv Funct Mater 2018;28:1705137.

[77] Wu MX, Yan HJ, Gao J, Cheng Y, Yang J, Wu JR, et al. Multifunctional supramolecular materials constructed from polypyrrole@uio-66 nanohybrids and pillararene nanovalves for targeted chemophotothermal therapy. ACS Appl Mater Interfaces 2018;10:34655–63.

[78] Lin W, Cui Y, Yang Y, Hu Q, Qian G. A biocompatible metal-organic framework as a pH and temperature dual-responsive drug carrier. Dalton Trans 2018;47:15882–7.

[79] Kim K, Lee S, Jin E, Palanikumar L, Lee JH, Kim JC, et al. MOF x biopolymer: collaborative combination of metal-organic framework and biopolymer for advanced anticancer therapy. ACS Appl Mater Interfaces 2019;11:27512–20.

[80] García Márquez A, Demessence A, Platero-Prats AE, Heurtaux D, Horcajada P, Serre C, et al. Green microwave synthesis of MIL-100(Al, Cr, Fe) nanoparticles for thin-film elaboration. Eur J Inorg Chem 2012;100:5165–74.

[81] Rojas S, Colinet I, Cunha D, Hidalgo T, Salles F, Serre C, et al. Toward understanding drug incorporation and delivery from biocompatible metal-organic frameworks in view of cutaneous administration. ACS Omega 2018;3:2994–3003.

[82] (a) Hartlieb KJ, Ferris DP, Holcroft JM, Kandela I, Stern CL, Nassar MS, et al. Encapsulation of ibuprofen in CD-MOF and related bioavailability studies. Mol Pharm 2017;14:1831–9.
(b) Bhadra BN, Ahmed I, Kim S, Jhung SH. Adsorptive removal of ibuprofen and diclofenac from water using metal-organic framework-derived porous carbon. Chem Eng J 2017;314:50–8.

[83] Loe J, Lizarán I, Fernández-Sanchez L, Alió JL, Cuenca N, Estrada A, et al. Metal-organic frameworks as drug delivery platforms for ocular therapeutics. ACS Appl Mater Interfaces 2019;11:1924–31.

[84] He C, Lu K, Lin W. Nanoscale metal-organic frameworks for real-time intracellular pH sensing in live cells. J Am Chem Soc 2014;136:12253–6.

This page intentionally left blank

Chapter 17

Metal-organic frameworks and permeable natural polymers for reasonable carbon dioxide fixation

M. Ramesh[1], M. Muthukrishnan[1] and Anish Khan[2,3]
[1]*Department of Mechanical Engineering, KIT-Kalaignarkarunanidhi Institute of Technology, Coimbatore, India,* [2]*Chemistry Department, Faculty of Science, King Abdulaziz University, Jeddah, Saudi Arabia,* [3]*Center of Excellence for Advanced Materials Research, King Abdulaziz University, Jeddah, Saudi Arabia*

17.1 Introduction

Global warming is real and it is increasing at an alarming pace compared to previous decades. This temperature increase has devastating effects on ecosystems with frequent forest fires, rise of sea level due to increased pace of ice melting at the polar regions, frequent draught, and adverse flash floods. Though global warming was persistent during the Jurassic period, the discovery of fossil fuels and exploitation of fossil-related fuels cause the accumulation of greenhouse gases (GHGs) such as CO_2, methane, chlorofluorocarbons (CFCs), and carbon monoxide. Ever since the advent of industrial revolution and with the invention of spark ignition engines, increased usage of fossil fuels has aggravated the accumulation of harmful GHGs.

Among the many harmful GHGs, CO_2 gas emission occupies 60% of all the GHGs combined. CO_2 gases are emitted from combustion of fossil fuels in automobiles, fossil fueled thermal power plants, industrial processed output, and hydrogen production from carbon rich feedstocks, which is the main concern for the increase in temperature [1]. Recent studies have indicated that the concentration of CO_2 gases is increased from 280 ppm during preindustrial revolution to 440 ppm in the recent years. Fossil fuels share the 81% of the world energy needs, and burning of the fossil fuels alone emits 30 Pg of CO_2 annually to the atmosphere. CO_2 emission increases by 2 ppm, and by 2100 the global CO_2 emission is estimated to be around 570 ppm which

Metal-Organic Frameworks for Chemical Reactions. DOI: https://doi.org/10.1016/B978-0-12-822099-3.00017-4

would result in 1.9° increase in atmospheric temperature and 3.8 m rise of sea level [2]. Also anything above 600 ppm will have adverse effects on the respiratory system of the human body.

Thus by reducing the CO_2 imprint in the atmosphere without affecting the annual energy consumption is the primary objective of the researchers all over the world. Researchers have proposed several methods to reduce the CO_2 emission: (1) reduce the use of fossil fuels by increasing the efficiency of the engines or developing engines that would comply with the current emission standards such as switching over from BS-IV to BS-VI. But it will take several years for developing high-emission standard engines and would indirectly curb the growth of automobile industry; (2) effective use of alternative energy resources such as renewable energy like solar, wind, and hydro, which would reduce the carbon footprint in the atmosphere. But the current nonfossil fuel resources do not meet the exceeding demand of the energy and are still in the incubation level for mass production; and (3) developing effective methods to capture CO_2 emission [3].

17.2 Carbon capture technologies and storage

Carbon capture and storage (CCS) in simple words follows three steps: (1) CO_2 capture, (2) transport CO_2 to storage, and (3) store the captured CO_2. Thus CCS is an amalgamation of technologies considered to avert the discharge of CO_2 through flue gases generated from conventional power plants, cement factories, and industrial processes. The technology involves capturing CO_2 from the flue gases and is compressed and stored in a separate place which prevents it from reaching the atmosphere again. The compressed CO_2 are transported through pipelines to the geological storage locations such as abandoned oil field, coal and mineral mines, and deep saline formations. Thus major objectives of CCS technologies are to improve the efficiency of capturing CO_2 from the gas compounds. Several methods are proposed and attempted and they are called capture technologies. In general, they are categorized into three methods based on the source point of CO_2 such as postcombustion, precombustion, and oxy-fuel combination. The key challenge of the CO_2 capturing technology depends on two factors: (1) the ability of the material to regenerate and the initial energy used to regenerate will affect the cost-effectiveness of the capturing technologies and (2) the ability of the gas or flue or exhaust mixture to separate CO_2 form the mixture.

17.3 Postcombustion capture

Postcombustion process involves segregating CO_2 gases from the flue gases, that is, postcombustion of fossil fuels from the industry in compounds such as NO_x, SO_x, and CO_2 and other gases. A typical flue gas released during combustion of fossil fuel at power plants comprises 15%−17% CO_2, 77%

N_2, and 7% water vapor. These flue gases are to be treated before releasing it to the atmosphere. But the key challenge is that the percentage of CO_2 present in the flue gas is more than 5%, and in certain cases, the percentage is found to be more than 10%. Another setback is that these CO_2 are present at low partial pressure in the high temperature flue gases [4]. Postcombustion CO_2 capture technology is suitable for retrofit applications and is mostly suitable for pulverized coal plants and natural gas combined thermal power plants. The conventional postcombustion CO_2 capture method is amine-based absorption technology. Similarly several other methods such as ammonia-based absorption, membranes; activated carbons have also been attempted. Metal-organic framework (MOF) is one of the emerging technologies used for carbon dioxide absorption from flue gases. The schematic representation of postcombustion process is presented in Fig. 17.1 [5].

17.3.1 Amine-based CO_2 capture

Amine or carbonate solvents are suitable for capturing CO_2 from the flue gases at low partial pressure. Amine absorbers are also called amine scrubbers that are widely used to enhance the reaction rate in CO_2 capturing technology. Amines are generally classified as primary, secondary, and tertiary amines based on the applications. Primary and secondary amines when reacted with CO_2 through fast nucleophilic reaction formed carbonates [6]. On the other hand, tertiary amines accept protons from the reaction of CO_2 and H_2O by acting as base carbonates. For example, in natural gas industry, mono-ethanolamine is one of the primary alkanolamine used to capture CO_2 from the flue gases at 60−70 atm pressure and at operating temperature of 50°C. This method has been in use for the past 60 years, they face several challenges like (1) demand for advanced amines to improve the efficiency of the CO_2 capture in power plants and industrial processes; (2) demand to improve energy efficiency during desorption of CO_2; and (3) stability of the amines in the presence of other gases such as O_2, O_x, and SO_x, which have degrading effects on amines, as a result other amines such as diethanolamine and methyldiethanolamine are in use for gas purification.

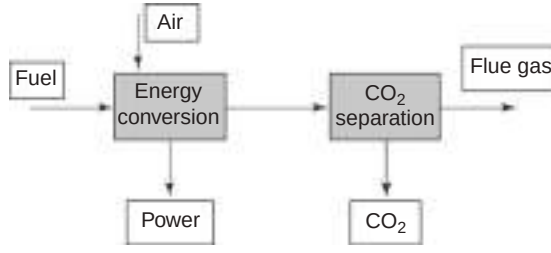

FIGURE 17.1 Schematic representation of postcombustion process [5].

17.3.2 Aqueous ammonia-based absorption

Aqueous ammonia-based absorption also works on the similar principle such as amines, but it has the advantage of working under lower heat of reaction, which results in significant energy savings. Ammonium carbonate reacts with CO_2 along with H_2O results in ammonium bicarbonate. Also aqueous ammonia solution captures SO_x, NO_x along with CO_2 which reduces significant cost in the harmful gases before leaving it to the atmosphere. It is a proven technology with the success rate of 90% regarding CO_2 capture. Aqueous ammonia is developed in different approaches that replace the traditional amine-based CO_2 capture. Chilled ammonia process is one among them where high concentration of aqueous ammonia solution (28%) at very low temperature preferably below 10°C is used to treat the flue gases [7]. But the energy consumption associated with the cooling of ammonia, washing plus regeneration of the washed water leads to higher energy costs than amine-based methods. Also ammonia at low temperature may results in solid precipitation that will affect the flow of circulating liquid [8]. In order to overcome the disadvantages associated with this process, it is proposed to reduce the concentration of ammonia from 28% to 6% at the cost of efficiency, where the effecting CO_2 stripping is affected by high energy consumption [9].

17.3.3 Membranes

Membranes have come into use in late 1980s to capture CO_2 in postcombustion process. Polymeric materials such as poly (ethylene oxide) are the commonly used material in membrane technology for CO_2 capturing process in the power plants. The two main properties of the membrane materials are permeability and selectivity. While permeability affects the degree of separation of CO_2 gases, selectivity determines the percentage of the concentration of CO_2 in the permanent gases. These membranes have better permeances for treating hydrogen, nitrogen, CO_2, and also other volatile compounds. Membranes carry out CO_2 separation from flue gases normally between 50 and 200 bar permeate pressures [10]. The temperature of the flue gases are reduced by wet scrubber before passing it the membranes. Membrane materials are classified as ceramic membrane, polymeric membrane, and hybrid membrane that contain metals [11]. Ceramic materials are inorganic, while polymer membranes are organic and hybrid materials are the combination of both organic and inorganic materials. Though several materials are attempted as membrane materials, they are likely to be limited by the low pressure gradient and low concentration of CO_2 present in the flue gases [12]. To compensate for the drawbacks of membrane capture method, membrane technology and research have proposed two stage process whereby recycled flue gas comprising CO_2 is feed to the boiler to increase the concentration to

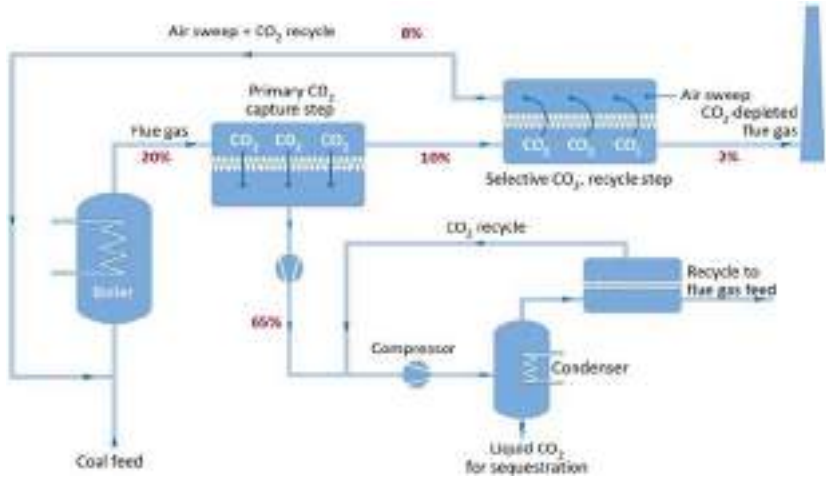

FIGURE 17.2 Postcombustion of two stage membrane process [14].

improve the CO_2 concentration as shown in Fig. 17.2. By this process the CO_2 capture rate is achieved around 90% [13,14].

17.3.4 Precombustion capture

Precombustion involves converting solid fuel such as coal and biomass to gaseous fuel under high pressure and temperature in the presence of water vapor. The resulting chemical reaction will yield hydrogen and carbon monoxide which is called syngas. The syngas is used to run the turbine generator to produce electricity. Carbon is extracted from the syngas before it passes to the gas turbine. To facilitate more CO_2 capture the syngas is passed into water−gas-shift (WGS) reaction and resulting carbon monoxide gas that is converted to CO_2 is captured. The hydrogen that is produced after the reaction is used for producing power by passing it into turbine. Precombustion of CO_2 is mainly used in integrated gasification combined cycle (IGCC) power plants. A schematic representation of the precombustion process is represented in Fig. 17.3. The main drawback of WGS reaction is the loss of energy due to large amount of steam that is used in the reaction. Another limited factor is the loss of heat recovery from the steam after WGS reaction and, hence, many research studies are going on to improve the efficiency of the CO_2 recovery. Also, the cost of setting up of IGCC plant is high.

17.3.5 Oxy-fuel combustion

It is a physical separation process where, instead of air that is commonly used in postcombustion process, pure oxygen is mixed with the flue gases for CO_2

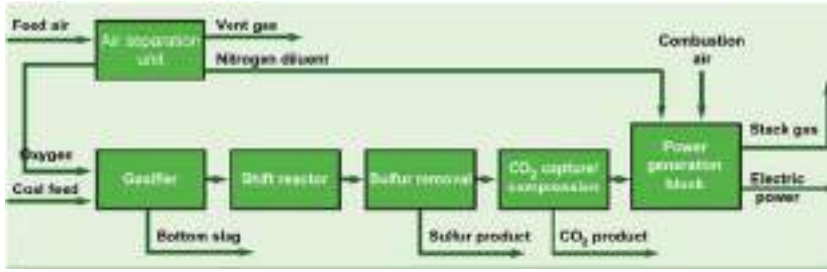

FIGURE 17.3 Precombustion of CO_2 capture in IGCC power plant [15]. *IGCC*, Integrated gasification combined cycle.

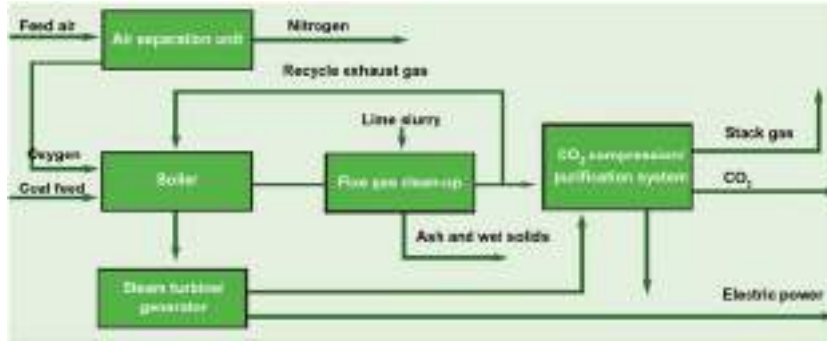

FIGURE 17.4 Oxy-fuel combustion capture process [16].

capture (Fig. 17.4). The key advantage of this process is that it prevents the formation of additional gases such as NO_x or SO_x and thus more concentration of CO_2 can be easily extracted. The advantage of this process is (1) simple process as CO_2 present in flue gases is over 80% and (2) additional solvents or reagents is not required and thus the operating cost is lower. The drawback is that the cost of oxygen is very high which will lead to high energy consumption. The comparison of the precombustion, postcombustion, and oxy-fuel combustion is represented in a schematic representation in Fig. 17.5. The application of these processes depends on the industry in which it is applied.

17.4 Metal-organic frameworks

MOFs are emerging crystalline porous materials based on inorganic metal clusters (Al^{3+}, Cr^{3+}, Cu^{2+}, Zn^{2+}, etc.) as core strongly bonded together by secondary building units called organic linkers to form 1D, 2D, and 3D structures [17]. These strong coordination bonds provide MOFs, a strong and rigid structure geometrically and crystallographically. The selection of primary and secondary building units of MOF, that is, inorganic metal cluster and organic

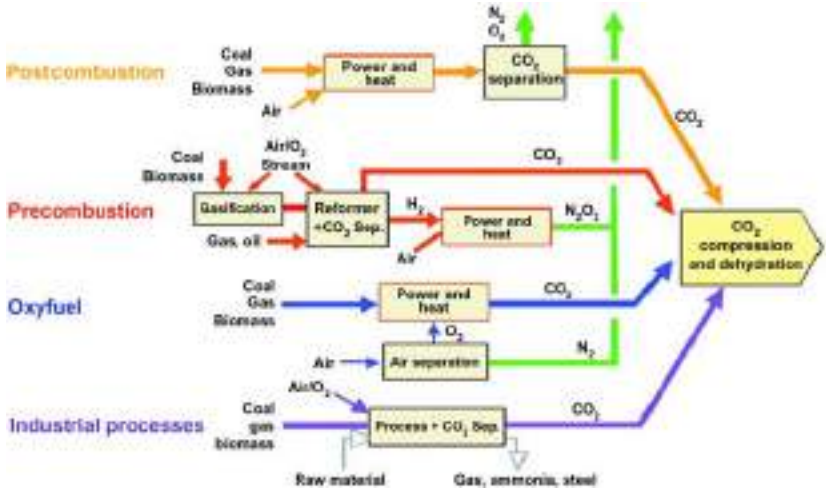

FIGURE 17.5 Comparison of the precombustion, postcombustion, and oxy-fuel combustion [15].

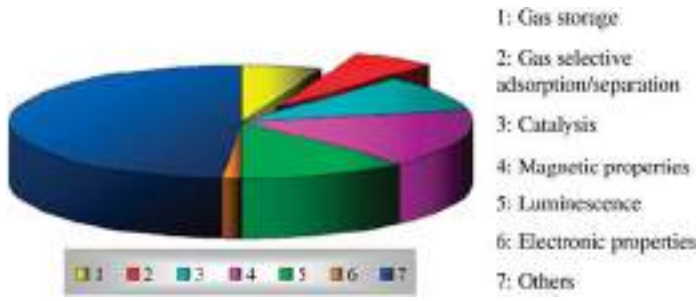

FIGURE 17.6 Potential applications of MOFs in various research areas [20]. *MOFs*, Metal-organic frameworks.

ligands are determined by the desired applications that determines the wide array of topological and structural features of MOFs [18]. MOFs are characterized by properties such as variable porosity, high specific surface area, better thermal and chemical stabilities, low densities ($0.21-1\ g\ cm^{-3}$) [19] and low void volume (50%–90%), potential functions as novel adsorbents, and easy tunability of the properties that makes it the potential candidate for mimicking DNA, molecular separation, drug delivery, separating petrochemicals, heavy metals removal, fluoride anions, hydrogen, and in gas storage [20]. The potential thrust areas where MOFs are in great demand are shown in Fig. 17.6.

For gas storage and separation applications, some of the design considerations of MOFs apart from metal clusters and ligands are temperature,

reaction time, optimization synthesis, reagent ratio and concentration, etc. These parameters determine the effectiveness of the gas separation and storage, and many initial reaction trials are required to identify the optimum MOF design. Thus new MOFs are synthesized under various technologies and these MOFs are generally categorized into (1) rigid MOFs, (2) flexible MOFs, (3) surface functionalized MOFs, and (4) open metal sites [21,22].

17.4.1 Rigid metal-organic frameworks

Rigid MOFs are stable and have robust and permanent porosity. They are based on stable organic secondary building blocks of phenyl, carboxylic acids, azolate, terephthalic acid, etc. The rigid MOFs such as Cu_3 (btc), MOF-74 are thermally stable and are able to retain their porosity even after adsorption and desorption. This is presented in Fig. 17.7.

On the other hand, flexible MOFs are subjected to framework transformation after adsorption and desorption of gas molecules and retain their porous geometry under high pressure. While rigid MOFs follow Type-I adsorption isotherm such as molecular sieving for CO_2 gases separation and storage, flexible MOF's pursue preferential adsorption/desorption are shown in Fig. 17.8. Compared to rigid MOFs, performance study and evaluation flexible dynamic MOFs are complicated. Some of the novel flexible MOFs used for CO_2 capture are MIL-53, MIL-88, SNU-M10, etc. [23,24].

17.4.2 Open metal sites

Open metal sites MOFs improve the CO_2 separation efficiency by providing selective adsorption mechanism for polar/nonpolar pairs. Thus CO_2 coordinates with MOFs metal center in an end fashion. Thus by dipole−quadruple interactions, CO_2 molecules bind to the porous surface by active metal sites. The water present in these MOFs has enhanced their CO_2 capture capacity. MOF $Cu_3(btc)_2$ (HKUST-1) is one of the prominent active open metal sites and the recent studies have shown that CO_2 capturing capacity has been improved by

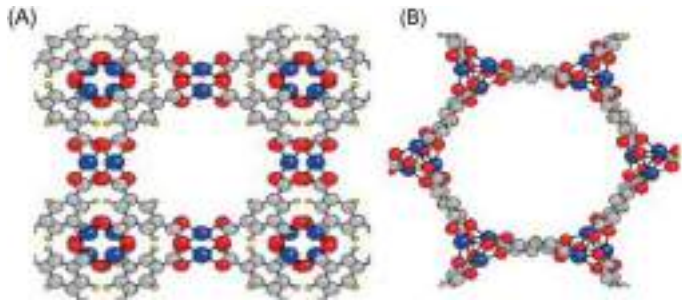

FIGURE 17.7 (A) Rigid MOF-Cu_3 (btc) and (B) MOF-74. *MOF*, Metal-organic framework.

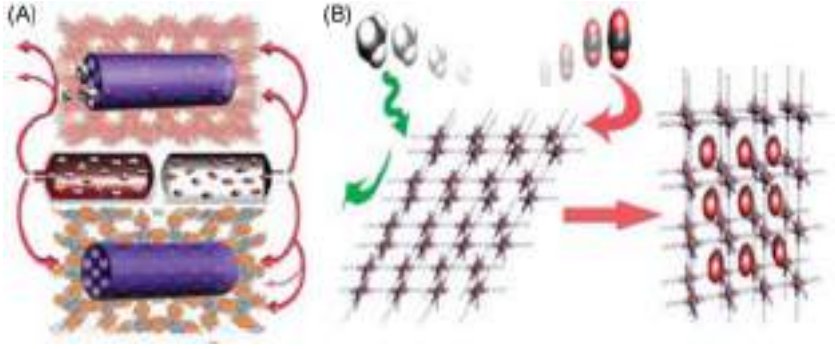

FIGURE 17.8 Gas adsorption mechanism in (A) rigid MOFs: molecular sieving effect and (B) preferential adsorption by flexible MOFs [20]. *MOFs*, Metal-organic frameworks.

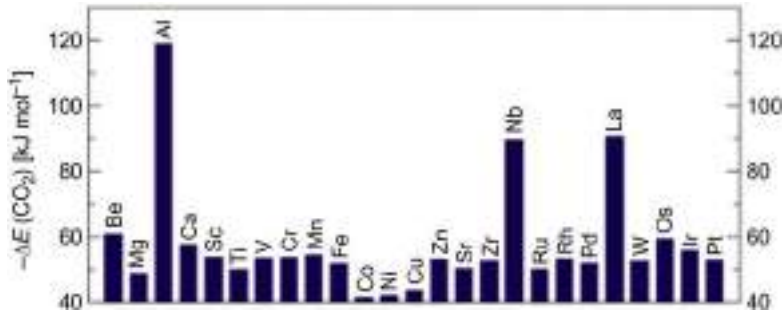

FIGURE 17.9 ΔE of CO_2 absorption of potential metal sites in M-MOF-74 [25]. *MOF*, Metal-organic framework.

four times than that of conventional absorbent zeolite by HKUST-1 posses 4% water capacity. Similarly studies on effect of active metal sites of iso-structural framework series like [M2(dobdc)(H_2O)] over CO_2 absorption revealed that [Mg_2(dodbc)] series have excellent CO_2 absorption capacity compared to other metal sites such as Mn, Ni, Zn, Co, and Fe [25,26].

Allison et al. [27] have studied MOF-74 and has developed a methodical procedure to estimate the adsorption isotherm accurately using computational approach during CO_2 interactions with activated field generated due to open metal sites. Apart from the studies of MOF-74 with open metal sites, HKUST-1, M-MIL-100, and M-MIL-101 are few of the most prominent frameworks that are widely studied by isolating the properties of the organic ligands, functional groups, and synthesis route of the framework. These studies have revealed that light metal sites facilitate more surface area for CO_2 capture at low pressures [28]. Similarly, computational approach on studies of noble metals Rh, Pd, Os, Ir, and Pt revealed them as potential candidates for CO_2 capture in M-MOF-74 [29−31]. The enthalpy of adsorption for CO_2 by open metal sites in M-MOF-74 is shown in Fig. 17.9.

Cabello et al. [32] investigated the MIL-100 framework with various unsaturated Cr(III) and Sc(III) metal sites for CO_2 capturing. The test studies using various temperature spectroscopies revealed that the enthalpy adsorption of the above metal sites was highest among the open metals sites considered for CO_2 adsorption on MOFs. Chaemchuen et al. [33] synthesized and studied the effect of open metal sites on CO_2 adsorption, pore volume, and surface area on M-DABCO series where the metals identified for the studies are Ni, Co, Cu, and Zn. Due to high charge density present at the metal center, Ni-DABCO series have shown better pore volume and higher specific surface area for CO_2 adsorption.

17.4.3 Surface functionalized metal-organic frameworks

Surface functionalized MOFs have functional groups that grafted to have high affinity for CO_2. Some of the functional groups considered for studies are arylamine [34], alkylamine [35], and hydroxyl [36]. These functional groups are grafted into surface of the porous materials or to coordinate active metal centers and facilitates selective interaction between CO_2 and functional molecule.

17.5 Strategies of CO_2 fixation

17.5.1 Selective CO_2 capture by the metal-organic frameworks constructed from flexible organic building blocks

Flexible MOFs (MOF-FL) are also called dynamic MOFs owing to their response to external stimuli. MOF-FLs are classified by their building blocks as Zn_4O-based MOFs, paddle−wheel−based MOFs with pillar linkers, copper paddle-wheel−based MOFs with open metal sites, and $Zr_6O_4(OH)_4$-based MOFs. For example MOF-FL, SNU-21({$[Cu_2(TCM)\ (H_2O)_2] \cdot 7DMF \cdot 3(1,4\text{-ioxane}) \cdot MeOH\}n$) has paddle-wheel type $\{Cu_2(O_2CR)_4\}$ building units that are connected by TCM4−tetrahedral building blocks to generate 3D channel frameworks [36]. Being sensitive to external response, these MOFs are stimulated by (1) supercritical CO_2 activation treatment and (2) extensive heat migration to form SNU-21S and SNU-21H. SNU-21H and SNU-21S have reported adsorption capabilities of CO_2 are 10.6 and 15.51 wt.% at 298K and 0.15 atm, respectively. Thus it was reported that SNU-21S shows more adsorption capacity of CO_2 than SNU-21H by losing more coordinated water molecules. Apart from CO_2 gases SNU-21S have greater adsorption capacity of N_2, O_2, H_2, and CH_4 by supercritical activation method, and it is found to be a superior method for CO_2 adsorption than heat migration method.

But at room temperature, MOFs should be flexible in nature to capture CO_2 as under normal conditions at room temperature, while many of the

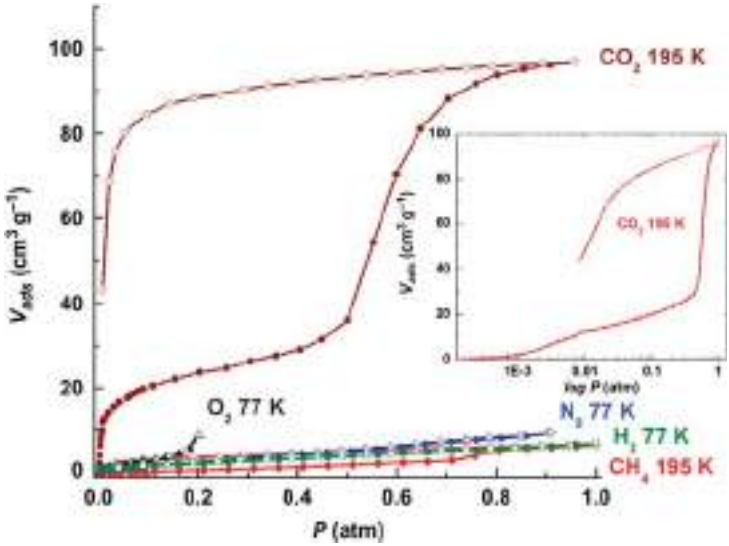

FIGURE 17.10 CO_2 adsorption capabilities of SNU-110 of various gases [37].

existing MOFs are not capable of CO_2 capture. SNU-110({[Zn_2 (*mpm*-PBODB)2bpy]3DMF}*n*) a flexible MOF, with super critical CO_2 fluid has adsorption of 97 $cm^3\ g^{-1}$ of CO_2 at 195K. Despite being smaller kinetic diameter of H_2, MOF is capable of adsorbing CO_2 owing to its high quadrupole and polarizability and they hardly adsorbs H_2 and N_2 gases. Adsorption capacities of SNU-110 over CO_2, H_2, and CH_4 and N_2 are given in Fig. 17.10.

17.5.2 CO_2 capture by flexible carboxyl pendants metal-organic framework

A flexible carboxyl pendant is another strategy used for CO_2 capture by modifying the stable MOF by ligand exchange method. For example, series of alkanedioic acids ($HO_2C(CH_2)n$-$2CO_2H$) are used to replace terephthalate ligand in MOF UiO-66 by ligand exchange method. The ligand substitution takes place by immersing the UiO-66 with terephthalate ligand in the solution of alkanedioic acids. The success of the ligand exchange depends on the immersion time that facilitates the incorporation of various carboxyl pendants (UiO-66-AD*n*: $n = 4$, 8, where n denotes the number of carbons in the pendant used for CO_2 capture). UiO-66-AD_6 facilitates more CO_2 uptake by 34% at 298K and by 58% at 323K. Various microstructural analysis such as TEM, IR indicates that the ratio of alkanediotic acid to terephthalate acid is 2:1 and the amount of exchange takes place from outer surface toward inner surface and allows more free carboxyl pendants in the pores [37].

17.5.3 Impregnating metal cations in anionic metal-organic framework CO_2 capture

In this method the CO_2 uptake is enhanced by impregnating the charged metals ions into the MOF as guest molecules which increases the interaction between the CO_2 gas molecules and MOF materials. In MOF SNU-100 $[[Zn_3(TCPT)_2(HCOO)]\ [NH_2(CH_3)_2] \cdot 5DMF$, TCPT = 2,4,6-tris-(4-carboxy-phenoxy)-1,3,5-triazine), the $NH_2(CH_3)^{2+}$ cations in the MOF pores are replaced by several metal ions such as Co^{2+}, Li^+, Mg^{2+}, Ca^{2+}, and Ni^{2+}. The electrostatic interactions between metal ions in the frame work and CO_2 aids in coordinating water molecules and significantly enhance CO_2 uptake capacity and selectivity by 16.8 wt.% of SNU-100 at 298K, 1 atm with isosteric heat of CO_2 increases to 40.4 kJ mol^{-1}. The CO_2 adsorption capacity SNU-100-Li^+, Ca^{2+}, and Ni^{2+} are 15.3, 15.1, and 16.6 wt.% (Fig. 17.11).

17.5.4 CO_2 capture by porous organic polymer impregnating flexible polymeric amine

Porous aromatic frameworks (PAFs) (Fig. 17.12) are of great interest in research area owing to its ultra large surface areas and excellent stability [39, 40]. In this method, PAF-5 is impregnated with the branched polyethyleneimine (PEI). PAF has Brunauer–Emmett–Teller (BET) surface area of 2070 $m^2\ g^{-1}$ and large pore size of 2.11 nm. The PAF-5 is also composed of phenyl ring fragments that make it suitable for modifying desired functional groups such as amine-based PEI that has strong interaction with the CO_2 which makes suitable for CO_2 adsorption. PAF-5 is loaded in PEI solution and by varying the wt.% of PEI and immersion time, PEI is strongly impregnated into the PAF-5. The impregnation of PAF-5 with PEI is presented in Fig. 17.13 [41]. The adsorption between PEI ethylene series and PAF phenyl

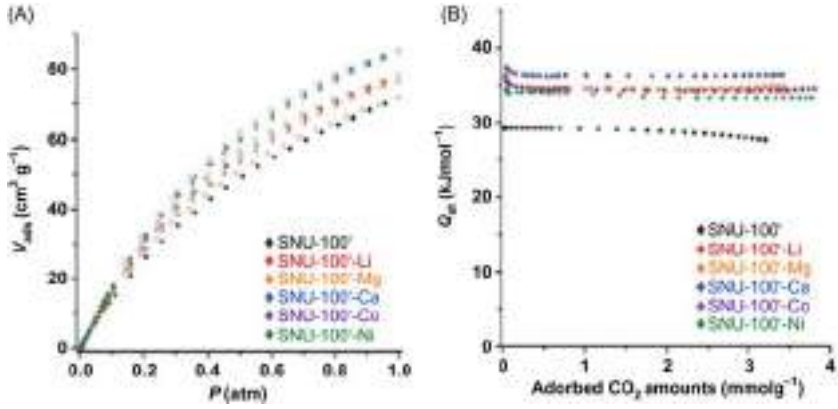

FIGURE 17.11 (A) SNU-100 CO_2 adsorption with various metal ions and (B) isosteric heat of CO_2 of various SNU-100 metal ions [38].

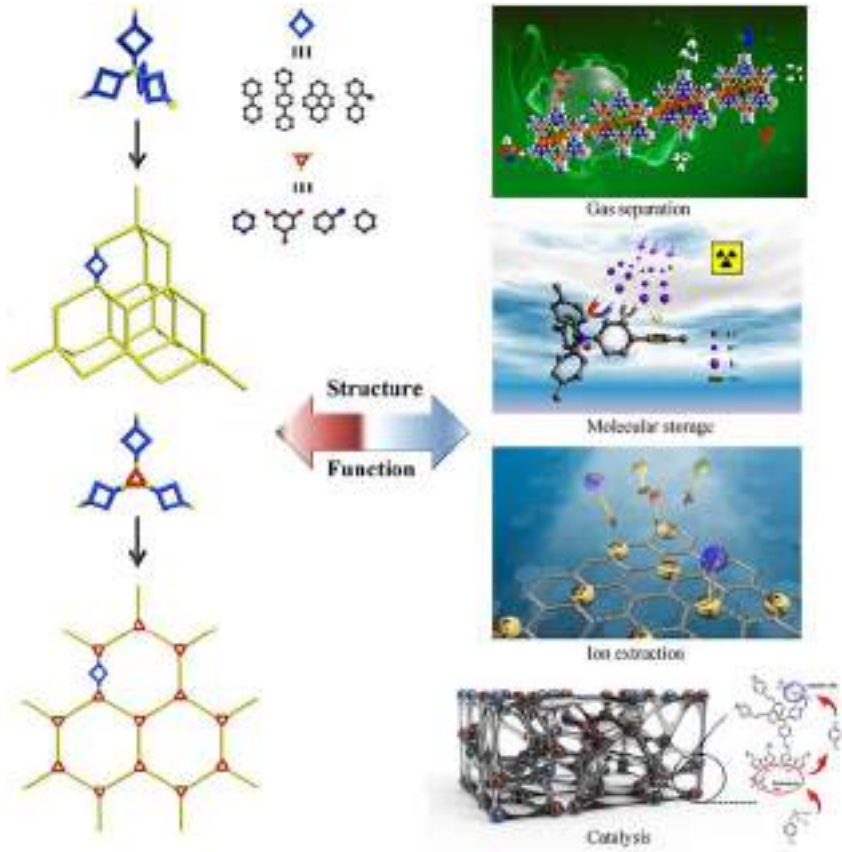

FIGURE 17.12 Targeted design and preparation of PAFs for gas separation, molecular storage, ion extraction, and catalysis.[40]. *PAFs*, Porous aromatic frameworks.

rings are so strong that it was not released even under activation of high vacuum. With the increase in PEI level, the amount of CO_2 adsorption increases at low CO_2 pressure (1.5 atm) coupled with drastically decreasing N_2 adsorption. On the other hand, PAF-5 with PEI-40 wt.% show 10, 14, and 16% increase CO_2 adsorption while comparing to pristine PAF-5 under 1.5 atm under temperature 298, 313, and 323K. Also, they exhibit faster adsorption and desorption kinetic; water stable and low-energy consumption makes it a suitable candidate for CO_2 capture.

Another PAF material, PAF-1 demonstrates strong adsorption capabilities even under extreme acidic and alkaline conditions. And their functional ligands with open pores are suitable for modifications [24]. PAF-1 is loaded with diarylethene (DArE) to synthesize DArE@PAF-1 as shown in Fig. 17.14. The effect of DArE in pore size distribution reduces DArE molecules photocyclization by aromatic stacking by enabling binding attraction between DArE with CO_2. It facilitates CO_2 adsorption and at the same time

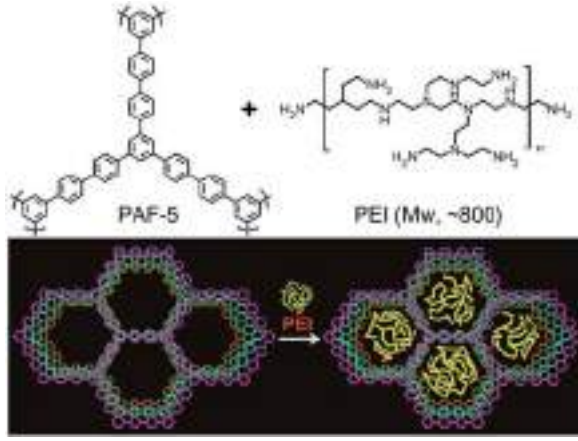

FIGURE 17.13 Impregnation of PAF-5 with PEI [41]. *PAF*, Porous aromatic framework; *PEI*, polyethyleneimine.

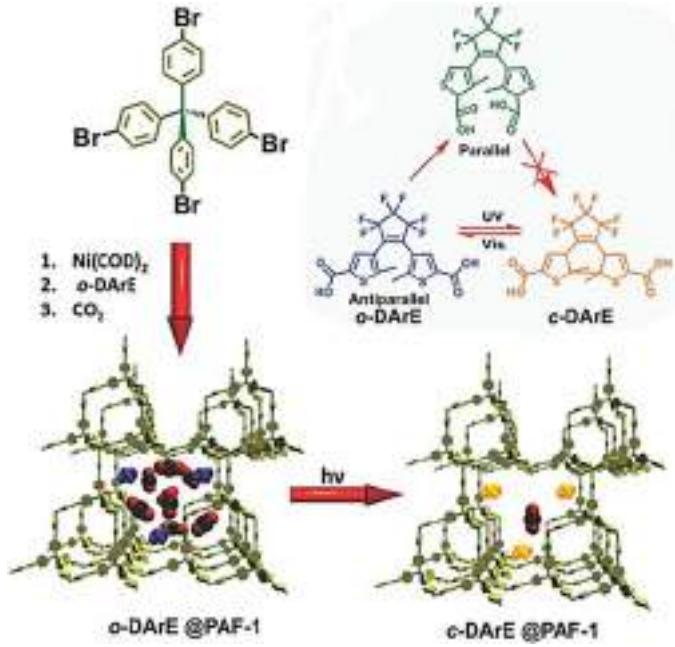

FIGURE 17.14 PAF-1 loaded with DArE [42]. *PAF*, Porous aromatic framework.

prevents H_2 interactions. Another PAF conformer o-DArE weakens the affinity between the adsorption sites and CO_2 which results in release of CO_2 instantaneously. Thus the modification of organic ligands enables CO_2 capture and release.

17.6 Evaluation of CO_2 adsorbent materials

The economics of the CO_2 separation process is determined by the ratio of CO_2 capture to that of the bulk flue gases components such as N_2, H_2, and O_2. This is called selectivity property of MOF, and high CO_2 selectivity is desirable for maximum efficiency of CO_2 adsorption. This CO_2 selectivity depends on (1) size exclusion and (2) gas−pore surface interaction. In size pore interaction the MOF pores do not allow gas−pore of certain kinetic diameter, whereas, in gas−pore surface interaction, the thermodynamic separation depends on polarizability and quadruple moments. The performance of the adsorbent material depends upon the CO_2 adsorbing capacity that depends more on the adsorbing kinetics over adsorption equilibrium. Kinetics of the adsorbent should exhibit adsorption/desorption capacity at a faster rate under the given operating conditions. Adsorption equilibrium of CO_2 capture can be measured for any adsorbent by (1) gravimetrically, that is, amount of CO_2 adsorbed in unit mass of flue gas and (2) volumetrically which determines the density of the CO_2 that is adsorbed with the material. In order to determine the energy requirements for adsorption and desorption, that is, heat efficiency of MOF, both the methods are widely used.

Another important factor for evaluation is the adsorption isotherms measure at ideal temperature and ambient pressure (generally low pressure to 1.2 atm) where CO_2 capture is maximum. Adsorbent's CO_2 adsorbing capacity is determined by the adsorption isotherm. Understanding the adsorption equilibrium capacity aids in the selection of suitable sorbent for the flue gas such as CO_2. Generally, the reference value for adsorption capacity is 2−4 mmol g^{-1}. These adsorption isotherms are highly influenced by the high surface area of MOF. Generally, most of the MOFs exhibit Langmuir shape isotherm, whereas few MOFs also exhibit other types of isotherm curves under varying pressure and temperature conditions such as stepwise isotherms, sigmoidal isotherms, and hysteretic isotherms. MOFs like MCF-19 have exhibited stepwise isotherms [43]. On the other hand, electrostatic interaction of MOF-5, MOF-177, and MOF-210 exhibits sigmoidal isotherm [44]. Seo and Chun [45] analyzed the hysteresis gas adsorption isotherm of CO_2 in MOF for Zn(2,7-ndc)(2,7-bdc = 2,7-naphthalene dicarboxylate).

The cost of adsorbent will increase with frequent change of adsorbent material during adsorption/desorption process. Thus the life of adsorbent depends upon the stability of the adsorbent material. A good adsorbent material should withstand severe operating conditions during CO_2 capture such as high temperature, vibration, and high rate of flue flow. Also, it should have tolerance over other impurities that are present in the flue gases. The characteristics of pore size and surface area are other deciding factors in CO_2 capturing, and Millward and Yaghi [33] investigated the effect of these variables over several MOFs adsorbents such as MOF-2 [46], MOF-505 and $Cu_3(BTC)_2$ [47], MOF-74 [48], IRMOF-11 and IRMOF-3 and 6 [49], IRMOF-1 [50], and MOF-177 [51]. The pore size and specific surface areas of various MOFs are shown in Fig. 17.15 and Table 17.1. It was found that CO_2 uptake capacity of

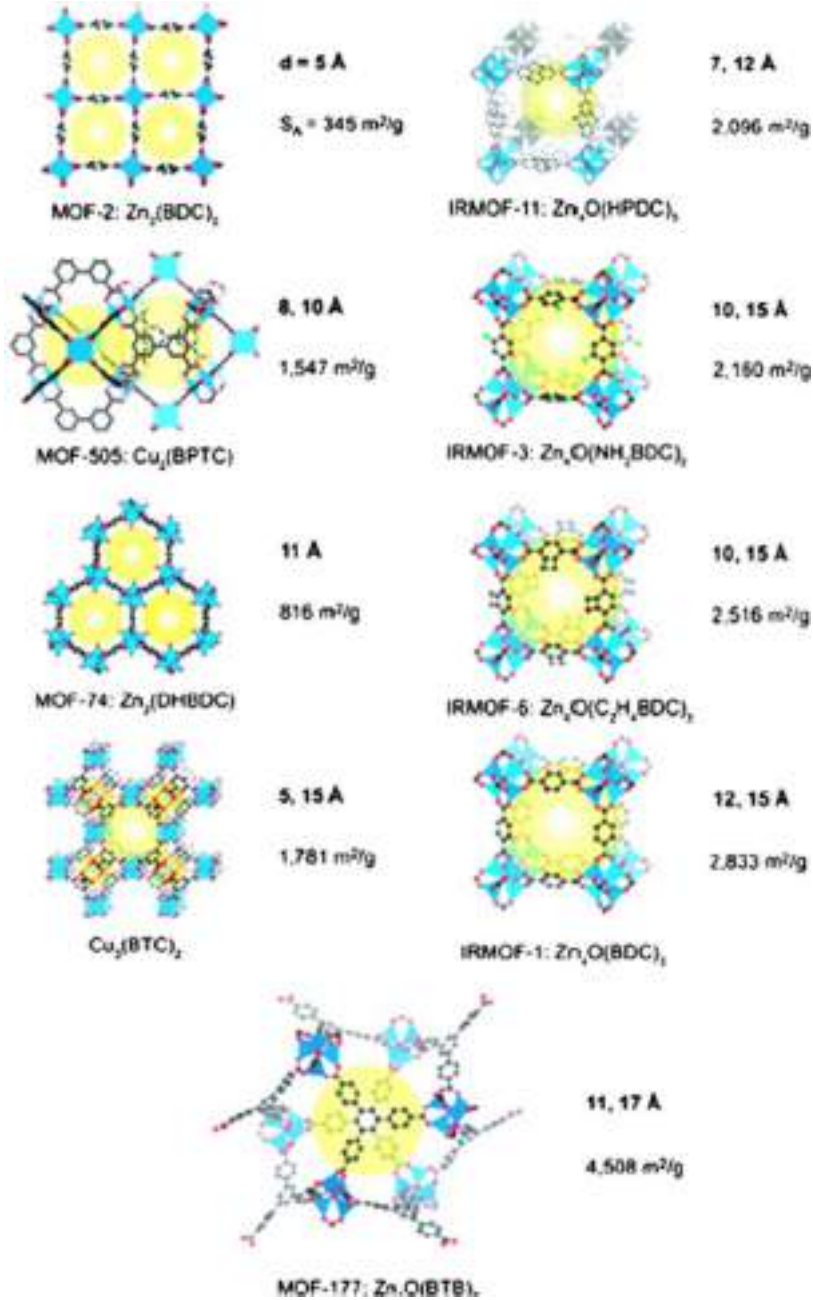

FIGURE 17.15 Evaluation of CO_2 adsorption with respect to pore size and surface area [44].

TABLE 17.1 CO_2 capturing capacities of various metal-organic framework (MOF) at low pressure.

S. No	Name of MOF	Surface area ($m^2\ g^{-1}$)		Uptake temperature	Uptake pressure	Capacity	Reference
		BET	Langmuir	(K)	(bar)	(wt.%)	
1	MOF-177	5,400	4690	298	1	3.6	[52]
2	MOF-74	1174	1733	298	1	5.8	[25]
3	$Cu_3(BTC)_2$	600	872	298	1	27	[53]
4	MOF-5, IRMOF-1	2304	2517	296	1	8.5	[54]
5	IRMOF-11	2096	3065	298	1	13.4	[55]
6	IRMOF-3	2160	–	298	1	5.1	[33]
7	MOF-505	1547	–	298	1	12.6	[33]
8	IRMOF-6	2516		298	1.2	4.6	[33]

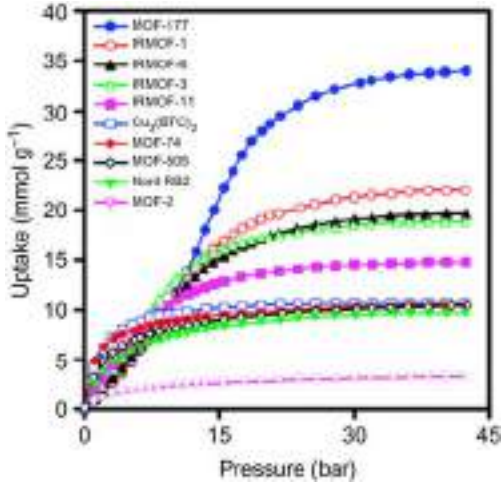

FIGURE 17.16 CO_2 uptake capacity of various MOFs under various pressures [44]. *MOFs*, Metal-organic frameworks.

MOF-505, MOF-74, and $Cu_3(BTC)_2$ is highest at low pressure, that is, 1 bar. However, MOF-177 gives the highest uptake of CO_2 among the concerned MOFs capacity at 35 bar (Fig. 17.16 and Table 17.2).

The advancement in the technological growth improvements of CO_2 capture and storage are playing a major role in the prevention of global warming, which is huge concern as discussed in the IPCC and the Conference of Parties. Below chart presented in Fig. 17.17 gives the technological readiness level of CO_2 capture at various scales, that is, laboratory, pilot, demonstration, and commercial scales. Also TRL scales are also categorized according to the applications of capture, transport, storage, and utilization. It can be seen that TRLs are showing their progress at TR3 to TR7 scale level but requires financial backup to make it commercially viable.

17.7 Conclusion

CO_2 is a significant contributor to global warming and would increase emissions from power plants, biomass or fuel combustion, vehicle exhaust, and from manufacturing processes. In this chapter we explored with a variety of examples how to fix CO_2 for MOFs and permeable natural polymers. It should be stressed that there are several other reactions which chemically fix CO_2 where MOFs play important roles. From the literature it is clear that the presence of open metal site and the high positive charge on the metal ion such as Cr^{3+}, Zr^{4+}, Al^{3+} will be very useful for the cycloaddition of CO_2 to

TABLE 17.2 CO_2 capturing capacities of various metal-organic frameworks (MOF) at high pressure.

S. No	Name of MOF	Surface area ($m^2\ g^{-1}$)		Uptake temperature	Uptake pressure	Capacity	Reference
		BET	Langmuir	(K)	(Bar)	wt.% $(mmol\ g)^{-1}$	
1	MOF-177	4500	5340	298	50	60.8	[33]
2	MOF-74	1542	–	298	36	68.9	[26]
3	$Cu_3(BTC)_2$	1270	–	313	30	42.8	[56]
4	MOF-5, IRMOF-1	2296	3840	298	35	21.7	[33]
5	IRMOF-11	2096	3840	298	40	14.7	[33]
6	IRMOF-3	2160	–	298	35	18.7	[33]
7	IRMOF-6	2296	3840	298	50	19.8	[33]

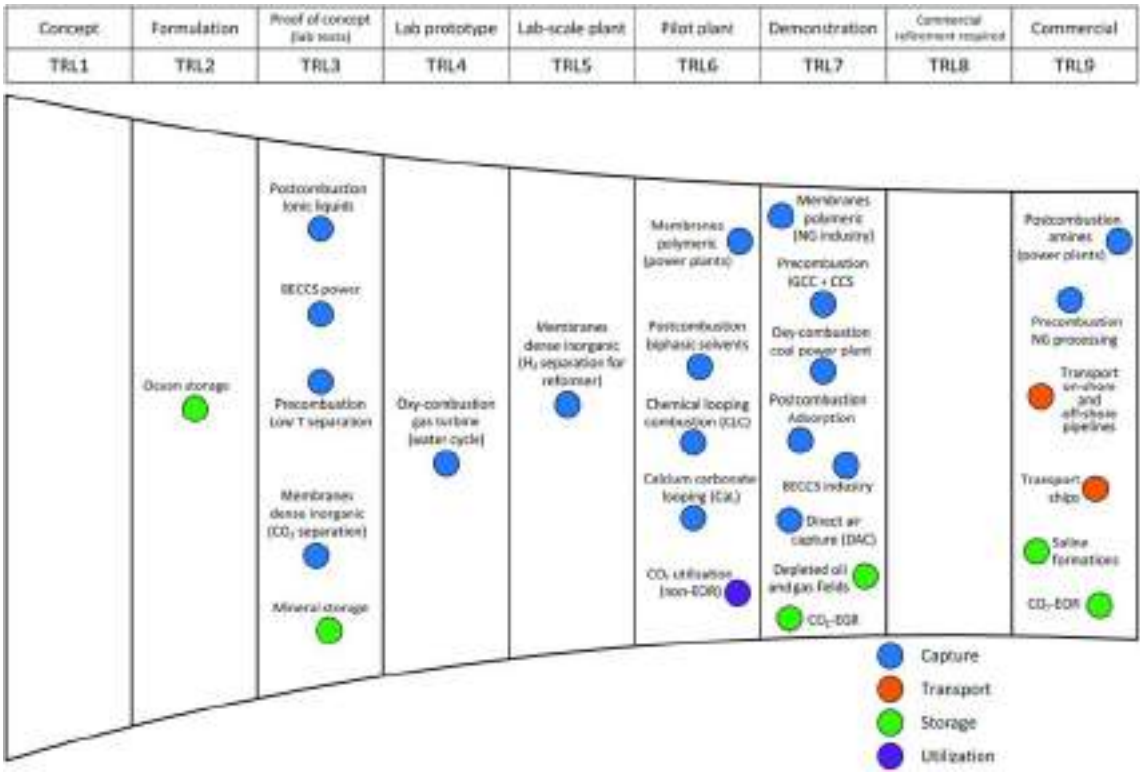

FIGURE 17.17 TRL of various CCS technologies [57]. *CCS*, Carbon capture and storage; *TRL*, technology readiness level.

epoxides. Until now, several technologies have been developed like CO_2 capture and geological sequestration. Production of heterogeneous catalysts based on MOF should be followed with vigor. Overall, MOF-based technology needs to be built urgently to achieve spot CO_2 fixation.

References

[1] Rackley SA. Carbon capture and storage. Burlington: Butterworth-Heinemann/Elsevier; 2017.

[2] Stewart C, Hessami M-A. A study of methods of carbon dioxide capture and sequestration-the sustainability of a photosynthetic bioreactor approach. Energy Conver Manage 2005;46:403–20. Available from: https://doi.org/10.1016/j.enconman.2004.03.009.

[3] Yang Q, Zhong C, Chen JF. Computational study of CO_2 storage in metal–organic frameworks. J Phys Chem 2008;112(5):1562–9.

[4] Olajire AA. CO_2 capture and separation technologies for end-of-pipe applications – a review. Energy 2010;35(6):2610–28.

[5] Feron PHM, Hendriks C. CO_2 capture process principles and costs. Oil Gas Sci Technol 2005;60(3):451–9.

[6] Conway W, Wang X, Fernandes D, Burns R, Lawrance G, Puxty G, et al. Comprehensive kinetic and thermodynamic study – with monoethanolamine (MEA) in aqueous solution. J Phys Chem A 2011;115:14340–9.

[7] Telikapalli V, Kozak F, Francois J, Sherrick B, Black J, Muraskin D. CCS with the Alstom chilled ammonia process development program—field pilot results. Energy Procedia 2011;4:273–81.

[8] Han K, Ahn CK, Lee MS, Rhee CH, Kim JY, Chun HD. Current status and challenges of the ammonia-based CO_2 capture technologies toward commercialization. Int J Greenh Gas Control 2013;14:270–81.

[9] Yu H, Qi G, Xiang Q, Wang S, Fang M, Yang Q. Aqueous ammonia based post combustion capture: results from pilot plant operation, challenges and further opportunities. Energy Procedia 2013;37:6256–64.

[10] Huang Y, Merkel TC, Baker RW. Pressure ratio and its impact on membrane gas separation processes. J Membr Sci 2014;463:33–40.

[11] Aaron D, Tsouris C. Separation of CO_2 from flue gas: a review. Sep Sci Technol 2005;40(1-3):321–48.

[12] Bernardo P, Drioli E, Golemme G. Membrane gas separation: a review/state of the art. Ind Eng Chem Res 2009;48(10):4638–63.

[13] Belaissaoui B, Favre E. Membrane separation processes for post-combustion carbon dioxide capture: state of the art and critical overview. Oil Gas Sci Technol – Rev IFP Energy Nouvelles 2013;69(6):1005–20.

[14] Merkel TC, Lin H, Wei X, Baker R. Power plant post-combustion carbon dioxide capture: an opportunity for membranes. J Membr Sci 2010;359:126–39.

[15] Kargari A, Ravanchi MT. Carbon dioxide: Capturing and utilizationAvailable from: https://www.intechopen.com/books/greenhouse-gases-capturing-utilization-and-reduction/carbon-dioxide-capturing-and-utilization.

[16] Algailani AZ. A discussion of ways to reduce greenhouse gases emission from chemical processes. Int J Innov Stud Sci Eng Tech 2015;1(1):1–6.

[17] Furukawa H, Cordova KE, O'Keeffe M, Yaghi OM. The chemistry and applications of metal-organic frameworks. Science 2013;341:1230444.

[18] Li M, Li D, O'Keeffe M, Yaghi OM. Topological analysis of metal−organic frameworks with polytopic linkers and/or multiple building units and the minimal transitivity principle. Chem Rev 2014;114:1343−70.

[19] Eddaoudi M, Moler DB, Li H, Chen B, Reineke TM, O'Keeffe M, et al. Modular chemistry: secondary building units as a basis for the design of highly porous and robust metal-organic carboxylate frameworks. Acc Chem Res 2001;34(4):319−30.

[20] Li JR, Kuppler RJ, Zhou HC. Selective gas adsorption and separation in metal−organic frameworks. Chem Soc Rev 2009;38:1477−504.

[21] Li JR, Ma YG, McCarthy MC, Sculley J, Yu JM, Jeong HK, et al. Carbon dioxide capture-related gas adsorption and separation in metal-organic frameworks. Coord Chem Rev 2011;255:1791−823.

[22] Biemmi E, Christian S, Stock N, Bein T. High-throughput screening of synthesis parameters in the formation of the metal-organic frameworks MOF-5 and HKUST-1. Microporous Mesoporous Mater 2009;117(1−2):111−17.

[23] Demessence A, D'Alessandro DM, Foo ML, Long JR. Strong CO_2 binding in a water-stable, triazolate-bridged metal-organic framework functionalized with ethylenediamine. J Am Chem Soc 2009;131:8784−6.

[24] Liang Z, Marshall M, Chaffee AL. CO_2 Adsorption-based separation by metal organic framework (Cu-BTC) versus Zeolite (13X). Energy Fuels 2009;23:2785−9.

[25] Caskey SR, Wong-Foy AG, Matzger AJ. Dramatic tuning of carbon dioxide uptake via metal substitution in a coordination polymer with cylindrical pores. J Am Chem Soc 2008;130:10870−1.

[26] Dietzel PDC, Besikiotis V, Blom R. Application of metal−organic frameworks with coordinatively unsaturated metal sites in storage and separation of methane and carbon dioxide. J Mater Chem 2009;19:7362−70.

[27] Allison LA, Mayer GS, Shoup RE. The *o*-phthalaldehyde derivatives of amines for high-speed liquid chromatography/electrochemistry. Anal Chem 1984;56:1089−96.

[28] Dzubak AL, Lin LC, Kim J, Swisher JA, Poloni R, Maximoff SN, et al. Ab initio carbon capture in open-site metal-organic frameworks. Nat Chem 2012;4:810−16.

[29] Yazaydin AO, Snurr RQ, Park TH, Koh K, Liu J, Levan MD, et al. Screening of metal-organic frameworks for carbon dioxide capture from flue gas using a combined experimental and modeling approach. J Am Chem Soc 2009;131:18198−9.

[30] Canepa P, Arter CA, Conwill EM, Johnson DH, Shoemaker BA, Soliman KZ, et al. High-throughput screening of small-molecule adsorption in MOF. J Mater Chem A 2013;1:13597−604.

[31] Hou X-J, He P, Li H, Wang X. Understanding the adsorption mechanism of C_2H_2, CO_2, and CH_4 in isostructural metal−organic frameworks with coordinatively unsaturated metal sites. J Phys Chem C 2013;117:2824−34.

[32] Cabello CP, Rumori P, Palomino GT. Carbon dioxide adsorption on MIL-100M (M = Cr, V, Sc) metal organic frameworks. IR spectrographic and metallographic studies. Microporous Mesoporous Mater 2014;190:234−9.

[33] Chaemchuen S, Zhou K, Kabir NA, Chen Y, Ke X, Van Tendeloo G, et al. Tuning metal sites of DABCO MOF for gas purification at ambient conditions. Microporous Mesoporous Mater 2015;201:277−85.

[34] Millward AR, Yaghi OM. Metal−organic frameworks with exceptionally high capacity for storage of carbon dioxide at room temperature. Am Chem Soc 2005;127:17998−9.

[35] Demessence A, D'Alessandro DM, Foo ML, Long JR. Strong CO_2 binding in a water-stable, triazolate-bridged metal–organic framework functionalized with ethylenediamine. J Am Chem Soc 2009;131:8784–6.
[36] Serre C, Bourrelly S, Vimont A, Ramsahye N A, Maurin G, Llewellyn P L, et al. An explanation for the very large breathing effect of a metal–organic framework during CO_2 adsorption. Adv Mater 2007;19:2246–51.
[37] Kim TK, Suh MP. Selective CO_2 adsorption in a flexible non-interpenetrated metal–organic framework. Chem Commun 2011;47:4258.
[38] Hong DH, Suh MP. Selective CO_2 adsorption in a metal–organic framework constructed from an organic ligand with flexible joints. Chem Commun 2012;48:9168.
[39] Park HJ, Suh MP. Enhanced isosteric heat, selectivity, and uptake capacity of CO_2 adsorption in a metal-organic framework by impregnated metal ions. Chem Sci 2013;4:685.
[40] Yuan Y, Zhu G. Porous aromatic frameworks as a platform for multifunctional applications. ACS Cent Sci 2019;5(3):409–18.
[41] Yang Y, Faheem M, Wang L, Meng Q, Sha H, Yang N, et al. Surface pore engineering of covalent organic frameworks for ammonia capture through synergistic multivariate and open metal site approaches. ACS Cent Sci 2018;4(6):748–54.
[42] Sung S, Suh MP. Highly efficient carbon dioxide capture with a porous organic polymer impregnated with polyethylenimine. J Mater Chem A 2014;2:13245.
[43] Ben T, Ren H, Ma S, Cao D, Lan J, Jing X, et al. Targeted synthesis of a porous aromatic framework with high stability and exceptionally high surface area. Angew Chem Int Ed 2009;48:9457–60.
[44] Zhang Y, Zhang W, Feng F, Zhang J, Chen X. A highly connected porous coordination polymer with unusual channel structure and sorption properties. Angew Chem Int Ed 2009;48:5287–90.
[45] Seo J, Chun H. Hysteretic gas sorption in a microporous metal–organic framework with nonintersecting 3D channels. Eur J Inorg Chem 2009;33:4946–9.
[46] Li H, Eddaoudi M, Groy TL, Yaghi OM. Establishing microporosity in open metal–organic frameworks: gas sorption isotherms for Zn(BDC) (BDC = 1,4-Benzenedicarboxylate). J Am Chem Soc 1998;120:8571–2.
[47] Chen B, Ockwig NW, Millward AR, Contreras DS, Yaghi OM. High H_2 adsorption in a microporous metal-organic framework with open metal sites. Angew Chem Int Ed Engl 2005;44:4745–9.
[48] Rosi NL, Kim J, Eddaoudi M, Chen B, O'Keeffe M, Yaghi OM. Rod packings and metal–organic frameworks constructed from rod-shaped secondary building units. J Am Chem Soc 2005;127:1504–18.
[49] Ockwig NW, Delgado-Friedrichs O, O'Keeffe M, Yaghi OM. Reticular chemistry: occurrence and taxonomy of nets and grammar for the design of frameworks. Acc Chem Res 2005;38:176–82.
[50] Eddaoudi M, Kim J, Rosi N, Vodak D, Wachter J, O'Keeffe M, et al. Systematic design of pore size and functionality in isoreticular MOFs and their application in methane storage. Science 2002;295(5554):469–72.
[51] Li H, Eddaoudi M, O'Keeffe M, Yaghi OM. Design and synthesis of an exceptionally stable and highly porous metal-organic framework. Nature 1999;402:276–9.
[52] Mason JA, Sumida K, Herm ZR, Krishna R, Long JR. Evaluating metal–organic frameworks for post-combustion carbon dioxide capture *via* temperature swing adsorption. Energy Environ Sci 2011;4:3030–40.

[53] Yazaydin AO, Benin AI, Faheem SA, Jakubczak P, Low JJ, Willis RR, et al. Modeling gas separation in metal-organic frameworks. Chem Mater 2009;21:1425–30.

[54] Zhao Z, Li Z, Lin YS. Adsorption and diffusion of carbon dioxide on metal–organic framework (MOF-5). Ind Eng Chem Res 2009;48:10015–20.

[55] Kim J, Yang S, Choi SB, Sim J, Kim J, Ahn W. Control of catenation in CuTATB-*n* metal–organic frameworks by sonochemical synthesis and its effect on CO_2 adsorption. J Mater Chem 2011;21:3070.

[56] Moellmer J, Moeller A, Dreisbach F, Glaeser R, Staudt R. High pressure adsorption of hydrogen, nitrogen, carbon dioxide and methane on the metal–organic framework HKUST-1. Microporous Mesoporous Mater 2011;138:140–8.

[57] Bui M, Adjiman CS, Bardow A, Anthony EJ, Boston A, Brown S, et al. Carbon capture and storage (CCS): the way forward. Energy Environ Sci 2018;11:1062–176.

Chapter 18

Nanomaterials derived from metal-organic frameworks for energy storage supercapacitor application

Lakshmanan Gurusamy[1], Sambandam Anandan[2] and Jerry J. Wu[1]
[1]*Department of Environmental Engineering and Science, Feng Chia University, Taichung, Taiwan,* [2]*Department of Chemistry, National Institute of Technology, Trichy, India*

18.1 Introduction

The MOFs (metal-organic frameworks) are well-developed materials due to their functionality, structural diversity, and multipurpose applications. MOFs as versatile functional materials produce highly controllable nanostructures because of their sacrificial precursors and achievement for energy storage devices [1]. The MOFs have been compared with the traditional inorganic porous materials, but MOFs have tunable pore sizes and topologies, multifunctionality, and naturally are of hybrid inorganic−organic frameworks [2,3]. The emerging avenue of MOFs nanostructures is fabricated through the highly tunable nature of ligands and metal ions. The porous nanostructured of MOFs can be converted by the controlled heating to produce a decidedly appropriate specific surface area. For instance, the porous Co_3O_4 nanostructures were prepared by using novel MOFs templated strategy, which has still remained a challenging [4−6]. Since Yaghi and coworkers first synthesized the MOFs in 1995 and had more interests in many application fields, for example, adsorption of gas and separation of gas, and electrocatalysis. Those MOFs possess high specific surface areas, porous nature, and outstanding thermal and structural stability. Motivated by this, the MOF electrode materials have greater performance in supercapacitor applications due to the porous structure of excellent specific surface areas, for example, to prepare porous Co_3O_4 [7,8]. The fluoride ions doped cobalt-coordination polymers (F-Co-CPs) look flower-like and are vertically grown on the ZIF-67 templates. The fluorine comes from the NH_4F, which has greater

Metal-Organic Frameworks for Chemical Reactions. DOI: https://doi.org/10.1016/B978-0-12-822099-3.00018-6

electronegativity than that of N_2 in 2-methylimidazole. The fluoride ion (F^-) was replaced by imidazole ($C_3N_2H_4$) ligand and was then coordinated with Co^{2+} ions to produce an F-Co-CPs electrode material.

MOF-derived hybrid nanoporous materials have been presented in high crystalline architectures and diverse functionalities for a variety of applications. MOFs could be quickly converted into metal oxides, metal sulfides, and porous carbons (PCs) as electroactive materials for energy storage devices. For electrical energy storage devices, MOFs have been used to provide greater surface areas with adequate redox reaction sites [9–12]. For instance, the dodecahedral structure of Co_3O_4 supported mesoporous carbon (MC) sponge (MCS) was prepared from commercially available melamine ($C_3H_6N_6$) foams and used as the precursor of zeolitic imidazolate framework-67 (ZIF-67) at the carbonization process. The ZIF-67 was used for the synthesis of Co_3O_4 nanoporous crystals owing to their low density with versatile specific surface areas and greater functionalities of ZIF-67. The charge storage space of ZIF-derived Co_3O_4 crystals was greater because the electrolyte ions can easily enter into the porous space and thus improve the electrochemical performance. Besides, the MCS works as excellent electrical conductivity and decreases the internal stress during the Co_3O_4 transformation to porous-Co_3O_4 using ZIF-67 precursor at thermal treatments. The obtained Co_3O_4/MCS can provide amazing electrochemical performance due to the synergistic effects for carbonaceous property from MCS and the metallic property derived from transition metal oxides (TMOs) [13,14].

Recently, MOFs have been widely used as potential electrode competitors for supercapacitor application due to their higher specific surface area and porosity with diverse morphology. MOFs could provide enough porous channels to facilitate the electron transportation in energy storage performances [15–17]. Moreover, MOFs can also act as a dual characters, such as precursors and templates, which are constructing hollow nanostructured for metal oxides and metal sulfides. The final products of MOFs exhibit high specific surface areas and rich porous structures to be applied in electrochemical energy storage devices. Besides, the MOFs could donate their derivatives with numerous compositions, which can increase the specific capacitance and cycling stability with rate performances of electrode materials [18,19]. The MOFs are potential electrode candidates due to their hallow nanovoids, controllable nanostructures, and noteworthy specific surface areas, thus improving energy storage performances in supercapacitor. For example, the hollow-concave $CoMoS_x$ was synthesized by two-step approach [20,21]. In addition, MOFs were extensively used as sacrificial templates or precursors in supercapacitor electrodes owing to the enormous internal surface area and rich electrochemical energetic components [22].

Electrochemistry application fields, including lithium-ion batteries, supercapacitors, and electrocatalysis, have been widely used as multifunctioning materials of MOFs [23]. The MOF nanostructures are well ordered porous,

which exhibit more redox-active sites for supercapacitor application and thus facilitate the transfer of ion and electron. For example, the electrode materials of Co-MOFs and Ni-MOFs have shown the exceptional reversibility [24]. The bi-MOFs show the double electrochemical behavior than that of mono-MOFs due to their greater redox-active sites. Nevertheless, the MOFs electronic conductivity plays an important role to become a major obstacle for their supercapacitors applications [25,26]. The preparation of PC materials (PCM) derived from MOFs procedures are unique by producing high carbon yield. For example, the PCM was formed via the carbonization process and exhibited admirable supercapacitive performance [27,28]. The MOF-derived PC compared with other PCM exhibits well-defined shape, uniform porosity, and higher surface area, thus achieving enhanced electrochemical performances in asymmetric supercapacitor (ASC) applications [29].

18.1.1 Metal-organic frameworks

More than 20 years ago, MOF's new kind of crystalline materials have been prepared through the coordination interactions of inorganic secondary building units to combine with multiple organic linkers [30]. MOFs are effortless structures and properties tailored through the postsynthetic modification (PSM) and functionality of the modules. According to the PSMs, more than 20,000 MOFs syntheses were employed for the fundamental development in the application fields. MOFs selectively catalyze some organic reactions owing to their controllable pore size (98 Å), corresponding low density ($0.13\ g\ cm^{-3}$), and high surface area ($10{,}000\ m^2\ g^{-1}$) [31,32]. MOFs were used for various applications, such as fuel cells, supercapacitors, and photocatalytic hydrogen evolution, which was highly attracted to materials science and chemistry communities. MOF-derived porous materials could act as excellent electrode materials in supercapacitor and fuel cell devices. Furthermore, MOFs might generate various nanostructures as shown in Fig. 18.1, such as directly supporting materials and integrate of metals, metal oxides, metal sulfide, bimetal oxides, and bimetal sulfide, respectively [33–35].

18.1.2 Composites of metal-organic frameworks

The MOF performance has been significantly improved by the MOFs combined with the different functional materials and thereby the new functionality was developed in practical application. For instance, the MOF composites of MOF–rGO, MOF–CNT, MOF–metal nanoparticles, MOF–metal oxide, MOF–metal sulfides, and MOF–complexes. The composite has extended its applications, for example, in catalysis, supercapacitor and conversion devices, and photo-induced H_2 generation, and so on [33]. The MOF composites not only provided multifunctionality but also created new

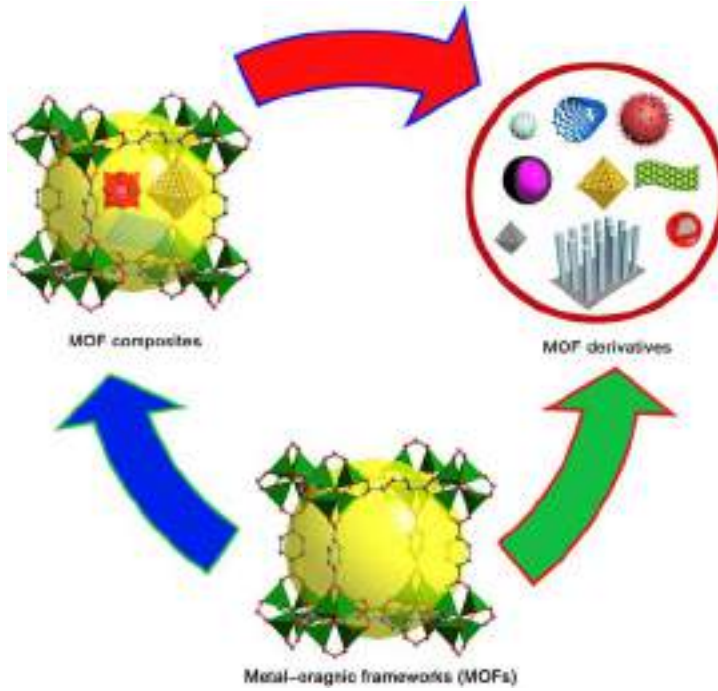

FIGURE 18.1 MOFs, MOF-composites, and MOF-derivatives schematic diagram as well as their conversions [1]. *MOF*, Metal-organic framework.

physiochemical properties, whereas these behaviors did not present in the single components. The composites of MOFs database would augment the sophisticated architectures and lead to new design strategies for the MOF composites [36].

18.1.3 Derivatives of metal-organic frameworks

The metals, metal oxides, metal sulfides, PCs and their hybrids, have been widely used in the field of nanoscience and nanotechnology. Especially, the nanoporous carbon electrode candidates have been employed for practical application of supercapacitor and conversion devices due to higher specific surface area, larger pore volume, and exceptional chemical and mechanical stability [37]. MOF-to-carbon structures were synthesized by the carbonization process in the presence of heating rate to obtain highly ordered pore structure, narrow pore-size distribution, tunable structures, and functionality. MOF-derived carbon nanorods have been prepared by the sonochemical approach followed by KOH activation method. The formation of 2−6 layered graphene nanoribbons establishes a new path for MOF-derived carbon materials according to the PSM with outstanding supercapacitor performance

[38]. Moreover, the preparation of inorganic nanomaterials, such as metals, bimetal oxides, and bimetal sulfides, used various synthetic procedures, but MOFs-derived nanostructured materials gave an effective route. The advantages of MOFs-derived nanostructure include low-cost precursors, size of the controllable morphology, and inimitable roles of MOFs-templates. The metals, metal oxides, metal sulfides, and their composites can be prepared through the MOF pyrolysis process and thereby MOF composites own excellently controllable morphology and augmented electrical conductivity in MOF derivatives in supercapacitor performances [39,40].

18.2 Metal-organic framework–derived metal oxide and composites

18.2.1 Porous Co_3O_4

According to a solvothermal reaction, the purple-colored ZIF-67 crystals were developed in between the Cobalt(II) nitrate hexahydrate and 2-methylimidazole (mIM) using the solvents of tetrahydrofuran and H_2O for 10 h at 150°C. Then, the porous-Co_3O_4 nanoparticles were prepared through the use of the calcination process of the ZIF-67 template that crystallizes in a cubic system with an $I-43m$ space group. The tetrahedral geometry can be formed by the four N atoms of four mIM ligands in N_4 environments coordinated with each Co(II) ion. The 3D framework of pores is formed by each $Co-N_4$ moieties connected to the other $Co-N_4$ moieties. The charge–discharge (CD) curves appearance is nonlinear at various current densities, which imitates the poor coulombic efficiency of the electrode materials. Galvanostatic charge and discharge (GCD) curves of constant slopes were observed at different current densities. The porous Co_3O_4 could attain maximum specific capacitance of 190 F g^{-1} at the 5 A g^{-1} and simultaneously the rate performance was determined to be 77.89% up to the current density of 20 A g^{-1}. Meanwhile, the Co_3O_4 showed battery-like behavior and, therefore, the different current density used for specific capacity was calculated. The greatest specific capacity of 95 C g^{-1} was obtained at a current density of 5 A g^{-1} and the rate capability performance achieved 74 C g^{-1} at 20 A g^{-1} [41].

18.2.2 Hollow α-Fe_2O_3 microboxes

The preparation processes are schematically illustrated in Fig. 18.2A. First, the polyvinyl pyrrolidone was transferred into the acidic nature of HCl and became a clear solution. Then 0.44 g of $K_4[Fe(CN)_6]\cdot 3H_2O$ was dissolved into the above mixture with magnetic stirring. Finally, the yellow color solutions of PB microcubes were heated at 80°C for 24 hours and subsequently washed several times by using water and ethanol, and then dried. Finally, the

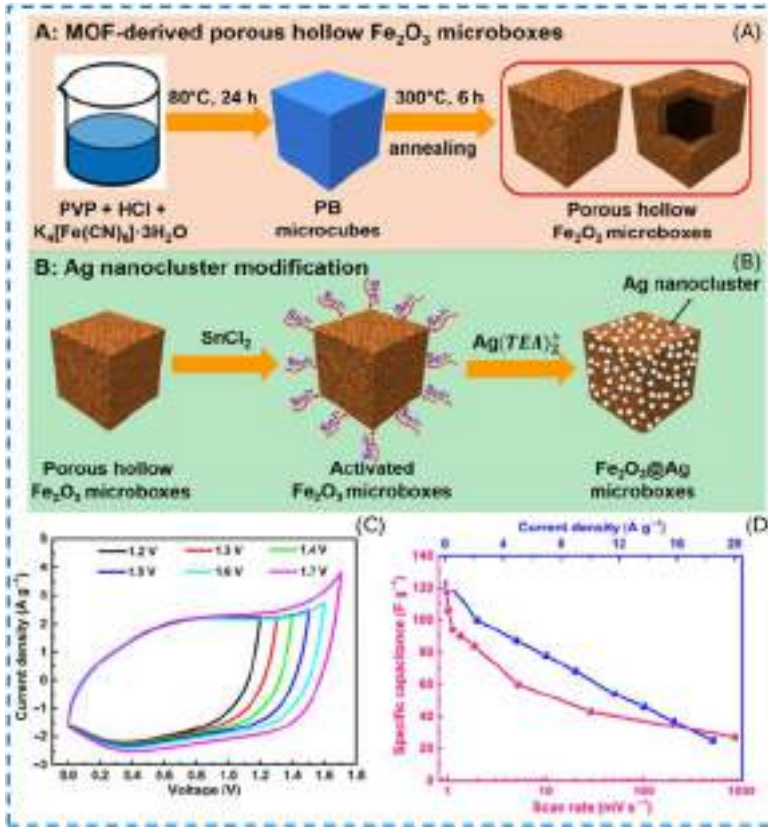

FIGURE 18.2 (A, B) The synthesis process schematic illustration of the Fe_2O_3@Ag micro boxes. ASC in 1 M Na_2SO_3 aqueous electrolyte: (C) CV data at different voltage windows. (D) Specific capacitances versus scan rates and current densities [42]. *ASC*, Asymmetric supercapacitor; *CV*, cyclic voltammetry.

Fe_2O_3 microboxes were formed by the PB microcubes calcined in an air atmosphere at the temperature of 300°C. As for the preparation of Fe_2O_3@Ag micro boxes, firstly 0.1 g of Fe_2O_3 microbiomes were added into 100 mL of ethanol and then 0.05 g of $SnCl_2 \cdot 2H_2O$ was added by the stirring followed by ultrasonication for 30 minutes. The Fe_2O_3 combined with Sn^{2+} was collected after centrifuging. Subsequently, the α-Fe_2O_3 was added in 50 mL of $(Ag\ TEA)_2^+$ solution under stirring for 2 hours to confirm that Ag^+ was reduced into the Ag by Sn^{2+}. In the end, the resultant product, Fe_2O_3@Ag was washed with ethanol, then dried as shown in Fig. 18.2B. The practical application of ASC was assembled by the anode materials of α-Fe_2O_3@Ag and cathode materials of activated carbon (AC) in 1 M Na_2SO_3 aqueous electrolyte solution. As depicted in Fig. 18.2C, the cyclic

voltammetry (CV) data exhibited at various operating potential windows from 1.2 to 1.7 V for the scan rate of 50 mV s^{-1}. This was originating from the oxidation−reduction reaction in while the operating potential window up to 1.7 V. According to the CV and GCD plots (Fig. 18.2D), the specific capacitance can achieve 123 and 118 F g^{-1} acquired at a scan rate of 1 mV s^{-1} and at an 0.1 A g^{-1}. The ASC apparatus revealed an excellent rate performance and specific capacitance of 27 F g^{-1} even at a higher current density of 20 A g^{-1} [42].

18.2.3 Co_3O_4/NiO/Mn_2O_3

The formation mechanism of Co_3O_4/NiO/Mn_2O_3 is schematically demonstrated in Fig. 18.3A. The terephthalic acid as an organic ligand coordinated with the metal ions of Co^{2+}, Ni^{2+}, Mn^{2+} (Co $(NO_3)_2$, Ni $(NO_3)_2$, and Mn $(NO_3)_2$) in the presence of the ethanol-DMF system. The CoNiMn-MOF was deposited under the coordination reaction over the nickel foam surface by the hydrothermal method, which was inveterate from the XRD pattern (pale-yellow product CoNiMn-MOF). The protection of the original framework of CoNiMn-MOF was made by the preheated pipe furnace under the N_2 atmosphere. The calcination process could obtain the metal oxide composite of Co_3O_4/NiO/Mn_2O_3, where the carbon was entirely oxidized and thus preserved the unique CoNiMn-MOF framework. The cyclic stability using

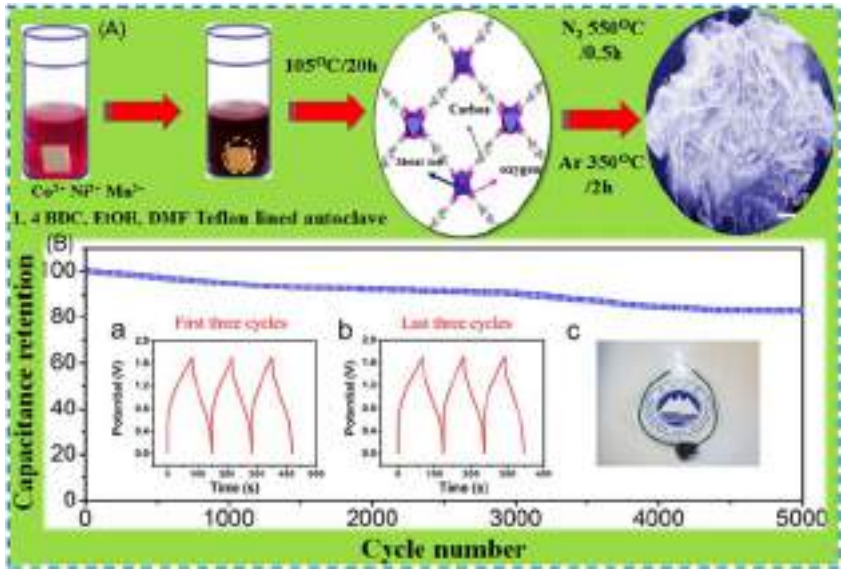

FIGURE 18.3 (A) The schematic diagrams of the Co_3O_4/NiO/Mn_2O_3 formation mechanism. (B) Cyclic stability of Co_3O_4/NiO/Mn_2O_3//rGO at a current density of 10 mA cm^{-2} (inset first and last three cycles, and the light-emitting diode lights up at 3 V) [43].

rGO//Co_3O_4/NiO/Mn_2O_3 electrode displays 82% capacitance retention after 5000 cycles evaluated at 10 mA cm^{-2} (Fig. 18.3B). The practical application of ASC has been tested for light-emitting diode (LEDs), which successfully lighted up at a working voltage of 3 V [43].

18.2.4 NiO/carbon nanofiber

MOFs fiber has been synthesized using the starting materials of Ni and Zn from $NiCl_2 \cdot 6H_2O$ and Zn from $Zn(Ac)_2 \cdot 2H_2O$, respectively, in the presence of trimesic acid (H_3BTC). Preparation procedure was followed that 1.25 g of H_3BTC was first added into the 50 mL of DMF solution at room temperature of 35°C. Then, the succeed addition of $(5(1-x)$ mmol) of $Zn(Ac)_2 \cdot 2H_2O$ and ($5x$ mmol) of $NiCl_2 \cdot 6H_2O$ (x was denoted as the Ni molar percentage). The resulting products were magnetically stirred for 30 minutes and transferred into a Teflon-lined stainless steel autoclave under heated for 12 hours at 140°C. The completion of reaction was done by the autoclave temperature cooling down to room temperature. The yielding of 100 × Ni-ZnBTC fibers was formed by washing and drying precursor solution.

Finally, the product of 100 × NiO/CNF composites (Fig. 18.4A) was formed by the dried materials which were pyrolyzed at 950°C for 2 hours. Moreover, the mechanically mixed electrode material, NiO/CNF (0.100 NiO−CNF-m), has been compared to the NiO/CNF composite (0.100 NiO/CNF-p) p-denoted as postgrafted. The FT-IR pattern of Ni, Zn-containing MOFs fiber displays stretching frequency at 1635, 1566, 1364, and 1250 cm^{-1} (Fig. 18.4B), which are corresponding to the phenol-bridged structures. As presented in Fig. 18.4C, the strong diffraction peaks of XRD data for 0.100 Ni-ZnBTC display from 5° to 20°, which belongs to the rutile-structured of $P4_2/mnm$ space group. The diffractions peaks of 0.100 NiO/CNF shows the $2\theta = 23°$ and 43° belonging to the crystalline planes (0 0 2) and (1 0 1). This strongly indicated that the crystalline-MOFs fibers were converted into the carbonaceous materials. Furthermore, the characteristic of the graphitic carbon structure was observed in-plane at $2\theta = 13°$, which represented the graphitic structures dominantly present in 0.100 NiO/CNF. Nyquist plots for the CNF and NiO/CNF of both the electrodes were presented in Fig. 18.4D, which can be divided into three regions, such as high, middle, and low-frequency regions. The 0.100 NiO/CNF electrode showed a smaller semicircle compared to other composites. Owing to its higher porosity, it presents in 0.100 NiO/CNF more efficient electron movement occurred from NiO to CNF. Also, the semicircle arc was intercepted on the real axis at high frequency, which indicates equivalent series resistance (ESR). The resistance of NiO/CNF composites solution is less than 0.72 Ω which excepts for that of 0.500 NiO/CNF. This suggested a superior electrical conductivity due to the NiO weight percentage dosage less than 0.43. Moreover, the stability of 0.100 NiO/CNF electrode was detected by the

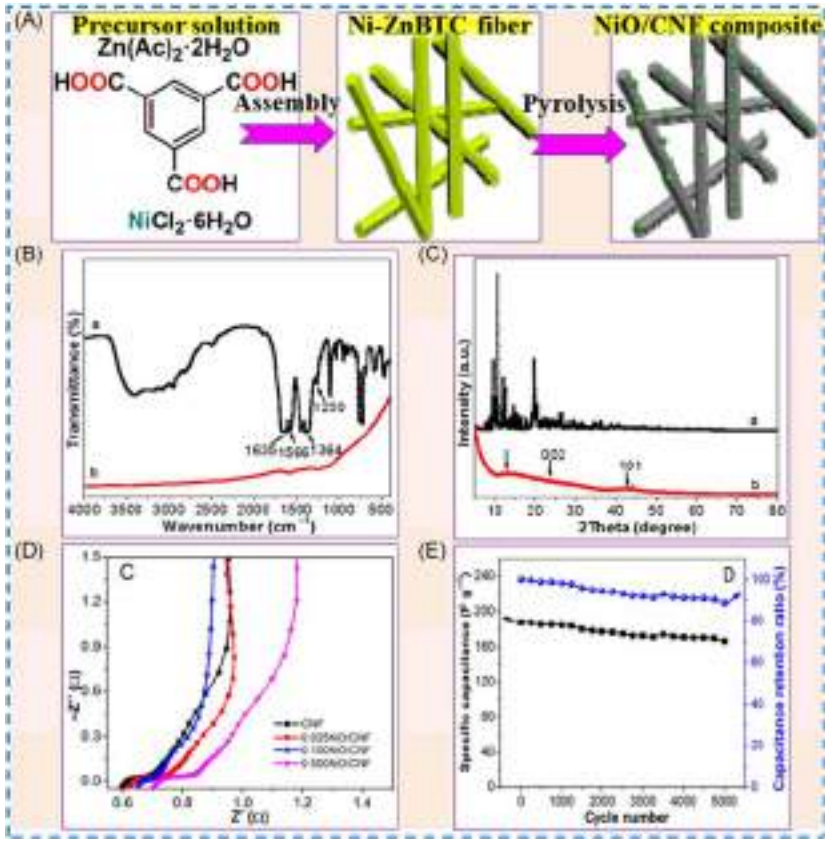

FIGURE 18.4 (A) Schematic description of NiO/CNF composite synthesis, (B) FT-IR pattern, (C) XRD pattern, (D) Nyquist plots of EIS data, and (E) cycling stability of 0.100 NiO/CNF [44].

long-term GCD curve behavior at a current density of 5 A g^{-1} as shown in Fig. 18.4E. The 0.100 NiO/CNF electrode reveals an outstanding cycling behavior due to the initial capacitance to be 90% after 5000 cycles and the capacity loss rate of 0.002% only for each cycle. The cycling performance of 0.100 NiO/CNF was greater than those of already reported pseudocapacitance-based electrode materials [44].

18.2.5 Co_3O_4@carbon flower

The solvent of CH_3OH was dissociated into the CH_3O^- and H^+ ions at the higher temperature, then F^- and CH_3O^- substituted at the location of 2-methylimidazole to steadily convert into 2D CPs (Co-coordination polymers) and schematically illustrated in Fig. 18.5A. FE-SEM image of morphology

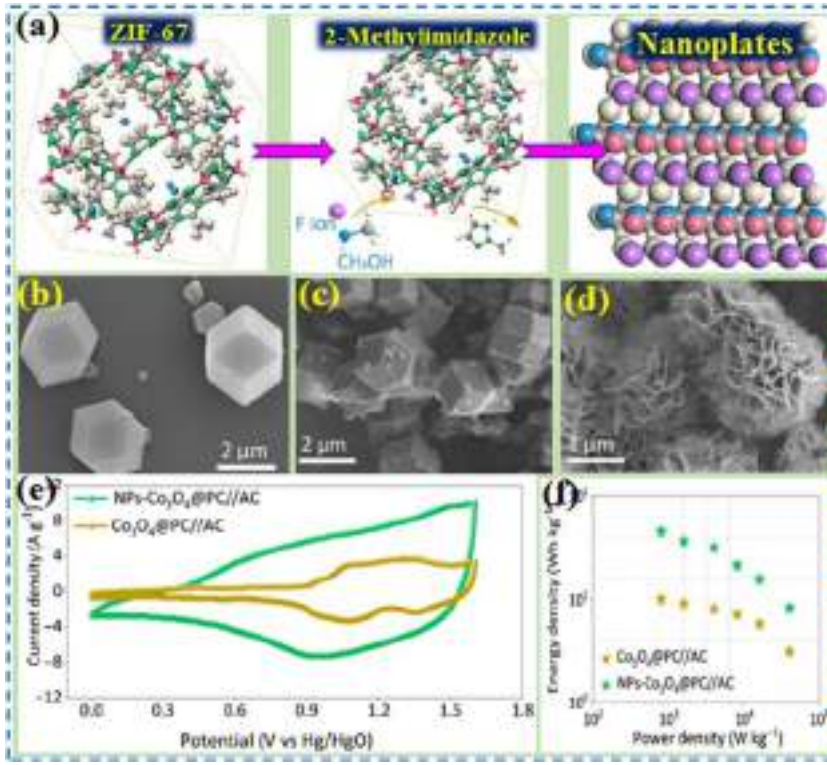

FIGURE 18.5 (A) The preparation process of F-Co-CPs. (B–D) ZIF-67, F-Co-CPs at the reaction of 0 h and F-Co-CPs at the reaction of 8 h (SEM image). (E) CV data of NS-Co_3O_4@PC//AC and Co_3O_4@PC//AC at 50 mV s^{-1}. (F) Ragone plots [45]. *AC*, Activated carbon; *CV*, cyclic voltammetry.

characterization and the development of the F-Co-CPs mechanism are presented in Fig. 18.5B. A uniform rhombic dodecahedron (without NH_4F) largely obtained without aggregation is observed in Fig. 18.5B. At different hydrothermal reaction time, such as 0, 1, 4, 8, and 12 hours, the precursor was collected, then the development process of these 2D-nanosheets (NSs) is shown in SEM images. As can be seen in Fig. 18.5C, few NSs deposited on the surface of the ZIF-67 templates. According to Fig. 18.5D, the assembled hollow microsphere by the interconnected in 2D NSs. Two adjacent NSs gaps 5–10 nm range were observed and thickness and average diameter of NSs were about 10 nm and 1–2.0 μm, respectively. Moreover, the AC and NS-Co_3O_4@PC electrode exhibited a potential window from −1 to 0 V and 0 to 0.6 V. Consequently, the ASC device voltage windows can be extended to 1.6 V. Based on Fig. 18.5E, the CV plots of NS-Co_3O_4@PC//AC and Co_3O_4@PC//AC were compared at the 50 mV s^{-1}, which show an integrated area of the NS-Co_3O_4@PC//AC electrode much larger than for

Co_3O_4@PC//AC. The energy/power density (P) are significant parameters to estimate the commercial ASCs application. As displayed in Fig. 18.5F, the NS-Co_3O_4@PC//AC ASC displayed a higher energy density of 45.23 Wh kg^{-1} at the 800 W kg^{-1}. For comparison, the Co_3O_4@PC//AC electrode merely displayed energy density of 10 Wh kg^{-1} at a power density of 40,000 W kg^{-1} [45].

18.2.6 CC@Co_3O_4

The cathode materials of CC@Co_3O_4 was used for electrochemical analysis in the potential windows from 0 to 0.6 V at the scan rates from 10 to 100 mV s^{-1} is presented in Fig. 18.6A. The CV data show oxidation (at 0.55 V) and reduction (at 0.45 V) peaks, which demonstrated the Faradaic reaction occurs between Co^{2+} and Co^{3+} in the presence of OH^- ions for better electrochemical reaction kinetics on the electrode surface. Likewise, the anode materials of the CC@NC electrode was studied at the three-electrode configuration, which represented the near-rectangular shape of CV plots in Fig. 18.6B. The electrode materials manufacture procedure and the architecture are schematically illustrated in Fig. 18.6C. The CC@Co-MOF nanocomposites prepared by the facile reaction occur between Co^{2+} and 2-methylimidazole in an aqueous medium. Meanwhile, a Co-MOF (2D sheet-like) was directly developed on the surface of carbon cloth. As shown in Fig. 18.6D, the anode of CC@NC combines with the cathode of CC@Co_3O_4 using the PVA-KOH electrolyte. The flexible ASC of the CC@Co_3O_4//CC@NC electrode has

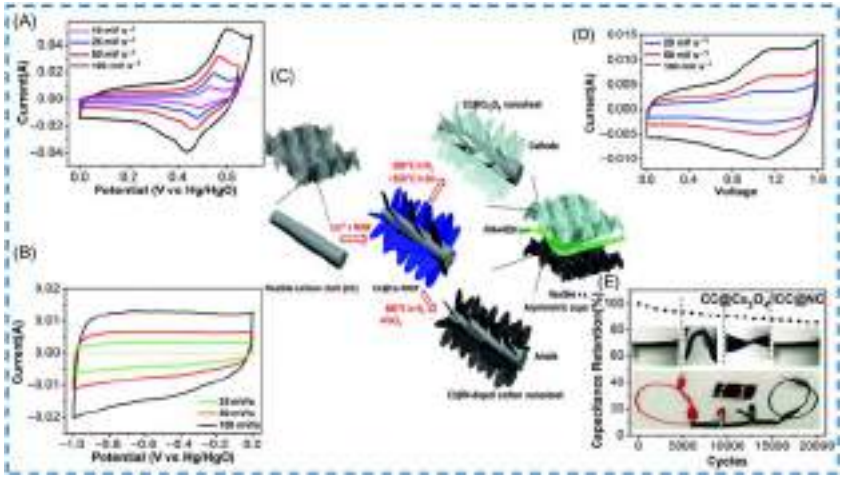

FIGURE 18.6 CV curves of (A) CC@Co_3O_4, (B) CC@NC. (C) schematic illustration of the 2D Co_3O_4 nanosheets and N-doped carbon nanosheets, (D) CV curves of CC@Co_3O_4//CC@NC. (E) The practical application in the three full cells (each size of $1 \times 2.5 \times 0.08$ cm^3) can light up eight orange LEDs [46]. *CV*, Cyclic voltammetry; *LED*, light-emitting diode.

shown the quasirectangular shape of the peaks even at the higher scan rate of 100 mV s^{-1}. The full-cell cycling test of CC@Co_3O_4//CC@NC electrode gave different bending/twisting conditions (inset in Fig. 18.6E). The 90.8% and 85.5% capacitance still retains after 10,000 cycles and 20,000 cycles due to the structural stability with outstanding cycling durability. The capacity loss is due to the nanostructure change and volume expansion during the cycling. The solid-state full-cell practical application for flexible/bendable electronics is further demonstrated in Fig. 18.6E. The LEDs can be lit in orange color, which connected three series ASCs ($3 \times 2.5 \times 0.08$ cm^3) under bending states [46].

18.2.7 Co_3O_4/3D macroporous carbon sponge

The fabrication process of Co_3O_4/3D macroporous carbon sponge synthesized by the melamine foam as the starting materials and 3D macroporous framework through thermal treatment are presented in Fig. 18.7A.

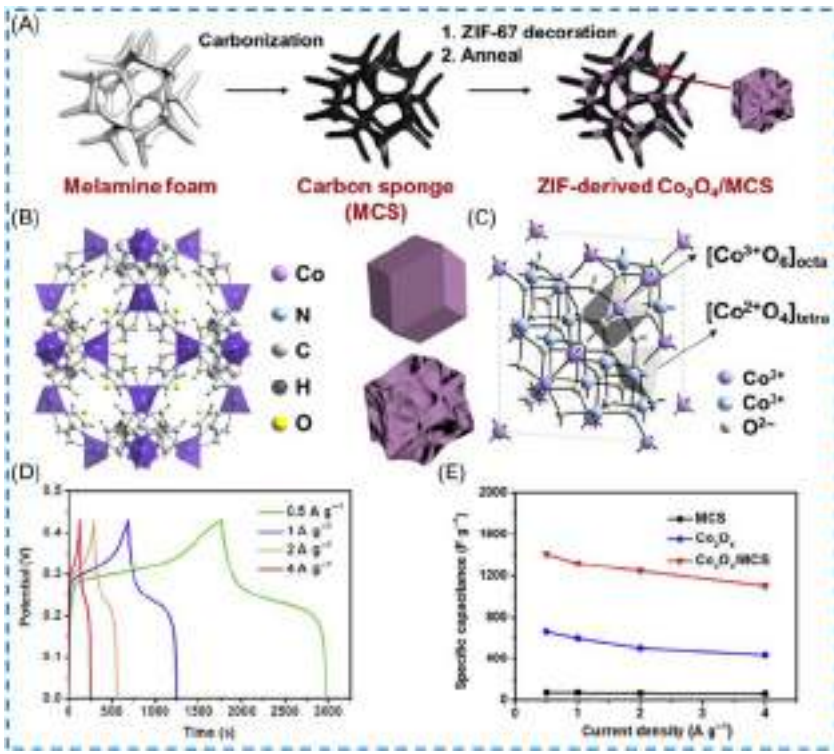

FIGURE 18.7 (A) The fabrication process of the Co_3O_4/MCS, (B) crystalline structure of ZIF-67; (C) crystalline structure of Co_3O_4 (ZIF-derived schematic morphology Co_3O_4). (D) GCD curves of Co_3O_4/MCS at different current densities, (E) specific capacitance versus different current densities [47]. *MCS*, Mesoporous carbon sponge.

The ZIF-67 and ZIF-derived Co_3O_4 crystalline structure and morphology have been depicted in Fig. 18.7B and C. Based on GCD curves, the specific capacitance increased from 4 to 0.5 A g^{-1} as shown in Fig. 18.7D and E. Meanwhile, MCS or Co_3O_4 showed insufficient electrochemically active surface area of materials [47].

18.3 Metal-organic framework-derived bimetal oxide nanostructures

18.3.1 Hollow spheres $CuCo_2O_4$

The yolk−shell spheres of bimetallic CuCo-ZIF prepared from CC-gly spheres is presented in Fig. 18.8A. Then, the CC-gly sphere was formed due to the 2-methylimidazole strongly coordinated with the copper and cobalt ions. The bimetallic CuCo-ZIF nanocrystals were developed on the surface of the outside sphere.

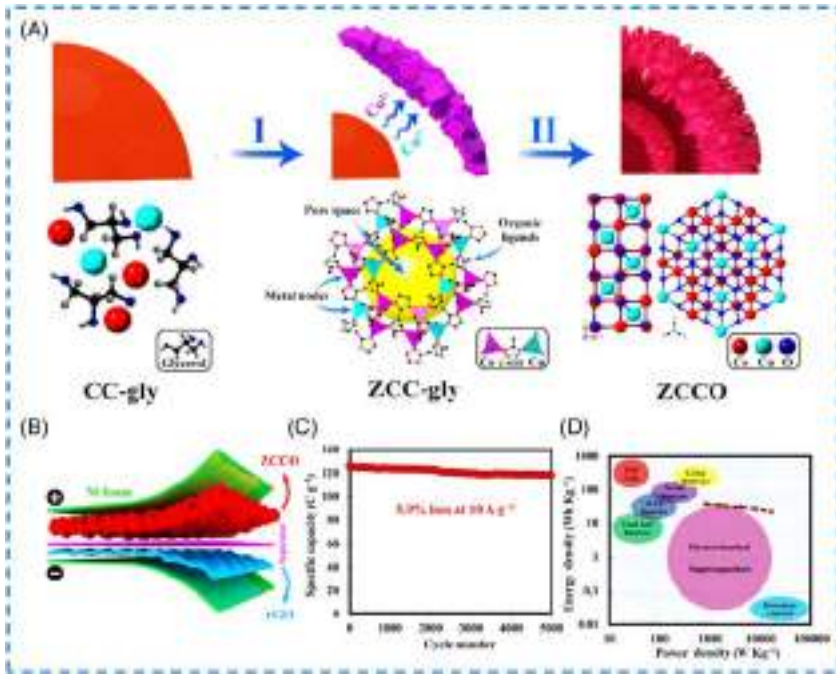

FIGURE 18.8 (A) The formation process of the crystal structures of CC-gly, ZCC-gly, and ZCCO. (B) Fabrication of a ZCCO/rGO asymmetric supercapacitor device. (C) Cycling stability of the device shows 5000 GCD cycles at a 10 A g^{-1}, and (D) Ragone plot has compared to the other ASC energy storage devices [48]. *ASC*, Asymmetric supercapacitor.

The yolk−shell arrangement could be created in an interior by the various cationic/anionic species diffused along with the nanostructure. The CuCo-ZIF shell grew completely over the solid sphere due to the smaller size of ions diffusing toward the surface solid structure. Finally, the double-shell of the $CuCo_2O_4$ hollow sphere has been formed by the ZCC-gly (yolk−shell) structure involved in the heat-treatment process. The electrochemical performance by the cathode materials of ZCCO (ZIF-CuCoO) combined with anode materials of rGO electrode using 3 M KOH solution as electrolyte and cellulose paper as a separator is presented in Fig. 18.8B. The sandwich-like ASC exhibits excellent rate capability via 60% of capacitance retention at different current density. After 5000 cycles, the cyclic stability has been determined through the 5.9% specific capacity loss at the 10 A g^{-1} (Fig. 18.8C). The Ragone plot can support the operation in terms of energy storage efficiency in devices through the energy and power density of hybrid supercapacitor (HSC) devices. The assembled HSC has been compared to the multiple energy storage devices, which revealed the extreme energy density of 38.4 Wh kg^{-1} at the power density 800 W kg^{-1} (Fig. 18.8D) [48].

18.3.2 Co-MOF@$CoCr_2O_4$ microplate

The fabrication process of the hollow and hierarchical Co-MOF@$CoCr_2O_4$ microplate arrays was made. According to the solvothermal reaction, the Co-MOF microplate was firstly deposited on the surface of NF. Next, the Co-MOF@$CoCr_2O_4$/NF was fabricated by the addition of $K_2Cr_2O_7$ in hydrothermal conditions. The hollow and hierarchical Co-MOF@$CoCr_2O_4$ microplate formation mechanism could be dependent on the three processes, such as ion exchange, reduction reaction, and in situ conversion strategy. The ultrathin layer of $CoCr_2O_4$ NS has been formed through the Co^{2+} (from Co-MOF surface) reacting quickly in $Cr_2O_7^{2-}$ ions, which helped as coordination between the inner Co^{2+} and outside $Cr_2O_7^{2-}$.

Generally, the diffusion rate of cationic species is greater than that of anions due to the smaller size in cations. At the same time, the hydrothermal reaction process was easily reduced to Cr^{3+} from Cr^{6+} with strong oxidation. The practical application of HSC cell was fabricated by the negative site working on AC/NF and positive site working on Co-MOF@$CoCr_2O_4$ electrode with the use of PVA/KOH gel electrolyte. The cyclic stability of the MOF@$CoCr_2O_4$/NF//AC device has been determined at CD tests at 30 mA cm^{-2}, where the capacity loss was 3.8% after 5000 times. The cyclic life performance was greater due to the active material strongly interacted with the core of Co-MOF and shell of $CoCr_2O_4$, which avoided the Co-MOF@$CoCr_2O_4$/NF structure to collapse through the long-term redox reaction [49].

18.4 Metal-organic framework–derived metal sulfide nanostructures

18.4.1 Hollow CoS_2 dodecahedrons

The porous-CoS_2 hollow dodecahedrons synthesis method is displayed in Fig. 18.9A. The yolk–shell Co_3O_4 hollow dodecahedron particles were prepared by using ZIF-67 particles at a controlled annealing process. The concave surfaces of CoS_2 nanoparticles were synthesized from the Co_3O_4 hollow dodecahedron (yolk–shell) by the precursor of S as a powder (sulfuration). The electrode preparation used slurry cast technology since the flat surface accepts the electrolyte ions limited as shown in Fig. 18.9B. The porous-CoS_2 nanostructures (concave) are able to have superior electrolyte distribution, which is attributed to the adjoin particle utilization on the contact surface. The

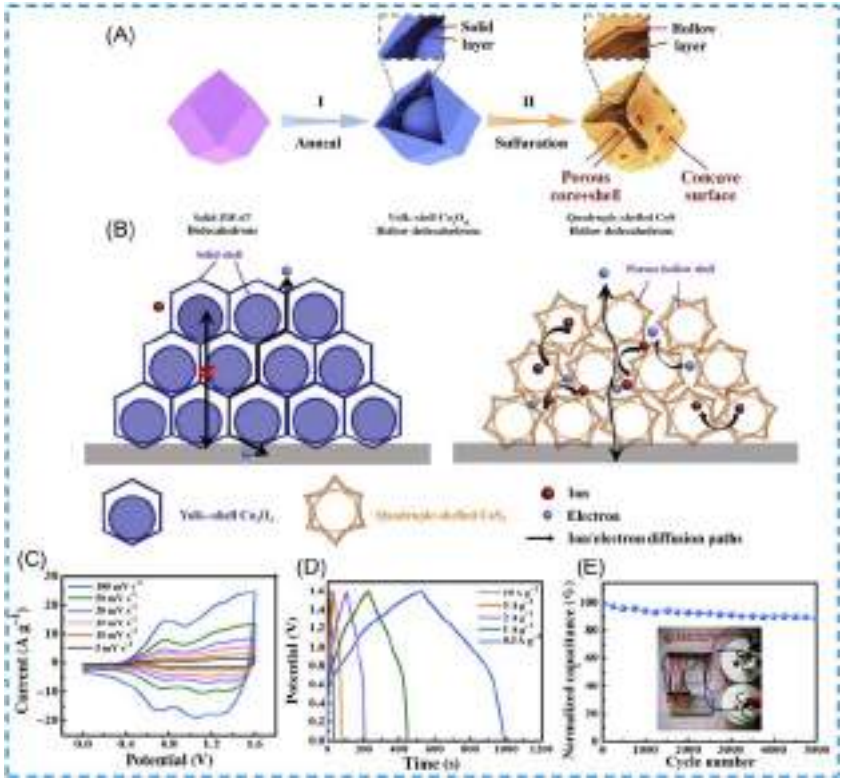

FIGURE 18.9 (A) The fabrication of schematic illustration for hollow-CoS_2 dodecahedrons electrodes. (B) Schematic illustration of hollow-CoS_2 dodecahedrons compared to the Co_3O_4 yolk–shell structures. Hollow-CoS_2 quadruple-shelled dodecahedrons//AC device: (C) CV curves (D) GCD curves. (E) Ragone plot of CoS_2 hollow dodecahedrons//AC device [50]. *AC*, Activated carbon; *CV*, cyclic voltammetry.

hollow shell of CoS_2 electrode materials utilized core materials by improving the electrolyte access into the inner parts. In conclusion, the hollow dodecahedron quadruple-shelled CoS_2 can offer short ions diffusion length, balanced electrolyte distribution, and enhanced structural stability compared with the Co_3O_4 (yolk−shell) dodecahedron particles. The CV curves of the ASC display redox peaks due to the presence of a faradaic reaction in CoS_2 as shown in Fig. 18.9C. Moreover, the GCD curves show almost symmetric feature in Fig. 18.9D, which indicates the greater coulombic efficiency and higher electrochemical reversibility. The ASC has exhibited specific capacitance is 146 F g^{-1} at 0.5 A g^{-1} and 105 F g^{-1} at a 10 A g^{-1} according to the discharge time. The 89% capacitance retention exhibits ASC after 5000 cycles at a 5 A g^{-1} (Fig. 18.9E). By assembling two ASCs in series, the LED bulbs show the practical application in several minutes and inset in Fig. 18.9E [50].

18.4.2 Hollow-concave $CoMoS_x$

The ASC configuration was fabricated by the anode materials of commercial AC and $CoMoS_x$ boxes (hollow-concave) as cathode materials as shown in Fig. 18.10A. The $CoMoS_x$ boxes (hollow-concave) CV curves display the voltage window of 0 to 0.6 V via a redox reaction. Meanwhile, the typical double-layer capacitive performance shows the AC electrode, which displays the operating potential window of −1 to 0 V at a scan rate of 30 mV s^{-1}. The operating potential windows of the ASC device was expected to be established up to 1.6 V. The ASC device of $CoMoS_x$//AC shows GCD curves at different current densities of 1−20 A g^{-1} (Fig. 18.10B). The specific capacitances (Cs) values for $CoMoS_x$//AC ASC were calculated according to the total mass of the active materials. The specific capacitances values are 104.2, 90.0, 76.7, 60.5, 48.2, 43.6, 38.9, and 30.6 F g^{-1}, which belongs to the current densities of 1, 2, 3, 5, 8,10, 12, and 20 A g^{-1}, respectively. The $CoMoS_x$ boxes (hollow-concave) formation mechanism is illustrated in Fig. 18.10C. First, according to the classical coordination chemistry theory the highly homogenous ZIF-67 was synthesized by a precipitating reaction. The $CoMoO_4$@ZIF-67 electrode was prepared by the templates of ZIF-67 cubes, then introduced molybdate ion (MoO_4^{2-}) via ion exchange process at controlling treatment time. The resultant product of $CoMoO_4$ cubes was washed, then removed unwanted impurities and excess of ZIF-67 templates 2-MIm and CTAB surfactant. In the end, the $CoMoO_4$ nanocubes can be converted into $CoMoS_x$ boxes (hallow concave) by the solvothermal method (sulfidation reaction). The exceptional $CoMoS_x$ concave structure has been formed due to the greater atomic radius of S atom than that of the O atom. As depicted in Fig. 18.10D, the CV curve purple regions indicated surface capacitive contribution, whereas remaining areas represented diffusion contribution at a 20 mV s^{-1}. At the scan rate of 50 mV s^{-1}, the capacitive contribution is more dominant (Fig. 18.10E), which means charge storage

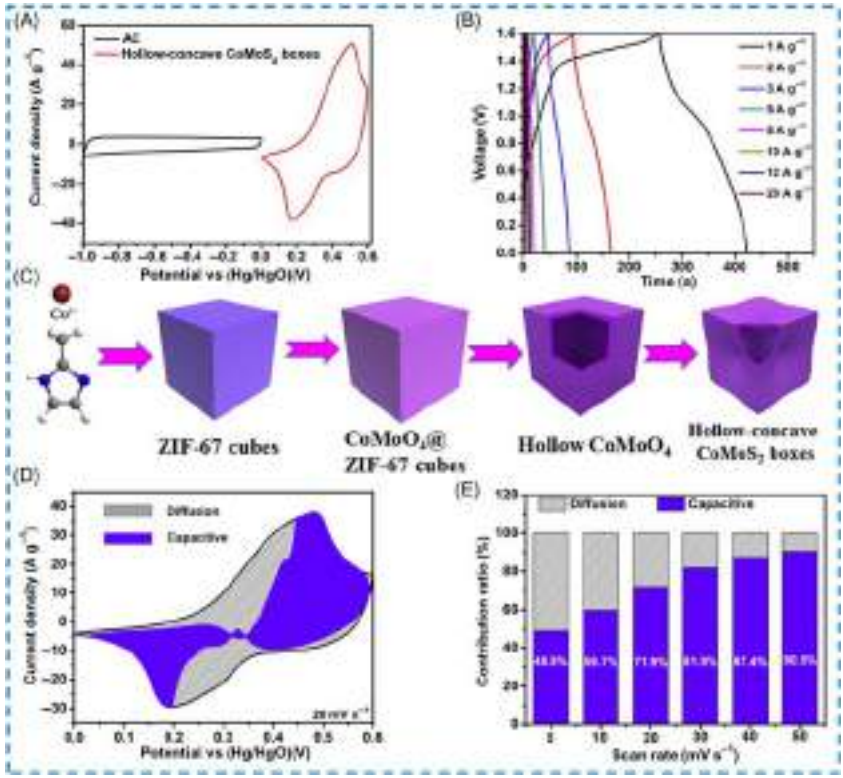

FIGURE 18.10 (A) The CoMoSx boxes (hollow-concave)//AC electrodes at scan rate of 30 mV s^{-1}. (B) The ASC device of GCD curves. (C) Hollow-concave $CoMoS_x$ boxes schematic illustration, (D) the CV curves of capacitive and diffusion-controlled contribution at a 20 mV s^{-1}. (E) Surface and diffusion-controlled contributions at different scan rates [51]. *AC*, Activated carbon; *ASC*, asymmetric supercapacitor; *CV*, cyclic voltammetry.

behavior is greater in $CoMoS_x$ boxes. At the scan rate of 5 mV s^{-1}, the diffusion-controlled process is significant, which means a slow electrochemical reaction. Higher capacitive contribution occurs due to shorter ion diffusion path and quick electronic transmission [51].

18.4.3 Metal-organic framework-derived metal sulfide ($MnCo_2S_4$/Co_9S_8) nanostructures

The schematically illustrated in the fabrication process of waxberry-like $MnCo_2S_4/Co_9S_8$ as presented in Fig. 18.11A. The precursor of MnCo-LDH was synthesized by a facile hydrothermal reaction. Then, the organic ligand of 2-methylimidazole and MnCo-LDH were mixed at room temperature in an aqueous medium. Finally, the $MnCo_2S_4/Co_9S_8$ composite produced by the

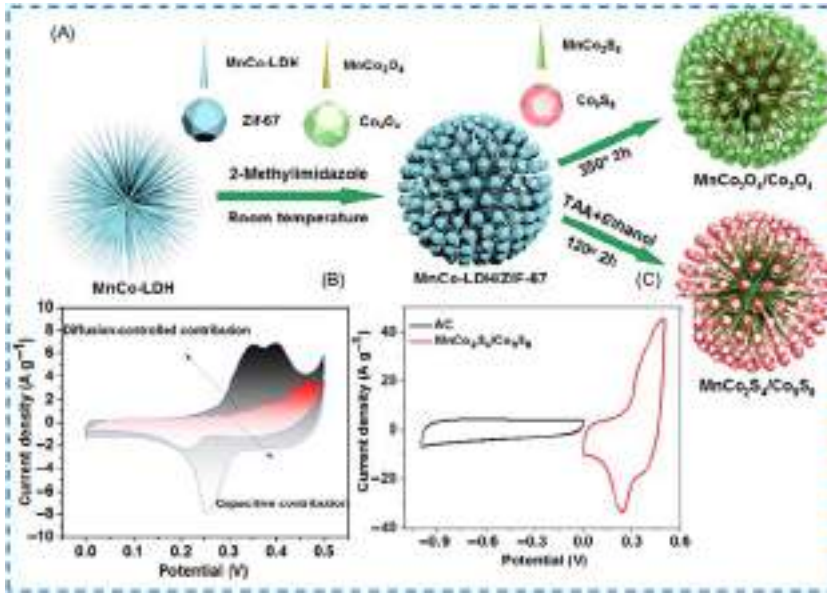

FIGURE 18.11 (A) The fabrication procedure of waxberry-like $MnCo_2S_4/Co_9S_8$ composite. (B) Diffusion and capacitive-controlled contributions of $MnCo_2S_4/Co_9S_8$ electrode materials at a 2 mV s^{-1}. (C) CV curves of AC and $MnCo_2S_4/Co_9S_8$ in three-electrode configuration at the scan rate of 50 mV s^{-1} [52]. *AC*, Activated carbon; *CV*, cyclic voltammetry.

MnCo-LDH/ZIF-67 reaction with the TAA in the presence of ethanol for 2 hours at 120°C. The energy storage mechanisms (Fig. 18.11B) were determined by the composites of $MnCo_2S_4/Co_9S_8$, which can be classified as diffusion-controlled contribution of ($h_2v^{1/2}$) and capacitive contribution (h_1v). According to Dunn's method, the CV curves charge storage properties were determined by the various scan rates. The exponential relations is followed as $i = h_1v + h_2v^{1/2}$, where (i) is the current response, v is the scan rate, and h_1 and h_2 are constants. The practical application of ASC can further evaluate the cathode materials of $MnCo_2S_4/Co_9S_8$ and anode materials of AC in the electrolyte solution of 6 M KOH as shown in Fig. 18.11C. The $MnCo_2S_4/Co_9S_8$// AC has been tested in a three-electrode system with the CV curves [52].

18.4.4 MnO_2@NiCo-LDH/CoS_2

A one-dimensional axial layered structure of the synthesizing process of MnO_2@NiCo-LDH/CoS_2 is illustrated in Fig. 18.12A. The core−shell structure of MnO_2@ZIF-67 formed by the negatively charged MnO_2 nanotubes reacts with the positive charge of cobalt ions through electrostatic interactions. A uniform ZIF-67 nanopolyhedron would accumulate on the surface of MnO_2 nanotubes to produce a MnO_2@ZIF-67, then 2-methylimidazole was

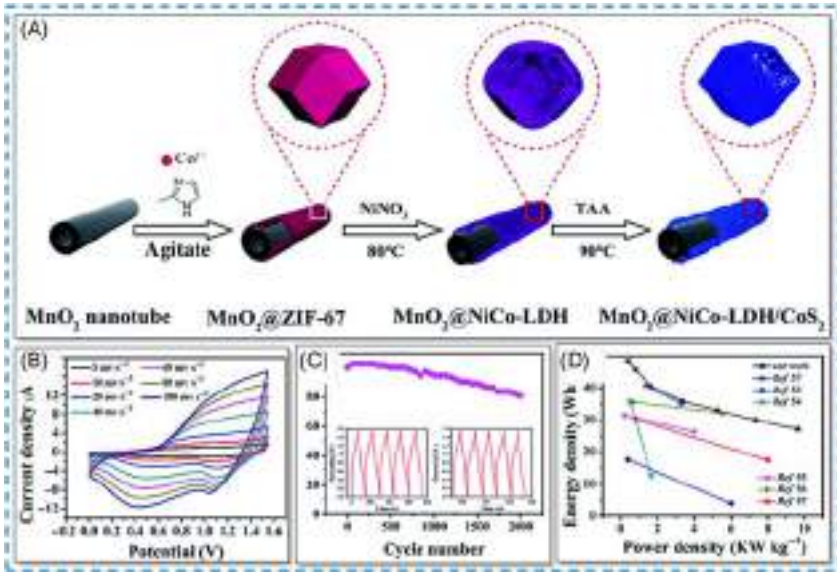

FIGURE 18.12 (A) The synthesis process of a schematic diagram for MnO_2@NiCo-LDH/CoS_2//AC. ASC of MnO_2@NiCo-LDH/CoS_2//AC: (B) CV curves, (C) cycling stability of the hybrid electrode (the inset is the first and last 5-GCD cycles at 10 A g^{-1}), (D) Ragone plot [53]. *AC*, Activated carbon; *ASC*, asymmetric supercapacitor; *CV*, cyclic voltammetry.

added. The coordination between 2-methylimidazole and Co^{2+} ions formed from the generated protons could enter the ZIF-67 skeleton at hydrolysis conditions. Then, Ni−Co double hydroxide formed by the nickel ions reacting with the released cobalt ions. Due to the Kirkendall effect, the hollow NiCo-LDH electrode with the ZIF-67 could slowly migrate to the surface of MnO_2 nanotubes. In the end, the sulfuration process at the heat treatment produced MOF-derived MnO_2 nanotubes@NiCo-LDH/CoS_2 composites. The ASC of CV curves was measured at various scan rates as depicted in Fig. 18.12B, where the curve shows electric double-layer behavior associated with pseudocapacitance properties. The ASC exhibited the cyclic stability performance of the MnO_2@NiCo-LDH/CoS_2//AC at a 10 A g^{-1} (Fig. 18.12C). The 81% initial capacitance will retain after 2000 cycles. As revealed in Fig. 18.12D, Ragone plots of MnO_2@NiCo-LDH/CoS_2//AC devices exhibited the energy and power density of 49.5 Wh kg^{-1} at a 391.5 W kg^{-1}, which can be compared with the other type of ASCs [53].

18.4.5 NiCoZn-S nanosheets coupled $NiCo_2S_4$

The NiCoZn-CH/NiCo-CH@CF was synthesized hydrothermally by the Ni/Co ion at the ratio of 1:1 for fabrication process as illustrated in Fig. 18.13A. The 3D NiCoZn-CH/NiCo-CH@CF constructed by the NiCo-CH nanowires

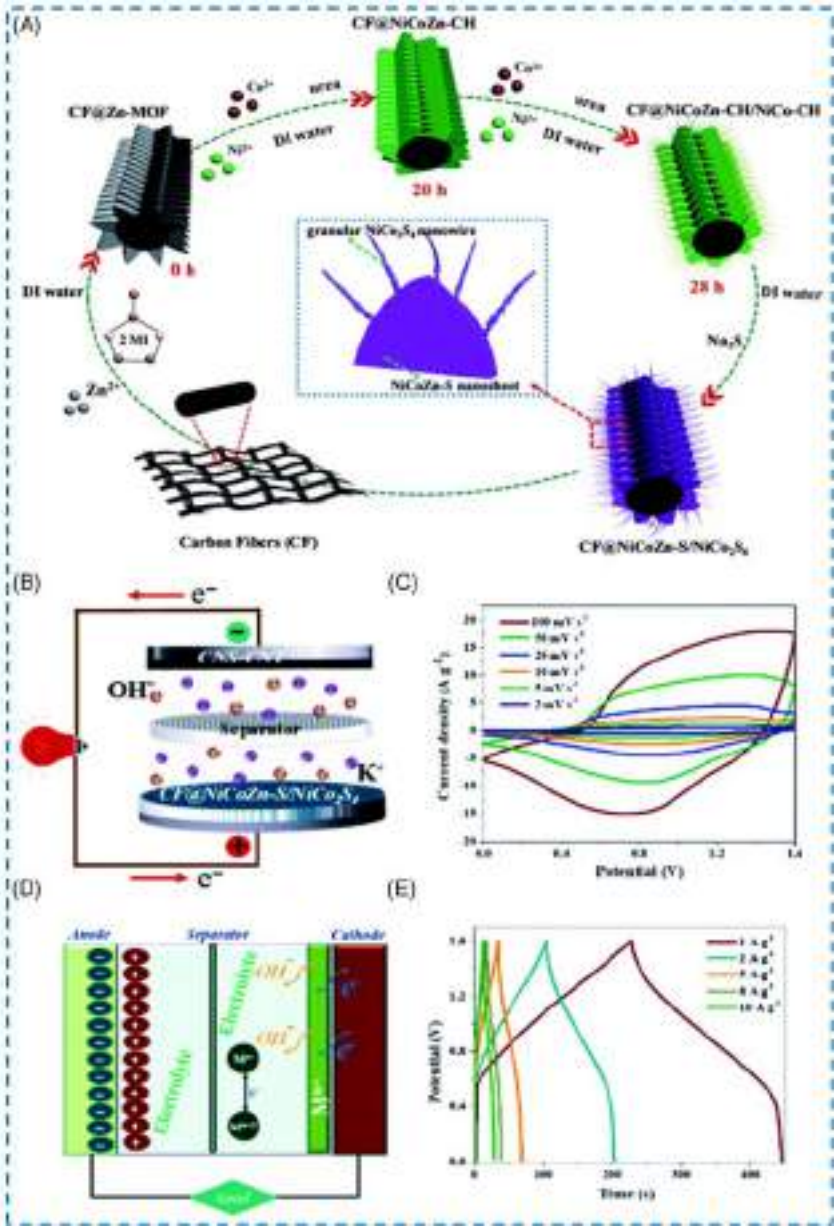

FIGURE 18.13 (A) The 3D-CF@NiCoZn-S/$NiCo_2S_4$ nanoarrays preparation process. (B) The CF@NiCoZn-S/$NiCo_2S_4$//CNS−CNT schematic diagram, (C) energy storage principle of HSCs, (D) CV curves, and (E) GCD curves [54]. *CV*, Cyclic voltammetry; *HSCs*, hybrid supercapacitors.

progressively grew on the NiCoZn-CH NSs, which required complete reaction time up to 28 hours with Zn-MOF precursors. HSC devices were schematically shown in Fig. 18.13b, where the cathode of CF@NiCoZn-S/$NiCo_2S_4$ and anode materials of CNS−CNT were connected in the electrolyte solution of 6 M KOH. The HSC energy storage principle briefly described by storing the charge depends on the redox reactions as presented in Fig. 18.13C. HSC device was tested (Fig. 18.13D) from the CV curves, which exhibit the operating potential window from 0 to 1.6 V at scan rates from 2 to 100 mV s^{-1}. At the scanning rate reaching 100 mV s^{-1}, the CV curves did not show obvious change that represented a satisfactory rate capability of the as-assembled HSC device. The specific capacitance (Cs) can be determined from the GCD curves (Fig. 18.13E) of the hybrid HSC as 137, 123, 108, 95, and 90.5 F g^{-1} at 1, 2, 5, 8, and 10 A g^{-1}, respectively [54].

18.5 Metal-organic framework–derived carbon nanostructures

18.5.1 Porous carbon

The pyrolysis process was used to prepare the hierarchical novel sponge-like 3D-interconnected PCs (Fig. 18.14A). Zn-based MOFs [Zn (tbip)] (tbip = 5-tert-butyl isophthalate) could be divided into two parts, such as Zn (tbip)-B (diameter of the average particles B = 0.5 mm) and Zn (tbip)-S (diameter of the average particles S = 600 nm).

Two kind of nano sized porous carbons (PC) could be produced by using the Zn-based MOFs (Zn (tbip)) and unwanted impurities of PEG K10 were further removed by ethanol and distilled water. The Zn (tbip)-B was denoted as C-B-*n* and Zn (tbip)-S represented as C-S-*n* (*n* = 800°C, 900°C, 1000°C). The micropores and mesopores preparation belongs to the gasification of the catalytic carbon using Zn metals at high evaporation etching. As depicted in Fig. 18.14A, the carbonization temperature can be deduced to the risky factor in the structural analysis of PCs. The supercapacitor performances have been dependent on the specific surface area, porosity, and electrical conductivity of the two-electrode cell materials (Fig. 18.14B). The two-electrode cell was fabricated by the anode for C-B-*n* and cathode for C-S-*n* at the scan rate of 50 mV s^{-1} in the electrolyte solution for 6 M KOH. The GCD curves revealed a nearly isosceles-triangular shape with a small Ohmic drop at different current densities (Fig. 18.14C), which indicated that the two-electrode cell possessed reversibility and ideal capacitive performances [55].

18.5.2 Porous carbon polyhedrons

ASCs were constructed by the PCs having a higher specific surface area and appropriate pore nanostructure. The unique polyhedral morphology of

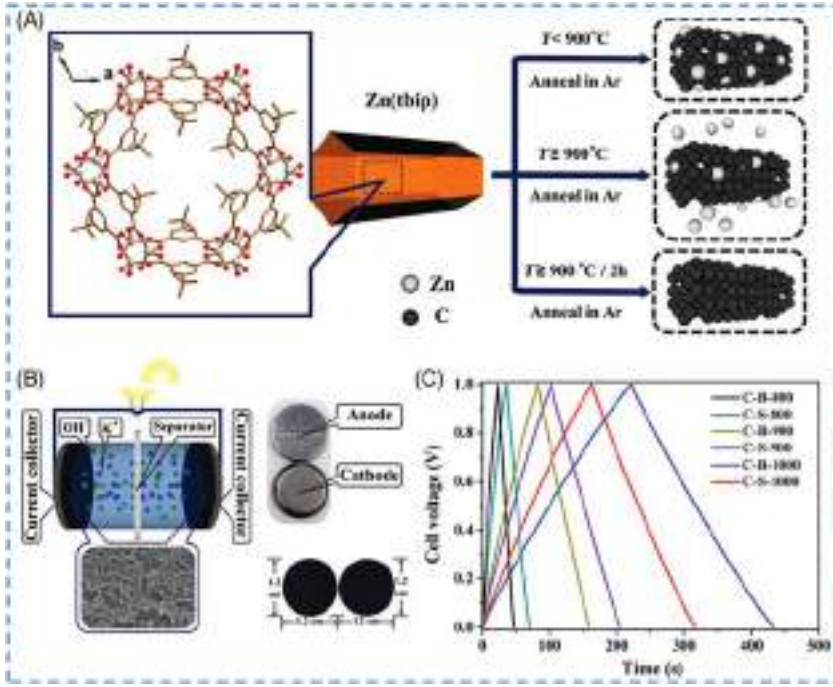

FIGURE 18.14 (A) Carbonization process of Zn (tbip). (B) Schematic illustration of the two-electrode cell, (C) GCD curves at current densities of 0.5 A g^{-1} [55].

MOF-derived electrode materials is PC polyhedrons (PCPs), where negative electrode materials are prepared via the carbonization process of ZIF-8 templates. As shown in Fig. 18.15A, the PCPs possess the excellent uniformity of the polyhedral morphology and the average size of the particles to be 500 nm. The PCPs exhibits well-defined polyhedral shape, truncated rhombic dodecahedron, and smooth surface as presented in Fig. 18.15B. The GCD curves of PCPs (Fig. 18.15C) show linear shape and good symmetry at 1 to 20 A g^{-1}, indicating the superior electrochemical reversibility of the PCPs electrode. The specific capacitance of PCP displays 245 F g^{-1} at 1 A g^{-1} and 162 F g^{-1} at 20 A g^{-1} (Fig. 18.15D). The polyhedral morphology of PCPs has revealed the following advantages. The well-defined polyhedral shapes can be generated from the secondary mesoporous structures owing to the high uniform shape of the polyhedral and greater packing density. Besides, the electrode/electrolyte contact area will greatly increase in porous structure and thereby capacitive performances are enhanced to achieve high rate capability.

The ASC has been fabricated via the composites of CNT@NiO positive site and negative sites of PCPs in 1 M KOH solution (Fig. 18.15E). The

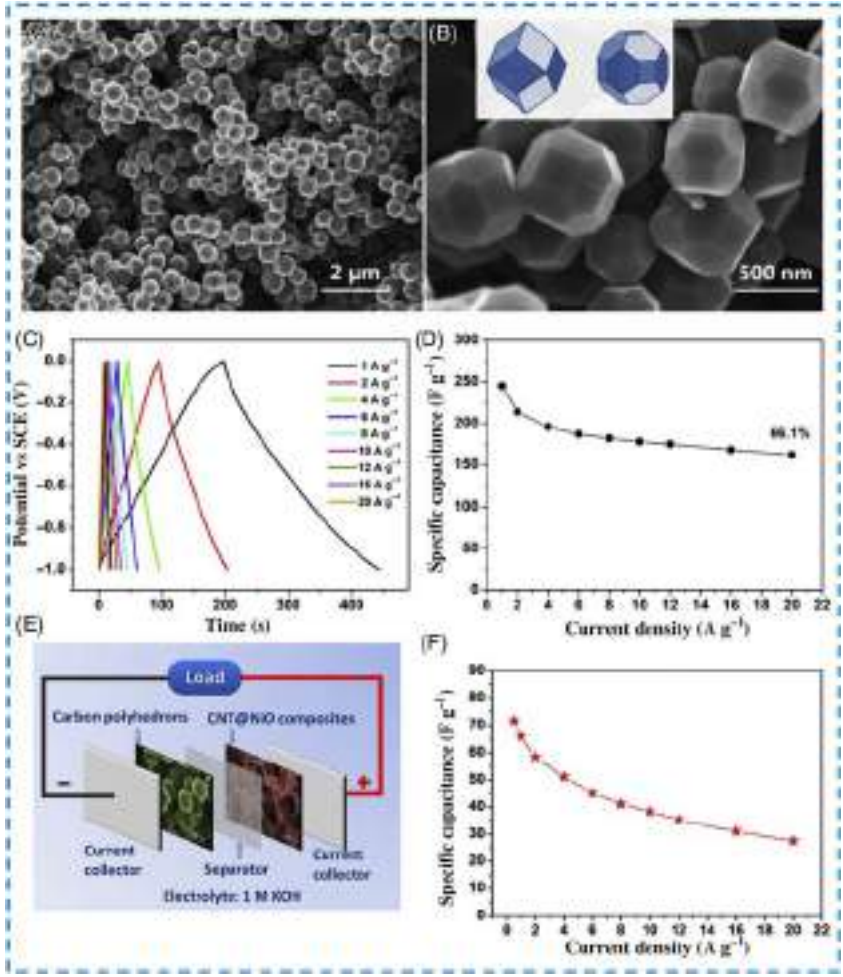

FIGURE 18.15 (A, B) Porous carbon polyhedrons (FE-SEM), (B) the schematic illustration of a rhombic dodecahedron and a truncated rhombic dodecahedron (inset), (C) CD curves at various current densities, (D) specific capacitance at different current densities, (E) ASC-assembled structure, and (F) specific capacitance at different current densities [56]. *ASC*, Asymmetric supercapacitor; *CD*, charge−discharge.

ASC shows that the specific capacitance values calculated from the discharging time depend on the active materials of the total mass (Fig. 18.15F). The maximum specific capacitance values can reach 72 F g^{-1} at 0.5 A g^{-1} compared to the higher current density of 20 A g^{-1}. The specific capacitance values decrease at higher current density values due to the low utilization efficiency of active materials [56].

18.5.3 Mesoporous carbon

The ZIF-8 can produce homogenous polyhedron at present in high-resolution SEM images as shown in Fig. 18.16A–C. The diameter of the average size of polyhedrons is around 500 nm. The positive electrode of Mn_2O_3@NF and negative electrode of MC connected with aqueous electrolytes would assemble the HSCs. As depicted in Fig. 18.16D, the positive electrode has the effective mass of active materials which allow more number of electrolyte ions to deeply diffuse into the porous electrode material at present cuboidal-like morphology. The mesoporous carbon (MC) plays a significant role for providing the pathways of fast electron transportation. Besides, HSC of Mn_2O_3@NF//MC also showed (Fig. 18.16E) admirable cycling stability at an applied potential window of 0.0–1.6 V. As depicted in Fig. 18.16E, HSC revealing the capacitance retains 86.73% after 5000 GCD cycles at 12 A g^{-1}. The inset first and last five GCD cycles stable and CD behavior smoothly in Fig. 18.16E. The EIS results were further confirmed to the outstanding performance of HSC shows (Fig. 18.16F) in ESR values = ~0.181 Ω and R_{ct} ~0.778 Ω), suggesting the good electrical conductivity of the electrodes materials. The ESR reveals the outstanding stability of the electrolyte due to the best contact of active materials with Ni-foam substrate during the cycling process [57].

18.6 NiCo-MOF@PNTs

The schematic preparation process of NiCo-MOF@PNTs nanocomposites is illustrated in Fig. 18.17A. The fibrillary reactive template was formed by Fe^{3+} reacting with methyl orange, which directly gave the growth of PNTs. Next, the DMF solution was presented by Ni^{2+}, Co^{2+}, PTA, and TEA that were dispersed in PNTs. The NiCo-MOF ultrathin NSs wrapping PNTs electrode materials were obtained by ultrasonicating the whole mixtures for 8 hours. As depicted in Fig. 18.17B, the ASC device was fabricated by the cathode materials of NiCo-MOF@PNTs and anode materials of AC, respectively. The mass ratios of positive and negative electrodes show the number of charges stored in each electrode. As depicted in Fig. 18.17C, the CV curves of fabricated NiCo-MOF@PNTs and AC exhibit the operating potential windows from −1.0 to 0.0 V and 0.0 to 0.6 V in a three-electrode configuration at a scan rate of 30 mV s^{-1}. As observed in Fig. 18.17D, ASC at different potential ranges of the CV curves exhibits similar areas and no polarization curves. The CV curve shapes change regularly and appear no polarization phenomenon when the operating potential window increases from 0 to 1.5 V. The ASC device of the NiCo-MOF@PNTs//AC (Fig. 18.17E) reveals 79.1% capacitance retention after the 10,000 cycles and the inset is the last 10 CD curve cycles [58].

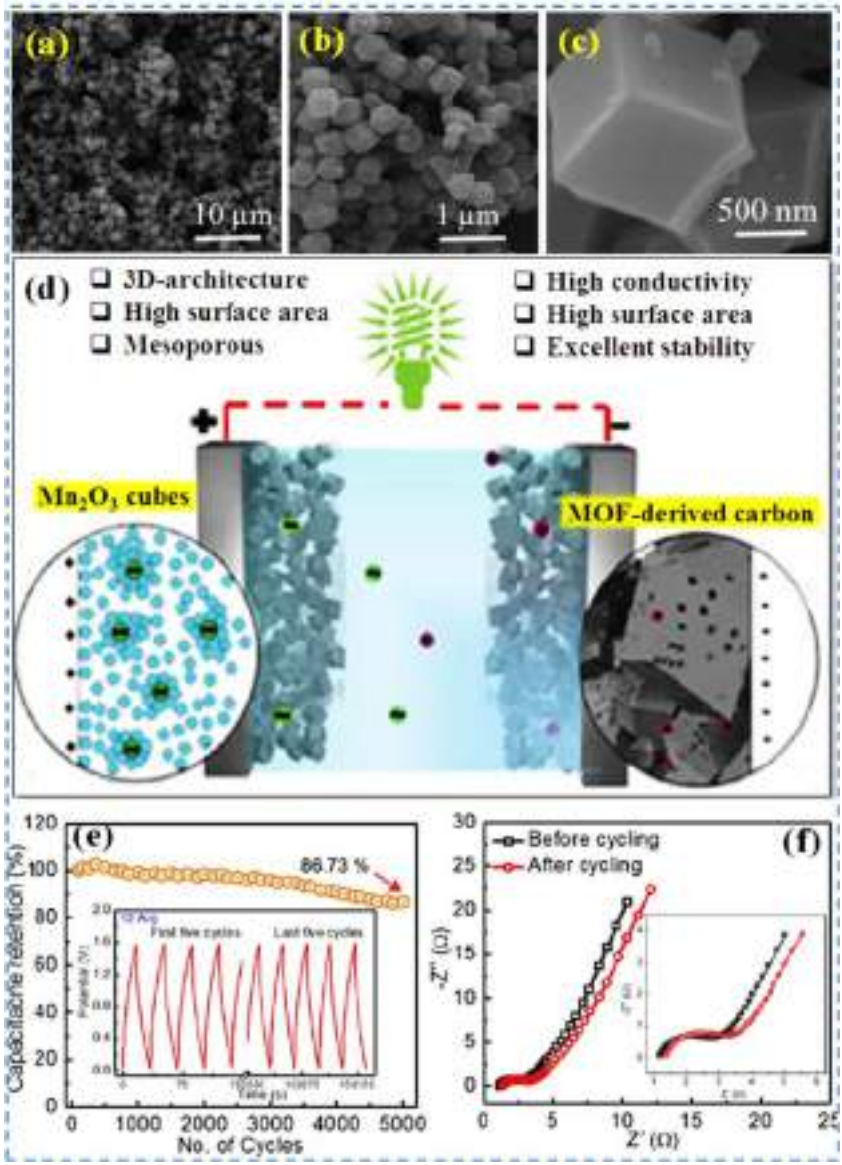

FIGURE 18.16 (A–C) MOF-derived mesoporous carbon polyhedrons of FE-SEM. Hybrid supercapacitor Mn_2O_3@NF//MC: (D) schematic diagram of charge storage mechanism and electrode designs for the hybrid device, (E) cyclic life test (insert the first and last five GCD cycles), and (F) Nyquist plot of hybrid SC (inset is the particular region at a high-frequency range) [57]. *MOF*, Metal-organic framework.

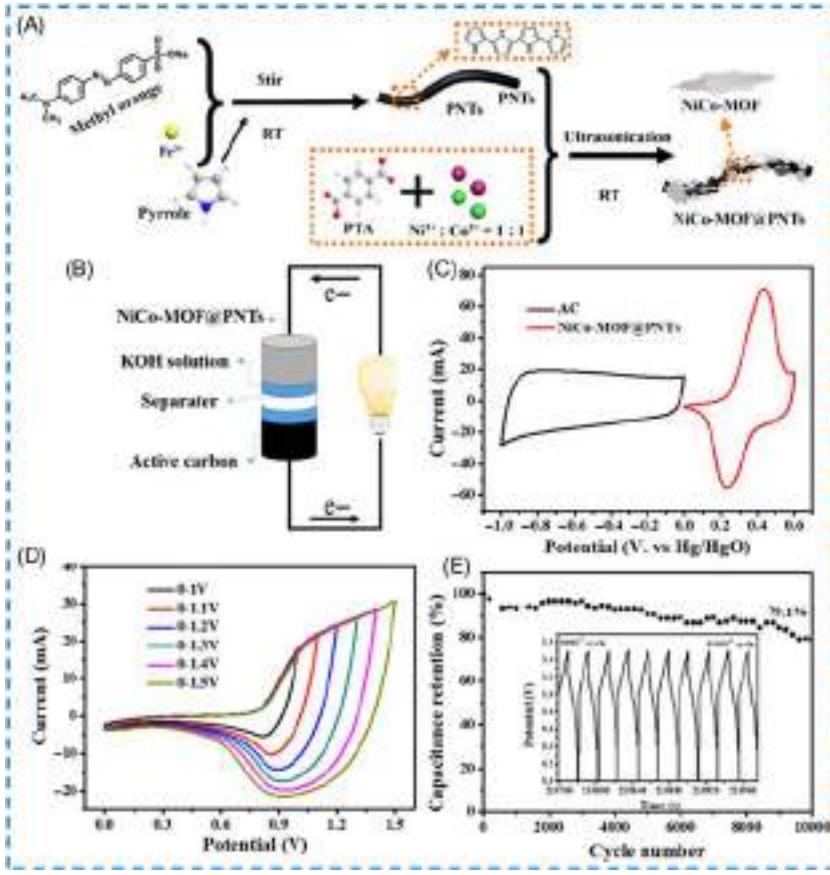

FIGURE 18.17 (A) The synthesis scheme of NiCo-MOF@PNTs. (B) The NiCo-MOF@PNTs// AC ASC device schematic diagram, (C) CV curves of ASC devices at a scan rate of 30 mV s^{-1}. (D) ASC of the CV curves at different potential windows. (E) The cyclic stability for 10,000 cycles and (inset shows the last 10 cycles) [58]. *AC*, Activated carbon; *ASC*, asymmetric supercapacitor; *CV*, cyclic voltammetry; *MOF*, metal-organic framework.

18.7 Conclusion and future perspective

In this chapter, the MOF-derived metal oxide/metal sulfides, bimetal oxide/metal sulfides, PCs, and corresponding nanocomposites have been highlighted. First, the preparation process of porous Co_3O_4, Fe_2O_3, NiO, and metal oxide supported carbon nanocomposites from MOFs and their supercapacitor performances have been discussed. The resulting metal oxides and their composites displayed higher electrical conductivity and excellent specific surface area, which are highly anticipated properties for the performance of supercapacitor. Moreover, the bimetal oxide and their nanocomposites have been discussed, for instance, hollow spheres of

$CuCo_2O_4$ and Co-MOF@$CoCr_2O_4$ electrode materials shows the ASC performances. Next, this chapter also contains metal sulfides, metal-doped metal sulfides, and their composites, such as CoS_2 dodecahedrons, hollow-concave $CoMoS_x$, and $MnCo_2S_4$/Co_9S_8. The resulting nanostructures of metal sulfide are presented in high surface areas of the porous structures which are used as the free motion of ions or electrons by facilitating electrode−electrolyte dynamics. Finally, the PCs have been derived from MOF-templates using Zn-metal as a catalyst for catalytic carbonization process. Generally, the PCs exhibits the electrical double-layer properties which have been used as the negative electrode for the fabrication of ASCs. Owing to their porous morphology, they helped the large number of electrolyte ions intensely penetrate the electrode/electrolyte interface.

Future perspectives of MOF-derivative materials include (1) the electrochemical performance study and resultant mechanism to determine the different types of MOFs branches; (2) a novel MOFs developed by the selecting fresh linkers with functional groups, such as oxidation/reduction group and hydrophilic group; (3) the synthesis equipment required to be produced to the various kind of MOF nanostructures materials; (4) the simplistic preparation process, such as at room temperature and atmospheric pressure and low-cost with less use of expensive solvents or chemicals; (5) optimization of different types of electrolytes, binders, and current collectors used in MOF-derived nanostructures; and (6) the several MOFs and MOF-based composites developed with superior performances and increased large-scale production in commercial aspects.

Acknowledgment

The authors wish to thank the financial support by Ministry of Science and Technology (MOST) in Taiwan under the contract numbers of MOST-107-2221-E-035-001-MY3 and MOST-108-2221-E-035-054-MY3.

References

[1] Wang H, Zhu QL, Zou R, Xu Q. Metal-organic frameworks for energy applications. Chem 2017;2(1):52−80.

[2] Eddaoudi M, Sava DF, Eubank JF, Adil K, Guillerm V. Zeolite-like metal−organic frameworks (ZMOFs): design, synthesis, and properties. Chem Soc Rev 2015;44(1):228−49.

[3] Kuppler RJ, Timmons DJ, Fang QR, Li JR, Makal TA, Young MD, et al. Potential applications of metal-organic frameworks. Coord Chem Rev 2009;253(23−24):3042−66.

[4] Lin SY, Zhang X. Two-dimensional titanium carbide electrode with large mass loading for supercapacitor. J Power Sources 2015;294:354−9.

[5] Kaneti YV, Tang J, Salunkhe RR, Jiang X, Yu A, Wu KC, et al. Nanoarchitectured design of porous materials and nanocomposites from metal-organic frameworks. Adv Mater 2017;29(12):1604898.

[6] Cousin Saint Remi J, Rémy T, Van Hunskerken V, van de Perre S, Duerinck T, Maes M, et al. Biobutanol separation with the metal−organic framework ZIF-8. ChemSusChem 2011;4(8):1074−7.
[7] Yaghi OM, Li H. Hydrothermal synthesis of a metal-organic framework containing large rectangular channels. J Am Chem Soc 1995;117(41):10401−2.
[8] Goswami S, Ray D, Otake KI, Kung CW, Garibay SJ, Islamoglu T, et al. A porous, electrically conductive hexa-zirconium (IV) metal−organic framework. Chem Sci 2018;9 (19):4477−82.
[9] Pachfule P, Shinde D, Majumder M, Xu Q. Fabrication of carbon nanorods and graphene nanoribbons from a metal−organic framework. Nat Chem 2016;8(7):718.
[10] Stassen I, Styles M, Grenci G, Van Gorp H, Vanderlinden W, De Feyter S, et al. Chemical vapour deposition of zeolitic imidazolate framework thin films. Nat Mater 2016;15(3):304−10.
[11] Cao F, Zhao M, Yu Y, Chen B, Huang Y, Yang J, et al. Synthesis of two-dimensional CoS1. 097/nitrogen-doped carbon nanocomposites using metal−organic framework nanosheets as precursors for supercapacitor application. J Am Chem Soc 2016;138 (22):6924−7.
[12] Gallego A, Hermosa C, Castillo O, Berlanga I, Gómez-García CJ, Mateo-Martí E, et al. Solvent-induced delamination of a multifunctional two dimensional coordination polymer. Adv Mater 2013;25(15):2141−6.
[13] Wang MX, Zhang J, Fan HL, Liu BX, Yi XB, Wang JQ. ZIF-67 derived Co_3O_4/carbon aerogel composite for supercapacitor electrodes. N J Chem 2019;43(15):5666−9.
[14] Wang KB, Bi R, Wang ZK, Chu Y, Wu H. Metal−organic frameworks with different spatial dimensions for supercapacitors. N J Chem 2020;44(8):3147−67.
[15] Xue Y, Zheng S, Xue H, Pang H. Metal-organic framework composites and their electrochemical applications. J Mater Chem A 2019;7(13):7301−27.
[16] Zhu G, Wen H, Ma M, Wang W, Yang L, Wang L, et al. A self-supported hierarchical Co-MOF as a supercapacitor electrode with ultrahigh areal capacitance and excellent rate performance. Chem Commun 2018;54(74):10499−502.
[17] Ma HM, Yi JW, Li S, Jiang C, Wei JH, Wu YP, et al. Stable bimetal-MOF ultrathin nanosheets for pseudocapacitors with enhanced performance. Inorg Chem 2019;58 (15):9543−7.
[18] Cai ZX, Wang ZL, Kim J, Yamauchi Y. Hollow functional materials derived from metal−organic frameworks: synthetic strategies, conversion mechanisms, and electrochemical applications. Adv Mater 2019;31(11):1804903.
[19] Han X, Tao K, Wang D, Han L. Design of a porous cobalt sulfide nanosheet array on Ni foam from zeolitic imidazolate frameworks as an advanced electrode for supercapacitors. Nanoscale 2018;10(6):2735−41.
[20] Shi X, Zhang S, Chen X, Tang T, Mijowska E. Three dimensional graphene/carbonized metal-organic frameworks based high-performance supercapacitor. Carbon. 2020;157:55−63.
[21] Li H, Liang M, Sun W, Wang Y. Bimetal−organic framework: one-step homogenous formation and its derived mesoporous ternary metal oxide nanorod for high-capacity, high-rate, and long-cycle-life lithium storage. Adv Funct Mater 2016;26(7):1098−103.
[22] Niu H, Zhang Y, Liu Y, Luo B, Xin N, Shi W. MOFs-derived Co_9S_8-embedded graphene/hollow carbon spheres film with macroporous frameworks for hybrid supercapacitors with superior volumetric energy density. J Mater Chem A 2019;7(14):8503−9.

[23] Duan J, Chen S, Zhao C. Ultrathin metal-organic framework array for efficient electrocatalytic water splitting. Nat Commun 2017;8(1):1–7.
[24] Jin J, Zheng Y, Huang SZ, Sun PP, Srikanth N, Kong LB, et al. Directly anchoring 2D NiCo metal–organic frameworks on few-layer black phosphorus for advanced lithium-ion batteries. J Mater Chem A 2019;7(2):783–90.
[25] Jian SL, Hsiao LY, Yeh MH, Ho KC. Designing a carbon nanotubes-interconnected ZIF-derived cobalt sulfide hybrid nanocage for supercapacitors. J Mater Chem A 2019;7(4):1479–90.
[26] Li YL, Zhou JJ, Wu MK, Chen C, Tao K, Yi FY, et al. Hierarchical two-dimensional conductive metal–organic framework/layered double hydroxide nanoarray for a high-performance supercapacitor. Inorg Chem 2018;57(11):6202–5.
[27] Liu B, Shioyama H, Jiang H, Zhang X, Xu Q. Metal–organic framework (MOF) as a template for syntheses of nanoporous carbons as electrode materials for supercapacitor. Carbon. 2010;48(2):456–63.
[28] Chaikittisilp W, Hu M, Wang H, Huang HS, Fujita T, Wu KC, et al. Nanoporous carbons through direct carbonization of a zeolitic imidazolate framework for supercapacitor electrodes. Chem Commun 2012;48(58):7259–61.
[29] Jiang HL, Liu B, Lan YQ, Kuratani K, Akita T, Shioyama H, et al. From metal–organic framework to nanoporous carbon: toward a very high surface area and hydrogen uptake. J Am Chem Soc 2011;133(31):11854–7.
[30] Furukawa H, Cordova KE, O'Keeffe M, Yaghi OM. The chemistry and applications of metal-organic frameworks. Science. 2013;341(6149):1230444.
[31] Li B, Wen HM, Cui Y, Zhou W, Qian G, Chen B. Emerging multifunctional metal–organic framework materials. Adv Mater 2016;28(40):8819–60.
[32] Zhang Z, Chen Y, Xu X, Zhang J, Xiang G, He W, et al. Well-defined metal–organic framework hollow nanocages. Angew Chem Int Ed 2014;53(2):429–33.
[33] Zhu QL, Xu Q. Metal–organic framework composites. Chem Soc Rev 2014;43(16):5468–512.
[34] Sun JK, Xu Q. Functional materials derived from open framework templates/precursors: synthesis and applications. Energy Environ Sci 2014;7(7):2071–100.
[35] Xia W, Mahmood A, Zou R, Xu Q. Metal-organic frameworks and their derived nanostructures for electrochemical energy storage and conversion. Energy Environ Sci 2015;8(7):1837–66.
[36] Ramaswamy P, Wong NE, Shimizu GK. MOFs as proton conductors-challenges and opportunities. Chem Soc Rev 2014;43(16):5913–32.
[37] Liu B, Shioyama H, Akita T, Xu Q. Metal-organic framework as a template for porous carbon synthesis. J Am Chem Soc 2008;130(16):5390–1.
[38] Hu J, Wang H, Gao Q, Guo H. Porous carbons prepared by using metal–organic framework as the precursor for supercapacitors. Carbon. 2010;48(12):3599–606.
[39] Dekrafft KE, Wang C, Lin W. Metal-organic framework templated synthesis of Fe_2O_3/TiO_2 nanocomposite for hydrogen production. Adv Mater 2012;24(15):2014–18.
[40] Xia BY, Yan Y, Li N, Wu HB, Lou XW, Wang X. A metal–organic framework-derived bifunctional oxygen electrocatalyst. Nat Energy 2016;1(1):1–8.
[41] Saraf M, Rajak R, Mobin SM. MOF derived high surface area enabled porous Co_3O_4 nanoparticles for supercapacitors. ChemistrySelect 2019;4(27):8142–9.
[42] Yu Z, Zhang X, Wei L, Guo X. MOF-derived porous hollow α-Fe_2O_3 microboxes modified by silver nanoclusters for enhanced pseudocapacitive storage. Appl Surf Sci 2019;463:616–25.

[43] Li S, Duan Y, Teng Y, Fan N, Huo Y. MOF-derived tremelliform Co_3O_4/NiO/Mn_2O_3 with excellent capacitive performance. Appl Surf Sci 2019;478:247−54.
[44] Yang Y, Yang F, Hu H, Lee S, Wang Y, Zhao H, et al. Dilute NiO/carbon nanofiber composites derived from metal organic framework fibers as electrode materials for supercapacitors. Chem Eng J 2017;307:583−92.
[45] Ding Y, Peng Y, Chen S, Li Z, Zhang X, Falaras P, et al. A competitive coordination strategy to synthesize Co_3O_4@carbon flower-like structures for high-performance asymmetric supercapacitors. Appl Surf Sci 2019;495:143502.
[46] Guan C, Zhao W, Hu Y, Lai Z, Li X, Sun S, et al. Cobalt oxide and N-doped carbon nanosheets derived from a single two-dimensional metal-organic framework precursor and their application in flexible asymmetric supercapacitors. Nanoscale Horiz 2017;2(2):99−105.
[47] Han X, Liu S, Shi L, Li S, Li Y, Wang Y, et al. ZIF-derived wrinkled Co_3O_4 polyhedra supported on 3D macroporous carbon sponge for supercapacitor electrode. Ceram Int 2019;45(12):14634−41.
[48] Saleki F, Mohammadi A, Moosavifard SE, Hafizi A, Rahimpour MR. MOF assistance synthesis of nanoporous double-shelled $CuCo_2O_4$ hollow spheres for hybrid supercapacitors. J Colloid Interface Sci 2019;556:83−91.
[49] Li Q, Zhou J, Zhao S, Li Y, Chen C, Tao K, et al. Hollow and hierarchical cobalt−metal organic framework@$CoCr_2O_4$ microplate array as a battery-type electrode for high-performance hybrid supercapacitors. ChemElectroChem 2020;7(2):437−44.
[50] Jia H, Wang Z, Zheng X, Cai Y, Lin J, Liang H, et al. Controlled synthesis of MOF-derived quadruple-shelled CoS_2 hollow dodecahedrons as enhanced electrodes for supercapacitors. Electrochim Acta 2019;312:54−61.
[51] Chen J, Zhang L, Bai W, Zhou Y, Li C, Guo T, et al. Unique hollow-concave $CoMoS_x$ boxes with abundant mesoporous structure for high-performance hybrid supercapacitors. Electrochim Acta 2020;337:135824.
[52] Jia H, Wang J, Fu W, Hu J, Liu Y. In-situ MOFs-derived hollow Co_9S_8 polyhedron welding on the top of $MnCo_2S_4$ nanoneedles for high performance hybrid supercapacitors. Chem Eng J 2019;391:123541.
[53] Wang X, Huang F, Rong F, He P, Que R. Unique MOF-derived hierarchical MnO_2 nanotubes@NiCo-LDH/CoS_2 nanocage materials as high performance supercapacitors. J Mater Chem A 2019;7(19):12018−28.
[54] Yang Q, Liu Y, Deng C, Yan M, Shi W. MOF-derived 3D hierarchical nanoarrays consisting of NiCoZn-S nanosheets coupled with granular $NiCo_2S_4$ nanowires for high-performance hybrid supercapacitors. J Mater Chem A 2019;7(45):26131−8.
[55] Cao XM, Sun ZJ, Zhao SY, Wang B, Han ZB. MOF-derived sponge-like hierarchical porous carbon for flexible all-solid-state supercapacitors. Mater Chem Front 2018;2(9):1692−9.
[56] Yi H, Wang H, Jing Y, Peng T, Wang X. Asymmetric supercapacitors based on carbon nanotubes@NiO ultrathin nanosheets core-shell composites and MOF-derived porous carbon polyhedrons with super-long cycle life. J Power Sources 2015;285:281−90.
[57] Javed MS, Shah HU, Shaheen N, Lin R, Qiu M, Xie J, et al. High energy density hybrid supercapacitor based on 3D mesoporous cuboidal Mn2O3 and MOF-derived porous carbon polyhedrons. Electrochim Acta 2018;282:1−9.
[58] Liu Y, Wang Y, Chen Y, Wang C, Guo L. NiCo-MOF nanosheets wrapping polypyrrole nanotubes for high-performance supercapacitors. Appl Surf Sci 2020;507:145089.

Index

Note: Page numbers followed by "*f*" and "*t*" refer to figures and tables, respectively.

C

D

E

F

G

N

O

P

Q

R

S

T

U

V

W

X

Y

Z

Metal-Organic Frameworks for Chemical Reactions

From Organic Transformations to Energy Applications

Features the latest information on metal-organic frameworks materials and covers recent technology in the fields of manufacturing and design

Metal-Organic Frameworks for Chemical Reactions: From Organic Transformations to Energy Applications covers different aspects of reactions from energy storage and catalysts, including preparation, design, and characterization techniques of metal-organic frameworks (MOFs) materials and applications. Due to their exceptional physical and chemical properties, metal-organic frameworks—which are nanoporous polymers made up of inorganic metal focuses connected by natural ligands—are useful in many different fields, including medicine, energy, and the environment. Choosing an appropriate synthetic technique that produces a product with homogenous morphology, small size dispersion, and high thermal stability is critical since combination conditions strongly affect the properties of these compounds.

This comprehensive resource is ideal for researchers and advanced students studying metal-organic frameworks in academia and industry.

Key Features:

- Covers the synthetic advantages and versatile applications of MOFs due to their organic-inorganic hybrid nature and unique porous structure
- Includes energy applications such as batteries, fuel storage, fuel cells, hydrogen evaluation reactions, and super capacitors
- Features information on using MOFs as replacements for conventional engineering materials as they are lightweight, lower cost, environmentally friendly, and sustainable

About the Editors

Anish Khan, Center of Excellence for Advanced Materials Research, King Abdulaziz University, Jeddah, Saudi Arabia

Francis Verpoort, State Key Laboratory of Advanced Technology for Materials Synthesis and Processing, Wuhan University of Technology, Wuhan, China
Ghent University - Global Campus, Yeonsu-Gu, Incheon, Republic of Korea

Abdullah M. Asiri, Chemistry Department, Faculty of Science, King Abdulaziz University, Jeddah, Saudi Arabia
Center of Excellence for Advanced Materials Research, King Abdulaziz University, Jeddah, Saudi Arabia

Md Enamul Hoque, Department of Biomedical Engineering at the Military Institute of Science and Technology (MIST), Dhaka, Bangladesh

Anwar L. Bilgrami, Department of Entomology, Rutgers University, New Jersey, USA
Deanship of Scientific Research, King Abdulaziz University, Jeddah, Saudi Arabia

Mohammad Azam, Associate Professor of Chemistry, King Saud University, Riyadh, Saudi Arabia

K. Chandra Babu Naidu, GITAM School of Science (GSS), GITAM Deemed-to-Be University, Bangalore, India

ISBN 978-0-12-822099-3

9 780128 220993

ELSEVIER elsevier.com/books-and-journals